Using metamorphic modelling techniques to investigate the thermal and structural evolution of the Himalayan-Karakoram-Tibetan orogen

by

Richard Mark Palin

Submitted for the degree of Doctor of Philosophy

at the Department of Earth Sciences, University of Oxford

July 2013

Supervised by M.P. Searle and D.J. Waters

UNIVERSITY OF OXFORD

DATE: 12 July 2013

AUTHOR: Richard Mark Palin

TITLE: Using metamorphic modelling techniques to investigate the thermal and structural evolution of the Himalayan-Karakoram-Tibetan orogen

DEPARTMENT: Earth Sciences

COLLEGE: Worcester

DEGREE: Doctor of Philosophy

SUPERVISORS: M.P. Searle and D.J. Waters

Permission is granted to University of Oxford to distribute and to have copied for non-commercial purposes, at its discretion, the above title on the request of individuals or institutions. The author reserves all other publication rights, and confirms that any copyrighted material appearing in the thesis has been properly and clearly acknowledged.

Although the work presented in this thesis has benefitted from discussion with supervisors, publication co-authors and suggested corrections as a result of the peer-review process, it remains solely the result of my own labour. This includes all data acquisition, analysis and interpretation, unless explicitly stated otherwise.

Signature of author

“Rocks are records of events that took place at the time they formed.

They are books. They have a different vocabulary, a different alphabet,

but you learn how to read them.” – John McPhee

Acknowledgements

I am truly indebted to both Mike Searle and Dave Waters for setting up this project and therefore allowing me to continue my academic career at Oxford. Mike was in constant contact during my year away in Australia and was relentless in encouraging me to give research another try. For that I am extremely grateful, as it was definitely the right decision. They were both incredibly supportive throughout my entire postgrad years and I could not have had two better supervisors at Oxford. Both Randy Parrish and Matt Horstwood at NIGL were incredibly helpful (and patient) in teaching me how to obtain an age for a rock. They are both world experts in the field of geochronology and I consider myself extremely lucky to have studied under them. Nick Roberts also taught me a lot about the acquisition and interpretation of geochronological data during my second stint at NIGL. He was vital in making the trip a success and helped me get some great data out of the Tibet and RRSZ projects. Marc St-Onge was also an invaluable source of discussion and inspiration, and I am extremely grateful for his advice and support in the field both in Assynt and during our ill-fated fieldwork in Tibet. Once again, I consider myself exceptionally lucky to call him a colleague.

I received the majority of my financial support for my research from NERC but also benefitted from occasional grants off the Earth Sciences Department (through the Burdett Coutts fund), the Metamorphic Studies Group of the Geological Society of London, and NIGL, who provided extra funding that allowed me to complete geochronological work at BGS Keyworth. I thank all of these institutions for making my work a possibility and I must also acknowledge the technical assistance provided by the department in various areas. Jeremy Hyde was invaluable in the preparation of thin sections and was always happy to speed the occasional job along when asked. He worked tirelessly and efficiently despite having many other students also begging for his time! Norman Charnley was also instrumental in teaching me how to use the SEM and, perhaps more importantly, how to fix it when it broke down.

Throughout my time as a postgrad, I have been extremely lucky to have worked closely with many of the undergrad MESc students in the petrology group. In particular, I would like to thank Jonathan, Sarah, Jamie, Andrew, Jack, Will, Paul, Tom, Robbie, Alan and Chris for allowing me to share ideas and have extremely useful and stimulating conversations regarding both my work and theirs. My fellow postgrads Owen Weller and Al White were a constant source of critical discussion

and many enjoyable cumulative hours under the microscope. With all of us being fairly competitive in nature, I'm sure that we inadvertently improved the quality of each other's work in an attempt to out-do each other! Although I only had the chance to swap ideas with Brendan for a short time whilst I was finishing off, I sincerely hope that we can work together in the future. The fortnightly 'Hard Rock Group' lunches were also immensely enjoyable, as well as useful, and I will miss them a lot. Finally I would like to thank Mum, Dad, Martin and Stella for their continued support and of course Liz, my incredibly patient wife, who put up with plenty of geological conversations and long nights of work, especially during my final year. This entire work is dedicated to her.

I would like to end my acknowledgements by sharing the most important piece of advice that I was given during my study at Oxford, whilst completing my MESc undergrad project. At first I was worried that it was a subtle message for me to work more independently, but I later realised that it was actually an insight that could only have been delivered from a lifelong petrologist who had the deepest understanding of the way that rocks, and science, works:

"If you have a question, go and ask the rock…" – Dr. Dave Waters

Using metamorphic modelling techniques to investigate the thermal and structural evolution of the Himalayan-Karakoram-Tibetan orogeny

Richard Mark Palin, Department of Earth Sciences, Worecster College, University of Oxford, Trinity Term 2013

Abstract

Metamorphic rocks constitute a vast volumetric proportion of the Earth's continental lithosphere and are invaluable recorders of the mechanisms and rates of deformation and metamorphism that occur at the micro-, meso- and macro-scale. As such, they have the potential to provide detailed insight into important tectonic processes such as the subductive transport of material into, and back from, mantle depths and also folding, faulting and thickening of crust that occurs during collisional orogeny. The Himalayan-Karakoram-Tibetan orogen is the youngest and most prominent example of a continent-continent collisional mountain belt on Earth today and is a product of the on-going convergence of the Indian and Asian plates that initiated in the Early Eocene. Thus, it provides an exceptional natural laboratory for the investigation of such processes. Recent advances in the computational ability to replicate natural mineral assemblages through a variety of metamorphic modelling techniques have led to improvements in the amount (and quality) of petrographic data that may be obtained from a typical metamorphic rock. In this study, phase equilibria modelling (pseudosection construction) using THERMOCALC, amongst other techniques, has been integrated with *in-situ* U–Pb and Th–Pb geochronology of accessory monazite in order to constrain the tectonothermal evolution of four regions intimately associated with the Himalayan-Karakoram-Tibetan orogen. These regions comprise the Karakoram metamorphic complex (north Pakistan), the Tso Morari massif (north-west India), the eastern Himalayan syntaxis (south-east Tibet) and the Day Nui Con Voi metamorphic core complex of the Red River shear zone (North Vietnam). Each case study documents previously unreported metamorphic, magmatic or deformational events that are associated with the India-Asia collision. These data have allowed original interpretations to be made regarding the tectonic evolution of each individual region as well as the large-scale evolution of the Himalayan-Karakoram-Tibetan orogenic system as a whole.

Extended abstract

Investigating the driving mechanisms and rates of plate tectonic processes is an essential step in understanding how the Earth's continental lithosphere has evolved over geological time, and how it will continue to change in the future. Metamorphic rocks offer the best chance to investigate these processes, as they often undergo sequential mineralogical or textural changes during deformation and metamorphism. Thus, within the crust there exist a range of metamorphic lithologies that formed at different times (t), that have equilibrated at different pressure (P) and temperature (T) conditions and that are associated with different tectonic events. If these units are subsequently exhumed to the surface, they can provide valuable insight into the tectonothermal history of a particular area. These results are often extrapolated to provide constraints on the larger-scale evolution of a region, such as an orogenic belt. Petrological and thermobarometric analysis of such metamorphic rocks can provide absolute P–T conditions that were reached during different stages of their evolution. When these data are combined with age constraints obtained through geochronology, the timing and rates of the processes responsible can also be calculated.

There is abundant geological evidence showing that continent-continent collisional orogeny has occurred throughout a large proportion of Earth history (e.g. Brown, 2007, 2009), the youngest such example being the Himalayan-Karakoram-Tibetan orogen, which was initiated at c. 50 Ma (Green *et al*., 2008) and formed as a result of the collision of India with Asia. Parts of the orogen are readily accessible, contain extensive exposures of exhumed deep-crustal lithologies and are still deforming today. As such, it provides a perfect natural laboratory for the investigation of plate tectonic processes and is the case study for this thesis.

Four regions associated with the Himalayan-Karakoram-Tibetan orogen have been the subject of integrated petrographic, thermobarometric and geochronological investigation using a variety of techniques, including phase diagram (pseudosection) construction using THERMOCALC, in order to produce new data that describe their local metamorphic and structural evolution. These data have also provided insight into the regional-scale processes that affect the evolution of the orogen as a whole. Regions containing high-grade rocks belonging to the southern Asian margin (the Karakoram metamorphic complex, north Pakistan, and the eastern Himalayan syntaxis, south-east Tibet) have provided understanding of the processes that operated prior to, during, and after initial collision with

the Indian indenter. Mafic eclogite from the Tso Morari massif (north-west India) has provided information describing the geodynamic evolution of subducted crustal material immediately preceding closure of the Neo-Tethys Ocean during the Early Eocene. Finally, an investigation of magmatic and metamorphic units of the Day Nui Con Voi massif (North Vietnam) situated in the Red River shear zone that separates the Indochina and South China blocks of south-east Asia has provided insight into the timing of metamorphism and crustal melting and the continental extrusion hypothesis. The results of these studies are summarised below.

Petrographic analysis of peraluminous metapelites from two separate regions of the Karakoram metamorphic complex (chapter 4) has produced new insights into the *P–T–t* evolution of the deep crust along the south Asian margin before and after the India-Asia collision. Conventional thermobarometry and *P–T* pseudosection construction in the MnO–Na_2O–CaO–K_2O–FeO–MgO–Al_2O_3–SiO_2–H_2O–TiO_2–O system have provided prograde and peak metamorphic conditions and *in-situ* U–Pb geochronology of metamorphic monazite has provided age constraints. Two new events in the tectonothermal evolution of the Hunza Valley have been documented within a single sample that exhibits a long and complex metamorphic history. Firstly, an andalusite-grade contact metamorphic event at unknown *P–T* conditions has been dated at 105.5 ± 0.8 Ma and is interpreted to be linked to widespread subduction-related granite magmatism caused by the Late Cretaceous closure of the Shyok suture and accretion of the Kohistan-Ladakh island arc to the southern margin of Asia. A separate episode of kyanite-grade metamorphism at 28.2 ± 0.8 Ma overprints an earlier sillimanite-grade assemblage in the same sample, the former having peak *P–T* conditions of ~7.8 kbar and 645 °C and is interpreted to be associated with the on-going India-Asia collision. A kyanite-grade event documented in the Baltoro region with similar peak *P–T* conditions of ~7.4–8.0 kbar and ~640–660 °C is interpreted to have occurred sometime after 21.8 ± 0.6 Ma. A calculated prograde *P–T* path for this kyanite-grade event indicates that garnet nucleated on an initial geothermal gradient of ~30 °C/km and grew during a significant increase in pressure of ~2.6 kbar and a temperature increase of ~100 °C. This initially high geotherm is interpreted to represent evidence for conductive heating of the middle crust during early stages of intrusion of components of the Baltoro Plutonic Unit of the Karakoram batholith, which has emplacement ages ranging between c. 25–13 Ma (Schärer *et al.*, 1990; Parrish & Tirrul, 1989; Searle *et al.*, 2010a). The subsequent increase in pressure is attributed

to either lateral migration of these early intrusive components (‘magmatic over-accretion’) or to be the result of continued crustal thickening and burial associated with the India-Asia collision.

Analysis of mafic eclogite from the Tso Morari massif (chapter 5) has provided new insight into the tectonothermal evolution of the leading edge of the Indian continental margin during subduction associated with the closure of the Neo-Tethys Ocean. Subsets of various mineral inclusions in poikiloblastic garnet core domains that lack significant compositional zoning are interpreted to represent an early prograde assemblage that formed during initial subduction, although the absolute *P*–*T* conditions of this event (M0) are uncertain. Strong compositional zoning and a variety of inclusions in garnet rim domains have allowed investigation of the latter stages of the prograde-to-peak metamorphic history of the eclogite. *P*–*T* pseudosections constructed in the Na_2O–CaO–K_2O–FeO–MgO–Al_2O_3–SiO_2–H_2O–TiO_2–O system suggest initial garnet rim growth at ~22.5 kbar and ~525 °C (M1) followed by prograde metamorphism associated with on-going subduction allowing inclusion of omphacite, paragonite, epidote/allanite, rutile, talc, calcite and quartz grains. Peak metamorphism (M2) is calculated to have occurred at 25.5–27.5 kbar and 630–645 °C, equivalent to a depth of subduction of ~90–100 km, with the variation in *P*–*T* conditions depending on whether the fractionation of cations into garnet is considered during thermodynamic modelling. This range in calculated peak M2 conditions is independently verified by THERMOCALC AvePT and conventional thermobarometry applied to a microstructurally-constrained peak paragenesis comprising garnet, omphacite, phengite, lawsonite, talc, epidote/allanite, rutile and quartz.

Compositionally zoned matrix amphibole containing barroisite/winchite cores and magnesiohornblende rims is interpreted to have formed as a result of hydration of this peak assemblage during exhumation to lower pressure M3 conditions. *P*–M(H_2O) pseudosection modelling of the effects of variable fluid content during exhumation show that it is possible to reproduce the observed amphibole compositions and proportions via the addition of H_2O, which is interpreted from field observations to have been derived from an external source, most likely the host metasediments and orthogneisses. An additional result of exhumation is the formation of symplectite colonies along matrix omphacite grain boundaries. Such colonies are composed of intergrown calcic-amphibole, diopside and plagioclase and are calculated to have formed at *P*–*T* conditions of 10.3–13.9 kbar and 461–554 °C with an apparent trend from low-pressure eclogite-

facies, through epidote-amphibolite-facies into blueschist-facies. Evidence for the retrograde breakdown of lawsonite during exhumation is given by the formation of porphyroblasts of clinozoisite and paragonite in the rock matrix and epidote-paragonite pseudomorphs within garnet rims. These data, which document stages in the prograde, peak, and retrograde evolution of the Tso Morari massif, demonstrate remarkable similarity to the documented evolution of the Kaghan eclogitic massif, Pakistan, suggesting a laterally continuous subduction-exhumation event along the leading edge of the Indian plate.

A combined petrological and geochronological study of pelitic lithologies from the north-west flank of the eastern Himalayan syntaxis (chapter 6) has documented previously unreported metamorphic events in the history of the south Lhasa block (Asian margin). U(–Th)–Pb *in-situ* dating of monazite suggests that fluid-absent sillimanite-grade leucosomes formed episodically between c. 71–50 Ma at *P–T* conditions greater than 6.3 ± 1.2 kbar and 750 ± 30 °C, whereas a separate episode of fluid-fluxed partial melting at kyanite-grade conditions occurred between c. 44–33 Ma at *P–T* conditions of 10.4 ± 1.0 kbar and 698 ± 20 °C. A staurolite-grade metapelite, that was subsequently mylonitised, experienced peak metamorphism at 23.6 ± 0.3 Ma at a maximum temperature of 650 °C at mid-crustal pressures. This event is interpreted to represent an additional and separate prograde metamorphic episode within the south Lhasa block, although the provenance of the protolith is uncertain. A major ductile shear zone separates these rocks from the Indian plate Namche Barwa Group units in the core of the syntaxis. Mylonitised metapelites now exposed in this shear zone record monazite ages between c. 16–11 Ma and c. 9.5–8.0 Ma that are interpreted to date the timing of shearing along the bounding Milin-Yanggudajue-Lulang-Parlung fault. Together, these data are interpreted to document an early (pre-collision) Lhasa block sillimanite-grade melting event that is most likely related to conductive heat transfer to the middle crust caused by emplacement of units of the Gangdese batholith, which was followed by a higher pressure-lower temperature kyanite-grade melting event associated with burial and crustal thickening during the on-going India-Asia collision. A comparison of the post-collisional *P–T–t* evolution of the eastern Himalayan syntaxis and south Lhasa block suggests the possibility that both regions may have acted as a paired metamorphic belt since ~44 Ma.

Various lithologies from the Day Nui Con Voi massif, the southernmost of four ductiley-deformed metamorphic core complexes situated along the Red River shear zone in south-east Asia, have provided new constraints on the tectonic and metamorphic evolution of this region prior to and following the initial India-Asia collision (chapter 7). Analysis of a weakly deformed anatectic paragneiss using *P–T* pseudosections constructed in the $MnO–Na_2O–CaO–K_2O–FeO–MgO–Al_2O_3–SiO_2–H_2O–TiO_2–O$ system has provided prograde, peak and retrograde metamorphic conditions and *in-situ* U–Th–Pb geochronology of metamorphic monazite has provided texturally controlled age constraints. Tertiary metamorphism and deformation, overprinting earlier Triassic metamorphism associated with the Indosinian orogeny, is characterised by peak metamorphic conditions of ~8.5 kbar and ~805 °C between c. 38–34 Ma. Exhumation from peak conditions occurred along a steep retrograde *P–T* path with final melt crystallising at the solidus at a pressure greater than ~5.5 kbar at ~790 °C. Further exhumation through *P–T* conditions of 4–5 kbar and 640–700 °C occurred in the subsolidus environment at c. 31 Ma. U–Pb geochronological analysis of monazite from a strongly deformed pre-kinematic granite dyke from the flank of the Day Nui Con Voi antiformal complex provides further evidence for exhumation at this time. Magmatic grains suggest initial emplacement at 66.0 ± 1.0 Ma, prior to the India-Asia collision, whereas grains with metamorphic characteristics indicate later deformation at 30.6 ± 0.4 Ma. Monazite grains from a cross-cutting post-kinematic dyke in the core of the antiform provide a minimum age constraint of 25.2 ± 1.4 Ma for the termination of fabric development. The cause of these high-grade Tertiary events is uncertain, but they are deemed likely to be be related to continued deformation during the evolution of the Himalayan-Karakoram-Tibetan orogeny, although these data are not supportive of the continental extrusion hypothesis. A disparate and significant episode of monazite growth at c. 83–69 Ma is suggested to be the result of fluid-assisted recrystallisation following the emplacement of magmatic units, although the cause of pre-collisional magmatic activity in this region is unidentified.

Table of contents

Acknowledgements 1

Abstract 3

Extended abstract 4

Table of contents 9

List of figures 14

List of tables 17

List of abbreviations 19

1. Introduction 20

1.1. A statement of the problem 20

1.2. Objectives, aims and motivation 21

1.3. Thesis structure 22

1.4. Geological setting of the HKTO 23

1.4.1. The Himalayan Range 24

1.4.2. The Tibetan plateau 26

1.4.3. The Karakoram Range 28

1.4.4. Red River shear zone 29

1.5. Metamorphic-magmatic evolution of the HKTO 31

1.5.1. The Greater Himalayan Sequence 31

1.5.2. The Lhasa block 32

1.5.3. The Karakoram metamorphic complex 34

1.5.4. Red River shear zone 35

2. Metamorphic petrology 37

2.1. Introduction 37

2.2. Thermodynamic principles 38

2.3. Thermobarometry 40

2.3.1. Conventional thermobarometry 41

2.3.2. Phase equilibria modelling 46

2.3.3. Limitations and uncertainties 48

2.4. Pseudosection construction and analysis 50

2.4.1. Model systems and activity-composition models 50
2.4.2. Bulk composition calculation 52
2.4.3. SEM-microprobe analysis methodology and analytical conditions 53
3. U–Th–Pb geochronology 55
3.1. The principles of radioactive decay 55
3.2. U–Th–Pb systematics 56
3.3. Uncertainty on calculated ages and the interpretation of U–Pb data 58
3.4. Monazite geochronology 60
3.4.1. The occurrence of monazite in metasedimentary rocks 61
3.4.2. Monazite chemistry 64
3.5. Work performed at the NERC Isotope Geosciences Laboratory 65
3.5.1. Analytical techniques, methodology and operating conditions 66
3.5.2. Data interpretation 67
4. Karakoram metamorphic complex 69
4.1. Chapter introduction 69
4.2. Geological setting 69
4.2.1. The Hunza Valley 70
4.2.2. The Baltoro region 72
4.3. Petrography and mineral chemistry 74
4.3.1. The Hunza Valley 74
4.3.2. The Baltoro region 76
4.4. Textural and compositional interpretation 80
4.4.1. The Hunza Valley 80
4.4.2. The Baltoro region 82
4.5. U–Pb monazite geochronology 83
4.5.1. Monazite chemistry and U–Pb ages 83
4.5.2. Interpretation 87
4.6. Thermobarometry and phase diagram modelling 90
4.6.1. AvePT and conventional thermobarometry 90
4.6.2. Pseudosection modelling 92

4.7. Summary and discussion 101
4.7.1. Tectonic implications for the Hunza Valley 101
4.7.2. Tectonic implications for the Baltoro region 103
4.7.3. Correlation along the Karakoram Range 105
5. Tso Morari massif 108
5.1. Chapter introduction 108
5.2. Geological setting and tectonothermal history 108
5.3. Petrography and mineral chemistry 112
5.4. Textural and compositional interpretation 118
5.5. Thermobarometry and phase diagram modelling 121
5.5.1. Early (pre-M1) metamorphism 123
5.5.2. M1 prograde metamorphism 127
5.5.3. M2 peak metamorphism 130
5.5.4. M3 conditions of exhumation 135
5.6. Summary and discussion 148
5.6.1. Modelling discrepancies 148
5.6.2. Tectonic-petrographic synthesis 152
6. Eastern Himalayan syntaxis 155
6.1. Chapter introduction 155
6.2. Geological setting 155
6.2.1. Metamorphic evolution of the EHS 158
6.2.2. Comparison of the Namche Barwa Group with the GHS and Nanga Parbat 161
6.3. Petrography, mineral chemistry and tectonic setting 162
6.3.1. Plutonic units 163
6.3.2. Ophiolitic fragments 168
6.3.3. Upper amphibolite-facies migmatites 170
6.3.4. Mylonites 178
6.4. Textural and compositional interpretation 185
6.4.1. Upper amphibolite-facies migmatites 185
6.4.2. Mylonites 188

6.5. U–Th–Pb monazite geochronology 189
6.5.1. Monazite chemistry and U–Pb ages 189
6.5.2. Interpretation of monazite geochronology 198
6.6. Thermobarometry of metamorphic units 200
6.6.1. Sillimanite-grade migmatisation 201
6.6.2. Kyanite-grade migmatisation 202
6.6.3. Mylonitisation of metapelites and prior prograde metamorphism 203
6.7. Summary and discussion 205
6.7.1. Partial melting in the B-L-M gneisses 205
6.7.2. Mylonite formation along the MYLP fault 209
7. Red River shear zone 211
7.1. Chapter introduction 211
7.2. Geological setting 211
7.2.1. Geochronology 213
7.2.2. Thermobarometry 214
7.3. Petrography and mineral chemistry 214
7.3.1. DNCV01 215
7.3.2. DNCV02 218
7.3.3. DNCV09 218
7.3.4. DNCV10 218
7.4. Thermobarometry and pseudosection modelling 219
7.4.1. Bulk composition calculation and pseudosection construction 219
7.4.2. Pseudosections for measured bulk composition (suprasolidus *P*–*T* evolution) 220
7.4.3. Melt-reintegration (inferred prograde *P*–*T* evolution) 223
7.4.4. *P*–*T* conditions of retrograde metamorphism 227
7.5. U–Th–Pb monazite geochronology 228
7.5.1. Analytical techniques 229
7.5.2. Monazite chemistry and U–Th–Pb ages 229
7.5.3. LA–MC–ICP–MS separated grain U–Pb ages 230
7.5.4. LA–SC–ICP–MS *in-situ* U–Th–Pb ages 234

7.5.5. Interpretation of monazite geochronology 239
7.6. Summary and discussion 240
7.6.1. Timing and *P*–*T* conditions of metamorphism and partial melting 240
7.6.2. Late Cretaceous monazite ages 242
8. Conclusions and discussion 245
8.1. Regional studies 245
8.1.1. Deep subduction of the leading edge of the Indian plate 245
8.1.2. Metamorphism and magmatism along the southern Asian margin 248
8.1.3. Lithospheric-scale strike-slip faults and the continental extrusion hypothesis 258
8.2. Implications for pseudosection modelling 260
8.3. On the application of different thermobarometric techniques to different lithologies 263
8.4. Future work 265
9. Reference list 267
10. Additional information 304
10.1. Conference proceedings 304
10.2. Peer-reviewed work 305
10.2.1. Palin *et al*. (2012) – The Karakoram metamorphic complex 305
10.2.2. Palin *et al*. (2013) – The Day Nui Con Voi metamorphic massif 305
10.2.3. Palin *et al*. (in press) – The eastern Himalayan syntaxis 305
10.2.4. St-Onge *et al*. (2013) – The Tso Morari massif 306
10.3. A historical account of the methods used for metamorphic petrology 306
11. Appendices 309
11.1. Description of external contributions 309
11.2. U–(Th–)Pb isotopic data for MC–ICP–MS and SC–ICP–MS analyses 310
11.3. Mass spectrometer technical specifications and operating conditions 317
11.4. ID-TIMS data for Stern, Moacyr and Manangotry monazite materials 318
11.5. THERMOCALC AvePT calculation end-member activities 319
11.6. Phase compositions and proportions used in bulk composition calculations 320

List of figures

Fig. 1.1 – Compound satellite imagery of the HKTO and environs 24

Fig. 1.2 – Generalised geology of the Himalayan Range 25

Fig. 1.3 – Cross-section through the central Himalaya-central Tibet 27

Fig. 1.4 – Schematic geological map of north Pakistan 28

Fig. 1.5 – Cross-section through the western Himalaya-Karakoram Range-western Tibet 29

Fig. 1.6 – Tectonic map of south-east Asia 30

Fig. 2.1 – Distribution coefficient and equilibrium constant contouring of *P*–*T* space 43

Fig. 2.2 – Example *P*–*T* projection 47

Fig. 2.3 – Example *P*–*T* and *T*–*X* pseudosection 48

Fig. 2.4 – Example SEM BSE contrast image used for modal proportion calculations 53

Fig. 3.1 – Schematic representation of the ^{238}U, ^{235}U and ^{232}Th decay schemes 57

Fig. 3.2 – Idealised plots for the interpretation of U–Pb data 59

Fig. 3.3 – Temperature and bulk rock CaO/Na_2O controls on monazite and allanite stability 62

Fig. 3.4 – Phase diagrams showing the relative stability fields of allanite and monazite 64

Fig. 4.1 – Geological map of the Hunza Valley and associated cross-section 71

Fig. 4.2 – Geological map of the Baltoro region and associated cross-section 73

Fig. 4.3 – Petrography of sample 20-199 75

Fig. 4.4 – Petrography of samples K146 and T17 77

Fig. 4.5 – Garnet compositional profile for sample 20-199 81

Fig. 4.6 – Garnet compositional profiles for samples K146 and T17 82

Fig. 4.7 – Tera-Wasserburg plots for samples 20-199 and K146. 84

Fig. 4.8 – Compositional maps of monazite from samples 20-199 and K146 84

Fig. 4.9 – Petrographic positions of monazite inclusions in garnet in sample 20-199 88

Fig. 4.10 – Thermobarometric results for peak metamorphism in sample 20-199 91

Fig. 4.11 – Schematic illustration of the method used for cation fractionation 94

Fig. 4.12 – Pseudosection modelling results for sample T17 97

Fig. 4.13 – Tectonic implications for the Hunza Valley 102

Fig. 4.14 – Compound tectonothermal time chart for events within the KMC 107

Fig. 5.1 – Field relations for lithological units of the TMM 109

Fig. 5.2 – *P–T* estimates for units of the TMM 111
Fig. 5.3 – Petrography of sample L08-03A 112
Fig. 5.4 – Garnet compositional profile for sample L08-03A 114
Fig. 5.5 – Sample L08-03A amphibole compositional variation 115
Fig. 5.6 – IMA compositional classification of clinoamphibole 115
Fig. 5.7 – Interpreted petrographic evolution in sample L08-03A 121
Fig. 5.8 – *P–T* pseudosection for sample L08-03A 124
Fig. 5.9 – *P–T* pseudosections for sample L08-03A with garnet isolines 125
Fig. 5.10 – *P–T* pseudosection for sample L08-03A showing garnet core growth regions 126
Fig. 5.11 – *P–T* pseudosections for sample L08-03A not accounting for a changing EBC 128
Fig. 5.12 – *P–T* pseudosections for sample L08-03A accounting for a changing EBC 132
Fig. 5.13 – *P–T* pseudosection for sample L08-03A with isopleths of Si in phengite 133
Fig. 5.14 – Sample L08-03A conventional thermobarometry results for M2 metamorphism 134
Fig. 5.15 – Compositional plots for sample L08-03A matrix amphibole 138
Fig. 5.16 – *P*–M(H_2O) pseudosections with isolines for amphibole properties 138
Fig. 5.17 – SEM BSE image of matrix amphibole compositional zoning in sample L08-03A 140
Fig. 5.18 – *P*–M(H_2O) pseudosection interpretation 141
Fig. 5.19 – SEM BSE images of symplectite occurrence and morphology in sample L08-03A 143
Fig. 5.20 – Hbl-Pl geothermometer results for symplectite colonies 146
Fig. 5.21 – Geobarometric and combined *P–T* results of symplectite thermobarometry 148
Fig. 5.22 – Tectonic synthesis for sample L08-03A 153
Fig. 6.1 – Geological map and cross-section of the EHS with sample localities 156
Fig. 6.2 – *P–T* conditions for metamorphic events in the EHS region 159
Fig. 6.3 – Petrography of S-type samples and associated enclaves 164
Fig. 6.4 – Field relations for sample ET10-19 167
Fig. 6.5 – Petrography of sample ET10-19 168
Fig. 6.6 – Field relations and petrography of sample ET10-14 170
Fig. 6.7 – Petrography of migmatite samples 171
Fig. 6.8 – Compositional garnet line profiles for migmatite samples 172
Fig. 6.9 – Detailed petrography of sample ET10-12 175

Fig. 6.10 – Field relations for mylonite samples 179
Fig. 6.11 – Petrography of granitoid, metabasite and quartzo-feldspathic mylonites 181
Fig. 6.12 – Petrography of mylonitised metapelites 183
Fig. 6.13 – Compositional garnet line profiles for mylonitised metapelite samples 184
Fig. 6.14 – Activity diagram for selected sillimanite-grade minerals 187
Fig. 6.15 – Mn-partitioning between garnet and ilmenite in samples ET10-13 and ET10-18a 189
Fig. 6.16 – Tera-Wasserburg plots for samples from the B-L-M region 191
Fig. 6.17 – SEM BSE images of monazite for samples from the B-L-M region 193
Fig. 6.18 – Interpreted *P–T–t* syntheses for samples from the B-L-M region 206
Fig. 7.1 – Geological map of the DNCV and environs 212
Fig. 7.2 – Field photographs and thin section images of samples from the DNCV 217
Fig. 7.3 – Garnet compositional profile for sample DNCV01 217
Fig. 7.4 – *P–T* pseudosection for sample DNCV01 using the observed bulk composition 222
Fig. 7.5 – Gmin output for DNCV01 225
Fig. 7.6 – *P–T* pseudosection for sample DNCV01 using the MRBC 227
Fig. 7.7 – SEM BSE images of monazite in samples DNCV02, DNCV09 and DNCV10 230
Fig. 7.8 – Tera-Wasserburg plots for samples DNCV02, DNCV09 and DNCV10 231
Fig. 7.9 – SEM BSE images and petrographic positions of monazite in sample DNCV01 235
Fig. 7.10 – Tera-Wasserburg and Th–Pb box plots for sample DNCV01 236
Fig. 7.11 – *P–T* synthesis for the DNCV massif 241
Fig. 7.12 – Summary timechart for geochronological data obtained in this study 243
Fig. 8.1 – Comparison of *P–T* data between sample L08-03A and the Kaghan eclogitic massif 247
Fig. 8.2 – Comparative magmatic-metamorphic evolution timechart for selected regions 251
Fig. 8.3 – Map summary of geochronological data currently available for the B-L-M region 254
Fig. 8.4 – Paired metamorphic belts within the EHS? 255
Fig. 8.5 – Cartoon cross-sections of the India-Asia collision over since 70 Ma 256

List of tables

Table 3.1 – Properties of the main radioactive isotopes of U and Th 57

Table 4.1 – Age data and isotopic dating methods for magmatic units in the KMC 72

Table 4.2 – Mineral compositions for samples 20-199, K146 and T17 77

Table 4.3 – Monazite compositions from samples 20-199 and K146 86

Table 4.4 – MC–ICP–MS U–Pb ages for samples 20-199 and K146 87

Table 4.5 – THERMOCALC AvePT results for samples 20-199, K146 & T17 91

Table 4.6 – Changes in sample T17 EBC during fractionation 95

Table 4.7 – Changes in sample T17 phase proportion during prograde metamorphism 96

Table 4.8 – THERMOCALC composition parameters calculated at peak *P*–*T* conditions 100

Table 5.1 – Mineral compositions for sample L08-03A 116

Table 5.2 – Changes in sample L08-03A EBC during fractionation 129

Table 5.3 – Changes in sample L08-03A phase proportion during prograde metamorphism 130

Table 5.4 – THERMOCALC AvePT results for sample L08-03A M2 metamorphism 135

Table 5.5 – EBCs for sample L08-03A *P*–M(H_2O) pseudosections 136

Table 5.6 – Mineral compositions for all symplectite colonies used for thermobarometry 143

Table 5.7 – Hbl-Pl geothermometer results for symplectite colonies 145

Table 5.8 – End-member activities used for symplectite AveP calculations 147

Table 5.9 – AveP geobarometer results for symplectite colonies 147

Table 6.1 – Petrography, GPS co-ordinates and structural information for EHS samples 163

Table 6.2 – Mineral compositions for plutonic igneous samples and associated enclaves 166

Table 6.3 – Mineral compositions for ophiolitic sample ET10-14 170

Table 6.4 – Mineral compositions for sillimanite-grade migmatite samples 174

Table 6.5 – Mineral compositions for kyanite-grade migmatite samples 177

Table 6.6 – Mineral compositions for granitoid, metabasite and quartzo-feldspathic mylonite samples 180

Table 6.7 – Mineral compositions for mylonitised metapelite samples 182

Table 6.8 – MC–ICP–MS U–Pb ages for samples ET09-05 and ET09-06 190

Table 6.9 – SC–ICP–MS U–Th–Pb ages for samples ET10-07, ET10-09 and ET10-10 194

Table 6.10 – SC–ICP–MS U–Th–Pb ages for samples ET10-13, ET10-18a and ET09-02. 196

Table 6.11 – Monazite compositions for all analysed migmatite and mylonite samples 197

Table 6.12 – THERMOCALC AvePT results for samples from the B-L-M region.....202

Table 6.13 – Mineral compositions used for garnet-ilmenite thermometry.....204

Table 7.1 – *P–T* estimates for various stages in the evolution of the DNCV massif.....214

Table 7.2 – Mineral compositions for sample DNCV01.....216

Table 7.3 – Mineral compositions for strain shadow assemblages in DNCV01.....228

Table 7.4 – Monazite compositions from samples DNCV02, DNCV09 and DNCV10.....233

Table 7.5 – MC–ICP–MS U–Pb ages for samples DNCV02, DNCV09 and DNCV10.....233

Table 7.6 – Monazite compositions from sample DNCV01.....236

Table 7.7 – SC–ICP–MS U–Th–Pb ages for sample DNCV01.....238

Table 11.1 – MC–ICP–MS isotopic data for samples K146, 20-199, ET09-05 and ET09-06.....310

Table 11.2 – SC–ICP–MS isotopic data for samples ET10-07, ET10-09,ET10-10, ET10-13, ET10-18a and ET09-02.....311

Table 11.3 – MC–ICP–MS isotopic data for samples DNCV02, DNCV09 and DNCV10.....314

Table 11.4 – SC–ICP–MS isotopic data for sample DNCV01.....315

Table 11.5 – ID-TIMS data for Stern, Moacyr and Manangotry monazite reference materials.....318

Table 11.6 – Activities for all end-members used for THERMOCALC AvePT calculations.....319

Table 11.7 – Phase compositions and proportions used for EBC calculation.....320

List of abbreviations

The following abbreviations for mineral compositional parameters are used frequently throughout this thesis and also occur as column headers in tables of mineral compositions. They are defined here with a full mineralogical description and are abbreviated elsewhere.

Parameter	Definition	Mineralogical description
XMg	$Mg/(Mg+Fe^{2+})$	Proportion of Mg in ferromagnesian minerals
XCa	Ca/(Ca+Na+K)	Anorthite content of feldspar
XMn	$Mn/(Mn+Fe^{2+})$	Pyrophanite content of ilmenite-group minerals
XK	K/(Ca+Na+K)	K-feldspar content of feldspar
Al^{IV}	$4\text{-}Si^{total}$ (for 11 oxygens)	Tetrahedral Al in mica-group minerals
Al^{VI}	$Al^{total}\text{-}Al^{IV}$	Octahedral Al in mica-group minerals
Almandine/alm	$Fe^{2+}/(Fe^{2+}+Mg+Ca+Mn)$	Almandine content of aluminosilicate garnet
Pyrope/prp	$Mg/(Fe^{2+}+Mg+Ca+Mn)$	Pyrope content of aluminosilicate garnet
Grossular/grs	$Ca/(Fe^{2+}+Mg+Ca+Mn)$	Grossular content of aluminosilicate garnet
Spessartine/sps	$Mn/(Fe^{2+}+Mg+Ca+Mn)$	Spessartine content of aluminosilicate garnet
XJd	Na/(Na+Ca)	Jadeite content of sodic clinopyroxene
XPs	$Fe^{3+}/(Al+Fe^{3+})$	Pistacite content of epidote-group minerals
XFe^{3+}	$Fe^{3+}/(Fe^{2+}+Fe^{3+})$	Proportion of Fe that is ferric
XH_2O	$H_2O/(H_2O+CO_2)$	H_2O content of fluid phase (binary system)

1. Introduction

1.1. A statement of the problem

The theory of plate tectonics provides a solid framework with which the evolution of the Earth's lithosphere may be described and understood (Vine & Matthews, 1963). Oceanic plate boundaries, for example, are characterised by narrow and well-defined regions of faulting, seismicity and magmatism where oceanic crust may be formed (mid-ocean ridges) or destroyed (subduction zones). The first-order processes that occur in the oceanic lithosphere are well understood (e.g. McKenzie & Bickle, 1988) whereas those that control the evolution of the continental lithosphere are commonly debated. Here, deformation is not restricted to plate boundaries and the intraplate effects of continent-continent collision can be noted vast distances away from them (e.g. Searle *et al*., 2011). The duration and timing of metamorphism and deformation occurring along collisional mountain belts, and the relationship between metamorphism, crustal anatexis, crustal thickening and mountain uplift are all major orogenic processes that this thesis will address.

The Himalayan-Karakoram-Tibetan orogen (hereafter referred to as the 'HKTO'), a result of the collision of India with Asia that initiated c. 50 Myr ago (Green *et al*., 2008), is the youngest continent-continent collisional belt on Earth. As such, it has received intense multidisciplinary study in an attempt to explain and understand the processes involved in its formation. This has been achieved through a combination of geophysical remote sensing, field investigation and laboratory study and has substantially improved our knowledge of how the continental lithosphere grows and deforms over time. Furthermore, as a young and well-exposed mountain belt that is still actively deforming today, the HKTO provides a unique opportunity to examine the tectonothermal processes that may have driven the formation and evolution of some older orogenic belts (cf. St-Onge *et al*., 2006; Streule *et al*., 2010). In order to pursue such investigations, one requires detailed knowledge of the process of metamorphism, which considers the whole spectrum of changes that occur in the Earth between the upper crustal zone of weathering and erosion, and the deep crustal zone in which the last solid constituents melt to produce magma. These changes generally begin at a temperature of ~150 °C and may continue up to ~1000 °C depending on factors such as confining pressure, lithology and the composition and abundance of coexisting fluid (Philpotts & Ague, 2009). As any

rock can be buried and heated, and hence metamorphosed, it is estimated that metamorphic rocks constitute a vast proportion (at least 60 volume percent) of the continents today (ibid).

Exhumed high-grade metamorphic rocks within the HKTO system that belong to both the Indian and Asian plates can be used to interpret the thermal evolution of the unobservable lower crust prior to, and during, orogenesis. The HKTO in particular provides the chance to investigate the response of a lithospheric plate that has been pre-conditioned as an Andean-type plate margin (the Asian plate) to a continental collision, in comparison to that of a colder and more rigid passive plate margin (the Indian plate). So, four regions where structural and field relationships are relatively well-known have been targeted for multidisciplinary study in this thesis, which allows the results of metamorphic investigation to be integrated directly into their tectonic framework. These comprise the Karakoram metamorphic complex in north Pakistan (chapter 4), the Tso Morari massif in north-west India (chapter 5), the eastern Himalayan syntaxis region in south-east Tibet (chapter 6) and the Day Nui Con Voi metamorphic complex of the Red River shear zone, North Vietnam (chapter 7). Lithologies from the Karakoram metamorphic complex and eastern Himalayan syntaxis record deformation of the Asian plate margin, whereas those from the Tso Morari massif document deformation of the leading edge of the Indian plate immediately preceding initial collision. Units from the Red River shear zone record distal deformation of the lithosphere in Southeast Asia that is supposedly related to the indentation of India with Asia. When studied together these regions allow investigation of the evolution of the HKTO on a broad temporal and spatial scale, the current understanding of which is introduced in chapter 1.4.

1.2. Objectives, aims and motivation

The four case studies noted above contain lithologies that record key events in the tectonothermal history of the HKTO and which formed in a range of tectonic settings (e.g. transpressive shear zone, subduction zone, and middle- and deep-crust of an orogenic core). Thus, they allow examination of a range of rock types (e.g. mylonites, migmatites, eclogites and Barrovian-type metasediments) with which to assess the strengths and weaknesses of various thermobarometric and metamorphic modelling techniques within the context of the tectonic evolution of the HKTO. The following approaches were used in each region investigated in this study:

1. Perform petrographic and thermobarometric investigation into sets of metamorphic and magmatic units to determine as accurately as possible a region's tectonothermal history.
2. Identify key samples with minerals useful for geochronology so as to provide absolute age constraints on specific metamorphic or deformational stages in each rock's history.
3. Integrate the above *P*–*T* and age results to provide new interpretations about the evolution of each region. In each case the implications of these data should be considered within the framework of the HKTO rather than just the limited geographical extent of the region.

Therefore, the two main objectives of this thesis can be summarised as follows:

- Investigate the tectonic processes that lead to large-scale deformation of the continental lithosphere, quantifying their magnitudes and timescales in the context of the HKTO, by combining geochronological analysis with a range of metamorphic modelling techniques.
- Investigate the advantages and limitations of the various metamorphic modelling techniques when applied to a wide range of petrological and tectonic situations. Consequently, suggest areas for improvement and future research directions in metamorphic modelling procedures.

This thesis presents the results of the above work in the form of four research papers, chapters 4–7. Methodologies and background principles that are common to all studies are described once in their relevant chapters (see below) in order to avoid unnecessary repetition. Each study is prefaced by an introduction to the region's geological setting, followed by a presentation of the new data obtained and its subsequent interpretation. Contributions to these studies made by collaborators and/or journal reviewers are clearly listed in Appendix 11.1; all other work is my own.

1.3. Thesis structure

Chapter 2 – In this chapter, the underlying thermodynamic principles of metamorphic petrology are discussed in relation to the calculation of evolving pressure and temperature conditions through time. The methodology describing the construction of phase equilibria diagrams that are used in this study is outlined, including model chemical systems, bulk composition calculations and the acquisition of mineral compositions by electron-beam microanalysis.

Chapter 3 – This chapter deals with the systematics of the U–Pb and Th–Pb radiogenic isotope systems and their use in the radiometric dating of rocks and minerals. In particular, monazite

geochronology is discussed alongside the factors that determine its appearance in rocks of different bulk compositions. Work performed at the NERC Isotope Geosciences Laboratory is described alongside an account of analytical techniques and data interpretation methods.

Chapters 4–7 – These chapters make up the majority of the thesis work and present detailed accounts of the work performed in each regional study. Regional introductions, geological backgrounds, literature reviews, calculated data and interpretations, and brief discussions and conclusions are presented in these sections.

Chapter 8 – The main results and conclusions of each individual study are compiled in this chapter and integrated into the framework of the HKTO as a whole. This chapter also discusses the implications of this work and gives suggestions for future research direction.

Chapter 10 – This chapter provides additional information concerning the work presented in this thesis including conference proceedings and peer-reviewed articles.

Chapter 11 – This chapter presents appendices that contain a variety of supplementary data and results relevant to the regional studies in this thesis.

1.4. Geological setting of the HKTO

The collision of India with Asia during the Early Eocene resulted in crustal thickening both along the northern margin of India (forming the Himalayan Range) and along the southern margin of Asia (forming the Hindu Kush, Karakoram Range and the Tibetan plateau; Fig. 1.1). Numerous geophysical, seismic and GPS investigations have shown that these regions are undergoing active deformation today (see Searle *et al.*, 2011 for a review) as a result of the continuing northward movement of the Indian plate at a rate of 58 ± 4 mm/yr (Bilham *et al.*, 1997). This convergence rate has reduced significantly following initial collision, when the northward motion of India was at least 150 mm/yr (Molnar & Stock, 2009; Copley *et al.*, 2010).

Thickened crust beneath Tibet, numerous southwards-propagating thrust systems and the occurrence of high-pressure metamorphic rocks in the Himalayan Range (below) suggest that a significant amount of shortening of the upper-middle crust has occurred post-collision. Most estimates of total shortening across the orogen range between 500–1000 km (see Johnson, 2002 for

discussion); however, recent investigation based on palaeomagnetic plate reconstruction and area conservation has argued for between 2600–3200 km instead (Van Hinsbergen *et al*., 2011). This deformational response by the upper-middle crust is in contrast to that of the lower crust, which has acted in a more rigid manner, with the Indian lithosphere purported to underplate Tibet by up to 400 km north of the collision zone at approximately ~33° N latitude (Kosarev *et al*., 1999). Deformation associated with the collision can also be observed at significant distances away from the HKTO, particularly in south-east Asia, where numerous large-scale strike-slip fault systems have been suggested to control the eastward and south-eastwardly motion of crustal blocks away from the Indian indenter (e.g. Tapponnier *et al*., 1986; see chapter 1.4.4). A brief summary of the main geological features of these regions associated with the HKTO is given below (after Le Fort, 1975; Hodges, 2000 and Yin & Harrison, 2000 unless otherwise stated).



Fig. 1.1 – Compound satellite imagery of the HKTO and environs showing major tectonic features (from Google Earth©). MBT = Main Boundary thrust; ITSZ = Indus Tsangpo suture zone; BNSZ = Bangong Nujiang suture zone; JSZ = Jinsha suture zone.

1.4.1. The Himalayan Range

The Himalayan Range (or 'Himalaya') stretches for ~2500 km from the Afghanistan-Pakistan border in the west to the South China (Yunnan)-Burma border in the east (Fig. 1.1). Despite its extent, it is merely a section of the much larger Himalaya-Alpine orogenic system that stretches from the Sumatran arc of Indonesia in the east to the Mediterranean Sea in the west. Lithostratigraphic units

of the Himalaya are those bounded between the Indus Tsangpo suture zone (ITSZ) to the north and the Main Frontal thrust (MFT) to the south (Fig. 1.2) and represent the leading edge of the Indian continent. These units are commonly divided into three major tectonic 'slices'. From north to south, these are the High Himalaya (comprised of the Tethyan Sedimentary Sequence (TSS) and Greater Himalayan Sequence (GHS)), the Lesser Himalaya (comprising the Lesser Himalayan Sequence (LHS)) and the Sub-Himalaya (the Siwaliks). These slices are separated by low-angle faults of Late Cenozoic age and are exposed at the surface today in a manner that is largely consistent along strike.

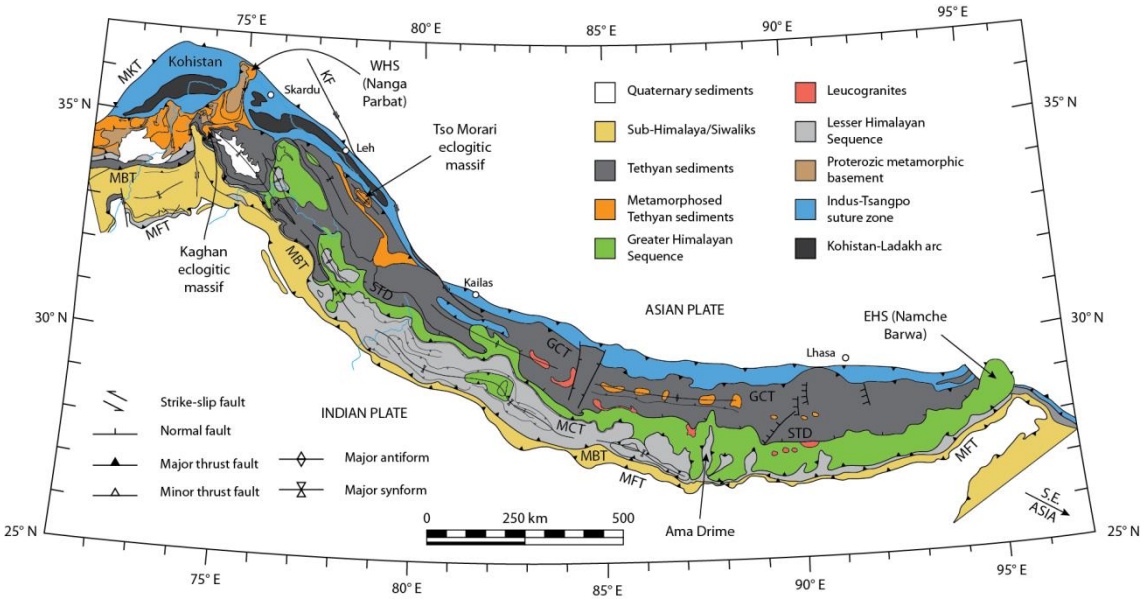


Fig. 1.2 – Generalised geology of the Himalayan Range (after DiPietro & Pogue, 2004 and Guillot *et al.*, 2008, and references therein).

The ITSZ marks the suture of the India-Asia collision and contains remnant constituents of the Neo-Tethys Ocean and related oceanic basins (ophiolitic mélange, flysch and occasional deformed island-arc volcanics). These units are separated from the underlying TSS by the Zanskar shear zone (ZSZ) in the west or the Great Counter thrust (GCT) in the east, a steep southward-dipping backthrust fault (Fig. 1.2). The TSS is the northernmost and structurally highest lithostratigraphic unit of the Himalaya and represents a series of marine sediments that were originally deposited along the passive margin of the Indian plate (Gaetani & Garzanti, 1991) and have since been strongly folded and weakly metamorphosed to lower greenschist-facies (Steck *et al.*, 1993). The TSS is bound at its base by a low-angle northward-dipping normal-sense shear zone, the South Tibetan Detachment System (STDS). This shear zone is characterised by a series of sub-

parallel detachments that are thought to have experienced displacement at different times and may have each undergone several periods of reactivation, although none are active today (Hodges *et al*., 1996; Grujic *et al*., 2011). On the basis of deep seismic profiling Nelson *et al*. (1996) suggested that the STDS, unlike the other major fault systems within the Himalaya, levels off in the upper-middle crust instead of merging with the Main Himalayan thrust (MHT) at depth.

A variety of metamorphic rocks are exposed in tectonic windows along the length of the TSS, including eclogite-facies lithologies at Tso Morari in the western Himalaya (Fig. 1.2) and granulite-facies gneiss and granite domes in the central-eastern Himalaya. The latter exposures are collectively called the 'north Himalayan gneiss domes' and are thought to have affinity with the underlying GHS (King *et al*., 2011). The GHS exists as a sequence of metamorphic units that primarily include amphibolite-facies gneiss, schist, calc-silicate and amphibolite; all interpreted to represent accreted continental crust derived from the subducting Indian plate. Following the onset of continental collision this sequence was buried and metamorphosed and has a complex thermal history, a detailed description of which is given in chapter 1.5.1. *In-situ* crustal anatexis within the core of the GHS has resulted in the migration of partial melt and emplacement of leucogranitic dykes and plutons at the highest structural levels, some of which follow basal strands of the STDS.

The Main Central thrust (MCT), a low-angle northward-dipping thrust fault, bounds the base of the GHS and emplaces it above the underlying LHS (Fig. 1.2). The LHS is characterised by a sequence of intercalated sedimentary and volcanic units, Cambro-Ordovician granites and gneisses and weakly metamorphosed NeoProterozoic pelitic and psammitic rocks (the Haimanta or Cheka Group). The LHS is in turn thrust over the Siwalik deformed foreland basin molasse deposits by the Main Boundary thrust (MBT) and the lower bound of the Siwaliks is the currently active Main Frontal thrust (MFT). Both the MBT and MFT are low-angle northward-dipping thrust faults that, on seismic evidence, are believed to converge with the basal detachment, the MHT, which is interpreted as the plane along which India is currently underthrusting southern Tibet today (Brown *et al*., 1996).

1.4.2. The Tibetan plateau

The Tibetan plateau (or 'Tibet') is situated north of the Himalayan Range (Fig. 1.1) and has a surface area of ~3500 by 1500 km, a mean elevation ~5000 m (Fielding *et al*., 1994) and a crustal

thickness between 70–90 km (Wittlinger *et al.*, 2004; Rai *et al.*, 2006). The plateau is structurally complex, having formed from the successive accretion of numerous microplates and island arcs to the southern margin of Eurasia since the Early Palaeozoic (Dewey *et al.*, 1988). The collision of the Indian plate, closure of the Neo-Tethys Ocean and associated formation of the Himalaya represent the most recent of these events. Thus the plateau may be divided into a number of approximately E–W trending terranes including, amongst others, the Lhasa and Qiangtang blocks.

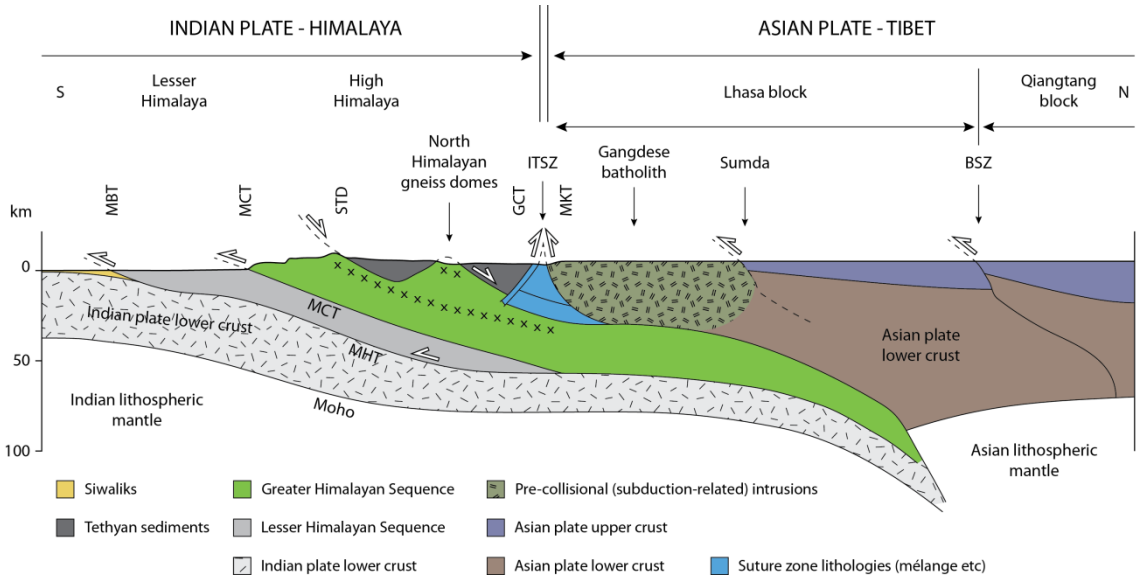


Fig. 1.3 – Cross-section through the central Himalaya-central Tibet showing the lithospheric structure and main geologic units (after Searle *et al.*, 2010a). 'x' within the GHS represents migmatites/partial melt (ibid).

The Lhasa block is the southernmost tectonic block in Tibet and is bounded by the ITSZ to the south and the Bangong-Nujiang suture zone (BNSZ) to the north (Fig. 1.1). It was accreted to the former Asian plate southern margin (the Qiangtang block) during the Late Jurassic (Dewey *et al.*, 1988). The Lhasa block is bounded to the west by the right-lateral strike-slip Karakoram fault, but can be correlated across this structure with the Kohistan-Ladakh arc in north-west India and north Pakistan (Searle, 1996; Robinson, 2009). Here, the BNSZ is referred to as the Shyok suture zone (SSZ) or Main Karakoram thrust (MKT). The Qiangtang block is located between the BNSZ and the Jinsha suture zone (JSZ) and is was accreted to the southern Asian plate margin during the Late Triassic-Early Jurassic (Dewey *et al.*, 1988). Like the Lhasa block, the Qiangtang block can be correlated across its western boundary, the Karakoram fault, becoming the lateral equivalent of the Karakoram Range (Tapponnier *et al.*, 1981; Yin & Nie, 1996). The Qiangtang block consists largely of supracrustal rocks that surround a central ~600 km long by ~150 km wide tectonic mélange of

blueschist- and eclogite-bearing blocks (Kapp *et al*., 2003; Zhang *et al*., 2006) in a greenschist-facies matrix of Triassic age (Pullen *et al*., 2011). Very little evidence of the tectonic processes operating around the time of the India-Asia collision can be found in these regions; hence, the tectonothermal evolution of this terrane is not discussed further. A cross-section through the Himalaya and central Tibet (at approximately 90 °E) illustrating the major features described above is shown in Fig. 1.3.

1.4.3. The Karakoram Range

The Karakoram Range is approximately 700 km long and 100–150 km wide and extends in a broad arc along the borders of Afghanistan, Pakistan, India and China (Fig. 1.4). Geophysical studies of the Karakoram Range show that very little seismic activity occurs in the upper and middle crust, with occasional seismicity at depths of 70–100 km (Chen & Molnar, 1983), indicating that the upper mantle is relatively cold (Brandon & Romanowicz, 1986). Caporali (2000) showed that the axis of the range corresponds with a line of large negative gravity anomalies (<-500 mGal) and high heat flow, suggesting the presence of a deep crustal root similar to that under Tibet today. As previously noted, the Karakoram Range is the lateral equivalent of the Qiangtang block in central Tibet and can be correlated across the Karakoram fault (Fig. 1.1); however, unlike the Qiangtang block, extensive crustal thickening, rock uplift and erosion in this region have produced extreme topography and large exposures of deep crustal lithologies.

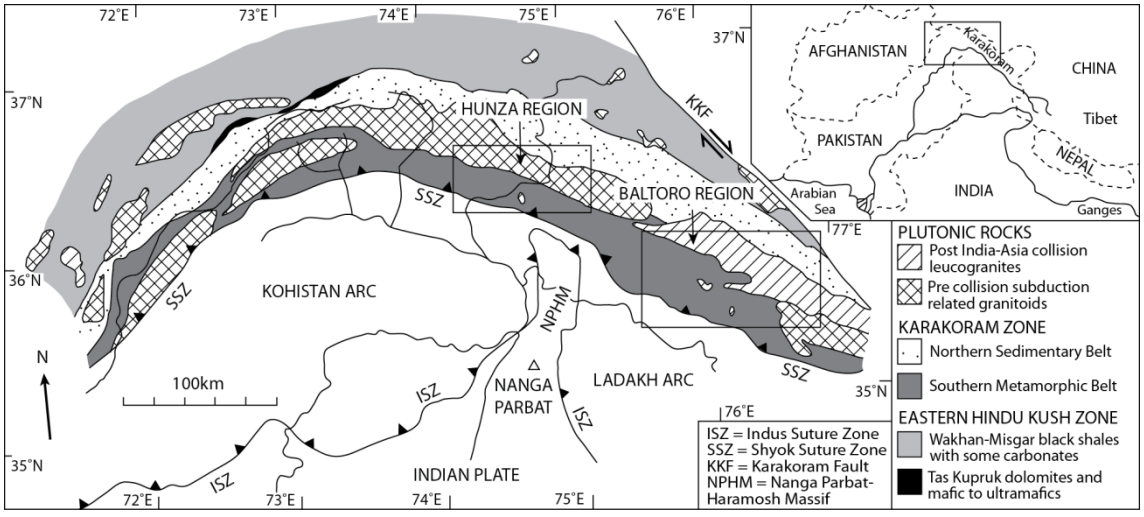


Fig. 1.4 – Schematic geological map of north Pakistan showing major geological relationships in the Karakoram Range (after Searle, 1991, Hildebrand *et al*., 1998, 2001, and Fraser *et al*., 2001).

Rocks exposed within the Karakoram Range record metamorphism and deformation of the southern extent of the Asian margin during the collision of the Kohistan-Ladakh island arc in the Late Cretaceous and the subsequent collision with the Indian plate during the Early Eocene (Searle *et al*., 1991, 2010a). A cross-section through the western Himalaya, Karakoram Range and western Tibet (at approximately 75–80 °E) is shown in Fig. 1.5 illustrating major structural relationships.

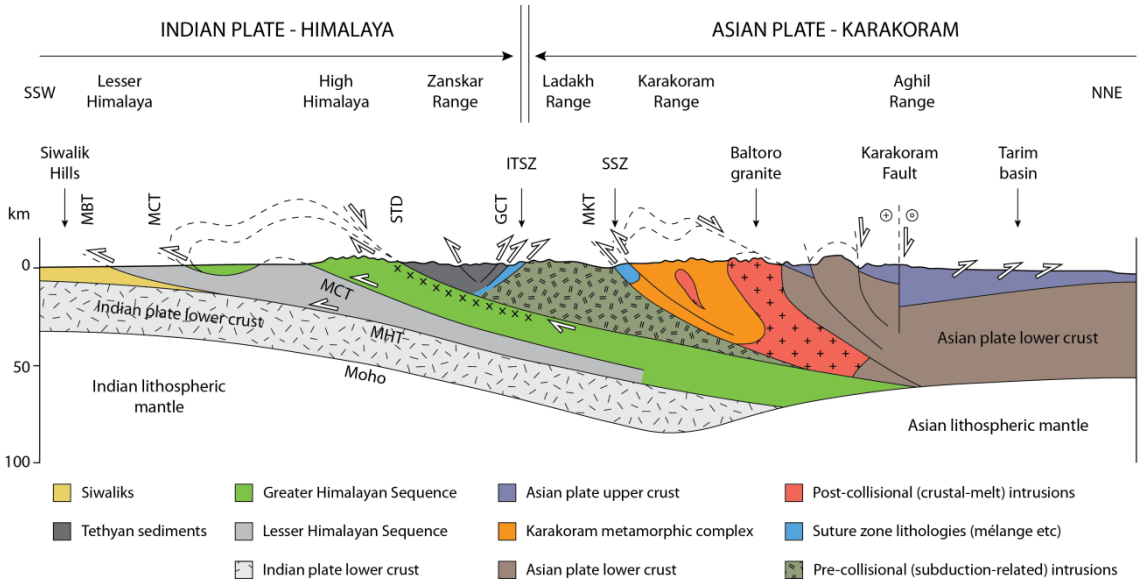


Fig. 1.5 – Cross-section through the western Himalaya-Karakoram Range-western Tibet showing the lithospheric structure and main geologic units (after Searle *et al.,* 2010a).

1.4.4. Red River shear zone

Although the effects of the collision of India with Asia are most prevalent in the aforementioned regions (the Himalaya, the Karakoram Range and Tibet) deformation allegedly attributed to this event can also be found in distant parts of south-east Asia. One of the tectonic models commonly used to explain the tectonics of south-east Asia (and Tibet) is that of 'continental extrusion', whereby regional-scale strike-slip fault systems control the eastward and south-eastward motion of large crustal blocks away from the Indian indenter (e.g. Tapponnier *et al*., 1986). In particular, left-lateral strike-slip shearing along the Red River shear zone (RRSZ), the Sagaing fault and the Wang Chao fault (Fig. 1.6) has reportedly accommodated displacement of the Indochina block by 500–1000 km during the Tertiary, a range calculated from apparent offsets of geological markers along each fault zone (Leloup *et al.*, 1993, 1995, 2001; Tapponnier *et al.*, 1986, 1990, 2001).

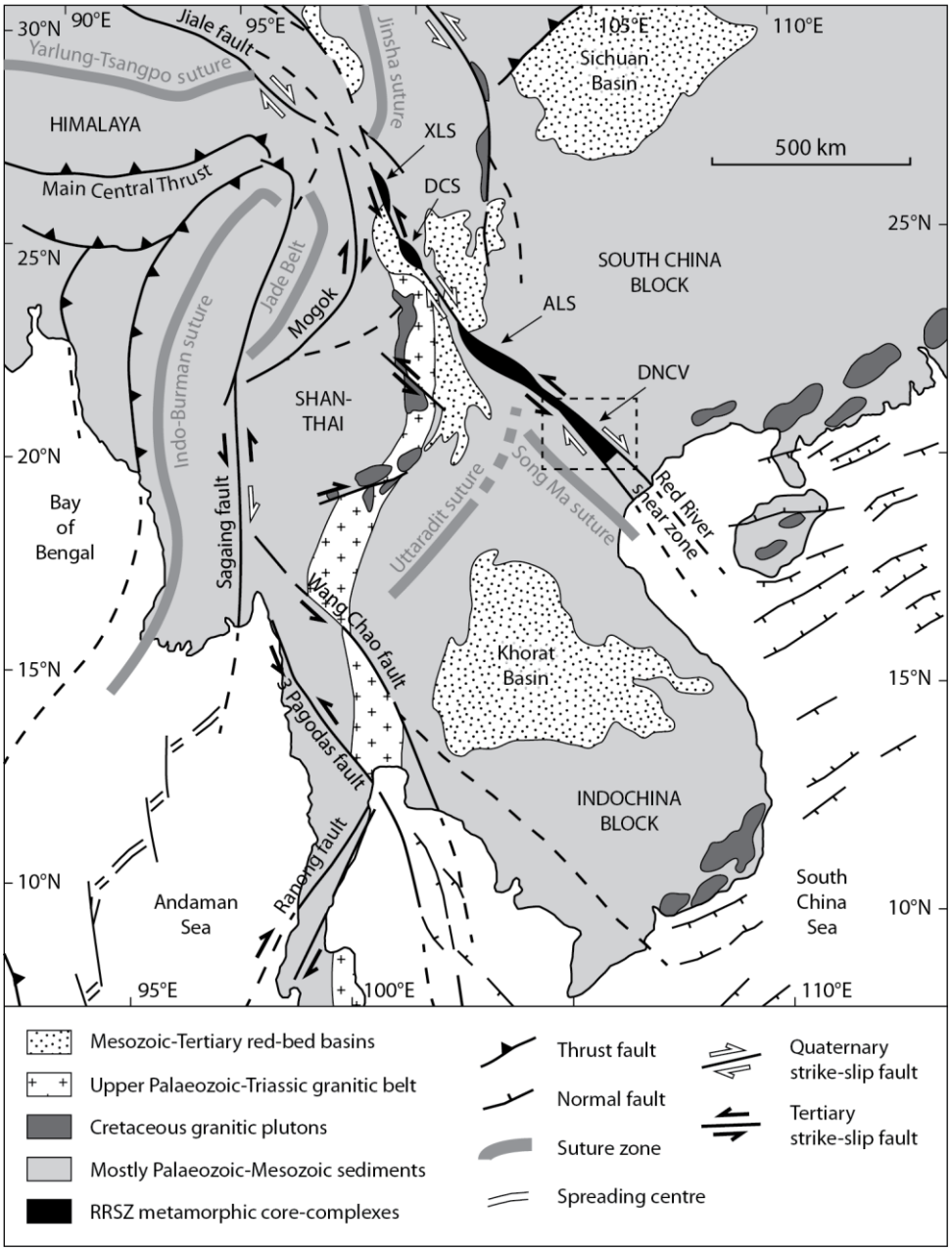


Fig. 1.6 – Tectonic map of south-east Asia showing the geological setting of the RRSZ and metamorphic core complexes (after Tapponnier *et al*., 1990, Leloup *et al*., 1995 and Gilley *et al*., 2003). Dashed box represents position of Fig. 7.1. XLS = Xuelong Shan, DCS = Diancang Shan, ALS = Ailao Shan, DNCV = Day Nui Con Voi.

By contrast, other recent studies of major strike-slip faults in Tibet and south-east Asia contest the scale of the continental extrusion model by suggesting that total displacements are much less than previously proposed and that the offset geological features used by previous workers lack definite pinning points (Searle, 2006; Yeh *et al*., 2008; Searle *et al*., 2010b, 2011). Despite this disagreement, monazite and zircon ages obtained from both igneous and metamorphic lithologies in the RRSZ indicate that strike-slip deformation was occurring during the Tertiary (e.g. Lin *et al*.,

2012). Such lithologies are exposed along the length of the RRSZ in four spatially distinct NW–SE aligned metamorphic core complexes: the Xuelong Shan, Diancang Shan and Ailao Shan in Yunnan, China, and the Day Nui Con Voi (DNCV) in North Vietnam (Fig. 1.6). These complexes are characterised by variably deformed orthogneiss and paragneiss, many of which exhibit strong mylonitic fabrics that are aligned with the Red River fault (RRF), a major structure in the RRSZ. The RRF is active today and exhibits dominantly right-lateral strike-slip motion (opposite in sense to Tertiary movement) coupled with a component of low-angle normal faulting along the margins (Tapponnier & Molnar, 1977; Allen *et al.*, 1984; Leloup *et al.*, 1995).

As the timing of motion and total offset along the RRSZ are fundamental to the continental extrusion hypothesis, accurately constraining the timing of metamorphism and deformation in these complexes is of great importance. Many previous studies have been unable to produce a coherent model for the formation of these metamorphic units; hence, a multidisciplinary investigation of metamorphic and magmatic lithologies from the DNCV was undertaken in an attempt to clarify the relationship between the RRSZ to the HKTO (see chapters 1.5.4 and 7).

1.5. Metamorphic-magmatic evolution of the HKTO

The previously described regions contain metamorphic and magmatic rocks that are inherently linked to deformation caused by the on-going India-Asia collision. This is most apparent when examining units of the GHS, most of which have been transformed from sedimentary protoliths into high-grade schists, gneisses or crustal melts. Studies of this lithostratigraphic unit have proven to be invaluable for elucidation of the evolution of the Indian plate margin before, during and after collision with Asia. However, in comparison with the Indian plate, exposures of similar high-grade metamorphic rocks on the Asian plate are unevenly distributed and thus the response in central Tibet to the collision is harder to quantify. The current understanding of the metamorphic and magmatic evolution of these individual regions is summarised below.

1.5.1. The Greater Himalayan Sequence

Numerous thermobarometric and geochronological studies of regional metamorphic units of the GHS have produced a 3-stage tectonothermal evolution that, with few exceptions, is largely uniform along-strike of the Himalaya. A brief summary of these stages is given below.

Initial ultra-high-pressure (UHP) metamorphism (M1) of the northern margin of the Indian plate is recorded in coesite-bearing eclogite that is exposed in two locations: the Kaghan Valley, Pakistan, and the Tso Morari massif (TMM), north-west India. Parrish *et al*. (2006) dated peak metamorphism of the former at 46.4 ± 0.1 Ma (U–Pb zircon and allanite) at *P–T* conditions of >27.5 kbar and 720–770 °C. The latter UHP locality (Tso Morari) has been studied by numerous workers, although strong disagreement exists concerning the timing of subduction and exhumation, and also the calculated peak metamorphic conditions (see O'Brien, 2006 for discussion). Mafic eclogite from this locality was studied in this thesis (chapter 5) and a synthesis of the available petrographic and geochronological data is given in that section.

Subsequent crustal thickening and Barrovian-type metamorphism along the Himalaya resulted in regional kyanite-grade metamorphism (M2) of the GHS that peaked between c. 37–30 Ma, identified from U–Pb dating of metamorphic monazite (Walker *et al*., 2001; Godin *et al*., 2001; Simpson *et al*., 2000) and Sm–Nd dating of garnet growth (Vance & Harris, 1999). Peak *P–T* conditions for this event range between 9–12 kbar and 550–680 °C (e.g. Vannay & Hodges, 1996 and others). Subsequent decompression and heating along a clockwise *P–T* path resulted in sillimanite-grade metamorphism (M3), extensive migmatisation and the formation of leucogranites (Searle *et al*., 2009). U–Pb ages of sillimanite-grade monazite mainly span the period between c. 24–15 Ma (Noble & Searle, 1995; Searle *et al*., 1997, 1999, 2003; Murphy & Harrison, 1999; Simpson *et al*., 2000; Viskupic & Hodges, 2001; Cottle *et al*., 2009a), though the youngest leucogranite dykes in the GHS are in Bhutan and are dated at c. 11 Ma (U–Pb zircon; Kellett *et al*., 2009). Two notable exceptions to this along-strike evolution are the Himalayan syntaxis regions; Nanga Parbat in the west and Namche Barwa in the east (Fig. 1.2). These regions contain high-grade migmatitic rocks with extremely young (Pliocene) ages, indicating that they have undergone distinct episodes of deformation that do not relate to the main body of the GHS. The eastern Himalayan syntaxis region (EHS) and the adjacent Asian plate south Lhasa block forms another case study in this thesis, and a detailed discussion of its tectonothermal evolution is given in chapter 6.2.2 alongside a comparison with Nanga Parbat and the main body of the GHS.

1.5.2. The Lhasa block

The surface geology of the Lhasa block is strongly heterogeneous, with lithologies documenting a protracted tectonometamorphic history prior to, and following, its collision with India. Pre-India-Asia collision metamorphism is documented by a discontinuous belt of mafic and ultramafic rocks situated in the central Lhasa block, over 100 km south of the BNSZ (Liu, 1988). Following their discovery, these units were interpreted as either tectonic slices of the BNSZ that have been displaced southwards along low-angle thrust faults (Girardeau *et al*., 1984) or as evidence for an additional suture within the Lhasa block (Hsü *et al*., 1995) that was previously unidentified. Samples of eclogite from this belt were analysed by Yang *et al*. (2009), who produced Permian ages between c. 292–242 Ma (U–Pb zircon), with an average value of 262 ± 5 Ma, and peak metamorphic conditions of 27 kbar and 730 °C. As a result of the concomitant identification of an E–W trending band of Carboniferous-Permian volcanic rocks to the north of this eclogite belt, the latter scenario of a previously unidentified suture zone within the Lhasa block was advocated (ibid).

Consequently, the Lhasa block has been divided into northern and southern segments separated by this eclogite belt. The northern segment exposes vast regions of flat-lying sediments of Ordovician to Jurassic age (Yu & Zheng, 1979), suggesting that no significant deformation related to the India-Asia collision affected the region. By contrast, the geology of the southern Lhasa block is dominated by the pre-collision Gangdese composite batholith, which is composed of subduction-related hornblende- and biotite-bearing diorites, granodiorites and granites, together with their extrusive equivalent calc-alkaline andesites, rhyolites and dacites (Chung *et al*., 2005). U–Pb zircon dating shows that these subduction-related units were emplaced between the Jurassic and Early Eocene, with the main episodes between c. 133–110 Ma and c. 66–57 Ma (Wen *et al*., 2008; Chiu *et al*., 2009; Lee *et al*., 2009). Smaller post-collisional intrusions are mostly adakitic and are sourced from the melting of garnet-bearing crustal rocks (Chung *et al*., 2003, 2005; Zhang *et al*., 2009).

In the south Lhasa block exposures of metamorphic rocks are rare. Intermittent exposures of amphibolite-facies sillimanite-bearing orthogneiss and garnet amphibolite have been reported by Dong *et al.* (2011) to be of Triassic age (c. 225–213 Ma; U–Pb zircon) and are suggested to be typical of the unobservable metamorphic middle crust. The only kyanite- or sillimanite-grade units currently documented to be of Tertiary age are those reported in the Bayi-Linzhi-Milin area in the far south-east of Tibet, in the immediate vicinity of the EHS (Zhang *et al.*, 2010; Xu *et al.*, 2010). These

young rocks are therefore extremely important to the investigation of the effects of the India-Asia collision on the south Lhasa block, and they constitute another case study in this thesis. A more detailed account of their metamorphic and magmatic evolution is given in chapter 6.

1.5.3. The Karakoram metamorphic complex

Rocks within the Karakoram Range that lie between the Karakoram batholith to the north and the Shyok suture zone to the south are collectively called the Karakoram metamorphic complex (KMC). Two particular regions of the KMC provide excellent exposure and have been targeted in the past for detailed study (Fig. 1.4): the Hunza Valley in the west (Zeitler, 1985; Crawford & Searle, 1993; Fraser *et al*., 2001) and the Baltoro region in the central-southeast (Searle & Tirrul, 1991; Searle *et al*., 1992, 2010a; Rolland *et al*., 2001, 2006). Although these regions are along strike of one another and are not separated by any major structural features, poor accessibility and limited exposure in the intermediate region does not allow for direct correlation of metamorphic units (Searle *et al*., 2010a). Lithologies in the KMC consist of abundant marbles, meta-marls and calc-silicates with subordinate metapelites and orthogneiss units (Desio, 1964; Searle *et al*., 1986, 1989; Searle, 1991; Rolland *et al*., 2006). A brief outline of the geological evolution of the Karakoram Range is presented below; however, discussion of metamorphic events utilises metapelites owing to their superior potential for recording changing *P*–*T*–*t* conditions.

Some units of the Karakoram Range preserve a metamorphic and magmatic record that predates the India-Asia collision. Early subduction of the Neo-Tethys Ocean beneath the south-western Asian margin resulted in formation of the Karakoram batholith, a composite intrusion that contains I-type granodiorites, quartz diorites and monzogranites with intrusion ages ranging between c. 95–105 Ma (Rb–Sr whole rock; Debon *et al*., 1987; U–Pb zircon; Le Fort *et al*., 1983, Fraser *et al*., 2001). Consequently, rocks of the Asian margin experienced high-temperature contact metamorphism (M0) associated with magma intrusion (see chapter 4.7.1). Such magmatism ceased upon the closure of the Shyok suture and the accretion of the Kohistan-Ladakh island arc to the Asian margin during the Late Cretaceous (Mahéo *et al*., 2004). This accretion event has been interpreted to be responsible for a period of sillimanite-grade metamorphism (M1) that occurred between c. 83–53 Ma (U–Pb monazite; Fraser *et al*., 2001; Foster *et al*., 2004). It should be noted

that data to constrain the duration of metamorphism pre- and post-SSZ closure is lacking, therefore it is possible (but unlikely; see chapter 4.5.2) that M0 and M1 constitute one continuous thermal event.

Following the subsequent closure of the Indus suture and onset of the India-Asia collision, thrusting of rocks to the south-west resulted in extensive crustal thickening and Barrovian-type kyanite- and sillimanite- grade metamorphism (M2) between c. 44–22 Ma at *P–T* conditions of 8–10 kbar and 600–700 °C (U–Pb monazite and zircon; Allen & Chamberlain, 1991; Searle & Tirrul, 1991; Bertrand *et al*., 1988; Lemennicier *et al*., 1996; Rolland *et al*., 2001; Searle *et al*., 1989, 2010a). In the Baltoro region this event culminated in extensive crustal melting leading to formation of the Baltoro Plutonic Unit (BPU) of the Karakoram batholith. This body contains numerous biotite monzogranite and garnet two-mica leucogranite components that crystallised between c. 25–13 Ma (U–Pb zircon and monazite; Parrish & Tirrul, 1989; Schärer *et al*., 1990; Searle *et al*., 2010a). At this time in the Hunza Valley, unrelated prograde staurolite-grade metamorphism (M3) peaked at 16.0 ± 1.0 Ma (U–Pb monazite; Fraser *et al*., 2001). Most recently, exhumed metamorphic units in the Baltoro region record sillimanite- and K-feldspar-grade overprinting of M2 assemblages, with associated partial melting dated at 5.4 ± 0.2 Ma (U–Pb monazite; Fraser *et al*., 2001) and 6.7 ± 0.5 Ma (U–Pb monazite; Smith, 1993) at pressures between 4–7.5 kbar (Villa *et al*., 1996).

This brief summary illustrates that major differences exist in the tectonothermal evolution of the Hunza Valley and Baltoro regions. Rocks from both have been studied in this thesis in order to provide insight into the causes of such disparity and to further explore the effects of the India-Asia collision on the Asian plate margin. Results of this work are given in chapter 4 and prefaced by a more detailed account of the geological evolution of the Karakoram Range as a whole.

1.5.4. Red River shear zone

The relative timing, cause and supposed inter-relationship between high-grade metamorphism, partial melting and strike-slip fault motion along the RRSZ are highly debated issues. In general, such hypotheses may be divided into two principal groups. Studies that support the continental extrusion hypothesis suggest that the high-grade metamorphism and magmatism within each core complex formed as a direct result of Tertiary shear heating along the RRSZ in response to the collision of India with Asia (Tapponnier *et al.*, 1990; Leloup *et al*., 1993, 1995, 2001, 2007). In this

model, motion along the RRF and RRSZ supposedly induced heating in the middle-lower crust, causing an increase in ambient crustal temperature of ~150 °C, leading to metamorphism and partial melting (Leloup *et al*., 1995). However, a later study by Gilley *et al*. (2003) showed through time-dependent conductive thermal modelling that up to 20 Myr of continual shearing would only raise temperatures by 60–80 °C, weakening, but not dismissing, this argument.

Other workers limit the RRF to the upper-middle brittle crust (Searle, 2006, Yeh *et al*., 2008), complying with the Sibson-Scholz model of fault zone architecture (Sibson, 1986), and suggest that the RRSZ includes all of the ductilely-deformed metamorphic rocks in the core complex. In this latter interpretation, all metamorphic rocks in the RRSZ formed during the Indosinian orogeny, prior to strike-slip motion, and have simply been exhumed as a result of fault motion so that current mylonitic fabrics have been imposed onto previous metamorphic foliations and lineations (Jolivet *et al*., 2001; Searle, 2006; Anczkiewicz *et al*., 2007; Yeh *et al*., 2008). The Indosinian orogeny represents the accretion of the Sibumasu continental block to Indochina/South China that occurred between c. 250–190 Ma (Metcalfe, 2000) and is poorly documented given the later reworking of many metamorphic units and the generally poor degree of exposure throughout south-east Asia.

Geochronological data obtained from each massif along the RRSZ support the existence of metamorphic and magmatic episodes during both the Triassic and the Tertiary. For example, U–Pb dating of orthogneiss from the Ailao Shan and Diancang Shan massifs by Searle *et al*. (2010b) revealed zircon cores of Indosinian age (between c. 243–239 Ma) and rims of Oligocene age (c. 26 Ma), the former interpreted to represent protolith emplacement and crystallisation and the latter to represent a metamorphic or magmatic overprint. Additionally, *in-situ* Th–Pb dating of monazite performed by Gilley *et al*. (2003) on DNCV paragneiss produced a large dataset spread between c. 220–21 Ma, with a significant cluster of young ages between c. 34–21 Ma interpreted as signifying an episode of garnet growth related to prograde metamorphism and dating left-lateral shearing along the RRSZ. Samples of variably deformed anatectic paragneiss and granite dykes that were collected from the DNCV have been analysed in this study in order to provide new insight into these disputes through the combination of *in-situ* monazite geochronology and thermodynamic modelling of high-grade metamorphism and partial melting. The results of this work are presented in chapter 7 in addition to a more detailed description of the *P*–*T*–*t* evolution of the DNCV and its surrounding area.

2. Metamorphic petrology

The word 'metamorphic' was first proposed by Charles Lyell following a trip to Norway in the early 19th century to describe Palaeozoic sedimentary rocks that had been *'changed by heat'* as a result of the emplacement of Permian granite-syenite intrusions (Lyell, 1833, 1838; Hestmark, 2011). Subsequent work has expanded on this initial notion (see chapter 10.3); thus, a more generalised definition would describe metamorphism as the process by which a rock responds to changes in ambient physical and/or chemical conditions. In the context of orogenesis, these are primarily pressure (*P*), temperature (*T*) and composition (*X*). Such changes induce physiochemical reactions between constituent solid and fluid phases that result in the formation of a new mineral assemblage and/or microstructure. Hence, minerals and microfabrics observed in rocks at the Earth's surface today are monitors of the changing *P–T–X* conditions over which those rocks formed. The principal aim of metamorphic petrology is to quantify the relative or absolute changes in these conditions over time and therefore understand the tectonic processes responsible. Further insight is gained by applying temporal constraints on these processes through microstructural analysis and isotopic dating to provide a relative or absolute geochronology. This chapter outlines the approach used to extract such *P–T–X* information from metamorphic rocks.

2.1. Introduction

The process of metamorphism acts to minimise a rock's internal free energy through a variety of mechanisms, for example by the recrystallisation of pre-existing minerals into a new fabric or by the growth of new minerals via chemical reaction. Ultimately, a rock tries to reach a state of chemical and textural *equilibrium* characterised by a particular mineral assemblage that is unique to a specific *P–T–X* condition and can be described by definite proportions and compositions of constituent phases. Chemical thermodynamics allows prediction of which mineral assemblage will be stable (i.e. has the lowest total free energy) in a rock at equilibrium conditions. Therefore utilising petrological techniques on a metamorphic rock is primarily a reverse modelling problem, where the geologist desires to calculate the *P–T–X* conditions at which the observed mineral assemblage formed.

Despite metamorphic rocks striving to reach a state of minimal free energy, in natural systems a state of equilibrium may never be fully achieved and rocks may instead preserve evidence of

previous stable assemblages, in a state of *disequilibrium*. This situation is often preferable to the geologist, as a rock preserving a state of perfect chemical and textural equilibrium is of limited use for the tectonic interpretation of an outcrop. Although peak metamorphic conditions are readily obtained in this latter situation, no information is provided about how the sample achieved (or departed from) those conditions. In most cases, the tectonic interpretation of an outcrop would significantly benefit from such information. By contrast, disequilibrium features can be used to determine numerous points along a *P–T* path that a rock must have travelled; the interpretation of which provides important geodynamic information about the tectonic processes responsible. In order to calculate these *P–T* conditions, knowledge of the underlying thermodynamic principles of thermobarometry is required; with the following treatment after Spear (1993).

2.2. Thermodynamic principles

In a multi-phase system, the thermodynamic potential for work to be performed governs the thermodynamic state of that system. When considering the state variables *T*, *P* and the number of moles (n_i) of components, this thermodynamic potential is referred to as the Gibbs free energy (G). For a rock with a particular bulk composition, numerous possible phase assemblages could theoretically exist at any *P–T* condition and the Gibbs free energy of the system (G_{sys}) would be different for each. The configuration with the lowest G_{sys} is termed the *stable assemblage* and would exist in a state of heterogeneous equilibrium – all other assemblages with higher values of G_{sys} are described as being *metastable*. If G_{sys} is not minimised, the constituent phases in the system will act to reduce the thermodynamic potential by means of heterogeneous reaction. During metamorphism and deformation a rock experiences many changes in ambient *P–T* conditions and will therefore undergo a series of continuous and discontinuous reactions in an attempt to achieve sequential equilibria, each representative of the current state of the system.

For a rock comprised of four phases (A, B, C and D), at heterogeneous equilibrium, all phases will have the same temperature and pressure and the free energy of the system will be minimised. As there is no potential for $G_{sys}$to change under these conditions, then:

$$dG_{sys} = 0 \tag{2.2.1}$$

As G_{sys} is the sum of the free energies of all phases within the system, it follows that:

$$dG_{sys} = 0 = dG_A + dG_B + dG_C + dG_D \quad (2.2.2)$$

If a state of heterogeneous equilibrium is disturbed by a change in ambient *P–T* conditions, subsequent physical or chemical reactions must occur between constituent phases to reach a new equilibrium condition, at which point the free energy available for further reaction (ΔG_R) is equal to zero. In a closed system, total mass is conserved over the course of any reaction. A similar relationship applies to the chemical potentials (μ) of phase components, whereby the sum of chemical potentials of products is equal to the chemical potentials of reactants. This is expressed as:

$$0 = \sum_{j=1}^{m} v_j \cdot \mu_j = \Delta G_R \quad (2.2.3)$$

Here, v_j represents the stoichiometric coefficient for each phase component (j) in a reaction where there are *m* phase components. Where a phase exhibits solid solution between multiple end-members (i.e. is impure), the chemical potential of each phase component is reduced from its pure state due to the entropy of mixing, as follows:

$$\mu_j = \mu_j^\circ + RT \ln a_j \quad (2.2.4)$$

In this relationship μ_j° is the chemical potential of phase component *j* at its standard state conditions (pure *j* at the *P* and *T* of interest), *R* is the gas constant (8.314 $J \cdot K^{-1}$ mol^{-1}), *T* is temperature (in Kelvin) and a_j is the activity of a component in a given phase.

Combining equations 2.2.3 and 2.2.4 produces the following relationship, where ΔG° is the change in Gibbs free energy between end-members in a reaction and K_{eq} is the equilibrium constant that relates the activities of reactants and products (see later):

$$\Delta G_R = 0 = \Delta G^\circ + RT \ln K_{eq} \quad (2.2.5)$$

The complete relationship between pressure, temperature and phase composition at equilibrium can be expressed as follows (Spear, 1993):

$$\begin{aligned} \Delta G_R = 0 = \Delta H_{298,1} + \int_{298}^{T} \Delta C_P \, dT + \int_{1}^{P} \Delta V \, dP \\ -T\left(\Delta S_{298,1} + \int_{298}^{T} \frac{\Delta C_P}{T} dT\right) + RT \ln K_{eq} \end{aligned} \quad (2.2.6)$$

Here, H, S, V and C_P are enthalpy, entropy, volume and heat capacity respectively and these thermodynamic properties are given at standard state conditions of 298 K and 1 bar. For volatile-

absent metamorphic reactions that occur in the subsolidus domain, this relationship may be simplified significantly. Although C_P is a function of *T*, the ΔC_P of a reaction is often negligible so can be approximated to zero. Likewise, if all phases have a similar compressibility then ΔV can be assumed to be constant. This leads to the much simplified relationship:

$$\Delta G_R = 0 = \Delta H + P\Delta V - T\Delta S + RT \ln K_{eq} \quad (2.2.7)$$

This equation can then be rearranged to express $\ln K_{eq}$ as a function of *T*, *P* and the remaining thermodynamic parameters:

$$\ln K_{eq} = \frac{T\Delta S - \Delta H - P\Delta V}{RT} \quad (2.2.8)$$

Alternatively, this may be expressed as a thermometer (2.2.9) or barometer (2.2.10):

$$T = \frac{P\Delta V + \Delta H}{\Delta S - R \ln K_{eq}} \quad (2.2.9) \qquad P = \frac{T\Delta S - RT \ln K_{eq} - \Delta H}{\Delta V} \quad (2.2.10)$$

For any equilibrium, values of $\Delta H, \Delta S$ and ΔV may be calculated from experimentally determined values for phases of interest and $\ln K_{eq}$ may be calculated from the measured or assumed compositions of reactants and products. Thus a univariant line representing a particular equilibrium can be positioned in *P*–*T* space, the slope of which is described by the Clausius-Clapeyron equation when considering pure phases (2.2.11) or those with solid solution (2.2.12):

$$\frac{dP}{dT} = \frac{\Delta S}{\Delta V} \quad (2.2.11) \qquad \frac{dP}{dT} = \frac{\Delta S - R \ln K_{eq}}{\Delta V} \quad (2.2.12)$$

2.3. Thermobarometry

From the treatment above it can be seen that *P*–*T* conditions of equilibration may be calculated from observed mineral assemblages, provided that they represent a frozen-in equilibrium. However, the extent to which this is achieved at various stages in a rock's evolution relies on two important factors: the *time* available for equilibrium to be reached at a particular *P*–*T* condition and the *scale* at which equilibrium forms (Powell, 1978). These two factors are closely related – the more time that a rock remains at a particular *P*–*T* condition, the larger the volume of the rock that should be able to reach equilibrium. After only a short amount of time, many small volumes may reach equilibrium even if the system as a whole is out of equilibrium – a situation termed local or mosaic equilibrium (ibid). In this case, careful petrographic analysis must be used to determine the state of an assemblage under consideration. Two main methods of investigation of changing *P*–*T*–*X* conditions

are often employed: conventional thermobarometry and phase equilibria modelling. The choice of method depends on many factors, notably the extent of equilibrium observed in a sample, and the methodology, advantages and limitations of each technique are outlined below.

2.3.1. Conventional thermobarometry

Although phase equilibria modelling has been suggested to be the most powerful method of extracting *P–T–X* information from a metamorphic rock (below), it cannot be applied uncritically in all situations. Such examples include large-scale mosaic equilibrium or when investigating rocks where the bulk composition is thought to have changed by an unquantifiable amount (e.g. mylonitised high-grade rocks). Here, conventional thermobarometry is often able to provide estimates of pressures and/or temperatures of equilibration instead.

Conventional thermobarometry allows equilibrium P or T conditions for a mineral assemblage to be calculated from the measured distribution of elements between particular phases. Good geothermometers have steep slopes in *P–T* space, a relatively large ΔS and a small ΔV and are typically cation exchange reactions. Good geobarometers have shallow slopes in *P–T* space, a large ΔV and relatively small ΔS and are typically net transfer reactions. The methodology for thermobarometric calculation is demonstrated by examination of equation 2.2.8. Thermodynamic parameters occurring on the right hand side of the equation, relevant to a specific reaction, may be used to produce a linear relationship between P and T with a specific gradient. The equilibrium constant on the left hand side provides a compositional constraint that determines the absolute position of this calculated relationship in *P–T* space. Using a single geothermometer, for example, suggests that a mineral assemblage equilibrated somewhere along the calculated line. However simultaneous solution of multiple thermometers and barometers allows calculation of a *P–T* point where these individual equilibria intersect.

2.3.1.1. Geothermometry

The distribution of Fe and Mg between garnet and biotite is temperature-dependent and can be used as a geothermometer in suitable rocks. The cation exchange equilibrium is expressed as follows:

$$\underset{\textit{phlogopite}}{KMg_3AlSi_3O_{10}(OH)_2} + \underset{\textit{almandine}}{Fe_3Al_2Si_3O_{12}} = \underset{\textit{annite}}{KFe_3AlSi_3O_{10}(OH)_2} + \underset{\textit{pyrope}}{Mg_3Al_2Si_3O_{12}} \qquad (2.3.1)$$

As thermodynamic data for most common mineral end-members are readily available (e.g. Helgeson *et al*., 1978), it can be seen from equation 2.2.9 that the temperature of equilibration at a given pressure is calculated simply with knowledge of K_{eq} for this reaction. The concept of the equilibrium constant was first described by Waage & Guldberg (1864), who noted that 'where a system is at equilibrium, a constant value is established by the multiplicative product of the concentrations of the products (each raised first to the power of its coefficient), then divided by the multiplicative product of the reactants (each raised first to the power of its coefficient)'.

$$aA + bB \leftrightarrow cC + dD \tag{2.3.2}$$

In the case of the above generic relationship between four phases (A, B, C and D) in a system, the equilibrium constant may be written as:

$$K_{eq} = \frac{(a_C)^c (a_D)^d}{(a_A)^a (a_B)^b} \tag{2.3.3}$$

And for the garnet-biotite thermometer, K_{eq} is:

$$K_{eq} = \frac{(a_{ann})(a_{prp})}{(a_{phl})(a_{alm})} \tag{2.3.4}$$

The compositions of minerals exhibiting solid solution are often reported in mole proportions of end-members; however, this is not equivalent to activity unless mixing is ideal. For example, aluminosilicate garnet ($X_3Al_2Si_3O_{12}$) is a solid solution between four end-members, where X is a different divalent cation in each; almandine (Fe), pyrope (Mg), grossular (Ca) and spessartine (Mn). Determination of the activity of each end-member in a natural garnet requires an ionic model describing the crystallographic sites over which cations may mix. For ideal mixing of α cations on a single site, the activity of each component is related to the mole fraction by equation 2.3.5:

$$a_i = (X_j)^{\alpha} \tag{2.3.5}$$

Here, the activity of component *i* is the mole fraction of the cation *j* raised to the power of the number of sites over which that cation may exchange. In the case of biotite and aluminosilicate garnet, if it is assumed that the divalent cations ideally mix over a single site, the activity of almandine in garnet, for example, is expressed as:

$$a_{alm} = (X_{alm})^3 = \left(\frac{Fe}{Fe + Mg + Ca + Mn}\right)^3 \tag{2.3.6}$$

The calculation of end-member activities can become increasingly complex where minerals exhibit cation mixing over several sites, where mixing is not ideal or it involves coupled substitutions (e.g. Tschermak's exchange). However, these activities must be quantified in order to determine the equilibrium constant and thus calculate *P* or *T* conditions of interest. If ideal solutions are assumed for the garnet-biotite thermometer then the equilibrium constant may be written as:

$$K_{eq} = \left(\frac{X_{Fe}^{Bt} X_{Mg}^{Grt}}{X_{Mg}^{Bt} X_{Fe}^{Grt}} \right)^3 \tag{2.3.7}$$

For the discussion of element partitioning between minerals, Spear (1993) notes that it is common to use the term distribution coefficient (K_D) that is a reduced form of K_{eq} without any exponents:

$$K_D = \frac{X_{Fe}^{Bt} X_{Mg}^{Grt}}{X_{Mg}^{Bt} X_{Fe}^{Grt}} = \frac{(Mg/Fe)^{Grt}}{(Mg/Fe)^{Bt}} = \left(K_{eq}\right)^{\frac{1}{3}} \tag{2.3.8}$$

Experimental investigation of Fe–Mg partitioning between biotite and garnet at constant pressures quantifies K_D and provides a link between the theoretical basis described above and natural samples. Thus, *P*–*T* space may be contoured for values of K_D for a particular reaction, for example as shown in Fig. 2.1a using the experimental data of Ferry & Spear (1978) for the garnet-biotite thermometer.

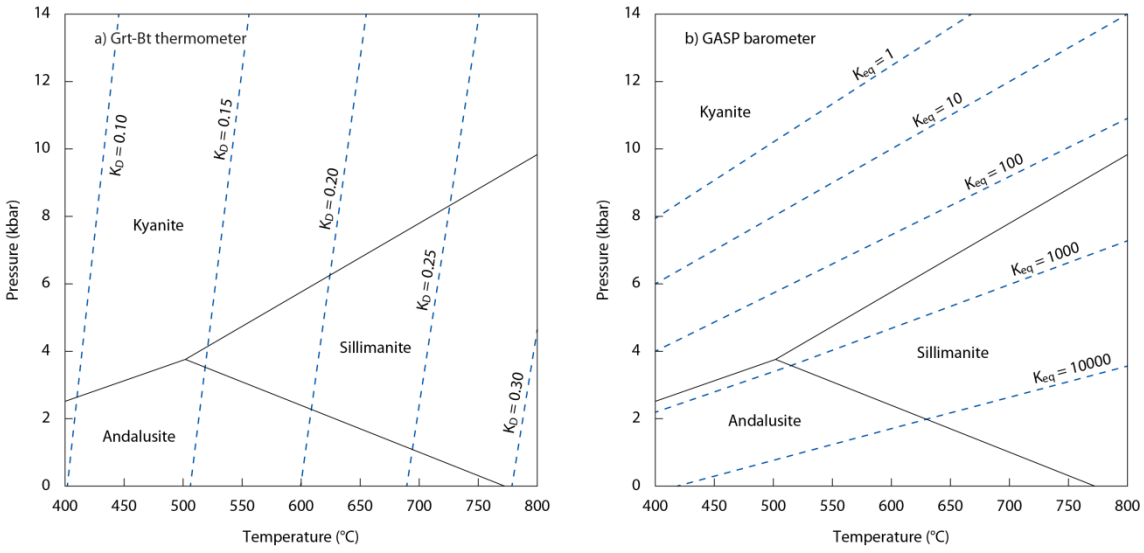


Fig. 2.1 – Distribution coefficient and equilibrium constant contouring of *P–T* space for (a) the Grt-Bt thermometer and (b) the GASP barometer (after Spear, 1993).

2.3.1.2. Geobarometry

While cation exchange reactions are mostly temperature sensitive, the consumption and production of mineral species is strongly pressure sensitive if the product and reactant assemblages have very

different molar volumes (i.e. densities). Here, a reaction has a large ΔV and is a good geobarometer. A common example is the garnet-aluminosilicate-silica-plagioclase (GASP) barometer that involves the exchange of Ca between plagioclase and garnet through the following relationship:

$$\underset{\textit{anorthite}}{3\ CaAl_2Si_2O_8} = \underset{\textit{grossular}}{Ca_3Al_2Si_3O_{12}} + \underset{\textit{kyanite}}{2\ Al_2SiO_5} + \underset{\textit{quartz}}{SiO_2} \tag{2.3.9}$$

Although the form of Al_2SiO_5 used here is kyanite, any polymorph may participate in this reaction. As before, by assuming ideal mixing and simple ionic solution models, the equilibrium constant is:

$$K_{eq} = \frac{X_{grs}^{Grt}\left(X_{Al2SiO5}^{Ky}\right)^2 X_{SiO2}^{Qz}}{\left(X_{an}^{Pl}\right)^3} = \frac{X_{grs}^{Grt}}{\left(X_{an}^{Pl}\right)^3} \tag{2.3.10}$$

As a result of aluminosilicate and quartz both exhibiting negligible solid solution, their activities are both set to 1 and are thus eliminated from the calculation. Experimental data for this reaction have been reported by Koziol & Newton (1988), which allows the contouring of *P*–*T* space for K_{eq}. For a rock containing pure grossular, anorthite, quartz and kyanite, where the activity of all phases is equal to 1, it can be seen that the above reaction would take place at high-pressure along the isoline labelled $K_{eq} = 1$ in Fig. 2.1b. More commonly, where solid solution occurs and the activities of grossular in garnet and anorthite in plagioclase are reduced, reaction 2.3.9 occurs at lower pressure conditions and is defined by a larger value of K_{eq} (Fig. 2.1b). Therefore, measurement of the ratio of grossular to anorthite content in the presence of quartz and aluminosilicate determines the value of K_{eq}, which can then be used to find the absolute pressure of equilibration for an assemblage (if an independent temperature estimate can be obtained).

2.3.1.3. Single phase ‘concentration thermobarometry’

Alongside cation exchange and net transfer reactions described above, an important and distinct type of thermobarometer uses the saturation concentration of a minor element in a single mineral. Thus, the concentration of the minor element may provide a pressure or temperature estimate if saturation levels are sensitive to these variables. Example thermometers include the Ti content of biotite (Henry *et al*., 2005), the Ti content of quartz (Wark & Watson, 2006) and the Zr content of rutile (Zack *et al*., 2004). Example barometers include the Al content of hornblende (Hammarstrom & Zen, 1986 and others) and the Ti content of phengite (Auzanneau *et al*., 2010).

If saturation conditions are not satisfied, so that the mineral in question incorporates a less-than-optimum concentration of the element in question, the calibration can provide limiting constraints. For example biotite that has recrystallised in the presence of ilmenite or rutile with a Ti content of 0.35 cations (per 22-oxygen formula unit) and an XMg = 0.5 suggests equilibration at a temperature of 685 °C with an associated uncertainty of ± 23 °C (Henry *et al*., 2005). If this analysis was taken in the absence of a Ti-saturating phase, so that the Ti content of the biotite was not maximised, this result would represent a minimum temperature of crystallisation.

2.3.1.4. Simultaneous solution of multiple independent reactions (AvePT)

Although individual geothermometers and geobarometers can provide single *P* or *T* conditions of equilibration, greater confidence is gained by the simultaneous solution of multiple independent reactions written between end-member phases in an equilibrium assemblage (Powell & Holland, 1994). In this study this is achieved using THERMOCALC version 3.33 and thermodynamic dataset ds55 (Powell & Holland, 1988; Holland & Powell, 1998, updated to August, 2004) in AvePT mode. Compositional analyses of phases judged to be in equilibrium (at the chosen stage of metamorphism) were recalculated into end-member activities for this process using the program AX (Holland, 2009).

The AvePT function provides substantial advantages over utilising individual conventional thermobarometers, in particular by providing detailed statistical information on the reliability and confidence level of the calculated result (see Powell & Holland, 1994). This information allows the user to exclude data that are suspected to be of a poor quality (e.g. from a phase not actually in chemical equilibrium with the rest of the assemblage). For calculations in this study, where fit indices exceeded the maximum allowable value for 95% confidence, the end-member with the most suspicious input activity (largest e*) was removed and the calculation re-run until all indices conformed (the χ^2 test, Powell & Holland, 1994). Additionally, AvePT allows the user to monitor the sensitivity of results to a variable fluid composition. In carbonate- or graphite-bearing rocks, AvePT may be employed over a range of XH_2O (where $XH_2O = H_2O/(H_2O+CO_2)$) in order to examine the resulting *P–T* conditions, or alternatively perform calculations in a fluid-absent environment. This gives much-improved flexibility over conventional thermobarometers, which in some cases may be only calibrated for particular rocks types or for restricted mineral compositional ranges.

2.3.2. Phase equilibria modelling

Phase equilibria modelling involves the relation of mineral assemblages and compositions observed in real rocks with calculated equilibrium assemblages that are represented graphically on a phase diagram. In this study, all such diagrams were constructed using THERMOCALC version 3.33 and thermodynamic dataset ds55 (Powell & Holland, 1988; Holland & Powell, 1998, updated to August, 2004). THERMOCALC constructs phase diagrams by solving sets of non-linear equations relating to an assemblage that represent balanced chemical reactions between end-members of phases that are in mutual equilibrium (i.e. they all satisfy equation 2.2.3). For each phase in a system that exhibits solid solution and contains e_k end-members, there are $e_k - 1$ compositional variables. So for P phases in an equilibrium assemblage, the number of end-members of phases (S) and compositional variables are determined by equations 2.3.11 and 2.3.12 respectively:

$$\sum_{k=1}^{P} e_k = S \qquad (2.3.11) \qquad \sum_{k=1}^{P} (e_k - 1) = S - P \qquad (2.3.12)$$

The number of independent reactions between these phases is equal to the number of components subtracted from the number of end-members, $S - C$, which is also equal to the number of unknowns that can be solved for (Powell & Holland, 1998). Thus, at equilibrium, there exist a total of $S - P + 2$ variables, which is equal to the number of compositional variables (equation 2.3.12) plus pressure and temperature. The total number of degrees of freedom (F) in the system is therefore the number of variables ($S - P + 2$) minus the number of solvable unknowns ($S - C$):

$$F = C - P + 2 \qquad (2.3.13)$$

This relationship is termed the Gibbs phase rule, and is of fundamental importance to the construction of phase diagrams.

Once a model chemical system and phases of interest in a rock have been identified, the various equilibria between those phases may be graphically presented in many ways. A ‘total phase diagram’ contains all of the phase equilibria in a system, so is able to define all possible stable assemblages, phase proportions and compositions in the limits of interest in *P–T–X* space. The number of axes required to describe a total phase diagram depends upon the number of components in that system, such that a total phase diagram in an n-component system would have axes of pressure, temperature and $n - 1$ independent compositional axes. However, as the graphical

representation and interpretation of 3-dimensional diagrams is challenging, it it often the case that lower-dimension representations of a total phase diagram are constructed instead. These include projections, sections and pseudosections, which are all 2-dimensional.

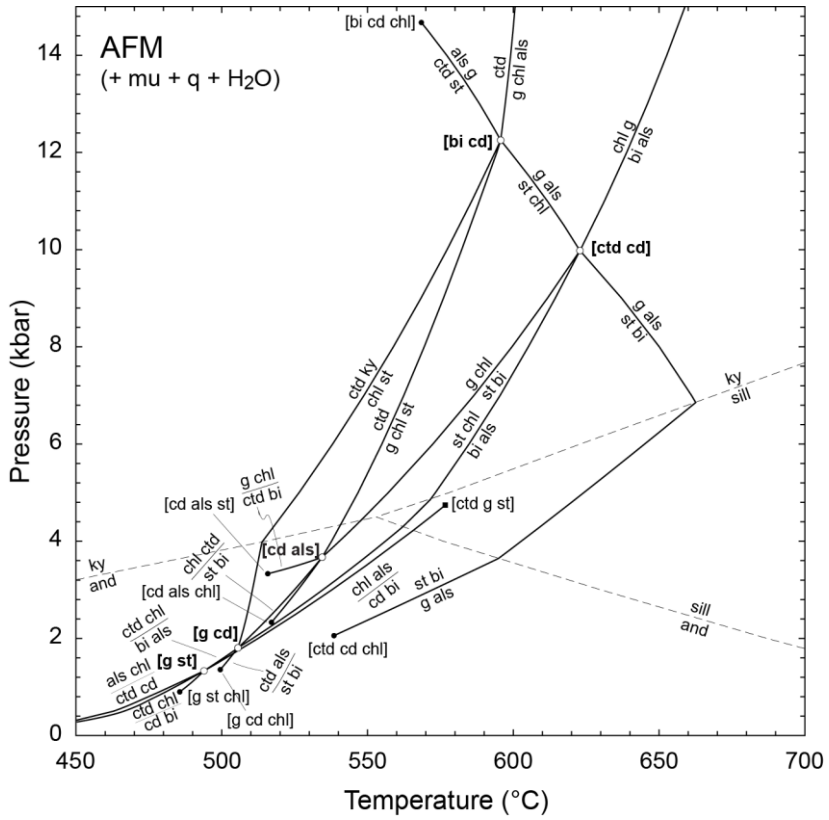


Fig. 2.2 – Example *P–T* projection(from Powell *et al.*, 1998).

Information from a total phase diagram can be *projected* onto an appropriate plane of reference. For example, projection can be made from all compositional variables onto *P–T* space to produce a '*P–T* projection' or 'petrogenetic grid' (Fig. 2.2). Such projections show all possible equilibria between considered phases in *P–T* space, although specific bulk compositions will only experience a small number of this total set. Furthermore, in order to keep such diagrams simple enough to visually interpret, model systems cannot contain large numbers of components, limiting their value for comparison with natural systems.

A total phase diagram may alternatively be *sectioned* with respect to an intensive variable (P, T or μ_i) or extensive variable (S, V or n_i). In the former case, all calculated assemblages will lie in the plane of the section as the value of any intensive variable is equal in all phases. In the latter case, compositions of phases in the system do not lie in a single sectioned plane and the calculated phase diagram is referred to as a *pseudosection* as a result. The most common (and useful) pseudosections

are those where the sectioning variable specifies the system's total composition and the two remaining variables (axes) are *P* and *T*, yielding a *P*–*T* pseudosection (Fig. 2.3). As such, the construction of a pseudosection by solving sets of non-linear equations for equilibrium relationships involves the simultaneous consideration of sets of equations describing mass balance constraints. These constraints require the phase compositions and proportions in each calculated assemblage to sum to the bulk rock composition. As a result, the equilibrium state of the (closed) system may be completely defined by two independent variables (a result known as Duhem's theorem). Hence, each *P*–*T* pseudosection uniquely portrays the equilibrium assemblages that occur in a rock composition.

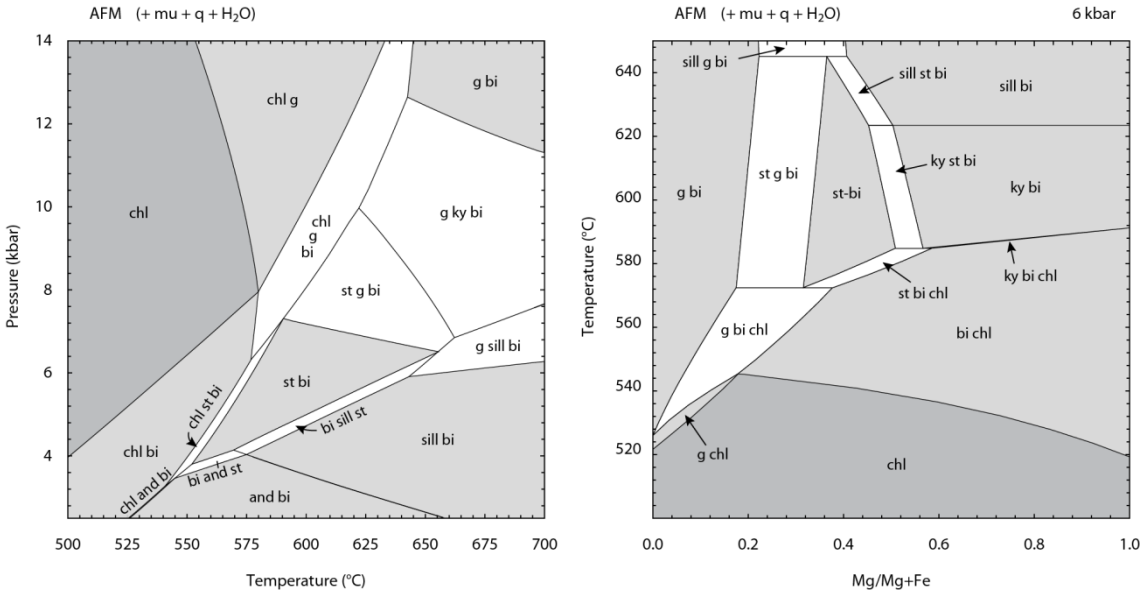


Fig. 2.3 – Example *P*–*T* and *T*–*X* pseudosection (from Powell *et al.*, 1998).

An alternative form of pseudosection fixes either *P* or *T* at a constant value and considers a compositional variable axis instead (Fig. 2.3). These *T*–*X* and *P*–*X* pseudosections can be used in many ways, for example to test the sensitivity of phase relations to a compositional variable (such as XMg) and can provide brackets for this value based on an observed assemblage. Alternatively the effects of metasomatism, retrogressive alteration and extraction or addition of partial melt may be investigated with the relevant choice of compositional vector.

2.3.3. Limitations and uncertainties

There are numerous sources of error that must be considered when employing any kind of thermobarometry. A fundamental source of uncertainty arises from whether the metamorphic mineral assemblage being used has achieved full equilibrium. The degree of equilibrium may be

assessed qualitatively by textural (microstructural) criteria that can suggest which minerals are most likely to represent a stable assemblage. For example, minerals that have formed through retrograde reaction (i.e. are not part of a peak assemblage) can be omitted from calculations. A quantitative assessment of equilibrium can be made with compositional criteria by simultaneously employing multiple thermobarometers. Here, all independent estimates of equilibration conditions should converge on a restricted region of *P–T* space if mutual equilibrium was achieved. This is commonly achieved with programs that can solve sets of independent reactions simultaneously, for example THERMOCALC in AvePT mode (as described in chapter 2.3.1.4).

A limitation to both conventional thermobarometers and phase diagrams is the reliance on idealised model systems, whereby omitted elements may significantly alter the stability of certain phases in *P–T* space (e.g. Mn in garnet, Zn in staurolite, Ti in biotite). Consideration of such components, that are otherwise unaccounted for, can cause considerable departure from formerly-calculated conditions. This also includes uncertainty regarding the oxidation state of certain cations in a phase (in particular, the Fe^{3+}/Fe^{total} ratio), which cannot be obtained through microprobe analysis, so must be estimated or calculated in another way. In the case of conventional thermobarometry this problem can be circumvented by strictly following the compositional constraints that are reported for each calibration. In addition, where thermobarometric calibrations are formulated experimentally (rather than empirically), extrapolation outside of the considered *P–T–X* ranges may propagate uncertainty in an unpredictable fashion.

A somewhat unavoidable source of uncertainty results from variation in experimental techniques and machine precision in different laboratories worldwide. Values for thermodynamic parameters such as *H, S* and *V* for individual phases are determined by such experiments and are therefore subject to both random and systematic uncertainty. This issue is avoided in the case of phase equilibria modelling where large datasets slightly adjust these data within their error brackets to make all values internally-consistent (cf. Holland & Powell, 1998).

An important source of uncertainty for conventional thermobarometry lies in the choice of activity models that are used to describe solid solutions in minerals of interest. For example, the GASP geobarometer assumes ionic solution models with ideal mixing; however, mixing in natural garnet and plagioclase is known to be non-ideal (Orville, 1972; Spear, 1993). More sophisticated

models that can better replicate observed traits require additional terms to describe the excess Gibbs free energy of mixing at intermediate compositions between two end-members, such as activity coefficients and interaction parameters (e.g. Green & Usdansky, 1986). Although, these values potentially carry large uncertainties themselves as a result of the difficulty in constraining them experimentally, they are employed in the vast majority of cases for activity-composition relationships used in THERMOCALC.

2.4. Pseudosection construction and analysis

The construction and interpretation of pseudosections is the preferred method of investigation of the tectonothermal evolution of metamorphic rocks (e.g. Vance & Mahar, 1998; Powell & Holland, 2008) and was chosen as the main interpretive tool for most samples in this project. The ability to define equilibrium relationships between minerals at different *P*–*T* conditions for a sample-specific bulk composition makes pseudosections extremely flexible for examining different stages in a rock's evolution. In addition, the ever-improving activity-composition relationships for minerals (e.g. Diener *et al*., 2007; White *et al*., 2000, 2005) and expansion of internally-consistent thermodynamic datasets (Holland & Powell, 1998, 2011) results in increasing reliability and accuracy in replicating natural chemical systems. Additionally, the potential accuracy of pseudosection construction and interpretation overshadows most conventional thermobarometry, where uncertainties on calculated *P*–*T* conditions are commonly at least ±1 kbar and ±50 °C (at 2σ; Powell & Holland, 2008). Calculated assemblage fields on a pseudosection that are relevant to observed assemblages may be much smaller than these aforementioned errors, or otherwise refinement of *P*–*T* conditions within large fields may be achieved by correlating observed modal proportions and individual compositions of phases with calculated values. All pseudosections presented in this study were constructed following the method of Powell *et al*. (1998) using THERMOCALC v3.33 and thermodynamic dataset ds55 (Powell & Holland, 1988; Holland & Powell, 1998; updated to August, 2004).

2.4.1. Model systems and activity-composition models

The model system chosen for thermodynamic modelling is a necessary simplification of a natural chemical system and the choice of components is effectively limited by the activity-composition relationships available for minerals of interest. The more components that comprise this model

system, the better the resulting phase diagram should reproduce the modelled sample. In this thesis pseudosection modelling was performed for samples from the KMC (chapter 4), the TMM (chapter 5) and the DNCV (chapter 7).

Samples from the KMC were modelled in the 11 component system MnO–Na_2O–CaO–K_2O–FeO–MgO–Al_2O_3–SiO_2–H_2O–TiO_2–O (MnNCKFMASHTO) considering the following solid solution models: silicate melt (White *et al.*, 2007), cordierite and staurolite (Mahar *et al.*, 1997; Holland & Powell, 1998), garnet and ilmenite (White *et al.*, 2005), chloritoid (White *et al.*, 2000; Mahar *et al.*, 1997), chlorite (Mahar *et al.*, 1997; Holland *et al.*, 1998), biotite (Mn-bearing model; White *et al.*, 2007), muscovite and paragonite (Coggon & Holland, 2002), K-feldspar and plagioclase (Holland & Powell, 2003), epidote (Holland & Powell, 1998) and magnetite (White *et al.*, 2000). Additional pure phases included andalusite, kyanite, sillimanite, rutile, quartz and H_2O.

Sample L08-03A from the TMM was modelled in the 10 component system Na_2O–CaO–K_2O–FeO–MgO–Al_2O_3–SiO_2–H_2O–TiO_2–O (NCKFMASHTO). Calculations at (U)HP conditions considered the following solid solution models: glaucophane, actinolite and hornblende (Diener *et al.*, 2007), diopside, omphacite and jadeite (Green *et al.*, 2007), muscovite and paragonite (Coggon & Holland, 2002), talc and epidote (Holland & Powell, 1998), chloritoid, magnetite, ilmenite and hematite (White *et al.*, 2000), chlorite (Holland *et al.*, 1998), garnet (White *et al.*, 2007), plagioclase and K-feldspar (Holland & Powell, 2003). Pure phases included clinozoisite, lawsonite, albite, rutile, titanite, quartz, coesite and H_2O. Calculations at LP conditions additionally included solid solution models for cummingtonite (Diener *et al.*, 2007) and biotite (Mn-bearing model; White *et al.*, 2007).

Sample DNCV01 from the DNCV metamorphic complex was modelled in the 11 component system MnNCKFMASHTO considering the following solid solution models: silicate melt (White *et al.*, 2007), cordierite (Mahar *et al.*, 1997; Holland & Powell, 1998), garnet and ilmenite (White *et al.*, 2005), orthopyroxene (White *et al.*, 2002), chlorite (Mahar *et al.*, 1997; Holland *et al.*, 1998), biotite (Ti-bearing model; White *et al.*, 2007), muscovite (Coggon & Holland, 2002), K-feldspar and plagioclase (Holland & Powell, 2003) and magnetite (suprasolidus model; White *et al.*, 2002). Pure phases included andalusite, kyanite, sillimanite, rutile, quartz and H_2O.

In each case, not all considered phases were necessarily calculated to be stable in the relevant *P*–*T* limits of each pseudosection and some were included in order to define limits to assemblage

fields of interest. Sample-specific detail regarding bulk composition calculations, thermodynamic modelling procedures and general analytical techniques is described in the relevant chapters.

2.4.2. Bulk composition calculation

Pseudosection construction follows Duhem's theorem and thus requires a unique bulk composition to be specified for each modelled sample – THERMOCALC requires this to be expressed in terms of proportions of oxide components. The process of obtaining a bulk composition suitable for modelling is non-trivial, as the full (actual) bulk composition of a sample of metamorphic rock can be calculated and subsequently reduced in various ways. Techniques such as X-ray fluorescence (XRF) are able to provide a full elemental analysis of a sample of rock; however, this method does not account for the existence of partial disequilibrium or compositional zoning in porphyroblasts, and also assumes that the analysed portion is representative of the rock as a whole. Furthermore, XRF cannot distinguish between different ion valence states and also provides contributions from elements that are not included in the model system and need to be accommodated for on reduction.

A more effective method that avoids many of these shortcomings is provided by the calculation of modal proportions and representative compositions of major modellable minerals (e.g. Meyre *et al*., 1997; Carson *et al*., 1999). In this way, the *actual* bulk composition is manually reduced to a *modellable* bulk composition by the omission of unmodellable phases. Crucially, this method allows for accommodation of partial disequilibrium whereby domains judged on textural or compositional criteria to be out of equilibrium with the larger reacting volume can be excluded from the bulk compositional contribution. Thus, even though some phases may be reproducible in a model, if they are part of a domain that is outside of the equilibration volume, they are excluded from the *effective* bulk composition. This method also ensures that the compositions and proportions of phases calculated through thermodynamic modelling may be directly compared to those in the thin section of interest. As the calculation of an equilibration volume, and hence the effective bulk composition, is the primary control on the geometry of a pseudosection (Stüwe, 1997), all bulk compositions were calculated using this latter method. Modal proportions of considered phases were obtained through analysis of thin section and SEM BSE images of representative areas (Fig. 2.4), the latter using the area calculation tool provided in the SEM imaging software.

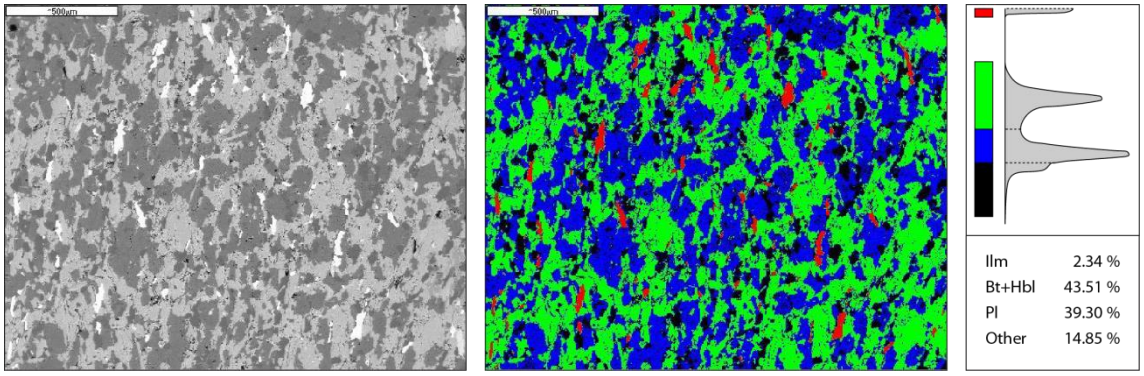


Fig. 2.4 – Example SEM BSE contrast image used for modal proportion calculations through inspection of individual mineral species count intensity. These proportions are then used in bulk composition calculations.

Representative compositions of each relevant mineral species were obtained through SEM-microprobe analysis following the techniques described below in chapter 2.4.3. Where phase compositions varied throughout petrographic position, analyses were chosen of phases that were judged to be in mutual equilibrium with each other at the desired conditions e.g. mica from the matrix foliation instead of included grains for the calculation of peak *P*–*T* conditions. Garnet was commonly observed to be internally chemically heterogeneous and a compositional contribution was obtained by the integration of concentric shells, assuming spherical geometry.

Accessory phases containing components outside of each model system were not considered for the bulk rock composition calculations (e.g. apatite). Omission of accessory phases in these cases is justified due to their total volume contribution being negligible compared to the bulk rock volume under analysis. To date, activity-composition relationships for use with internally-consistent dataset ds55 mostly consider major rock-forming minerals, although thermodynamic modelling of zircon has been successfully undertaken by Kelsey & Powell (2011).

2.4.3. SEM-microprobe analysis methodology and analytical conditions

For each studied sample, multiple thin sections were examined using a petrographic microscope in order to determine characteristic mineral assemblages and microstructural evidence for the sequence of deformation events and mineral growth. Representative polished thin sections were chosen for further examination in order to obtain mineral compositional data for use in thermobarometry and phase diagram construction. All chemical analyses were performed in the University of Oxford Earth Science Department on a JEOL JSM-840A SEM-microprobe equipped with an Oxford Instruments

Isis 300 energy-dispersive analytical system. Operating conditions were consistent for all analyses, including a working distance of 15 mm, an acceleration voltage of 20.0 kV and a beam current of 6.00 nA. The beam current was checked regularly and the count rate calibrated every 120 minutes using a pure cobalt metal standard. The instrument was calibrated for the analysed elements with a range of natural and synthetic standards and a ZAF correction procedure was applied. Each point analysis was performed for a 100 second live time and multiple analyses were obtained across individual grains and throughout each sample in order to determine the extent of chemical heterogeneity. Compositional profiles across garnets were determined by accumulating counts along a 256-channel line scan for approximately 45 minutes. The profiles were corrected for background counts and calibrated against six point analyses taken at known positions along the profile in order to calculate mole fractions of garnet end-members. Multiple lines and point analyses were taken across each garnet as a check to ensure that compositional zoning was concentric and similar in all directions. For particular grains of interest, compositional maps were obtained via a cumulative area scan for approximately 30 minutes at the same operating conditions as for point and line analyses.

Anhydrous phase compositions were calculated to standard numbers of oxygens per formula unit (Deer *et al.*, 1992) whereas mica compositions were calculated to a total of 11, epidote-group minerals to 12.5, amphibole to 23, chlorite to 28 and staurolite to 46 oxygens. For hydrous phases, H_2O content was assumed to be present in stoichiometric amounts (except for biotite in sample DNCV01; see chapter 7.4.1). Amphibole analyses were transformed to the general chemical formula $AB_2{}^{VI}C_5{}^{IV}T_8O_{22}(OH)_2$ according to the method of Leake *et al*. (1997) to allow estimation of Fe^{3+} and individual cation site allocations. For all mineral species aside from amphibole, where stoichiometric criteria can be applied, the proportion of Fe^{3+}/Fe^{total} was calculated from SEM-microprobe analyses using the software AX (Holland, 2009). Mineral compositions presented in tables that show a proportion of Fe_2O_3 represent original SEM-microprobe analyses that have been recalculated through AX in order to calculate this value. All mineral abbreviations in the text, figures, and tables of this thesis follow the guidelines given by Whitney & Evans (2010).

3. U–Th–Pb geochronology

In the late 19th century the physicist William Thompson, later to become Lord Kelvin, published a landmark paper suggesting that the age of the Earth lay between 20 and 400 Ma, based upon the length of time required for a homogeneous molten Earth to cool to its current surface temperature (Kelvin, 1863). Critically, however, Kelvin did not consider convection in a layered Earth, nor did he envisage any additional sources of heat. As a result even the upper limit of this range fell far short of that required to account for many geological phenomena. Insight into this 'young Earth' problem was provided approximately 30 years later by the French chemist Henri Becquerel who accidentally discovered radioactivity whilst investigating phosphorescence in uranium salts (Becquerel, 1896). Subsequent investigation of this phenomenon has had a major impact on the field of geology, as radioactive decay provides a means by which the age of the Earth, or individual rocks in it, can be determined absolutely and thus allows the timescales and rates of major tectonic processes to be measured accurately. This chapter summarises the methodology and scope of this technique.

3.1. The principles of radioactive decay

Radioactive decay describes the probability that a constituent particle of the nucleus of an atom will overcome the potential energy barrier binding it to the nucleus, therefore escaping from the atom and creating a new nuclide. In addition, the rate of radioactive decay is exponential and independent of varying physical or chemical conditions that may occur in the Earth (Rutherford & Soddy, 1902). In the following discussion the term 'parent' is applied to the radioactive atom at the start of a decay chain, which ultimately produces a stable 'daughter' atom at the end of the decay chain, with several intermediate radioactive nuclides in-between.

The rate of decay of any parent atom is directly proportional to the number of those atoms (N) present in the system at any time (t) through the following relationship:

$$-\frac{dN}{dt} \propto N \tag{3.1.1}$$

Variation in the rate of decay of different elements is represented by an associated decay constant (λ), which is assumed to have remained unchanged over the whole of Earth history:

$$-\frac{dN}{dt} = \lambda N \tag{3.1.2}$$

This equation can then be rearranged to relate the number of parent atoms present at any time since decay began to the initial number of parent atoms (N_0):

$$\frac{N}{N_0} = e^{-\lambda t} \tag{3.1.3}$$

If no radiogenic daughter atoms are present at the start of decay ($t = 0$), then the total number that have been produced by decay (D^*) at any time can be related to N_0 via the following relationship:

$$D^* = N_0\left(1 - e^{-\lambda t}\right) \tag{3.1.4}$$

Alternatively, if the original number of parent atoms is unknown, D^* may then be related simply to N by rearranging and substituting equation 3.1.3:

$$D^* = N\left(e^{\lambda t} - 1\right) \tag{3.1.5}$$

In the latter case, which is relevant to most geological problems, the total number of daughter atoms (D_{tot}) present in a system is the sum of those initially present (D_0) at the start of decay and those that have been produced as a result of the decay process:

$$D_{tot} = D_0 + D^* \tag{3.1.6}$$

As such, a fundamental relationship can be found between the number of parent and daughter atoms in a system and the time elapsed since the start of decay:

$$D_{tot} = D_0 + N\left(e^{\lambda t} - 1\right) \tag{3.1.7}$$

Analysis of a sample via mass spectrometry allows measurement of D_{tot} and N, whereas D_0 may be assumed or calculated based on the known behaviour of individual metamorphic minerals. As the decay constant for a particular radioactive isotope is known, this equation may then be solved for t, allowing the calculation of an age since decay initiated.

3.2. U–Th–Pb systematics

Uranium has three naturally occurring radioactive isotopes, ^{238}U, ^{235}U and ^{234}U, although only ^{238}U and ^{235}U exist in sufficient abundance to be used for geochronology (Table 3.1). These two parent isotopes ultimately produce the stable daughter isotopes ^{206}Pb and ^{207}Pb through the *'uranium series'* and *'actinium series'* respectively; ^{234}U exists solely as an intermediate nuclide in the uranium series (Fig. 3.1). Thorium exists in nature almost exclusively as ^{232}Th and ultimately produces the stable daughter isotope ^{208}Pb through the *'thorium series'* (Fig. 3.1).

Isotope	Abundance (%)	Decay constant (λ)	Half life (yr)
^{238}U	99.274	1.551 x 10^{-10}	4.468 x 10^{9}
^{235}U	0.721	9.849 x 10^{-10}	0.704 x 10^{9}
^{232}Th	100.000	4.948 x 10^{-11}	14.01 x 10^{9}

Table 3.1 – Properties of the main radioactive isotopes of U and Th (from Wetherill, 1966; Steiger & Jäger, 1977).

The total decay schemes for these isotopes involve the emission of α and β radiation and the release of energy as follows:

$$^{238}U \rightarrow {}^{206}Pb + 8\alpha + 6\beta^{-} + 47.4 \text{ MeV/atom} \quad (3.2.1)$$

$$^{235}U \rightarrow {}^{207}Pb + 7\alpha + 4\beta^{-} + 45.2 \text{ MeV/atom} \quad (3.2.2)$$

$$^{232}Th \rightarrow {}^{208}Pb + 6\alpha + 4\beta^{-} + 39.8 \text{ MeV/atom} \quad (3.2.3)$$

Although intermediate daughter nuclides exist in these decay schemes (Fig. 3.1), the half lives of the parent U and Th isotopes are many orders of magnitude longer than these products (Faure, 1986). As such, the production rate of each stable Pb isotope is limited by the rate of decay of each parent, so U and Th are effectively considered to decay directly to Pb in a state of so-called secular equilibrium.

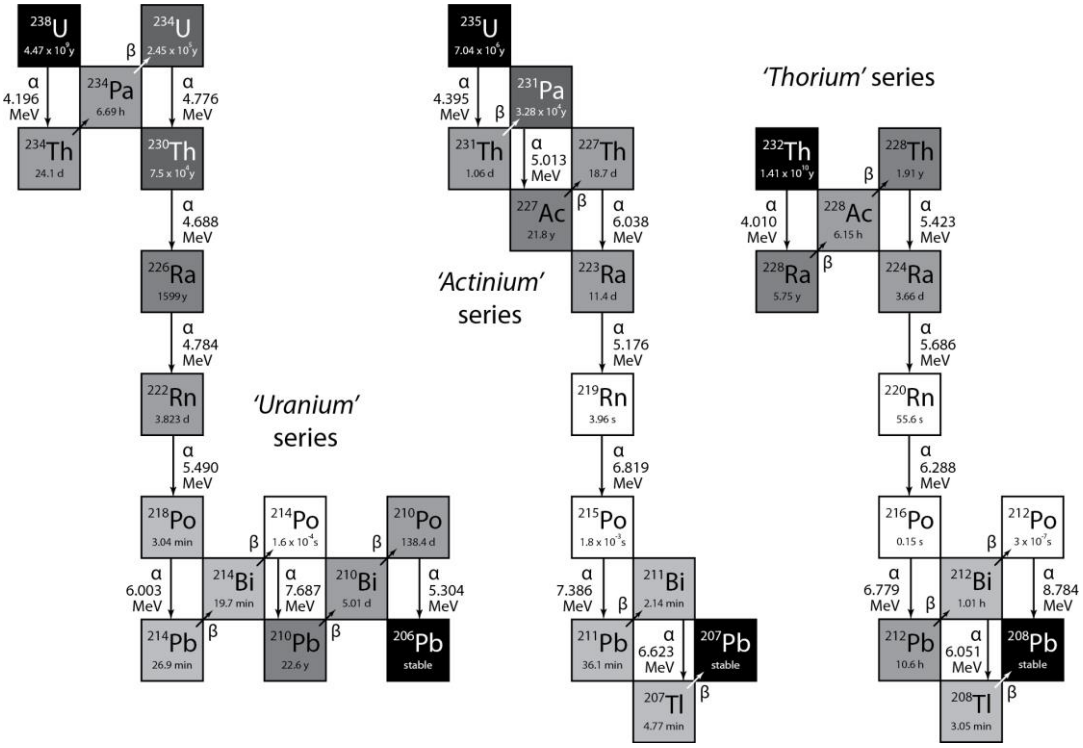


Fig. 3.1 – Schematic representation of the ^{238}U, ^{235}U and ^{232}Th decay schemes (after Faure, 1986). Greyscale reflects half life, with darker shades representing longer half lives.

The production of each daughter Pb isotope is defined by the following governing equations, where concentrations are normalised to ^{204}Pb, the sole non-radiogenic lead isotope (Faure, 1986):

$$\left(\frac{^{206}Pb}{^{204}Pb}\right)_t = \left(\frac{^{206}Pb}{^{204}Pb}\right)_0 + \left(\frac{^{238}U}{^{204}Pb}\right)_t \cdot \left(e^{\lambda_{238}^t} - 1\right) \quad (3.2.4)$$

$$\left(\frac{^{207}Pb}{^{204}Pb}\right)_t = \left(\frac{^{207}Pb}{^{204}Pb}\right)_0 + \left(\frac{^{235}U}{^{204}Pb}\right)_t \cdot \left(e^{\lambda_{235}^t} - 1\right) \quad (3.2.5)$$

$$\left(\frac{^{208}Pb}{^{204}Pb}\right)_t = \left(\frac{^{208}Pb}{^{204}Pb}\right)_0 + \left(\frac{^{232}Th}{^{204}Pb}\right)_t \cdot \left(e^{\lambda_{232}^t} - 1\right) \quad (3.2.6)$$

Three independent ages may be obtained by solving these equations for time, all of which should be similar within error (*concordant*), provided various conditions are met. Where these ages do not agree (are *discordant*), any of a range of factors may be responsible; the causes of this discrepancy and the interpretation of such data are discussed below.

3.3. Uncertainty on calculated ages and the interpretation of U–Pb data

The accuracy and reliability of a calculated age depend on multiple assumptions. Most importantly the mineral under examination is assumed to have remained closed to the loss or gain of parent or daughter atoms since radioactive decay began. From equations 3.24–3.26 it can be seen that the initial number of daughter atoms must also be known (or can be estimated with confidence) and the current number of parent and daughter atoms must be measured accurately using mass spectrometry. Additionally, it is assumed that the relevant decay constant is precisely known and has remained the same over the whole of Earth history. If these conditions are met, ages calculated from equations 3.24–3.26 will be in agreement; yet, as this is often not the case, a variety of methods have been developed to assess the reasons behind disagreements and aid the interpretation of discordant data.

The U–Pb isotope system is uniquely useful for dating of geological materials, as two independent age determinations can be obtained through a single measurement of U and Pb concentrations in a mineral (via the uranium and actinium decay series). The classical interpretation of such U–Pb data is performed on a Wetherill plot, which plots $^{207}Pb/^{235}U$ concentration against $^{206}Pb/^{238}U$ concentration (Fig. 3.2a). The solution to equation 3.1.5 for both U–Pb decay series over geological time produces a curve known as concordia, which is the geometric locus of concordant analyses/ages satisfying all assumptions outlined above. Discordant analyses may plot either above or below concordia and are interpreted using a straight line best-fit (called discordia) plotted through

these points (Fig. 3.2a). Discordia may occur on a Wetherill plot as a result of continual or episodic loss of Pb (or gain of U) from the analysed mineral at some time after initial crystallisation. This is commonly as a result of a high-temperature metamorphic overprint reaching conditions above the closure temperature of the mineral in question and allowing for open system behaviour of U or Pb through cation diffusion. The discordia chord may intersect concordia curve at either one or two locations. The upper (older) intercept, which should always be present, is inferred to represent the time of initial formation of the analysed minerals and when U–Pb decay began (Wetherill 1956a). The lower (younger) intercept, if present, is taken to represent the timing of a later episode of Pb loss (or U gain), for example a metamorphic overprint (Wetherill, 1965b).

Although the Wetherill plot is used extensively for the interpretation of Precambrian U–Pb data, the curvature of concordia becomes extremely weak for Phanerozoic ages, approximating a straight line for Tertiary ages and younger. As a result, discordia chords for such young analyses can plot sub-parallel to concordia, hindering interpretation and leading to large uncertainties for intercepts. It follows, therefore, that this plot is unsuitable for the analysis of 'Himalayan' data.

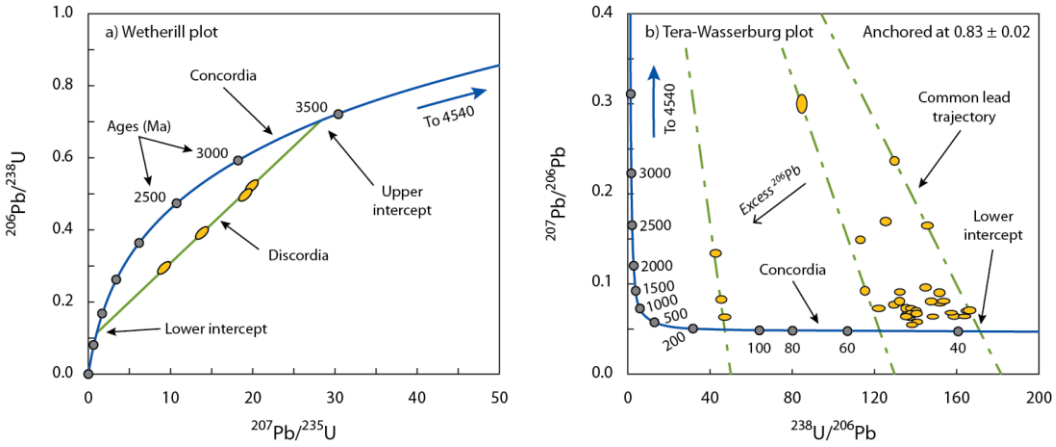


Fig. 3.2 – Idealised plots for the interpretation of U–Pb data illustrating associated nomenclature (a) Wetherill plot (b) Tera-Wasserburg plot.

An alternative method of interpretation for such young data is performed on a Tera-Wasserburg plot, which plots $^{207}Pb/^{206}Pb$ concentration against $^{238}U/^{206}Pb$ concentration (Fig. 3.2b). Due to the different gradient of curvature of concordia on a Tera-Wasserburg plot, significantly higher resolution is obtained when interpreting young age data. As with Wetherill plots, discordant data may occur as a result of open system behaviour during later metamorphism if temperatures are sufficient for the mineral in question to allow intracrystalline diffusion of U and/or Pb and so modify

the $^{207}Pb/^{206}Pb$ and $^{238}U/^{206}Pb$ ratios acquired at the time of first growth. Alternatively, a cause of discordia that results in data points trending towards the origin on a Tera-Wasserburg plot is that of 'excess ^{206}Pb' where a disequilibrium amount of daughter ^{206}Pb is present, when compared to the amount of parent ^{238}U (Fig. 3.2). This may result from either the incorporation of radiogenic ^{230}Th during monazite crustallisation, an intermediate isotope in the $^{238}U–^{206}Pb$ decay scheme (Fig. 3.1), or by inclusion of additional ^{206}Pb that was produced during an earlier (and presumably disparate) episode of ^{238}U radiogenic decay. The former case is more likely as Th and U are considerably more compatible with monazite than Pb (Parrish, 1990); however, either may cause a wide spread of data if different grains (or internal domains) behaved significantly differently during crystallisation.

Data populations on Tera-Wasserburg plots are interpreted with straight-line regressions termed 'common lead trajectories'. Upper intercepts for trajectories may be anchored at assumed initial $^{207}Pb/^{206}Pb$ ratios obtained during crystallisation (cf. Stacey & Kramers, 1975), or calculated where analysed monazite contains sufficient variation in common lead concentrations throughout the grain. Such trajectories can also bracket durations of crystallisation for protracted metamorphic or anatectic events (e.g. Kellett *et al*., 2010; Palin *et al*., 2013). Tera-Wasserburg plots are used in the analysis of all U–Pb geochronological data in this study, with sample-specific methods used to interpret ages and their geological implications. Detailed accounts of these individual interpretation methods are provided in chapter 3.5.2 and the relevant regional study (chapters 4–7).

3.4. Monazite geochronology

Monazite is a rare earth element (REE) phosphate commonly found as an accessory mineral in metaluminous and peraluminous granitic and metapelitic rocks (Spear & Pyle, 2002). It is often the *mineral of choice* for geochronological work on these lithologies due to its propensity for incorporation of high concentrations of Th and U (Kohn & Malloy, 2004) alongside very low initial concentrations of common lead (Parrish, 1990). Monazite is also extremely resistant to U–Th–Pb internal diffusion at temperatures less than 900 °C (Cherniak *et al*., 2004), which can allow successive phases of growth to be recorded in a rock that has undergone multiple metamorphic episodes (e.g. Kohn *et al*., 2005). Furthermore, geochronological analysis using *in-situ* laser ablation from thin section can provide a robust petrographic context to any age data obtained (e.g. Foster &

Parrish, 2003; Foster *et al*., 2004). For example, monazite included in garnet can potentially become isolated from the reacting matrix, allowing evidence of former metamorphic events to be preserved, even if matrix crystals are partially reset during subsequent metamorphism (Montel *et al.,* 2000).

3.4.1. The occurrence of monazite in metasedimentary rocks

Isotope geochronology allows a geologist the valuable opportunity to assign absolute ages to a metamorphic or igneous rock by dating the radiogenic minerals within. By associating these ages with calculated *P–T* conditions of metamorphism and deformation, insight is gained into the tectonic processes involved in its formation. However, it is the responsibility of the geologist to make interpretations on exactly what those ages signify, avoiding common pitfalls. For example, an age obtained from a grain of monazite included in a garnet does not necessarily date the timing of host garnet growth. This uncertainty can be significantly reduced if a direct chemical, petrographic or textural link can be made between the timing of growth of the dated mineral and a significant event in the rock's history (e.g. major mineral growth). This non-trivial question '*at what point in a rock's metamorphic history did a particular grain of monazite grow*?' has invoked intense study in recent years and is actively researched today. The current understanding of this problem is outlined below.

Monazite has been reported in a range of metasedimentary rocks at-and-above the greenschist-facies (Spear & Pyle, 2002 and references therein) and is thought to be involved in metamorphic reactions with major (e.g. Foster & Parrish, 2003; Kohn & Malloy, 2004) and accessory minerals (e.g. Finger *et al*., 1998; Foster *et al*., 2000). In general, albeit strongly dependent on bulk composition, monazite in metasedimentary rocks occurs both at low- and high-grade, with allanite more stable at intermediate *P–T* conditions. In many cases, some monazite grains in low-grade metasedimentary rocks may be detrital in nature, as they are able to withstand sedimentation and diagenetic processes (Morton & Hallsworth, 1999). Although such grains are expected to become unstable during the early stages of metamorphism (below), detrital monazite has also been reported from greenschist and amphibolite-facies terranes (Williams, 2001; Krenn *et al*., 2008) While these detrital grains have only minor use for geochronological analysis of their host rocks, metamorphic overgrowths on inherited grains have also been reported (Janots *et al*., 2008) and as such can be valuable for age determinations. A detailed study of detrital monazite from

metamorphosed sandstones and conglomerates by Rasmussen & Muhling (2009) showed that such grains are commonly pseudomorphed by (or recrystallise into) metamorphic monazite and are often associated with neocrystallised chlorite, quartz and sericite.

With increasing metamorphic grade, allanite commonly takes over from monazite as the dominant REE-bearing accessory phase (Spear & Pyle, 2002). Mass balance calculations performed on a range of metapelitic rocks by Yang & Pattison (2006) showed that garnet and other major silicate minerals do not contain sufficient REEs to be initial low-grade precursors to allanite formation. Instead, textural evidence of allanite forming at the expense of low-grade monazite has been documented at 450 ± 25 °C (Fig. 3.3), roughly coincidental with the appearance of biotite (Wing *et al*., 2003) or chloritoid (Janots *et al*., 2008). Several reactions have been proposed for this transition based on commonly observed mineralogical associations in meta-marls (reaction 3.4.1; Wing *et al*., 2003), metapelites (reaction 3.4.2 – unbalanced; Janots *et al*., 2008) and metapsammites (reaction 3.4.3; Rasmussen & Muhling, 2009):

$$\text{3 monazite + 3 muscovite + 8 ankerite + 4 siderite + 9 quartz + 2 } H_2O \rightarrow \text{3 allanite + 3 biotite + apatite + 20 } CO_2 \quad (3.4.1)$$

$$\text{monazite + chlorite + anorthite ± hematite} \rightarrow \text{allanite + xenotime + apatite + chloritoid + fluid} \quad (3.4.2)$$

$$\text{3 monazite + chlorite + 11 } Ca^{2+} \text{ + 4 quartz} \rightarrow \text{3 allanite + apatite + 0.06 huttonite + 1.5 } LREE^{3+} \quad (3.4.3)$$

The reverse of these reactions can produce low-grade monazite from allanite breakdown during retrograde metamorphism and can thus date the timing of exhumation through the ~450 °C isotherm.

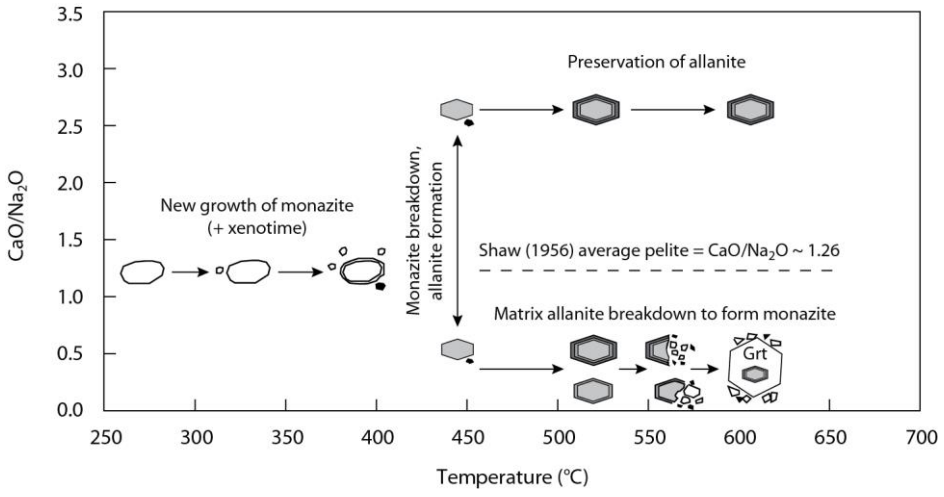


Fig. 3.3 – Temperature and bulk rock CaO/Na_2O controls on monazite and allanite stability (after Janots *et al*., 2008).

Monazite may reappear in a metasediment during prograde metamorphism as a result of the breakdown of allanite which, depending on its individual chemistry, may also form additional xenotime, plagioclase, epidote or clinozoisite (Janots *et al.*, 2008). The stability of allanite with increasing grade is strongly dependent on rock bulk composition and it may alternatively persist to high-temperatures in high-Ca metasediments (Fig. 3.3). In low-Ca bulk compositions, many studies have noted that the transition occurs in the middle amphibolite-facies, coincident with the staurolite or kyanite isograd and facilitated by the simultaneous breakdown of P-bearing phases such as apatite (Spear & Pyle, 2002; Kohn & Malloy, 2004; Janots *et al.*, 2008 and others). Textural relations observed in metapelitic bulk compositions by Wing *et al*. (2003) suggest that the formation of monazite from allanite coincides with the first appearance of an 'Al-rich mineral reactant', and that all rocks with metamorphic monazite also contain apatite, muscovite, biotite, plagioclase and quartz. From this the following amphibolite-facies reaction was proposed:

$$\text{3 allanite + apatite + muscovite + 4 andalusite/kyanite + 3 quartz} \rightarrow \qquad (3.4.4)$$

$$\text{3 monazite + biotite + 8 plagioclase + 2 } H_2O\text{-rich fluid}$$

Recent attempts to replicate these monazite-allanite relationships with phase equilibria modelling have met with partial success. *P–T–X* pseudosection construction in P_2O_5- and Ce_2O_3-bearing model systems by Janots *et al*. (2007) and Spear (2010) have reproduced the observed dependence of the prograde allanite-monazite transition to CaO and Al_2O_3 bulk rock content. The latter study used the average metapelitic bulk composition of Shaw (1956), which contains 2.17 wt% CaO and has a CaO/Na_2O ratio of ~1.26 (cf. Fig. 3.3). Initial modelling in the minimum CaO–FeO–Al_2O_3–SiO_2–H_2O–P_2O_5–Ce_2O_3 (CFASHPCe) system suggested that the transition occurred at high-temperature (~725 °C at 5 kbar), whereas halving the total CaO greatly stabilised monazite, with the transition occurring instead at <450 °C (Fig. 3.4a). Coexisting monazite and allanite were calculated to occur only in a limited region of *P–T* space (dark grey bands in Fig. 3.4a). In a more realistic model system for natural samples (MnO–Na_2O–CaO–K_2O–FeO–MgO–Al_2O_3–SiO_2–H_2O–P_2O_5–Ce_2O_3; MnNCKFMASHPCe) this transition was calculated to lie between ~450–550 °C at 5–10 kbar (Fig. 3.4b), too low-grade to account for monazite appearances at staurolite and kyanite isograds as documented by previous studies. It is clear from these results that further investigation is required before these phases can be successfully modelled in this way.

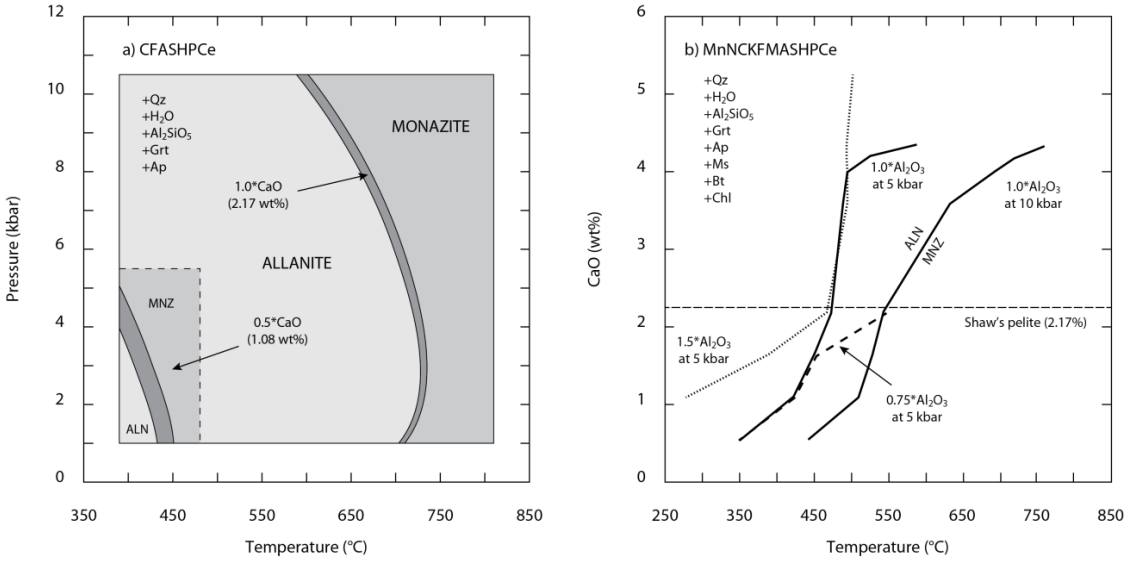


Fig. 3.4 – Phase diagrams showing the relative stability fields of allanite and monazite (modified from Spear, 2010). (a) *P–T* pseudosection in CFASHPCe illustrating phase relations with variable CaO bulk rock content. (b) The effect of temperature, CaO and Al_2O_3 bulk rock content on the transition (in MnNCKFMASHPCe).

At higher-grade conditions, sufficient for partial melting to occur, the behaviour of monazite is debated. Some studies suggest that grains become unstable and dissolve into early formed silicate melt, recrystallising on melt solidification (Hawkins & Bowring, 1999; Rubatto *et al.*, 2001). Yet, other studies report through laboratory experiments that monazite has a relatively low solubility in peraluminous melts (Wolf & London, 1995; Montel, 1993) and pre-anatectic (prograde) monazite may be preserved alongside younger grains that formed from partial melting processes. Chemical characteristics (below) can discriminate between different generations of growth in these cases.

It can be seen that the *P–T* conditions at which a particular grain of monazite might first form or later recrystallise varies greatly according to rock type and bulk composition, hence interpretation requires careful investigation on a sample-specific basis. Although textures suggestive of particular monazite-producing reactions are not always present, *in-situ* petrographic relationships between monazite and major minerals and fabrics may be used as an interpretative tool for ages obtained. These observations may be paired with chemical analyses to provide greater consistency and reliability, with diagnostic compositional characteristics outlined below.

3.4.2. Monazite chemistry

Monazite, described by the general composition $(REE)PO_4$, is composed mostly of the LREEs La, Ce and Nd, which make up ~75% of the cation total, excluding P (Spear & Pyle, 2002). In addition,

most metamorphic monazite also contains variable proportions of Th, U, Ca, Si, HREE, Y, and Pb according to numerous substitution mechanisms. For example, Y may substitute for other LREEs to produce a solid solution series with xenotime (YPO_4). The addition of Th or U can be achieved through one of two substitution mechanisms: U + Th + Si = REE + P (where Si replaces P in the tetrahedral site) and Th or U + Ca = 2REE (where Ca replaces an additional REE in the 8-fold site; Spear & Pyle, 2002). These replacements lead to enrichment in the huttonite ($ThSiO_4$) and cheralite ($CaTh(PO_4)_2$) components respectively, and it is these substitutions that produce the compositional zonation that is common in many monazite grains.

Many previous studies have shown that particular chemical characteristics of monazite are indicators of the coexisting mineral assemblage with which a particular grain (or internal domain) grew (e.g. Foster *et al*., 2000 and others). In particular, the combined HREE and Y content of monazite may be linked to episodes of formation (or breakdown) of garnet (Yang & Pattison, 2006). During prograde metamorphism garnet incorporates the bulk of a rock's available Y+HREE budget in preference to other REE-bearing minerals (Pyle & Spear, 1999; Foster *et al*., 2000). Consequently, if monazite growth occurs *before* garnet nucleation then it will typically have a significantly higher Y+HREE content than a similar grain that formed *during* or *after* garnet growth had occurred (Yang & Pattison, 2006). This relationship is useful in determining the timing of monazite growth in subsolidus metapelites where the prograde allanite-monazite transition may overlap with periods of garnet growth through the amphibolite-facies. Likewise, where peritectic garnet is produced in metapelites that have undergone partial melting, its subsequent replacement by biotite (as a result of back-reaction upon melt crystallisation) would liberate Y into the reacting matrix and allow for the growth of Y(+HREE)-rich monazite (Pyle & Spear, 2003; Kohn *et al*., 2005). Compositional analysis of monazite was undertaken in three of the four regional studies presented in this thesis in order to provide constraints on the timing of growth through the characteristics described above (no geochronology was performed on the TMM).

3.5. Work performed at the NERC Isotope Geosciences Laboratory

All geochronological work undertaken in this study was performed at the Natural Environment Research Council Isotope Geosciences Laboratory (NIGL), UK, on two separate occasions. On each

occasion analyses were performed on a different mass spectrometer; a summary of data obtained and procedures undertaken for both is presented below. A more detailed account of technical specifications and operating conditions is given in Appendix 11.3

3.5.1. Analytical techniques, methodology and operating conditions

Prior to geochronological analysis, investigative chemical and textural examination of monazite was performed at the University of Oxford Earth Science Department on a JEOL JSM-840A SEM-microprobe with working conditions and techniques as described in chapter 2.4.3. Internal compositional domains, where present, were identified through examination of enhanced contrast back scattered electron (BSE) images, which primarily highlight variations in Th and/or Y content (Gibson *et al.*, 2004). Where separate domains could be identified, subsequent ablation spot localities were chosen so that individual domains were analysed in order to avoid or minimise potential mixing of different ages. The accurate measurement of many HREE was often impossible due to extremely low concentrations in the majority of grains. However, Y content may be used as a reliable proxy for HREE concentration in metamorphic monazite (e.g. Foster *et al*., 2000, 2002) given the similar ionic radii of Y^{3+} and Ho in 8- and 9-fold coordination (Atkins *et al*., 2010) and was used as such in all cases in this study.

3.5.1.1. Nu Plasma MC–ICP–MS

Monazite from samples ET09-05, ET09-06 (chapter 6) and K146 and 20-199 (chapter 4) was analysed *in-situ* from thin section in July 2010 on a Nu Plasma multi-collector inductively coupled plasma mass spectrometer (MC–ICP–MS) coupled to a New Wave Research UP193SS laser ablation system. Only U–Pb data were collected on this mass spectrometer. Ablation spot sizes of 10 μm (20-199), 15 μm (K146) and 20 μm (ET09-05 and ET09-06) were used due to variation in average grain size and target domains. In all cases U–Pb data were normalised to the primary monazite reference material 'Manangotry' (559 ± 1 Ma (2 S.D.), ID-TIMS ^{238}U–^{206}Pb age; NIGL in-house data, Appendix 11.4). Separated monazites from samples DNCV02, DNCV09 and DNCV10 (chapter 7) were analysed from mounts in June 2010 on the same Nu Plasma MC–ICP–MS by R.R. Parrish using a spot size of 20 μm. U–Pb data were normalised to the primary monazite reference material 'Moacyr' (515.6 ± 1.4 Ma (2 S.D.), ID-TIMS ^{238}U–^{206}Pb age; NIGL in-house data, Appendix 11.4).

3.5.1.2. Nu Attom SC–ICP–MS

Monazite from samples ET10-07, ET10-09, ET10-10, ET10-13, ET10-18a, ET09-02 (chapter 6) and DNCV01 (chapter 7) was analysed *in-situ* from thin section in February 2012 using a Nu Attom single-collector inductively coupled plasma mass spectrometer (SC–ICP–MS) with a New Wave Research UP193FX laser ablation system. Monazite was analysed with an ablation spot size of 20 μm diameter and both U–Pb and Th–Pb data were collected. All U–Th–Pb data were normalised to the monazite reference material 'Stern' (512.1 ± 1.9 Ma (2 S.D.), ID-TIMS ^{238}U–^{206}Pb average age; NIGL in-house data, Appendix 11.4).

3.5.2. Data interpretation

The interpretation of all U–Pb data was performed using Tera-Wasserburg plots to allow for variable common lead. Regressions for samples K146, 20-199, ET09-05, ET09-06, ET10-18a, DNCV01, DNCV02, DNCV09 and DNCV10 assumed a $^{207}Pb/^{206}Pb$ ratio of 0.83 ± 0.02 based on the predicted initial lead composition for Phanerozoic mineral growth (Stacey & Kramers, 1975) whereas sample-specific $^{207}Pb/^{206}Pb$ ratios for samples ET09-02, ET10-07, ET10-09, ET10-10 and ET10-13 were obtained from peak metamorphic minerals that contain minimal common lead. Average analysis correction values were normalised to the reference material NIST612 (Woodhead & Hergt, 2001) and were measured to be: 0.85 ± 0.02 (ET09-02; muscovite and biotite), 0.83 ± 0.02 (ET10-07; biotite), 0.83 ± 0.02 (ET10-09; biotite), 0.85 ± 0.02 (ET10-10; muscovite and plagioclase) and 0.72 ± 0.04 (ET10-13; muscovite and biotite). The calculated accuracy of ^{238}U–^{206}Pb ages is within 3% according to secondary monazite reference materials (see Appendix 11.3). Interpreted ^{238}U–^{206}Pb ages are based on Tera-Wasserburg plot regressions through coherent populations, if present. Where U–Pb data could not be interpreted using this method, durations of crystallisation are delimited with general age limits (cf. Kellett *et al*., 2010); absolute errors are only given for regressed populations with a calculated MSWD value. All quoted uncertainties and ellipses on Tera-Wasserburg plots are at the 2σ confidence interval and all calculations used the 'Isoplot' Excel add-in (Ludwig, 2003).

Analyses on Nu Attom SC–ICP–MS collected both U–Pb and Th–Pb data, so allow independent age determinations to be made through the U–Pb and Th–Pb decay schemes. However, the preferential incorporation of Th in place of U can result in significant amounts of radiogenic

^{230}Th, a daughter nuclide in the ^{238}U–^{206}Pb decay chain, being incorporated during crystallisation (Schärer, 1984). Consequently, the resultant excess ^{206}Pb causes calculated ^{238}U–^{206}Pb apparent ages to be older than the true crystallisation age, this effect becoming increasingly significant in Cenozoic monazite (Schärer, 1984; Parrish, 1990). As the Th–Pb system is unaffected by this disequilibrium, ^{232}Th–^{208}Pb ages should be the most reliable estimates of the timing of monazite growth, although low ^{208}Pb concentrations often result in large uncertainties. The ^{235}U–^{207}Pb system is also unaffected by excess ^{206}Pb; however, the generally low abundance of ^{207}Pb also precludes precise age determinations. Interpreted ages for samples analysed on the Nu Attom SC–ICP–MS are thus discussed primarily with reference to the ^{238}U– ^{206}Pb isotopic system, unless otherwise stated.

4. Karakoram metamorphic complex

Part of the work presented here forms the basis of the paper Palin et al. (2012) published in the Journal of Metamorphic Geology (cf. chapter 10.2.1).

4.1. Chapter introduction

Multidisciplinary investigations of the Karakoram Range have been undertaken by many previous students at Oxford, notably including focused studies of the metamorphic and magmatic evolution of the Hunza Valley and Baltoro regions of the KMC performed by J. Fraser and A. Thow respectively. The general lack of metamorphic rocks exposed within the Lhasa and Qiangtang crustal blocks (chapter 1.4.2) has hindered investigation into the deformational response of the Asian plate to the continental collision process. As such, the KMC provides an important study area that offers an along-strike analogue and exposes deep-crustal units that may be equivalent to those at varying depths in Tibet today. Constraining the tectonothermal evolution of the Asian margin is important for understanding the response of a lithospheric plate that has been pre-conditioned as an Andean-type plate margin to a continental collision, in comparison to that of the colder and more rigid Indian plate. New field investigation of the KMC was not achieved during this study, so three rocks that had been previously collected (but not studied in detail) were chosen for further examination in this work; sample 20-199 (documented in Fraser (2000) and Fraser *et al.*, 2001), sample T17 (Thow, 2004) and sample K146 (Searle & Tirrul, 1991). Previous investigation has been unable to constrain the *P–T* conditions or age of key tectonothermal episodes in the KMC, including pre-collision andalusite-grade metamorphism and post-collision kyanite-grade overprinting of sillimanite-grade units in the Hunza Valley. In addition, it is unknown as to why the prograde evolution of different kyanite-grade units in the Baltoro region appears to differ, despite them being in close proximity today. These aforementioned samples all preserve petrographic evidence of these events and so were studied using modern analytical and modelling techniques with the aim of solving these problems.

4.2. Geological setting

The KMC exposes a variety of metamorphic and igneous rocks that offer analogues for lithologies thought to exist at different depths in the Asian crust along strike to the east (see chapter 1.4.3). The tectonothermal history of the KMC is complex and although recent studies have established a broad

framework (Fraser *et al*., 2001; Searle *et al*., 2010a) some aspects are still unclear. In particular, there exists a contrast in the interpreted metamorphic history between the Hunza Valley in the west, where there is a record of an extended metamorphism between c. 83–53 Ma (U–Pb zircon; Foster *et al*., 2004), and the Baltoro region in the east, which lacks any metamorphic ages older than c. 28 Ma (Searle *et al*., 2010a). Moreover, the large crustally-derived Baltoro granite batholith, emplaced between c. 25–13 Ma (Table 4.1, below) is unmatched in the Hunza Valley. Such differences suggest that the tectonic evolution of both regions is significantly different, although the reasons for this are unknown in view of their close proximity along-strike. Key samples, such as Hunza Valley metapelite 20-199 (Fraser *et al*., 2001), retain microstructural evidence of a polyphase metamorphic history and careful analysis can provide added insight into this sequence of events.

4.2.1. The Hunza Valley

Several north-east-dipping thrust faults in the Hunza Valley juxtapose different tectonostratigraphic units against one another, resulting in a general increase in metamorphic grade and age northwards. From north to south, numbered 1–5 on Fig. 4.1, these are the Hunza thrust, the Hassanabad thrust, the North and South Murtazabad thrusts and the Main Karakoram thrust. Metamorphic rocks are bound to the north by the Hunza Plutonic Unit (HPU) of the Karakoram batholith (Fig. 4.1). The HPU consists mainly of subduction-related quartz diorites and granodiorites with documented crystallisation ages between c. 95–105 Ma, which were intruded by a suite of monzogranite and leucogranite dykes (set 1) between c. 52–50 Ma (Table 4.1). Both the HPU and the set 1 Hunza dykes were similarly deformed during southward motion along the Hunza thrust associated with the India-Asia collision (Fraser *et al*., 2001). Younger undeformed dykes (set 2) cut across fabrics in the HPU and metamorphic units immediately to the south (Fig. 4.1) and were intruded at 35.0 ± 1.0 Ma (Table 4.1), thus providing a minimum age for thrusting. The northernmost metamorphic unit of the Hunza Valley, the sillimanite zone, may be divided into two sections. These comprise the relatively higher-grade K-feldspar-bearing migmatitic ‘upper sillimanite zone’ (USZ) and the lower-grade muscovite-bearing ‘lower sillimanite zone’ (LSZ) units (Fig. 4.1). Field observations suggest that the USZ may have been juxtaposed against the LSZ by an E–W trending thrust fault situated between Aliabad and the Hassanabad Valley; however, this feature is not fully exposed and may instead represent localised brittle deformation (Fraser, 2000).

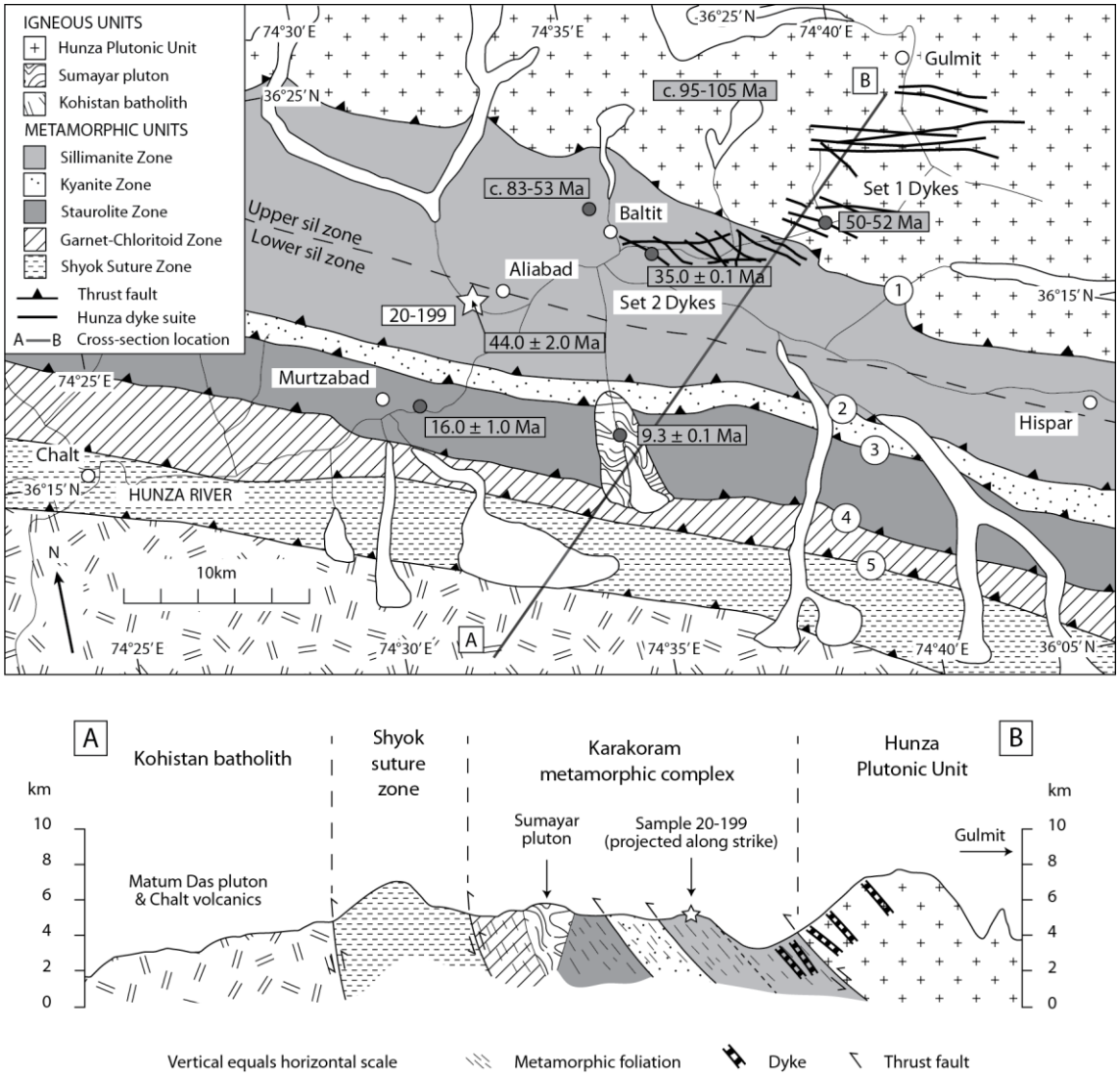


Fig. 4.1 – Geological map of the Hunza Valley and associated cross-section showing tectonic relations (after Searle, 1991 and Fraser *et al.,* 2001). Sample 20-199 outcrop locality is marked with a star. See text for sources of age data.

Migmatitic sillimanite gneiss from the USZ dated by Fraser *et al.* (2001) produced U–Pb ages ranging between 82.9 ± 6.1 Ma and 63.3 ± 0.4 Ma from palaeosome monazite, and between 56.3 ± 0.3 Ma and 53.4 ± 0.3 Ma for leucosome monazite. Further work by Foster *et al.* (2004) delimited four significant U–Pb monazite age populations in the same sample at c. 82 Ma, c. 66–59 Ma, c. 56–53 Ma and c. 46 Ma. Using garnet-xenotime thermometry and THERMOCALC AvePT, Foster *et al.* (2004) suggested that this older age of c. 82 Ma recorded initial M1 sillimanite-grade conditions at temperatures of ~550 °C, coincident with the closure of the Shyok suture. Monazite growth at c. 56–53 Ma was interpreted to record garnet breakdown during rapid exhumation and partial melting; however, the conditions and mechanism of final monazite growth at c. 46 Ma were undetermined. As a result of the spread of ages obtained in each case, Fraser *et al.* (2001) and Foster *et al.* (2004)

both proposed that M1 could represent a continuous prograde metamorphic event in the Hunza, lasting at least ~30 Myr from c. 83 to c. 53 Ma culminating in widespread migmatisation in the USZ.

Region	Lithology	Age (Ma)	Method	Study
Hunza Valley	Hunza Plutonic Unit	95 +4/-6	U–Pb zircon	Le Fort *et al*. (1983)
Hunza Valley	Hunza Plutonic Unit	97 + 17	Rb–Sr whole rock	Debon *et al*. (1987)
Hunza Valley	Hunza Plutonic Unit	105.7 ± 0.5	U–Pb zircon	Fraser *et al*. (2001)
Hunza Valley	Set 1 Hunza dykes	52–50	U–Pb zircon	Fraser *et al*. (2001)
Hunza Valley	Set 2 Hunza dykes	35 ± 1	U–Pb zircon	Fraser *et al*. (2001)
Hunza Valley	Sumayar granite	9.3 ± 0.1	U–Pb uraninite	Fraser *et al*. (2001)
Baltoro	Hushe gneiss igneous protolith	200–145	U–Pb zircon, K–Ar hornblende	Searle *et al*. (1989)
Baltoro	Baltoro Plutonic Unit	21 ± 0.5	U–Pb zircon	Parrish & Tirrul (1989)
Baltoro	Baltoro Plutonic Unit	19–17	U–Pb monazite	Parrish & Tirrul (1989)
Baltoro	Baltoro Plutonic Unit	25.5 ± 0.8	U–Pb monazite	Schärer *et al*. (1990)
Baltoro	Baltoro Plutonic Unit	21.4 ± 0.6	U–Pb monazite	Schärer *et al*. (1990)
Baltoro	Baltoro Plutonic Unit	25–13	U–Pb zircon and monazite	Searle *et al*. (2010a)
Baltoro	Mango Gusar granite	26.4 ± 1.3	Th–Pb allanite	Fraser *et al*. (2001)
Baltoro	Chingkang-la granite	34 ± 1	U–Pb zircon	Searle *et al*. (2010a)

Table 4.1 – Age data and isotopic dating methods for magmatic units in the KMC

The timing of peak M2 metamorphism was identified by Fraser *et al*. (2001) who dated a sample of sillimanite schist from the LSZ (sample 20-199 in this study) and produced a younger U–Pb monazite age of 44.0 ± 2.0 Ma. Notably, this is similar to the c. 46 Ma age of 'uncertain' origin identified in the USZ by Foster *et al*. (2004). Overprinting of LSZ units to kyanite-grade can be observed in localised outcrops (Fraser, 2000), although the relationship of such samples to the documented 'kyanite zone' further south is unknown. A separate and younger prograde staurolite-grade event (M3), dated at 16.0 ± 1.0 Ma (U–Pb monazite; Fraser *et al*., 2001), is documented in rocks exposed in the southern parts of the region. No data are currently available to constrain the timing of peak metamorphism in the kyanite and garnet-chloritoid zones shown in Fig. 4.1. Thrusting in the southern Hunza Valley is constrained by the youngest phase of crustal magmatism, intrusion of the Sumayar granite (Fig. 4.1), dated at 9.3 ± 0.1 Ma (Table 4.1). This granite truncates deformational fabrics associated with the emplacement of kyanite-grade units onto staurolite-grade units and also induced localised contact metamorphism in the host units (Crawford & Searle, 1993).

4.2.2. The Baltoro region

Metamorphic rocks exposed in Baltoro region extend from the MKT in the south to the BPU of the Karakoram batholith to the north and show a general increase in metamorphic grade from the Hushe region in the south-east towards the Dassu and Bullah regions in the north-west (Fig. 4.2; Searle & Tirrul, 1991; Rolland *et al*., 2001). The Hushe gneisses represent original igneous components of the

Karakoram batholith that were emplaced between c. 200–145 Ma (Table 4.1), all of which have been subsequently metamorphosed and deformed. Low-pressure, high-temperature andalusite- and garnet-bearing metapelites are spatially associated with the deformed Hushe gneisses and were interpreted by Searle *et al*. (1989) and Crawford & Searle (1992) to record contact metamorphism (M0) synchronous with subduction of the Neo-Tethys Ocean preceding closure of the SSZ.

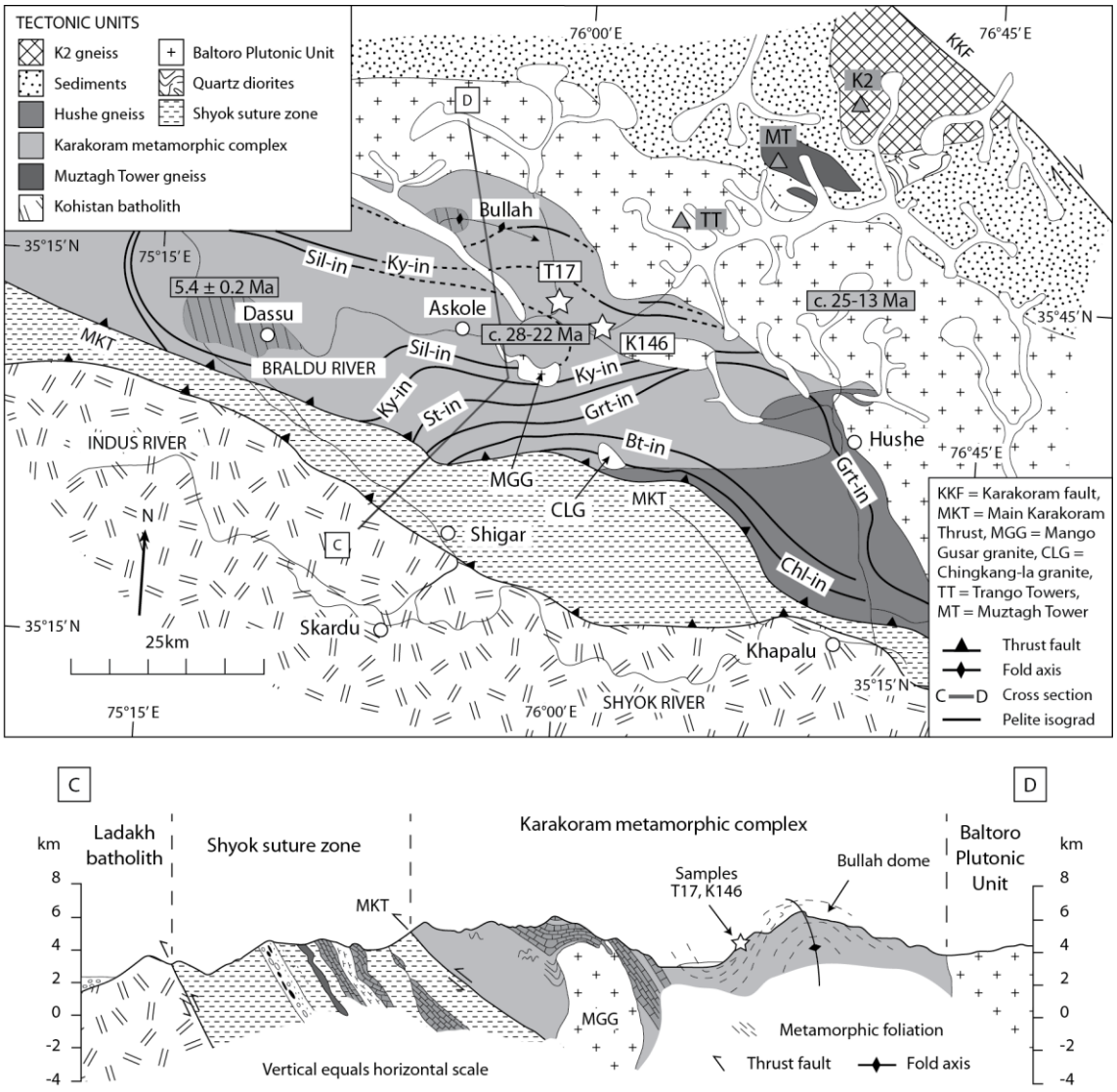


Fig. 4.2 – Geological map of the Baltoro region and associated cross-section showing tectonic relations (after Searle, 1991). Outcrop localities for samples T17 and K146 are marked with stars. Metapelite isograds are after Rolland *et al*. (2001) and Searle & Tirrul (1991).

Prolonged Late Cretaceous-Eocene sillimanite-grade metamorphism and partial melting (M1) recorded in Hunza Valley units is absent in the Baltoro region. The main body of the Baltoro metapelitic units preserves an amphibolite-facies Barrovian metamorphic sequence (M2) ranging from chlorite- to sillimanite-grade (Fig. 4.2). Peak kyanite-grade metamorphism reportedly occurred

between 28.0 ± 0.5 Ma (U–Pb monazite; Fraser *et al*., 2001) and 22.0 ± 0.3 Ma (U–Pb monazite; Searle *et al*., 2010a) at *P–T* conditions between 6–10 kbar and 650–700 °C (Bertrand *et al*., 1988; Allen & Chamberlain, 1991; Rolland *et al*., 2001). M2 deformation must have initiated prior to intrusion of the Chingkang-la granite pluton (Fig. 4.2), which crystallised at 34 ± 1 Ma (Table 4.1) and locally cuts across early metamorphic fabrics. The later formation of the BPU is interpreted by Searle *et al*. (2010a) to be a result of extensive crustal thickening, heating and partial melting of the lower crust during the Oligocene-Miocene. The batholith is largely undeformed and crystallisation ages for various components range between c. 25–13 Ma (Table 4.1). The BPU cross-cuts kyanite-grade M2 metamorphic fabrics and has a contact metamorphic aureole along its southern margin, which contains andalusite-, sillimanite- and cordierite-bearing hornfels (Searle & Tirrul, 1991).

Young sillimanite-K-feldspar-grade metamorphism and partial melting (M4) in the Baltoro is exposed in the cores of the Dassu and Bullah gneiss domes (dashed regions on Fig. 4.2; Rolland *et al*., 2001; Searle *et al*., 2010a). Migmatites from the Dassu dome document peak *P–T* conditions for this event between 3.8–7.6 kbar and 630–750 °C (Villa *et al*., 1996; Searle *et al*., 2010a). M4 metamorphism is dated at 5.4 ± 0.2 Ma (U–Pb monazite; Fraser *et al*., 2001) and 6.7 ± 0.5 Ma (U–Pb monazite; Smith, 1993), with cooling through the ~300 °C isotherm at 4.7 ± 0.2 Ma (K–Ar biotite; Searle *et al*., 1989). Undeformed and cross-cutting tourmaline-bearing pegmatite dykes with crystallisation ages of 3.5 ± 0.1 Ma (U–Pb zircon and monazite; Searle *et al*., 2010a) constrain the cessation of M4 metamorphism. Such doming and associated migmatisation has been suggested by Rolland *et al*. (2006) to be caused by mantle-derived syenite magma intrusions into the cores of each dome; with such diapirs dated at 8.4 ± 0.1 Ma (Ar–Ar muscovite; Villa *et al*., 1996). However, other workers dispute this and suggest instead that both doming and partial melting were associated with post-Miocene north-south shortening along the MKT (Searle & Tirrul, 1991; Fraser *et al*., 2001).

4.3. Petrography and mineral chemistry

Petrographic and compositional analysis was performed following the method given in chapter 2.4.3.

4.3.1. The Hunza Valley

Sample 20-199 was collected from the LSZ of the Hunza Valley, west of Aliabad, at approximate latitude-longitude co-ordinates 36° 19’ 52.0” N and 74° 34’ 43.8” E (estimated from Google Earth©

satellite imagery compared against field photographs and outcrop maps presented in Fraser, 2000). Kyanite partially replaces sillimanite in isolated outcrops within the LSZ (Fraser, 2000), as is observed in sample 20-199. Previous work on sample 20-199 performed by Fraser *et al*. (2001) quantified the timing of sillimanite-grade metamorphism. It was chosen for further study in this thesis to determine the *P–T* conditions and timing of kyanite-grade overprinting.

20-199 – Kyanite-sillimanite schist

Sample 20-199 is a metapelitic schist containing porphyroblasts of garnet and aluminosilicate, which are wrapped by a spaced foliation defined by biotite, muscovite and graphite.

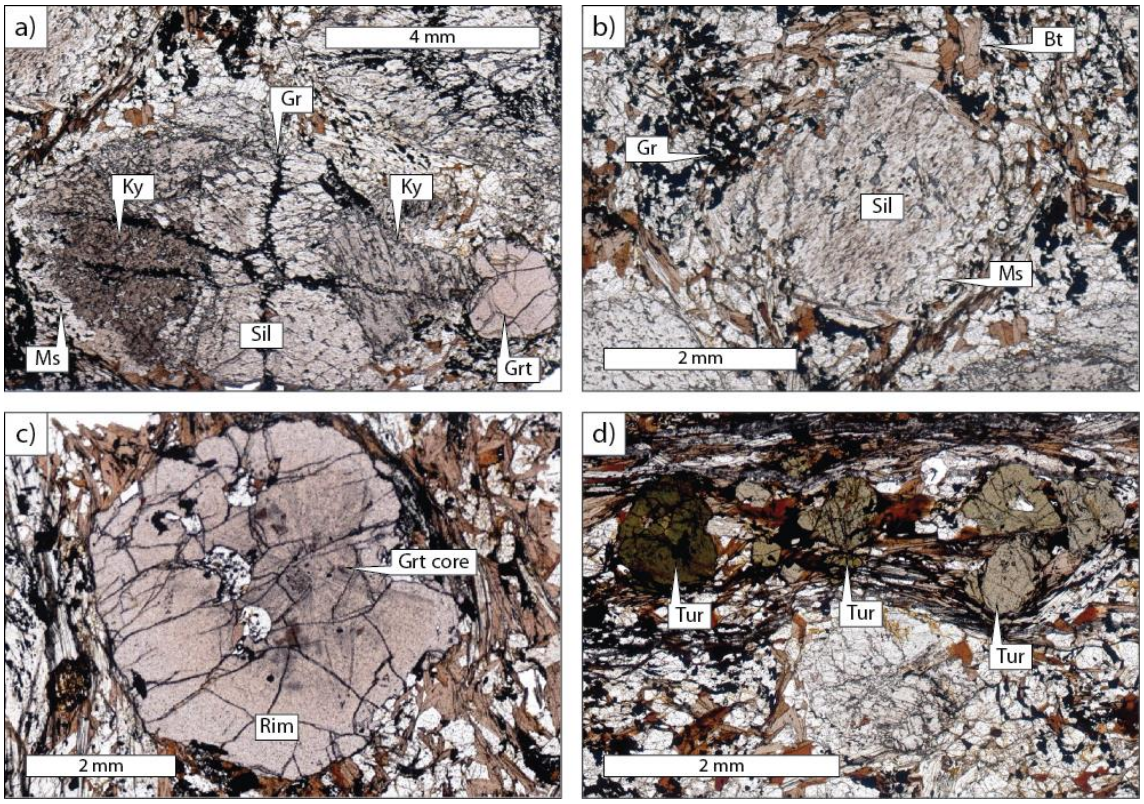


Fig. 4.3 – Petrography of sample 20-199 from the Hunza Valley. All thin section images viewed under plane polarised light. (a) Original porphyroblast of andalusite that has been pseudomorphed by sillimanite and kyanite. (b) Graphite-free circular clusters of prismatic sillimanite (c) Garnet porphyroblasts showing core-rim textural relations (d) Tourmaline grains wrapped by the metamorphic foliation.

Matrix minerals include plagioclase, ilmenite and quartz alongside accessory tourmaline, apatite, monazite and zircon. Aluminosilicate porphyroblasts are characterised by kyanite partially replacing sillimanite, the latter having previously pseudomorphed earlier andalusite (Fig. 4.3a). Sillimanite also occurs as small circular clusters that lack graphite (Fig. 4.3b). Garnet porphyroblasts have a

diameter up to 5 mm and contain core and rim regions that can be differentiated through texture and composition. Broad cores trap biotite, plagioclase, rutile and radiating sets of fluid inclusions (Fig. 4.3c) and show minor compositional variation. By contrast, thin rim regions retain strong compositional gradients and have rare inclusions of biotite. Compositions in core regions range between 14–17% pyrope, 4–6% grossular and 4–5% spessartine, whereas from the core-rim boundary to the outer rim grossular content increases to 11% and both spessartine and pyrope decrease to 1% and 14% respectively (Table 4.2). Almandine exhibits no systematic variation from core to rim, ranging between 73–76%.

Biotite occurs dominantly within the matrix foliation and has XMg = 0.48–0.49 and Ti = 0.12–0.14 cpfu, rare inclusions in garnet rims have XMg = 0.54–0.55 and Ti = 0.12–0.13 cpfu and grains within garnet strain shadows have XMg = 0.51–0.53 and Ti = 0.08–0.11 cpfu. Fine grained muscovite occurs in the matrix foliation and coarser grains occur as thin rims on aluminosilicate aggregates (Fig. 4.3a–b). Plagioclase in the matrix contains XCa = 0.29–0.33 and inclusions in garnet cores are slightly more calcic with XCa = 0.31–0.37 (Table 4.2). Anhedral porphyroblasts of tourmaline (Fig. 4.3d) are commonly wrapped by the matrix foliation.

4.3.2. The Baltoro region

Two samples that had been collected during previous fieldwork and placed in storage at University of Oxford (chapter 4.1) were re-examined in this thesis so as to investigate the prograde *P–T* conditions and use *in-situ* dating to constrain the timing of M2 kyanite-grade metamorphism in the Baltoro region. Both samples were originally collected from the central Baltoro region (Fig. 4.2), north-east of the Mango Gusar granite at approximate latitude-longitude co-ordinates 35° 40’ 59.3” N and 75° 58’ 07.8” E (sample T17) and 35° 38’ 50.6” N and 76° 02’ 17.4” E (sample K146). Latitude-longitude co-ordinates are estimated from Google Earth© satellite images when compared against outcrop locality information documented in Thow (2004) and Searle & Tirrul (1991).

K146 – Garnet-kyanite schist

Sample K146 is characterised by a widely spaced foliation defined by muscovite and biotite and a matrix composed mostly of quartz, ilmenite, apatite, monazite and zircon. This foliation wraps inclusion-rich poikiloblasts of plagioclase, but is overgrown by porphyroblasts of kyanite and garnet.

Rare staurolite is present as small inclusions in garnet rims and as anhedral grains in the matrix that are associated with kyanite and biotite.

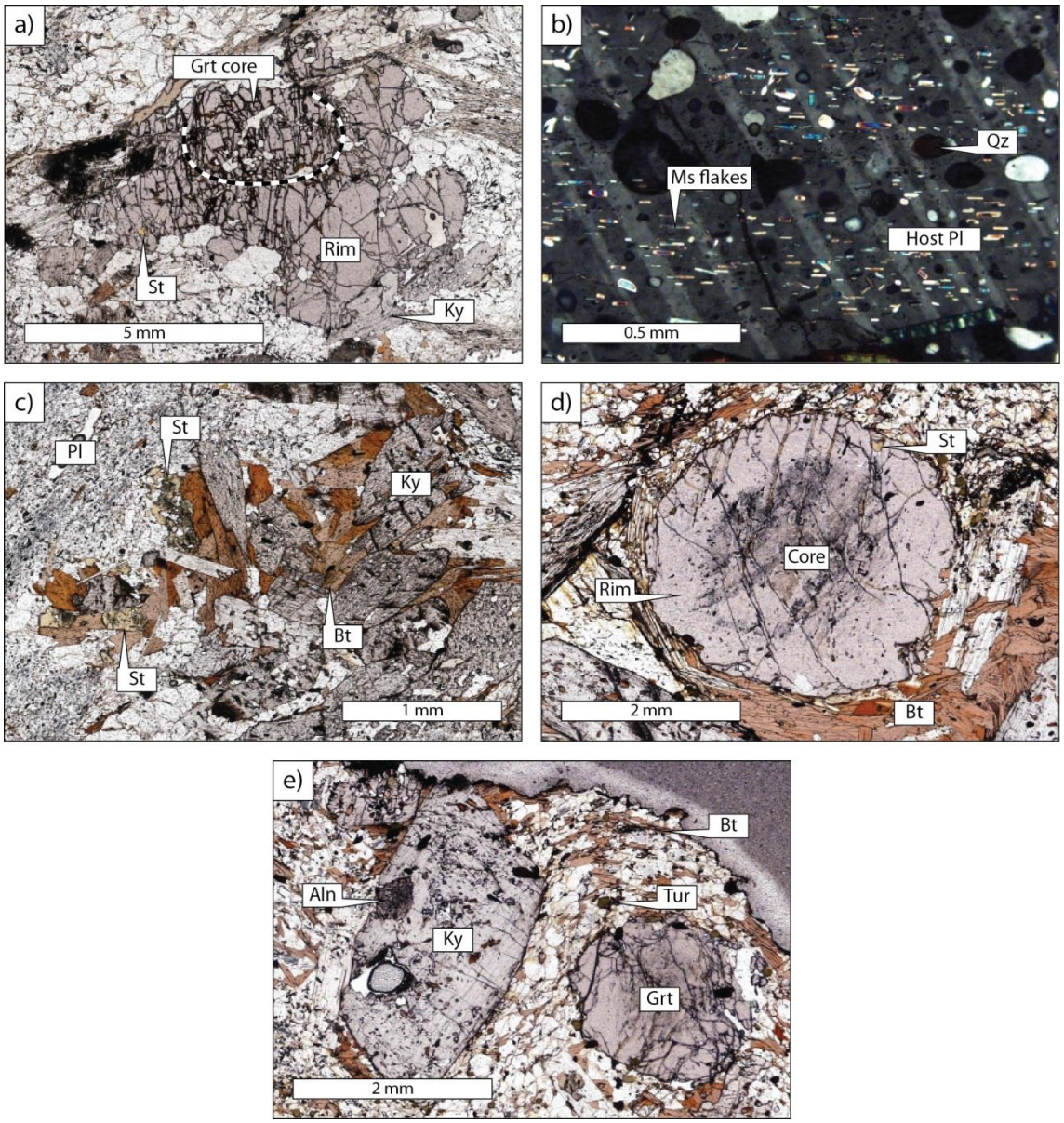


Fig. 4.4 – Petrography of samples K146 and T17 from the Baltoro region. All thin section images are viewed in plane polarised light except Fig. 4.4b (a) Garnet porphyroblasts in sample K146 contain staurolite inclusions in rim regions and also form interlocking mutual boundaries with matrix kyanite. (b) Large plagioclase porphyroblasts contain abundant quartz inclusions and preserve a relic linear internal fabric defined primarily by muscovite flakes (viewed under crossed polars). (c) Sample K146 also contains aggregates of undeformed biotite and kyanite, commonly surrounding staurolite. (d) Garnet in sample T17 contains a core region with arcuate graphitic inclusion trails surrounded by graphite-free rim regions, which also contain rare inclusions of staurolite. (e) Subhedral kyanite in sample T17 encloses biotite, quartz and allanite.

Table 4.2 – Mineral compositions for samples 20-199, K146 and T17 (overleaf)

Sample	Mineral	Location	SiO_2	TiO_2	Al_2O_3	Fe_2O_3	FeO	MnO	MgO	CaO	Na_2O	K_2O	**Total**	Si	Ti	Al	Fe^{3+}	Fe^{2+}	Mn	Mg	Ca	Na	K	**Sum**	Ox	XMg	XCa	XMn	Al(iv)	Al(vi)	Alm	Prp	Grs	Sps
K146	Bt	Matrix	35.15	2.50	19.01	0.00	20.21	0.01	8.73	0.05	0.18	9.65	**95.49**	2.69	0.14	1.71	0.00	1.29	0.00	0.99	0.00	0.03	0.94	**7.79**	11	0.43	-	-	1.31	0.40	-	-	-	-
	Bt	Adjacent to matrix St	34.65	2.39	18.85	0.00	19.86	0.00	8.81	0.03	0.19	9.54	**94.32**	2.68	0.14	1.72	0.00	1.28	0.00	1.02	0.00	0.03	0.94	**7.81**	11	0.40	-	-	1.32	0.40	-	-	-	-
	Grt	Core	37.16	0.00	21.44	1.38	33.15	0.66	3.25	3.53	0.00	0.00	**100.57**	2.96	0.00	2.02	0.04	2.25	0.04	0.39	0.30	0.00	0.00	**8.00**	12	0.15	-	-	-	-	0.76	0.13	0.10	0.01
	Grt	Rim	36.78	0.02	21.33	1.61	36.54	0.07	3.27	2.03	0.00	0.01	**101.66**	2.97	0.00	2.01	0.04	2.40	0.01	0.39	0.18	0.00	0.00	**8.00**	12	0.14	-	-	-	-	0.81	0.13	0.06	0.00
	Ilm	Matrix	0.34	53.16	0.35	0.00	44.90	0.06	0.60	0.06	0.04	0.00	**99.51**	0.01	1.00	0.01	0.00	0.96	0.00	0.02	0.00	0.00	0.00	**2.00**	3	-	-	0.00	-	-	-	-	-	-
	Ms	Inc in Pl poikiloblast	46.01	1.05	35.42	0.00	1.21	0.02	0.73	0.04	0.89	10.42	**95.79**	3.05	0.05	2.77	0.00	0.07	0.00	0.07	0.00	0.11	0.88	**7.01**	11	0.52	-	-	0.95	1.82	-	-	-	-
	Ms	Matrix	45.56	0.96	35.55	0.00	1.32	0.01	0.69	0.03	0.71	10.06	**94.89**	3.04	0.05	2.80	0.00	0.07	0.00	0.07	0.00	0.09	0.86	**6.98**	11	0.50	-	-	0.96	1.84	-	-	-	-
	Pl	Poikiloblast core	61.28	0.00	24.82	0.01	0.00	0.00	0.02	5.78	7.75	0.10	**99.76**	2.72	0.00	1.30	0.00	0.00	0.00	0.00	0.29	0.69	0.00	**5.00**	8	-	0.30	-	-	-	-	-	-	-
	Pl	Poikiloblast rim	59.78	0.01	25.45	0.02	0.00	0.00	0.00	6.49	7.51	0.09	**99.35**	2.67	0.00	1.34	0.00	0.00	0.00	0.00	0.34	0.65	0.00	**5.00**	8	-	0.34	-	-	-	-	-	-	-
	St	Matrix	26.68	0.79	54.06	0.00	13.88	0.03	1.45	0.02	0.16	0.00	**97.07**	7.48	0.17	17.86	0.00	3.25	0.01	0.61	0.01	0.09	0.00	**29.48**	46	0.16	-	-	-	-	-	-	-	-
T17	Bt	Matrix	35.97	2.83	19.08	0.00	17.40	0.02	10.18	0.07	0.03	9.88	**95.46**	2.70	0.17	1.69	0.00	1.11	0.00	1.14	0.00	0.01	0.96	**7.78**	11	0.51	-	-	1.30	0.39	-	-	-	-
	Grt	Core	36.16	0.03	20.92	0.39	30.08	4.94	2.34	4.49	0.00	0.00	**99.35**	2.98	0.00	2.01	0.01	2.01	0.31	0.29	0.39	0.00	0.00	**8.00**	12	0.13	-	-	-	-	0.67	0.10	0.13	0.10
	Grt	Inner rim	37.02	0.01	21.54	0.84	31.37	0.37	4.03	4.09	0.00	0.00	**99.27**	2.98	0.00	2.03	0.03	2.10	0.03	0.48	0.35	0.00	0.00	**8.00**	12	0.19	-	-	-	-	0.71	0.16	0.12	0.01
	Ilm	Matrix	0.27	54.82	0.45	0.00	40.59	3.40	0.14	0.02	0.00	0.02	**99.71**	0.01	1.01	0.00	0.00	0.90	0.07	0.01	0.00	0.00	0.00	**2.00**	3	-	-	0.07	-	-	-	-	-	-
	Ms	Matrix	45.36	1.33	34.74	0.00	1.33	0.00	0.90	0.05	0.28	10.09	**94.08**	3.05	0.07	2.76	0.00	0.08	0.00	0.09	0.00	0.04	0.87	**6.96**	11	0.53	-	-	0.95	1.81	-	-	-	-
	Pl	Matrix	56.46	0.01	27.48	0.07	0.00	0.01	0.00	8.97	6.07	0.08	**99.15**	2.55	0.00	1.46	0.00	0.00	0.00	0.00	0.45	0.53	0.01	**5.00**	8	-	0.45	-	-	-	-	-	-	-
	St	Inc in Grt rim	26.72	0.78	53.90	0.00	11.98	0.05	2.43	0.04	0.00	0.01	**95.91**	7.55	0.17	17.95	0.00	2.60	0.01	1.02	0.01	0.00	0.00	**29.31**	46	0.28	-	-	-	-	-	-	-	-
20-199	Bt	Matrix	35.52	2.20	19.08	0.00	18.50	0.02	10.47	0.10	0.65	9.77	**96.31**	2.67	0.12	1.69	0.00	1.17	0.00	1.17	0.01	0.10	0.94	**7.87**	11	0.50	-	-	1.33	0.36	-	-	-	-
	Bt	Grt strain shadow	35.42	1.92	19.08	0.00	18.07	0.00	10.53	0.12	0.51	10.11	**95.75**	2.68	0.11	1.70	0.00	1.14	0.00	1.19	0.01	0.07	0.98	**7.88**	11	0.51	-	-	1.32	0.38	-	-	-	-
	Grt	Core	36.23	0.09	20.52	3.29	32.23	1.94	4.02	1.92	0.13	0.00	**100.37**	2.94	0.01	1.97	0.19	2.11	0.12	0.47	0.17	0.02	0.00	**8.00**	12	0.18	-	-	-	-	0.74	0.16	0.06	0.04
	Grt	Inner rim	35.71	0.19	20.57	3.51	31.66	1.76	3.94	1.85	0.22	0.00	**99.41**	2.91	0.01	1.98	0.21	2.09	0.12	0.48	0.16	0.04	0.00	**8.00**	12	0.19	-	-	-	-	0.73	0.17	0.06	0.04
	Grt	Outer rim	35.72	0.00	20.57	3.77	31.59	0.45	3.59	3.23	0.23	0.01	**99.16**	2.91	0.00	1.98	0.23	2.09	0.03	0.44	0.28	0.04	0.00	**8.00**	12	0.17	-	-	-	-	0.74	0.15	0.10	0.01
	Ilm	Matrix	0.16	53.46	0.37	0.00	45.31	0.21	0.30	0.00	0.00	0.04	**99.85**	0.00	1.01	0.01	0.00	0.97	0.00	0.01	0.00	0.00	0.00	**2.00**	3	-	-	0.00	-	-	-	-	-	-
	Ms	Mantling Ky/Sil	45.85	0.98	35.59	0.00	1.20	0.00	0.78	0.06	0.86	10.64	**95.96**	3.04	0.05	2.78	0.00	0.07	0.00	0.08	0.00	0.11	0.90	**7.03**	11	0.53	-	-	0.96	1.82	-	-	-	-
	Ms	Matrix	45.23	1.23	35.41	0.00	1.21	0.02	1.20	0.08	0.81	10.68	**95.87**	3.01	0.06	2.78	0.00	0.07	0.00	0.12	0.01	0.10	0.91	**7.06**	11	0.63	-	-	0.99	1.79	-	-	-	-
	Pl	Matrix	60.79	0.01	25.37	0.02	0.00	0.02	0.34	6.29	7.61	0.12	**100.57**	2.68	0.00	1.32	0.00	0.00	0.00	0.01	0.32	0.66	0.01	**5.00**	8	-	0.32	-	-	-	-	-	-	-

Garnet porphyroblasts are large (up to 10 mm in diameter) and all observed examples are highly anhedral. They commonly exhibit fractured core regions that contain inclusions of biotite, quartz and graphite, and are surrounded by broad rims with rarer inclusions of biotite and staurolite. Outer rim regions occasionally share common growth faces with, and partially enclose, kyanite in the matrix (Fig. 4.4a). Minor compositional variation occurs within garnet porphyroblasts whereby core regions contain 9–10% grossular, 13–15% pyrope and 71–76% almandine whereas rim regions contain 5–7% grossular, 12–13% pyrope and 73–81% almandine. Both core and rim regions are Mn-poor and have a spessartine content of ~1% (Table 4.2). Poikiloblasts of plagioclase up to 15 mm in length contain an internal fabric defined by muscovite, biotite, ilmenite and graphite (Fig. 4.4b) that is discordant to the matrix foliation. Such poikiloblasts have XCa = 0.29–0.30 and occasionally have thin inclusion-free rim regions that are more calcic (XCa = 0.34–0.37; Table 4.2). Staurolite in the matrix is spatially associated with clusters of kyanite and coarse randomly orientated biotite (Fig. 4.4c). These staurolite grains, as well as inclusions in garnet rims (Fig. 4.4a), have a similar XMg = 0.15–0.16. Biotite in the matrix foliation has XMg = 0.41–0.45 and Ti = 0.13–0.16 cpfu and coarse unfoliated crystals associated with matrix staurolite have XMg = 0.42–0.46 and Ti = 0.14–0.16 cpfu (Table 4.2). Muscovite in the matrix foliation has Na/(Na+K) = 0.09–0.10 whereas inclusions in plagioclase poikiloblasts contain Na/(Na+K) = 0.11–0.12 (Table 4.2).

T17 – Garnet-kyanite schist

Sample T17 contains porphyroblasts of garnet and kyanite that are wrapped by a discontinuous foliation defined by muscovite and biotite (Fig. 4.4d). The matrix additionally contains biotite, muscovite, plagioclase, quartz, rutile, staurolite, tourmaline, allanite, zircon and apatite. Garnet porphyroblasts may be divided into core and rim regions according to textural and compositional characteristics. Core regions contain randomly orientated inclusions of ilmenite and rutile in addition to curved graphitic inclusion trails (Fig. 4.4d). Rim regions lack graphite but do contain rutile and staurolite inclusions. Garnet porphyroblasts preserve prominent compositional zoning profiles – spessartine content decreases from 10% in the core to <1% at the rim, grossular content decreases from between 13–15% in the core to a minimum of 10% inside the outer rim, followed by a slight increase to just over 11% at the extreme rim, and pyrope content increases from 9–10% in the core

to 16% at the rim. Biotite in the matrix has XMg = 0.50–0.54 and Ti = 0.15–0.18 cpfu, matrix muscovite has Na/(Na+K) = 0.03–0.05 and plagioclase contains XCa = 0.44–0.47 (Table 4.2). Staurolite both in the matrix and as inclusions in garnet rims has XMg = 0.28–0.29.

4.4. Textural and compositional interpretation

The textural and compositional information pertaining to the metamorphic evolution of samples 20-199, K146 and T17 is discussed below within the context of the tectonothermal history of the KMC.

4.4.1. The Hunza Valley

Garnet compositional zoning

Garnet compositional zoning profiles have been documented by many studies to form mainly as a consequence of changing pressure and temperature conditions during growth (e.g. Tracy, 1982 and references therein). Equilibrium prograde metamorphism of a metapelitic bulk composition along a regional metamorphic thermal gradient has been shown by Woodsworth (1977) to preferentially concentrate Ca and Mn into garnet cores, if available, and Fe and Mg into the rims. As garnet strongly partitions Mn in preference to other minerals likely to be present, spessartine content should decrease from core to rim during growth (Hollister, 1966); otherwise it is likely that cation diffusion has altered the original growth profile (e.g. Florence & Spear, 1991).

The largest garnet observed and analysed in sample 20-199 has a radius of ~2.5 mm and contains texturally distinguishable core and rim regions (Fig. 4.3c). Both regions preserve different compositional profiles whereby broad cores (~2.2 mm radius; Fig. 4.5) lack significant zonation in any cation and thin rims (~0.3 mm radius; Fig. 4.5) preserve relatively steep compositional gradients in both Ca and Mn. This profile suggests that core and rim regions did not grow during a single continuous metamorphic event. Given that abundant Mn exists in garnet core regions (up to ~5% molar proportion), 'bell-shaped' spessartine profiles would have formed during initial growth as a result of the continual fractionation of cations from the matrix (Hollister, 1966). Instead, the flat-to-slightly-concave Mn profile observed in the core region (Fig. 4.5) is suggestive of diffusional modification over some period of time following initial growth. The presence of a steep Mn gradient in rim regions indicates that a second (and unrelated) stage of garnet growth occurred after core compositions had formed (and subsequently had any zoning removed).

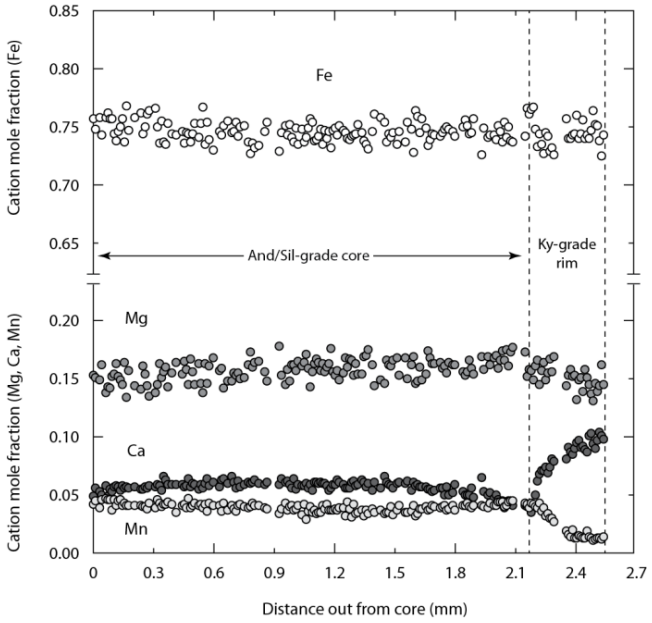


Fig. 4.5 – Garnet compositional profile for sample 20-199 from the Hunza Valley. Line profile is non-continuous due to traverses crossing inclusions and fractures.

Other petrographic features of sample 20-199 allow interpretation of this garnet profile. Here, aluminosilicate preserves evidence of three stages of metamorphism; firstly at andalusite-grade, secondly at sillimanite-grade and finally at kyanite-grade (also noted in Fraser *et al.*, 2001). Additionally, garnet rims can be seen enclosing kyanite replacements of prior aluminosilicate (Fig. 4.3a), indicating that rim growth post-dates at least andalusite formation. From these textural relationships it is interpreted that garnet rim growth occurred during the most recent metamorphic event, at kyanite-grade conditions, which must have occurred *after* diffusional modification of core compositions in order to preserve the observed steep Mn and Ca gradients. However, insufficient evidence exists to define whether garnet core growth occurred at andalusite- or sillimanite-grade.

Matrix mineralogy

Sample 20-199 contains aggregates of prismatic sillimanite that are circular and lack graphite inclusions (Fig. 4.3b), so appear to have a different origin from the rhombohedral pseudomorphs of sillimanite after andalusite (Fig. 4.3a). If these aggregates do represent a different precursor mineral, it must also predate sillimanite-grade events, thus likely coexisted with andalusite. Therefore, one must consider minerals that occur in Al-rich bulk compositions and are also stable at low-pressure. The association of cordierite with aluminosilicate is common in contact metamorphic rocks of pelitic bulk composition, forming via the prograde destabilisation of chlorite (Deer *et al.*, 1992):

$$\text{muscovite} + \text{chlorite} + \text{quartz} \rightarrow \text{cordierite} + \text{aluminosilicate} + \text{biotite} + H_2O \qquad (4.4.1)$$

Thus, these circular aggregates are interpreted to represent former cordierite porphyroblasts, which likely existed alongside andalusite during M0 contact metamorphism that is suggested to have affected rocks of the Hunza Valley during the Late Cretaceous (Crawford & Searle, 1992).

4.4.2. The Baltoro region

Garnet compositional zoning

Garnet compositional zoning profiles in samples K146 and T17 both show an increase in XMg from core to rim (Table 4.2), which indicates that they formed during a single episode of prograde metamorphism (Kohn & Spear, 2000). This is supported by the presence of a 'bell-shaped' spessartine profile in sample T17 – the absence of such a profile in sample K146 being interpreted as a result of an extremely low overall Mn bulk rock content whereby fractionation from the matrix could not occur. Nonetheless, it is expected that compositional zoning profiles in both samples would record the same metamorphic process, given their close proximity in outcrop (Fig. 4.2). Observed outer rim compositions are interpreted to represent those obtained at peak metamorphism due to the absence of inflections (or 'kicks') in either Mn or XMg (cf. Kohn & Spear, 2000).

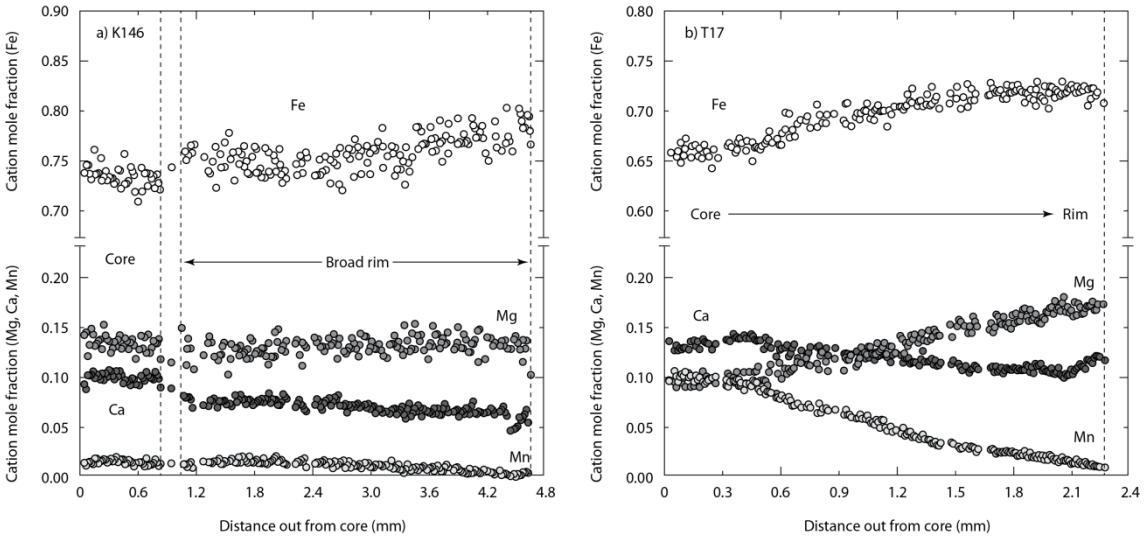


Fig. 4.6 – Garnet compositional profiles for samples K146 and T17 from the Baltoro region. Line profiles are non-continuous due to traverses crossing inclusions and fractures. (a) K146 (b) T17.

Matrix mineralogy

Samples K146 and T17 both contain textural evidence for the prograde breakdown of staurolite to produce biotite, Fe-Mg garnet and kyanite. Staurolite occurs as inclusions in garnet rims in both

cases and, in sample K146, matrix grains are associated with coarse unfoliated biotite and kyanite porphyroblasts (Fig. 4.4c). Furthermore, interlocking growth faces between kyanite porphyroblasts and garnet rims in sample K146 (Fig. 4.4a) suggest that garnet outer rims formed simultaneously with kyanite. Together, these relationships suggest that garnet rims, kyanite and associated coarse biotite are derived from the same prograde breakdown reaction (Deer *et al*., 1992):

$$\text{staurolite} + \text{muscovite} + \text{quartz} \rightarrow \text{Fe-Mg garnet} + \text{kyanite} + \text{biotite} + H_2O \qquad (4.4.2)$$

4.5. U–Pb monazite geochronology

Monazite is present in samples 20-199 and K146, and was analysed in order to constrain the timing of metamorphism and deformation in the Hunza Valley and Baltoro regions of the KMC. By contrast, sample T17 contains allanite so was unable to undergo geochronological analysis as a result of the current lack of suitable reference materials. All geochronological data collection, analysis and interpretation follows the methods outlined in chapter 3.5. Tera-Wasserburg plots are shown in Fig. 4.7 and SEM-microprobe compositional analyses for individual grains and internal domains are presented in Table 4.3. U–Pb ages for monazite in samples 20-199 and K146 are given in Table 4.4 and MC–ICP–MS data are given in Table 11.1. Compositional maps of all monazite grains, shown in Fig. 4.8, highlight spatial variation in cerium, thorium, uranium and yttrium. Although a slight overlap of uranium Mβ and potassium Kα1 EDS peaks can result in adjacent mica appearing apparently U-rich, the relative concentrations in monazite grains are proposed to be of value due to the exclusion of potassium from the monazite structure (Deer *et al*., 1992).

4.5.1. Monazite chemistry and U–Pb ages

20-199

Monazite from sample 20-199 is located in the cores and rims of garnet and is typically anhedral and very small (~30 μm diameter). Three analyses were obtained from grain 1, located in a garnet core and 10 analyses were obtained from 3 grains located in garnet rims (grains 2–4; Fig. 4.7a). Three analyses were rejected from grain 4 due to high common lead content and uneven ablation profiles during analysis. Grain 1 is relatively ThO_2-poor (4.30–5.52 wt%), UO_2-poor (0.02–0.25 wt%) and Y_2O_3-rich (1.44–1.80 wt%) with no systematic zoning (Fig. 4.8). By contrast, monazite inclusions in garnet rims are relatively Y_2O_3-poor (0.00–0.81 wt%) and contain a variety of zoning in ThO_2 and

UO_2 content (Fig. 4.8). Grains 3 and 4 contain broad ThO_2-poor bodies (4.92–5.49 wt%) that are surrounded by discontinuous thin ThO_2-rich rims (20.84–26.15 wt%). Grain 2 lacks such a rim, but still contains minor internal variation in ThO_2 (4.43–5.30 wt%). A regression of data for grain 1 on a Tera-Wasserburg plot produced a U–Pb lower intercept age of 105.5 ± 0.8 Ma (MSWD = 0.077; Fig. 4.7b). A regression of 7 data points from grains 2 and 3 produced a much younger U–Pb lower intercept age of 28.2 ± 0.8 Ma (MSWD = 0.80; Fig. 4.7c).

K146

Monazite from sample K146 is anhedral and 40–150 μm in diameter. A total of 22 analyses were obtained from 7 grains, though 3 analyses were rejected as a result of high common lead content.

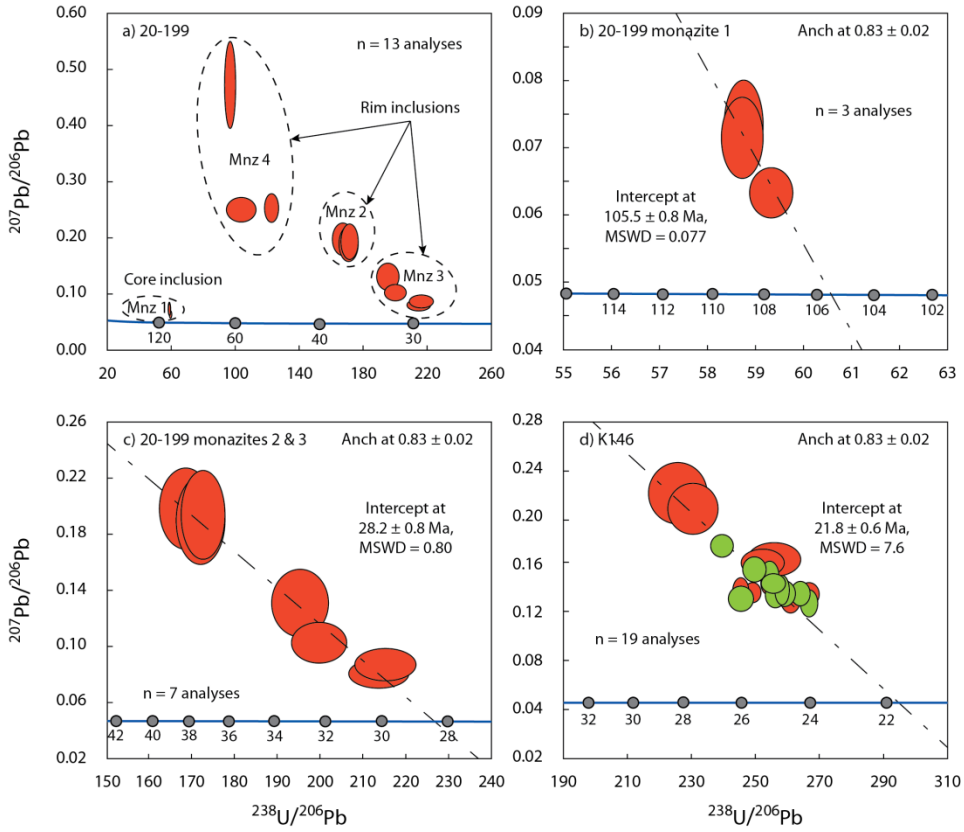
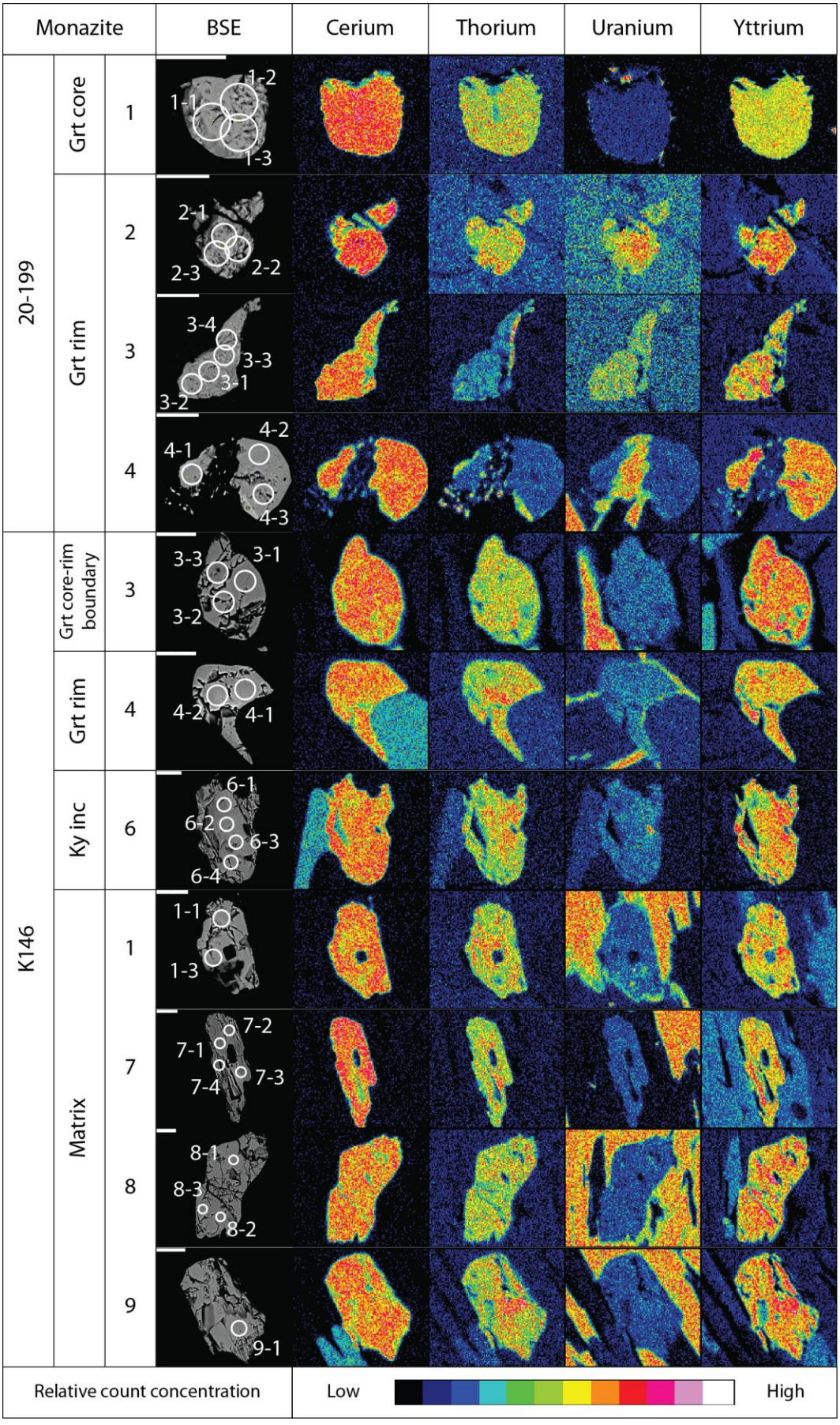


Fig. 4.7 – Tera-Wasserburg plots for samples 20-199 and K146. Red ellipses show analyses from monazite inclusions in garnet and green ellipses show matrix grain analyses. (a) All data for sample 20-199 (b) Regression for monazite grain 1, sample 20-199 (c) Regression for monazite grains 2 and 3, sample 20-199 (d) All data for sample K146.

Fig. 4.8 – Compositional maps of monazite from samples 20-199 and K146 (overleaf). SEM BSE images of each monazite show the location of ablation spots alongside compositional maps for cerium, thorium, uranium and yttrium. Scale bar in top left-hand corner for each monazite image is equal to 20 microns. Colour scale runs from 'cold' (black-dark blue) to 'warm' (red-pink) from low to high count rate respectively.


Monazite
BSE
Cerium
Thorium
Uranium
Yttrium
20-199
Grt core
Grt rim
K146
Grt core-rim boundary
Grt rim
Ky inc
Matrix
1
2
3
4
6
7
8
9
1-1
1-2
1-3
2-1
2-2
2-3
3-1
3-2
3-3
3-4
4-1
4-2
4-3
6-1
6-2
6-3
6-4
7-1
7-2
7-3
7-4
8-1
8-2
8-3
9-1
Relative count concentration
Low
High

Analysis	Petrographic position	Internal domain	SiO_2	P_2O_5	CaO	FeO	Y_2O_3	La_2O_3	Ce_2O_3	Pr_2O_3	Nd_2O_3	Sm_2O_3	Eu_2O_3	Gd_2O_3	Tb_2O_3	Dy_2O_3	Ho_2O_3	Er_2O_3	Tm_2O_3	Yb_2O_3	Lu_2O_3	PbO	ThO_2	UO_2	**Total**
20-199 Mnz 1	Inclusion in Grt core	Core	0.39	26.70	1.08	1.43	1.50	14.63	26.76	2.86	10.17	2.27	0.01	2.21	0.32	0.72	0.30	0.54	0.22	0.17	0.10	b.d.l	4.30	0.19	**96.86**
20-199 Mnz 1	Inclusion in Grt core	Core	0.40	28.44	1.08	1.06	1.80	14.33	27.64	3.14	10.59	1.56	0.24	1.36	0.32	0.59	0.05	0.21	b.d.l	b.d.l	0.22	0.07	5.52	0.17	**98.79**
20-199 Mnz 1	Inclusion in Grt core	Rim	0.05	25.65	0.92	1.57	1.70	15.17	28.59	3.21	10.97	2.25	0.54	1.35	0.25	0.33	0.05	0.09	b.d.l	b.d.l	b.d.l	b.d.l	4.41	0.25	**97.34**
20-199 Mnz 1	Inclusion in Grt core	Rim	0.15	28.32	1.06	1.59	1.44	15.15	28.15	2.88	11.26	1.56	0.29	0.93	0.28	0.06	b.d.l	b.d.l	b.d.l	b.d.l	0.05	b.d.l	5.30	0.05	**98.54**
20-199 Mnz 2	Inclusion in Grt rim	Core	0.07	27.22	1.08	2.18	0.42	14.89	28.15	3.07	10.77	1.93	0.53	1.64	0.27	0.00	b.d.l	b.d.l	b.d.l	b.d.l	0.13	b.d.l	4.43	0.54	**97.33**
20-199 Mnz 2	Inclusion in Grt rim	Rim	0.82	26.65	1.29	2.14	0.81	14.59	27.69	2.78	10.66	1.92	0.22	1.78	0.42	0.21	b.d.l	b.d.l	b.d.l	b.d.l	b.d.l	0.01	5.30	0.41	**97.71**
20-199 Mnz 3	Inclusion in Grt rim	Th-rich rim	5.03	20.57	2.02	3.45	0.81	8.90	18.79	2.46	8.07	1.24	0.37	0.79	0.06	0.10	b.d.l	0.12	0.03	0.02	0.11	0.05	26.15	0.26	**99.41**
20-199 Mnz 3	Inclusion in Grt rim	Dull core	0.29	29.50	1.04	0.97	0.06	14.39	28.54	2.78	10.88	1.88	0.02	1.14	0.16	0.38	b.d.l	b.d.l	b.d.l	b.d.l	b.d.l	0.02	4.92	0.31	**97.27**
20-199 Mnz 4	Inclusion in Grt rim	Th-rich rim	2.68	22.90	1.88	0.68	0.00	10.88	21.69	2.04	9.09	1.22	0.13	0.79	0.04	0.10	b.d.l	b.d.l	b.d.l	b.d.l	b.d.l	0.08	20.84	0.19	**95.23**
20-199 Mnz 4	Inclusion in Grt rim	Dull core	0.00	27.90	1.04	0.68	0.25	13.94	28.24	3.27	10.78	1.73	0.12	1.25	0.00	0.46	0.03	0.20	b.d.l	0.01	0.06	0.14	5.49	0.31	**95.91**
K146 Mnz 1	Matrix	Body	0.04	28.73	1.52	0.23	0.73	14.27	25.96	2.86	8.94	2.04	0.43	1.81	0.22	0.71	b.d.l	0.26	b.d.l	0.20	0.25	0.08	8.25	0.53	**98.06**
K146 Mnz 1	Matrix	Body	0.15	29.03	1.70	0.21	0.68	13.87	25.41	3.38	9.38	1.52	0.00	1.31	0.15	0.76	0.09	0.33	0.12	0.43	0.25	0.12	9.92	0.54	**99.34**
K146 Mnz 3	Inclusion in Grt rim	Body	0.10	28.19	1.61	0.47	1.22	14.74	26.81	2.84	9.48	1.65	0.04	0.86	0.14	0.45	0.27	0.03	b.d.l	0.04	0.03	b.d.l	8.96	0.89	**98.81**
K146 Mnz 3	Inclusion in Grt rim	Body	0.10	28.38	1.57	0.34	0.22	14.42	26.47	3.30	9.15	1.62	0.00	1.39	0.16	0.74	0.08	0.23	b.d.l	0.17	0.03	0.18	9.16	0.34	**98.03**
K146 Mnz 4	Inclusion in Grt rim	Body	0.31	27.60	2.41	0.69	0.03	13.03	23.69	3.01	8.47	1.43	0.00	1.32	0.41	0.54	0.02	0.15	b.d.l	b.d.l	0.12	b.d.l	14.70	1.13	**99.05**
K146 Mnz 4	Inclusion in Grt rim	Body	0.35	28.05	2.23	0.99	0.06	12.26	23.48	2.57	8.58	1.82	0.41	1.51	0.38	0.47	0.12	0.26	b.d.l	0.05	b.d.l	0.11	13.75	1.05	**98.49**
K146 Mnz 6	Inclusion in Ky	Th-rich core	0.04	29.22	2.20	0.06	0.93	12.70	23.47	2.89	9.12	1.48	0.00	1.33	0.00	1.01	b.d.l	b.d.l	b.d.l	0.06	b.d.l	0.01	12.53	1.10	**98.14**
K146 Mnz 6	Inclusion in Ky	Th-poor rim	0.00	28.75	1.41	0.18	0.57	14.36	25.99	2.81	9.40	1.97	0.56	1.76	0.52	1.09	0.13	0.28	0.06	b.d.l	0.09	0.06	7.68	0.47	**98.14**
K146 Mnz 7	Matrix	Body	0.16	29.43	1.54	0.10	1.00	14.14	25.65	2.84	9.79	1.61	0.22	1.39	0.27	0.88	0.28	0.39	0.21	0.18	0.01	b.d.l	8.87	0.42	**99.39**
K146 Mnz 7	Matrix	Body	0.33	28.90	1.62	0.04	0.88	13.44	25.46	2.90	9.12	1.75	0.26	1.42	0.13	0.92	0.26	0.45	0.02	0.11	0.17	0.11	10.05	0.60	**98.93**
K146 Mnz 8	Matrix	Body	0.03	28.71	1.68	0.08	0.17	13.85	25.02	3.27	9.30	1.68	0.33	1.53	0.30	1.00	0.43	0.47	0.10	0.10	0.01	0.05	9.87	0.73	**98.71**
K146 Mnz 8	Matrix	Body	0.00	29.09	1.72	0.20	0.96	14.16	25.60	2.96	9.27	1.65	0.01	1.60	0.34	1.00	b.d.l	0.02	b.d.l	b.d.l	b.d.l	0.19	9.53	0.50	**98.78**
K146 Mnz 9	Matrix	Th-poor mantle	0.19	29.23	1.36	0.16	0.82	14.52	26.29	2.87	9.65	1.40	0.26	1.69	0.44	0.73	0.06	0.19	b.d.l	0.03	b.d.l	0.08	7.93	0.65	**98.56**
K146 Mnz 9	Matrix	Th-rich core	0.12	29.33	1.73	0.00	1.28	14.40	25.46	2.62	8.97	1.48	0.20	1.49	0.31	0.72	b.d.l	0.46	0.05	b.d.l	0.06	0.14	9.76	0.79	**99.37**

Table 4.3 – Monazite compositions from samples 20-199 and K146 shown in weight % oxide.

Analysis	Position	Calculated age (Ma)						Corrected age (Ma)	
		$^{207}Pb/^{206}Pb$ 2σ (abs)		$^{206}Pb/^{238}U$ 2σ (abs)		$^{207}Pb/^{235}U$ 2σ (abs)		$^{206}Pb/^{238}U$ 2σ (abs)	
K146 Mnz 1-1	Matrix	2661	73	26.7	0.3	99.9	4.3	22.1	0.4
K146 Mnz 1-3	Matrix	2173	113	26.0	0.3	74.1	4.7	23.1	0.4
K146 Mnz 3-1	Inclusion in Grt rim	3025	152	28.3	0.9	130.5	12.2	21.8	1.1
K146 Mnz 3-2	Inclusion in Grt rim	2925	137	27.7	0.8	120.8	10.1	21.9	0.9
K146 Mnz 3-3	Inclusion in Grt rim	2251	115	26.0	0.2	77.4	5.0	22.9	0.4
K146 Mnz 4-1	Inclusion in Grt rim	2521	98	25.3	0.6	87.8	5.2	21.5	0.6
K146 Mnz 4-2	Inclusion in Grt rim	2551	116	25.0	0.7	88.1	6.2	21.1	0.7
K146 Mnz 6-1	Inclusion in Ky	2220	100	24.0	0.2	70.3	4.0	21.1	0.4
K146 Mnz 6-2	Inclusion in Ky	2335	90	25.2	0.2	78.5	4.0	21.9	0.3
K146 Mnz 6-3	Inclusion in Ky	2240	86	25.7	0.2	75.8	3.7	22.6	0.3
K146 Mnz 6-4	Inclusion in Ky	2170	127	24.5	0.2	69.8	4.9	21.7	0.4
K146 Mnz 7-1	Matrix	2227	106	24.2	0.2	71.2	4.3	21.3	0.4
K146 Mnz 7-2	Matrix	2463	92	25.6	0.3	85.8	4.6	21.9	0.4
K146 Mnz 7-3	Matrix	2330	80	25.0	0.3	77.9	3.6	21.8	0.4
K146 Mnz 7-4	Matrix	2227	112	24.7	0.3	72.5	4.6	21.8	0.4
K146 Mnz 8-1	Matrix	2216	115	25.0	0.3	72.9	4.7	22.0	0.4
K146 Mnz 8-2	Matrix	2263	125	24.8	0.2	74.2	5.2	21.7	0.4
K146 Mnz 8-3	Matrix	2120	126	24.0	0.2	66.5	4.6	21.4	0.4
K146 Mnz 9-1	Matrix	2408	111	25.1	0.2	81.7	5.2	21.6	0.4
20-199 Mnz 1-1	Inclusion in Grt core	991	232	108.4	1.0	158.3	16.6	105.1	1.5
20-199 Mnz 1-2	Inclusion in Grt core	730	166	107.3	1.1	139.6	10.3	105.2	1.2
20-199 Mnz 1-3	Inclusion in Grt core	1038	241	108.4	1.0	161.7	17.7	104.8	1.5
20-199 Mnz 2-1	Inclusion in Grt rim	2742	220	37.5	1.1	144.5	18.2	30.7	1.5
20-199 Mnz 2-2	Inclusion in Grt rim	2776	216	37.4	1.0	146.9	18.2	30.4	1.5
20-199 Mnz 2-3	Inclusion in Grt rim	2814	192	38.4	1.2	153.6	17.2	30.9	1.5
20-199 Mnz 3-1	Inclusion in Grt rim	1360	211	29.7	0.8	54.7	6.0	28.2	0.9
20-199 Mnz 3-2	Inclusion in Grt rim	1674	216	32.1	0.9	69.3	8.0	29.8	1.0
20-199 Mnz 3-3	Inclusion in Grt rim	1208	209	29.9	0.8	51.1	5.5	28.6	0.9
20-199 Mnz 3-4	Inclusion in Grt rim	2114	266	32.8	1.0	89.7	13.2	29.3	1.2
20-199 Mnz 4-1	Inclusion in Grt rim	3214	128	52.2	1.5	255.1	19.2	38.4	1.9
20-199 Mnz 4-2	Inclusion in Grt rim	3193	112	61.7	4.5	292.1	25.6	45.7	3.7
20-199 Mnz 4-3	Inclusion in Grt rim	4166	198	66.1	1.9	524.3	54.6	30.0	5.6

Table 4.4 – MC–ICP–MS U–Pb ages for samples 20-199 and K146

Matrix grains contain small cores with ThO_2 up to 10.05 wt% (e.g. grain 7; Fig. 4.8 & Table 4.3), which are surrounded by rims that have lower ThO_2 (as little as 7.93 wt%). Y_2O_3 and UO_2 contents range between 0.17–1.28 wt% and 0.42–0.79 wt% respectively, showing no correlation with ThO_2 zoning. Monazite inclusions in kyanite and garnet have a similar Y_2O_3 content to those grains in the matrix (0.03–1.22 wt%) but contain higher ThO_2 (7.68–14.70 wt%) and UO_2 (0.34–1.13 wt%). All data points, including monazite in the matrix (green ellipses; Fig. 4.7d) and grains included in garnet and kyanite (red ellipses; Fig. 4.7d) were interpreted with a single regression on a Tera-Wasserburg plot, producing a U–Pb lower intercept age of 21.8 ± 0.6 Ma (MSWD = 7.6). Although this MSWD is high for a single population, there is no apparent difference in common lead corrected ages between grains in different textural positions so growth populations cannot be established.

4.5.2. Interpretation

Samples 20-199 and K146 both lack textural evidence relating to the timing or nature of possible monazite-forming reactions (e.g. the absence of relic allanite preserved within early phases). Hence,

microstructural relationships between monazite grains and major minerals are used to apply a petrographic context to the ages obtained.

20-199

Andalusite pseudomorphs (Fig. 4.3a) show that sample 20-199 has experienced three separate metamorphic episodes, most recently involving a partial kyanite-grade overprint of Hunza Valley LSZ units. In addition, interpretation of garnet compositional zoning profiles (Fig. 4.5) has inferred that rims formed during this most recent kyanite-grade metamorphism, whereas cores predate this event and may have formed during either andalusite- or sillimanite-grade metamorphism. Monazite from sample 20-199 was analysed as inclusions in the core (grain 1) and rim (grain 2) regions of the same garnet porphyroblast (Fig. 4.9a), thus the ages obtained can be related directly to one another in terms of the tectonic history of the sample. Additionally, although grain 1 is located along a garnet fracture, no hydrous minerals occur as infill (Fig. 4.9b) and the absence of compositionally distinct overgrowths observed in compositional maps of the monazite grain (Fig. 4.8) suggests that there has been no hydrothermal alteration of this grain (cf. Carson *et al.*, 2004). Grain 1 also contains more Y_2O_3 than grains included in garnet rims (Table 4.3), which suggests that grain 1 crystallised prior to garnet growth (see chapter 3.4.2) and that the U–Pb ages obtained are representative of a primary metamorphic episode rather than fluid-assisted recrystallisation at some later time.

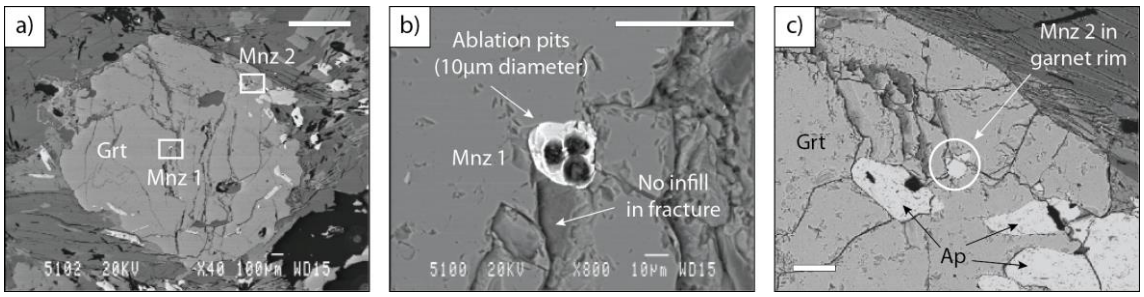


Fig. 4.9 – Petrographic positions of monazite inclusions in garnet in sample 20-199. Monazite inclusions 1 and 2 are located within the same garnet core and rim regions respectively. Scale bar equals 500 microns. Boxes indicate approximate locations of Fig. 4.9b–c. (b) SEM BSE image of grain 1 post-ablation. Compositional analysis shows a total lack of infill along the garnet fracture along which grain 1 lies. Scale bar equals 50 microns. (c) SEM BSE image of grain 2 included in the garnet rim. Scale bar equals 50 microns.

Protracted crustal thickening in the Hunza Valley during closure of the Neo-Tethys Ocean between c. 83–53 Ma (chapter 4.2.1) resulted in extended periods of muscovite-dehydration sillimanite-grade metamorphism and melting (M1). Foster et al. (2004) used garnet-xenotime

thermometry to interpret this oldest episode of monazite growth as representing the initiation of sillimanite-grade metamorphism at ~550 °C. These new data indicating monazite growth at 105.5 ± 0.8 Ma are considerably older than this event; therefore, if it were to also represent growth during sillimanite-grade conditions, the duration of M1 would increase from at least 30 Myr to over 52 Myr. This scenario is implausible as it directly conflicts with the data of Foster *et al*. (2004), so the age of 105.5 ± 0.8 Ma is interpreted to represent monazite growth during previous andalusite-grade contact metamorphism (M0) associated with emplacement of the Karakoram batholith during early subduction and closure of the Neo-Tethys Ocean. This is supported by the oldest ages documenting intrusion of the HPU of 105.7 ± 0.5 Ma (Table 4.1). Additionally, rare andalusite-bearing hornfels in the Baltoro region is spatially associated with the deformed Hushe gneisses, which represent original igneous components of the Karakoram batholith that have been subsequently metamorphosed during the India-Asia collision (Searle *et al*., 1989; Crawford & Searle, 1992). Although no age data for these andalusite-bearing units has been documented, it is likely that early metamorphism in sample 20-199 represents their along-strike equivalent in the Hunza Valley.

A U–Pb age of 28.2 ± 0.8 Ma obtained from monazite grains 2 and 3 provides a maximum age constraint on the timing of garnet rim growth and therefore peak kyanite-grade metamorphism. Previous study of sample 20-199 by Fraser *et al*. (2001) produced a U–Pb monazite age of 44.0 ± 2.0 Ma that was interpreted as representing peak sillimanite-grade metamorphism in the LSZ of the Hunza Valley. However, these data were obtained via isotope dilution thermal ionization mass spectrometry (ID-TIMS) on three separated grains; therefore, the true petrographic significance of the age is uncertain. Despite this, this interpreted age of 44.0 ± 2.0 Ma supports microstructural and compositional evidence showing that kyanite-grade metamorphism post-dates both sillimanite- and andalusite-grade metamorphism. No geochronology has been performed on rocks from the kyanite-zone in the southern Hunza Valley (Fig. 4.1), so it is unclear whether this partial overprint on LSZ units is comparable with those units – further work on suitable samples is required to determine this.

K146

Monazite from sample K146 is situated in the matrix and as inclusions in garnet and kyanite porphyroblasts. With this variation in textural setting, different grains could potentially provide age

constraints on the timing of different stages of metamorphism if monazite formation was simultaneous with the later stages of prograde metamorphism and precise dating was achieved. However, green ellipses on Fig. 4.7d represent data obtained from matrix grains and red ellipses represent data from monazite inclusions in garnet and kyanite. It is evident that common lead corrected U–Pb ages for individual grains are indistinguishable and all analyses form a co-linear relationship along a single regression that produced an age of 21.8 ± 0.6 Ma (Fig. 4.7d). This suggests that all monazite growth occurred prior to staurolite breakdown and these grains were subsequently included into garnet and kyanite. This is supported by the lack of significant distinction in Y_2O_3 content between grains included in garnet and those in the matrix (Table 4.3). This age of 21.8 ± 0.6 Ma is therefore interpreted to provide a minimum age constraint on kyanite-grade conditions in sample K146, which must have peaked sometime afterwards.

4.6. Thermobarometry and phase diagram modelling

Peak *P–T* conditions of kyanite-grade metamorphism in the Baltoro region (samples K146 & T17) and the Hunza Valley (sample 20-199) were calculated using AvePT and conventional thermobarometry. Sample T17 was also used for investigation of its prograde *P–T* history as a result of its apparently unmodified garnet compositional growth zoning. This method involved the construction of *P–T* pseudosections that examined the effects of cation sequestration into garnet, thus dynamically changing the effective bulk composition (EBC) during metamorphism.

4.6.1. AvePT and conventional thermobarometry

Hunza Valley

Sample 20-199 contains graphite in the matrix foliation, implying dilution of the fluid phase with a proportion of CO_2 during peak metamorphism. Many temperature-sensitive equilibria are also sensitive to the composition of a coexisting metamorphic fluid; thus, AvePT was employed over a range of XH_2O in order to examine the dependence of calculated kyanite-grade peak *P–T* conditions to fluid composition. Fluid composition was constrained to a maximum XH_2O of 0.85 in accordance with the predicted CO_2 content of a metamorphic fluid coexisting with graphite at mid-crustal pressures in the upper amphibolite-facies (Ohmoto & Kerrick, 1977). Calculations with a fluid of composition XH_2O = 0.85 produced peak *P–T* conditions of 8.4 ± 1.1 kbar and 698 ± 24 °C (Table

4.5), whereas, for comparison, calculations with pure H_2O produced peak *P–T* conditions of 8.6 ± 1.1 kbar and 711 ± 25 °C. Calculations omitting fluid as a phase component produced *P–T* conditions of 7.8 kbar and 644 °C (Fig. 4.10), with larger associated uncertainties of ± 1.4 kbar and 85 °C (Table 4.5). The input activities of all end-members used are given in Appendix 11.5. As actual fluid composition during metamorphism is undeterminable, the best estimate of peak *P–T* conditions uses fluid-absent equilibria. Hence, the latter result of 7.8 kbar and ~645 °C is used for peak kyanite-grade conditions for this event in the Hunza Valley. This is supported by the Ti content of biotite in the matrix foliation, also a fluid-independent geothermometer, and which produced a temperature range between 628–639 °C (± 23 °C) through the calibration of Henry *et al*. (2005).

Sample	Calculation assemblage	XH_2O	T (°C)	1 S.D.	P (kbar)	1 S.D.	Cor	Sig Fit	N	End-members excluded
K146	Grt, St, Ms, Pl, Bt, Ky, Ilm, Qz, H_2O	1.00	642	21	7.4	0.8	0.14	0.67	8	spss, ilm, pnt, geik, pa
T17	Grt, St, Ms, Pl, Bt, Ky, Rt, Qz, H_2O	1.00	661	22	8.0	0.8	0.21	0.37	7	ru, mst, pa
20-199	Grt, Ms, Pl, Bt, Ky, Ilm, Qz, H_2O	1.00	711	25	8.6	1.1	0.80	0.61	5	spss, ilm, pnt, geik
20-199	Grt, Ms, Pl, Bt, Ky, Ilm, Qz, H_2O	0.85	692	24	8.3	1.1	0.80	0.52	5	spss, ilm, pnt, geik
20-199	Grt, Ms, Pl, Bt, Ky, Ilm, Qz	N/A	644	85	7.8	1.4	0.82	0.50	4	spss, ilm, pnt, geik, H_2O

Table 4.5 – THERMOCALC AvePT results for samples 20-199, K146 & T17. Cor = correlation, Sig Fit = significant fit, N = number of independent reactions used in calculation (after Powell & Holland, 1994).

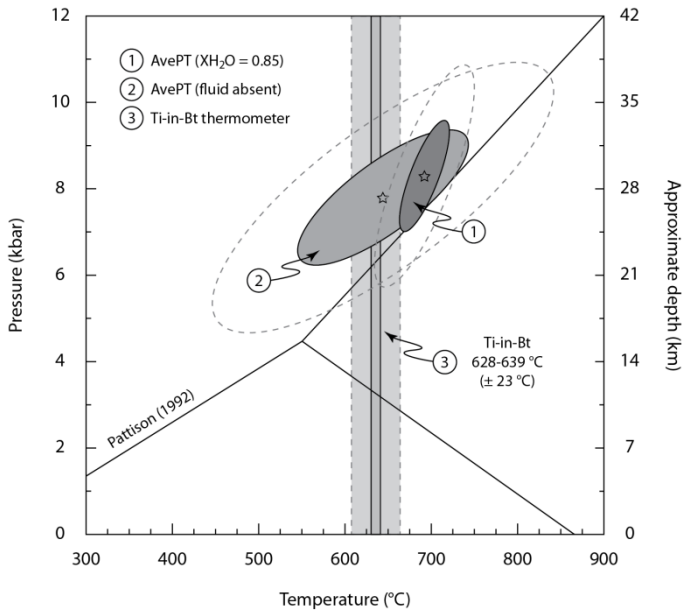


Fig. 4.10 – Thermobarometric results for peak metamorphism in sample 20-199 from the Hunza Valley. Aluminosilicate phase relations and triple point are after Pattison (1992).

Baltoro region

Peak kyanite-grade conditions in the Baltoro region were calculated through analysis of samples K146 and T17. A set of 8 independent reactions for sample K146 produced an AvePT result of 7.4 ±

0.8 kbar and 642 ± 21 °C (Table 4.5). An independent check on these conditions is provided by the Ti content of biotite throughout the sample; coarse unfoliated grains associated with staurolite breakdown contain XMg = 0.42–0.46 and Ti = 0.14–0.16 cpfu (Table 4.2) and produced temperatures of 624–658 °C (± 23 °C). AvePT calculations for sample T17 produced *P–T* conditions of 8.0 ± 0.8 kbar and 661 ± 22 °C (Table 4.5) for peak kyanite-grade metamorphism, whereas the Ti content of matrix biotite produced results of 675–690 °C (± 23 °C). Thus, AvePT results from both samples are within uncertainty and suggest that peak kyanite-grade conditions lie between ~7.4–8.0 kbar and ~640–660 °C. This *P–T* range is supported, within error, by the analysis of biotite compositions and is similar to peak conditions of 7.8 kbar and ~645 °C as suggested for kyanite-grade conditions in the Hunza Valley in sample 20-199.

4.6.2. Pseudosection modelling

The retention of compositional growth zoning in garnet in sample T17 allows examination of the prograde *P–T* evolution up to peak kyanite-grade conditions in the Baltoro via pseudosection modelling. Initial pseudosection construction and bulk composition calculations were undertaken following the methods outlined in chapter 2.4. As a result of the subsolidus nature of sample T17 H_2O was assumed to be in excess for initial pseudosection construction. Phase compositions and volume proportions used in bulk composition calculation are given in Appendix 11.6. The modelled bulk composition for sample T17 is SiO_2 – 67.97; Al_2O_3 – 16.00; FeO – 4.98; MgO – 3.98; CaO – 1.49; K_2O – 2.99; Na_2O – 0.84; TiO_2 – 1.57; MnO – 0.13; O – 0.04 (mole %).

The fundamental method of prograde *P–T* path calculation using a compositional zoning profile in garnet relies on the construction of a pseudosection for a specific bulk composition, which is subsequently contoured for isopleths relevant to the analysed porphyroblast (e.g. Vance & Mahar, 1998; Wei & Song, 2008). Measured compositions (e.g. from core-to-rim) can be tracked across *P–T* space by following intersecting isopleths and the resulting path will pass through each intersection. This methodology is theoretically sound if the EBC remains fixed; however, due to the physical resistance of garnet to recrystallisation during deformation, coupled with slow intracrystalline rates of cation diffusion (Carlson, 2006), this simplification is often untrue – even if the rock itself acts as a closed system on the scale of examination.

It is commonly reported in the literature that garnet growth is an efficient mechanism for the removal of cations from the reacting matrix and, once sequestered into a growing garnet, they are unavailable for further reaction such that the matrix becomes 'depleted' (e.g. Konrad-Schmolke *et al*., 2008). This is an effect that becomes increasingly important as the grains grow, as garnet volume increases proportionally to the cube of the radius (assuming spherical geometry). The result of such 'fractionation' on a bulk rock composition has been considered by many previous studies, all of which conclude that it can have a significant effect on the calculated peak metamorphic assemblage, if garnet volume is sufficiently large (e.g. Marmo *et al*., 2002 and others). Various methodologies used to model fractionation have been outlined in the literature and the particular one used in this study is outlined below.

Fractionation methodology

From an initial bulk composition, representing that present before first garnet nucleation, the successive removal of garnet 'domains' during growth was achieved by manipulation of the read-bulk-info (RBI) matrix that is produced by THERMOCALC (using the *readbulkinfo yes* script). The RBI code defines a bulk composition in terms of a matrix of modal proportions and compositions (in moles of oxide system components) of all considered phases. Manipulating individual elements of the matrix allows reduction of garnet modal proportion (to zero) in order to sequester constituent cations from the total bulk composition, thus fractionating (cf. White, 2010).

The analysed garnet compositional zoning profile must be sectioned into multiple parts divided by points that are spaced out from core to rim. Each section defines an episode of garnet growth and the composition at each point can be located on a *P–T* pseudosection via isopleth intersections. In this study, isopleths representing pyrope and grossular content are used as monitors. Initial core nucleation may be located on a pseudosection constructed using the initial EBC at the intersection of 'core isopleths'. These isopleths should overlap with the garnet-in field boundary (within calculated error) and at this point the rock has zero garnet volume (Fig. 4.11).

The isopleth intersection representing the next rimward point along the garnet zoning profile is then located in *P–T* space. The RBI matrix at this new point shows the proportion of garnet that has grown, with other matrix phase modal proportions changing accordingly. As prograde garnet

growth occurs largely through dehydration reactions, this method of fractionation does not function properly if H_2O remains in excess in THERMOCALC (D.J. Waters *pers comms*, 2010). As a result, fluid is treated as a compositional variable from the point of first garnet growth and any H_2O liberated into the matrix is likely to be lost from the rock. Thus, adjustment of garnet and H_2O modal proportion to zero fractionates this first portion of garnet from the EBC and the modified RBI matrix is then used as the new rock bulk composition (Fig. 4.11). This process is repeated for successive compositions, manually reducing garnet and H_2O modal proportion to zero each time, until rim compositions have been located. This method also allows numerous data to be monitored at each step, including modal proportions and compositions of all phases calculated to be stable in addition to the evolving EBC of the reacting matrix. The total volume of garnet formed can be found from a summation of all steps and should match the final observed garnet proportion in the sample rock. The proportions of matrix phases presented (other than garnet and H_2O) are adjusted in order to account for the fact that a volume of garnet has already formed, thus the new assemblage does not constitute exactly 100% of the rock volume. Table 4.7 (below) demonstrates this effect by showing the modal proportions calculated at each step prior to, and following, adjustment.

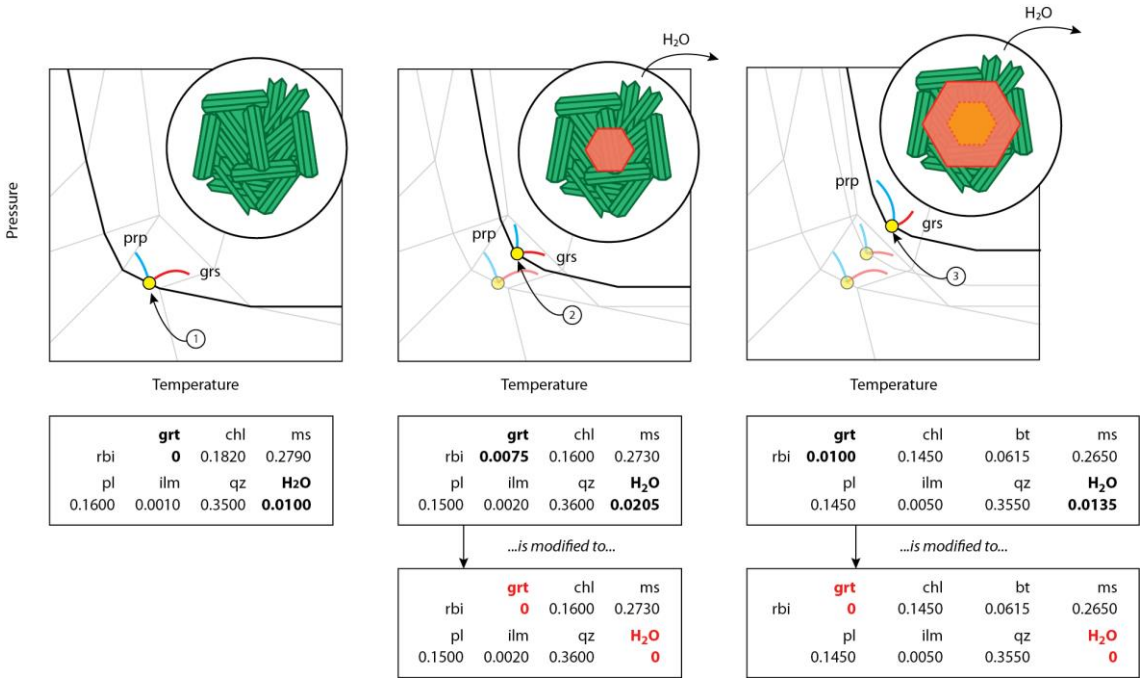


Fig. 4.11 – Schematic illustration of the method used for cation fractionationduring thermodynamic modelling. The bulk composition as defined by the RBI matrix is sequentially changed to model the removal of garnet and loss of metamorphic fluid following the method described in the text.

Results

A *P–T* pseudosection for sample T17 (calculated with a fixed EBC) is presented in Fig. 4.12a and allows preliminary interpretation of the prograde evolution of kyanite-grade units in the Baltoro region. Garnet-absent assemblage fields have been calculated, but are not shown, as the focus of the investigation concerns prograde garnet growth. The peak assemblage of grt–bt–ms–pl–ky–rt–qz–H_2O exists as a single field located between ~7–11.5 kbar and ~590–690 °C and has considerable overlap in *P–T* space with the calculated AvePT ellipse centred on 8 kbar and 661 °C. The upper temperature limit for peak conditions is provided by the appearance of silicate melt, although it should be noted that suprasolidus regions of Fig. 4.12a–c are likely to be unrealistic due to calculation with excess H_2O. Compositional isopleths for pyrope and grossular content (Fig. 4.12b) intersect at high angles, thus providing unique intersection points with a strong degree of confidence for tracking garnet composition evolution. A prograde *P–T* path has been calculated for both a fixed (Fig. 4.12c) and fractionating (Fig. 4.12d) EBC. For the latter, 9 equally spaced steps were chosen from core to rim of the analysed garnet in sample T17 (Fig. 4.6b); step 1 represents the garnet core and step 9 represents the garnet rim. Shaded boxes in Fig. 4.12 represent 1 S.D. uncertainties on intersection points as calculated by THERMOCALC. Compositions used at each step for tracking isopleth intersections are presented in Table 4.6 with changes in the calculated EBC following each fractionation step. Table 4.7 shows the changing modal proportions of coexisting phases during prograde metamorphism, with and without considering the effects of cation fractionation.

Step	prp	grs	H_2O	SiO_2	Al_2O_3	CaO	MgO	FeO	K_2O	Na_2O	TiO_2	MnO	O	P (kbar)	T (°C)
1	0.097	0.138	Excess	67.97	16.00	1.49	3.98	4.98	2.99	0.84	1.57	0.13	0.04	5.03	561.3
2	0.107	0.134	11.32	60.28	14.19	1.32	3.53	4.42	2.65	0.75	1.39	0.12	0.04	5.15	568.5
3	0.118	0.123	11.18	60.41	14.22	1.32	3.54	4.40	2.66	0.75	1.40	0.11	0.04	5.12	575.5
4	0.130	0.114	11.07	60.53	14.24	1.31	3.54	4.37	2.67	0.75	1.40	0.10	0.04	5.31	581.5
5	0.138	0.105	7.39	63.13	14.83	1.36	3.68	4.47	2.79	0.78	1.47	0.07	0.04	5.47	596.4
6	0.143	0.111	7.33	63.18	14.84	1.35	3.68	4.47	2.79	0.79	1.47	0.07	0.04	6.56	627.1
7	0.154	0.107	6.24	64.43	15.05	1.31	3.68	4.03	2.89	0.81	1.52	0.03	0.04	7.13	654.3
8	0.158	0.109	6.24	64.76	15.08	1.27	3.65	3.69	2.93	0.82	1.54	0.01	0.04	7.38	660.7
9	0.167	0.113	6.28	64.93	15.08	1.24	3.62	3.48	2.95	0.83	1.55	0.00	0.04	7.81	669.2

Table 4.6 – Changes in sample T17 EBC during fractionation expressed as molar proportions of oxides. Pyrope and grossular contents used to calculate *P–T* intersection loci at each step are also shown.

Garnet core isopleths (0.097 prp) and (0.138 grs) predict initial nucleation at ~5 kbar and ~560 °C in an assemblage field of chl–ms–st–pl–ilm–rt–qz–H_2O (Fig. 4.12c). Without considering cation fractionation into garnet, biotite becomes stable in the place of chlorite during prograde

metamorphism between ~569 and 574 °C, the latter being consumed from an initial modal proportion of 0.149 to zero over ~20 °C (Table 4.7). The consumption of chlorite coincides with a sharp increase in the modal proportion of staurolite over the same temperature interval. From an initial proportion of 0.051, this increases to 0.129 with no fractionation and 0.128 with fractionation, adjusted for garnet, at the same point.

No fractionation

Step	Grt	St	Chl	Bt	Ms	Pl	Ky	Ilm	Rt	Qz	H_2O	Grt^C	P (kbar)	T (°C)
1	0.000	0.051	0.149		0.374	0.077		0.027	0.001	0.321	Excess	0.000	5.03	561.3
2	0.001	0.054	0.144		0.372	0.078		0.029	0.000	0.321	Excess	0.001	5.15	568.5
3	0.001	0.064	0.125	0.017	0.358	0.081		0.029	0.000	0.325	Excess	0.001	5.10	574.3
4	0.006	0.129		0.160	0.246	0.091		0.009	0.009	0.351	Excess	0.006	5.25	581.7
5	0.014	0.054		0.181	0.224	0.096	0.065	0.018	0.004	0.345	Excess	0.014	5.87	610.0
6	0.036			0.186	0.221	0.093	0.107	0.017	0.005	0.337	Excess	0.036	6.49	623.7
7	0.053			0.178	0.223	0.092	0.103	0.009	0.009	0.332	Excess	0.053	6.98	646.5
8	0.062			0.173	0.228	0.090	0.101	0.005	0.010	0.330	Excess	0.062	7.17	651.0
9	0.079			0.160	0.240	0.086	0.097	0.001	0.013	0.326	Excess	0.079	7.57	658.0

Fractionated modal proportions of each phase calculated at each step

Step	Grt	St	Chl	Bt	Ms	Pl	Ky	Ilm	Rt	Qz	H_2O	Grt^C	P (kbar)	T (°C)
1	0.000	0.051	0.149		0.374	0.077		0.027	0.001	0.321	0.000	0.000	5.03	561.3
2	0.001	0.054	0.144		0.372	0.078		0.029	0.000	0.321	0.002	0.001	5.15	568.5
3	0.002	0.056	0.141		0.370	0.080		0.029	0.000	0.321	0.002	0.003	5.12	575.5
4	0.003	0.124		0.154	0.238	0.087		0.008	0.009	0.337	0.040	0.006	5.31	581.5
5	0.001	0.131		0.161	0.243	0.094		0.008	0.010	0.352	0.001	0.007	5.47	596.4
6	0.019			0.190	0.213	0.095	0.109	0.021	0.003	0.337	0.013	0.026	6.56	627.1
7	0.013			0.194	0.217	0.100	0.112	0.014	0.007	0.344	0.001	0.039	7.13	654.3
8	0.008			0.192	0.224	0.100	0.112	0.010	0.009	0.346	0.000	0.047	7.38	660.7
9	0.018			0.181	0.236	0.097	0.108	0.004	0.012	0.344	0.000	0.065	7.81	669.2

Fractionated modal proportions of each phase calculated at each step after accounting for garnet that has already formed

Step	Grt	St	Chl	Bt	Ms	Pl	Ky	Ilm	Rt	Qz	H_2O	Grt^C	P (kbar)	T (°C)
1	0.000	0.051	0.149		0.374	0.077		0.027	0.001	0.321	0.000	0.000	5.03	561.3
2	0.001	0.054	0.144		0.372	0.078		0.029	0.000	0.321	0.002	0.001	5.15	568.5
3	0.002	0.056	0.141		0.370	0.080		0.029	0.000	0.321	0.002	0.003	5.12	575.5
4	0.003	0.128		0.159	0.246	0.090		0.008	0.009	0.348	0.040	0.006	5.31	581.5
5	0.001	0.130		0.160	0.242	0.093		0.008	0.010	0.350	0.001	0.007	5.47	596.4
6	0.019			0.188	0.210	0.094	0.108	0.021	0.003	0.333	0.013	0.026	6.56	627.1
7	0.013			0.187	0.209	0.096	0.108	0.013	0.007	0.331	0.001	0.038	7.13	654.3
8	0.008			0.183	0.213	0.095	0.107	0.010	0.009	0.330	0.000	0.046	7.38	660.7
9	0.017			0.169	0.221	0.091	0.101	0.004	0.011	0.322	0.000	0.063	7.81	669.2

Table 4.7 – Changes in sample T17 phase proportion during prograde metamorphism with and without considering fractionation. The first set of values for fractionation represent the modal proportion of that phase calculated at each step, with an additional column (Grt^C) for the cumulative total of garnet produced. The final set of values normalises these calculated values to account for the fact that a volume of garnet is already present, thus the new assemblage does not constitute exactly 100% of the rock volume.

Garnet growth is minimal during progression through staurolite-bearing assemblages, reaching a modal proportion of 0.014 (unfractionated) and 0.007 cumulative total (fractionated; Table 4.7). However, staurolite breakdown between ~610 and 624 °C causes biotite and garnet modal proportions to increase, as well as initiating kyanite growth (Table 4.7).

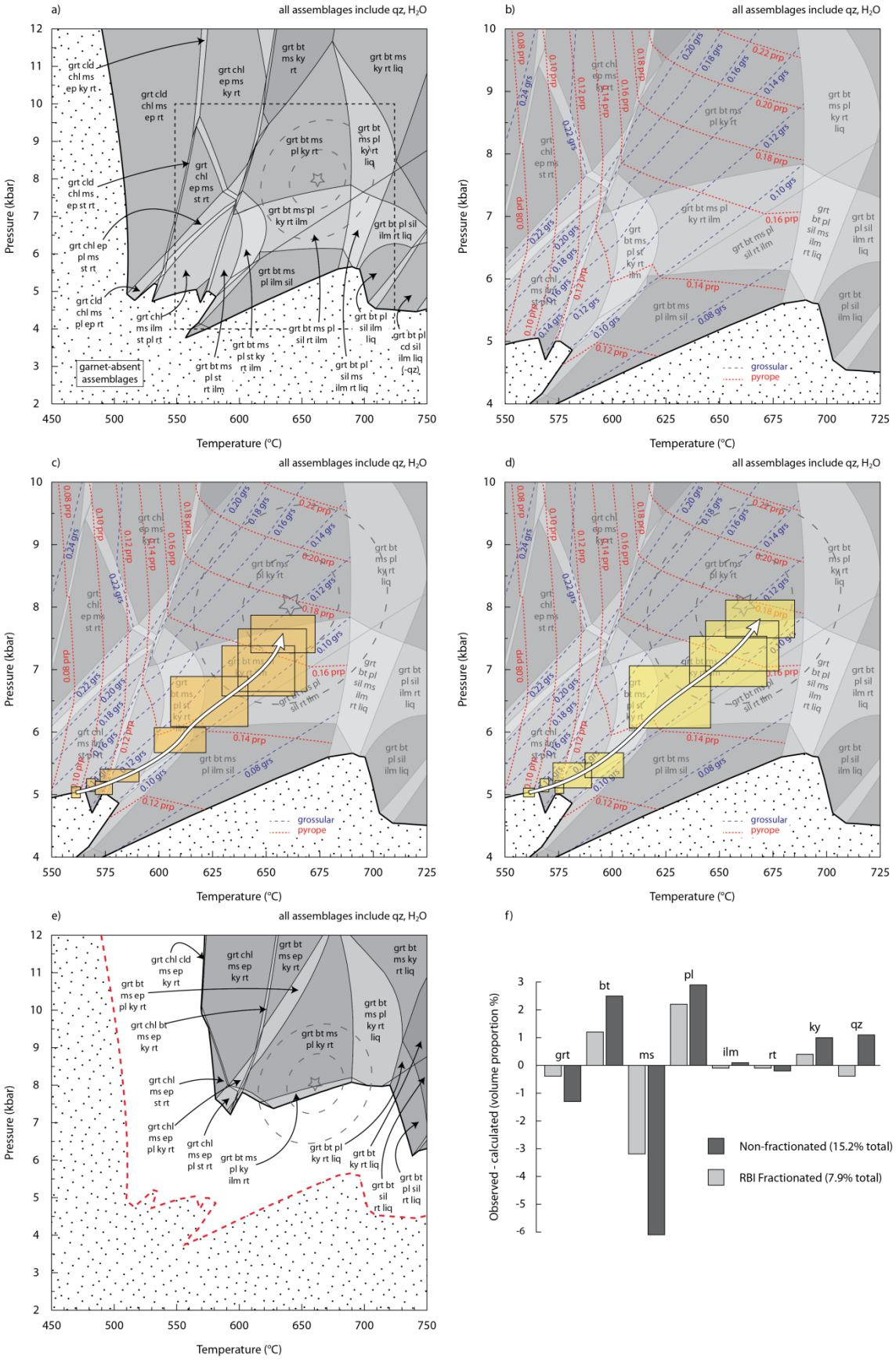


Fig. 4.12 – Pseudosection modelling results for sample T17. (a) *P–T* pseudosection showing calculated garnet-bearing assemblages. Dashed box represents extent of Fig. 4.12b–d. (b) Isopleths for pyrope (prp) and grossular

(grs) calculated according to a fixed EBC calculated prior to first garnet growth. (c) Prograde *P–T* path constructed via isopleth intersections without fractionation of the EBC. Boxes represent calculated 1 S.D. uncertainty on isopleth intersection loci. AvePT result is shown by a star with dashed ellipses representing uncertainty at 1 and 2 S.D. (d) Prograde *P–T* path constructed via isopleth intersections with a fractionating EBC. Boxes represent calculated 1 S.D. uncertainty on isopleth intersection loci. (e) *P–T* pseudosection showing garnet-bearing assemblages calculated using the EBC obtained at the end of the fractionation process. (f) Bar chart showing differences in peak assemblage volume proportions calculated via both methods, compared to observed proportions. Fractionated proportions are those after adjustment for garnet volume. See text for discussion.

This microstructural feature was inferred from both Baltoro samples, most prominently in sample K146, which contains matrix staurolite surrounded by coarse biotite and kyanite (Fig. 4.4c). Mutual growth faces between garnet rims and kyanite in sample K146 (Fig. 4.4a) also suggest that both formed at the same time.

Garnet rim isopleths (0.167 prp) and (0.113 grs) intersect in the assemblage field grt–bt–ms–pl–ky–ilm–rt–qz for both unfractionated (Fig. 4.12c) and fractionated (Fig. 4.12d) paths. Peak *P–T* conditions inferred from these rim isopleths are calculated to be ~7.6 kbar and ~660 °C (unfractionated) and ~7.8 kbar and ~670 °C (fractionated). Both results lie within 1 S.D. of peak conditions calculated by AvePT and it can be seen that each prograde *P–T* path is similar within calculated error. Therefore, as all methods carry their own individual associated uncertainties, peak *P–T* conditions for this kyanite-grade event in the Baltoro region are suggested to lie between ~7.4–8.0 kbar and ~640–660 °C. A pseudosection calculated for an EBC following total garnet fractionation is shown in Fig. 4.12e and the mismatch between calculated and observed volume proportions of major phases in sample T17 is shown in Fig. 4.12f. For this latter plot, molar proportions of each phase calculated by THERMOCALC were converted to volume proportions by multiplying by each relevant molar volume. All volume data were then normalised to 100%, allowing for straightforward comparison with the proportions observed in thin section.

Discussion of modelling results

Compositional zoning in garnet from sample T17 was used to construct prograde *P–T* paths with and without considering a changing EBC during growth. The calculated *P–T* conditions along both paths for each equivalent point agree within uncertainty, even when the assemblage field differs (cf. Table 4.7). This observation suggests that, at least in this sample, an isopleth's position in *P–T* space is more dependent on absolute *P–T* conditions than on the EBC (within any plausible variation for a

metapelitic bulk composition). Despite this, there are some inconsistencies in the modelled results with the main textural and compositional features documented in chapter 4.3. Garnet is seen to be texturally zoned with core regions containing graphite inclusion trails that are absent from rim regions. This observation may be taken to suggest two episodes of garnet growth, between which graphite was eliminated from the rock matrix (e.g. Olimpio & Anderson, 1978), or otherwise that the kinetics of growth of garnet changed after a certain point so that it did not include matrix graphite, if still present. However, as no graphite currently exists in the sample, the former scenario is more suitable. A two-stage growth scenario is also supported from textural constraints outlined in chapter 4.4.2 that show that staurolite breakdown produced garnet, kyanite and biotite (reaction 4.4.2).

Inspection of changing modal proportions of phases during prograde metamorphism from pseudosection analysis shows that garnet proportion increases sharply as a direct result of the breakdown of staurolite, as expected (Table 4.7). However, graphite-bearing core regions comprise ~20–25 volume % of the analysed garnet grain (assuming spherical geometry), whereas garnet in staurolite-bearing assemblage fields (in a non-fractionating bulk composition) makes up a maximum of ~18% of the total garnet volume that is predicted to form at peak metamorphism (i.e. 0.014/0.079*100). This proportion reduces to ~11% in a fractionating EBC (i.e. 0.007/0.063*100). These data suggest that the garnet volume present in staurolite-bearing assemblage fields is underestimated in both cases, assuming that the graphite-free rims are correctly interpreted to have formed from staurolite-breakdown.

More complexity is added by the observation that staurolite occurs as small, rare and anhedral grains in the matrix, yet is not present in the calculated peak assemblage fields (Fig. 4.12c–d). At its peak abundance, staurolite is predicted to have comprised 0.129 modal proportion of the sample (Table 4.7) although this volume should have broken down entirely during prograde metamorphism if full chemical and textural equilibrium was achieved. When discounting the effects of fractionation, staurolite is consumed to produce kyanite, garnet and biotite after ~580 °C, between steps 4 and 5 in Table 4.7 (the first appearance of kyanite). By contrast, when considering fractionation, the first appearance of kyanite must occur after ~596 °C (step 5 in Table 4.7). It would appear that the sequestration of cations into garnet must stabilise staurolite, the breakdown of which controls the appearance of kyanite in this case (Fig. 4.12a). This implies that minor staurolite persists

metastably up to peak kyanite-grade conditions, although it is not currently possible to realistically account for metastability in this way during calculations.

Phase	THERMOCALC parameter	Coding reference	Observed range	Fractionated result	Unfractionated result
Biotite	x(bi) = Fe/(Fe+Mg)	White *et al*. (2007)	0.46–0.50	0.43 ± 0.02	0.42 ± 0.01
	y(bi) = Al in M1 site	White *et al*. (2007)	0.37–0.39	0.35 ± 0.02	0.34 ± 0.02
Muscovite	fe(mu) = Fe/(Fe+Mg)	Coggon & Holland (2002)	0.43–0.48	0.43 ± 0.02	0.41 ± 0.01
	y(mu) = XAl in M2A site	Coggon & Holland (2002)	0.93–0.96	0.93 ± 0.00	0.94 ± 0.00
	na(mu) = XNa in A site	Coggon & Holland (2002)	0.03–0.05	0.10 ± 0.00	0.12 ± 0.01
Plagioclase	ca(pl) = Ca/(Na+Ca+K)	Holland & Powell (2003)	0.44–0.47	0.47 ± 0.01	0.48 ± 0.01

Table 4.8 – THERMOCALC composition parameters calculated at peak *P–T* conditions for fractionated and unfractionated paths, expressed as molar proportions of oxides and compared against observed values.

Finally, it can be seen that the modal proportions and compositions of phases calculated to comprise the peak assemblage vary according to whether fractionation calculations are employed. Comparing results in this way is a powerful check on the validity of calculated *P–T* conditions, given that the actual sample under study must represent the 'correct answer' (Stüwe & Powell, 1995). When considering the calculated peak assemblage, modal proportions of phases calculated at the end of a fractionated *P–T* path, once adjusted for garnet, provide a much closer match to observed proportions than those discounting fractionation, with 7.9% and 15.2% total volume discrepancies respectively (Fig. 4.12f). The same is true for calculated compositions in this instance, whereby coexisting phases exhibiting solid solution show variable correlation with observed compositional ranges. Table 4.8 illustrates this result and, although many results are similar within calculated uncertainty, for most parameters fractionation causes results to trend towards observed values. In particular, parameters involving Fe–Mg distribution appear to show better matches to observed compositions e.g. x(bi) and fe(mu).

It can be seen from the above discussion that accounting for the fractionation of cations into garnet during metamorphism appears to be beneficial in producing more reliable phase diagrams in some cases, but not in others. Although theoretically there should be a clear benefit in applying fractionation in this way, factors that are not considered in the modelling process may have an overriding control on results. For example, an examination of the (apparent) metastability of staurolite should consider the effect of omitting Zn from the model system, which stabilises staurolite with increasing grade (Deer *et al*., 1992). However, the current lack of Zn-bearing activity-composition models for metapelitic minerals precludes this as a possibility. It can be concluded,

therefore, that although the above pseudosections have some shortcomings, they represent the best attempt at investigation of the prograde history of sample T17 that can be made with the current 'tools' available. Further discussion on the advantages and disadvantages of this fractionation technique is given in chapter 5.6.1 with data from another case study (chapter 5.5.3).

4.7. Summary and discussion

4.7.1. Tectonic implications for the Hunza Valley

Pre-India-Asia collision contact metamorphism

Subduction of the Neo-Tethys Ocean beneath the southern Asian margin during the Cretaceous led to emplacement of the Hunza Plutonic Unit of the Karakoram batholith, components of which have intrusion ages ranging between c. 95–105 Ma (Table 4.1). No geochronological evidence for metamorphism associated with this event has been reported, prior to this study, most likely due to the polymetamorphic nature of the high-grade units of the northern Hunza Valley. However, Montel *et al*. (2000) showed that monazite shielded within garnet can successfully avoid recrystallisation or resetting of its composition, even if the rock undergoes later high-grade metamorphism. The same scenario is envisioned here for sample 20-199. Petrographic analysis has suggested that andalusite and cordierite coexisted during early low-pressure contact metamorphism associated with the formation of the Karakoram batholith. A monazite grain included within a garnet core in this sample produced a U–Pb age of 105.5 ± 0.8 Ma, interpreted to represent the timing of this event. Similar ages are likely to be preserved within other units of the KMC that were in close proximity to emplaced members of the Karakoram batholith at that time; therefore additional investigation into suitable samples may confirm this and corroborate these findings.

Post-India-Asia collision metamorphism and deformation

Metamorphic units exposed in the Hunza Valley show a general increase in age and peak *P–T* conditions northwards and are juxtaposed against one another via numerous approximately E–W-trending thrust faults (Fig. 4.1; Fraser, 2000; Fraser *et al*., 2001). Metamorphic *P–T–t* data for certain tectonostratigraphic units (kyanite- and garnet-chloritoid-grade) are currently unknown and the timing of motion along particular bounding faults is uncertain. As a result, the understanding of the tectonic evolution of the Hunza Valley following the India-Asia collision is incomplete. The new

U–Pb age data for kyanite-grade overprinting of LSZ units presented above constrains the timing of thrust faulting and allows the timing of metamorphism in some units to be predicted.

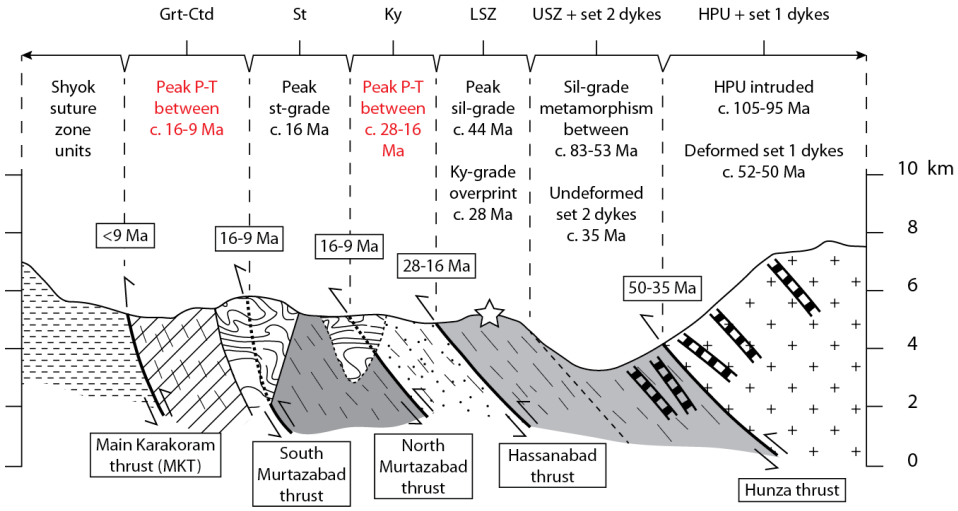


Fig. 4.13 – Tectonic implications for the Hunza Valley. Schematic cross-section showing new constraints on the metamorphic and kinematic evolution of different tectonic units and bounding thrust faults. Geological units, shading and fills are the same as those in Fig. 4.1. Red labels denote predicted ages (see text for discussion of data).

The timing of motion along the Hunza thrust, which places the HPU on top of USZ metamorphic units, is constrained by the intrusion of set 1 and set 2 Hunza dykes. Set 1 dykes, emplaced at c. 52–50 Ma (Table 4.1), intrude the HPU and are similarly deformed as a result of southward motion along the Hunza thrust (Fraser, 2000). Set 2 dykes cut across fabrics in the HPU and USZ metamorphic units and were intruded at 35.0 ± 1.0 Ma (Table 4.1). This constrains final motion along the Hunza thrust to between c. 50–35 Ma (Fig. 4.13). Younger staurolite-grade metamorphism exposed in the southern part of the Hunza Valley is dated at 16.0 ± 1.0 Ma (U–Pb monazite; Fraser *et al*., 2001). Kyanite-grade units have been thrust on top of these units along the North Murtazabad thrust, and these kyanite-grade units are themselves separated from structurally overlying LSZ units by the Hassanabad thrust fault (Fig. 4.13). Peak sillimanite-grade metamorphism in the LSZ is suggested to have occurred at 44.0 ± 2.0 Ma (U–Pb monazite; Fraser *et al*., 2001) and U–Pb monazite data from this study shows that a younger kyanite-grade overprint occurred no earlier than 28.2 ± 0.8 Ma, while these units were at a depth of ~28 km. These data limit peak kyanite-grade metamorphism (in the 'kyanite zone') and the timing of motion along the Hassanabad thrust to between c. 28–16 Ma. Although evidence is lacking to suggest the relative timing of these events, they must both have occurred in this period.

The lowest-grade metamorphic units (garnet-chloritoid) in the Hunza Valley are exposed along the southern margin and are overthrust by staurolite-grade units along the South Murtazabad thrust (Fig. 4.13). The timing of metamorphism in these low-grade units, and also motion along the bounding thrust, is constrained by emplacement of the Sumayar granite at 9.3 ± 0.1 Ma (Table 4.1). This body cuts across both Murtazabad faults, truncates thrust-related deformational fabrics in metamorphic units and is surrounded by a small thermal aureole (Crawford & Searle, 1993). Therefore peak metamorphism in the garnet-chloritoid zone is suggested to have occurred between c. 16–9 Ma. Further geochronological study of these units will be able to confirm or refine these age ranges and complete our understanding of the evolution of this region.

4.7.2. Tectonic implications for the Baltoro region

Duration and timing of peak metamorphism

Samples T17 and K146 used in this study were collected from outcrops less than 10 km along strike of each other at the same apparent structural level (Fig. 4.2). Both samples contain common textural features that indicate a similar *P–T* history and document similar peak *P–T* conditions; thus monazite U–Pb analyses from sample K146 are deemed suitable to be applied to calculated *P–T* conditions obtained from sample T17 for prograde metamorphism. A U–Pb age of 21.8 ± 0.6 Ma (sample K146) represents an upper age limit for kyanite-grade conditions, given that monazite grains from the matrix and within kyanite porphyroblasts produced similar ages. A calculated peak temperature of ~660 °C for M2 metamorphism alongside knowledge of the analysed garnet radius (~2.3 mm) provide preliminary constraints upon the maximum duration spent at peak conditions. Caddick *et al*. (2010) report that a garnet of radius 1.5 mm will only retain an unmodified zoning profile at a temperature ≥650 °C if the total prograde and exhumation cycle lasts less than or equal to 5 Myr. By contrast, for a garnet of radius 2.5 mm this increases to ~20 Myr (ibid). Thus, although the timing of exhumation of samples K146 and T17 is not constrained, comparisons with the results of intracrystalline cation diffusion modelling performed by Caddick *et al*. (2010) suggest that the entire M2 metamorphic cycle in the Baltoro region could have occurred during the Oligocene-Miocene.

Variations in M2 P–T path morphology

Peak *P–T* conditions of kyanite-grade metamorphism (M2) in the Baltoro region of the KMC have been calculated to lie between ~7.4–8.0 kbar and ~640–660 °C. Furthermore, pseudosection analysis has provided insight into the prograde *P–T* evolution of sample T17, which shows that garnet core growth initiated at ~5 kbar and ~560 °C, equivalent to an apparent geothermal gradient of ~30 °C/km. Assuming a crustal density of 2800 kg/m^3 and a pressure-depth ratio of ~3.6 km/kbar, this implies growth over a temperature interval of ~100 °C and an increase in pressure of ~2.6 kbar; equivalent to burial from ~17 km to ~26 km over an effective geothermal gradient of ~10 °C/km. Analysis of changing molar proportions during prograde metamorphism shows that the majority of garnet growth occurred due to staurolite breakdown during an increase in pressure that initiated from an already-elevated geothermal gradient.

The cause of this steep *P–T* path morphology initiating from a high geotherm is not immediately apparent when comparing this result with previous thermobarometry performed in the region. Rolland *et al.* (2001) document a typical kyanite- and sillimanite-bearing M2 metapelite from the Dassu region of the Baltoro (Fig. 4.2) with a clockwise *P–T* path decompressing from ~8 kbar and ~600 °C to peak conditions of ~6 kbar and ~675 °C. This Barrovian-type evolution is consistent with field observations of isoclinally folded amphibolite-facies metapelites in the central Baltoro, showing that episodes of crustal thickening have affected these units (Rolland *et al.*, 2001, 2006; Searle *et al.*, 2010a). This scenario presented by Rolland *et al.* (2001) shows that the geothermal gradient leading up to peak metamorphism increased from ~20 °C/km to ~30 °C/km, whereas garnet in sample T17 nucleated on an elevated geotherm of ~30 °C/km *before* experiencing an increase in pressure with further prograde metamorphism, suggesting that a different process (other than crustal thickening) was responsible for this initial growth on the elevated geotherm.

One tectonic scenario relevant to the Baltoro region that could account for this involves over-accretion due to magmatic migration, for example from an early intrusive element of the BPU. Thermal modelling of rocks undergoing magmatic over-accretion in the middle crust has been performed by Wells (1980), who found that resultant *P–T* paths show similar steep morphologies to that calculated for sample T17. In addition, the same study proposed that such prograde paths should be common in continent-continent collision scenarios that are associated with extensive plutonic activity, akin to the Baltoro region. The earliest component of the BPU *sensu stricto* has been dated

at 25.5 ± 0.8 Ma (Table 4.1), although it has been suggested by Searle *et al*. (2010a) that the nearby Mango Gusar granite (Fig. 4.2), which crystallised slightly earlier at 26.4 ± 1.3 Ma (Table 4.1) is likely to be an early phase of intrusion that was later deformed along with adjacent kyanite-grade units. Although the Mango Gusar granite itself lies ~10km away from samples K146 and T17 (Fig. 4.2), it indicates that magmatism occurred in the vicinity prior to burial and deformation.

If sample T17 experienced magmatic over-accretion and was buried as a result of lateral migration of magma at a higher structural level, the intrusion responsible is clearly unobservable in the Baltoro region today; thus, the mechanism is presented as a possibility only. It is also possible that the documented pressure increase resulted from crustal thickening in the central Baltoro associated with the on-going India-Asia collision, as inferred by Rolland *et al*. (2001, 2006) and Searle *et al*. (2010a). Notwithstanding, early magmatic activity would certainly account for garnet core formation on an initially high geothermal gradient if heat was conducted to the surrounding crust. If such early magmatism was unevenly distributed throughout the region, this could account for the different reported *P–T* evolutions for rocks of a similar age and structural level elsewhere (e.g. Rolland *et al*., 2001). In these other cases, folding and crustal thickening account for the more familiar clockwise *P–T* paths associated with collision.

4.7.3. Correlation along the Karakoram Range

With the new data presented in this study it is possible to refine the tectonothermal history of both regions of the KMC (Fig. 4.14). The Hunza Valley and Baltoro region are along strike of one another, with no significant tectonic structures in the intermediate region (Fig. 1.4), thus the reasons behind the apparent differences in their metamorphic and magmatic histories are unclear. The possibility of a diachronous evolution along the length of the Karakoram Range has been proposed by Rolland *et al*. (2006) and Searle *et al*. (2010a) as a solution to this problem. In this case, one should not expect events to occur simultaneously. Alternatively, if most events are common to both regions, differences in the rock record may be solely a result of variable exhumation along strike. For example, the tectonic arrangement of the Hunza Valley is controlled primarily by sets of north-dipping thrust faults that have experienced punctuated periods of activity following the initial India-Asia collision (Fig. 4.13) and may be responsible for the elevation of metamorphic units in their

respective hanging walls. By contrast, exhumation in the Baltoro region is largely the result of folding, rather than thrusting, as suggested by M2 metamorphic isograds trending around the exhumed cores of the Dassu and Bullah domes (Fig. 4.2; Searle, 1991; Rolland *et al*., 2001).

Further complications occur when interpreting U–Pb monazite age data from metapelitic rocks that lack microstructural constraints on the mechanism of monazite growth. Differences in 'peak' metamorphic ages reported for an event may be a result of variation in the timing of monazite growth on a sample-specific basis and the ages are dating different sections of the same *P–T* evolution. Alternatively, small age ranges for events such as kyanite-grade (M2) metamorphism in the Baltoro (Fig. 4.14), albeit only 6 Myr, could occur from sampling outcrops of similar grade that are at slightly different structural levels. Thermal modelling performed by England & Richardson (1977) has shown that maximum temperature ('peak metamorphism') is reached at a later time at successively greater depths within a vertical sequence of rocks that experience a similar burial and exhumation cycle. In this case, although the absolute conditions and timing of peak metamorphism differ, the rocks within the column may be described as undergoing the same 'event'.

Therefore, a direct comparison of pre-India-Asia collision metamorphism (M0–M1) along the Karakoram Range is not possible without similar data from the Baltoro region. The only 'common' event is provided by age data from sample 20-199 that appears to show that M2 kyanite-grade crustal thickening was occurring in both the Hunza Valley and Baltoro regions at c. 28 Ma (Fig. 4.14). Subsequent metamorphic episodes M3 and M4 are unique to the Hunza Valley and Baltoro regions respectively. Staurolite-grade metamorphism (M3) is reported to have peaked at 16.0 ± 1.0 Ma (Fig. 4.14), but must have ended by c. 9 Ma in order for the Sumayar granite to truncate metamorphic fabrics. However, M4 metamorphism within the Baltoro region relates to an episode of decompressional melting of units within the cores of domal structures. From their structural position, these gneiss domes appear to contain lithologies that would have previously experienced M2 Barrovian-type metamorphism to kyanite (or sillimanite) grade. Given the nature of such an event, M4 metamorphism would not be expected to be present in the Hunza Valley, as doming does not occur. Nonetheless, further study of currently undated units of the KMC would greatly improve on this synthesis and would complete our understanding of the response of the southern Asian margin to the India-Asia collision, and thus the evolution of the unobservable deep crust of central Tibet.

Further discussion of the evolution of the KMC in comparison to the south Lhasa block adjacent to the eastern Himalayan syntaxis is given in chapter 8.1.2.

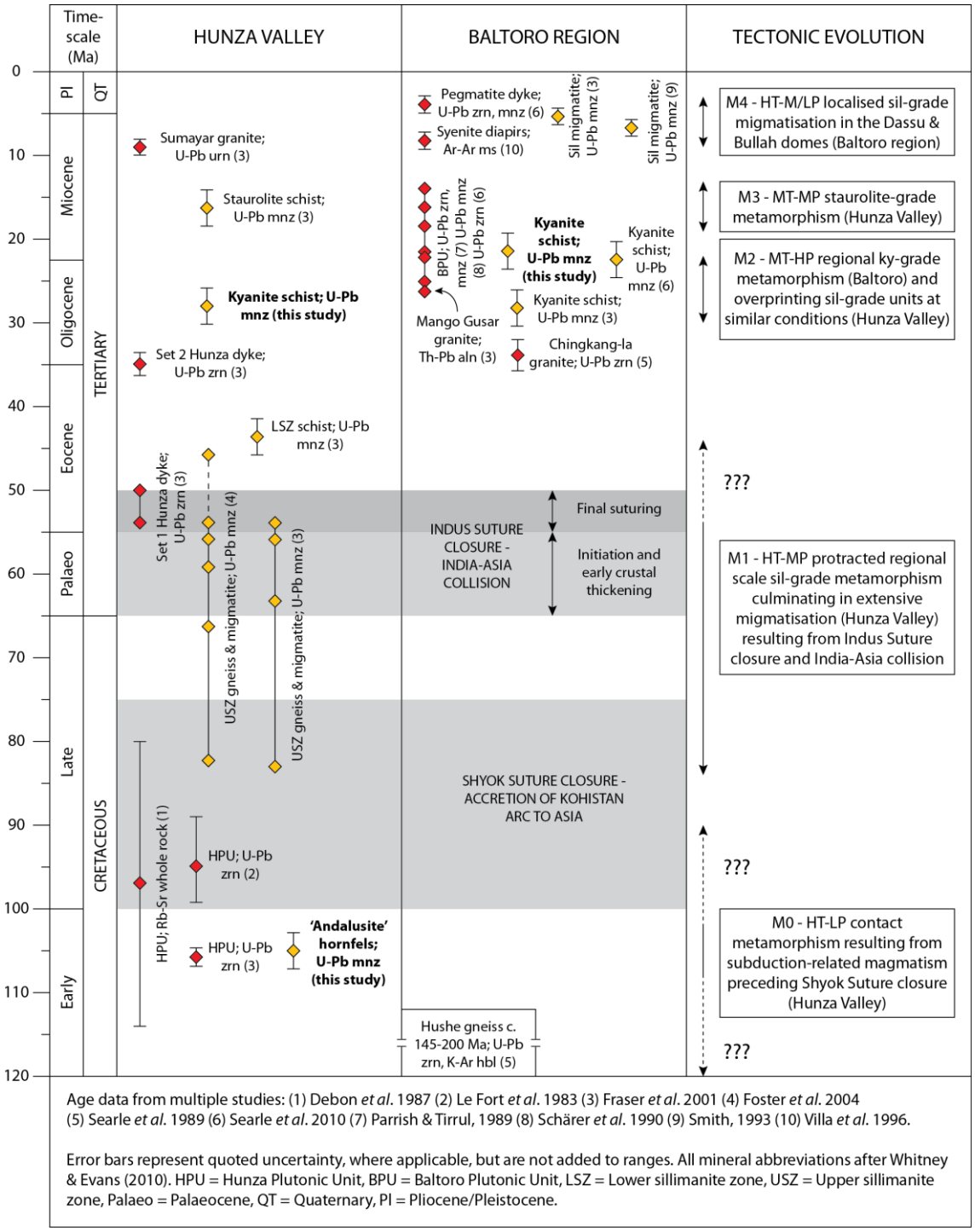


Fig. 4.14 – Compound tectonothermal time chart for events within the KMC. Horizontal shaded bars represent approximate age ranges of accretion of the Kohistan-Ladakh island arc to Asia (Petterson & Windley, 1985; Treloar *et al.*, 1989) and the India-Asia collision (Searle *et al.*, 1987; Green *et al.*, 2008).

5. Tso Morari massif

Parts of the petrography and phase equilibria modelling of mafic eclogite sample L08-03A presented here form the basis of the relevant sections in the paper St-Onge et al. (2013) in the Journal of Metamorphic Geology (cf. chapter 10.2.4).

5.1. Chapter introduction

Deep subduction of the leading edge of the Indian plate immediately preceding the onset of the India-Asia collision resulted in UHP metamorphism of packets of thinned continental crust and associated mafic intrusions (Guillot *et al*., 2008; see chapter 1.4.1). Understanding this event is crucial in order to form reliable geodynamic models describing the early evolution of the HKTO; however, only two localities in the Himalayan Range expose such Tertiary eclogites – Tso Morari (north-west India) and Kaghan (Pakistan) – thus few data are available and are restricted to these geographical regions. Furthermore, considerable previous study of the TMM has failed to produce a *P–T–t* history that is agreed upon, with strong debate continuing today (e.g. O'Brien, 2006). This is mainly a result of the extremely short timescales involved in the subduction-exhumation cycle as most disparity concerns the timing and *P–T* conditions of peak eclogite-facies conditions, rather than the Barrovian overprint, which is readily observed in the host gneisses. Previously reported estimates for peak pressure, for example, range between ~20 kbar and >39 kbar (see chapter 5.2 for a full discussion) and have either been based on the reported presence of particular index minerals or have been made using conventional thermobarometry. On the other hand, recent progress in the ability of phase equilibria modelling to reproduce HP and UHP assemblages, particularly with improvements to relevant eclogite-facies activity-composition relationships (white mica, amphibole, sodic pyroxene etc.), provide the best opportunity to accurately model mafic parageneses at these conditions. As a result, this method was employed in an attempt to yield a more robust tectonothermal history for the TMM, the results of which are presented below.

5.2. Geological setting and tectonothermal history

The TMM has been interpreted as a remnant of the distal margin of the Indian continent that underwent subduction during the closure of the Neo-Tethys Ocean, reaching UHP conditions of metamorphism (Guillot *et al*., 2008). In outcrop, mafic eclogite exists as boudins and lenses in

paragneiss and orthogneiss (Fig. 5.1a). This relationship has been interpreted to represent mafic intrusions into continental crust of Ordovician age (Girard & Bussy, 1999; Epard & Steck, 2008), with both units since having experienced a common *P–T–t* history. Previous work has identified five individual stages in the Tertiary evolution of the TMM. These comprise subduction-related prograde (M1) metamorphism, peak (M2) UHP eclogite-facies metamorphism, exhumation (M3) under lower amphibolite-facies conditions followed by a separate prograde metamorphic overprint (M4) up to upper amphibolite-facies conditions, and finally a greenschist-facies episode of retrograde recrystallisation (M5) documenting the final stages of exhumation in the upper crust.

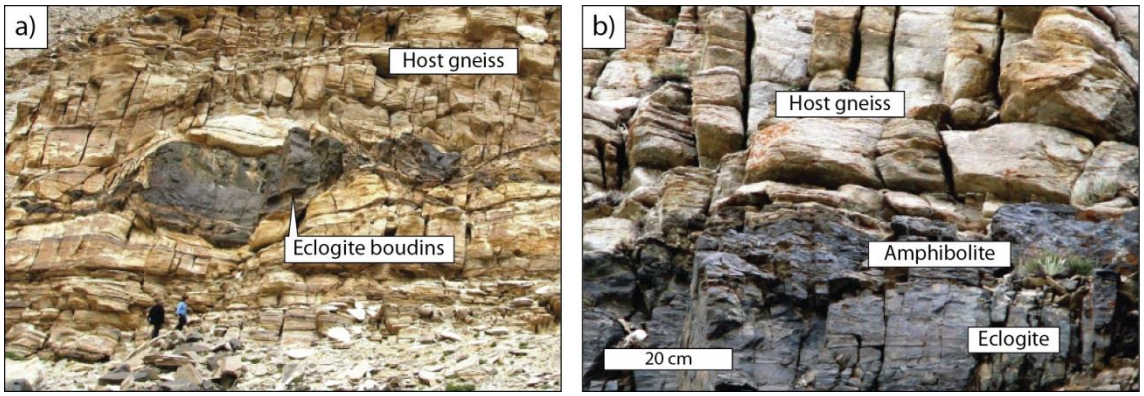


Fig. 5.1 – Field relations for lithological units of the TMM (photographs provided by M. St-Onge). (a) Boudins of mafic eclogite in host orthogneiss. Sample L08-03A used in this study was collected from the core of the large boudin in the centre of the photograph. People at base of outcrop provide scale. (b) Contact between mafic eclogite boudin and host orthogneiss showing the foliated amphibolitised margin.

No quantitative studies of the prograde (M1) evolution have been documented, although conditions of ~10 kbar and ~450 °C are quoted by Guillot *et al.* (2008) as conditions experienced during subduction, without reference to the source of data. By contrast, estimates of peak M2 UHP eclogite-facies *P–T* conditions are abundant and highly variable. Early studies suggest *P–T* conditions between 17–23 kbar and 520–640 °C (de Sigoyer *et al.*, 1997; Guillot *et al.* 1997), equivalent to at least 60 km subduction depth (Fig. 5.2). The later discovery of coesite (Sachan *et al.*, 2004 and others) increased pressure estimates to a minimum of 28 kbar (~100 km depth), whereas a subsequent report of microdiamond inclusions in zircon (Mukherjee *et al.*, 2005) led to peak conditions of >39 kbar and >750 °C being proposed, equivalent to >130 km depth of subduction. A further claim of majoritic garnet (Pandey *et al.*, 2010), implying a pressure of ~60 kbar (~200 km depth), has since been retracted, but nevertheless illustrates the disagreement over peak *P–T*

conditions that exists within the literature. Peak M2 conditions are recorded in metabasic eclogite lenses by assemblages dominated by garnet, omphacite, Si-rich phengite (3.56 cpfu), zoned amphibole, zoisite and rutile (e.g. de Sigoyer *et al*., 2000) with rarer paragonite (Gouzu *et al*., 2006; Epard & Steck, 2008), calcite (Gouzu *et al*., 2006), talc or kyanite (Mukherjee *et al*., 2003). Minor evidence of eclogite-facies metamorphism is preserved in host orthogneiss where primary igneous plagioclase and biotite have reacted to form Ca-rich garnet, kyanite, phengite (3.36 Si cpfu) and zoisite (de Sigoyer *et al*., 2004), and in metasediments that contain garnet, glaucophane, jadeite, chloritoid, paragonite, phengite (3.24–3.58 Si cpfu), zoisite, biotite, chlorite and quartz (Guillot *et al*., 1997; de Sigoyer *et al*., 2000; Epard & Steck, 2008). Proposed ages for peak M2 metamorphism range between 55 ± 7 Ma (Sm–Nd garnet, glaucophane, whole rock; de Sigoyer *et al*., 2000), 53.3 ± 0.7 Ma (U–Pb zircon; Leech *et al*., 2007) and 50.8 ± 1.4 Ma (U–Pb zircon; St-Onge *et al*., 2013).

The exhumation history of Tso Morari units has been divided into two stages involving an initial decompression (M3) followed by a minor prograde overprint (M4) in the middle crust (Fig. 5.2). Exhumation from peak M2 conditions reportedly occurred to a depth of 40–30 km (11 ± 2 kbar, de Sigoyer *et al*. 1997; 13 kbar, Guillot *et al*., 1997) under temperature conditions of 580 ± 60 °C (de Sigoyer *et al*., 1997) and 550 ± 50 °C (Guillot *et al*., 1997). During exhumation, the margins of large metabasic eclogite boudins are reported to have been extensively retrogressed (cf. Fig. 5.1b), forming an amphibolite-facies assemblage including calcic-amphibole, clinozoisite, biotite, chlorite, albite, calcite, titanite and quartz, whilst preserving relic garnet, phengite and rutile (de Sigoyer *et al*. 2000). Even the core regions of such lenses have experienced partial retrogression, documented by partial replacement of garnet and omphacite and the formation of matrix amphibole (de Sigoyer *et al*., 1997; Guillot *et al*., 1997; O'Brien *et al*., 2001; Girard, 2001).

Prograde M4 metamorphism is poorly documented in mafic eclogites, but is widely recorded in metapelite and metagreywacke host units by biotite and kyanite/sillimanite replacing staurolite, phengite and chlorite, recording a temperature increase up to 610 ± 70 °C at 9 ± 3 kbar (de Sigoyer *et al*., 1997), 650 ± 50 °C at 9 ± 1 kbar (Girard, 2001) and 630 ± 30 °C at 9 ± 2 kbar (Guillot *et al*., 1997). Host orthogneiss has M4 assemblages are characterised by quartz, K-feldspar, albite, oligoclase, phengite (3.10–3.28 Si cpfu), biotite, Ca-poor garnet and ilmenite (Epard & Steck, 2008). Occasional units exhibit thin cordierite coronae around garnet, which are reported by St-Onge *et al*.

(2013) to have formed at conditions of 7.1 ± 1.0 kbar and 725 ± 50 °C. The age of M3–M4 metamorphism has been reported between 47.5 ± 0.5 Ma and 45.2 ± 0.7 Ma (U–Pb zircon; Leech *et al*., 2007), 48 ± 2 Ma (Ar–Ar phengite; de Sigoyer *et al*., 2004), 45 ± 4 Ma (Rb–Sr phengite, apatite; de Sigoyer *et al*., 2004) and 45.3 ± 1.1 Ma (Th–Pb monazite; St-Onge *et al*., 2013).

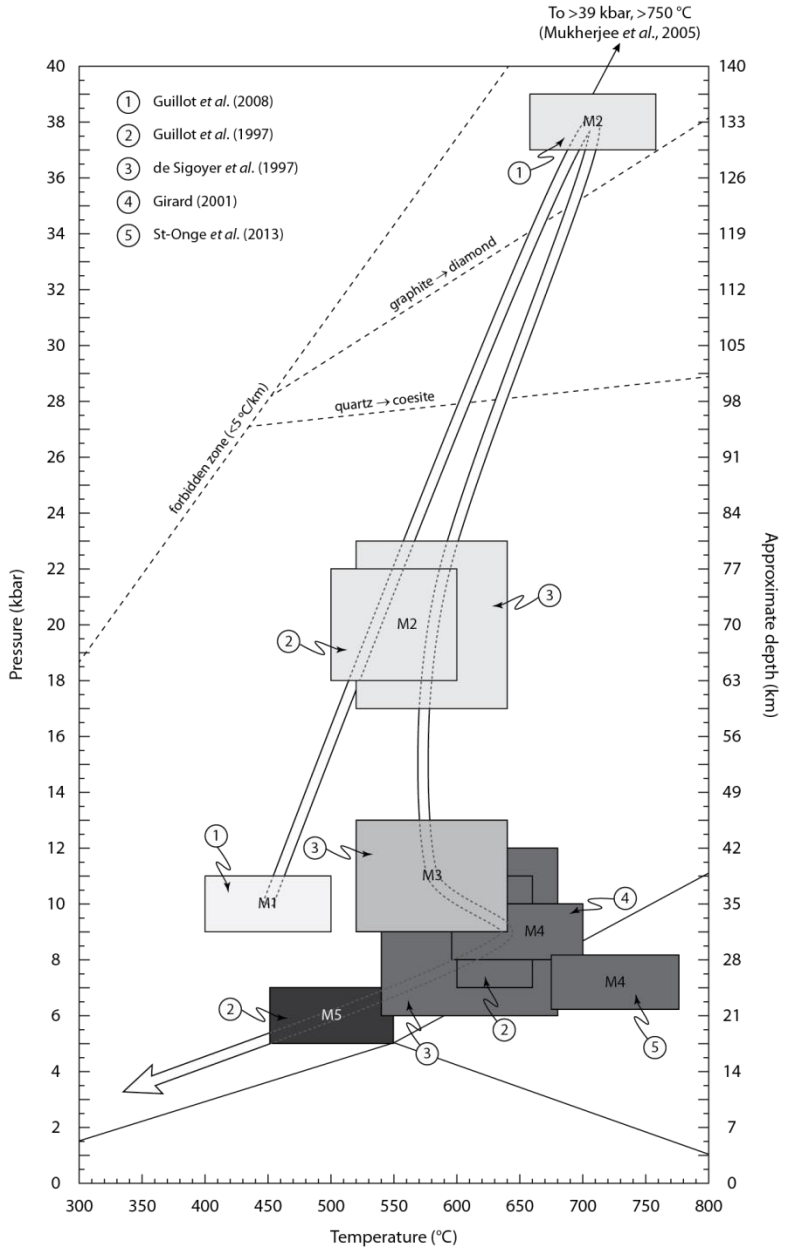


Fig. 5.2 – *P–T* estimates for units of the TMM. See text for sources and discussion of data.

Late M5 deformation is recorded in extensional shear bands of recrystallised chlorite, biotite and muscovite (3.00–3.10 Si cpfu) in metagreywackes, with additional calcite and chloritoid in calc-schists and metapelites (Epard & Steck, 2008). These reportedly formed under greenschist-facies conditions of 5–7 kbar and 500 ± 50°C (Guillot *et al*., 1997) at a crustal depth of ~20 km (Fig. 5.2).

5.3. Petrography and mineral chemistry

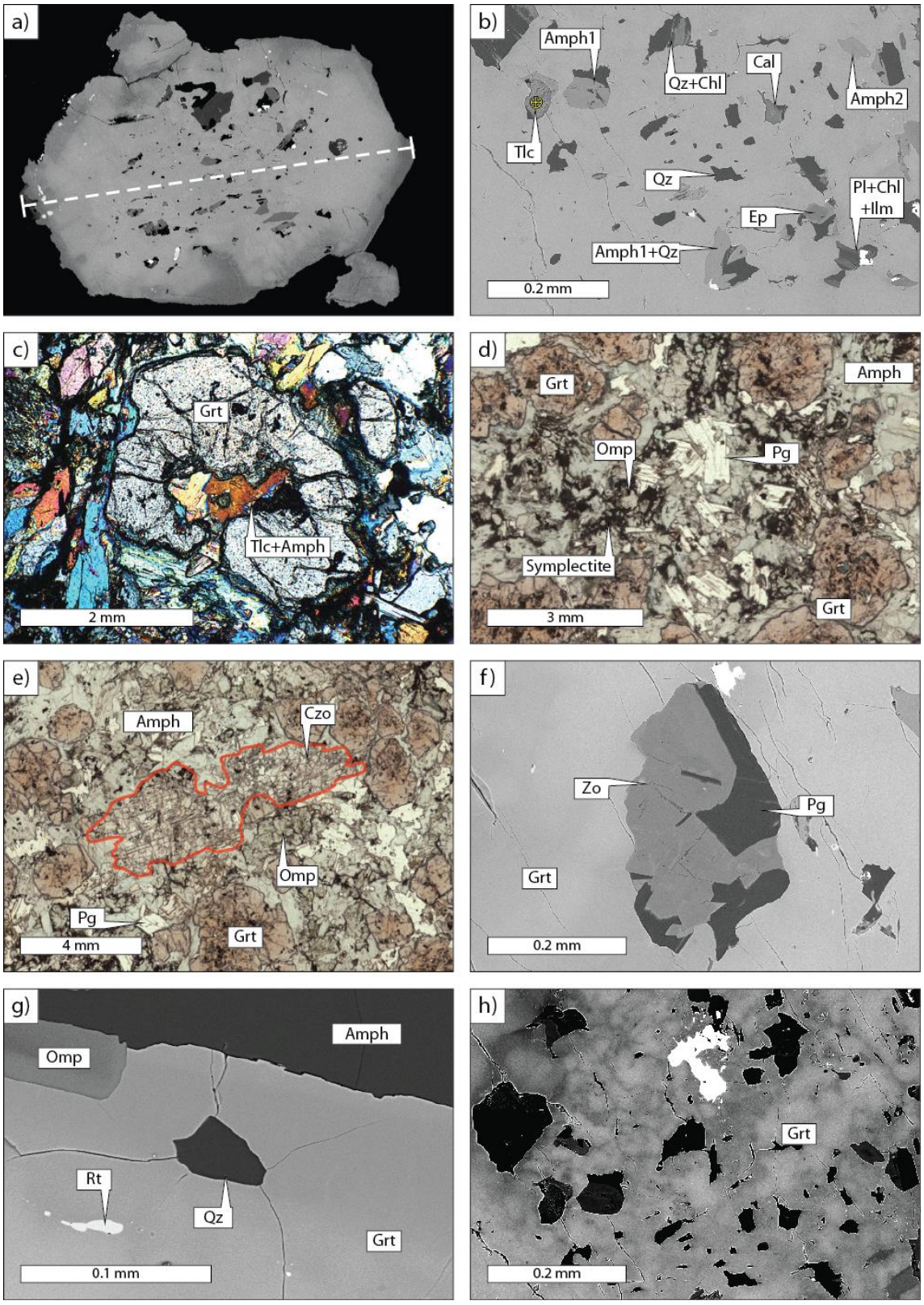
Sample L08-03A is a medium- to coarse-grained mafic eclogite that exhibits a granoblastic texture, comprising garnet and omphacite in a matrix of abundant calcic- and sodic-calcic amphibole and minor phengite, epidote/allanite, apatite, rutile, calcite and quartz. Porphyroblasts of clinozoisite, paragonite and dolomite overgrow this matrix and trap varied inclusions. Compositions of major minerals are given in Table 5.1 and thin section and SEM petrographic images in Fig. 5.3.

Garnet occurs as euhedral/subhedral porphyroblasts that are approximately 1–2 millimetres in diameter and exhibit marked optical, textural and compositional zoning (Fig. 5.3a). Orange-pink cores contain abundant inclusions that often exhibit a shape-preferred orientation, possibly representing a previous planar fabric. Such inclusions consist of subsets of calcic- and sodic-calcic amphiboles, chlorite, chloritoid, epidote, ilmenite, titanite, paragonite, calcite, albitic plagioclase, zircon and quartz (Fig. 5.3b). Rare grains show 'atoll'-like structures with cores replaced by calcic-amphibole and, to a lesser extent, talc (Fig. 5.3c). Inclusion-rich core regions (domain 1) have compositions of 60–67% almandine, 7–12% pyrope, 24–30% grossular and 3–4% spessartine (Fig. 5.4). Inclusion-poor rims contain minor omphacite, paragonite, epidote/allanite, talc, rutile, calcite and quartz. Compositional zoning in rim regions allows division into an inner, middle and outer rim.

The inner rim (domain 2) contains zoning profiles that transition between those of the core and middle rim (domain 3). Grossular content decreases from 25% to 18% whereas almandine and pyrope contents increase from 67% to 73% and 9% to 10% respectively. Spessartine content shows a steady decrease from 4% at the core-inner rim boundary to less than 1% in the outer rim (Fig. 5.4). The garnet middle rim shows extreme compositional change with almandine content falling from 73% to meet the outer rim composition of 46%, pyrope content increasing from 10% to 34% and grossular content showing a slight increase to 20%. Excluding minor diffusional effects adjacent to matrix minerals, the outer rim (domain 4) shows very little heterogeneity, with an approximate composition 46% almandine, 34% pyrope, 20% grossular and <1% spessartine (Fig. 5.4).

Fig. 5.3 – Petrography of sample L08-03A (overleaf). (a) SEM BSE image of a typical euhedral garnet with a core-rim structure. Dashed line indicates position of compositional profile shown in Fig. 5.4 (1.6 mm in length). Image provided by M. St-Onge. (b) SEM BSE image of a typical inclusion suite in garnet core domains. (c) Atoll-like garnet exhibiting partial replacement of its core by calcic amphibole and talc (viewed under crossed polars with quarter-wave accessory plate). (d) Paragonite porphyroblasts, matrix amphibole, dark symplectite surrounding omphacite

and garnet showing optical zonation from orange-pink cores to paler rims (plane polarised light). (e) Large clinozoisite lath (outlined in red) overgrowing matrix amphibole (plane polarised light). (f) SEM BSE image of a composite paragonite-Fe-poor epidote (zoisite) inclusion with pseudo-rhombohedral outline in garnet rim (domain 3, in this instance). (g) SEM BSE image of a quartz inclusion in garnet outer rim (domain 4) with radiating cracks. Note that quartz lacks a polycrystalline texture. (h) SEM BSE image of garnet core with a patchy/mottled texture.



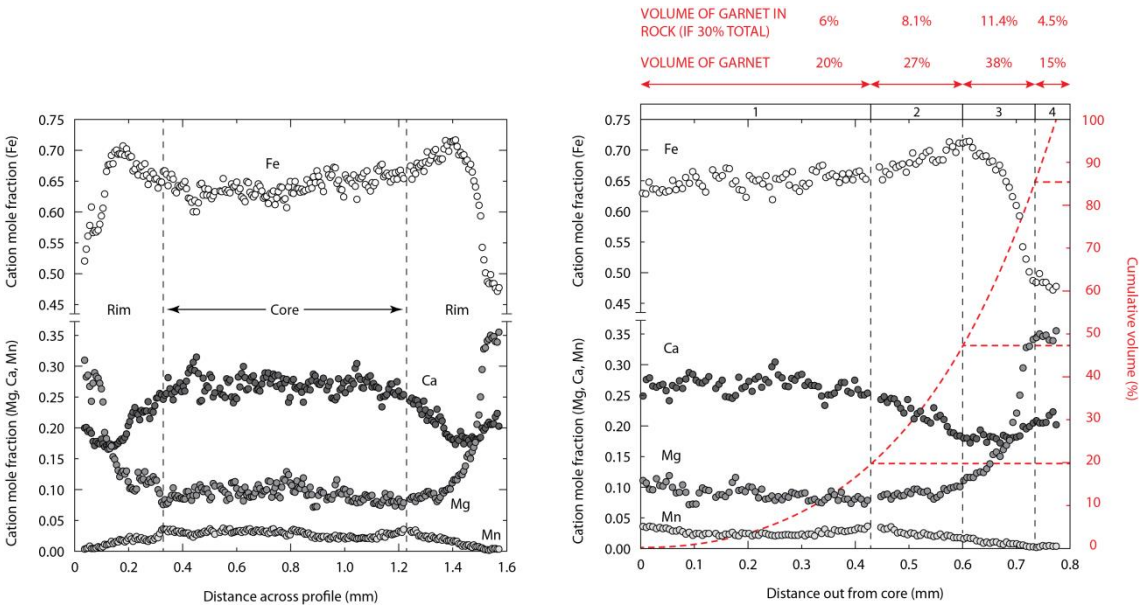


Fig. 5.4 – Garnet compositional profile for sample L08-03A. Line profile is non-continuous due to traverse crossing inclusions and fractures. Individual domains (numbered 1–4) are delimited based on various textural and compositional characteristics (see text for discussion).

Amphibole occurs in multiple textural positions and shows considerable compositional variation throughout (Fig. 5.5). Inclusions in garnet cores consist of three main compositional populations, comprising Si-poor sodic-calcic and calcic amphibole (taramite-pargasite) with Si = 6.11–6.46 cpfu, XMg = 0.27–0.57 and Na_B (M4 site) = 0.34–0.52 cpfu, Si-intermediate sodic-calcic amphibole (barroisite) containing Si = 7.22–7.40 cpfu, XMg = 0.63–0.74 and Na_B (M4 site) = 0.97–1.05 cpfu and Si-rich calcic amphibole (actinolite) with Si = 7.51–7.96 cpfu, XMg = 0.69–0.81 and Na_B (M4 site) = 0.13–0.24 cpfu (after IMA clinoamphibole classification scheme of Leake *et al.*, 1997, 2004; Fig. 5.6). Dark green calcic amphibole (ferropargasite) exists as thin (5–10 μm) rims mantling garnet porphyroblast outer rims and has Si = 5.76–5.82 cpfu, XMg = 0.46–0.50 and Na_B (M4 site) = 0.23–0.30 cpfu. Matrix amphibole appears pale green in thin section (Fig. 5.3d) and is compositionally zoned from a broad sodic barroisite-winchite core to a thinner, more calcic, magnesiohornblende rim. The core contains Si = 7.33–7.58 cpfu, XMg = 0.81–0.88 and Na_B (M4 site) = 0.51–0.81 cpfu, whereas the rim has Si = 7.13–7.29 cpfu, XMg = 0.75–0.81 and Na_B (M4 site) = 0.32–0.39 cpfu. Amphibole is also present as a constituent of symplectite colonies and ranges between magnesiohornblende and actinolite, with Si = 7.31–7.88 cpfu, XMg = 0.74–0.85 and Na_B (M4 site) = 0.10–0.41 cpfu (Table 5.1).

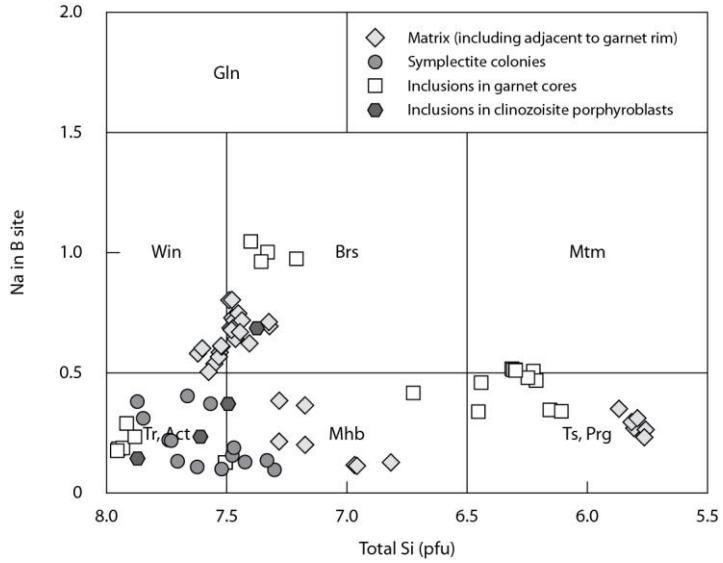


Fig. 5.5 – Sample L08-03A amphibole compositional variation (for subgroup classification see Fig. 5.6 below).

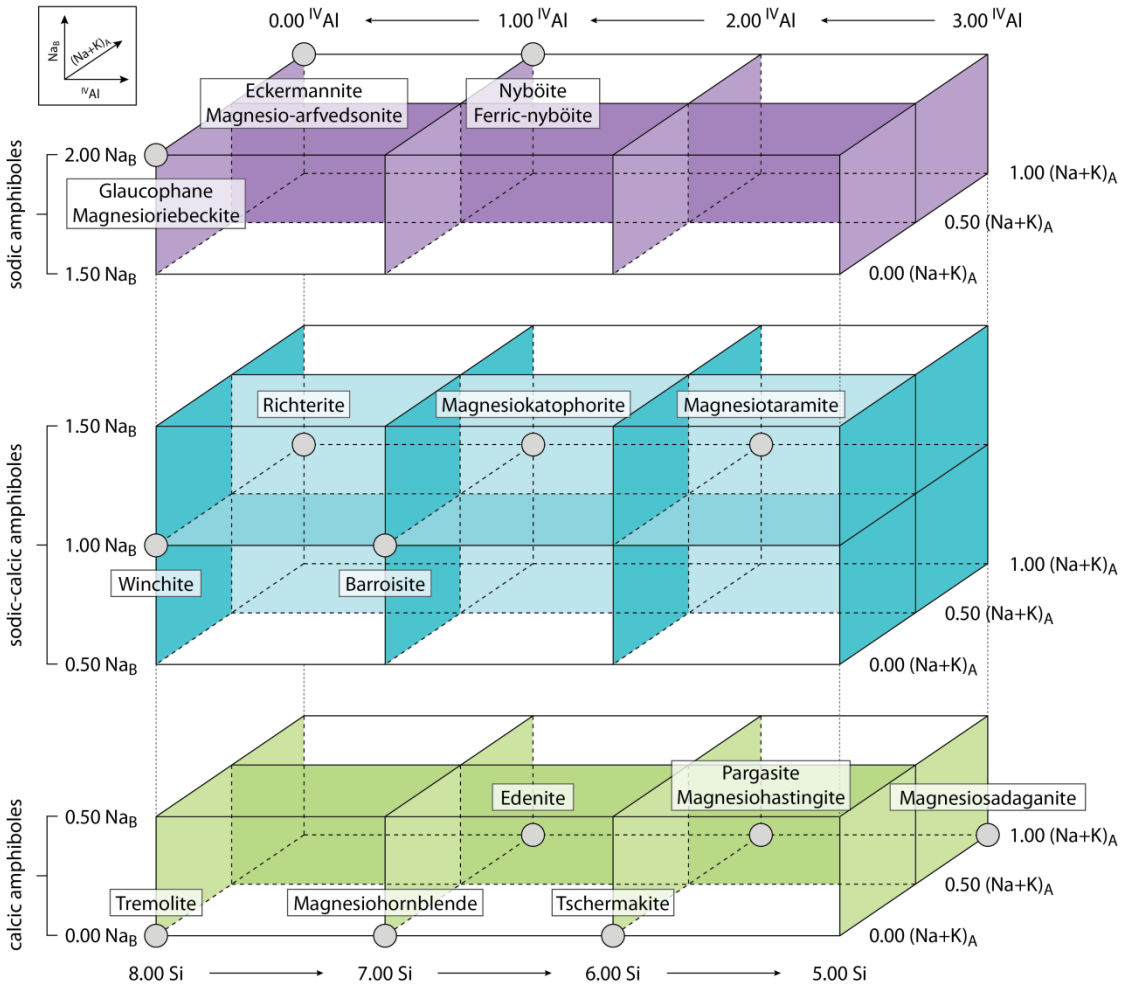


Fig. 5.6 – IMA compositional classification of clinoamphibole (modified from Leake *et al.*, 1997, 2004). Only Mg end-members are shown for clarity; however, all labelled phases have an equivalent Fe end-member. Group 2 (calcic amphiboles) require $(Ca+Na)_B \geq 1.00$ and $Na_B < 0.5$. Group 3 (sodic-calcic amphiboles) require $(Ca+Na)_B \geq 1.00$ and $0.5 < Na_B < 1.5$. Group 4 (sodic amphiboles) require $(Ca+Na)_B \geq 1.00$ and $Na_B > 1.5$.

Mineral	Location	SiO_2	TiO_2	Al_2O_3	Fe_2O_3	FeO	MnO	MgO	CaO	Na_2O	K_2O	**Total**	Si	Ti	Al	Fe^{3+}	Fe^{2+}	Mn	Mg	Ca	Na	K	**Sum**	Ox	XMg	XCa	XMn	Al(iv)	Al(vi)	Alm	Prp	Grs	Sps	Jd	XFe^{3+}	XPs
Act	Inclusion in Grt core	55.71	0.08	1.63	1.36	8.65	0.16	18.20	10.92	0.91	0.03	**97.65**	7.86	0.01	0.27	0.14	1.02	0.02	3.83	1.65	0.25	0.01	**15.06**	23	0.79	-	-	-	-	-	-	-	-	-	0.12	-
Brs	Inclusion in Grt core	50.70	0.25	10.03	4.80	9.46	0.26	11.69	5.05	4.28	0.00	**96.52**	7.29	0.03	1.70	0.52	1.14	0.03	2.50	0.78	1.19	0.00	**15.18**	23	0.69	-	-	-	-	-	-	-	-	-	0.31	-
Cal	Inclusion in Grt core and rim	0.13	0.00	0.12	0.00	2.84	0.92	0.70	52.75	0.00	0.01	**57.47**	0.01	0.00	0.01	0.00	0.08	0.03	0.02	1.85	0.00	0.00	**2.00**	6	-	-	-	-	-	-	-	-	-	-	-	-
Chl	Inclusion in Grt core	25.71	0.09	20.63	0.00	19.83	0.19	18.28	0.07	0.00	0.00	**84.80**	2.73	0.01	2.58	0.00	1.76	0.02	2.89	0.01	0.00	0.00	**10.00**	14	0.62	-	-	-	-	-	-	-	-	-	-	-
Cld	Inclusion in Grt core	24.36	0.03	40.83	0.97	20.00	0.17	5.00	0.05	0.00	0.01	**91.42**	1.00	0.00	1.97	0.03	0.69	0.01	0.31	0.00	0.00	0.00	**4.01**	6	0.31	-	-	-	-	-	-	-	-	-	-	-
Ep	Inclusion in Grt core (core comp)	38.55	0.10	29.89	5.86	0.00	0.04	0.19	23.99	0.00	0.00	**98.62**	2.95	0.01	2.70	0.34	0.00	0.01	0.02	1.97	0.00	0.00	**8.00**	12.5	-	-	-	-	-	-	-	-	-	-	-	0.11
Ep	Inclusion in Grt core (rim comp)	37.37	0.15	23.08	14.70	0.00	0.15	0.07	23.37	0.00	0.01	**98.90**	2.96	0.01	2.15	0.88	0.00	0.01	0.01	1.98	0.00	0.00	**8.00**	12.5	-	-	-	-	-	-	-	-	-	-	-	0.29
Ep	Composite Ep-Pg inclusion in Grt	38.39	0.16	30.29	4.80	0.00	0.05	0.21	24.14	0.00	0.01	**98.05**	2.96	0.01	2.75	0.28	0.00	0.00	0.02	1.99	0.00	0.00	**8.00**	12.5	-	-	-	-	-	-	-	-	-	-	-	0.09
Grt	Core	37.34	0.18	20.53	1.39	27.77	1.34	2.63	9.36	0.00	0.00	**100.54**	2.95	0.01	1.93	0.08	1.90	0.09	0.28	0.77	0.00	0.00	**8.00**	12	0.13	-	-	-	-	0.63	0.09	0.25	0.03	-	-	-
Grt	Outer rim	39.26	0.01	22.44	1.37	21.62	0.17	8.95	7.19	0.00	0.00	**101.01**	2.96	0.00	2.00	0.08	1.37	0.01	1.01	0.58	0.00	0.00	**8.00**	12	0.42	-	-	-	-	0.46	0.34	0.20	0.00	-	-	-
Ilm	Inclusion in Grt core	0.10	52.89	0.16	0.56	45.94	1.19	0.17	0.08	0.02	0.02	**101.13**	0.00	0.99	0.01	0.01	0.96	0.03	0.00	0.00	0.00	0.00	**2.00**	3	-	-	0.03	-	-	-	-	-	-	-	-	-
Omp	Inclusion in Grt outer rim	55.50	0.07	9.48	1.89	3.78	0.02	8.49	13.73	6.45	0.00	**99.41**	2.00	0.00	0.40	0.05	0.11	0.00	0.46	0.53	0.45	0.00	**4.00**	6	0.81	-	-	-	-	-	-	-	-	0.46	0.31	-
Pg	Inclusion in Grt core	46.09	0.18	39.91	0.00	1.16	0.02	0.15	0.35	7.62	0.08	**95.56**	2.95	0.01	3.01	0.00	0.06	0.00	0.02	0.03	0.95	0.01	**7.02**	11	0.20	-	-	1.06	1.96	-	-	-	-	-	-	-
Pg	Composite Ep-Pg inclusion in Grt	44.98	0.07	39.12	0.00	0.93	0.01	0.13	0.53	6.85	0.21	**92.83**	2.95	0.00	3.03	0.00	0.05	0.00	0.01	0.04	0.87	0.02	**6.97**	11	0.17	-	-	1.05	1.98	-	-	-	-	-	-	-
Pl	Inclusion in Grt core	67.66	0.07	20.65	0.49	0.00	0.05	0.00	1.22	9.80	0.00	**99.94**	3.00	0.00	1.08	0.02	0.00	0.00	0.00	0.06	0.84	0.00	**5.00**	8	-	0.07	-	-	-	-	-	-	-	-	-	-
Trm	Inclusion in Grt core	40.76	0.39	14.98	4.23	18.20	0.26	5.46	8.12	4.03	0.06	**96.49**	6.27	0.05	2.72	0.49	2.34	0.03	1.25	1.34	1.20	0.01	**15.70**	23	0.35	-	-	-	-	-	-	-	-	-	0.17	-
Brs	Matrix grain (core comp)	53.22	0.12	9.48	0.04	5.97	0.02	16.04	9.16	3.14	0.15	**97.34**	7.41	0.01	1.56	0.00	0.70	0.00	3.33	1.37	0.85	0.03	**15.26**	23	0.83	-	-	-	-	-	-	-	-	-	0.00	-
Cal	Matrix rim on Dol	0.09	0.01	0.09	0.00	0.95	0.04	1.19	53.25	0.00	0.01	**55.63**	0.00	0.00	0.00	0.00	0.03	0.00	0.06	1.91	0.00	0.00	**2.00**	6	-	-	-	-	-	-	-	-	-	-	-	-
Dol	Matrix	0.05	0.02	0.10	0.00	4.06	0.02	13.70	27.73	0.00	0.00	**45.68**	0.00	0.00	0.00	0.00	0.13	0.00	0.76	1.11	0.00	0.00	**2.00**	6	-	-	-	-	-	-	-	-	-	-	-	-
Ep	Inclusion in Dol	39.26	0.13	29.75	5.98	0.00	0.01	0.29	24.30	0.00	0.01	**99.73**	2.98	0.01	2.65	0.35	0.00	0.00	0.04	1.97	0.00	0.00	**8.00**	12.5	-	-	-	-	-	-	-	-	-	-	-	0.12
Fprg	Matrix (adjacent to Grt rim)	38.15	0.05	19.73	3.41	13.83	0.10	7.49	9.63	3.68	0.16	**96.23**	5.78	0.01	3.52	0.39	1.75	0.01	1.69	1.56	1.08	0.03	**15.82**	23	0.49	-	-	-	-	-	-	-	-	-	0.18	-
Mhb	Matrix grain (rim comp)	51.21	0.07	9.64	3.23	9.01	0.14	15.43	9.03	1.61	0.07	**99.44**	7.13	0.01	1.58	0.34	1.05	0.02	3.20	1.35	0.44	0.01	**15.13**	23	0.75	-	-	-	-	-	-	-	-	-	0.24	-
Omp	Matrix	55.38	0.07	10.23	0.21	4.56	0.02	7.83	12.97	6.71	0.00	**97.98**	2.01	0.00	0.44	0.01	0.14	0.00	0.42	0.51	0.47	0.00	**4.00**	6	0.75	-	-	-	-	-	-	-	0.48	0.07	-
Pg	Matrix	45.59	0.07	38.41	0.00	0.34	0.01	0.22	0.35	6.54	1.04	**92.57**	3.00	0.01	2.98	0.00	0.02	0.00	0.02	0.03	0.84	0.09	**6.97**	11	0.50	-	1.00	1.98	-	-	-	-	-	-	-	-
Ph	Matrix	52.31	0.26	26.39	0.00	1.26	0.00	4.37	0.02	0.33	10.99	**95.93**	3.45	0.02	2.06	0.00	0.07	0.00	0.43	0.00	0.05	0.93	**7.00**	11	0.86	-	0.55	1.51	-	-	-	-	-	-	-	-
Ph	Inclusion in Omp	51.85	0.28	27.70	0.00	1.38	0.02	3.78	0.08	0.75	10.48	**96.32**	3.41	0.02	2.15	0.00	0.08	0.00	0.37	0.01	0.10	0.88	**6.99**	11	0.83	-	0.60	1.55	-	-	-	-	-	-	-	-
Wnc	Matrix core	53.92	0.12	6.81	1.27	4.98	0.02	17.41	9.26	2.73	0.13	**96.65**	7.55	0.01	1.12	0.13	0.58	0.00	3.63	1.39	0.74	0.02	**15.17**	23	0.86	-	-	-	-	-	-	-	-	-	0.18	-
Brs	Inclusion in Czo porphyroblast	52.84	0.06	9.57	0.76	4.11	0.01	16.80	8.61	3.39	0.16	**96.31**	7.38	0.01	1.58	0.08	0.48	0.00	3.50	1.29	0.92	0.03	**15.27**	23	0.88	-	-	-	-	-	-	-	-	-	0.14	-
Czo	Porphyroblast	39.11	0.08	32.75	1.59	0.00	0.01	0.06	24.87	0.00	0.01	**98.48**	2.96	0.01	2.92	0.09	0.00	0.00	0.01	2.01	0.00	0.00	**8.00**	12.5	-	-	-	-	-	-	-	-	-	-	-	0.03
Dol	Inclusion in Czo porphyroblast	0.04	0.03	0.10	0.00	4.50	0.04	15.42	28.82	0.00	0.01	**48.96**	0.00	0.00	0.00	0.00	0.13	0.00	0.79	1.08	0.00	0.00	**2.00**	6	-	-	-	-	-	-	-	-	-	-	-	-
Mhb	Inclusion in Czo porphyroblast	54.02	0.12	6.28	0.81	3.50	0.01	19.35	10.97	2.06	0.08	**97.20**	7.49	0.01	1.03	0.09	0.41	0.00	4.00	1.63	0.55	0.01	**15.22**	23	0.91	-	-	-	-	-	-	-	-	-	0.18	-
Omp	Inclusion in Czo porphyroblast	56.23	0.06	10.31	0.64	3.91	0.01	8.27	13.42	6.78	0.00	**99.63**	2.01	0.00	0.43	0.02	0.12	0.00	0.44	0.51	0.47	0.00	**4.00**	6	0.79	-	-	-	-	-	-	-	0.48	0.14	-
Pg	Inclusion in Czo porphyroblast	46.92	0.00	39.66	0.00	0.34	0.00	0.18	0.49	7.24	0.51	**95.34**	3.00	0.00	2.99	0.00	0.02	0.00	0.02	0.04	0.90	0.04	**6.99**	11	0.43	-	-	1.01	1.98	-	-	-	-	-	-	-
Tlc	Inclusion in Czo porphyroblast	62.12	0.03	0.40	0.00	3.23	0.00	28.52	0.07	0.01	0.02	**94.40**	4.01	0.00	0.03	0.00	0.17	0.00	2.75	0.01	0.00	0.00	**6.97**	11	0.94	-	-	-	-	-	-	-	-	-	-	-
Tr	Inclusion in Czo porphyroblast	57.05	0.02	3.46	0.73	2.27	0.03	21.69	12.26	1.01	0.04	**98.56**	7.74	0.00	0.55	0.08	0.26	0.00	4.39	1.78	0.27	0.01	**15.08**	23	0.94	-	-	-	-	-	-	-	-	-	0.24	-
Act	Symplectite constituent	53.80	0.24	3.81	0.22	7.98	0.08	17.67	12.40	0.82	0.13	**97.15**	7.63	0.03	0.64	0.02	0.95	0.01	3.74	1.88	0.22	0.02	**15.14**	23	0.80	-	-	-	-	-	-	-	-	-	0.02	-
Di	Symplectite constituent	54.48	0.09	3.28	0.00	5.28	0.02	13.19	21.82	1.81	0.01	**99.98**	1.99	0.00	0.14	0.00	0.16	0.00	0.72	0.86	0.13	0.00	**4.00**	6	0.82	-	-	-	-	-	-	-	0.13	0.00	-
Mhb	Symplectite constituent	51.78	0.13	5.79	0.21	8.74	0.02	16.42	12.12	1.24	0.15	**96.60**	7.43	0.01	0.98	0.02	1.05	0.00	3.51	1.86	0.34	0.03	**15.23**	23	0.77	-	-	-	-	-	-	-	-	0.02	-
Pl	Symplectite constituent	67.72	0.00	19.91	0.13	0.00	0.00	0.00	0.46	10.90	0.00	**99.12**	3.00	0.00	1.04	0.00	0.00	0.00	0.00	0.02	0.94	0.00	**5.00**	8	-	0.02	-	-	-	-	-	-	-	-	-	-

Table 5.1 – Mineral compositions for sample L08-03A

Clinopyroxene occurs in multiple petrographic positions in sample L08-03A. Omphacite exists in the matrix (Na = 0.44–0.50 cpfu), commonly surrounded by symplectite, as inclusions in the garnet outer rim (Na = 0.43–0.47 cpfu) and as inclusions in clinozoisite porphyroblasts (Na = 0.44–0.49 cpfu). All omphacite occurrences have largely similar compositions (Table 5.1). Clinopyroxene within symplectite colonies is diopsidic and has Na = 0.07–0.20 cpfu and XMg = 0.76–0.84. Such symplectite colonies appear dark in thin section owing to the extremely fine nature of the intergrowths (Fig. 5.3d).

White mica occurs as paragonite and phengite in various textural positions. Phengite occurs in the matrix (Si = 3.45–3.51 cpfu, Na/(Na+K) = 0.03–0.06) and as inclusions in omphacite (Si = 3.40–3.42 cpfu, Na/(Na+K) = 0.09–0.10). Paragonite occurs as stubby grains in the matrix (Fig. 5.3d), as inclusions in garnet cores, as 'composite' inclusions associated with epidote in garnet rims and as inclusions in clinozoisite porphyroblasts. Compositions of all grains are given in Table 5.1.

Epidote group minerals occur as inclusions in garnet cores, large subhedral clinozoisite porphyroblasts/laths in the matrix (Fig. 5.3e), inclusions associated with paragonite in the garnet rim (Fig. 5.3f), and zoned REE-rich grains ('allanite') that are present both in the matrix and as inclusions in the garnet rim. Epidote included in garnet cores is zoned with core compositions of XPs = 0.11 and rim compositions of XPs = 0.29. Inclusions in garnet rims associated with paragonite have XPs = 0.09–0.12 and epidote rims around REE-rich cores ('allanite') have XPs = 0.10. Clinozoisite laths in the matrix have XPs = 0.03 and contain inclusions of sodic-calcic amphibole, omphacite, dolomite, talc, apatite, rutile, paragonite and quartz.

Dolomite occurs as inclusions in clinozoisite porphyroblasts and as euhedral grains in the matrix that have thin calcite rims; calcite also occurs as inclusions in garnet cores. Plagioclase inclusions in garnet cores contain XCa = 0.04–0.13 and those crystals occurring as part of symplectites have XCa = 0.02–0.14. Chloritoid and chlorite are found as inclusions in garnet cores and have XMg = 0.27–0.33 and XMg = 0.56–0.67 respectively. Talc occurs only as inclusions in garnet and clinozoisite and exhibits a limited range of compositions with XMg = 0.94–0.95; it was not observed in the matrix. Accessory zircon occurs in the matrix and as inclusions in garnet and omphacite. Rare quartz occurs in the matrix and as inclusions in garnet rims (domain 4); the latter being ubiquitously associated with radiating cracks in the host porphyroblast (Fig. 5.3g).

5.4. Textural and compositional interpretation

Most petrographic information in sample L08-03A documents peak eclogite-facies and retrograde conditions. In response to re-orientated stress regimes and extreme changes in *P*–*T* conditions, successive episodes of metamorphism and deformation have eliminated early parageneses, such that inclusions in garnet porphyroblasts provide the only record of assemblages that were present during prograde metamorphism. The observed Mn content in domain 1 of the analysed garnet (Fig. 5.4) is flat to slightly concave, whereas domains 2–4 show a decreasing Mn content, the latter profile being typical of prograde growth zoning (Spear, 1993). Furthermore, some of the minerals included in domain 1 are atypical of high-*P* conditions (e.g. ilmenite and plagioclase, amongst others), whereas those in domains 2–4 are demonstrably eclogite-facies minerals (e.g. omphacite and phengite, amongst others). Similar compositional variation and distribution of inclusions in eclogitic garnets has been used to suggest multiple (discrete) episodes of growth over the course of one single tectonothermal event (Medaris *et al*., 1995; O'Brien & Vrána, 1995).

Hence, the associations described above are interpreted as documenting two stages of garnet growth; firstly prior to M1 (see chapter 5.5.1, below), and secondly during prograde metamorphism up to peak conditions (between M1–M2). The flattened spessartine profile observed in garnet core domain 1 would normally be attributed to intracrystalline cation diffusion homogenising a former Rayleigh fractionation profile (Woodsworth, 1977). However, as a result of the generally short timescales and low-temperatures involved in the subduction process, thermal diffusion is unlikely. Instead, this profile could possibly have formed while intergranular cation transport was too slow (possibly as a result of these low-temperatures) relative to the dissolution rate of reactant minerals in order for any significant fractionation of the matrix to occur during core formation. Aligned inclusions in domain 1 suggest that initial garnet core growth likely initiated at low-pressure conditions where it overgrew and included a paragenesis that is now preserved as a pre-M1 relic fabric (Fig. 5.3a). Analysis of the *P*–*T* conditions of first nucleation is presented in chapter 5.5.1.

Garnet rims (domains 2–4) contain inclusions of omphacite, phengite, talc, epidote/allanite, paragonite associated with epidote, rutile, calcite and quartz, all of which are interpreted as representing relics of prior prograde parageneses. Such paragonite-epidote associations (Fig. 5.3f) commonly exhibit rhombohedral outlines and have been interpreted in similar metabasic lithologies

by Hoschek (2001), Tsujimori *et al*. (2006), Song *et al*. (2007) and Angiboust *et al*. (2011) as pseudomorphs after lawsonite. This suggests that garnet growth during prograde metamorphism occurred in the lawsonite stability field and that replacement occurred at some time afterwards. Lawsonite replacement can occur at high (reaction 5.4.1) or low (reaction 5.4.2) pressure conditions, being accompanied by the consumption of jadeite or albite respectively (Deer *et al*., 1992):

$$4 \text{ lawsonite} + 1 \text{ jadeite} \rightarrow 1 \text{ paragonite} + 2 \text{ zoisite} + 1 \text{ quartz} + 6\ H_2O \qquad (5.4.1)$$

$$4 \text{ lawsonite} + 1 \text{ albite} \rightarrow 1 \text{ paragonite} + 2 \text{ zoisite} + 2 \text{ quartz} + 6\ H_2O \qquad (5.4.2)$$

The occurrence of clinozoisite and paragonite porphyroblasts in the matrix supports the above interpretation; lawsonite included in garnet during prograde metamorphism is now only preserved as pseudomorphs and the remaining matrix grains that were not shielded have since broken down to form the noted porphyroblasts, although it is unclear as to which reaction is responsible.

This interpretation is supported by the observation that the composition of epidote (that is associated with paragonite) differs in XPs content from the range of compositions reported for individual zoned epidote inclusions in garnet cores (Table 5.1). Furthermore, these associations are only found in garnet rim domains, whereas paragonite (as monomineralic inclusions) is only present in core domains. In order to facilitate retrograde breakdown, one must infer that there was potential for chemical communication between the included grains and the rock matrix, as reactions 5.4.1 and 5.4.2 involve a Na-bearing reactant in addition to lawsonite. However, re-orientated stress regimes during metamorphism (discussed above) may allow brittle fracture of host garnet porphyroblasts and so there is potential for reaction of the included grains with the matrix. The ΔV of reactions 5.4.1 and 5.4.2 are 6.79 J/bar and 5.09 J/bar respectively (using molar volumes from Holland & Powell, 1998) and so, as would be expected, the progress of these reactions during exhumation would result in volume expansion of included relics. In an analogous fashion to arguments commonly invoked for radiating fracture patterns surrounding relic coesite inclusions or their pseudosemorphs (O'Brien *et al*., 2001), fracturing of the host garnet (or augmentation of fractures already present) forms potential pathways for the exfiltration of the liberated H_2O into the rock matrix. This fluid may carry reactant or product components in solution and thus conserve mass balance over the course of the reaction.

The euhedral shape and lack of a Mn inflection at the analysed garnet outer rim, which would otherwise represent retrograde resorbtion or diffusional alteration (Kohn & Spear, 2000), leads to the

conclusion that garnet outer rim compositions represent the final stage of garnet growth. Hence, texturally stable inclusions in domain 4 are reliable indicators of the stable paragenesis present during peak metamorphism. Thus, a peak M2 eclogite-facies assemblage is interpreted to comprise garnet, omphacite, phengite, lawsonite, talc, epidote/allanite, rutile and quartz. With the exception of 'lawsonite' and talc all of these included phases are also observed in the matrix.

Comparison with previous interpretations

Previous studies of mafic eclogite in the TMM (summarised by Epard & Steck, 2008) corroborate these conclusions, with the sole exception of the petrographic interpretation of matrix amphibole. Pronounced compositional zonation in matrix amphibole is commonly documented and, in general, comprises sodic- or sodic-calcic amphibole cores surrounded by calcic-amphibole rim overgrowths. Cores have been interpreted to represent part of the M2 peak assemblage (e.g. de Sigoyer *et al*., 1997), whereas rims are interpreted to have formed during subsequent medium/low-pressure Barrovian overprinting (e.g. Epard & Steck, 2008). Prograde and peak parageneses in this study have been inferred from texturally stable inclusions in garnet domains. Given the lack of amphibole in these domains, the addition of observed barroisitic cores to the peak assemblage seems unwarranted.

De Sigoyer *et al*. (1997) report that '*numerous blue amphiboles [glaucophane or barroisite] are observed [in the metamorphic foliation] associated with garnet, omphacite, phengite, quartz, rutile and pyroxene-plagioclase symplectite'* in mafic eclogite from the TMM. This matrix assemblage is then asserted to represent that present at peak metamorphism, despite a lack of microstructural evidence. Furthermore, thermobarometry performed on these assemblages produced *P*–*T* conditions of 21–25 kbar and 540–580 °C, which were purported to represent peak eclogite-facies (M2) conditions. Given the subsequent identification of coesite in the TMM, this result is now known to be wrong and these conditions are interpreted here to represent a partial equilibrium that formed via re-hydration during exhumation of the eclogite. The sodic-calcic amphibole cores in sample L08-03A are thus interpreted to have formed at retrograde (but near-peak) conditions.

This conclusion is supported by Massonne (2012) who showed via phase equilibria modelling of metabasic bulk compositions that porphyroblasts of zoned amphibole and clinozoisite in eclogite commonly form as a result of fluid infiltration during exhumation. Notwithstanding, sample L08-

03A wholly lacks the glaucophane described in previous studies, therefore direct comparisons of mineral assemblages may not be appropriate. Such differences likely represent variations in rock bulk composition between different occurrences across the TMM. The interpreted petrological evolution of sample L08-03A as discussed above is shown in Fig. 5.7.

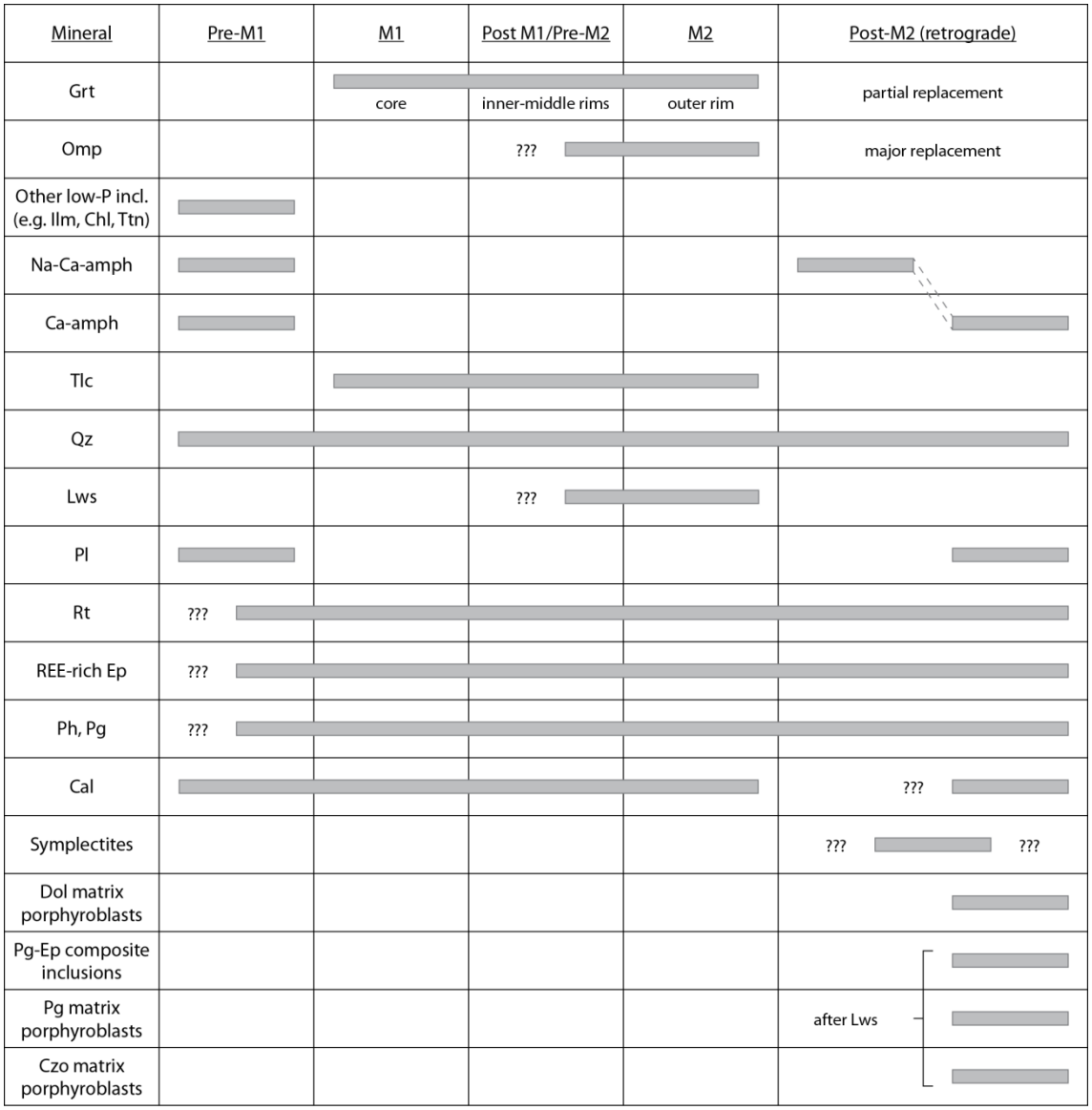


Fig. 5.7 – Interpreted petrographic evolution in sample L08-03A.

5.5. Thermobarometry and phase diagram modelling

In addition to the petrographic observations and preliminary interpretations documented above, thermobarometry and phase equilibria modelling were employed in order to provide quantitative constraints on the total *P–T* evolution of sample L08-03A. Pseudosections were constructed following the methodology outlined in chapter 2.4, but owing to the abundance of garnet and strong

internal compositional variation from core to rim, cation fractionation was applied in order to account for changes in the EBC during prograde metamorphism. Assumptions and model parameters specific to sample L08-03A are outlined below, and a description of the technique used for fractionation calculations is given in chapter 4.6.2.

The prograde history of a mafic eclogite typically involves the growth of anhydrous phases, such as garnet and omphacite, from the destruction of hydrous minerals, such as epidote and amphibole, releasing water (Carson *et al*., 1999). Such a protolith subjected to its first metamorphic cycle would be H_2O-saturated during initial metamorphism up to peak conditions, only (possibly) becoming H_2O-undersaturated towards the final stages of prograde metamorphism (Carson *et al*., 1999, 2000; Guiraud *et al*., 2001). Hydrous inclusions of phengite, talc and 'lawsonite' in sample L08-03A garnet rim regions indicate that fluid was readily available at near-peak conditions – therefore pseudosections were constructed with H_2O in excess (except for fractionation calculations – see chapter 4.6.2). In addition, as a result of the current absence of appropriate melt models, the high-*T* regions of some mafic pseudosections would be metastable with respect to melt-bearing assemblages. H_2O-saturated melting in the NCFMASH system is estimated to begin between 750–800 °C (e.g. Wolf & Wyllie, 1994; Pattison, 2003), hence an upper temperature limit of 725 °C was imposed for thermodynamic modelling so that all calculated fields represent stable configurations.

MnO was not included as a model system component due to its low concentration in garnet and negligible amount in other mineral phases. Although consideration of MnO during phase equilibria modelling expands the stability field of garnet to lower pressures and temperatures, the lack of Mn-bearing activity models for other major eclogite-facies phases (clinopyroxene, amphibole, white mica) precludes the examination of mutual stability. Also, due to Mn content falling to ~1% at outer rim regions (Fig. 5.4), omission of MnO will not have a noticeable effect on the position of pyrope and grossular isopleths, which are used for *P*–*T* determination. As a result, activity-composition parameters for garnet in sample L08-03A are: m(g) = Mg/(Mg+Fe+Ca), ca(g) = Ca/(Mg+Fe+Ca) and x(g) = Fe/(Mg+Fe) (White *et al*., 2007). The total sum of inclusions in garnet constitutes negligible volume, so were excluded as contributions to the bulk composition. As a result of uncertainty regarding mixed fluid compositions at high-pressure, carbonate phases were also excluded from EBC calculation, an omission that is also justified by their low abundance. In total,

calcite inclusions in garnet are rare and matrix dolomite porphyroblasts number approximately 1–4 grains per slide, of typical diameter 2 mm. Phase compositions and volume proportions used in the initial bulk composition calculation are given in Appendix 11.6 and the calculated initial modelled EBC for sample L08-03A is SiO_2 – 50.93; Al_2O_3 – 10.32; FeO – 11.94; MgO – 13.43; CaO – 9.83; K_2O – 0.35; Na_2O – 2.37; TiO_2 – 0.52; O – 0.33 (mole %). Finally, the names for amphibole species are reported *sensu lato* in accordance with wide compositional ranges that can occur as a result of identical activity-composition THERMOCALC codings (Diener *et al*., 2007).

5.5.1. Early (pre-M1) metamorphism

Inclusion populations in garnet core regions may represent parts of assemblages that existed during early prograde metamorphism (subduction). However, conventional thermobarometry and AvePT both failed to calculate equilibrium *P–T* conditions of formation for this included assemblage. This may be a result of many factors – most likely, some included phases do not belong to an equilibrium prograde paragenesis. For example, some phases may have been metastable during inclusion or otherwise have since formed due to the breakdown of former phases. The latter scenario would require exposure of garnet core domains to the reacting matrix and the infiltration of metamorphic fluid to catalyse reactions. Evidence for this process is observed in SEM BSE images of garnet core regions that show dendritic/mottled regions of light and dull colouration (Fig. 5.3h) that correlate with different Ca/Mg compositional ratios. Here, dull regions contain a higher Mg/Ca ratio compared with brighter regions. As it is the duller regions that demarcate the ‘channels’ it can be assumed that they represent the modified parts of the garnet core. Similar patterns with associated compositional variation in eclogitic garnet have been documented by Erambert & Austrheim (1993) and Engvik *et al*. (2001) and have been interpreted to represent healed fractures. This scenario fits the observations in sample L08-03A whereby high Mg/Ca rims are known to have formed at high-pressure conditions (Fig. 5.4) and thus this ‘composition’ should not occur within core regions that formed early in the prograde history. These alterations imply that fluid filtrated through core domains whilst the garnet was at high-pressure conditions, forcing compositional equilibration. It is plausible, therefore, that some ‘inclusions’ could have formed during this process and may not have been part of the initial early (pre-garnet) metamorphic fabric.

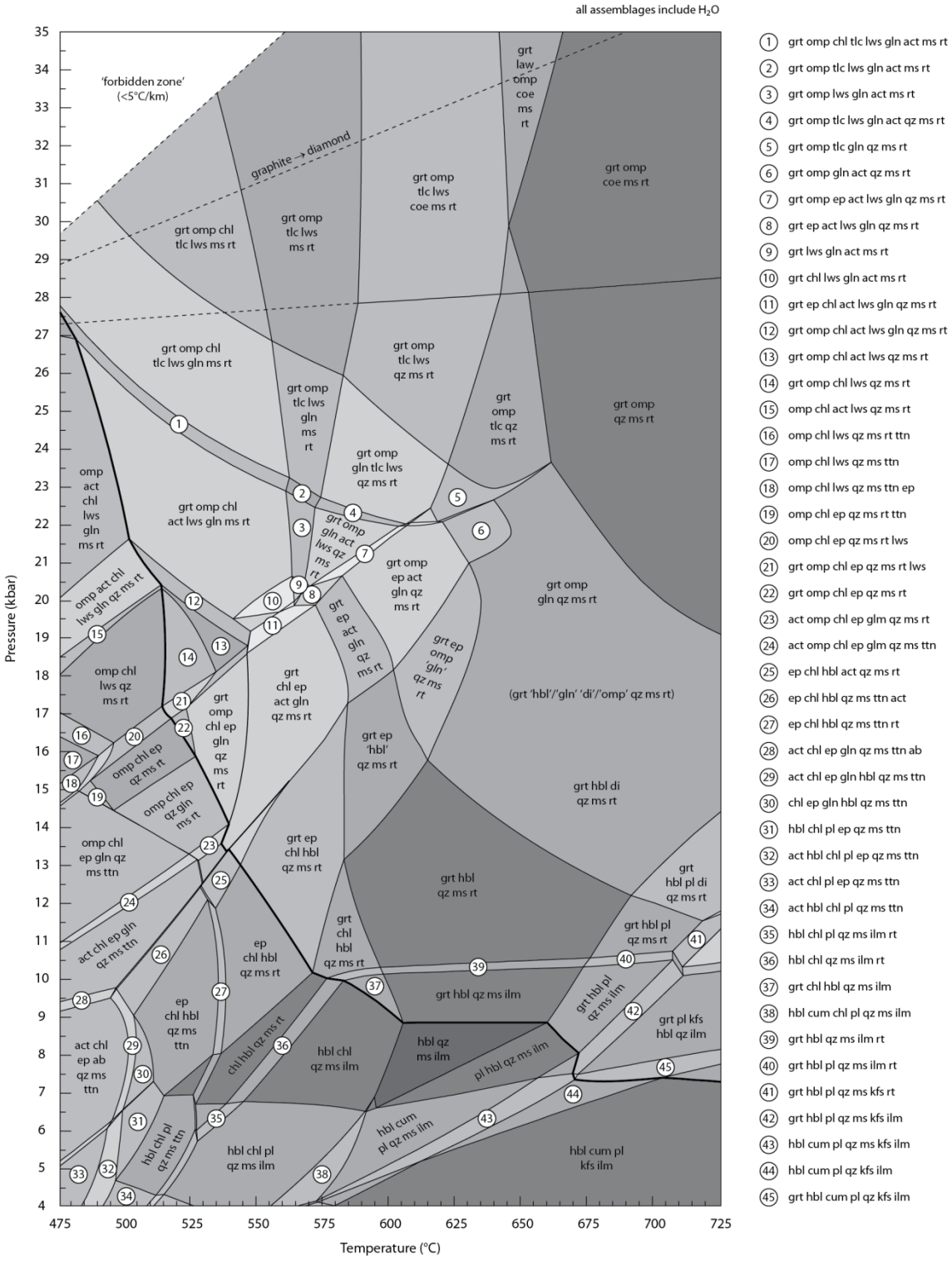


Fig. 5.8 – *P–T* pseudosection for sample L08-03A

Despite this, a preliminary investigation into possible conditions of garnet core formation was performed by inferring approximate boundaries on a *P–T* pseudosection, constructed for the full bulk rock composition, that are delimited by the total range of compositions observed in the analysed garnet core.

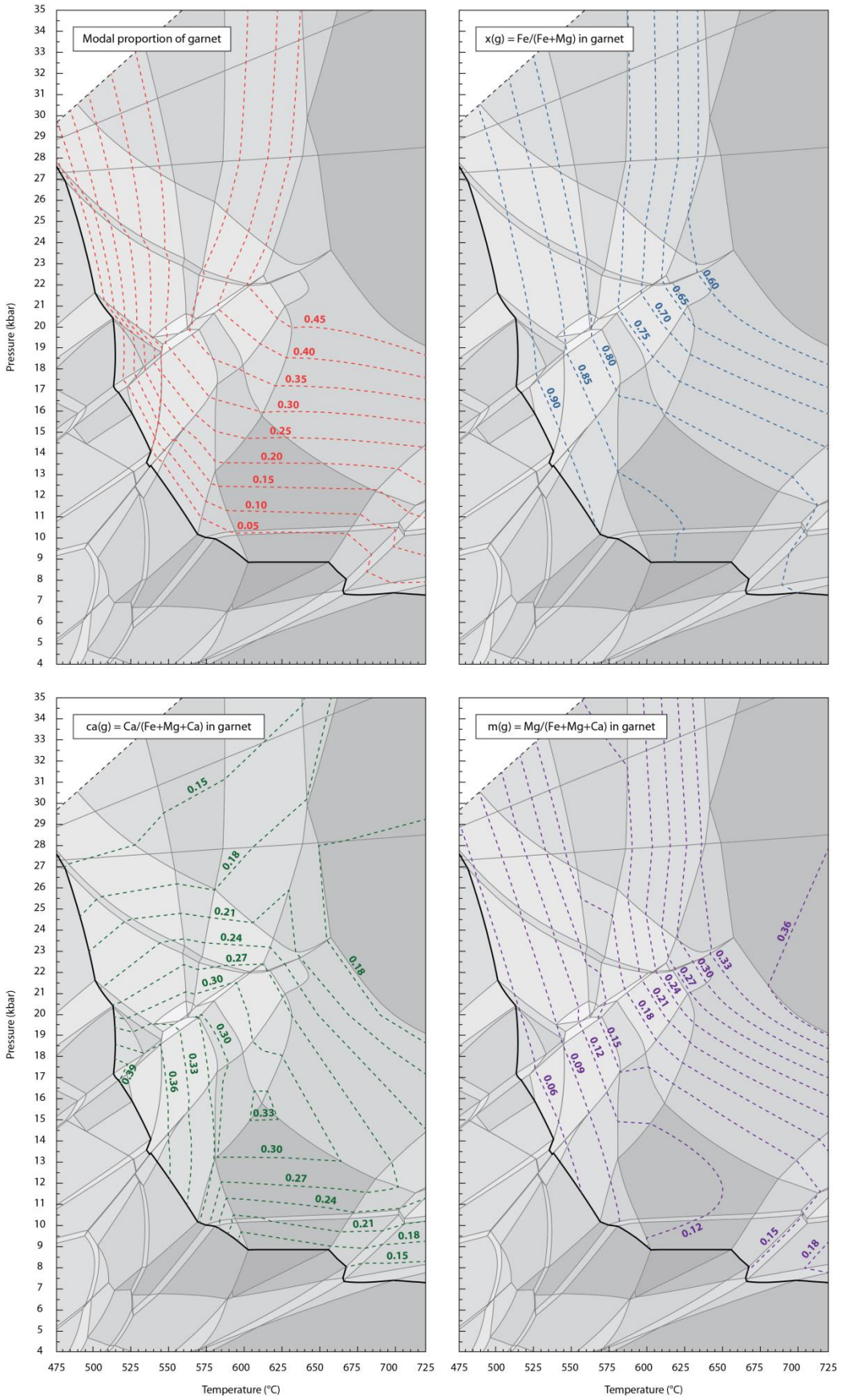


Fig. 5.9 – *P*–*T* pseudosections for sample L08-03A with garnet isolines for compositional parameters x(g), ca(g), m(g) and garnet modal proportion contours.

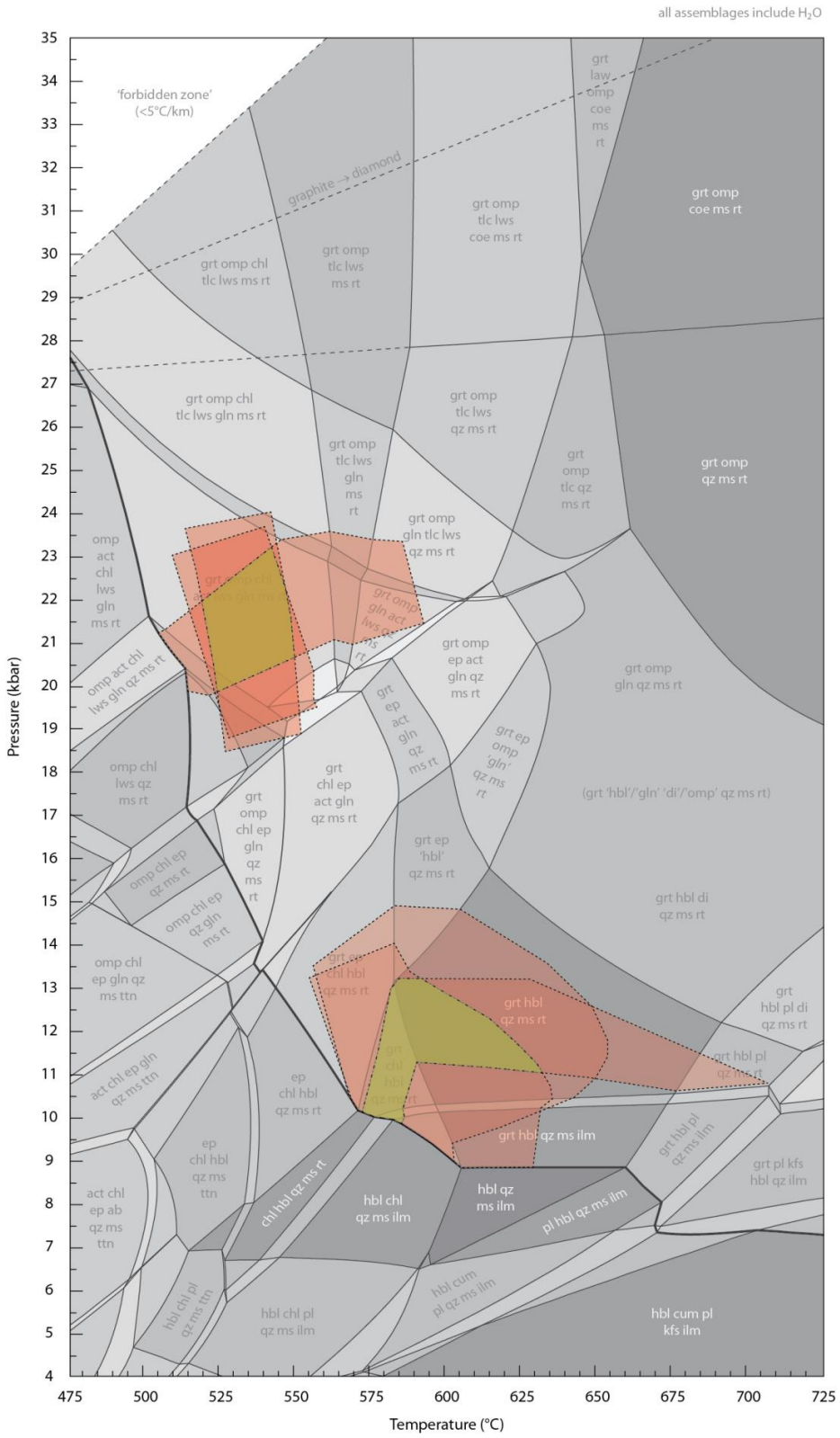


Fig. 5.10 – *P–T* pseudosection for sample L08-03A showing garnet core growth regions

The resultant pseudosection, constructed between the *P–T* limits of 4–35 kbar and 475–725 °C, is presented in Fig. 5.8. Isolines for relevant garnet compositional parameters and garnet modal proportion over this *P–T* range are shown in Fig. 5.9. The compositional ranges that occur within

garnet core regions comprise ca(g) = 0.24–0.30, m(g) = 0.07–0.12 and x(g) = 0.85–0.90 (Fig. 5.11b). These ranges define two regions in *P–T* space where core compositions could theoretically have formed, including a low-pressure range between ~10–13 kbar and ~575–625 °C and a high-pressure range between ~20–23 kbar and ~520–550 °C (Fig. 5.10). The coexisting mineral assemblage calculated at low-pressure comprises hornblende, muscovite, rutile and quartz, with or without chlorite, ilmenite, plagioclase or epidote. At high-pressure the assemblage is calculated to be omphacite, chlorite, actinolite, glaucophane, lawsonite, phengite and rutile, with or without quartz. However, the full suite of inclusions observed in garnet core domains, (calcic- and sodic-calcic amphibole, chlorite, chloritoid, epidote, ilmenite, titanite, paragonite, calcite, albitic plagioclase and quartz) cannot be unambiguously assigned to either of the calculated fields. Given the uncertainties discussed above regarding the possible metastability of some included phases, probable modification (leaching) of some garnet core compositions and the apparent lack of equilibrium conditions indicated by the flattened spessartine profile in domain 1, conditions of metamorphism during subduction leading up to M1 conditions (below) remain unknown (see chapter 5.6.1 for discussion).

5.5.2. M1 prograde metamorphism

Conditions of M1 prograde metamorphism were investigated using a series of pseudosections constructed with and without considering a changing EBC during garnet growth. In rocks where garnet is a relatively small volumetric constituent, the effects of cation sequestration may be minor (see chapter 4.6.2); however, as garnet is a major component of sample L08-03A (~30% of the rock volume; Appendix 11.6), considering cation fractionation during prograde metamorphism is necessary. An unfractionated pseudosection (with a fixed EBC) was constructed for comparison and to provide a reference point for the changing *P–T* conditions associated with an evolving EBC. The method used for cation fractionation is the same as that outlined for sample T17 in chapter 4.6.2. Fractionation points were initially chosen to coincide with the compositional domain boundaries shown in Fig. 5.4, although as domain 3 represents a large volume proportion of the analysed garnet (~38%; Fig. 5.4) an additional intermediate step at 700 µm was chosen, making four steps in total. EBCs produced at each stage of this method are presented in Table 5.2. Given the uncertainty on the timing and *P–T* conditions of growth of core domain 1, the first fractionating EBC was calculated

without a contribution from this domain (i.e. 'garnet core' was removed from the composition-proportion matrix given in Appendix 11.6).

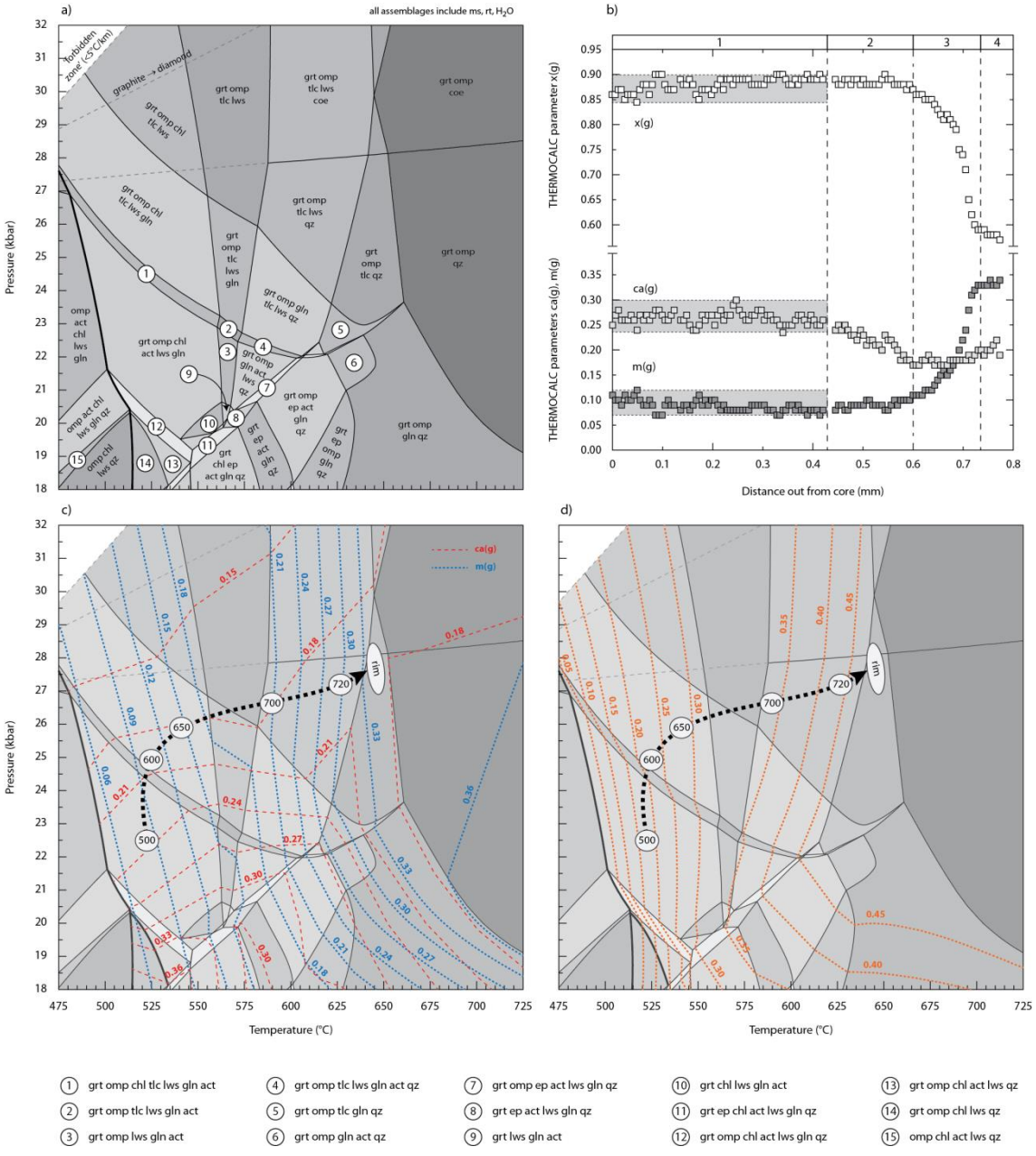


Fig. 5.11 – *P–T* pseudosections for sample L08-03A not accounting for a changing EBC (a) *P–T* pseudosection showing calculated assemblages; minor fields are unlabeled for clarity. (b) THERMOCALC activity-composition coding parameters for analysed garnet. (c) Compositional isopleths ca(g) and m(g) and calculated prograde *P–T* path. See text for discussion. Circled numbers along the *P–T* path represent distances along garnet zoning profile from domain 2 to 4. (d) Garnet ismode contours and calculated prograde *P–T* path.

The calculated *P–T* pseudosection for sample L08-03A using a fixed EBC is shown in Fig. 5.11a. Fig. 5.11b shows the analysed garnet compositional line profile after conversion into THERMOCALC activity-coding parameters x(g), ca(g) and m(g) and shaded boxes delimit the

range of calculated parameters for domain 1. Isopleths relevant to these recalculated parameters are shown in Fig. 5.11c and isolines for the modal proportion of garnet are shown in Fig. 5.11d. These contours were used to ensure that the calculated prograde path produced continual garnet growth. Results suggest that the garnet inner rim (domain 2) initially grew in equilibrium with the assemblage omphacite, chlorite, actinolite, lawsonite, glaucophane, phengite and rutile at *P–T* conditions of ~22.5 kbar and ~525 °C (Fig. 5.11c). Calculated modal proportions show that this assemblage would be largely actinolite, glaucophane, garnet and lawsonite, whereas omphacite, chlorite, rutile and phengite would be present as minor constituents (Table 5.3). Continued growth occurred over an approximately isothermal increase in pressure to 24.5 kbar where talc is calculated to become a stable phase in place of actinolite and both phases coexist in a thin divariant assemblage field. The disappearance of actinolite and appearance of talc across this field coincides with an increase in modal proportion of omphacite from 0.07 to 0.23 and a decrease in modal proportion of glaucophane from 0.19 to 0.10. Modelling of the garnet middle rim (domain 3) indicates that with increasing *P–T* conditions, chlorite is consumed at the expense of garnet and leaves the stable assemblage at ~26.5 kbar and ~555 °C. This increase in garnet modal proportion is accompanied by a decrease in modal proportion of glaucophane and lawsonite, with the eventual loss of glaucophane immediately preceding the appearance of quartz (Fig. 5.11c). Significant garnet growth then occurs across the broad quadrivariant field containing garnet, omphacite, talc, lawsonite, quartz, phengite and rutile. In this unfractionated scenario, lawsonite is calculated to become unstable at ~27.25 kbar and ~635 °C, just short of (M2) peak pressure metamorphism.

Step	Fig.	H_2O	SiO_2	Al_2O_3	CaO	MgO	FeO	K_2O	Na_2O	TiO_2	O
Initial (total) bulk composition	5.11	Excess	50.93	10.32	9.83	13.43	11.94	0.35	2.37	0.52	0.33
Bulk composition omitting 0-420 µm (domain 1)	5.12a	11.94	45.40	8.88	8.52	12.39	9.58	0.33	2.24	0.49	0.24
After fractionation of 420-600 µm (domains 1 & 2)	5.12b	14.97	45.78	7.59	8.07	14.33	5.16	0.40	2.74	0.60	0.36
After fractionation of 420-700 µm (intermediate step)	5.12c	12.12	48.63	7.22	8.56	15.73	2.95	0.48	3.21	0.71	0.41
After fractionation of 420-720 µm (domains 1, 2 & 3)	5.12d	10.82	49.73	7.14	8.76	16.09	2.39	0.50	3.37	0.74	0.43

Table 5.2 – Changes in sample L08-03A EBC during fractionation expressed as molar proportions of oxides.

The sensitivity of the calculated prograde *P–T* conditions to the effects of a changing EBC can be seen in Fig. 5.12. Early sections of the prograde evolution of sample L08-03A are similar to those calculated without fractionation. This is most likely a result of significant compositional change first occurring in the middle rim (domain 3). It can be seen by comparing Fig. 5.11a with Fig. 5.12a that the omission of domain 1 from the initial bulk composition does not change the topology

of the calculated phase diagram significantly, despite it constituting approximately 20% of the garnet grain (and ~6% of the total rock volume; Fig. 5.4). Fractionation of domain 2 from the previously calculated bulk composition translates the new garnet-in line up-temperature by ~30 °C (Fig. 5.12b) although almost all assemblage field boundaries that are largely independent of bulk composition (e.g. the lawsonite-epidote transition) remain unaffected. Despite this, the assemblage field garnet, omphacite, talc, lawsonite and quartz expands. Similar results are seen in the pseudosection constructed following garnet growth up to a 700 μm radius (Fig. 5.12c), where the high-temperature limit of the lawsonite stability field increases relative to the unfractionated pseudosection topology. Table 5.3 shows that the modal proportion of garnet does not increase as quickly (or by as much) as in the unfractionated case prior to peak metamorphism. With a fractionating EBC, garnet modal proportion reaches 0.321 just prior to rim growth compared to 0.474 with a fixed EBC.

No fractionation

Step	py(g)	ca(g)	Grt	Act	Omp	Ms	Ta	Chl	Gl	Law	Ru	Qtz	Grt^C	P (kbar)	T (°C)
500	0.09	0.23	0.191	0.211	0.048	0.040		0.085	0.209	0.212	0.004		0.191	22.52	527.4
600	0.10	0.20	0.209		0.239	0.041	0.150	0.080	0.082	0.194	0.005		0.209	25.20	521.1
700	0.21	0.18	0.349		0.314	0.043	0.161			0.124	0.005	0.004	0.349	26.61	590.6
720	0.30	0.19	0.445		0.343	0.045	0.067			0.033	0.006	0.032	0.445	27.05	627.6
rim	0.34	0.19	0.474		0.364	0.046	0.015				0.005	0.046	0.474	27.49	645.0

Fractionated modal proportions of each phase calculated at each step (after removal of 0-420 μm core region)

Step	py(g)	ca(g)	Grt	Omp	Ms	Ta	Chl	Gl	Law	Ru	Qtz	H_2O	Grt^C	P (kbar)	T (°C)
0-420	-	-	0.200	-	-	-	-	-	-	-	-	-	0.200	-	-
600	0.10	0.20	0.026	0.256	0.052	0.183	0.090	0.151	0.227	0.006		0.010	0.226	25.04	525.1
700	0.21	0.18	0.101	0.306	0.054	0.205	0.019	0.090	0.172	0.006		0.046	0.327	26.25	564.9
720	0.30	0.19	0.029	0.421	0.063	0.291			0.170	0.007		0.012	0.356	25.45	620.0
rim	0.34	0.19	0.010	0.447	0.066	0.293			0.168	0.007	0.003	0.005	0.366	25.51	630.2

Fractionated modal proportions calculated at each step (after removal of 0-420 μm core region) accounting for garnet that has already formed

Step	py(g)	ca(g)	Grt	Omp	Ms	Ta	Chl	Gl	Law	Ru	Qtz	H_2O	Grt^C	P (kbar)	T (°C)
0-420	-	-	0.200	-	-	-	-	-	-	-	-	-	0.200	-	-
600	0.10	0.20	0.020	0.201	0.041	0.144	0.071	0.119	0.178	0.005		0.010	0.220	25.04	525.1
700	0.21	0.18	0.074	0.225	0.040	0.151	0.014	0.066	0.126	0.004		0.046	0.295	26.25	564.9
720	0.30	0.19	0.020	0.289	0.043	0.200			0.117	0.005		0.012	0.315	25.45	620.0
rim	0.34	0.19	0.007	0.300	0.044	0.196			0.113	0.005	0.002	0.005	0.321	25.51	630.2

Table 5.3 – Changes in sample L08-03A phase proportion during prograde metamorphism with and without considering fractionation. Grt^C represents the total garnet produced during fractionation of inner rim in addition to the core contribution (0.200) prior to fractionation.

5.5.3. M2 peak metamorphism

Garnet outer rim compositions are used to constrain peak M2 conditions. Investigation using a fixed EBC during prograde metamorphism shows that isopleths of ca(g) = 0.19 and m(g) = 0.34 intersect at ~27.5 kbar at ~645 °C in the assemblage field garnet, omphacite, talc, quartz, phengite and rutile (Fig. 5.11c). At these conditions, garnet and omphacite together would have comprised almost 90%

of the rock, with phengite, quartz, rutile and talc present as minor constituents (Table 5.3). Uncertainties on the location of these isopleths produced by THERMOCALC are 5 °C and 0.4 kbar (1 S.D.). Although this error is small, it does not account for any uncertainty in activity-composition models or the analytical uncertainty associated with measured phase compositions; such isopleth errors are derived through propagation of uncertainties on the thermodynamic dataset enthalpies.

By contrast, the calculated prograde *P–T* conditions for an evolving EBC begins as partly concordant to the previous result, but then deviates away to an increasing degree (Fig. 5.12e). In this scenario isopleths representing peak metamorphic conditions intersect at ~25.5 kbar and ~630 °C (with associated location uncertainties of 5 °C and 0.4 kbar) in the peak assemblage field garnet, omphacite, talc, lawsonite, quartz, phengite and rutile, which is the same as the peak assemblage identified in thin section through microstructural constraints. A notable difference is that lawsonite is predicted to be stable at peak conditions with a fractionating EBC, unlike with a fixed EBC. The cumulative total modal proportion of garnet that is predicted to have been formed during the fractionation process is ~32% with omphacite making up the majority of the coexisting assemblage (~30%). In the case of a fixed EBC, garnet modal proportion at peak conditions was significantly higher (~47%; Table 5.3).

These data show that numerous differences exist between calculated peak conditions between models. In order to obtain further constraints on the depth of subduction, the peak pressures calculated above from garnet rim compositions were checked against the measured Si content of phengite, an independent compositional criterion that is commonly used as a geobarometer in the study of mafic eclogites (e.g. Waters & Martin, 1993; Carswell *et al.*, 1997; O'Brien *et al.*, 2001; Krogh Ravna & Terry, 2004). These studies show that the Si content of the tetrahedral site in white-mica increases with increasing pressure. Phengite in sample L08-03A has variable Si content whereby inclusions in omphacite contain Si = 3.40–3.42 cpfu and grains in the matrix contain Si = 3.45–3.51 cpfu (Table 5.1). These data are interpreted in that inclusions in omphacite were trapped during subduction and were unable to further equilibrate at peak pressure, unlike matrix grains that contain a higher Si content. Thus, matrix grain compositions constrain maximum pressure.

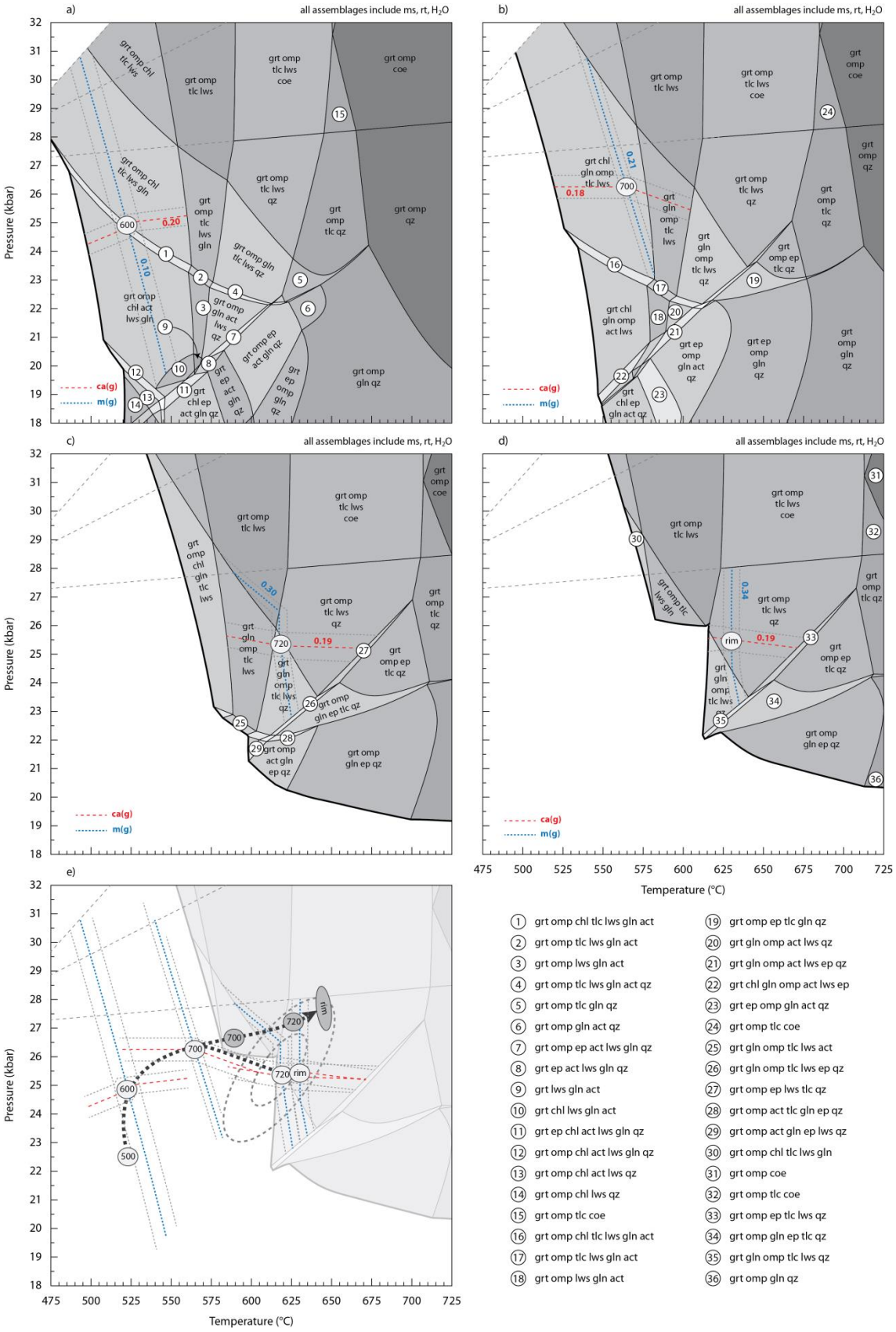


Fig. 5.12 – *P–T* pseudosections for sample L08-03A accounting for a changing EBC. Garnet-absent assemblages are not shown for clarity. Dashed lines representing polymorphic transitions and the location of the 'forbidden zone' are from Fig. 5.11a. Dashed lines located parallel to isopleths represent error envelopes (1 S.D.) as calculated by

THERMOCALC. (a) *P–T* pseudosection constructed following growth of domain 1 with isopleths representing the next fractionation point marked ca(g) = 0.20 and m(g) = 0.10. (b) *P–T* pseudosection constructed for an EBC following growth of domains 1 and 2. The next fractionation point is marked ca(g) = 0.18 and m(g) = 0.21. (c) *P–T* pseudosection constructed for an EBC following growth of garnet core up to 700 µm (domains 1, 2 and part of 3). The next fractionation point is marked ca(g) = 0.19 and m(g) = 0.30. (d) *P–T* pseudosection constructed for an EBC following growth of domains 1, 2 and 3. Isopleths representing the garnet composition of the outer rim are marked as ca(g) = 0.19 and m(g) = 0.34. (e) Comparison of prograde *P–T* paths calculated via both methods. AvePT results for peak M2 conditions are shown with dashed error ellipses at both 1 and 2 S.D.

Compositional isopleths of tetrahedral Si in phengite calculated for both a fixed and dynamic EBC and are shown in Fig. 5.13; the latter calculation using the most fractionated bulk composition (Table 5.2) relevant for peak conditions. For a fixed EBC, isopleths representing matrix phengite overlie the final stages of prograde metamorphism and peak conditions (Fig. 5.13a) whereas for a fractionating EBC this range occurs at notably higher pressures (Fig. 5.13b). This shows a greater agreement between garnet and phengite pseudosection peak pressure constraints with a fixed EBC, which is an unexpected outcome. Further discussion of this point is given in chapter 5.6.1.

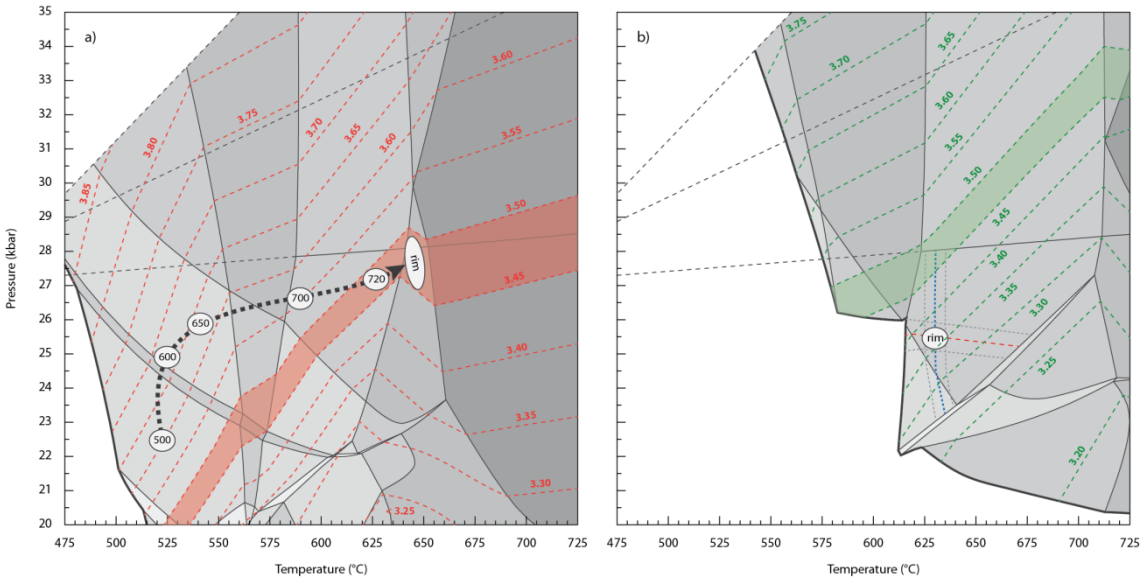


Fig. 5.13 – *P–T* pseudosection for sample L08-03A with isopleths of Si in phengite. Isopleths show the total compositional range between the limits 20–35 kbar and 475–725 °C. Measured compositions of matrix phengite lie approximately in the shaded region for both (a) un-fractionated and (b) fractionated EBCs.

Conventional thermobarometry

Various conventional thermobarometers were employed in order to provide additional independent checks on peak *P–T* conditions that have been obtained through phase equilibria modelling (above). Štípská & Powell (2005) suggest that a minimum uncertainty of ± 70 °C (1 S.D.) should be applied

to temperatures obtained from the garnet-clinopyroxene thermometer mainly due to uncertainty regarding calculation of the XFe^{3+} ratio of both phases. Additionally, the simplification of assuming that all iron in omphacite is Fe^{2+} biases estimates strongly up-temperature (ibid). Such uncertainties do not allow for precise geothermometry when compared to the *potential* accuracy of phase equilibria modelling; however, few other independent checks are available for eclogitic parageneses therefore the calibrations are used as an investigative tool in this case.

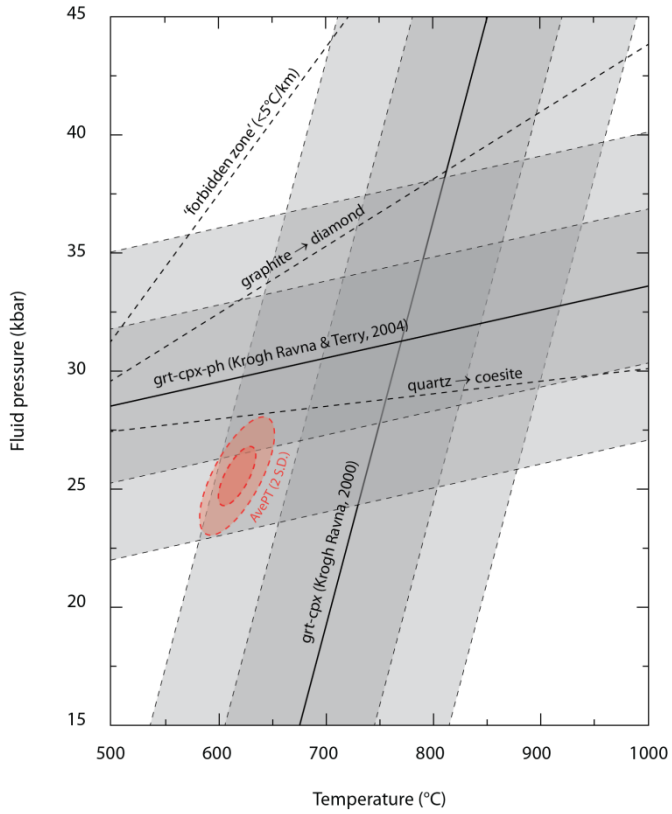


Fig. 5.14 – Sample L08-03A conventional thermobarometry results for M2 metamorphism. Results are shown at 1 S.D. and 2 S.D. in all cases.

Peak conditions were calculated by combining the garnet-clinopyroxene thermometer (Krogh Ravna, 2000) and the garnet-clinopyroxene-phengite barometer (Krogh Ravna & Terry, 2004). For the garnet-clinopyroxene thermometer, compositions of the analysed garnet outer rim and an associated omphacite inclusion (Table 5.1) were used to calculate an equilibrium lying between 705–792 °C and 20–35 kbar respectively. This equilibrium has a dT/dP ~6 °C/kbar and its position in *P*–*T* space is shown in Fig. 5.14. For the garnet-clinopyroxene-phengite barometer, the aforementioned garnet and omphacite compositions were used alongside a matrix phengite composition to calculate an equilibrium lying between 27.5–33.6 kbar and 400–1000 °C respectively (with an associated 1

S.D. of ± 3.2 kbar in the coesite stability field). This equilibrium has a dP/dT of ~0.01 kbar/°C and lies above the quartz-coesite transition (Fig. 5.14). End-member activities were calculated by the spreadsheet GCPKS (Krogh Ravna & Terry, 2004) using the garnet model of Ganguly *et al*. (1996), the pyroxene model of Holland (1990) and the white mica model of Holland & Powell (1998). Calculated activities are as follows: 0.02760 (alm), 0.04095 (grs), 0.2014 (prp), 0.1084 (hed), 0.4287 (di), 0.4342 (jd), 0.3976 (mu), 0.1587 (cel) and 0.0325 (fcel).

The AvePT function of THERMOCALC was also used to calculate peak *P–T* conditions of equilibration for garnet outer rims and associated inclusions that are otherwise not considered by the above thermobarometry. Considered phases that exhibit solid solution include garnet, omphacite, phengite and talc, whereas pure end-member compositions were used for quartz, rutile, lawsonite and H_2O. The input activities of all end-members are presented in Appendix 11.5. A fluid composition of $X(H_2O) = 1.0$ produced a result of 25.5 ± 1.2 kbar and 617 ± 17 °C (1 S.D.) from 5 independent reactions (Table 5.4). Investigation into the effect of a coexisting fluid of mixed H_2O–CO_2 composition on AvePT results, as suggested by the presence of minor carbonate, showed inconsequential change. A fluid composition of $X(H_2O) = 0.9$ produced 25.5 ± 1.2 kbar and 607 ± 18 °C, and $X(H_2O) = 0.8$ produced 25.5 ± 1.3 kbar and 602 ± 18 °C, all within error of initial calculations. The resulting AvePT error ellipse is shown on Fig. 5.14. It is also notable that the 2 S.D. confidence interval overlaps with both predicted final *P–T* conditions as obtained through thermodynamic modelling (Fig. 5.12e). As all thermobarometric methods involve various assumptions and limitations (chapter 2.3.3), it is concluded that peak M2 conditions most likely lie between 25.5–27.5 kbar and 630–645 °C, a region of *P–T* space common to the majority of results.

Sample	Calculation assemblage	XH_2O	T (°C)	1 S.D.	P (kbar)	1 S.D.	Cor	Sig Fit	N	End-members excluded
L08-03A	Grt, Ph, Omp, Tlc, Lws, Rt, Qz, H_2O	1.00	617	17	25.5	1.2	0.70	1.36	5	fcel, ru, hed
	Grt, Ph, Omp, Tlc, Lws, Rt, Qz, H_2O	0.90	607	18	25.5	1.2	0.70	1.43	5	fcel, ru, hed
	Grt, Ph, Omp, Tlc, Lws, Rt, Qz, H_2O	0.80	602	18	25.5	1.3	0.71	1.48	5	fcel, ru, hed

Table 5.4 – THERMOCALC AvePT results for sample L08-03A M2 metamorphism. Cor = correlation, Sig Fit = significant fit, N = number of independent reactions used in calculation (after Powell & Holland, 1994).

5.5.4. M3 conditions of exhumation

Investigation into the retrograde evolution of sample L08-03A was performed using two techniques. Firstly, the effect of fluid addition ('re-hydration') on the largely anhydrous peak M2 assemblage

was investigated through construction of *P*–M(H_2O) pseudosections that attempted to replicate the formation of abundant matrix amphibole, microstructurally determined to have formed post-M2 metamorphism. Secondly, the *P–T* conditions of formation of symplectite colonies surrounding matrix omphacite were investigated through the combination of various conventional thermobarometers. The methodology and results for both studies are outlined below.

5.5.4.1. *P*–M(H_2O) pseudosections

The formation of zoned amphibole in mafic eclogites has been suggested to be a direct result of fluid addition during exhumation (Massonne, 2012), which results in the breakdown of omphacite and, to a lesser extent, garnet through the following reaction (Zhang *et al*., 2003):

$$\text{omphacite} + \text{garnet} + H_2O \rightarrow \text{plagioclase} + \text{Na-Ca amphibole} \pm \text{clinopyroxene} \qquad (5.5.1)$$

Here, the source of fluid may be internal to the eclogite, for example by the breakdown of constituent hydrous phases, or external via infiltration from the dehydration of adjacent lithologies. In order to investigate whether the compositionally zoned matrix amphibole observed in sample L08-03A could have formed via re-hydration, pseudosections were constructed that show calculated assemblages over a range of bulk H_2O contents. These pseudosections were used to investigate the effects of gain (or loss) of H_2O during exhumation from peak M2 conditions. An EBC was calculated that utilised all observed matrix phases and a nominal contribution from garnet outer rim regions (1% rock volume) due to the existence of pargasite kelyphites/mantles around some garnet rims, indicative of retrograde reaction. H_2O content of the EBC was calculated by considering the individual H_2O contents of each hydrous matrix phase (with H_2O assumed to be present in stoichiometric amounts). The *incomplete* replacement of omphacite suggests that H_2O availability during exhumation was not in excess (Štípská & Powell, 2005), so is suitable for this method.

Bulk composition	H_2O	SiO_2	Al_2O_3	CaO	MgO	FeO	K_2O	Na_2O	TiO_2	O
Anhydrous	0.00	55.04	8.48	10.10	16.64	4.81	0.51	3.50	0.77	0.16
Calculated fluid content	6.21	51.62	7.95	9.47	15.61	4.51	0.48	3.28	0.72	0.15

Table 5.5 – EBCs for sample L08-03A *P*–M(H_2O) pseudosections

The observation that the calculated fluid content in Table 5.5 is less than that predicted to be present at peak metamorphism (the 'fully fractionated' EBC obtained during *P–T* pseudosection modelling) indicates that there may be complex interplay between fluid release from the breakdown

of hydrous phases (e.g. talc and lawsonite) during exhumation and the infiltration of fluid from an external source (below). As this behaviour is unquantifiable without isotopic techniques to trace the source of fluids, a composition calculated from observed phases is the most realistic estimate of the bulk rock fluid content during exhumation and is used as an end-member in this case.

The H_2O content of the bulk rock is designated M(H_2O) in order to avoid confusion with X(H_2O) that describes fluid composition. The range of values for M is defined by the bulk compositions in Table 5.5, from 0 (anhydrous) to 1 (H_2O content defined by the observed hydrated matrix assemblage). Finally, in order to examine the effect of varying proportions of H_2O in the EBC during exhumation, temperature was fixed at 640 °C. This was due to previous studies of the TMM suggesting that exhumation from M2 to M3 conditions was more-or-less isothermal (Fig. 5.2), with the value of 640 °C chosen following the results of M2 thermobarometry (above). At a certain point during exhumation under these conditions the EBC for sample L08-03A must cross the H_2O-saturation line as free H_2O is consumed in the formation of hydrous minerals. At this point, the lack of free H_2O should effectively 'freeze in' the solid mineral assemblage and compositions, as further discontinuous reaction in the absence of fluid can be sluggish (Carson *et al*., 1999; Guiraud *et al*., 2001). In reality rocks may not remain closed to external fluid and retrogressive change may be further enhanced by influx after this point; however, microstructural evidence for or against this scenario is absent and quantification is most likely impossible. Likewise, prograde metamorphism is known to have occurred following exhumation to M3 conditions (Fig. 5.2); thus, the idea that sample L08-03A was re-hydrated during exhumation and *not* subsequently dehydrated again, is unlikely to be true. The presented modelling is thus considered as a preliminary investigation into the effect of varying proportions of H_2O in the EBC and the parageneses produced. Additionally, as matrix amphibole formation at the expense of omphacite is the investigated phenomenon, discussion of the calculated *P*–M(H_2O) pseudosections deals explicitly with this result.

Amphibole compositions and pseudosection results

The range of matrix amphibole compositional variation is shown in Fig. 5.15, displayed as functions of common amphibole exchange vectors. Compositional additive vectors can be demonstrated by inspection of Fig. 5.6, initiating at starting composition $Ca_2Mg_5Si_8O_{22}(OH)_2$ (tremolite).

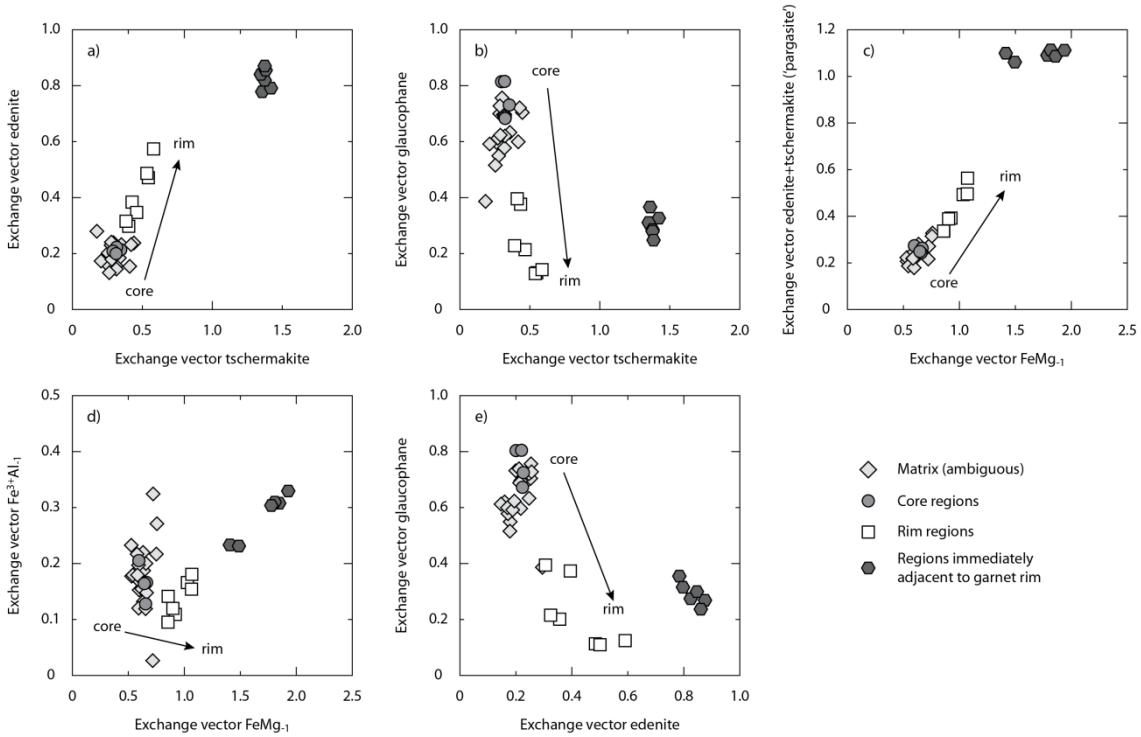
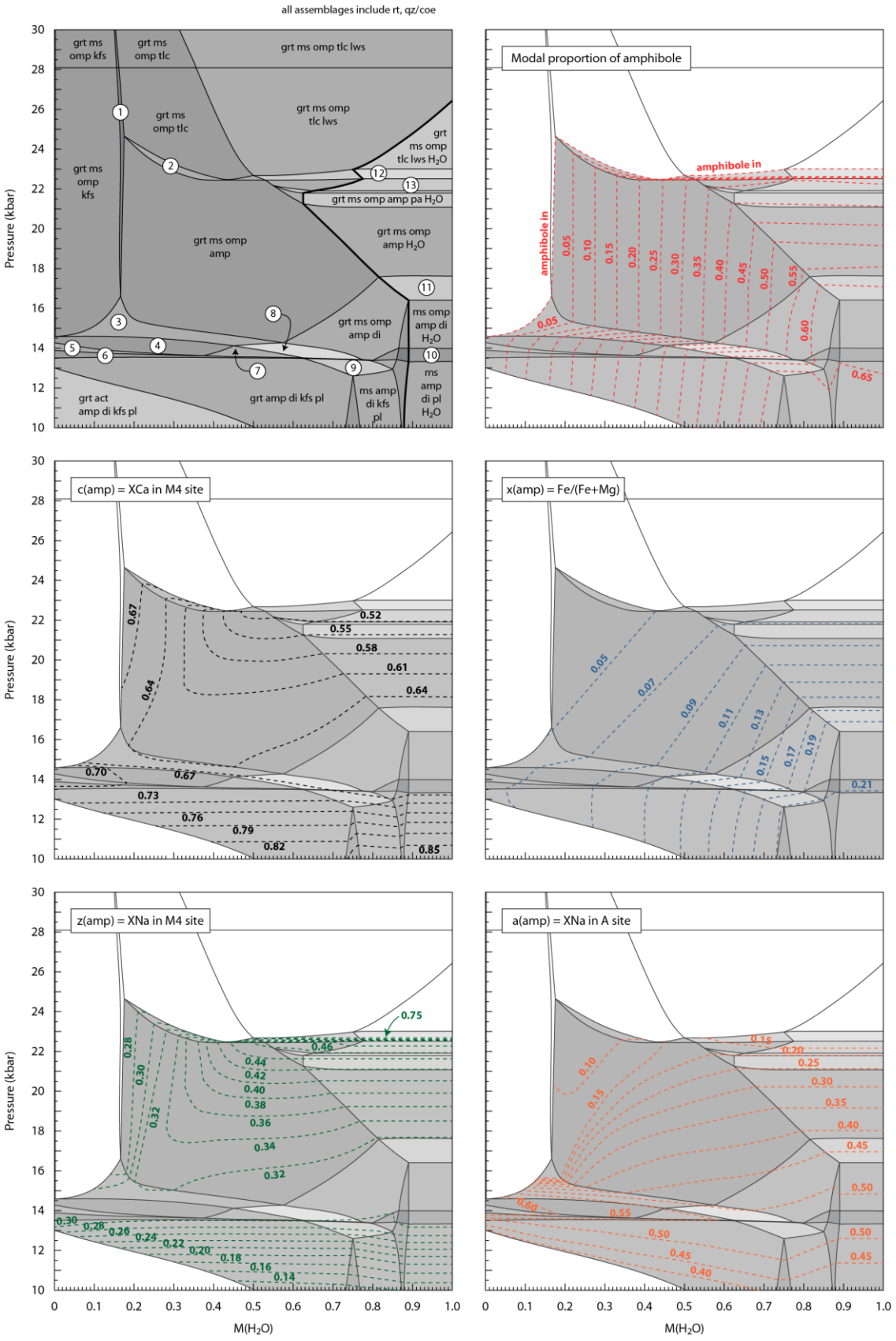


Fig. 5.15 – Compositional plots for sample L08-03A matrix amphiboleexpressed in terms of exchange vectors. Compositional trends from cores to rims of matrix laths are marked by arrows. It can be seen that pargasitic amphibole bands mantling garnet porphyroblasts have a distinctly different composition than matrix amphibole situated away from garnet. (a) Exchange vector edenite (Na+K in A site) vs. exchange vector tschermakite ($Al_2Mg_{-1}Si_{-1}$). (b) Exchange vector glaucophane (Na in B site) vs. exchange vector tschermakite ($Al_2Mg_{-1}Si_{-1}$). (c) Exchange vector edenite+tschermakite ('pargasite') vs. exchange vector $FeMg_{-1}$. (d) Exchange vector $Fe^{3+}Al_{-1}$ vs. exchange vector $FeMg_{-1}$. (e) Exchange vector glaucophane (Na in B site) vs. exchange vector edenite (Na+K in A site).

For example, the transformation of tremolite to edenite involves the addition of both Na+K to the A site whereas transformation to glaucophane involves addition of Na to the B site only. For simplicity Fig. 5.6 deals with Mg end-members only and the $FeMg_{-1}$ vector cannot be shown. Fig. 5.15 shows that some compositional vectors have clearer differences between sodic-calcic cores and calcic rims than others, so should be better discriminants in compositional space. For example, the exchange vector $Fe^{3+}Al_{-1}$ is relatively poor, as the measured ranges in core and rim regions overlap in the range ~0.1–0.2 (Fig. 5.15d). By contrast, there is minimal overlap between core and rim compositions when considering the glaucophane exchange vector (Fig. 5.15b).

Fig. 5.16 – *P*–M(H_2O) pseudosections with isolines for amphibole properties (overleaf). All assemblages contain rt+qz/coe. Numbered fields are: (1) grt ms omp (2) grt ms omp tlc amp (3) grt ms omp amp kfs (4) grt omp amp kfs (5)grt omp amp kfs pl (6) grt omp amp kfs pl di (7) grt omp amp kfs di (8) grt ms omp amp kfs di (9) grt ms amp di kfs pl (10) ms di amp H_2O (11) grt ms omp amp di H_2O (12) grt ms omp tlc amp lws H_2O (13) grt ms omp amp lws H_2O.



Amphibole compositional parameters monitored by THERMOCALC activity-composition relationships include x(amp) = Fe/(Fe+Mg), z(amp) = mole fraction of Na on the M4 site, a(amp) =

Na on the A site and c(amp) = mole fraction of Ca on the M4 site (Diener *et al*., 2007). Isopleths representing these compositional variables are presented in Fig. 5.16 on *P*–M(H_2O) pseudosections that show that matrix amphibole would first form in sample L08-03A at pressures between 23–25 kbar if the EBC was restricted to a value of M(H_2O) > 0.16. Otherwise, the first appearance of amphibole occurs at ~15–17 kbar.

It can be seen from Fig. 5.16 that large variations in calculated amphibole composition occur in *P*–M(H_2O) space; for example the proportion of Na in the M4 site (parameter z(amp)) ranges from 0.28 to 0.75 between ~23–24 kbar and ~0.25–0.50 M(H_2O). The inferred peak M2 assemblage in L08-03A contains minor phengite, lawsonite and talc as hydrous phases (chapter 5.5.3). This assemblage occurs at M(H_2O) > 0.4 at a pressure of 28 kbar on Fig. 5.16, which may be taken as a minimum for H_2O bulk rock content at the start of exhumation from HP conditions. Within this M(H_2O) range, contours for amphibole modal proportion show that significant growth occurs as a result of talc and lawsonite breakdown at ~22–23 kbar. Here, a modal proportion up to 0.35 may form over an extremely small pressure interval. Otherwise, amphibole proportion is calculated to increase steadily with decreasing pressure within H_2O-saturated assemblages, whereas growth is largely insensitive to pressure elsewhere, changing only as a function of M(H_2O).

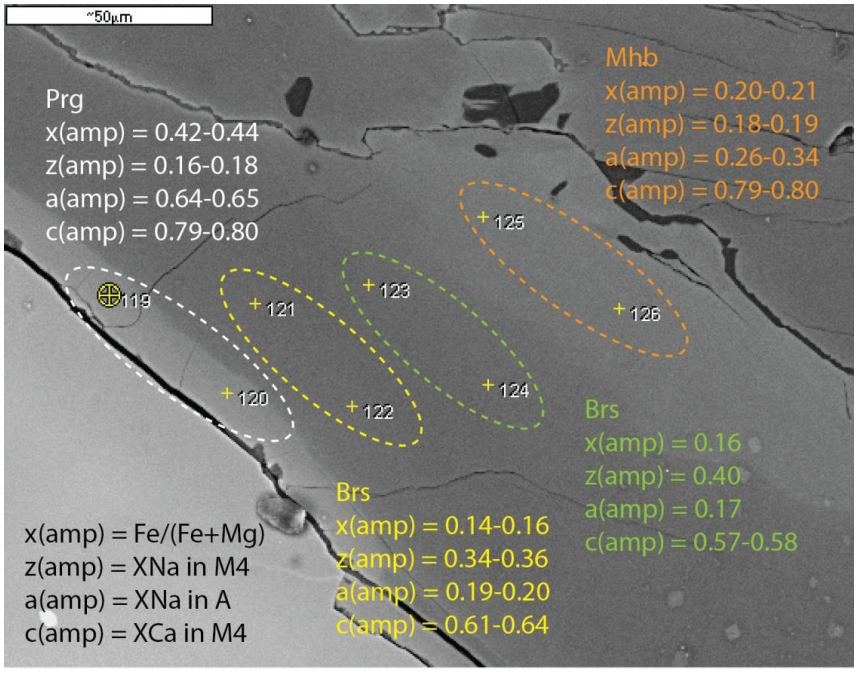


Fig. 5.17 – SEM BSE image of matrix amphibole compositional zoning in sample L08-03A showing calculated THERMOCALC composition coding parameters in core and rim regions as described in the text. Pargasitic mantles occur against garnet grains (bright phase in bottom left-hand corner).

In order to interpret this pseudosection, ranges in THERMOCALC compositional parameters were obtained from numerous large matrix amphibole laths (e.g. Fig. 5.17). Isopleths representing the total range of measured compositions are as follows: x(amp) = 0.11–0.19, z(amp) = 0.26–0.40, a(amp) = 0.10–0.25 and c(amp) = 0.57–0.72 (barroisite cores) and x(amp) = 0.19–0.24, z(amp) = 0.06–0.20, a(amp) = 0.25–0.51, c(amp) = 0.79–0.92 (magnesiohornblende rims).

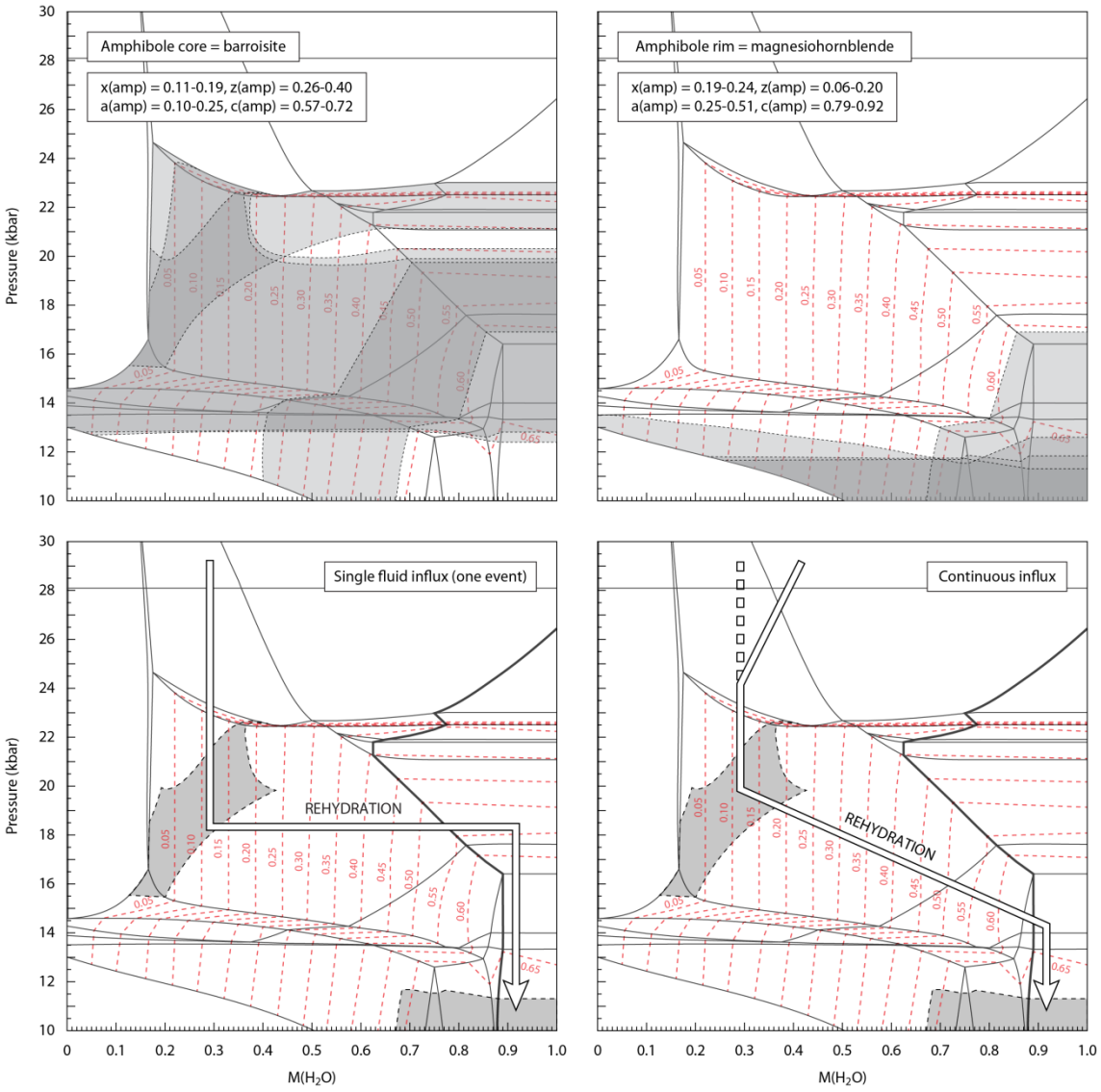


Fig. 5.18 – *P*–M(H_2O) pseudosection interpretation showing possible regions of *P*–M(H_2O) space where core and rim compositions could form.

These ranges for core and rim regions are shown in *P*–M(H_2O) space in Fig. 5.18. With the exception of x(amp), compositional ranges relevant to barroisitic core regions intersect at a pressure between 16–23 kbar and M(H_2O) between 0.16–0.40 (Fig. 5.18). It is notable that Fe-Mg exchange was a poor discriminating factor between core and rim growth in Fig. 5.15; therefore, it is possible to

find a somewhat similar composition for core regions in *P*–M(H_2O) space at 640 °C to those observed in sample L08-03A. All four compositional parameters for magnesiohornblende rims intersect at pressures between 10–12 kbar and M(H_2O) > 0.67 (Fig. 5.18). These data encouragingly suggest that compositions matching amphibole observed in sample L08-03A can be located in *P*–M(H_2O) space, and isomode contours show that amphibole would comprise a modal proportion of up to 0.25 of the calculated assemblage for core regions and at least 0.62 for rim regions (Fig. 5.18).

Matrix amphibole in sample L08-03A constitutes a ~38% volume proportion of the total rock. Additionally, garnet comprises ~30% total volume of sample L08-03A. Given that only 1% of garnet was considered as a contributor to the EBC and is therefore largely not considered within the calculated assemblage, these modal proportions for amphibole cores and rims reduce to ~0.18 and ~0.44 (i.e. multiplication by 0.71; assuming that modal proportion is approximately equal to volume proportion for ease of conversion). This suggests that modal proportions are in good agreement with observed volume proportions, in addition to compositions. Although the nature of re-hydration is unknown, different hypothetical scenarios do not change the calculated result significantly (Fig. 5.16). As a result of the large assemblage field grt–ms–omp–amp–ru–qz that connects core and rim regions in *P*–M(H_2O) space, there is minor change in coexisting assemblage whether influx occurs at a single pressure or whether fluid is added over a range of pressures during exhumation. In addition, it can also be seen that fluid release associated with the breakdown of lawsonite and/or talc, which may or may not be lost from the rock, will not affect amphibole growth above ~25 kbar. However, if fluid was retained and the M(H_2O) was relatively high (e.g. >0.5), initial amphibole growth could occur as a highly-sodic composition (e.g. glaucophane). This may affect the reported variation in amphibole composition across the TMM.

5.5.4.2. Symplectite thermobarometry

High-pressure minerals breaking down to fine intergrowths of lower pressure minerals (symplectites) are common in most exhumed HP and UHP metabasites (Eskola, 1921; Droop *et al.*, 1990; Zhao *et al.*, 2001). Some eclogites contain intergrowths of orthopyroxene, sapphirine, spinel, corundum or anorthite that are interpreted to have formed during decompression under granulite-facies conditions (O'Brien & Vrána, 1995; O'Brien, 1997a,b). Conversely, amphibole-bearing

symplectites have been interpreted to have formed at lower temperature conditions of the amphibolite-facies (Messiga & Bettini, 1990; Medaris *et al*., 1995; Waters, 2002). However, examination of the minerals in a symplectic intergrowth cannot be used to infer the *P–T* conditions of exhumation without further information, as the mineral compositions and assemblages present may also depend on the activity of components such as H_2O or SiO_2 (Štípská & Powell, 2005).

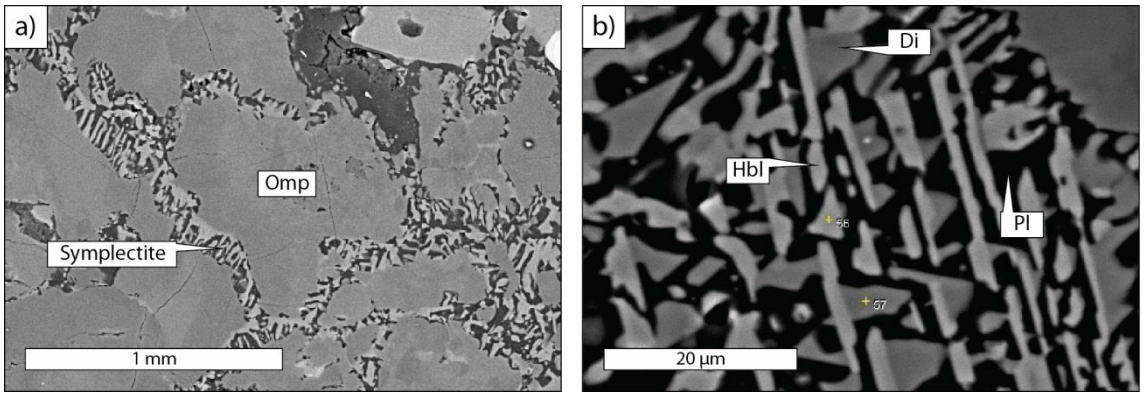


Fig. 5.19 – SEM BSE images of symplectite occurrence and morphology in sample L08-03A (a) Symplectite colonies rim omphacite and most likely demarcate the position of prior omphacite-omphacite grain boundaries. Note that no symplectite has developed at the top right-hand corner of the central grain, which is adjacent to the matrix. (b) Highly magnified view of a typical symplectite colony showing the lath- or plate-like morphology of hornblende. Plagioclase can be seen as the dark 'background' phase.

In sample L08-03A, symplectites located along the grain boundaries of omphacite (Fig. 5.19a) are extremely fine and composed of platelets of actinolite/hornblende, diopside and albitic plagioclase, commonly 4–8 µm in width (Fig. 5.19b). Thermobarometric analysis of symplectite colonies involved selecting discrete occurrences throughout sample L08-03A that were sufficiently coarse to enable SEM-microprobe investigation of individual coexisting plagioclase-amphibole-pyroxene platelets. Visual inspection of multiple colonies suggests that there is no obvious growth direction, thus it was not possible to distinguish early vs. late growth of constituents (if indeed growth occurred over an extended period). Nonetheless, no systematic differences in composition of any phase were identified between different spatial positions throughout the sample. A total of 8 out of 17 plagioclase-amphibole-pyroxene triplets analysed on the SEM-microprobe were suitable for both pressure and temperature determination, compositions of which are presented in Table 5.6.

Table 5.6 – Mineral compositions for all symplectite colonies used for thermobarometry (overleaf).

Colony	Mineral	SiO_2	TiO_2	Al_2O_3	Fe_2O_3	FeO	MnO	MgO	CaO	Na_2O	K_2O	**Total**	Si	Ti	Al	Fe^{3+}	Fe^{2+}	Mn	Mg	Ca	Na	K	**Sum**	Ox
S1	Di	53.12	0.09	2.78	1.33	4.57	0.03	12.81	22.15	1.68	0.00	**98.56**	1.98	0.00	0.12	0.04	0.14	0.00	0.71	0.88	0.12	0.00	**4.00**	6
	Mhb	51.78	0.13	5.79	0.21	8.74	0.02	16.42	12.12	1.24	0.15	**96.60**	7.43	0.01	0.98	0.02	1.05	0.00	3.51	1.86	0.34	0.03	**15.24**	23
	Pl	67.05	0.00	19.71	0.13	0.00	0.00	0.00	0.46	10.79	0.00	**98.14**	3.00	0.00	1.04	0.00	0.00	0.00	0.00	0.02	0.93	0.00	**5.00**	8
S4	Di	54.02	0.14	2.78	0.78	4.60	0.04	13.54	22.49	1.53	0.00	**99.92**	1.98	0.00	0.12	0.02	0.14	0.00	0.74	0.88	0.11	0.00	**4.00**	6
	Mhb	50.53	0.19	6.46	0.52	8.91	0.05	15.99	12.18	1.24	0.18	**96.25**	7.31	0.02	1.10	0.06	1.08	0.01	3.45	1.89	0.35	0.03	**15.28**	23
	Pl	65.91	0.01	19.14	0.26	0.00	0.01	0.19	0.93	9.43	0.00	**95.88**	3.00	0.00	1.04	0.01	0.00	0.00	0.01	0.05	0.88	0.00	**5.00**	8
S7	Act	52.24	0.24	4.68	0.31	7.95	0.03	17.08	12.24	0.89	0.11	**95.77**	7.53	0.03	0.79	0.03	0.96	0.00	3.67	1.89	0.25	0.02	**15.17**	23
	Di	54.75	0.11	2.75	0.95	4.26	0.04	13.97	22.20	1.71	0.01	**100.75**	1.99	0.00	0.12	0.03	0.13	0.00	0.76	0.86	0.12	0.00	**4.00**	6
	Pl	65.84	0.00	19.22	0.20	0.00	0.01	0.23	0.93	9.90	0.00	**96.33**	3.00	0.00	1.04	0.01	0.00	0.00	0.02	0.05	0.89	0.00	**5.00**	8
S10	Di	53.33	0.23	6.89	0.20	4.37	0.09	11.82	19.37	2.91	0.04	**99.25**	1.95	0.01	0.30	0.01	0.13	0.00	0.64	0.76	0.21	0.00	**4.00**	6
	Mhb	53.08	0.38	5.54	0.02	6.08	0.01	18.26	12.20	1.15	0.18	**96.90**	7.48	0.04	0.92	0.00	0.72	0.00	3.84	1.84	0.31	0.03	**15.19**	23
	Pl	64.54	0.08	18.56	0.34	0.00	0.02	0.85	1.64	10.02	0.00	**96.05**	2.95	0.00	1.00	0.01	0.00	0.00	0.06	0.08	0.89	0.00	**5.00**	8
S13	Act	55.74	0.18	6.34	0.00	7.41	0.06	16.53	12.53	1.96	0.17	**100.92**	7.57	0.02	1.02	0.00	0.84	0.01	3.35	1.82	0.52	0.03	**15.17**	23
	Di	55.58	0.00	5.12	0.00	4.68	0.00	12.08	19.47	2.88	0.00	**99.81**	2.01	0.00	0.22	0.00	0.14	0.00	0.66	0.77	0.20	0.00	**4.00**	6
	Pl	67.66	0.00	18.07	0.75	0.00	0.01	1.43	2.42	9.74	0.00	**100.08**	2.99	0.00	0.94	0.03	0.00	0.00	0.09	0.11	0.83	0.00	**5.00**	8
S14	Act	55.99	0.10	5.64	0.00	6.49	0.01	17.14	11.99	1.96	0.11	**99.43**	7.67	0.01	0.91	0.00	0.74	0.00	3.50	1.76	0.52	0.02	**15.13**	23
	Di	54.27	0.20	4.58	0.04	5.20	0.00	13.07	22.14	1.77	0.00	**101.27**	1.96	0.01	0.20	0.00	0.16	0.00	0.70	0.86	0.12	0.00	**4.00**	6
	Pl	64.46	0.00	18.23	0.43	0.00	0.00	0.84	1.63	9.71	0.00	**95.30**	2.98	0.00	0.99	0.02	0.00	0.00	0.06	0.08	0.87	0.00	**5.00**	8
S15	Di	55.28	0.06	2.95	0.00	6.23	0.06	13.07	22.14	1.74	0.04	**101.57**	2.00	0.00	0.13	0.00	0.19	0.00	0.70	0.86	0.12	0.00	**4.00**	6
	Mhb	52.18	0.15	5.67	0.00	9.50	0.05	15.68	12.17	1.44	0.21	**97.05**	7.48	0.02	0.96	0.00	1.14	0.01	3.35	1.87	0.40	0.04	**15.25**	23
	Pl	66.09	0.04	19.42	0.41	0.00	0.06	0.07	0.77	10.58	0.00	**97.44**	2.98	0.00	1.03	0.01	0.00	0.00	0.01	0.04	0.93	0.00	**5.00**	8
S17	Di	54.56	0.07	3.64	0.00	5.45	0.01	13.17	21.50	1.80	0.00	**100.20**	2.00	0.00	0.16	0.00	0.17	0.00	0.72	0.84	0.13	0.00	**4.00**	6
	Mhb	51.27	0.26	6.60	0.00	9.41	0.07	15.84	12.20	1.41	0.20	**97.26**	7.34	0.03	1.11	0.00	1.13	0.01	3.38	1.87	0.39	0.04	**15.29**	23
	Pl	65.99	0.00	18.99	0.16	0.00	0.02	0.05	0.46	10.96	0.02	**96.65**	2.99	0.00	1.01	0.01	0.00	0.00	0.00	0.02	0.96	0.00	**5.00**	8

For calculations, uncertainty regarding unknown fluid composition/activity was eliminated by only considering anhydrous equilibria. Holland & Blundy (1994) provide such equilibria with two thermometers based on cation exchange between amphibole and plagioclase:

edenite + 4 quartz = tremolite + albite (5.5.2)

edenite + albite = richerite + anorthite (5.5.3)

The calibrations presented in Holland & Blundy (1994) allow for partitioning ('underflow') of Ca onto the M1 and M3 sites in the amphibole structure, which in certain situations can result in a

negative proportion of cummingtonite on calculation of end-member proportions (D.J. Waters *pers comms*, 2011). This is a result of the IMA stoichiometric criterion that the cation total (excluding K+Na+Ca) should not be less than 13 and thus should restrict Ca to the M4 site (Appenix 2 in Leake *et al.*, 1997), whereas a limit of 12.9 is employed by Holland & Blundy (1994) such that it is possible for a recalculation to have some Ca on the M1 or M3 sites. To avoid this, an adjustment to the formula recalculation was performed using the spreadsheet HBPL94 (D.J. Waters *pers comms*, 2011) where no Ca underflow onto the M1 and M3 sites can occur and the cation total (excluding K+Na+Ca) is reset to 13. This led to two slightly different structural formulae being used (below).

Results

Pressures between 6–18 kbar were utilised as reference values for initial temperature calculations, and show that both equilibria (5.5.2 and 5.5.3) have a very small dT/dP of ~2–4 °C/kbar in *P–T* space. As such, the reference pressure used for thermometry does not control the result significantly. Thus, an estimated pressure of 12 kbar was chosen for final calculations, producing results for reaction 5.5.2 ranging between 462–552 °C (Ca underflow) and 465–547 °C (no underflow). Reaction 5.5.3 produced a range of 468–558 °C (Ca underflow) and 455–550 °C (no underflow) under the same pressure conditions (Table 5.7). The quoted uncertainty for both Holland & Blundy (1994) calibrations ranges between ± 35–40 °C.

Colony	XCa	Calculated temperature (°C)				
		Ed-Tr^1	Ed-Tr^2	Ed-Ri^1	Ed-Ri^2	**Ed-Ri ave**
S1	0.02	527	524	468	455	**461**
S4	0.05	552	547	515	494	**505**
S7	0.05	498	508	507	487	**497**
S10	0.08	506	515	548	534	**541**
S13	0.11	490	482	558	550	**554**
S14	0.08	462	465	530	532	**531**
S15	0.04	515	511	496	483	**489**
S17	0.02	543	536	474	460	**467**

Table 5.7 – Hbl-Pl geothermometer results for symplectite colonies using both formula recalculations in both reactions from Holland & Blundy (1994). Superscript 1 = Ca underflow, superscript 2 = no Ca underflow.

Reaction 5.5.3 (edenite + albite = richerite + anorthite) is most applicable to the observed mineralogy, instead of reaction 5.5.2 (edenite + 4 quartz = tremolite + albite), given the lack of quartz within symplectite colonies. In addition, Fig. 5.20 shows that results from reaction 5.5.2 have a poor correlation with the Ca content of plagioclase (R^2 = 0.456 and 0.504), whereas temperatures

obtained from reaction 5.5.3 show strong correlations (R^2 = 0.913 and 0.957). It should be noted that the majority of the analysed feldspars are strongly albitic, therefore the small proportion of anorthite present likely results in relatively high uncertainties on calculated activities (of anorthite) following SEM-microprobe analysis. Despite this, given the strong correlation for both stoichiometry recalculations, a more suitable mineralogical calibration and all results being within uncertainty of each other, an average of temperatures obtained from reaction 5.5.3 was used for each data pair as a reference point (Table 5.7) for subsequent geobarometry.

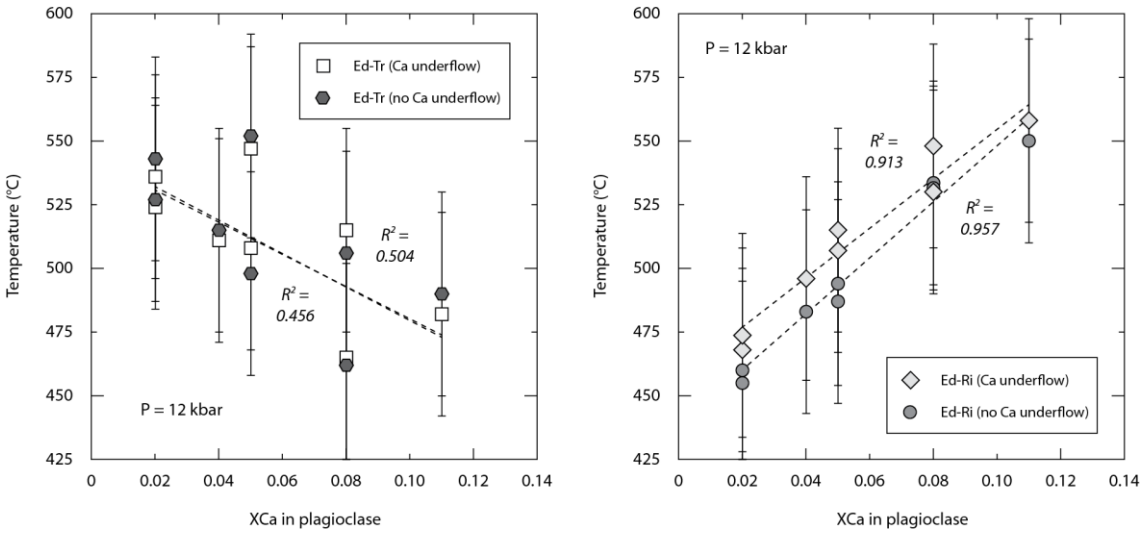


Fig. 5.20 – Hbl-Pl geothermometer results for symplectite colonies using both formula recalculations in both reactions from Holland & Blundy (1994). The associated error on each calculated temperature is shown as ± 40 °C

Pressures of symplectite formation were calculated through three silica- and fluid-independent barometers using the THERMOCALC AveP function:

tremolite + tschermakite + 8 jadeite = 2 pargasite + 6 albite (5.5.4)

tremolite + anorthite + 5 jadeite = pargasite + 4 albite + diopside (5.5.5)

4 tremolite + ferro-actinolite + 5 anorthite + 25 jadeite = 5 pargasite + 20 albite + 5 hedenbergite (5.5.6)

The activities of amphibole and feldspar end-members were calculated using the software AX whereas those for pyroxene were calculated using a disordered (C2/c) non-ideal two-site model after Holland (1990). This was performed using the spreadsheet ax-cpx-04 (D.J. Waters *pers comms*, 2011) as a result of the inability AX to calculate the activity of jadeite for clinopyroxene with low Na content. All end-member activities are presented in Table 5.8.

Colony	Mineral	End-member activities and calculated uncertainties											
S1	Di	di	0.6646	0.066	hed	0.1791	0.018	jd	0.3002	0.03			
	Mhb	tr	0.282	0.0353	fact	0.00021	0.000106	ts	0.0031	0.002	parg	0.083	0.0103
	Pl	an	0.04	0.0055	ab	0.98	0.0244						
S4	Di	di	0.6847	0.068	hed	0.1699	0.017	jd	0.2083	0.021			
	Mhb	tr	0.291	0.0364	fact	0.00022	0.000109	ts	0.0022	0.0021	parg	0.074	0.0093
	Pl	an	0.09	0.0112	ab	0.95	0.0237						
S7	Act	tr	0.30	0.0369	fact	0.00019	0.000094	ts	0.0046	0.0017	parg	0.078	0.0098
	Di	di	0.6817	0.068	hed	0.1511	0.015	jd	0.2277	0.023			
	Pl	an	0.086	0.0108	ab	0.95	0.0238						
S10	Di	di	0.5874	0.058	hed	0.1408	0.014	jd	0.3939	0.039			
	Mhb	tr	0.34	0.0425	fact	0.00004	0.000023	ts	0.007	0.0025	parg	0.142	0.0178
	Pl	an	0.143	0.0157	ab	0.92	0.023						
S13	Act	tr	0.256	0.032	fact	0.000098	0.000052	ts	0.008	0.0025	parg	0.107	0.0134
	Di	di	0.6337	0.064	hed	0.2216	0.022	jd	0.3075	0.031			
	Pl	an	0.21	0.0195	ab	0.88	0.022						
S14	Act	tr	0.28	0.0347	fact	0.000055	0.000304	ts	0.01	0.0027	parg	0.103	0.0129
	Di	di	0.6526	0.065	hed	0.1765	0.018	jd	0.2519	0.025			
	Pl	an	0.147	0.016	ab	0.92	0.0229						
S15	Di	di	0.6542	0.065	hed	0.2153	0.022	jd	0.2431	0.024			
	Mhb	tr	0.232	0.0291	fact	0.00032	0.000155	ts	0.003	0.0018	parg	0.09	0.0113
	Pl	an	0.068	0.0088	ab	0.96	0.024						
S17	Di	di	0.6685	0.067	hed	0.203	0.02	jd	0.2796	0.028			
	Mhb	tr	0.257	0.0321	fact	0.00026	0.000128	ts	0.0024	0.002	parg	0.089	0.0112
	Pl	an	0.039	0.0055	ab	0.98	0.0244						

Table 5.8 – End-member activities used for symplectite AveP calculations. N.B. A 10% uncertainty was applied to calculated activities for pyroxene end-members. All other uncertainties were calculated by AX.

Pressures obtained from reaction 5.5.4 range between 10.3–13.9 kbar, whereas reactions 5.5.5 and 5.5.6 produced results between 1.0–1.5 kbar lower (Table 5.9 and Fig. 5.21a); however, all results are equal within uncertainty. Results from reaction 5.5.4 were combined with previously calculated average temperatures to produce a *P–T* array for symplectite formation between 461–554 °C and 10.3–13.9 kbar with an apparent trajectory from low-pressure eclogite-facies, through epidote-amphibolite-facies into blueschist-facies conditions (Fig. 5.21b). The tectonic implications of these results are discussed below in chapter 5.6.2.

Colony	Reference temp (°C)	Calculated pressure (kbar)					
		Barometer 5.5.4	1 S.D.	Barometer 5.5.5	1 S.D.	Barometer 5.5.6	1 S.D.
S1	461	10.9	0.8	9.2	0.9	9.4	0.9
S4	505	10.3	1.1	9.3	1.1	9.6	1.1
S7	497	10.9	0.9	9.5	1.1	9.9	1.1
S10	541	13.9	0.7	13.7	0.8	13.7	0.8
S13	554	13.5	0.9	13.2	0.9	13.0	1.0
S14	531	12.2	0.9	11.1	1.0	11.0	1.1
S15	489	10.4	0.9	9.1	1.0	9.2	1.0
S17	467	10.4	0.9	8.8	0.9	9.0	1.0

Table 5.9 – AveP geobarometer results for symplectite colonies

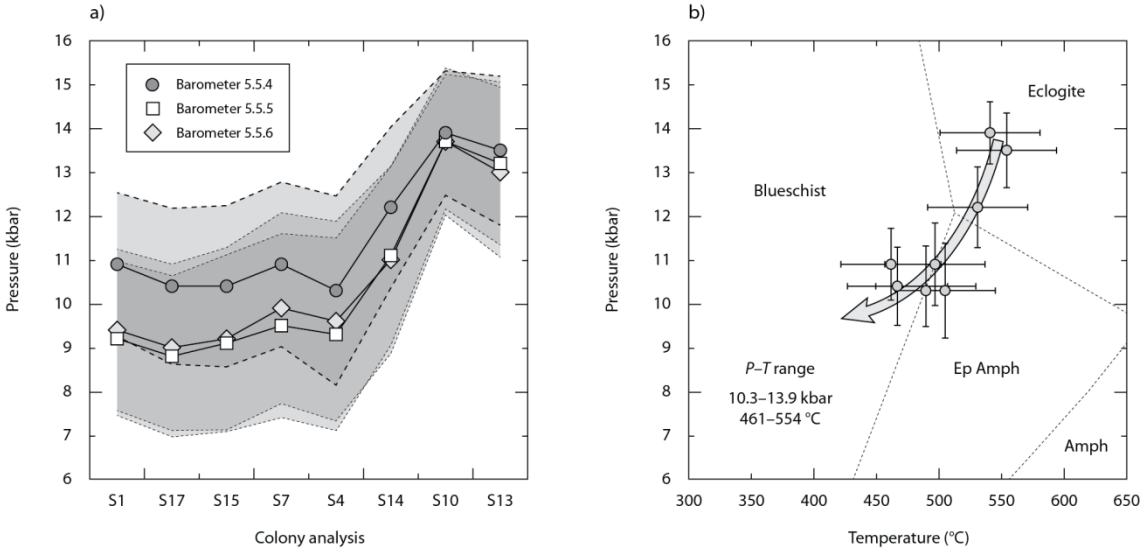


Fig. 5.21 – Geobarometric and combined *P–T* results of symplectite thermobarometry. (a) Results of AveP geobarometry for each reaction (b) Total array combining temperatures and pressures for each colony. Metamorphic facies boundaries are after Takasu *et al.* (1989).

5.6. Summary and discussion

5.6.1. Modelling discrepancies

Thermobarometry and phase equilibria modelling have provided insight into the *P*–*T*–M(H_2O) conditions experienced by sample L08-03A during subduction and exhumation; however, numerous discrepancies exist between observed parageneses and compositions and those that are predicted in each model. These are outlined below, alongside a discussion of possible causes.

Fractionated vs. unfractionated P–T path morphologies

There is a clear difference in the morphology of the calculated peak *P*–*T* path derived from the consideration (or not) of a fractionating bulk composition during prograde metamorphism. Each temperature is constrained by the calculated position of the relevant pyrope isopleth, with the garnet outer rim composition determining peak M2 conditions. The consideration (or not) of cation fractionation has only a minor effect on this result, with a difference of ~20 °C calculated between both situations. Instead, calculated pressures are determined by the position in *P*–*T* space of each grossular isopleth, with peak M2 pressure corroborated by the Si content of phengite. As a result, the changing Ca and Si budget of the fractionating EBC is greatly influential upon final result.

In a study of a similar mafic eclogite from the TMM, Konrad-Schmolke *et al.* (2008) noted that the grossular content of prograde garnet is controlled by the breakdown of epidote and

sodic/sodic-calcic amphibole in the blueschist- and eclogite-facies respectively. Microstructural observation shows that both epidote and sodic-calcic amphibole exist as inclusions in garnet core regions in sample L08-03A, but are absent from rims (with the exception of REE-rich epidote/allanite). Notably, pseudosection modelling indicates that glaucophane (*sensu lato*) is calculated to be stable only during the early stages of prograde metamorphism in an unfractionated scenario, but persists to higher temperatures when considering fractionation. Additionally, it is not until the latter stages of garnet growth that the *P*–*T* paths deviate from one another, with grossular content inferring a lower peak pressure in the latter case. Deviation first occurs after fractionation of domain 3, which is unsurprising as the middle rim contains extreme compositional variation and constitutes a large volume (~38%) of the analysed garnet grain (Fig. 5.4). Its removal should therefore cause significant change to the matrix EBC.

The mismatch between calculated peak conditions is possibly a result of the calculated presence of glaucophane (*sensu lato*) during the latter stages of garnet growth; a condition that has been interpreted to be inaccurate due to its absence in the studied garnet grain rims. A calculated sodic or sodic-calcic amphibole would sequester Ca and Si from the EBC, resulting in a garnet rim region that is calculated to be relatively grossular-depleted compared to the measured grains. An influence on the actual EBC may also be made by the presence of prograde epidote/allanite, which would fractionate Ca and Si from the matrix, but due to the current lack of REE-bearing activity-composition models for such phases, this effect could not be investigated. This problem highlights the limitations that exist on certain thermodynamic models at the current time and although the data presented are suggested to be useful evidence for the prograde and peak metamorphic evolution of the TMM, it is acknowledged that further work is needed, preferably on fresher samples that better preserve the peak metamorphic assemblage. Notwithstanding, AvePT results, which are unaffected by the intricacies of bulk composition calculation, produce similar conditions for M2 metamorphism.

Absence of coesite at M2 metamorphism

Numerous studies have shown through the presence of coesite and/or its pseudomorphs that parts of the TMM experienced UHP conditions during M2 metamorphism (e.g. Sachan *et al*., 2004; Gouzu *et al*., 2006; Epard & Steck, 2008). However, the interpreted peak pressure range for sample L08-03A

lies between 25.5–27.5 kbar (at 630–645 °C) so is insufficient for quartz to transform to coesite. Furthermore, quartz inclusions in garnet outer rims (Fig. 5.3g) are surrounded by radiating fractures in the host porphyroblasts. Such features imply that some volume-expansion of quartz had occurred following its inclusion (i.e. during exhumation), although grains are not polycrystalline – a common feature of reverted SiO_2 (Krogh Ravna & Terry, 2004). Additionally, Gouzu *et al*. (2006) described mafic eclogite from the same L08-03A outcrop locality and also documented a lack of UHP indicators, in contrast to similar localities a few kilometres away, supportive of this result.

Nevertheless, the absence of coesite in L08-03A does not explicitly dismiss the possibility of UHP conditions being attained by the sample. If coesite did form within the matrix, it is possible that all evidence has been lost through polymorphic inversion if neither garnet nor omphacite experienced any significant growth/recrystallisation during UHP conditions. The lack of garnet/clinopyroxene growth in the coesite stability field has been suggested by Wilke *et al*. (2010) and Konrad-Schmolke *et al*. (2008) to be the reason behind the absence of coesite in specific samples from Kaghan and the Western Gneiss Region, Norway. Alternatively, it is also possible that different mafic eclogite exposures in the TMM reached slightly different peak metamorphic conditions. Indeed, if the 'average' peak pressure is somewhat close to the upper limit of the proposed range in this thesis (27.5 kbar at 645 °C), extremely subtle variations (on the order of magnitude of 1 kbar or less) would be sufficient to cause discrimination between HP and UHP samples. Nevertheless, the joint interpretation of petrographic constraints, phase equilibria modelling (with acknowledged limitations) and independent thermobarometry are wholly unsupportive of the apparent existence of diamond (as suggested by Mukherjee *et al.*, 2005).

Inclusions in garnet as indicators of previous equilibrium assemblages

The extreme pressures and dynamic stress regimes associated with the subduction and exhumation of mafic eclogites can cause rigid garnet porphyroblasts to develop fractures during deformation, which may subsequently heal at some later time (Matthews *et al*., 1992; Erambert & Austrheim, 1993; Engvik *et al*., 2001). Garnet observed in sample L08-03A often contains open fractures that connect core and rim regions to the matrix. Such 'channels' allow free fluid to access porphyroblast interiors and induce metamorphic reactions, such as the breakdown of lawsonite. Thus, the presence

of a mineral apparently 'included' in garnet may not be certain evidence that it was part of the stable assemblage at the time of garnet growth. A discriminating factor is whether the inclusion appears to be in textural and compositional equilibrium with associated phases, as well with the garnet itself.

This is of particular significance for garnet core assemblages, as some constituents are almost certainly not in mutual equilibrium with the population as a whole. The phase rule dictates that a stable divariant assemblage may contain a number of phases less than or equal to the amount of components in the chemical system (chapter 2.2). In the model system NCKFMASHTO, sufficient to describe the major chemistry of all considered phases (excluding carbonate minerals), a total of 10 components may only make 8 or fewer solid phases in the presence of water (which are overgrown by garnet). Documented 'inclusions' comprise 11 solid phases: three distinct amphibole populations, chlorite, chloritoid, epidote, ilmenite, titanite, paragonite, albitic plagioclase and quartz. Hence, the entire population could not be stable together and an equivalent assemblage field on a pseudosection, which considers stable assemblages only, can never be found. Additional work to carefully detail the composition, distribution and morphology of each inclusion would greatly improve the interpretation of the prograde history of this sample and other eclogites that contain similar features.

Amphibole growth during exhumation

P–M(H_2O) pseudosection modelling at a fixed temperature of 640 °C attempted to replicate the composition and modal proportion of matrix amphibole in sample L08-03A by changing the H_2O content of the EBC. This has shown that two regions of *P*–M(H_2O) space could replicate the main compositional parameters for amphibole core and rim growth, also with an approximately similar modal proportion to that observed in thin section following rim growth. However, regularly spaced isomode contours between these two regions suggest that amphibole would have grown at a steady rate with the addition of H_2O, which is in dispute with an abrupt change in greyscale intensity observed in SEM BSE imagery (Fig. 5.17b). Such a feature likely represents two distinct episodes of growth, so a continuous compositional transition in *P*–M(H_2O) space would not be expected.

The calculated pseudosection provides indications of problem that may account for these differences. Although considered during modelling, clinozoisite/epidote was not calculated to be stable at any pressure (at 640 °C), and paragonite exhibits a very restricted region of stability

between 21–22 kbar at M(H_2O) > 0.55. These are both significant in the retrograde evolution of sample L08-03A, occurring in the matrix as the breakdown products of lawsonite. The cations within the matrix EBC that would otherwise be taken up by these phases may alter the topology of the calculated pseudosection, showing that more investigation is needed in order to attempt to stabilise these two phases in accordance with observations in sample L08-03A. Alternatively it is possible that exhumation was associated with cooling to below ~640 °C; hence the true evolution of L08-03A cannot even be represented within the plane of the calculated pseudosection. Finally, a wide range of possible re-hydration scenarios can occur during eclogite exhumation; therefore, these compositional and modal proportion data only allow a preliminary assessment of the evolution of sample L08-03A.

5.6.2. Tectonic-petrographic synthesis

A wide range of petrographic information preserved in sample L08-03A has allowed investigation of various stages in the deformational and metamorphic history of the TMM. Subsets of various mineral currently inclusions in garnet core domains are interpreted to represent a prograde assemblage that equilibrated in the middle/upper blueschist-facies during early subduction – parts of which were later included into garnet cores. However, petrographic evidence of subsequent fluid exchange between garnet core regions and the matrix during exhumation indicates that some observed inclusions may not be primary constituents of this prograde assemblage. The absolute *P–T* conditions of this early fabric forming prograde event (M0) are uncertain.

A calculated *P–T* pseudosection highlights two possible regions in *P–T* space where observed garnet core compositions could theoretically have formed (10–13 kbar and 575–625 °C, and 20–23 kbar and 520–550 °C). However, kinetic constraints suggesting a degree of disequilibrium during growth, coupled with probable modification of core compositions associated with fluid transport along healed fractures has prevented elucidation of the absolute *P–T* conditions of core formation. Prograde metamorphism (M1) associated with on-going subduction resulted in the growth of garnet rim domains over progressively changing metamorphic parageneses, allowing incorporation of omphacite, paragonite, epidote/allanite, rutile, talc and quartz inclusions. Garnet inner rim growth initiated at *P–T* conditions of ~22.5 kbar and ~525 °C. Garnet rim growth is calculated to terminate at a peak temperature of ~640 °C and a pressure ranging between 25.5–27.5 kbar, depending on

whether the fractionation of cations into garnet is considered in thermodynamic modelling. These peak M2 conditions are independently verified by conventional thermobarometry and AvePT and corroborate microstructural observations of the peak assemblage comprising garnet, omphacite, phengite, lawsonite, talc, epidote/allanite, rutile and quartz. This peak pressure range indicates a maximum depth of subduction of ~90–100 km, notably less than some previous studies of the TMM.

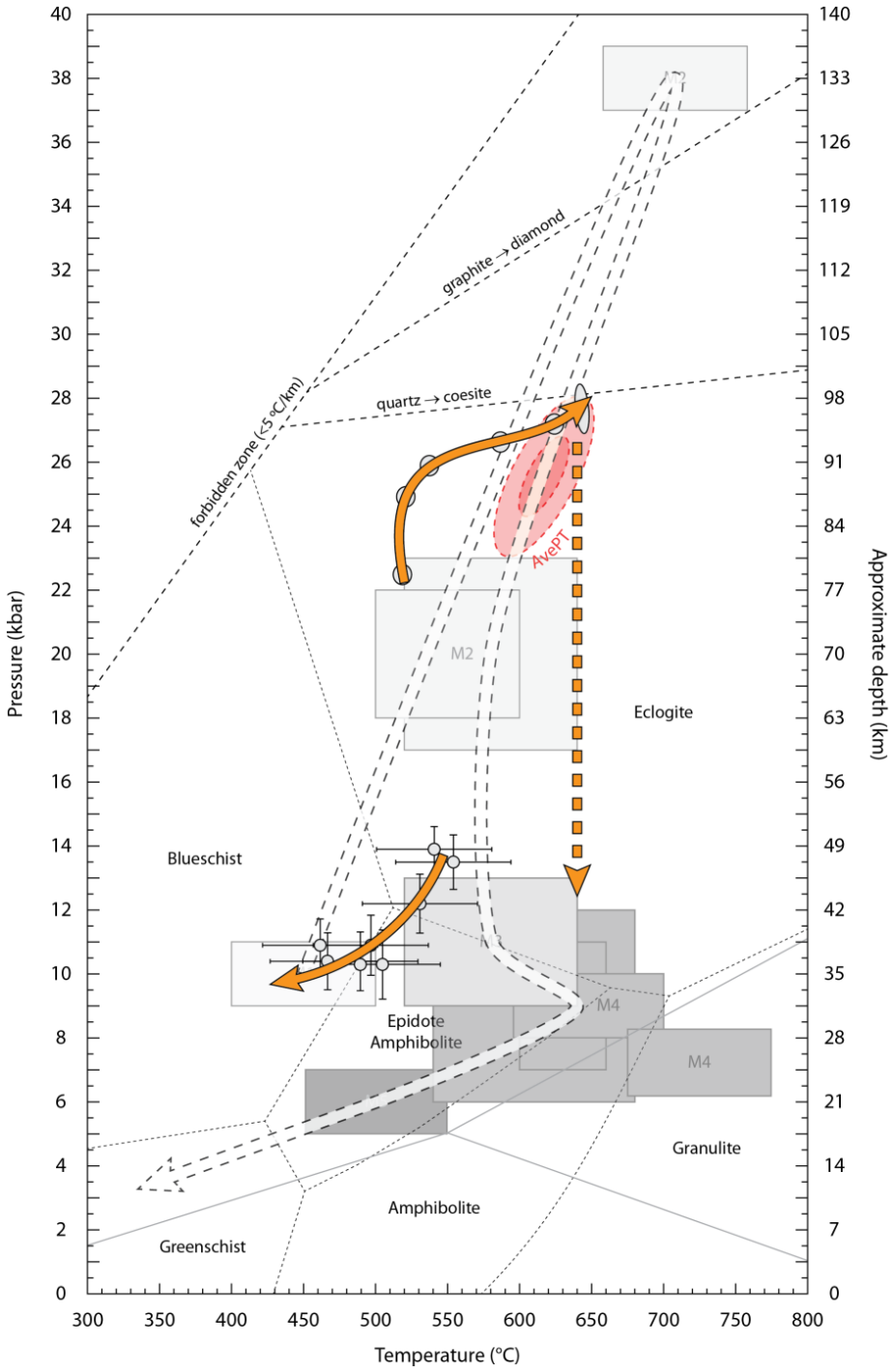


Fig. 5.22 – Tectonic synthesis for sample L08-03A. The selected results of prograde and retrograde phase equilibria modelling and thermobarometry are compared against previous studies' data.

Exhumation from peak pressure (M3) was associated with re-hydration of the matrix, either from external input or from the decomposition of peak M2 talc and lawsonite. This is shown by the occurrence of retrograde matrix amphibole with barroisite/winchite cores and magnesiohornblende rims. Phase equilibria modelling using *P*–M(H_2O) pseudosections shows that it is possible to replicate the main compositional ranges for amphibole core and rim regions, with first growth occurring at 23–25 kbar (at T = 640 °C). Although the final modal proportion matches the observed volume proportion, this model cannot account for an inferred two-stage growth. Microstructural constraints show that the retrograde breakdown of lawsonite formed clinozoisite and paragonite porphyroblasts in the matrix and epidote-paragonite pseudomorphs as inclusions in garnet.

An additional result of exhumation is a discrete episode of omphacite breakdown, resulting in the formation of extremely fine symplectite colonies at mutual grain boundaries that are composed of intergrown calcic-amphibole, diopside and albitic plagioclase. Thermobarometry performed on such symplectites produced a *P*–*T* array between 10.3–13.9 kbar and 461–554 °C with an apparent evolution from low-pressure eclogite-facies, through epidote-amphibolite-facies into blueschist-facies (Fig. 5.21). However, the trajectory and *P*–*T* conditions of this array is discrepant with the well-documented occurrence of further prograde metamorphism (M4) of the TMM up to a temperature of 650 °C (Girard, 2001) immediately following initial exhumation (Fig. 5.22). However, previous workers have noted that relatively fresh mafic eclogite situated in the cores of boudins does not record evidence of prograde overprinting to the same extent as host metasediments. Further investigation into this problem is required, given that the thermobarometric methods employed do not appear to violate any petrographic or calibration constraints.

6. Eastern Himalayan syntaxis

Part of the work presented here forms the basis of the paper Palin et al. (in press) in the journal Gondwana Research (cf. chapter 10.2.3).

6.1. Chapter introduction

An investigation of the tectonic, metamorphic and magmatic evolution of the EHS was undertaken during two short field seasons in August 2009 and September 2010. A range of lithologies was collected by various workers (chapter 11.1) from roadside outcrops along the western and north-western flank of the EHS, hereafter referred to as the Bayi-Linzhi-Milin (B-L-M) region (Fig. 6.1). Although fieldwork allowed sampling and examination of the major road sections, a systematic regional mapping campaign was not able to be completed due to severe political restrictions that did not allow off-road access. The EHS has been the focus of intense study in recent years as a result of its important tectonic setting in the framework of the India-Asia collision, with many investigations into its structural and geomorphic evolution (Burg *et al*., 1998; Craw *et al*., 2005; Geng *et al*., 2006; Finnegan *et al*., 2008; Seward & Burg, 2008) and also the petrology of magmatic and metamorphic units (Liu & Zhong, 1997; Ding *et al*., 2001; Booth *et al*., 2004, 2009; Liu *et al*., 2006; Zhang *et al*., 2009; Shen *et al*., 2010; Xu *et al*., 2010; Zhang *et al*., 2010; Guilmette *et al*., 2011; Guo *et al*., 2012). The suite of rocks collected from the B-L-M region has produced new insight into the tectonothermal evolution of the EHS; in particular, the behaviour of the adjacent southern Asian margin during the India-Asia collision. The combination of detailed petrography, thermobarometry and *in-situ* U–Th–Pb monazite geochronology reports new metamorphic and deformational events in the *P–T–t* history of the region, the results of which are detailed below.

6.2. Geological setting

The EHS forms the north-eastern boundary of the Indian plate lower crust and is a region of extreme topography that contains the peaks of Namche Barwa (7756 m) and Gyala Peri, (7294 m) and is cut through by the Yarlung Tsangpo River (Fig. 6.1; Burg *et al*., 1997). In this region the Late Eocene to Miocene south-vergent thrust systems of the Himalaya have been subsequently deformed by the later culmination, exhumation and uplift of the deeper crustal rocks of the EHS (ibid). The present day margins of the syntaxis are a series of young ductile shear zones and faults that bound the rapidly

exhuming deeper crustal rocks (Xu *et al*., 2012) and which cut across overlying thrust sheets. Consequently most of the ITSZ rocks, including the ophiolitic mélange, have been exhumed and eroded and the present boundaries of the Indian and Asian plates are young faults exhibiting dominantly transtensional characteristics (ibid).

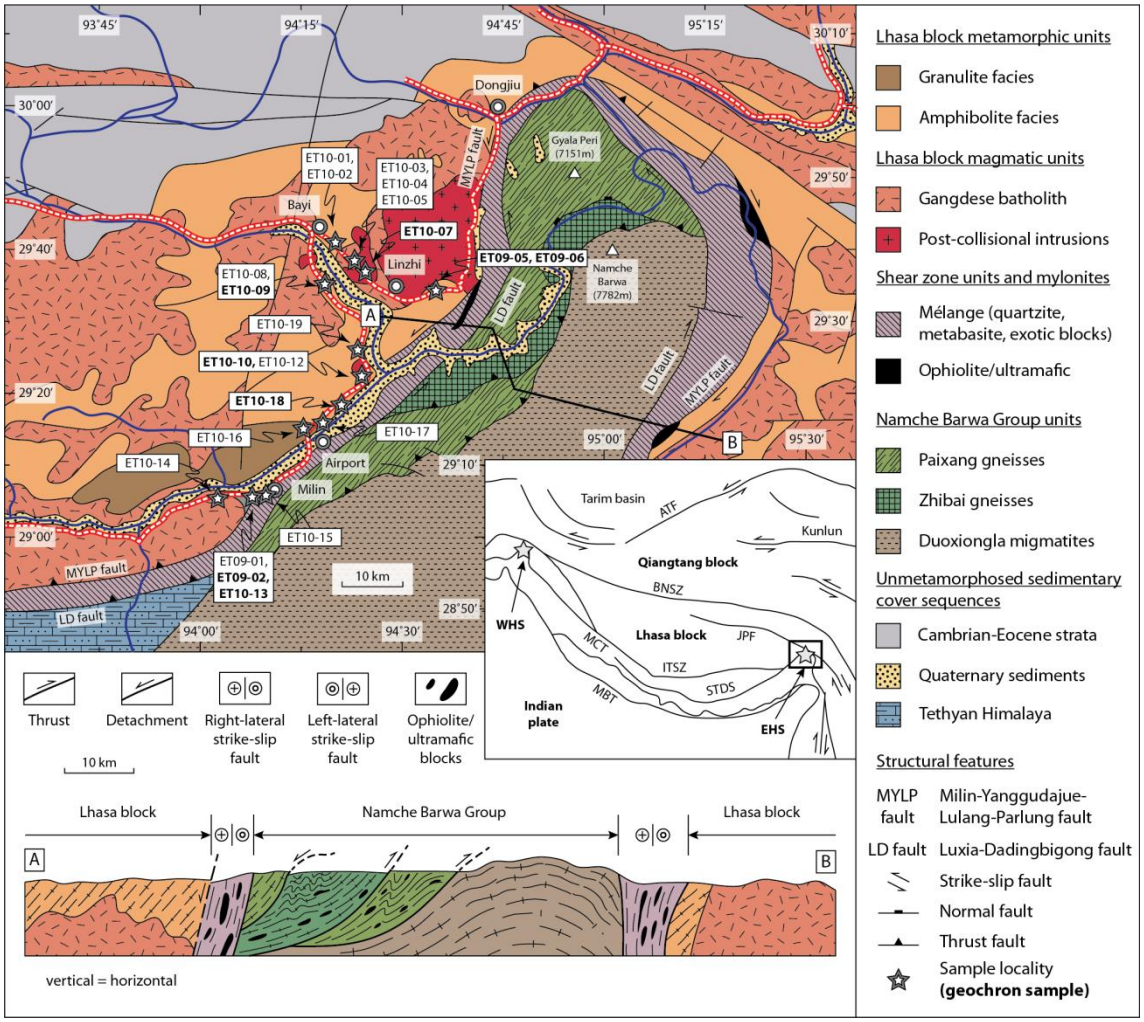


Fig. 6.1 – Geological map and cross-section of the EHS with sample localities (after Geng *et al*., 2006, Zhang *et al*., 2010, Guilmette *et al*., 2011; Xu *et al*., 2012). Highways are shown with a thick red line with dashed stroke.

The EHS is expressed as a broad north-east plunging antiform that exposes three main tectonostratigraphic units (Fig. 6.1). The structurally lowest unit, forming the core of the EHS, comprises mostly high-grade metamorphic rocks of the Namche Barwa Group. Geng *et al*. (2006) divide this Group into three lithostratigraphic units containing high-pressure garnet pyroxenite boudins in kyanite-bearing felsic gneiss (the Zhibai gneiss), felsic migmatite and banded gneiss (the Duoxiongla migmatite) and felsic and minor calc-silicate gneiss (the Paixiang gneiss). Towards the south-west, moving away from the EHS, these units are overlain by deformed units of the TSS.

Structurally above the Namche Barwa Group lies a band of highly deformed and mylonitised lithologies that are exposed in a 2–10 km wide shear zone that mantles the antiform. These units are separated from the overlying Lhasa block units by the Milin-Yanggudajue-Lulang-Parlung (MYLP) fault and separated from the underlying Namche Barwa Group by the Luxia-Dadingbigong (LD) fault (Fig. 6.1). This sequence has previously been interpreted as sheared packets of marine sediments and oceanic crust that once formed part of the Neo-Tethyan Ocean prior to the India-Asia collision (Zhang *et al*., 2010); namely, representing the ITSZ. This is owing to the occurrence of ultramafic and mafic lenses of a dismembered ophiolite suite of back-arc affinity (Hao *et al*., 1999) and exotic blocks of felsic gneiss and marble, reportedly contained in greenschist-facies metabasite and quartz-mica schist (Geng *et al*., 2006). However, recent work by Xu *et al*. (2012) has shown that the LD and MYLP faults were active between c. 22–2 Ma (Ar–Ar biotite, hornblende), suggesting that they are accommodating the rapid exhumation of deeper crustal rocks in the EHS core. As a result, they are unlikely to faithfully represent the position of the original India-Asia plate boundary, and fieldwork in this study shows that mylonite exposed along the MYLP fault is of extremely varied petrographic parentage including plutonic granitoids, metabasite, metapelite, and quartzo-feldspathic schist. It is therefore more likely that these Miocene structures have disrupted the original ITSZ mélange rocks, some of which remain as fragments in host mylonite units. The provenance of these mylonites is therefore uncertain, and may be marine sediments of the Neo-Tethyan Ocean, or crustal rocks of the Asian or Indian plate.

The uppermost structural unit bounding the EHS is the southern part of the Asian plate Lhasa block, which consists mostly of high-grade metamorphic rocks (otherwise termed the ‘Nyingchi Group’, ‘Nyingchi Complex’ or ‘Nyainqentanglha Group’ in other literature) including banded migmatite and biotite- and granitic-gneiss with minor marble lenses (Geng *et al*., 2006). Zhang *et al*. (2010) broadly divided these units by metamorphic grade into those preserving amphibolite- or granulite-facies assemblages and noted that, further to the north and west of the EHS, these units are overlain by intercalated sedimentary and volcanic units of Cambrian to Eocene age (Fig. 6.1). All units of the southern Lhasa block have been intruded by abundant calc-alkaline composite plutons of the Gangdese batholith, with emplacement ages between c. 133–110 Ma and c. 66–57 Ma, that are related to pre-collision northward oceanic subduction beneath Asia (Wen *et al*., 2008; Chiu *et al*.,

2009; Lee *et al*., 2009). Other adakitic post-collisional intrusions occur in the B-L-M region and are reported by numerous studies to be partially sourced from the melting of garnet-bearing crustal rocks (e.g. Chung *et al*., 2003, 2005; Zhang *et al*., 2009).

6.2.1. Metamorphic evolution of the EHS

Lhasa block

As a result of limited exposures of metamorphic units in the south Lhasa block, the vast majority of petrological studies have focused on the Mesozoic magmatism (Chung *et al*., 2005 and references therein). However, a recent study by Dong *et al*. (2011) of upper amphibolite-facies garnet-sillimanite paragneiss and garnet-amphibolite located ~400 km west of the EHS suggested that the main body of metamorphic basement of the south Lhasa block is Triassic in age (c. 225–213 Ma; U–Pb zircon). The lack of information concerning the *P–T–t* evolution of the south Lhasa block is cause for concern, as with a limited understanding of the metamorphic history, tectonic models for the evolution of the southern Asian margin will remain incomplete. This is particularly important in light of the wide range of ages and compositions that are reported for magmatic contributions to the Gangdese batholith (above), which demonstrate that it is clearly not a single batholithic complex.

B-L-M region

Tertiary ages documented for kyanite- and sillimanite-bearing gneiss, migmatite and two-mica leucogranite in the B-L-M region of the EHS discredit the above view that the main episodes of metamorphism and anatexis within the Lhasa block are of Triassic age. These data imply that there is either a miscorrelation between the two areas or that the south-east region of the Lhasa block has experienced a different tectonometamorphic history. Therefore, lithologies within the B-L-M region are treated separately from the western and central regions of the south Lhasa block until the *P–T–t* history of both areas can be more clearly defined.

In comparison to the Namche Barwa Group (below), thermobarometric studies of the metamorphic units of the B-L-M region are rare, and units can simply be divided into those preserving peak *P–T* conditions at granulite- or amphibolite-facies conditions (Fig. 6.2a). Zhang *et al*. (2010) document extensive exposures of both facies occurring on the north side of the Yarlung Tsangpo River, north of Milin (Fig. 6.1), and also that granulite-facies blocks and lenses may be

found in amphibolite-facies hosts, although the contacts are often gradational and some blocks may be fully retrogressed. Zhang *et al*. (2010) report initial granulite-facies metamorphism with peak *P–T* conditions of 9–13 kbar and 830–900 °C at c. 90 Ma (U–Pb zircon), followed by an amphibolite-facies overprint at c. 36–33 Ma (U–Pb zircon) at *P–T* conditions of 8–11 kbar and 590–660 °C. Amphibolite-facies paragneiss situated south of Bayi has been reported by Booth *et al*. (2009) to document slightly higher-grade *P–T* conditions of 8–12 kbar and 600–800 °C, although no constraints on the timing of peak metamorphism are presented. Guo *et al.* (2012) report U–Pb zircon ages from a sample of orthogneiss from east of Linzhi that suggest a magmatic crystallisation age of 83.4 ± 1.2 Ma followed by subsequent metamorphism between c. 65–46 Ma. An associated granite sill was also documented with a U–Pb zircon crystallisation age of 64.4 ± 0.7 Ma and two subsequent episodes of metamorphism at 55.1 ± 1.3 Ma and 41.4 ± 2.3 Ma (ibid).

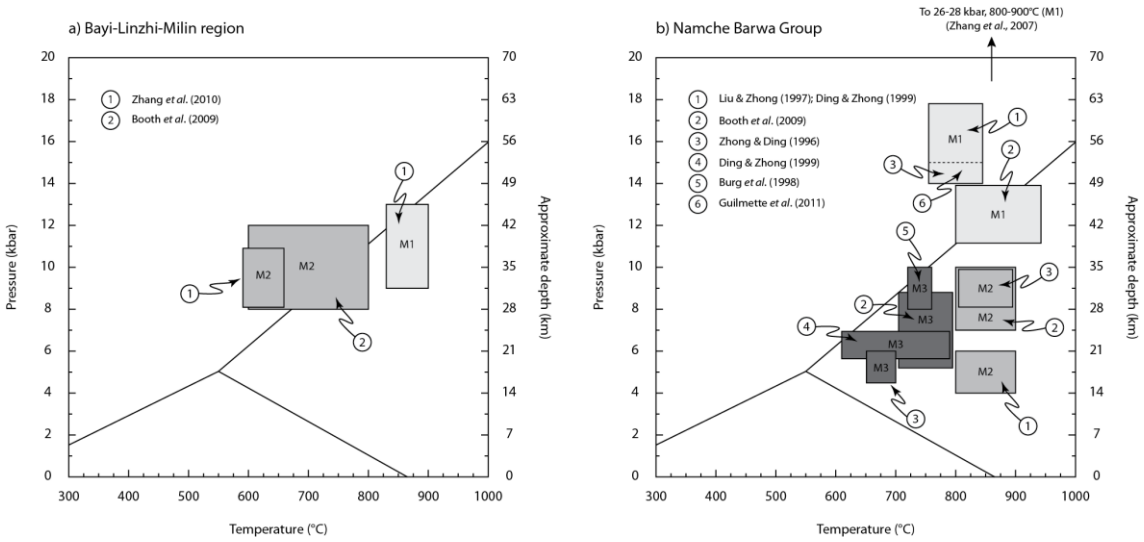


Fig. 6.2 – *P–T* conditions for metamorphic events in the EHS region Aluminosilicate phase relations and triple point are after Pattison (1992). Boxes represent peak *P–T* conditions or ranges with 1 S.D. uncertainty, if available. An error of ±50 °C is added to temperatures where no uncertainty is quoted. Approximate depth is calculated using a conversion factor of 3.5 km per kilobar. (a) B-L-M region (b) Namche Barwa Group.

High-grade metamorphic rocks of the B-L-M region are also intruded by numerous post-collisional plutonic rocks (Fig. 6.1), locally resulting in agmatite complexes (R.R. Parrish *pers comms*, 2012). A major- and trace-element geochemical study of three such granitic bodies was undertaken by Zhang *et al*. (2009) who showed that they are of Asian plate continental affinity, rather than being subduction-related, and formed from a mixed source comprising garnet-bearing crustal rocks of the Lhasa block and a Gangdese batholith component. U–Pb zircon ages of 22 ± 1

Ma and 25.4 ± 0.3 Ma are reported for the intrusion of two large bodies, the Bayi and Lunan granites (250 and >1000 km^2 in areal extent respectively), as well as an older age of 49.1 ± 0.4 Ma for a smaller sheeted intrusion (the Confluence granite). The location and relative size of these bodies within the B-L-M region compared to magmatic contributions from the Gangdese batholith are shown on Fig. 6.1. These data show that, unlike the rest of the Lhasa block away from the EHS, a major magmatic input into the B-L-M region is Oligocene-Miocene in age.

Namche Barwa Group

Numerous studies of the Namche Barwa Group have produced evidence for a *P–T* history comprising three stages of metamorphism (M1–3; Fig. 6.2b). An initial high-pressure granulite-facies event (M1) is documented in garnet- and kyanite-bearing paragneiss, mafic granulite and garnet-clinopyroxene mafic boudins with *P–T* conditions between 11–18 kbar and 750–950 °C (Liu & Zhong, 1997; Ding & Zhong, 1999, Zhong & Ding, 1996; Ding *et al*., 2001; Booth *et al*., 2009; Guilmette *et al*., 2011). More extreme peak pressures of 26–28 kbar (at 800–900 °C) have been proposed by Zhang *et al*. (2007) for a sample of garnet-pyroxenite collected from the core of the syntaxis, suggesting that some units of the Namche Barwa Group may have experienced an early eclogite-facies metamorphism. The age of peak M1 metamorphism is highly disputed and has been suggested to be c. 40 Ma (U–Pb zircon; Ding *et al*., 2001), between c. 37–32 Ma (U–Pb zircon; Zhang *et al*., 2010) and 24.0 ± 0.3 Ma (U–Pb zircon; Xu *et al*., 2010); the youngest age being documented in metamorphic zircon cores thought to have grown at high-pressure plagioclase-absent conditions. An older age for M1 of 53.9 ± 1.1 Ma (U–Pb zircon) has been proposed by Xu *et al*. (2012) to represent the initial oblique collision between the eastern corner of the Indian plate and the Lhasa block; however, this sample of mylonitised felsic gneiss was collected from the northern section of the ductile shear zone and therefore is of possible Asian-plate affinity.

Subsequent medium-pressure high-temperature metamorphism (M2; Fig. 6.2b) is recorded in mafic granulite by the replacement of early (M1) garnet by two-pyroxene-plagioclase symplectites at *P–T* conditions between 8–10 kbar and 800–900 °C (Zhong & Ding, 1996). M2 assemblages in pelitic gneisses contain sillimanite, cordierite and spinel and record *P–T* conditions of equilibration of 4–6 kbar and 800–900 °C (Liu & Zhong, 1997; Ding & Zhong, 1999) and 7–10 kbar and 800–900

°C (Booth *et al*., 2009). Xu *et al*. (2010) suggest that zircon rims with a U–Pb age of 18.8 ± 0.3 Ma could record the timing of peak M2 granulite-facies metamorphism. A younger M3 episode is defined by a low-to-medium-pressure, medium-temperature amphibolite-facies event (Fig. 6.2b) that overprints M2 assemblages at *P–T* conditions of 4.5–10 kbar and 600–800 °C (Zhong & Ding, 1996; Ding & Zhong, 1999; Booth *et al*., 2009; Burg *et al*., 1998). This event is characterised in mafic granulites by the replacement of pyroxene (± garnet) by hornblende, plagioclase and biotite. The timing of this M3 event is poorly constrained with proposed ages ranging between c. 25–11 Ma (U–Pb zircon; Ding *et al.*, 2001), 17.0 ± 0.4 Ma (U–Pb zircon; Xu *et al.*, 2010), 16.0 ± 2.5 Ma (Sm–Nd garnet, whole-rock metapelite; Burg *et al.*, 1998), c. 30–8 Ma (U–Pb zircon; Zhang *et al.*, 2012) and c. 29–16 Ma (U–Pb zircon; Zhang *et al.*, 2010). Notably, many of the upper limits of these ranges predate the suggested age of M2 metamorphism, complicating this situation. Very young metamorphism (M4?) in the EHS has been proposed by Booth *et al*. (2009) at *P–T* conditions of 7–8 kbar and 550–650 °C, with ages between 3.9–2.9 Ma (U–Th–Pb xenotime, thorite; Burg *et al.*, 1998) and c. 10–3 Ma (U–Th–Pb monazite, titanite; Booth *et al.*, 2009) reported for cordierite- and biotite-bearing amphibolite-facies migmatites. These ages are similar to zircon and apatite fission-track results by Seward & Burg (2008) who suggest that the EHS began to decompress at c. 4 Ma.

6.2.2. Comparison of the Namche Barwa Group with the GHS and Nanga Parbat

The central body of the Namche Barwa Group (the Zhibai gneiss) is thought to have geochemical affinity to the GHS (Xu *et al*., 2010) and therefore the tectonothermal evolution of both units should show a degree of similarity. The structural and metamorphic evolution of the GHS has been well-constrained through multidisciplinary investigations in the western and central Himalaya, notably in Pakistan, Zanskar and Nepal (see chapter 1.5.1 for a detailed summary). UHP eclogite-facies units exposed at Kaghan reached peak conditions of >27.5 kbar and 720–770 °C at 46.4 ± 0.1 Ma (U–Pb zircon and allanite; Parrish *et al*., 2006), whereas the main body of the GHS records evidence of prograde Barrovian metamorphism that first reached kyanite-grade *P–T* conditions of 9–12 kbar and 550–680 °C between c. 37–30 Ma (U–Pb monazite; Walker *et al*., 2001; Godin *et al*., 2001; Simpson *et al*., 2000; Vance & Harris, 1999) and then sillimanite-grade *P–T* conditions of 4.5–7 kbar and 650–770 °C between c. 24–15 Ma (U–Pb monazite; Noble & Searle, 1995; Searle *et al*., 1997, 1999,

2003; Murphy & Harrison, 1999; Simpson *et al*., 2000; Viskupic & Hodges, 2001; Cottle *et al*., 2009a). Partial melting accompanied this sillimanite-grade event, facilitating channel flow and extrusion of the GHS during the Miocene (Searle *et al*., 2003, 2006; Godin *et al*., 2006).

As detailed above, the Namche Barwa Group also contains rocks that show initial kyanite-grade metamorphism followed by a lower pressure sillimanite-grade overprinting, although the peak *P–T* conditions for each event (Fig. 6.2b) are significantly higher-grade than those for the GHS. Sillimanite-grade metamorphism, for example, reached temperatures of 800–900 °C (Fig. 6.2b) in comparison with temperatures of 650–770 °C for the equivalent event in the GHS. Furthermore, poor geochronological constraints on individual metamorphic episodes in the Namche Barwa Group render temporal comparisons with the GHS difficult. Here, high-pressure kyanite-grade M1 metamorphism in the Namche Barwa Group has been suggested to have occurred somewhere between c. 54 Ma (Xu *et al*., 2012) and c. 24 Ma (Xu *et al*., 2010), in comparison the equivalent metamorphism in the GHS that is tightly constrained between c. 37–30 Ma.

In the Ama Drime massif in the far northern part of the GHS (Nepal), original eclogite-facies assemblages have been overprinted by a granulite-facies metamorphism at 7–8 kbar and 750 °C at <13.2 Ma, with post-kinematic leucogranite dykes emplaced at 11.6 Ma (Cottle *et al*., 2009b). This indicates that the deep structural levels of the GHS in the northern-most exposures were undergoing high-grade metamorphism at later than the main body of the GHS. Even younger high-grade metamorphism has been reported by Crowley *et al*. (2009) at Nanga Parbat in the western Himalayan syntaxis with biotite-dehydration melting (at 5 kbar and 720 °C) occurring at ~1.7 Ma (U–Pb monazite). The same study described garnet- and cordierite-bearing neosomes that crystallised at ~1.0 Ma (U–Pb xenotime) at 3.5 kbar and tourmaline-bearing leucogranite veins that crystallised at ~0.7 Ma (U–Pb zircon). As both syntaxis regions have experienced rapid uplift during the Miocene-Pliocene (Zeitler *et al*., 2001), the young c. 3–10 Ma cordierite- and biotite-bearing melts reported from the EHS core (described above) may be analogous to those within Nanga Parbat.

6.3. Petrography, mineral chemistry and tectonic setting

Fieldwork and sample collection for lithologies prefixed with ET09- was conducted by M.P. Searle and M.R. St-Onge in August 2009. Fieldwork and collection of ET10- units was performed by R.M

Palin over the course of one and a half days in September 2010. During both field seasons samples were collected from roadside outcrops on highway S306, which connects Milin in the south to Bayi in the north via the local airport, and highway G318, which heads east from Bayi and Linzhi, turning north at the Sirchi-La Pass towards Donjiu (Fig. 6.1). Lithologies observed along both highways can be broadly divided into plutonic units, fragments of ophiolitic material, mylonites of varied parentage and amphibolite-facies migmatites. Outcrops along these roads have previously been mapped as Gangdese batholith, amphibolite- and granulite-facies gneiss of the Lhasa block and mélange of the ITSZ (Booth *et al*., 2004, 2009; Geng *et al*., 2006; Xu *et al*., 2010; Zhang *et al*., 2010). Petrography, GPS co-ordinates and structural information for all analysed samples in the B-L-M region are presented in Table 6.1 and descriptions of each major group are given below.

Sample	Lithology	Northing			Easting			Elevation (m)	Dip-dip direction
ET09-01	Mylonitised granitoid	29	11	22.0	94	11	2.6	2867	58-318
ET09-02	Mylonitised metapelite	29	11	22.0	94	11	2.6	2867	58-318
ET09-05	Sillimanite migmatite	29	36	38.4	94	39	6.0	4564	-
ET09-06	Sillimanite migmatite	29	37	16.8	94	42	24.3	4238	-
ET10-01	Biotite monzogranite	29	39	6.2	94	22	0.1	2969	-
ET10-02	Biotite gneiss enclave	29	39	6.2	94	22	0.1	2969	-
ET10-03	Sillimanite migmatite	29	36	32.2	94	24	13.6	2930	72-322
ET10-04	Garnet-bearing enclave	29	36	32.2	94	24	13.6	2930	72-322
ET10-05	Two-mica-garnet monzogranite	29	36	32.2	94	24	13.6	2930	72-322
ET10-07	Sillimanite migmatite	29	36	5.1	94	25	2.7	2963	-
ET10-08	Garnet-tourmaline leucogranite	29	35	36.1	94	22	55.1	2943	-
ET10-09	Sillimanite migmatite	29	35	36.1	94	22	55.1	2943	-
ET10-10	Garnet-kyanite migmatite	29	26	1.2	94	27	10.0	2861	74-314
ET10-12	Calc-/semi-pelite migmatite	29	26	1.2	94	27	10.0	2861	74-314
ET10-13	Mylonitised metapelite	29	11	22.0	94	11	2.6	2867	58-318
ET10-14	Ophiolite fragments	29	11	50.0	94	4	49.5	2897	-
ET10-15a	Quartzo-feldspathic mylonite	29	11	15.7	94	11	45.2	2833	54-316
ET10-15b	Mylonitised metabasite	29	11	15.7	94	11	45.2	2833	54-316
ET10-15c	Mylonitised metabasite	29	11	15.7	94	11	45.2	2833	54-316
ET10-16a	Mylonitised metabasite	29	19	7.6	94	20	11.5	2901	58-322
ET10-16b	Mylonitised metabasite	29	19	7.6	94	20	11.5	2901	58-322
ET10-17a	Quartzo-feldspathic mylonite	29	19	26.5	94	21	14.5	2896	54-334
ET10-17b	Quartzo-feldspathic mylonite	29	19	26.5	94	21	14.5	2896	54-334
ET10-18a	Mylonitised metapelite	29	21	47.5	94	24	16.1	2909	52-320
ET10-18b	Quartzo-feldspathic mylonite	29	21	47.5	94	24	16.1	2909	52-320
ET10-19	Epidote monzogranite enclave	29	26	45.8	94	26	4.9	2904	-

Table 6.1 – Petrography, GPS co-ordinates and structural information for EHS samples (see Fig. 6.1). GPS co-ordinates are given in D-M-S notation.

6.3.1. Plutonic units

Although the south Lhasa block is dominated by subduction-related ('I-type') plutonic units of the Gangdese batholith, numerous garnet-, tourmaline- and muscovite-bearing crustal melts were encountered during fieldwork in the B-L-M region. Given the wide range in accuracy and level of

detail between published geological maps of the EHS region, correlation of specific samples between studies is difficult. However, GPS co-ordinates and petrological characteristics of the units denoted 'S-type' (below) suggest that they are equivalent to the Bayi and Lunan granites of Zhang *et al*. (2009) that are described in chapter 6.2. Samples of both 'types' were collected to provide petrographic context to the host metamorphic units, although the fieldwork restrictions outlined in chapter 6.1 did not allow their sizes or tectonic relations with host units to be characterised.

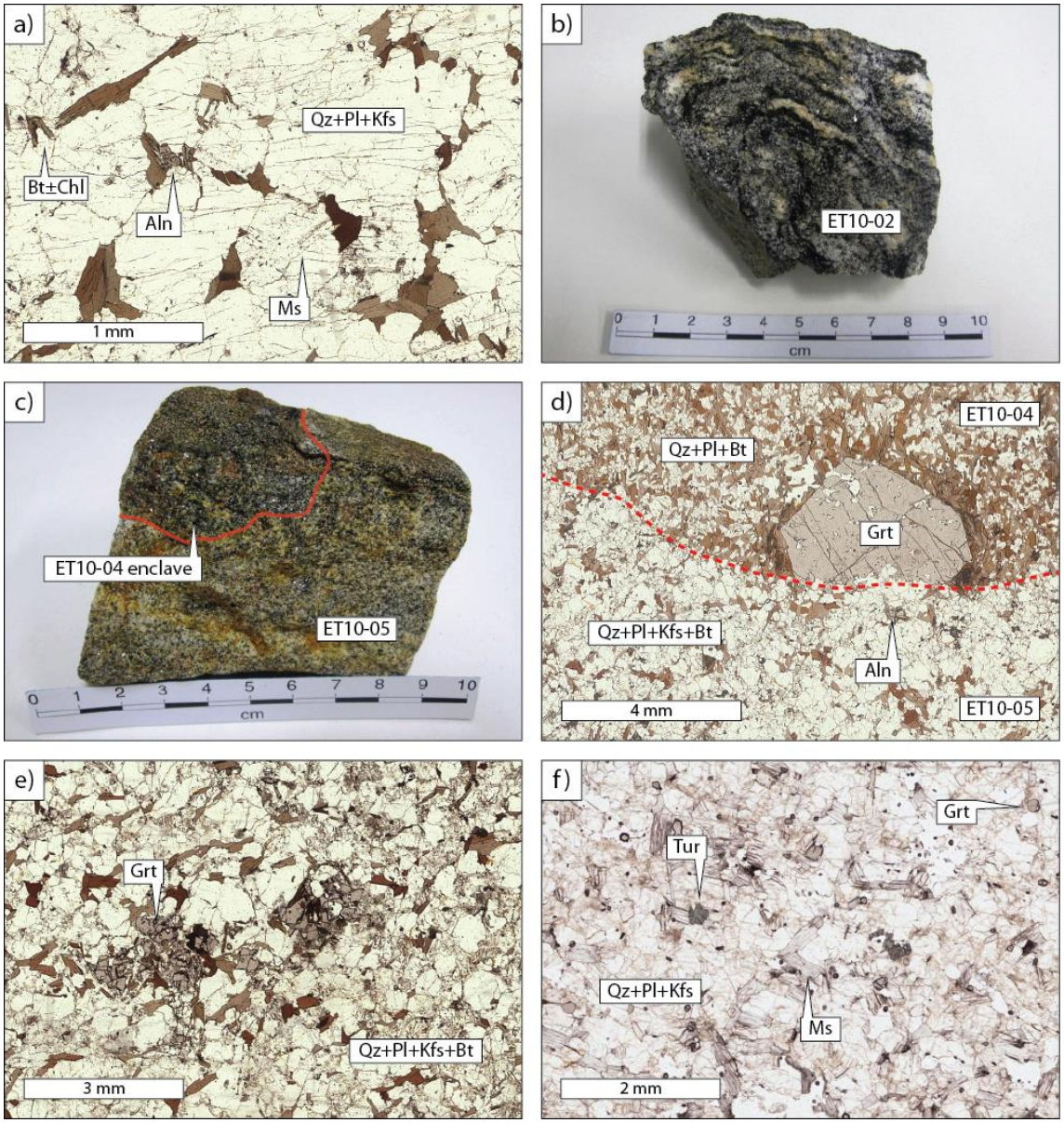


Fig. 6.3 – Petrography of S-type samples and associated enclaves All thin section images in plane polarised light. (a) Sample ET10-01. (b) Hand specimen of enclave sample ET10-02. (c) Hand specimen showing ET10-04 (enclave) and ET10-05 (host monzogranite) relationship. (d) Thin section showing the ET10-04 (enclave) and ET10-05 (monzogranite) interface. (e) Skeletal garnet in sample ET10-05 in a fine crystalline groundmass. (f) Sample ET10-08 with small garnet, muscovite and tourmaline in a groundmass of granitic composition.

Sample	Mineral	Location	SiO_2	TiO_2	Al_2O_3	Fe_2O_3	FeO	MnO	MgO	CaO	Na_2O	K_2O	**Total**	Si	Ti	Al	Fe^{3+}	Fe^{2+}	Mn	Mg	Ca	Na	K	**Sum**	Ox	XMg	XCa	XMn	Al(iv)	Al(vi)	Alm	Prp	Grs	Sps	XFe^{3+}	XPs
ET10-01	Bt	Groundmass	35.25	3.79	16.31	0.00	21.26	0.41	8.09	0.01	0.09	10.00	**95.21**	2.74	0.22	1.49	0.00	1.38	0.03	0.94	0.00	0.01	0.99	**7.80**	11	0.40	-	-	1.26	0.23	-	-	-	-	-	-
	Ilm	Groundmass	0.08	53.05	0.14	0.00	39.36	7.16	0.15	0.02	0.00	0.00	**99.96**	0.00	1.01	0.00	0.00	0.83	0.15	0.01	0.00	0.00	0.00	**2.00**	3	-	-	0.16	-	-	-	-	-	-	-	-
	Kfs	Groundmass	63.55	0.38	18.64	0.01	0.00	0.03	0.01	0.02	0.56	15.75	**98.95**	2.97	0.01	1.03	0.00	0.00	0.00	0.00	0.00	0.05	0.94	**5.00**	8	-	0.00	-	-	-	-	-	-	-	-	-
	Ms	Groundmass	45.39	0.35	30.52	2.62	1.01	0.04	1.63	0.07	0.07	9.58	**91.28**	3.16	0.02	2.51	0.14	0.06	0.00	0.17	0.01	0.01	0.85	**6.92**	11	0.74	-	-	0.84	1.67	-	-	-	-	-	-
	Pl	Groundmass	57.94	0.02	26.51	0.06	0.00	0.00	0.01	8.18	6.45	0.16	**99.33**	2.62	0.00	1.41	0.00	0.00	0.00	0.00	0.40	0.56	0.01	**5.00**	8	-	0.41	-	-	-	-	-	-	-	-	-
ET10-02	Bt	Matrix	35.77	3.44	18.39	0.00	19.98	0.35	8.73	0.02	0.07	10.18	**96.93**	2.70	0.20	1.64	0.00	1.26	0.02	0.98	0.00	0.01	0.98	**7.79**	11	0.44	-	-	1.30	0.33	-	-	-	-	-	-
	Kfs	Matrix	64.17	0.44	19.12	0.01	0.00	0.01	0.04	0.04	1.17	15.31	**100.31**	2.94	0.01	1.04	0.00	0.00	0.00	0.00	0.00	0.10	0.90	**5.00**	8	-	0.00	-	-	-	-	-	-	-	-	-
	Pl	Matrix	57.58	0.02	25.63	0.02	0.00	0.01	0.06	7.45	6.85	0.21	**97.83**	2.63	0.00	1.38	0.00	0.00	0.00	0.00	0.36	0.61	0.01	**5.00**	8	-	0.37	-	-	-	-	-	-	-	-	-
ET10-04	Bt	Inclusion in Grt	36.80	3.72	15.92	0.00	18.82	0.33	11.23	0.00	0.18	9.58	**96.58**	2.77	0.21	1.41	0.00	1.18	0.02	1.26	0.00	0.03	0.92	**7.79**	11	0.52	-	-	1.24	0.18	-	-	-	-	-	-
	Bt	Matrix	36.45	3.11	16.68	0.00	20.13	0.19	10.06	0.06	0.16	9.81	**96.65**	2.76	0.18	1.49	0.00	1.27	0.01	1.13	0.01	0.02	0.95	**7.81**	11	0.47	-	-	1.25	0.24	-	-	-	-	-	-
	Bt	Matrix adjacent to Grt	36.25	3.25	16.36	0.00	19.99	0.19	9.83	0.09	0.14	9.49	**95.59**	2.77	0.19	1.47	0.00	1.28	0.01	1.12	0.01	0.02	0.92	**7.78**	11	0.47	-	-	1.23	0.24	-	-	-	-	-	-
	Grt	Core	36.99	0.03	20.95	2.05	25.05	5.54	2.89	6.58	0.00	0.00	**100.08**	2.95	0.00	1.97	0.12	1.67	0.37	0.34	0.56	0.00	0.00	**8.00**	12	0.17	-	-	-	-	0.57	0.12	0.19	0.13	-	-
	Grt	Rim	36.69	0.03	21.00	2.10	24.74	5.12	2.35	7.59	0.01	0.00	**99.63**	2.94	0.00	1.99	0.13	1.66	0.35	0.28	0.65	0.00	0.00	**8.00**	12	0.14	-	-	-	-	0.56	0.10	0.22	0.12	-	-
	Ilm	Matrix	0.15	53.06	0.16	0.00	41.10	5.29	0.14	0.03	0.00	0.13	**100.06**	0.00	1.00	0.01	0.00	0.86	0.11	0.01	0.00	0.00	0.00	**2.00**	3	-	-	0.11	-	-	-	-	-	-	-	-
	Pl	Matrix	51.85	0.01	30.98	0.04	0.00	0.01	0.00	13.28	4.02	0.03	**100.22**	2.35	0.00	1.65	0.00	0.00	0.00	0.00	0.64	0.35	0.00	**5.00**	8	-	0.64	-	-	-	-	-	-	-	-	-
ET10-05	Grt	Small grains in groundmass	35.57	0.05	20.53	2.30	32.37	4.51	1.86	1.61	0.06	0.00	**98.86**	2.93	0.00	2.00	0.14	2.23	0.32	0.23	0.14	0.01	0.00	**8.00**	12	0.09	-	-	-	-	0.77	0.08	0.05	0.11	-	-
	Kfs	Groundmass	64.48	0.20	19.01	0.00	0.00	0.04	0.00	0.05	1.03	15.25	**100.06**	2.97	0.01	1.03	0.00	0.00	0.00	0.00	0.00	0.09	0.90	**5.00**	8	-	0.00	-	-	-	-	-	-	-	-	-
	Bt	Groundmass	34.42	3.81	17.67	0.00	24.18	0.17	6.08	0.02	0.11	9.88	**96.34**	2.67	0.22	1.62	0.00	1.57	0.01	0.70	0.00	0.02	0.98	**7.79**	11	0.31	-	-	1.33	0.29	-	-	-	-	-	-
	Pl	Groundmass	58.03	0.00	25.55	0.01	0.00	0.01	0.00	7.36	6.98	0.26	**98.20**	2.64	0.00	1.37	0.00	0.00	0.00	0.00	0.36	0.62	0.02	**5.00**	8	-	0.36	-	-	-	-	-	-	-	-	-
	Ilm	Groundmass	0.13	53.78	0.19	0.00	43.66	1.90	0.17	0.06	0.00	0.02	**99.91**	0.00	1.02	0.01	0.00	0.92	0.04	0.01	0.00	0.00	0.00	**2.00**	3	-	-	0.04	-	-	-	-	-	-	-	-
	Ms	Small flakes in groundmass	47.61	0.39	33.28	2.14	0.82	0.02	1.38	0.00	0.08	9.89	**95.61**	3.15	0.02	2.60	0.11	0.05	0.00	0.14	0.00	0.01	0.84	**6.90**	11	0.75	-	-	0.85	1.75	-	-	-	-	-	-
	Ms	Large laths in groundmass	45.70	0.89	33.78	0.00	2.07	0.02	0.97	0.00	0.25	11.13	**94.81**	3.08	0.05	2.69	0.00	0.12	0.00	0.10	0.00	0.03	0.96	**7.02**	11	0.46	-	-	0.92	1.77	-	-	-	-	-	-
ET10-08	Grt	Groundmass	35.73	0.03	20.56	2.16	28.78	11.42	0.85	0.68	0.00	0.00	**100.21**	2.94	0.00	1.99	0.13	1.98	0.80	0.11	0.06	0.00	0.00	**8.00**	12	0.05	-	-	-	-	0.67	0.04	0.02	0.27	-	-
	Kfs	Groundmass	64.85	0.01	18.91	0.01	0.00	0.01	0.01	0.02	1.02	15.21	**100.05**	2.98	0.00	1.03	0.00	0.00	0.00	0.00	0.00	0.09	0.89	**5.00**	8	-	0.00	-	-	-	-	-	-	-	-	-
	Pl	Groundmass	65.45	0.01	21.92	0.03	0.00	0.01	0.00	2.53	9.73	0.21	**99.89**	2.89	0.00	1.14	0.00	0.00	0.00	0.00	0.12	0.83	0.01	**5.00**	8	-	0.12	-	-	-	-	-	-	-	-	-
	Ms	Groundmass	45.30	0.19	35.64	0.00	1.53	0.03	0.45	0.03	0.50	10.89	**94.56**	3.05	0.01	2.83	0.00	0.09	0.00	0.05	0.00	0.07	0.94	**7.03**	11	0.34	-	-	0.95	1.88	-	-	-	-	-	-
	Tur	Groundmass	35.59	0.38	34.81	0.00	9.91	0.10	3.80	0.30	2.00	0.04	**86.94**	5.83	0.05	6.72	0.00	1.11	0.01	0.93	0.05	0.63	0.01	**15.34**	24.5	0.46	-	-	-	-	-	-	-	-	-	-
ET10-19	Prg	Groundmass	40.90	1.40	11.81	2.46	15.89	0.43	9.18	11.30	1.66	1.75	**96.78**	6.28	0.16	2.14	0.29	2.04	0.06	2.10	1.86	0.49	0.34	**15.76**	23	0.51	-	-	-	-	-	-	-	-	0.12	-
	Ep	Rim on Aln	37.63	0.14	24.10	11.59	1.04	0.22	0.10	23.50	0.00	0.01	**98.33**	2.97	0.01	2.24	0.69	0.07	0.01	0.01	1.99	0.00	0.00	**8.00**	12.5	-	-	-	-	-	-	-	-	-	-	0.24
	Bt	Groundmass	36.66	2.82	15.19	0.00	18.56	0.30	11.39	0.06	0.10	9.90	**94.98**	2.81	0.16	1.37	0.00	1.19	0.02	1.30	0.01	0.02	0.97	**7.84**	11	0.52	-	-	1.19	0.18	-	-	-	-	-	-
	Kfs	Groundmass	62.98	0.61	18.64	0.04	0.00	0.02	0.04	0.01	0.94	14.83	**98.11**	2.96	0.02	1.03	0.00	0.00	0.00	0.00	0.00	0.09	0.89	**5.00**	8	-	0.00	-	-	-	-	-	-	-	-	-
	Pl	Groundmass	61.25	0.01	24.91	0.09	0.00	0.01	0.00	6.02	7.50	0.27	**100.06**	2.73	0.00	1.31	0.00	0.00	0.00	0.00	0.29	0.65	0.02	**5.00**	8	-	0.30	-	-	-	-	-	-	-	-	-
	Ttn	Groundmass	30.32	38.52	1.58	0.00	0.86	0.10	0.10	28.66	0.00	0.01	**100.14**	0.99	0.95	0.06	0.00	0.02	0.00	0.00	1.00	0.00	0.00	**3.03**	5	-	-	-	-	-	-	-	-	-	-	-
	Rt	Exsolved lamellae in T-mag	0.07	97.93	0.16	0.00	1.59	0.02	0.16	0.02	0.00	0.02	**99.95**	0.00	0.99	0.00	0.00	0.02	0.00	0.00	0.00	0.00	0.00	**1.01**	2	-	-	-	-	-	-	-	-	-	-	-
	T-Mag	Groundmass	0.13	12.90	0.27	40.00	41.24	0.14	0.15	0.02	0.00	0.00	**94.85**	0.01	0.39	0.01	1.20	1.38	0.01	0.01	0.00	0.00	0.00	**3.00**	4	-	-	0.00	-	-	-	-	-	-	0.47	-
	Usp	Groundmass	0.12	33.23	0.22	1.77	59.72	0.08	0.15	0.20	0.12	0.01	**95.62**	0.01	0.97	0.01	0.05	1.94	0.00	0.01	0.01	0.01	0.00	**3.00**	4	-	-	0.00	-	-	-	-	-	-	0.03	-

Table 6.2 – Mineral compositions for plutonic igneous samples and associated enclaves ET10-01, ET10-02, ET10-05, ET10-08 and ET10-19 (overleaf).

'S-type'

Three 'S-type' units have been analysed in this study. Sample ET10-01 is a biotite-monzogranite that has an undeformed magmatic texture and contains coarse plagioclase, K-feldspar, biotite and quartz (Fig. 6.3a) with minor muscovite, ilmenite, zircon, apatite and allanite. Enclaves of foliated biotite gneiss (ET10-02; Fig. 6.3b) occur in sample ET10-01 and contain plagioclase, K-feldspar, biotite and quartz. Poor exposure did not allow examination of the outcrop field relations, although it is possible that sample ET10-02 may represent the host unit into which ET10-01 intrudes. Sample ET10-05 is a two-mica-garnet monzogranite that also contains abundant enclaves of gneiss (sample ET10-04; Fig. 6.3c). The latter contain garnet, biotite, plagioclase, K-feldspar, ilmenite, and quartz (Fig. 6.3d) whereas the host unit contains garnet, K-feldspar, biotite, plagioclase, muscovite, ilmenite and quartz (Fig. 6.3e) with accessory zircon, apatite and allanite (Fig. 6.3d). Sample ET10-08 is a leucogranite containing small tourmaline and garnet in a groundmass of K-feldspar, plagioclase, muscovite, quartz, apatite and zircon (Fig. 6.3f). Sample ET10-08 likely intrudes across host sillimanite migmatite (sample ET10-09, below), though the direct contact is unobservable in the field. Mineral compositions are given in Table 6.2.

'I-type'

The outcrop from which sample ET10-19 was collected contains a wide range of lithologies with complex structural relations. Host orthogneiss is intruded by foliation-parallel hornblende-rich mafic sills (Fig. 6.4a) and elsewhere contains discrete shear zones, several metres in width, with cm- to metre-scale basaltic, dioritic and monzogranitic enclaves (Fig. 6.4b–d). These units have a significantly different petrography from the previously described S-type granitic units and are likely closely related to the Gangdese lithologies that occur throughout the Lhasa block. However, the immediate curtailment of fieldwork at this outcrop meant that no structural work could be performed and only one sample (a monzogranitic enclave; ET10-19) was obtained.

Sample ET10-19 is undeformed and preserves an original magmatic texture (Fig. 6.5a) characterised by allanite, epidote, K-feldspar, plagioclase, amphibole, biotite, quartz, titanite and

titanomagnetite with rutile lamellae. Accessory zircon and apatite are also present. Dark brown allanite is generally euhedral and exhibits overgrowths of epidote (Fig. 6.5b) that have XPs = 0.22–0.25 (Table 6.2). Subhedral-to-anhedral amphibole (Fig. 6.5c) shows minor compositional variation with Si = 6.19–6.38 cpfu, XMg = 0.48–0.52 and Na_B (M4 site) = 0.07–0.08 cpfu; thus, are compositionally classed as pargasite (Leake *et al.*, 1997, 2004). Repeated rutile lamellae occur in host titanomagnetite crystals in the groundmass (Fig. 6.5d) and some grains are rimmed by titanite or ulvöspinel (Fig. 6.5c). Plagioclase composition ranges between XCa = 0.29–0.31, but grains have no systematic zonation. Compositions for all major minerals are presented in Table 6.2.

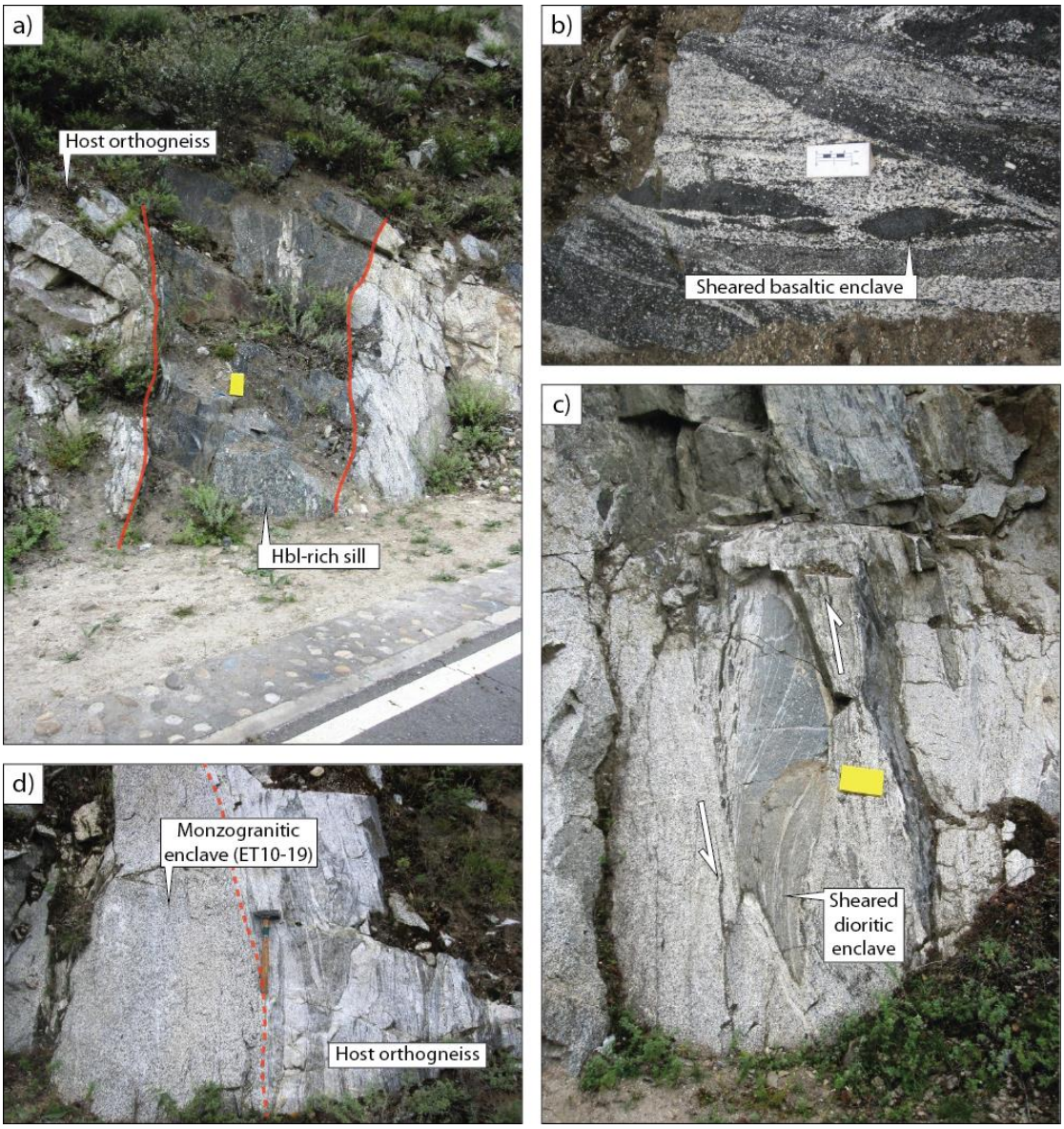


Fig. 6.4 – Field relations for sample ET10-19. (a) Hornblende-rich sill intruding orthogneiss. (b) Various enclaves in orthogneiss (basaltic to dioritic in composition). (c) Large diorite enclave with macroscopic shear sense indicators. (d) Monzogranitic enclave sample ET10-19.

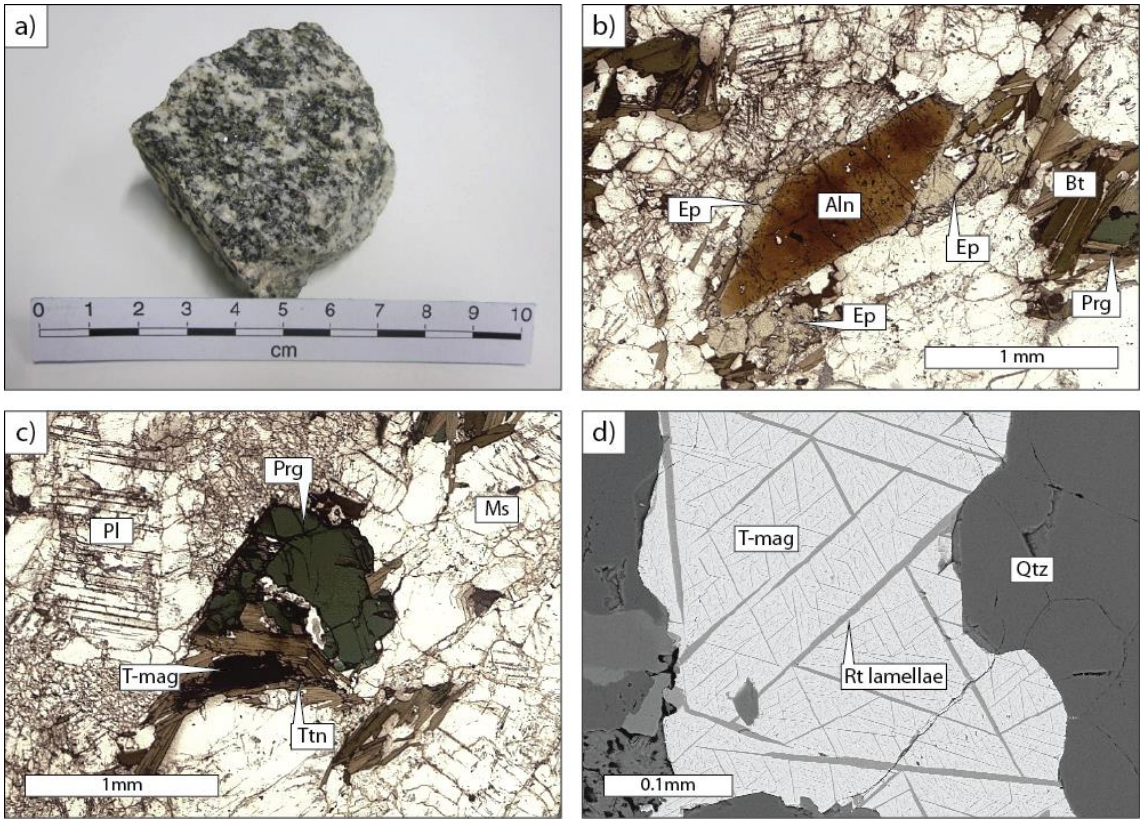


Fig. 6.5 – Petrography of sample ET10-19. (a) Hand specimen showing an undeformed magmatic texture. (b) Thin section showing euhedral allanite and (c) pargasite crystals (plane polarised light). (d) SEM BSE image showing rutile lamellae in a titanomagnetite host crystal.

6.3.2. Ophiolitic fragments

Blocks of ophiolitic material (sample ET10-14) occur in unconsolidated road-side sediment (Fig. 6.6a) west of Milin (Fig. 6.1). Although most specimens exhibit moderate-to-significant degrees of retrogressive alteration, the freshest samples contain abundant clinopyroxene (diopside) and olivine, suggesting that they were originally wehrlite. Orthopyroxene was not documented in any examples.

Some samples contain large tan-coloured amphibole that is interstitial to relic pyroxene and olivine grains (Fig. 6.6b) whereas others show a granoblastic texture with well-annealed grain boundaries (Fig. 6.6c). Accessory magnetite contains up to ~7 wt% Cr_2O_3 and olivine contains XMg = 0.75–0.76 (Table 6.3). Diopside compositions show minor variation with XMg = 0.83–0.85 and Ca = 0.94–0.97 cpfu and commonly contain discontinuous Fe-rich exsolution lamellae (Fig. 6.6d) that trend at a ~90° angle to cleavage. Such lamellae have sub-micron widths and so cannot be compositionally analysed for further information. Compositions for all major minerals are presented in Table 6.3.

Sample	Mineral	Location	SiO_2	TiO_2	Al_2O_3	Cr_2O_3	Fe_2O_3	FeO	MnO	MgO	CaO	Na_2O	K_2O	**Total**	Si	Ti	Al	Cr^{3+}	Fe^{3+}	Fe^{2+}	Mn	Mg	Ca	Na	K	**Sum**	Ox	XMg	XMn	XFe^{3+}	XPs
ET10-14	Amph	Interstitial in matrix	42.79	1.10	12.23	0.13	2.55	6.00	0.12	15.29	12.44	2.05	0.55	**95.25**	6.33	0.12	2.13	0.02	0.28	0.74	0.02	3.37	1.97	0.59	0.10	**15.68**	23	0.82	-	0.28	-
	Cpx	Matrix	52.13	0.53	3.47	0.36	0.82	4.18	0.09	14.99	24.80	0.00	0.01	**101.38**	1.90	0.01	0.15	0.01	0.02	0.13	0.00	0.81	0.97	0.00	0.00	**4.00**	6	0.86	-	0.15	-
	Cpx	Core (with exsolution stripes)	51.23	0.40	3.20	0.25	1.04	4.11	0.14	14.72	23.88	0.12	0.00	**99.09**	1.91	0.01	0.14	0.01	0.03	0.13	0.00	0.82	0.95	0.01	0.00	**4.00**	6	0.86	-	0.18	-
	Cpx	Rim (against matrix amphibole)	51.17	0.24	2.45	0.10	2.44	2.74	0.16	15.09	23.88	0.21	0.01	**98.49**	1.91	0.01	0.11	0.00	0.07	0.09	0.01	0.84	0.96	0.02	0.00	**4.00**	6	0.91	-	0.45	-
	Ol	Relic within amphibole matte	37.79	0.01	0.00	0.10	0.00	21.43	0.25	38.43	0.00	0.01	0.00	**98.02**	1.00	0.00	0.00	0.00	0.00	0.47	0.01	1.52	0.00	0.00	0.00	**3.00**	4	0.76	-	-	-
	Mt	Matrix	0.10	1.42	1.57	7.01	56.00	31.73	0.43	0.10	0.06	0.00	0.00	**98.42**	0.00	0.04	0.07	0.21	1.63	1.02	0.01	0.01	0.00	0.00	0.00	**3.00**	4	-	0.01	0.61	-
	Ep	Alteration	37.84	0.15	22.68	0.01	13.69	0.00	0.06	0.00	23.99	0.00	0.00	**98.42**	3.00	0.01	2.13	0.00	0.82	0.00	0.00	0.00	2.04	0.00	0.00	**8.00**	12.5	-	-	-	0.28

Fig. 6.6 – Field relations and petrography of sample ET10-14 (overleaf). (a) Blocks of ophiolitic material in outcrop occurring in poorly consolidated sediment. (b) Thin section of interstitial tan-coloured matrix amphibole between clinopyroxene and olivine grains (plane polarised light). (c) Well-annealed grain boundaries between clinopyroxene with ~120° interfacial angles (viewed under crossed polars). (d) SEM BSE image of cleavage planes and exsolution features in clinopyroxene.

Table 6.3 – Mineral compositions for ophiolitic sample ET10-14 (overleaf).

6.3.3. Upper amphibolite-facies migmatites

Many samples of high-grade metamorphic rock collected from the B-L-M region preserve upper amphibolite-facies parageneses and exhibit petrographic and microstructural evidence of *in-situ* partial melting. These units can be divided into those that experienced peak metamorphism and anatexis under sillimanite-grade conditions (ET09-05, ET09-06, ET10-07 and ET10-09) or kyanite-grade conditions (ET10-10 and ET10-12). The petrography of these units is described below.

ET09-05 and ET09-06 – Muscovite-poor sillimanite migmatite

Samples ET09-05 and ET09-06 both contain the minerals garnet, biotite, plagioclase, K-feldspar, sillimanite (fibrolite), muscovite, quartz, chlorite, monazite, zircon, and apatite. In addition, sample ET09-05 contains ilmenite and sample ET09-06 contains pyrite. In both cases mesosome and leucosome regions are well-defined (e.g. Fig. 6.7a). The former are composed of sheaves of fibrolite and biotite and the latter are of a granitic composition, containing approximately equal proportions of quartz, plagioclase and K-feldspar alongside minor garnet, biotite, fibrolite and muscovite (Fig. 6.7b). Leucosome garnet in both samples ranges in diameter from <1 mm to ~4 mm. Porphyroblasts in sample ET09-05 contains weak compositional zoning in with decreasing almandine and pyrope content from core to rim between 75% to 71% and 14% to 12% respectively (Fig. 6.8a). Garnet from sample ET09-06 is similar, with almandine and pyrope content decreasing from 75% to 74% and 11% to 8% from core to rim respectively (Fig. 6.8b). Grossular shows extremely limited variation in both samples, remaining approximately constant at ~3% (ET09-05) and ~5% (ET09-06). Core regions contain spessartine profiles that are either convex (ET09-05; Fig. 6.8a) or flat (ET09-06; Fig. 6.8b) with concentrations that increase at outer rim regions from 8% to 13% (ET09-05) and 9% to 13% (ET09-06). Mineral compositions are presented in Table 6.4.

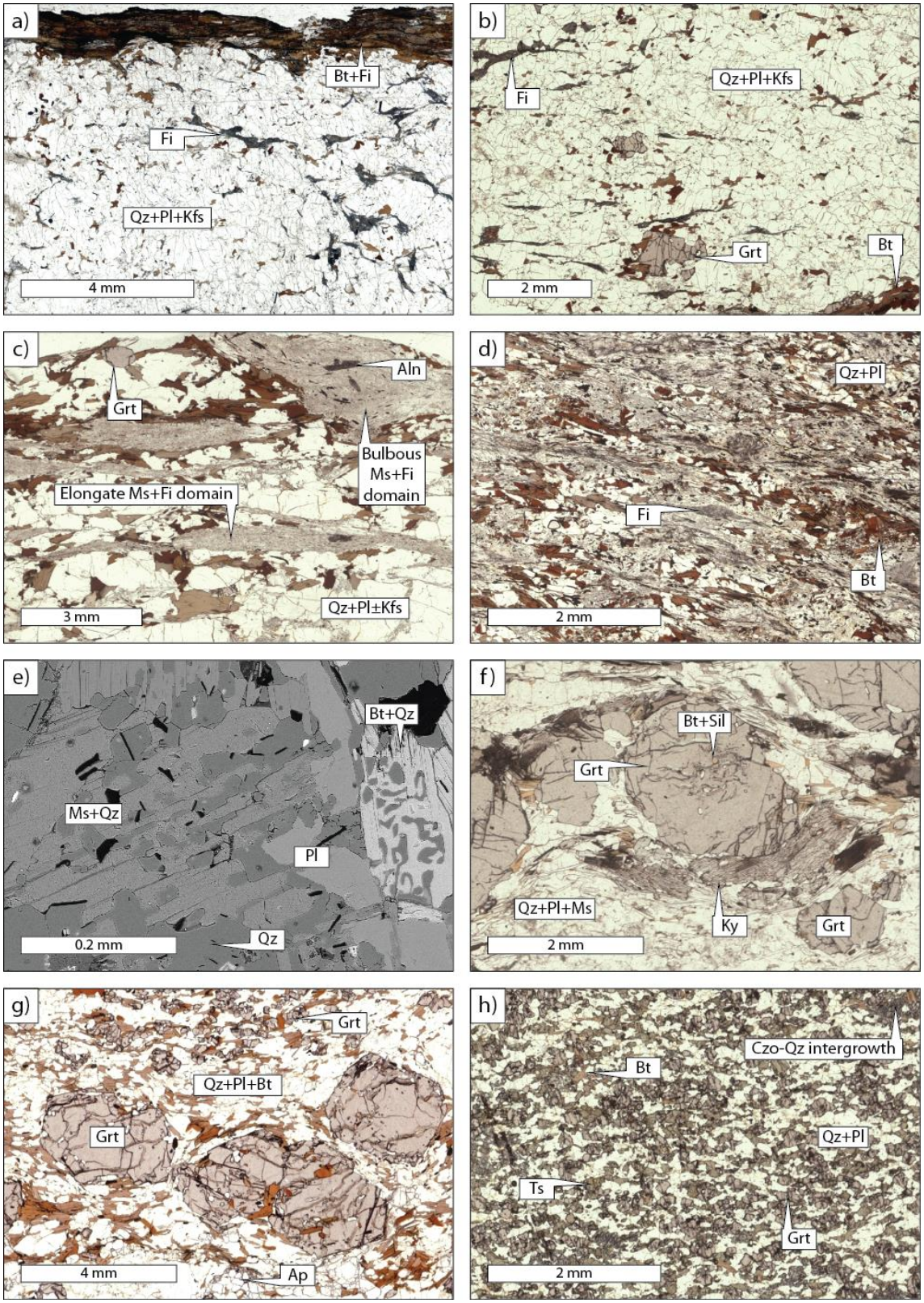


Fig. 6.7 – Petrography of migmatite samples. Thin sections viewed in plane polarised light (a) Sample ET09-05 showing a distinct boundary between leucosome and mesosome domains. (b) Typical leucosome in sample ET09-06 with a granitic mineralogy. (c) Fine crystalline muscovite-fibrolite aggregates in sample ET10-07 occur either as large bulbous domains or as elongate sheaths. Allanite occurs in the cores of some aggregates. (d) Sample ET10-09. (e) SEM BSE image of muscovite-quartz and biotite-quartz intergrowths in sample ET10-09 leucosome. (f) Sample ET10-

10 showing a quartz- and plagioclase-rich leucosome and garnet with sillimanite in its core. Smaller leucosome garnet has idioblastic faces. Kyanite is mostly aligned with the mesosome foliation and may be bent against garnet rims. (g) Sample ET10-12 semi-pelite leucosome with large euhedral type 2 garnet porphyroblasts. (h) Sample ET10-12 calc-pelite band comprised mostly of tschermakitic amphibole, type 1 garnet, quartz and plagioclase.

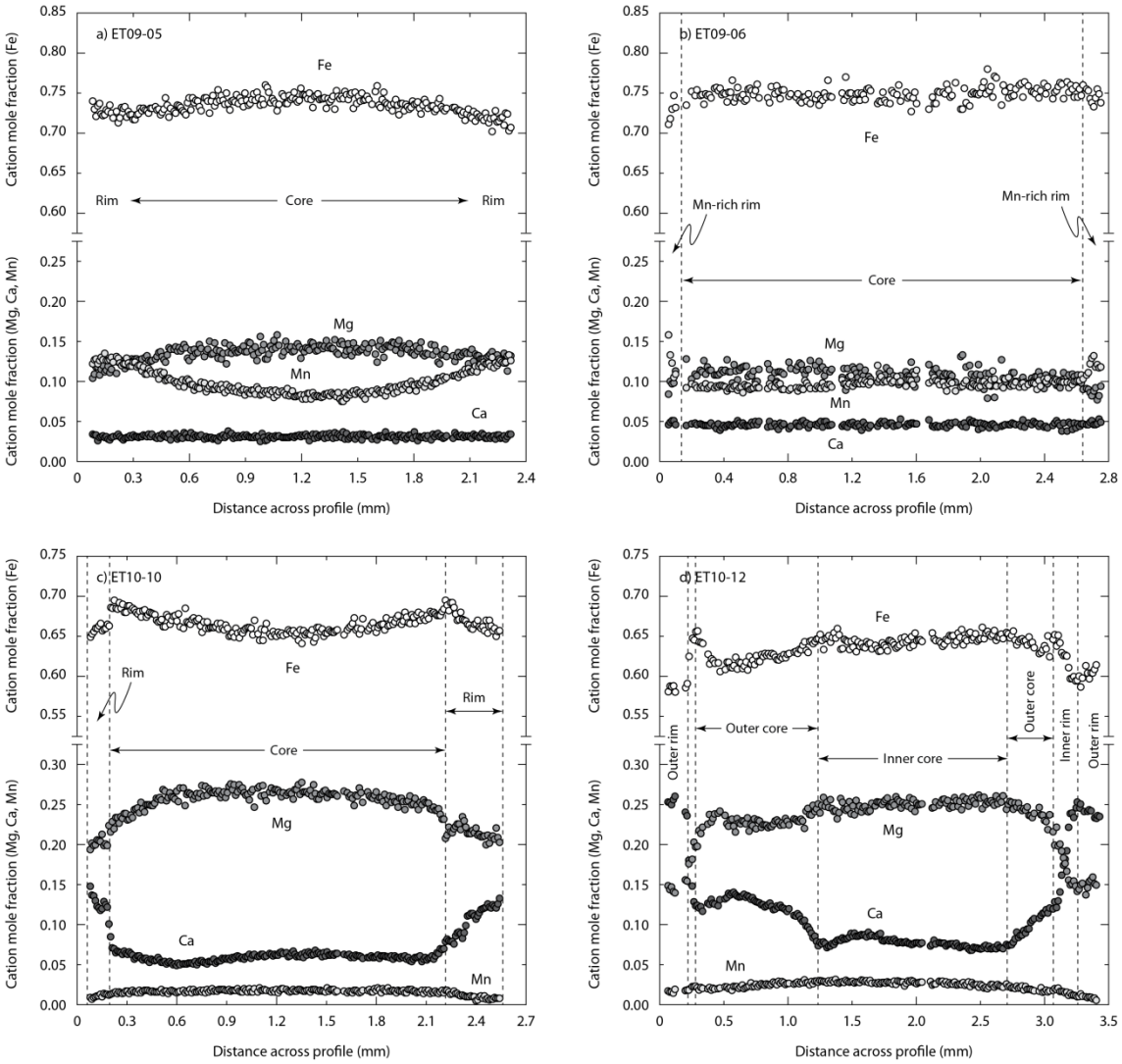


Fig. 6.8 – Compositional garnet line profiles for migmatite samples (a) ET09-05, (b) ET09-06, (c) ET10-10 (d) ET10-12. All profiles run from rim-to-rim and are non-continuous as traverses cross inclusions and fractures.

ET10-07 and ET10-09 – Muscovite-rich sillimanite migmatite

Samples ET10-07 and ET10-09 both contain muscovite, biotite, quartz and plagioclase with minor sillimanite (fibrolite), K-feldspar, ilmenite, apatite, monazite and zircon. Minor garnet and allanite also occur in sample ET10-07 (Fig. 6.7c). Both samples contain substantially more muscovite and less K-feldspar than ET09-05 and ET09-06. Small (<1 mm) garnet in ET10-07 is compositionally homogenous with 73% almandine, 13% spessartine, 10% pyrope, 4% grossular. Minor spessartine enrichment (to 14%) and pyrope depletion (to 9%) occurs at extreme rims when adjacent to biotite.

Sample	Mineral	Location	SiO_2	TiO_2	Al_2O_3	Fe_2O_3	FeO	MnO	MgO	CaO	Na_2O	K_2O	**Total**	Si	Ti	Al	Fe^{3+}	Fe^{2+}	Mn	Mg	Ca	Na	K	**Sum**	Ox	XMg	XCa	XMn	Al(iv)	Al(vi)	Alm	Prp	Grs	Sps	XFe^{3+}	XPs
ET09-05	Bt	Leucosome	35.40	4.38	18.74	0.00	20.63	0.19	7.15	0.05	0.12	10.38	**97.04**	2.68	0.25	1.67	0.00	1.30	0.01	0.81	0.00	0.02	1.00	**7.74**	11	0.38	-	-	1.32	0.35	-	-	-	-	-	-
	Grt	Core	36.72	0.01	21.23	1.83	32.17	3.77	3.63	1.06	0.00	0.03	**100.45**	2.93	0.00	2.00	0.07	2.23	0.24	0.43	0.09	0.00	0.00	**8.00**	12	0.16	-	-	-	-	0.75	0.14	0.03	0.08	-	-
	Grt	High-Mn rim	36.43	0.01	20.98	1.95	30.07	5.70	3.10	1.17	0.05	0.00	**99.46**	2.97	0.00	2.00	0.08	2.09	0.40	0.37	0.10	0.00	0.00	**8.00**	12	0.15	-	-	-	-	0.71	0.13	0.03	0.14	-	-
	Ilm	Leucosome	0.33	53.17	0.14	0.00	43.87	2.08	0.18	0.03	0.08	0.00	**99.88**	0.00	1.01	0.00	0.00	0.94	0.04	0.01	0.00	0.00	0.00	**2.00**	3	-	-	0.04	-	-	-	-	-	-	-	-
	Kfs	Leucosome	63.73	0.12	19.04	0.02	0.00	0.02	0.00	0.10	1.24	15.71	**99.98**	2.97	0.00	1.03	0.00	0.00	0.00	0.00	0.00	0.09	0.91	**5.00**	8	-	0.00	-	-	-	-	-	-	-	-	-
	Ms	Leucosome	45.68	1.48	35.33	0.00	1.39	0.01	1.04	0.05	0.40	11.32	**96.70**	3.02	0.07	2.75	0.00	0.08	0.00	0.10	0.00	0.05	0.96	**7.03**	11	0.56	-	-	0.98	1.77	-	-	-	-	-	-
	Pl	Leucosome	61.44	0.02	24.51	0.00	0.00	0.01	0.36	5.18	8.14	0.28	**99.94**	2.73	0.00	1.28	0.00	0.00	0.00	0.01	0.25	0.71	0.02	**5.00**	8	-	0.26	-	-	-	-	-	-	-	-	-
ET09-06	Bt	Leucosome	34.39	2.54	17.63	0.00	24.54	0.57	6.38	0.14	0.11	10.29	**96.59**	2.68	0.15	1.62	0.00	1.60	0.04	0.74	0.01	0.02	1.02	**7.88**	11	0.32	-	-	1.32	0.30	-	-	-	-	-	-
	Grt	Core	36.44	0.01	20.81	0.93	32.06	5.49	3.05	1.49	0.00	0.01	**100.29**	2.95	0.00	1.98	0.02	2.29	0.27	0.35	0.14	0.00	0.00	**8.00**	12	0.13	-	-	-	-	0.75	0.11	0.05	0.09	-	-
	Grt	High-Mn rim	36.03	0.00	20.72	0.81	31.46	6.31	2.67	1.49	0.10	0.03	**99.62**	2.96	0.00	1.99	0.02	2.23	0.39	0.25	0.14	0.01	0.00	**8.00**	12	0.10	-	-	-	-	0.74	0.08	0.05	0.13	-	-
	Kfs	Leucosome	64.88	0.10	18.96	0.00	0.00	0.03	0.19	0.09	1.51	14.94	**100.70**	2.97	0.00	1.02	0.00	0.00	0.00	0.01	0.00	0.13	0.87	**5.00**	8	-	0.00	-	-	-	-	-	-	-	-	-
	Ms	Leucosome	46.21	0.65	33.89	0.64	1.78	0.02	1.35	0.10	0.35	10.68	**95.67**	3.08	0.03	2.67	0.03	0.10	0.00	0.14	0.01	0.05	0.93	**7.04**	11	0.58	-	-	0.92	1.75	-	-	-	-	-	-
	Pl	Leucosome	62.40	0.01	23.64	0.00	0.00	0.03	0.29	4.59	7.96	0.36	**99.28**	2.77	0.00	1.24	0.00	0.00	0.00	0.02	0.23	0.71	0.03	**5.00**	8	-	0.24	-	-	-	-	-	-	-	-	-
ET10-03	Bt	Matrix	34.17	3.18	17.59	0.00	24.09	0.18	6.41	0.02	0.12	9.93	**95.69**	2.67	0.19	1.62	0.00	1.58	0.01	0.75	0.00	0.02	0.99	**7.83**	11	0.32	-	-	1.33	0.30	-	-	-	-	-	-
	Ilm	Matrix	0.06	53.30	0.19	0.00	44.05	2.17	0.16	0.01	0.02	0.01	**99.97**	0.00	1.01	0.01	0.00	0.93	0.05	0.01	0.00	0.00	0.00	**2.00**	3	-	-	0.05	-	-	-	-	-	-	-	-
	Kfs	Relic matrix	64.53	0.08	18.64	0.01	0.00	0.03	0.02	0.00	0.22	16.12	**99.65**	3.00	0.00	1.02	0.00	0.00	0.00	0.00	0.00	0.02	0.96	**5.00**	8	-	0.00	-	-	-	-	-	-	-	-	-
	Ms	Fine matte	45.52	0.60	35.39	0.00	1.72	0.02	0.59	0.05	0.26	11.42	**95.57**	3.05	0.03	2.79	0.00	0.10	0.00	0.06	0.00	0.03	0.98	**7.03**	11	0.38	-	-	0.96	1.84	-	-	-	-	-	-
	Ms	Large lath	45.25	0.85	36.01	0.00	1.56	0.02	0.55	0.03	0.40	11.24	**95.91**	3.01	0.04	2.83	0.00	0.09	0.00	0.05	0.00	0.05	0.96	**7.03**	11	0.38	-	-	0.99	1.84	-	-	-	-	-	-
	Pl	Poikiloblast	64.75	0.02	21.95	0.04	0.00	0.01	0.00	2.77	9.17	0.09	**98.80**	2.90	0.00	1.16	0.00	0.00	0.00	0.00	0.13	0.80	0.01	**5.00**	8	-	0.14	-	-	-	-	-	-	-	-	-
ET10-07	Bt	Adjacent to Grt rim	35.08	2.90	17.95	0.00	23.23	0.25	6.87	0.01	0.00	9.87	**96.16**	2.71	0.17	1.63	0.00	1.50	0.02	0.79	0.00	0.00	0.97	**7.79**	11	0.34	-	-	1.29	0.34	-	-	-	-	-	-
	Bt	Mesosome foliation	34.18	3.65	18.01	0.00	23.42	0.25	6.62	0.01	0.07	10.06	**96.27**	2.65	0.21	1.65	0.00	1.52	0.02	0.76	0.00	0.01	1.00	**7.82**	11	0.33	-	-	1.35	0.30	-	-	-	-	-	-
	Grt	Core	36.78	0.02	20.58	0.96	31.47	5.97	2.33	1.26	0.00	0.00	**99.37**	2.96	0.00	1.99	0.06	2.19	0.40	0.29	0.11	0.00	0.00	**8.00**	12	0.12	-	-	-	-	0.73	0.10	0.04	0.13	-	-
	Ilm	Matrix	0.11	53.96	0.30	0.00	40.45	4.67	0.21	0.01	0.00	0.01	**99.72**	0.00	1.01	0.01	0.00	0.87	0.10	0.01	0.00	0.00	0.00	**2.00**	3	-	-	0.10	-	-	-	-	-	-	-	-
	Kfs	Leucosome	64.03	0.20	18.67	0.00	0.00	0.00	0.03	0.00	0.84	15.71	**99.48**	2.97	0.01	1.02	0.00	0.00	0.00	0.00	0.00	0.08	0.92	**5.00**	8	-	0.00	-	-	-	-	-	-	-	-	-
	Ms	Fine matte	45.40	0.49	35.14	0.00	1.69	0.03	0.65	0.04	0.35	11.25	**95.04**	3.05	0.03	2.78	0.00	0.10	0.00	0.07	0.00	0.04	0.97	**7.04**	11	0.41	-	-	0.95	1.83	-	-	-	-	-	-
	Ms	Coarse lath	45.67	0.94	34.50	0.00	1.66	0.00	0.67	0.04	0.40	10.78	**94.66**	3.07	0.05	2.74	0.00	0.09	0.00	0.07	0.00	0.05	0.93	**7.00**	11	0.44	-	-	0.93	1.81	-	-	-	-	-	-
	Pl	Matrix	61.26	0.00	24.91	0.00	0.00	0.01	0.00	5.88	7.46	0.21	**99.73**	2.73	0.00	1.30	0.00	0.00	0.00	0.00	0.29	0.67	0.01	**5.00**	8	-	0.30	-	-	-	-	-	-	-	-	-
ET10-09	Bt	Bt-Qz intergrowth	35.11	3.22	18.11	0.00	21.77	0.23	8.15	0.00	0.13	10.13	**96.85**	2.68	0.19	1.63	0.00	1.39	0.02	0.93	0.00	0.02	0.98	**7.84**	11	0.40	-	-	1.32	0.31	-	-	-	-	-	-
	Bt	Matrix foliation	35.13	3.49	18.17	0.00	21.49	0.26	7.81	0.01	0.11	10.19	**96.66**	2.68	0.20	1.64	0.00	1.37	0.02	0.89	0.00	0.02	0.99	**7.81**	11	0.39	-	-	1.32	0.32	-	-	-	-	-	-
	Kfs	Matrix	64.41	0.20	18.80	0.12	0.00	0.00	0.00	0.01	1.16	15.34	**100.04**	2.98	0.00	1.02	0.00	0.00	0.00	0.00	0.00	0.10	0.90	**5.00**	8	-	0.00	-	-	-	-	-	-	-	-	-
	Ms	Coarse lath enclosing Sil	46.79	1.53	35.56	0.00	1.15	0.07	0.62	0.00	0.23	10.49	**96.44**	3.07	0.08	2.75	0.00	0.06	0.00	0.06	0.00	0.03	0.88	**6.93**	11	0.50	-	-	0.93	1.82	-	-	-	-	-	-
	Ms	Ms-Qz intergrowth	46.51	0.88	35.94	0.00	1.34	0.00	0.53	0.00	0.19	10.02	**95.41**	3.08	0.04	2.80	0.00	0.07	0.00	0.05	0.00	0.02	0.85	**6.91**	11	0.42	-	-	0.92	1.88	-	-	-	-	-	-
	Pl	Matrix	63.11	0.02	23.44	0.10	0.00	0.00	0.00	4.52	8.56	0.15	**99.90**	2.80	0.00	1.22	0.00	0.00	0.00	0.00	0.21	0.76	0.01	**5.00**	8	-	0.21	-	-	-	-	-	-	-	-	-

Table 6.4 – Mineral compositions for sillimanite-grade migmatite samples (overleaf).

Coarse muscovite laths in sample ET10-07 leucosome regions have slightly higher Si (3.04–3.08 cpfu) and Ti (0.03–0.05 cpfu) than muscovite in mesosome domains, which exists as a fine crystalline mat and contains Si = 3.04–3.05 cpfu and Ti = 0.01–0.03 cpfu (Table 6.4). Fibrolite occurs as turbid clusters in the cores of such mats (Fig. 6.7c). Muscovite in sample ET10-09 occurs similarly as laths with associated fibrolite (Fig. 6.7d) or as symplectic intergrowths with quartz. These intergrowths are also associated with either biotite-quartz symplectite (Fig. 6.7e) or myrmekite (plagioclase-quartz intergrowths). Muscovite in sample ET10-09 has a similar composition, with Si = 3.01–3.08 cpfu and Ti = 0.04–0.09 cpfu, whether occurring as laths or as muscovite-quartz intergrowths. Compositions of all major minerals are presented in Table 6.4.

ET10-10 – Kyanite-bearing migmatite

Sample ET10-10 is a stromatic migmatite with mm-scale leucosome and mesosome banding. Mesosome folia are defined by muscovite, biotite and graphite and leucosome segregations consist dominantly of quartz and plagioclase (in approximately equal proportions) alongside lesser biotite, muscovite, kyanite, garnet and rutile (Fig. 6.7f). Accessory minerals include apatite, zircon, monazite and allanite. Garnet occurs in the leucosome as porphyroblasts ranging from <1 mm to 8 mm in diameter, with the mesosome foliation commonly wrapping around the largest grains. This range of sizes commonly correlates with morphology, with smaller grains being idioblastic, and larger ones showing subhedral-to-anhedral faces (Fig. 6.7f). All large porphyroblasts exhibit similar compositional zoning profiles, with broad cores and thin rims (Fig. 6.8c). Core regions exhibit homogenous spessartine contents (~2%). By contrast, almandine content increases from 65% to 70% towards the core-rim transition with grossular and pyrope decreasing from 6% to 5% and 27% to 24% respectively over the same interval. Garnet outer rims are marked by lower almandine, spessartine and pyrope contents of 65%, <1% and 20% respectively, whereas grossular content increases to 15%. A representative compositional zoning profile is presented in Fig. 6.8c.

Sillimanite occurs in garnet cores with quartz, biotite and rutile (Fig. 6.7f), but is not found in garnet rims or the matrix. Kyanite is found primarily as subhedral-to-euhedral blades that show a preferred alignment with mesosome folia, contain inclusions of rutile, biotite, muscovite and quartz

and are commonly bent around garnet rims exhibiting no mutual growth faces (Fig. 6.7f). Less abundant and smaller kyanite grains occur in clusters in the leucosome and show anhedral morphologies. Compositions of major minerals are presented in Table 6.4.

ET10-12 – Calc-pelite/semi-pelite migmatite

Sample ET10-12 was collected from an outcrop of migmatitic paragneiss that contains semi-pelite and calc-pelite bands separated by gradational 'transition zones'. Calc-pelite domains (Fig. 6.7h) occur on a cm-scale between much thicker semi-pelite bands, with leucosome restricted to the latter. The petrography of each band is summarised in Fig. 6.9.

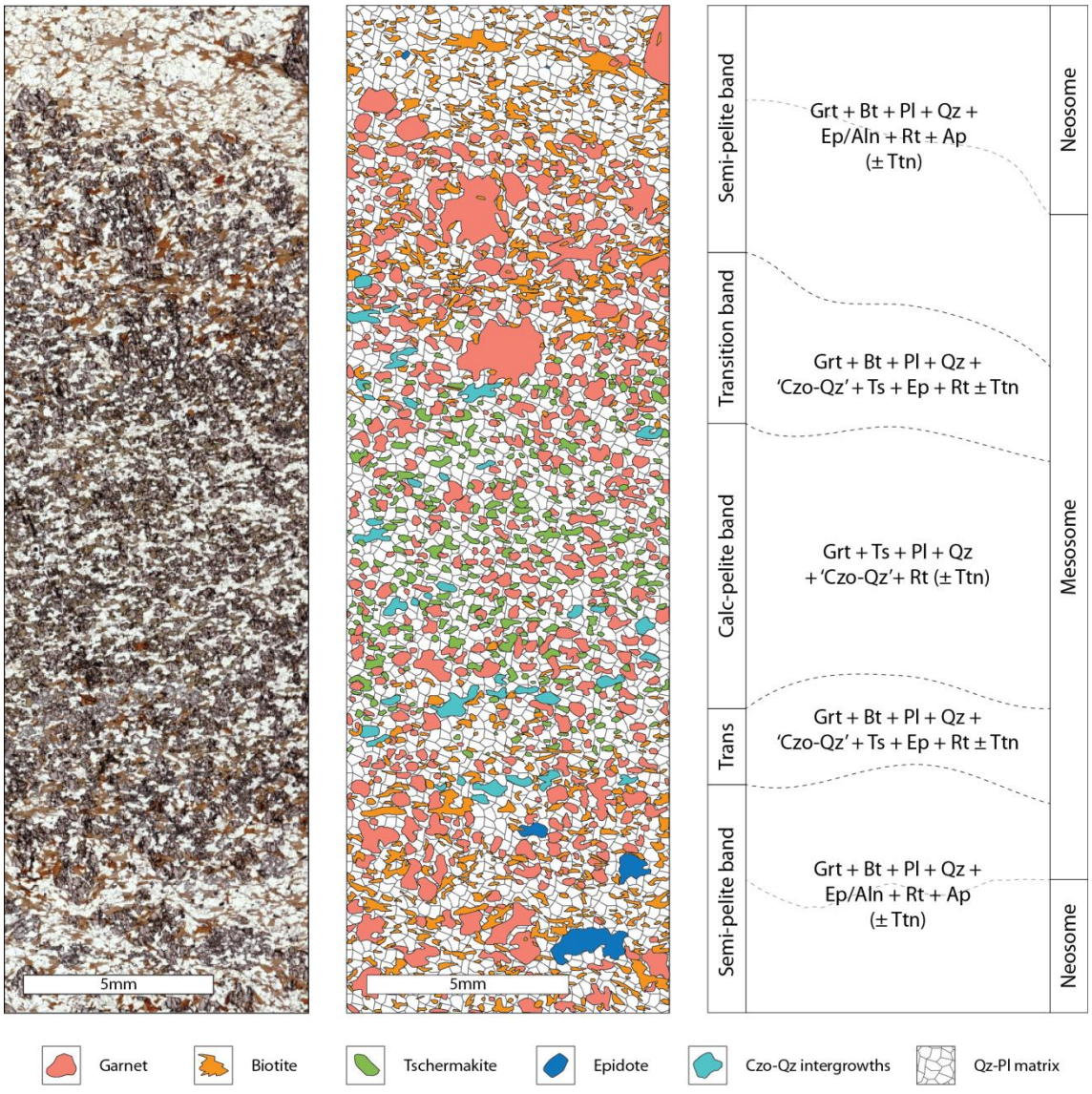


Fig. 6.9 – Detailed petrography of sample ET10-12 highlighting the gradation from amphibole-bearing calc-pelite bands into semi-pelitic bands with associated K-poor leucosomes. A schematic tracing of a photomicrograph of the different bands emphasises the separate parageneses.

Amphibole occurs in calc-pelite bands (Fig. 6.7h) and in transitional zones in diminishing proportion towards semi-pelite bands, where it is fully absent (Fig. 6.9). It invariably occurs as small stubby crystals that define a weak shape-preferred foliation. Grains exhibit no systematic compositional variation between calc-pelite and transition zones and contain Si = 6.06–6.36 cpfu, XMg = 0.58–0.64, Na_B (M4 site) = 0.07–0.11 cpfu and Na+K (A site) = 0.41–0.50, so are tschermakite ('calcic-amphibole'; Leake *et al*., 1997, 2004). Biotite is abundant in semi-pelite and leucosome domains and defines a weak foliation parallel to the dominant compositional banding. Biotite appears to coexist with amphibole in the semi- to calc-pelite transition zones, and their relative abundances show an inverse relationship. Biotite from semi-pelite/leucosome domains has XMg = 0.57–0.58, whereas those crystals from transition bands have XMg = 0.60–0.63 (Table 6.4).

Garnet occurs throughout sample ET10-12 but shows substantial textural and compositional variation in each band. Garnet (type 1) located in calc-pelite bands is small (<0.2 mm diameter; Fig. 6.7h) but abundant and shares straight crystal faces with amphibole. Ilmenite occurs in the cores of some grains. Similar type 1 garnet occurs in transition zones alongside rare skeletal porphyroblasts that are up to 4 mm diameter and enclose biotite, amphibole, quartz, plagioclase and rutile. Type 1 garnet shows slight compositional zoning from core to rim with pyrope content decreasing from 19% to 15% and almandine content increasing from 57% to 62%. Grossular shows minor variation from core to rim, ranging between 21% and 23%, and spessartine content is homogenous at ~2%.

Semi-pelite and leucosome regions contain euhedral/subhedral garnet porphyroblasts (type 2) up to 5 mm in diameter (Fig. 6.7g). These contain inclusions of ilmenite, rutile, biotite and quartz and exhibit approximately concentric compositional zoning, as shown in Fig. 6.8d. Inner core regions are Ca- and Mn-poor, with grossular and spessartine content as low as 7% and 3% respectively, but Mg- and Fe-rich with up to ~25% pyrope and ~65% almandine. The outer core is characterised by an increase in grossular content up to 15% and a steady decrease in spessartine and almandine contents to ~2% and ~62% respectively, with pyrope remaining approximately constant. Thinner rims with significantly different compositions surround these outer core regions, where grossular content reaches 24–25% and pyrope and almandine contents are much lower at 14–15% and ~60% respectively (Fig. 6.8d). Spessartine content is just over 1% in these regions.

Sample	Mineral	Location	SiO_2	TiO_2	Al_2O_3	Fe_2O_3	FeO	MnO	MgO	CaO	Na_2O	K_2O	**Total**	Si	Ti	Al	Fe^{3+}	Fe^{2+}	Mn	Mg	Ca	Na	K	**Sum**	Ox	XMg	XCa	XMn	Al(iv)	Al(vi)	Alm	Prp	Grs	Sps	XFe^{3+}	XPs
ET10-10	Bt	Inc in Grt core	38.28	2.80	18.74	0.00	11.77	0.03	15.02	0.06	0.36	9.31	**96.37**	2.76	0.15	1.59	0.00	0.71	0.00	1.61	0.00	0.05	0.86	**7.73**	11	0.69	-	-	1.24	0.35	-	-	-	-	-	-
	Bt	Leucosome	38.44	1.83	19.37	0.00	13.23	0.01	13.25	0.04	0.15	9.46	**95.78**	2.80	0.10	1.67	0.00	0.81	0.00	1.44	0.00	0.02	0.90	**7.74**	11	0.64	-	-	1.20	0.47	-	-	-	-	-	-
	Bt	Mesosome foliation	38.99	1.91	18.99	0.00	13.44	0.02	13.93	0.07	0.19	9.31	**96.85**	2.81	0.10	1.61	0.00	0.81	0.00	1.50	0.01	0.03	0.89	**7.76**	11	0.65	-	-	1.19	0.42	-	-	-	-	-	-
	Grt	Core	37.47	0.00	21.68	0.72	30.23	0.99	6.62	1.99	0.05	0.00	**99.75**	2.98	0.00	2.01	0.04	1.93	0.07	0.79	0.18	0.00	0.00	**8.00**	12	0.29	-	-	-	-	0.65	0.27	0.06	0.02	-	-
	Grt	Rim	37.38	0.07	21.53	0.96	28.46	0.24	5.37	5.41	0.00	0.01	**99.43**	2.98	0.00	2.00	0.05	1.91	0.02	0.60	0.45	0.00	0.00	**8.00**	12	0.24	-	-	-	-	0.64	0.20	0.15	0.01	-	-
	Ms	Leucosome	46.16	1.29	34.26	0.00	1.12	0.01	1.32	0.03	0.91	10.20	**95.30**	3.07	0.07	2.69	0.00	0.06	0.00	0.13	0.00	0.12	0.87	**7.01**	11	0.68	-	-	0.93	1.76	-	-	-	-	-	-
	Ms	Mesosome foliation	46.52	1.05	34.46	0.00	1.14	0.00	1.29	0.02	0.84	10.32	**95.64**	3.09	0.05	2.69	0.00	0.06	0.00	0.13	0.00	0.11	0.87	**7.00**	11	0.68	-	-	0.91	1.78	-	-	-	-	-	-
	Pl	Leucosome	58.15	0.01	26.50	0.02	0.00	0.01	0.01	8.01	6.79	0.05	**99.55**	2.62	0.00	1.40	0.00	0.00	0.00	0.00	0.39	0.59	0.00	**5.00**	8	-	0.40	-	-	-	-	-	-	-	-	-
ET10-12 semi-pelite bands	Bt	Neosome foliation	37.26	2.65	18.52	0.00	15.90	0.02	12.08	0.03	0.15	9.73	**96.34**	2.75	0.15	1.61	0.00	0.98	0.00	1.33	0.00	0.02	0.92	**7.76**	11	0.58	-	-	1.25	0.36	-	-	-	-	-	-
	Ep	Rims on Aln in neosome	38.29	0.34	29.92	4.89	0.00	0.00	0.11	24.05	0.00	0.00	**97.60**	2.96	0.02	2.73	0.28	0.00	0.00	0.01	1.99	0.00	0.00	**8.00**	12.5	-	-	-	-	-	-	-	-	-	-	0.09
	Grt	Core (neosome p-blast)	38.73	0.07	21.61	0.82	28.28	1.04	6.56	3.23	0.00	0.00	**100.34**	2.96	0.00	1.99	0.05	1.95	0.08	0.76	0.22	0.00	0.00	**8.00**	12	0.28	-	-	-	-	0.65	0.25	0.07	0.03	-	-
	Grt	Rim (neosome p-blast)	38.68	0.05	21.51	0.74	26.43	0.70	4.22	8.09	0.01	0.00	**100.43**	2.96	0.00	2.00	0.04	1.78	0.03	0.45	0.73	0.00	0.00	**8.00**	12	0.20	-	-	-	-	0.60	0.15	0.24	0.01	-	-
	Pl	Inc in Grt in neosome	55.06	0.01	28.49	0.13	0.00	0.01	0.00	10.55	5.47	0.04	**99.76**	2.48	0.00	1.52	0.00	0.00	0.00	0.00	0.52	0.48	0.00	**5.00**	8	-	0.52	-	-	-	-	-	-	-	-	-
	Pl	Neosome	56.90	0.03	27.17	0.04	0.00	0.01	0.02	8.89	6.34	0.08	**99.48**	2.57	0.00	1.44	0.00	0.00	0.00	0.00	0.43	0.55	0.01	**5.00**	8	-	0.43	-	-	-	-	-	-	-	-	-
ET10-12 calc-pelite and trans bands	Bt	Transition band	37.22	2.36	17.65	0.00	14.26	0.03	13.00	0.14	0.14	9.21	**94.01**	2.79	0.13	1.56	0.00	0.89	0.00	1.45	0.01	0.02	0.88	**7.73**	11	0.62	-	-	1.21	0.35	-	-	-	-	-	-
	Czo	Intergrowth with Qz	38.84	0.16	32.63	1.53	0.00	0.03	0.05	24.80	0.00	0.00	**98.04**	2.95	0.01	2.92	0.09	0.00	0.00	0.01	2.02	0.00	0.00	**8.00**	12.5	-	-	-	-	-	-	-	-	-	-	0.03
	Grt	Calc-pelite band	38.11	0.01	21.63	1.72	25.05	0.68	4.72	8.96	0.00	0.00	**100.88**	2.96	0.00	1.98	0.07	1.72	0.05	0.55	0.69	0.00	0.00	**8.02**	12	0.24	-	-	-	-	0.57	0.18	0.23	0.02	-	-
	Ilm	Inc in Grt core	0.10	54.09	0.18	0.00	43.73	0.96	1.03	0.00	0.08	0.01	**100.18**	0.00	1.00	0.01	0.00	0.93	0.02	0.04	0.00	0.00	0.00	**2.00**	3	-	-	0.02	-	-	-	-	-	-	-	-
	Kfs	Transition band	64.54	0.04	18.83	0.14	0.00	0.00	0.01	0.30	0.03	16.21	**100.10**	2.97	0.00	1.03	0.01	0.00	0.00	0.00	0.02	0.00	0.98	**5.00**	8	-	0.02	-	-	-	-	-	-	-	-	-
	Pl	Calc-pelite band	56.19	0.01	27.58	0.04	0.00	0.01	0.00	9.51	6.02	0.06	**99.42**	2.54	0.00	1.47	0.00	0.00	0.00	0.00	0.46	0.53	0.00	**5.00**	8	-	0.46	-	-	-	-	-	-	-	-	-
	Ts	Calc-pelite band	42.18	0.88	16.45	1.13	11.73	0.04	10.36	11.85	1.27	1.02	**96.91**	6.22	0.10	2.86	0.13	1.45	0.01	2.28	1.87	0.36	0.19	**15.47**	23	0.61	-	-	-	-	-	-	-	-	0.08	-
	Ttn	Calc-pelite band	30.16	38.91	1.84	0.00	0.20	0.01	0.09	28.67	0.00	0.00	**99.88**	0.99	0.96	0.05	0.00	0.00	0.00	0.00	1.00	0.00	0.00	**3.00**	5	-	-	-	-	-	-	-	-	-	-	-

Table 6.5 – Mineral compositions for kyanite-grade migmatite samplesET10-10 and ET10-12

Plagioclase occurs in all petrographic domains and also as inclusions in type 2 leucosome garnet. Individual grains lack internal zoning and show no ternary character, although there is significant compositional variation between these petrographic positions. Leucosome grains contain XCa = 0.43–0.46, anhedral crystals in calc-pelite and transitional regions contain XCa = 0.44–0.50, whereas inclusions in leucosome garnet are more calcic with XCa = 0.52–0.53. Rare K-feldspar exists as extremely small (<100 μm) crystals in calc-pelite bands and transition zones, with XK = 0.98, but is wholly absent from semi-pelite regions and leucosomes. Euhedral-to-subhedral epidote commonly contains dark REE-rich cores and is restricted to semi-pelite/leucosome regions. Grains are weakly zoned with increasing XPs from 0.07 at the rims to 0.10 towards REE-bearing cores. Clinozoisite occurs as individual grains and also as symplectic intergrowths with quartz in calc-pelite and transitional bands. Quartz is abundant throughout each domain in addition to minor amounts of zircon, apatite and rutile. Rutile is occasionally rimmed by ilmenite or titanite, the latter containing trace amounts of aluminium (0.05 cpfu).

6.3.4. Mylonites

Samples of mylonite from the ductile shear zone that separates the B-L-M region from the core of the EHS (between the MYLP and LD faults; Fig. 6.1) were collected to investigate the timing and *P–T* conditions of peak protolith metamorphism and subsequent deformation. The studied outcrops dip moderately towards the north-west (Fig. 6.10a) and show isoclinal folding, most obvious in quartzo-feldspathic horizons (Fig. 6.10b–c), and boudinage in more competent metabasic layers (Fig. 6.10d). Because of their varied petrographic parentage, samples are subsequently grouped and described according to their interpreted protolith lithology.

Granitoid protolith

Sample ET09-01 is a blastomylonite containing abundant porphyroclasts of plagioclase and K-feldspar, alongside rarer garnet and allanite, that occur within a ductilely-deformed matrix of quartz, epidote, biotite, muscovite, titanite, ilmenite and magnetite (Fig. 6.11a). K-feldspar porphyroclasts contain inclusions of biotite, chlorite, ilmenite, muscovite, magnetite and plagioclase. Garnet ranges between 1–2 mm in diameter and exhibits compositional zoning from core to rim, characterised by an increase in almandine content from 39% to 53%, a decrease in spessartine content from 18% to

8% and a slight decrease in grossular from 45% to 38% over the same interval. Pyrope content is uniformly low at ~1–2%. The protolith for this sample is interpreted to be a plutonic granitoid rock based on the abundance of large plagioclase and K-feldspar grains (originally as phenocrysts) alongside magnetite and allanite. Mineral compositions are presented in Table 6.6.

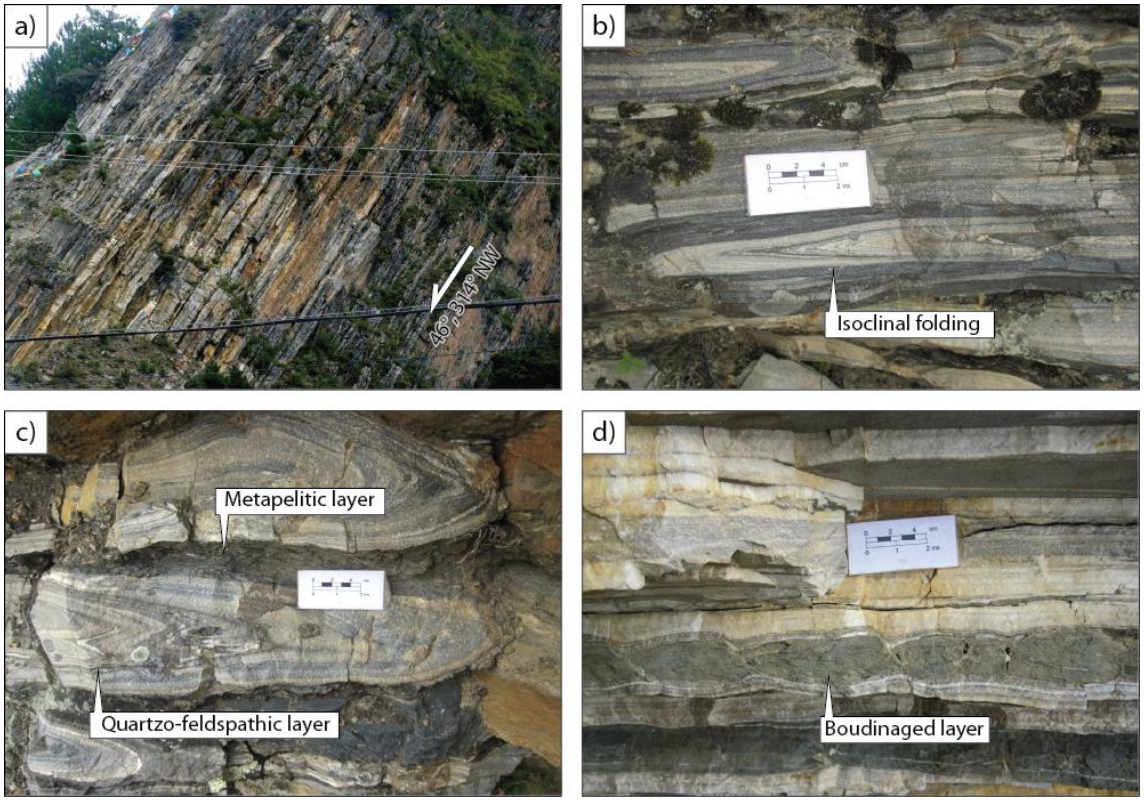


Fig. 6.10 – Field relations for mylonite samples (a) Outcrop photograph showing mylonitised lithologies, looking north-east, with ~20m of structural thickness visible. (b) Isoclinal folding in quartzo-feldspathic mylonite sample ET10-15a. (c) Petrographic variation occurs on a decimetre-scale. (d) Boudinage structures in sample ET10-15b.

Metabasite (amphibolite) protolith

Samples ET10-15b, ET10-15c and ET10-16 all contain amphibolite-facies assemblages diagnostic of a mafic bulk composition, but show a variety of microstructures. Samples ET10-15b and ET10-15c both exhibit an S-C fabric (Fig. 6.11b) with cleavage domains defined by biotite and microlithons containing amphibole (magnesiohornblende), plagioclase, ilmenite and quartz. Sample ET10-16 lacks an S-C fabric, but instead contains large amphibole laths (tschermakite-ferrotschermakite) that are strongly aligned (Fig. 6.11c) and define the mylonitic foliation. Sample ET10-16 has significantly less biotite than samples ET10-15b and ET10-15c and has a matrix composed of plagioclase, quartz and minor ilmenite. Clusters of epidote also occur and are wrapped by the sample foliation (Fig. 6.11c). Mineral compositions are given in Table 6.6.

Sample	Mineral	Location	SiO_2	TiO_2	Al_2O_3	Fe_2O_3	FeO	MnO	MgO	CaO	Na_2O	K_2O	**Total**	Si	Ti	Al	Fe^{3+}	Fe^{2+}	Mn	Mg	Ca	Na	K	**Sum**	Ox	XMg	XCa	XMn	Al(iv)	Al(vi)	Alm	Prp	Grs	Sps	XFe^{3+}	XPs
ET09-01	Bt	Matrix	33.62	2.45	15.24	0.00	29.64	0.82	3.23	0.09	0.17	9.85	**95.11**	2.75	0.15	1.47	0.00	2.02	0.06	0.39	0.01	0.03	1.03	**7.90**	11	0.16	-	-	1.26	0.21	-	-	-	-	-	-
	Bt	Inclusion in Kfs	36.76	0.91	16.61	0.00	25.36	0.29	7.24	0.09	0.28	10.68	**98.22**	2.81	0.05	1.50	0.00	1.62	0.02	0.83	0.01	0.04	1.04	**7.93**	11	0.34	-	-	1.19	0.31	-	-	-	-	-	-
	Chl	Inclusion in Kfs	22.94	0.10	20.54	1.50	37.49	0.71	5.32	0.01	0.20	0.03	**88.84**	2.59	0.01	2.73	0.13	3.54	0.07	0.89	0.00	0.04	0.00	**10.00**	14	0.20	-	-	-	-	-	-	-	-	-	-
	Ep	Matrix	37.44	0.00	22.55	14.66	0.00	0.12	0.37	21.42	0.00	0.04	**96.60**	3.03	0.00	2.15	0.89	0.00	0.01	0.04	1.86	0.00	0.00	**8.00**	12.5	-	-	-	-	-	-	-	-	-	-	0.29
	Grt	Core	36.29	0.14	20.10	2.92	15.58	8.48	0.38	14.56	0.00	0.00	**98.45**	2.94	0.01	1.92	0.18	1.06	0.58	0.05	1.27	0.00	0.00	**8.00**	12	0.04	-	-	-	0.36	0.02	0.43	0.20	-	-
	Grt	Rim	36.01	0.01	20.06	2.25	23.40	3.71	0.45	11.72	0.02	0.00	**97.63**	2.96	0.00	1.94	0.14	1.61	0.26	0.06	1.03	0.00	0.00	**8.00**	12	0.03	-	-	-	0.54	0.02	0.35	0.09	-	-
	Ilm	Inclusion in Kfs	1.48	54.58	0.50	0.00	28.57	14.80	0.26	0.03	0.34	0.05	**100.61**	0.04	1.02	0.01	0.00	0.59	0.31	0.01	0.00	0.02	0.00	**2.00**	3	-	-	0.02	-	-	-	-	-	-	-	-
	Kfs	Porphyroclast	63.81	0.09	18.72	0.04	0.00	0.01	0.28	0.08	0.67	16.64	**100.34**	2.93	0.00	1.01	0.00	0.00	0.00	0.02	0.00	0.06	0.97	**5.00**	8	-	0.00	-	-	-	-	-	-	-	-	-
	Kfs	Matrix	63.71	0.10	18.60	0.00	0.00	0.00	0.36	0.07	0.51	16.86	**100.21**	2.93	0.00	1.01	0.00	0.00	0.00	0.02	0.00	0.05	0.99	**5.00**	8	-	0.00	-	-	-	-	-	-	-	-	-
	Ms	Inclusion in Kfs	48.96	0.31	27.99	1.90	3.23	0.01	2.39	0.05	0.18	10.83	**95.85**	3.30	0.02	2.22	0.10	0.18	0.00	0.24	0.00	0.02	0.93	**7.01**	11	0.57	-	-	0.71	1.52	-	-	-	-	-	-
	Mt	Inclusion in Kfs	0.26	0.15	0.47	64.95	30.14	0.09	0.05	0.01	0.00	0.03	**96.15**	0.01	0.01	0.02	1.95	1.01	0.00	0.00	0.00	0.00	0.00	**3.00**	4	-	-	0.00	-	-	-	-	-	-	0.66	-
	Mt	Matrix	0.22	0.23	0.35	66.53	30.83	0.03	0.08	0.05	0.01	0.00	**98.33**	0.01	0.01	0.02	1.95	1.01	0.00	0.00	0.01	0.00	0.00	**3.00**	4	-	-	0.00	-	-	-	-	-	-	0.66	-
	Pl	Matrix	64.07	0.03	21.86	0.20	0.00	0.02	0.44	2.58	9.40	0.16	**98.76**	2.86	0.00	1.15	0.01	0.00	0.00	0.03	0.12	0.81	0.01	**5.00**	8	-	0.13	-	-	-	-	-	-	-	-	-
	Pl	Inclusion in Kfs	64.28	0.01	20.58	0.06	0.00	0.00	0.28	1.74	9.97	0.17	**97.09**	2.91	0.00	1.10	0.00	0.00	0.00	0.02	0.08	0.88	0.01	**5.00**	8	-	0.09	-	-	-	-	-	-	-	-	-
ET10-15b	Amph	Matrix	44.95	0.43	13.23	3.60	9.15	0.30	12.44	11.23	1.25	0.32	**96.90**	6.55	0.05	2.27	0.40	1.11	0.04	2.70	1.75	0.35	0.06	**15.28**	23	0.71	-	-	-	-	-	-	-	-	0.26	-
	Pl	Matrix	63.57	0.04	23.03	0.22	0.00	0.00	0.00	4.00	7.70	0.37	**98.93**	2.87	0.00	1.23	0.01	0.00	0.00	0.00	0.19	0.67	0.02	**5.00**	8	-	0.22	-	-	-	-	-	-	-	-	-
	Bt	Matrix	37.68	2.87	15.53	0.00	14.29	0.14	14.86	0.24	0.14	9.49	**95.24**	2.80	0.16	1.36	0.00	0.89	0.01	1.65	0.02	0.02	0.90	**7.81**	11	0.65	-	-	1.20	0.17	-	-	-	-	-	-
ET10-16	Ep	Cluster	36.62	0.17	23.24	12.28	0.00	0.20	0.07	23.14	0.00	0.00	**95.72**	2.98	0.01	2.23	0.75	0.00	0.01	0.01	2.01	0.00	0.00	**8.00**	12.5	-	-	-	-	-	-	-	-	-	-	0.25
	Amph	Porphryoblast rim	41.70	0.45	14.69	5.29	12.54	0.46	8.87	11.79	1.13	0.32	**97.24**	6.23	0.05	2.59	0.59	1.57	0.06	1.97	1.89	0.33	0.06	**15.33**	23	0.56	-	-	-	-	-	-	-	-	0.28	-
	Amph	Porphryoblast core	41.29	0.42	16.52	4.41	15.17	0.29	7.42	10.35	1.55	0.38	**97.80**	6.16	0.05	2.90	0.50	1.89	0.04	1.65	1.65	0.45	0.07	**15.36**	23	0.47	-	-	-	-	-	-	-	-	0.21	-
	Chl	Matrix associated with Kfs	25.35	0.04	20.85	0.00	18.40	0.31	18.44	0.03	0.04	0.02	**83.48**	2.71	0.00	2.63	0.00	1.65	0.03	2.94	0.00	0.01	0.00	**9.98**	14	0.64	-	-	-	-	-	-	-	-	-	-
	Ilm	Matrix	0.17	49.82	0.13	7.47	41.20	3.43	0.11	0.11	0.00	0.00	**102.44**	0.00	0.93	0.00	0.14	0.85	0.07	0.00	0.00	0.00	0.00	**2.00**	3	-	-	0.02	-	-	-	-	-	-	-	-
	Kfs	Matrix associated with Chl	63.54	0.12	18.48	0.33	0.00	0.04	0.11	0.00	0.00	17.14	**99.76**	2.95	0.00	1.01	0.01	0.00	0.00	0.01	0.00	0.00	1.01	**5.00**	8	-	0.00	-	-	-	-	-	-	-	-	-
	Mt	Matrix	0.06	0.17	0.23	67.48	30.09	0.03	0.14	0.03	0.07	0.04	**98.34**	0.00	0.01	0.01	0.98	0.98	0.00	0.01	0.00	0.01	0.00	**3.00**	4	-	-	0.00	-	-	-	-	-	-	0.67	-
	Pl	Matrix	59.22	0.00	26.10	0.04	0.00	0.00	0.00	7.78	6.81	0.09	**100.04**	2.65	0.00	1.38	0.00	0.00	0.00	0.00	0.37	0.59	0.01	**5.00**	8	-	0.38	-	-	-	-	-	-	-	-	-
ET10-17	Ep	Matrix	37.57	0.16	22.60	15.01	0.00	0.30	0.01	23.88	0.00	0.02	**99.54**	2.97	0.01	2.10	0.89	0.00	0.01	0.00	2.02	0.00	0.00	**8.00**	12.5	-	-	-	-	-	-	-	-	-	-	0.30
	Ilm	Matrix	0.00	52.41	0.16	0.39	43.15	3.67	0.10	0.07	0.00	0.00	**99.95**	0.00	0.99	0.01	0.01	0.91	0.08	0.00	0.00	0.00	0.00	**2.00**	3	-	-	0.02	-	-	-	-	-	-	-	-
	Bt	Matrix	37.88	1.93	18.45	0.00	16.51	0.18	12.19	0.00	0.06	10.56	**97.76**	2.77	0.11	1.59	0.00	1.01	0.01	1.33	0.00	0.01	0.99	**7.82**	11	0.57	-	-	1.23	0.37	-	-	-	-	-	-
	Chl	Matrix	25.34	0.10	22.17	0.00	20.47	0.33	18.02	0.05	0.00	0.00	**86.48**	2.64	0.01	2.72	0.00	1.78	0.03	2.80	0.01	0.00	0.00	**9.99**	14	0.61	-	-	-	-	-	-	-	-	-	-
	Ms	Matrix	45.41	0.75	34.55	1.61	0.89	0.00	0.87	0.02	0.69	9.34	**94.13**	3.05	0.04	2.74	0.08	0.05	0.00	0.09	0.00	0.09	0.80	**6.94**	11	0.64	-	-	0.95	1.79	-	-	-	-	-	-
	Pl	Matrix	68.03	0.00	19.76	0.09	0.00	0.00	0.00	0.34	10.67	0.00	**98.89**	3.03	0.00	1.04	0.00	0.00	0.00	0.00	0.02	0.92	0.00	**5.00**	8	-	0.02	-	-	-	-	-	-	-	-	-

Table 6.6 – Mineral compositions for granitoid, metabasite and quartzo-feldspathic mylonite samples ET09-01, ET10-15b, ET10-16 and ET10-17.

Quartzo-feldspathic schist protolith

Mylonite samples ET10-15a, ET10-17 and ET10-18b are interpreted to have been derived from quartzo-feldspathic protoliths given their lack of typical pelitic metamorphic minerals (e.g. garnet, staurolite or aluminosilicate) and low proportions of phyllosilicates. These lithologies contain abundant quartz and plagioclase with minor epidote, ilmenite, muscovite and chlorite in microlithons, whereas cleavage domains are characterised by Ti-poor biotite (Fig. 6.11d). Mineral compositions from sample ET10-17, which are typical of all samples, are presented in Table 6.6

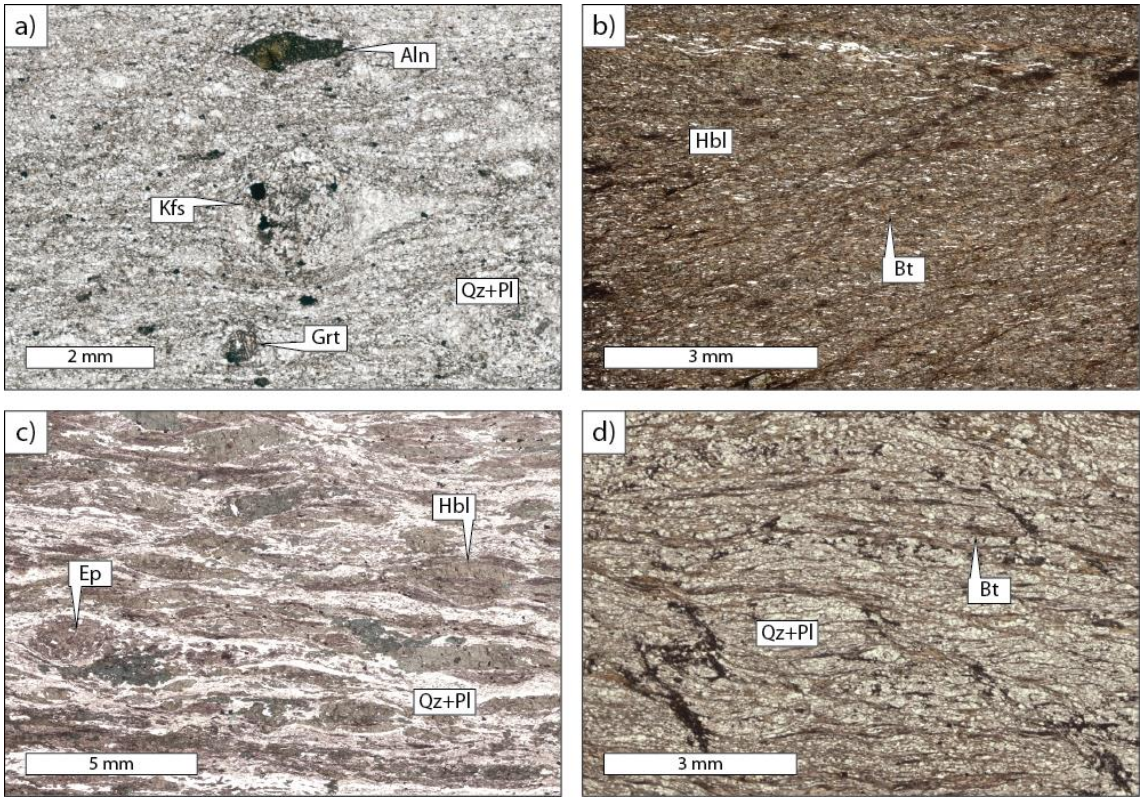


Fig. 6.11 – Petrography of granitoid, metabasite and quartzo-feldspathic mylonites (viewed in plane polarised light). (a) ET09-01. (b) S-C fabric in sample ET10-15b defined by biotite with hornblende in microlithons. (c) Strongly foliated sample ET10-16 with aligned hornblende grains and clusters of epidote. (d) ET10-17b quartzo-feldspathic mylonite with weak S-C fabric and cleavage domains defined by biotite.

Metapelite protolith

Samples ET09-02, ET10-13 and ET10-18a contain abundant phyllosilicate minerals alongside additional Barrovian-type index minerals that are characteristic of pelitic bulk compositions. Hence their protoliths are interpreted as amphibolite-facies metapelites. Compositions of constituent minerals from these samples are presented in Table 6.7.

Sample	Mineral	Location	SiO_2	TiO_2	Al_2O_3	Fe_2O_3	FeO	MnO	MgO	CaO	Na_2O	K_2O	**Total**	Si	Ti	Al	Fe^{3+}	Fe^{2+}	Mn	Mg	Ca	Na	K	**Sum**	Ox	XMg	XCa	XMn	Al(iv)	Al(vi)	Alm	Prp	Grs	Sps	XFe^{3+}
ET09-02	Bt	Matrix foliation	36.18	2.11	18.41	0.00	16.71	0.11	12.29	0.07	0.53	10.29	**96.70**	2.70	0.12	1.62	0.00	1.04	0.01	1.37	0.01	0.08	0.98	**7.93**	11	0.57	-	-	1.30	0.32	-	-	-	-	-
	Chl	Matrix foliation	25.47	0.13	21.56	0.95	18.38	0.23	18.66	0.04	0.19	0.23	**85.84**	2.66	0.01	2.65	0.08	1.61	0.02	2.90	0.00	0.04	0.03	**10.00**	14	0.64	-	-	-	-	-	-	-	-	-
	Ms	Matrix foliation	45.13	0.79	33.32	0.05	2.80	0.02	1.28	0.11	0.71	10.79	**95.00**	3.06	0.04	2.66	0.00	0.16	0.00	0.13	0.01	0.09	0.93	**7.08**	11	0.45	-	-	0.94	1.72	-	-	-	-	-
	Mt	Matrix	0.35	0.09	0.34	67.51	30.68	0.06	0.25	0.00	0.00	0.00	**99.28**	0.01	0.00	0.02	1.96	0.99	0.00	0.02	0.00	0.00	0.00	**3.00**	4	-	-	0.00	-	-	-	-	-	-	0.66
	Pl	Matrix	60.92	0.01	24.37	0.04	0.00	0.01	0.34	5.51	7.99	0.18	**99.37**	2.73	0.00	1.28	0.00	0.00	0.00	0.02	0.27	0.69	0.01	**5.00**	8	-	0.28	-	-	-	-	-	-	-	-
ET10-13	Bt	Matrix	36.35	1.90	19.39	0.00	19.11	0.00	10.28	0.10	0.08	9.46	**96.67**	2.71	0.11	1.71	0.00	1.19	0.00	1.14	0.01	0.01	0.90	**7.78**	11	0.49	-	-	1.29	0.42	-	-	-	-	-
	Bt	Within Grt strain shadow	36.40	0.77	20.70	0.00	18.79	0.02	9.84	0.08	0.17	9.21	**95.98**	2.72	0.04	1.83	0.00	1.18	0.00	1.10	0.01	0.03	0.88	**7.79**	11	0.48	-	-	1.28	0.55	-	-	-	-	-
	Chl	Within Grt strain shadow	24.51	0.17	20.84	0.00	25.37	0.05	14.04	0.07	0.07	0.08	**85.20**	2.67	0.01	2.68	0.00	2.31	0.01	2.28	0.01	0.01	0.01	**9.99**	14	0.50	-	-	-	-	-	-	-	-	-
	Grt	Core	36.47	0.21	20.77	1.13	24.48	7.27	0.78	8.19	0.00	0.00	**99.30**	2.97	0.01	1.97	0.09	1.73	0.43	0.11	0.70	0.00	0.00	**8.00**	12	0.06	-	-	-	-	0.58	0.04	0.24	0.14	-
	Grt	Rim	37.11	0.06	21.03	0.53	34.48	0.35	3.14	3.11	0.00	0.00	**99.81**	2.96	0.00	1.98	0.03	2.41	0.07	0.27	0.28	0.00	0.00	**8.00**	12	0.10	-	-	-	-	0.80	0.09	0.09	0.02	-
	Ilm	Inclusion in Grt core	0.40	52.76	0.25	0.00	45.52	1.08	0.39	0.02	0.01	0.01	**100.44**	0.01	0.99	0.01	0.00	0.95	0.02	0.02	0.00	0.00	0.00	**2.00**	3	-	-	0.02	-	-	-	-	-	-	-
	Ilm	Matrix	0.12	54.03	0.17	0.00	45.01	0.37	0.01	0.00	0.00	0.00	**99.71**	0.00	1.02	0.01	0.00	0.96	0.01	0.00	0.00	0.00	0.00	**2.00**	3	-	-	0.01	-	-	-	-	-	-	-
	Ms	Matrix	46.61	0.62	34.73	0.00	1.29	0.01	0.98	0.05	0.94	10.09	**95.32**	3.10	0.03	2.72	0.00	0.07	0.00	0.10	0.00	0.12	0.86	**7.00**	11	0.59	-	-	0.90	1.82	-	-	-	-	-
	Ms	Within Grt strain shadow	46.82	0.84	36.36	0.00	1.12	0.01	0.60	0.04	0.80	9.08	**95.67**	3.07	0.04	2.81	0.00	0.06	0.00	0.06	0.00	0.10	0.76	**6.90**	11	0.50	-	-	0.93	1.88	-	-	-	-	-
	Pl	Matrix	65.89	0.00	22.33	0.02	0.00	0.00	0.00	3.02	8.91	0.07	**100.24**	2.88	0.00	1.15	0.00	0.00	0.00	0.00	0.15	0.82	0.00	**5.00**	8	-	0.15	-	-	-	-	-	-	-	-
	Pl	Within Grt strain shadow	61.12	0.01	23.87	0.26	0.00	0.00	0.00	5.54	8.02	0.00	**98.82**	2.75	0.00	1.26	0.01	0.00	0.00	0.00	0.27	0.71	0.00	**5.00**	8	-	0.28	-	-	-	-	-	-	-	-
ET10-18a	Bt	Matrix	36.21	1.66	18.52	0.00	20.09	0.03	10.26	0.03	0.16	9.52	**96.48**	2.73	0.09	1.65	0.00	1.27	0.00	1.15	0.00	0.02	0.92	**7.83**	11	0.48	-	-	1.27	0.38	-	-	-	-	-
	Bt	Within Grt strain shadow	35.42	1.38	19.61	0.00	20.59	0.06	9.31	0.00	0.07	10.08	**96.52**	2.68	0.08	1.75	0.00	1.30	0.00	1.05	0.00	0.01	0.97	**7.84**	11	0.45	-	-	1.32	0.43	-	-	-	-	-
	Chl	Inclusion in Grt core	22.60	0.03	20.99	0.00	36.50	0.39	5.33	0.06	0.00	0.00	**85.90**	2.61	0.00	2.86	0.00	3.53	0.04	0.92	0.01	0.00	0.00	**9.97**	14	0.21	-	-	-	-	-	-	-	-	-
	Chl	Within Grt strain shadow	22.64	0.03	21.85	0.31	30.69	0.15	9.79	0.02	0.00	0.04	**85.52**	2.54	0.00	2.89	0.03	2.88	0.02	1.64	0.00	0.00	0.01	**10.01**	14	0.36	-	-	-	-	-	-	-	-	-
	Grt	Core	36.32	0.11	20.69	1.43	25.07	10.05	0.52	5.73	0.00	0.00	**99.92**	2.98	0.01	1.97	0.08	1.73	0.69	0.06	0.48	0.00	0.00	**8.00**	12	0.03	-	-	-	-	0.58	0.02	0.16	0.23	-
	Grt	Rim	36.63	0.05	20.96	1.04	32.96	0.07	2.69	4.68	0.00	0.00	**99.08**	2.98	0.00	1.99	0.06	2.26	0.01	0.30	0.40	0.00	0.00	**8.00**	12	0.12	-	-	-	-	0.76	0.10	0.13	0.00	-
	Ilm	Inclusion in Grt core	0.10	54.65	0.21	0.00	42.99	2.23	0.22	0.00	0.00	0.00	**100.40**	0.00	1.02	0.01	0.00	0.92	0.05	0.01	0.00	0.00	0.00	**2.01**	3	-	-	0.05	-	-	-	-	-	-	-
	Ilm	Matrix	0.07	52.68	0.27	0.00	46.60	0.02	0.47	0.00	0.00	0.00	**100.11**	0.00	1.00	0.01	0.00	0.98	0.00	0.02	0.00	0.00	0.00	**2.01**	3	-	-	0.00	-	-	-	-	-	-	-
	Ms	Matrix	46.25	0.45	36.25	0.00	1.18	0.02	0.58	0.03	1.07	10.18	**96.01**	3.05	0.02	2.82	0.00	0.07	0.00	0.06	0.00	0.14	0.86	**7.02**	11	0.46	-	-	0.95	1.87	-	-	-	-	-
	Ms	Within Grt strain shadow	46.79	0.27	35.81	0.00	1.66	0.00	0.56	0.01	0.67	10.08	**95.85**	3.09	0.01	2.79	0.00	0.09	0.00	0.06	0.00	0.09	0.85	**6.98**	11	0.40	-	-	0.91	1.88	-	-	-	-	-
	Pl	Matrix	59.48	0.00	24.02	0.00	0.00	0.00	0.04	5.89	7.81	0.05	**97.29**	2.71	0.00	1.29	0.00	0.00	0.00	0.00	0.30	0.70	0.00	**5.00**	8	-	0.30	-	-	-	-	-	-	-	-
	Pl	Within Grt strain shadow	60.33	0.00	24.59	0.23	0.00	0.02	0.00	6.17	7.77	0.05	**99.16**	2.69	0.00	1.30	0.01	0.00	0.00	0.00	0.30	0.70	0.00	**5.00**	8	-	0.30	-	-	-	-	-	-	-	-
	St	Inclusion in Grt rim	26.35	0.54	51.74	0.00	13.15	0.00	1.91	0.00	0.93	0.00	**94.62**	7.59	0.12	17.57	0.00	3.17	0.00	0.82	0.00	0.52	0.00	**29.79**	46	0.21	-	-	-	-	-	-	-	-	-
	St	Matrix	26.82	0.54	52.10	0.00	12.80	0.13	1.76	0.00	0.79	0.00	**94.94**	7.67	0.12	17.57	0.00	3.06	0.03	0.75	0.00	0.44	0.00	**29.64**	46	0.20	-	-	-	-	-	-	-	-	-

Table 6.7 – Mineral compositions for mylonitised metapelite samples ET09-02, ET10-13 and ET10-18a.

Sample ET09-02 contains biotite, muscovite, plagioclase, chlorite, quartz, rutile, magnetite, apatite, tourmaline, zircon, allanite and monazite. The dominant foliation occurs as a spaced cleavage and is defined by thick bands of finely-crystalline muscovite and biotite between thinner bands of quartz and plagioclase. This fabric is strongly crenulated (Fig. 6.12a). Randomly orientated clusters of chlorite occur throughout the sample, commonly in the hinge regions of microfolds (Fig. 6.12a).

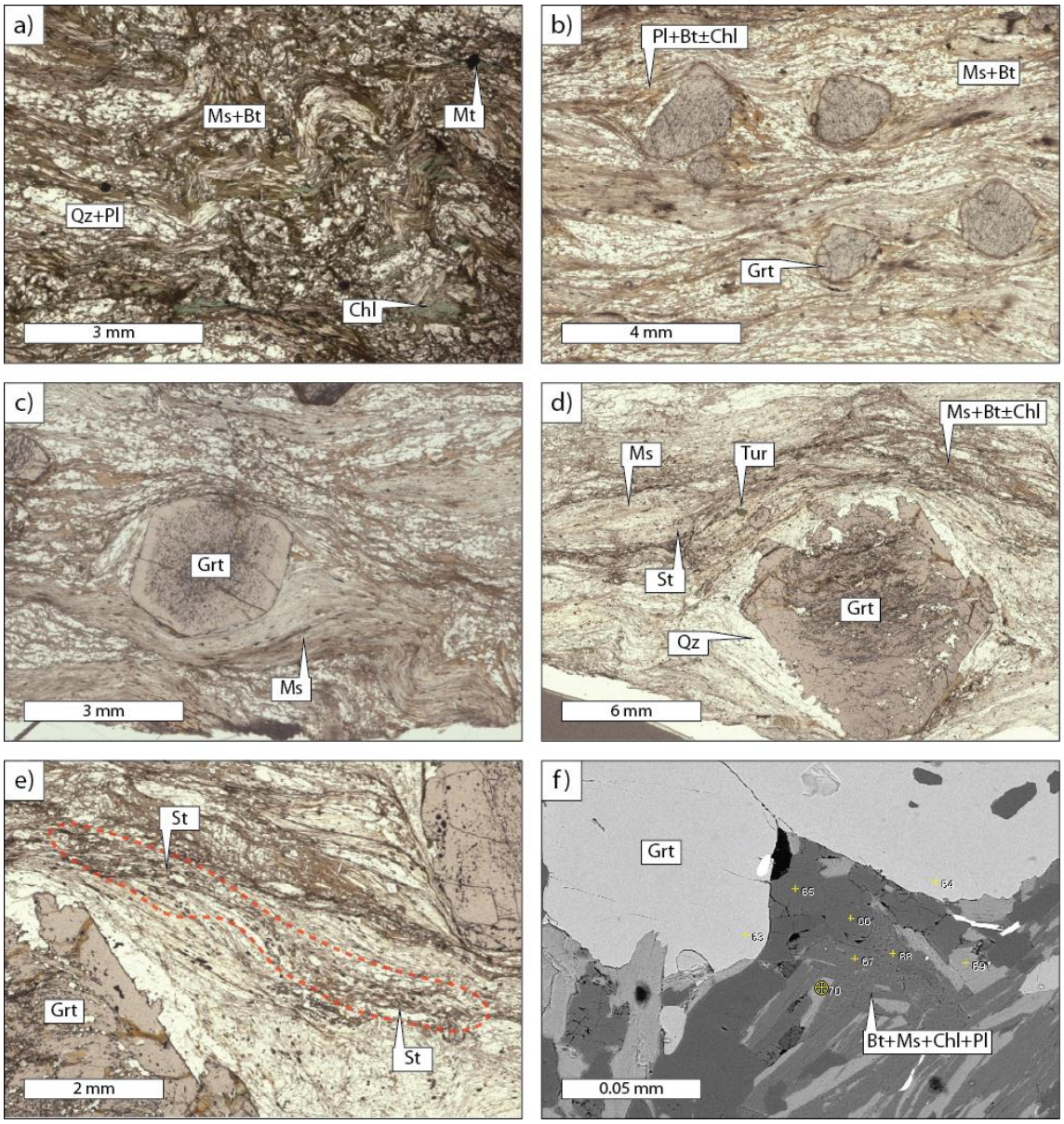


Fig. 6.12 – Petrography of mylonitised metapelites. Thin section images viewed under plane polarised light. (a) Sample ET09-02 with a strongly crenulated fabric defined largely by biotite and muscovite (b) Sample ET10-13 with rotated porphyroclasts of garnet showing randomly orientated inclusion trails that are discordant to the matrix foliation. (c) Sheaths of muscovite in ET10-13 exhibit complex folding. (d) Sample ET10-18a with large garnet porphyroclasts that contain sinusoidal inclusion trails in cores and inclusion-poor rims. (e) Sample ET10-18a with staurolite fragments present along specific foliation planes. (f) SEM BSE image of neocrystallised chlorite, biotite, muscovite and plagioclase in garnet strain shadow (in ET10-13).

Samples ET10-13 and ET10-18a contain the mineral assemblage garnet, ilmenite, epidote, plagioclase, tourmaline, biotite, muscovite, chlorite, quartz, zircon, apatite and monazite. Additional staurolite occurs in sample ET10-18a as fragments along specific foliation planes (Fig. 6.12e) and also as inclusions in garnet outer rims. Allanite occurs in garnet cores in both samples and additionally in the matrix in sample ET10-13, the latter having epitaxial overgrowths of epidote and being associated with apatite, xenotime and monazite. Garnet in both samples occurs as euhedral/subhedral porphyroclasts that contain compositionally and texturally distinct core and rim regions (Fig. 6.12c–d). Cores contain sigmoidal inclusion trails, defined primarily by quartz and ilmenite, which truncate against thin inclusion-poor rims. Representative compositional profiles are presented in Fig. 6.13. In both cases spessartine and grossular contents decrease from core to rim, whereas almandine and pyrope contents show the opposite trend. Garnet in sample ET10-18a shows an additional outer rim region that is richer in Ca and depleted in Fe (Fig. 6.13b). In both samples the Mn content of ilmenite inclusions in garnet shows a strong positive correlation with the spessartine content of garnet. Inclusions in garnet cores contain up to XMn = 0.05 (ET10-18a) and XMn = 0.03 (ET10-13) and those in garnet outer rims and the matrix contain XMn <0.01 (Table 6.7).

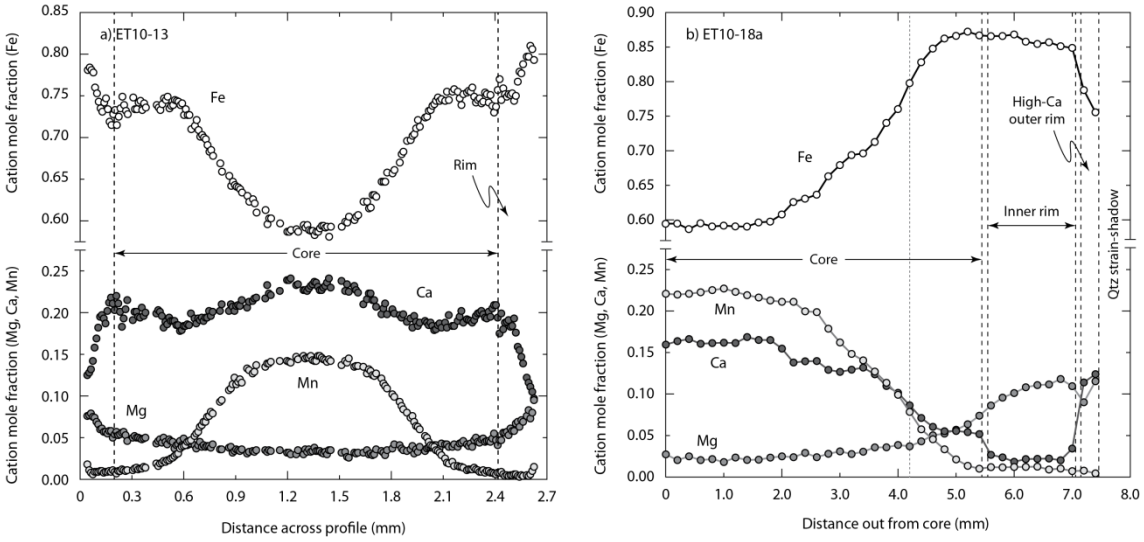


Fig. 6.13 – Compositional garnet line profiles for mylonitised metapelite samples (a) ET10-13 (rim-to-rim) and (b) ET10-18a (core-to-rim). Line profiles are non-continuous as traverses cross inclusions and fractures.

The dominant mylonitic foliation in both samples wraps garnet (e.g. Fig. 6.12b) and is defined by muscovite, biotite, and minor ilmenite. In places tight microfolds appear to have formed by deformation of an original fabric (Fig. 6.12c), supported by the observation that inclusions patterns

in garnet are different throughout the same thin section plane; therefore, rotation of the previous microstructure must have taken place. Garnet strain shadows are populated by randomly orientated quartz, chlorite, biotite, muscovite and plagioclase grains (Fig. 6.12f). Chlorite does not occur in the matrix in either sample. Compositions of all major minerals are presented in Table 6.7.

6.4. Textural and compositional interpretation

6.4.1. Upper amphibolite-facies migmatites

K-feldspar-bearing migmatites (ET09-05, ET09-06, ET10-03, ET10-07 and ET10-09)

In upper amphibolite-facies metapelites at mid-crustal pressures, the first appearance of anatectic melt can be attributed to the intersection of the wet granite solidus and destabilisation of primary muscovite through either of the following reactions (Pëto, 1976; Patiño Douce & Harris, 1998):

$$\text{muscovite} + \text{quartz} + \text{plagioclase} + H_2O \rightarrow \text{aluminosilicate} + \text{melt} \quad (6.4.1)$$

$$\text{muscovite} + \text{quartz} + \text{plagioclase} + \text{K-feldspar} + H_2O \rightarrow \text{melt} \quad (6.4.2)$$

However, the volume of melt produced from either of these reactions is very small, unless a substantial external supply of fluid is available (Thompson, 1982; Pattison & Tracy, 1991). Instead, with continued prograde metamorphism, volumetrically significant melting will occur via the fluid-absent dehydration melting reaction 6.4.3, often referred to as the 'upper sillimanite' or 'second sillimanite isograd', forming a K-rich neosome (García-Casco *et al*., 2003):

$$\text{muscovite} + \text{quartz} + \text{plagioclase} \rightarrow \text{K-feldspar} + \text{aluminosilicate} + \text{melt} \quad (6.4.3)$$

Leucosomes in samples ET09-05 and ET09-06 contain minor muscovite and abundant K-feldspar, whereas the reverse is true for samples ET10-03, ET10-07 and ET10-09; however, in all cases partial melt is interpreted to have formed through reaction 6.4.3. Melt formation is thought unlikely to have occurred through reactions 6.4.1 and 6.4.2, which do not produce K-feldspar, because compositional and textural relationships between muscovite, sillimanite and K-feldspar in each sample (described below) indicate that varying degrees of retrogression have taken place.

Ashworth (1975) notes that K-feldspar is often absent from sillimanite-grade migmatites in which it was likely present at peak metamorphism, most commonly having been replaced by muscovite. This can be demonstrated by identifying between different generations of muscovite through textural or compositional characteristics. Primary (prograde) muscovite that survives the

partial melting process commonly occurs as flakes orientated in the mesosome foliation (Tyler & Ashworth, 1982). By contrast, secondary (retrograde) muscovite mostly occurs as fine grained randomly orientated mats (Tyler & Ashworth, 1982), as large lath-like porphyroblasts that include sillimanite, or as symplectic intergrowths with quartz (Ashworth, 1975, 1979). Furthermore, primary muscovite commonly contains higher paragonite content than secondary muscovite that has formed during the replacement of K-feldspar (Ashworth, 1975; Evans & Guidiotti, 1966). Low Si content (<3.10 cpfu per 11-oxygens) coupled with high Ti content (up to 0.08 cpfu) is also typical of high-grade and magmatic muscovite (Miller *et al*., 1981; Guidiotti, 1984).

Muscovite in leucosomes in all samples is low in Si and contains a moderate-to-high Ti content (Table 6.4), suggesting that all primary grains were consumed during anatexis (reaction 6.4.3) and those currently present formed either during melt crystallisation or retrogressively whilst still at high-temperature. This compositional evidence is supported by textural features in samples ET10-07 and ET10-09, which have muscovite laths containing abundant fibrolite inclusions (Fig. 6.7c–d) and also muscovite-quartz symplectitic intergrowths (Fig. 6.7e). These features are typical of retrograde replacement of K-feldspar whilst at sillimanite-grade conditions (Evans & Guidiotti, 1966; Ashworth 1975; Brown, 2002), the reversal of reaction 6.4.3. The overall lack of retrograde replacement of K-feldspar (and garnet) in samples ET09-05 and ET09-06 suggests that a large proportion of vapour was lost from the local system during melt crystallisation and thus subsolidus cooling took place in a fluid-poor environment (Peterson & Grove, 2010; White & Powell, 2002).

The petrological effects of whether fluid is lost or retained in these lithologies have been shown by Wintsch (1975), who calculated activity diagrams in the system $KAlSi_3O_8$–$NaAlSi_3O_8$–SiO_2–H_2O–HCl and investigated the effects of pressure, temperature and aH_2O on the stability of aluminosilicate, K-feldspar, albite, muscovite and paragonite (Fig. 6.14). At a nominal mid-crustal pressure (5 kbar), assuming excess fluid for reactions, cooling through the ~650 °C isotherm with a fluid that had previously equilibrated with a muscovite-absent assemblage will induce the breakdown of K-feldspar, plagioclase and aluminosilicate. With decreasing temperature and a fixed fluid composition, muscovite will form in place of these aforementioned phases (Fig. 6.14). This process may also occur via the infiltration of externally-derived fluid moving down a temperature gradient, for example fluid released during melt crystallization at deeper crustal levels.

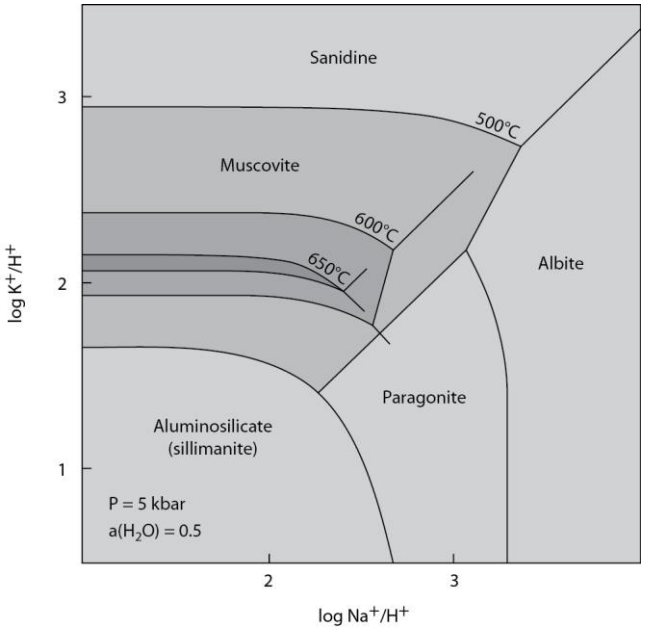


Fig. 6.14 – Activity diagram for selected sillimanite-grade minerals showing the relative stability of each according to coexisting fluid composition (after Wintsch, 1975). The stability field of muscovite in compositional space is shown by successively darker shades of grey that vary with temperature.

K-feldspar-absent migmatites (ET10-10 and ET10-12)

Samples ET10-10 and ET10-12 do not exhibit any of the K-feldspar replacement features described above, suggesting that their leucosomes were never of a granitic composition and thus a K-feldspar-absent melting reaction must be responsible for their formation. The range in *P–T* space over which such K-feldspar-absent reactions operate is extended to lower temperatures in the presence of excess H_2O (García-Casco *et al*., 2001, 2003; Cruciani *et al*., 2008). Increasing pressure also favours fluid-saturated melting reactions prior to attainment of conditions that favour dehydration melting (during an increase in temperature). The inverse correlation between pressure and plagioclase stability causes an increase in the plagioclase/muscovite ratio consumed in melting reactions with increasing pressure (Patiño Douce & Harris, 1998), and increasing H_2O activity leads to preferential solution of plagioclase components by lowering the Pl+Qz solidus (Conrad *et al*., 1988). These conditions result in the shift of H_2O-fluxed melting towards tonalitic/trondhjemitic compositions being more evident at high-pressure (Cruciani *et al*., 2008).

Garnet porphyroblasts in leucosome segregations (e.g. type 2 garnet in sample ET10-12) often exhibit idioblastic rims (Fig. 6.7f–g), a microstructural feature in migmatites that is often interpreted to represent growth in the presence of melt (Whitney & Irving, 1994; Guilmette *et al*., 2011). This

inference is supported by distinctly different core and rim compositions (cf. sample ET10-12; Fig. 6.8d) suggesting that garnet growth occurred in two stages, each at different *P–T* conditions (chapter 4.4.1). In the case of Fe and Ca content, rim compositions may be separated from core compositions by an abrupt step (Fig. 6.8c–d); otherwise, the transition is gradational. Smooth transitions, where developed, are interpreted as diffusion profiles that formed between two initially separate compositional regions (e.g. Caddick *et al.*, 2010). In sample ET10-10, this two-stage growth scenario is also supported by the presence of sillimanite inclusions in garnet cores and kyanite in the matrix. Additionally, kyanite is commonly aligned with the mesosome foliation and wraps against garnet rims (Fig. 6.7f), indicating that partial melting occurred at high-pressure. In sample ET10-10, partial melting may therefore have occurred through the following reaction that has been proposed by García-Casco *et al*. (2001) for similar kyanite-bearing migmatites:

$$\text{biotite} + \text{muscovite} + \text{plagioclase} + \text{quartz} + H_2O \rightarrow \text{garnet} + \text{kyanite} + \text{melt} \quad (6.4.4)$$

However, Winchester (1974) has shown that an Al-poor rock (i.e. semi-pelite domains in sample ET10-12), which thus has a relatively higher CaO/Al_2O_3 bulk compositional ratio than a typical metapelite, does not allow aluminosilicate to achieve equilibrium in the presence of excess silica. Here, the equilibrium 6.4.5 leads to plagioclase forming instead (ibid):

$$CaO + \text{quartz} + \text{aluminosilicate} \rightarrow \text{anorthite} \quad (6.4.5)$$

K-poor neosomes in sample ET10-12 therefore likely formed through the following sample-specific reaction, a combination of reactions 6.4.4 and 6.4.5, which also results in the production of peritectic garnet, consistent with the observations outlined above:

$$\text{biotite} + \text{muscovite} + \text{albitic plagioclase} + \text{quartz} + H_2O \rightarrow \text{garnet} + \text{melt} \quad (6.4.6)$$

6.4.2. Mylonites

Analysed mylonites have a wide range in interpreted protolith, although granitoid, metabasite and quartzo-feldspathic units retain little useful evidence of their pre-mylonitisation tectonothermal history. By contrast, metapelitic units have a much superior potential to document changes in *P–T* conditions, as prograde parageneses may be included in garnet porphyroblasts. Furthermore, the presence of monazite in these samples allows age constraints to be obtained. Garnet in samples ET10-13 and ET10-18a contains bell-shaped spessartine profiles (Fig. 6.13), characteristic of continuous prograde growth through the upper greenschist and/or amphibolite-facies (Harte &

Henley, 1966; Chinner, 1962; Tracy, 1982). The sigmoidal inclusion pattern of quartz and ilmenite in core regions, which truncates sharply at inclusion-free rims (e.g. Fig. 6.12c–e), is interpreted as syn-tectonic rotational growth during deformation/metamorphism (Passchier & Trouw, 2004).

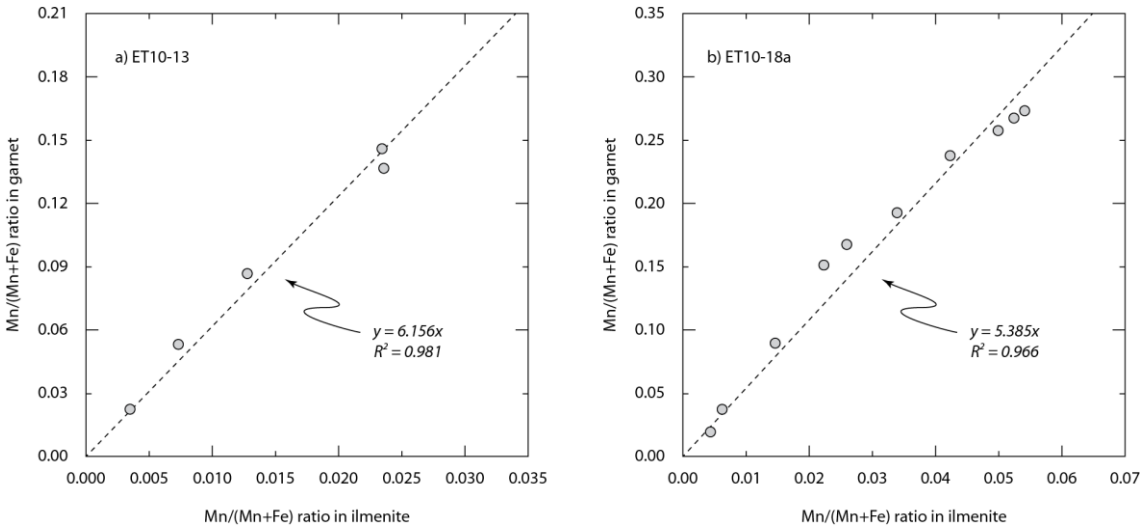


Fig. 6.15 – Mn-partitioning between garnet and ilmenite in samples ET10-13 and ET10-18a. Best-fit trendlines are constrained to pass through the origin (0,0).

The decreasing Mn content of ilmenite inclusions from garnet core to rim in both samples (Fig. 6.15) supports this interpretation since, in a situation where garnet grew helicitically over an already formed sinusoidal fabric, entrapped ilmenite compositions would all be approximately similar. Thermobarometric analysis of these inclusions and host garnet allows investigation into the maximum temperature of prior prograde metamorphism (shown later in chapter 6.6.3).

6.5. U–Th–Pb monazite geochronology

Geochronological analysis was performed on a subset of monazite-bearing samples, comprising upper-amphibolite facies migmatite samples ET09-05, ET09-06, ET10-07, ET10-09 and ET10-10, and mylonitised metapelite samples ET09-02, ET10-13 and ET10-18a. By selecting samples with assemblages suitable for thermobarometry, geochronological data could be used to constrain the *P*–*T*–*t* evolution of the B-L-M region.

6.5.1. Monazite chemistry and U–Pb ages

Geochronological analysis was performed following the methods outlined in chapter 3.5.1 and all U–Pb data are interpreted on Tera-Wasserburg plots that are shown in Fig. 6.16. U–Pb ages for

monazite in samples ET09-05 and ET09-06 are given in Table 6.8. U–Th–Pb ages for samples ET10-07, ET10-09, ET10-10, ET10-13, ET10-18a and ET09-02 are given in Table 6.9 and Table 6.10. Relevant MC–ICP–MS and SC–ICP–MS isotopic data are given in Table 11.1 and Table 11.2. Compositions of monazite domains for all samples are given in Table 6.11 and are from grains shown in Fig. 6.17. As noted in chapter 3.5.1, Y_2O_3 is used as a proxy for HREE concentration.

ET09-05 and ET09-06 – Muscovite-poor sillimanite migmatite

Monazite exists in leucosome segregations in samples ET09-05 and ET09-06 and additionally as garnet rim inclusions in sample ET09-05. Grains in both textural positions in sample ET09-05 are typically concentrically zoned (Fig. 6.17a) and contain variable Y_2O_3 and ThO_2 contents (Table 6.11). Although Y_2O_3 zonation is not systematic between core and rim domains, the monazite inclusions generally have a higher Y_2O_3 content (1.52–1.80 wt%) than the grains in the leucosome (0.85–1.26 wt%), suggesting that grains in the leucosome formed after the onset of garnet growth. Grains in sample ET09-06 have chaotic internal zoning patterns visible in SEM BSE images (Fig. 6.17b), although their large size (~200 μm) allowed individual internal domains to be analysed.

Analysis	Position	Calculated age (Ma)						Corrected age (Ma)	
		$^{207}Pb/^{206}Pb$ 2σ (abs)		$^{206}Pb/^{238}U$ 2σ (abs)		$^{207}Pb/^{235}U$ 2σ (abs)		$^{206}Pb/^{238}U$ 2σ (abs)	
ET09-05 mnz 2_1	Leucosome	214	20	69.1	1.4	73.3	1.7	68.8	1.4
ET09-05 mnz 2_2	Leucosome	237	16	65.7	1.2	70.5	1.5	65.4	1.2
ET09-05 mnz 2_3	Leucosome	244	19	71.1	1.3	76.4	1.6	70.8	1.3
ET09-05 mnz 4_1	Inclusion in Grt rim	102	18	68.7	1.3	69.7	1.4	68.7	1.2
ET09-05 mnz 4_2	Inclusion in Grt rim	235	29	71.0	1.3	76.0	1.7	70.7	1.2
ET09-05 mnz 4_3	Inclusion in Grt rim	107	18	62.9	1.1	64.0	1.3	62.8	1.1
ET09-05 mnz 4_4	Inclusion in Grt rim	533	32	72.0	1.2	87.5	2.0	71.0	1.2
ET09-05 mnz 4_5	Inclusion in Grt rim	250	21	72.6	1.3	78.1	1.6	72.2	1.3
ET09-05 mnz 4_6	Inclusion in Grt rim	109	21	64.3	1.1	65.5	1.3	64.2	1.1
ET09-05 mnz 4_7	Inclusion in Grt rim	530	195	61.8	1.3	75.4	7.1	61.0	1.3
ET09-05 mnz 4_8	Inclusion in Grt rim	206	22	69.1	1.2	73.1	1.5	68.8	1.2
ET09-05 mnz 5_1	Leucosome	144	20	68.1	1.2	70.3	1.4	68.0	1.2
ET09-05 mnz 5_2	Leucosome	213	24	70.4	1.2	74.6	1.5	70.1	1.2
ET09-06 mnz 1_1	Leucosome	327	50	69.8	1.4	77.7	2.4	69.3	1.4
ET09-06 mnz 1_2	Leucosome	142	31	72.6	1.5	74.7	1.9	72.5	1.4
ET09-06 mnz 1_3	Leucosome	190	34	67.7	1.4	71.2	1.8	67.5	1.3
ET09-06 mnz 1_4	Leucosome	202	39	65.9	1.3	69.8	1.9	65.7	1.3
ET09-06 mnz 1_5	Leucosome	122	20	63.7	1.5	65.2	1.7	63.6	1.5
ET09-06 mnz 1_6	Leucosome	68	23	48.4	1.0	48.8	1.2	48.5	1.0
ET09-06 mnz 1_7	Leucosome	117	25	56.7	1.2	58.1	1.4	56.6	1.2
ET09-06 mnz 3_1	Leucosome	97	20	62.7	1.2	63.6	1.4	62.6	1.2
ET09-06 mnz 3_2	Leucosome	86	17	60.2	1.2	60.9	1.3	60.2	1.1
ET09-06 mnz 3_3	Leucosome	278	22	68.5	1.4	74.7	1.8	68.1	1.4
ET09-06 mnz 3_4	Leucosome	185	19	68.2	1.3	71.5	1.6	68.0	1.3
ET09-06 mnz 3_5	Leucosome	169	22	66.4	1.3	69.3	1.5	66.3	1.3
ET09-06 mnz 3_6	Leucosome	68	20	59.4	1.2	59.6	1.3	59.4	1.1
ET09-06 mnz 3_7	Leucosome	770	78	67.4	1.4	91.2	4.0	65.8	1.3

Table 6.8 – MC–ICP–MS U–Pb ages for samples ET09-05 and ET09-06.

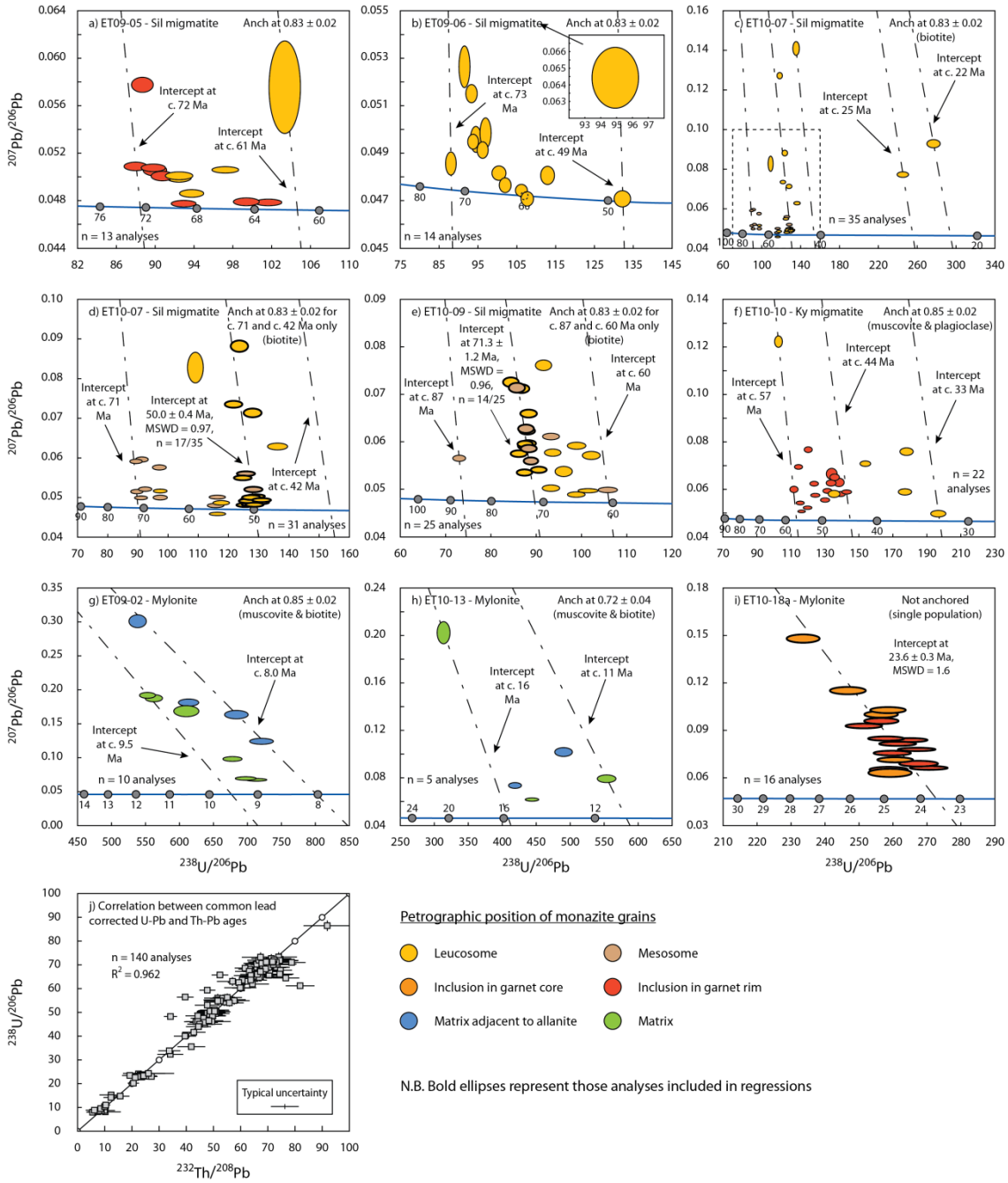


Fig. 6.16 – Tera-Wasserburg plots for samples from the B-L-M region. Dashed lines indicate regressions from sample-specific measured common lead ratios, unless a population is unanchored, and all ages represent intersections with concordia. (a) ET09-05. (b) ET09-06. (c) ET10-07. (d) ET10-07 detail on main population. (e) ET10-09. (f) ET10-10. (g) ET09-02. (h) ET10-13. (i) ET10-18. (j) Correlation between common lead corrected U–Pb ages and Th–Pb ages, each plotted with an associated uncertainty. The uncertainty on some U–Pb results is smaller than the symbol used. A reference 1:1 line for U–Pb ages and Th–Pb ages is shown marked at 10 Myr intervals.

Significant variation in ThO_2 content exists amongst bright and dull domains (between 9.47–16.86 wt%) with UO_2 content up to 2.15 wt% (Table 6.11). Y_2O_3 content shows an inverse-correlation with ThO_2 content, with the most Y_2O_3-rich domains (0.84 wt%) being Th-poor (9.47

wt%; Table 6.11). A total of 14 spot analyses were obtained from 3 grains in sample ET09-05 and 14 spot analyses were obtained from 2 large grains in sample ET09-06. One analysis was rejected from sample ET09-05 owing to very high common lead content. Sample ET09-05 produced a range of U–Pb lower intercept ages between c. 72–61 Ma (Fig. 6.16a) and sample ET09-06 leucosome grains gave a range of U–Pb lower intercept ages between c. 73–49 Ma (Fig. 6.16b).

ET10-07 and ET10-09 – Muscovite-rich sillimanite migmatite

Monazite in samples ET10-07 and ET10-09 occurs in leucosome and mesosome segregations, is commonly large (up to ~150 μm in diameter) and contains distinct core-rim relations. Grains in sample ET10-07 occasionally show small bright core regions surrounded by multi-layered darker rims (Fig. 6.17c) or more typically contain broad dull cores mantled by thin rims (Fig. 6.17d). Small bright cores (Fig. 6.17c) have high concentrations of ThO_2 (14.46–17.41 wt%) but low Y_2O_3 content (1.91–1.93 wt%), whereas duller rim regions are ThO_2-poor (6.07–7.75 wt%) and Y_2O_3-rich (3.78–4.08 wt%). Monazite in sample ET10-09 typically contains simple core-rim relations with bright spots that are ThO_2-rich (11.78–15.36 wt%) and Y_2O_3-rich (2.94–3.01 wt%) surrounded by dull rims with a much lower ThO_2 content (4.05–5.82 wt%) but are equally Y_2O_3-rich (2.65–3.40 wt%).

Garnet is absent from sample ET10-09 and is a very minor mineral in sample ET10-07, often surrounded by biotite, indicating post-peak replacement. Muscovite-quartz and biotite-quartz symplectites in both samples (e.g. Fig. 6.7e) suggest that a proportion of melt was retained in leucosomes and, on crystallisation, released fluid that facilitated retrogressive garnet breakdown (White & Powell, 2002). Although monazite cores in sample ET10-07 are Y_2O_3-poor, so likely grew in environment containing garnet, other relatively Y_2O_3-rich rims (ET10-07) and Y_2O_3-rich grains (ET10-09) are interpreted to have crystallised during or after retrograde garnet breakdown.

A total of 35 spot analyses obtained from 12 grains in sample ET10-07 produced a range of U–Pb lower intercept ages between c. 71–42 Ma (Fig. 6.16d) for the vast majority of analyses (n = 33/35); although, two spot analyses in the same grain produced much younger U–Pb ages of c. 25 Ma and c. 22 Ma (Fig. 6.16d). Given the large number of data points for each sample, some were selectively excluded from regressions on a statistical basis, whereby their inclusion resulted in an increase in the calculated MSWD value too far above the ‘expectation’ value of 1.00 (Wendt & Carl,

1991). This limiting value was calculated as MSWD = 1 + 2*(2/(n-2))$^{1/2}$, where n is the number of data points included in the regression, and a result above this value is taken to imply that the considered points have < 5% probability of representing a single population (ibid).

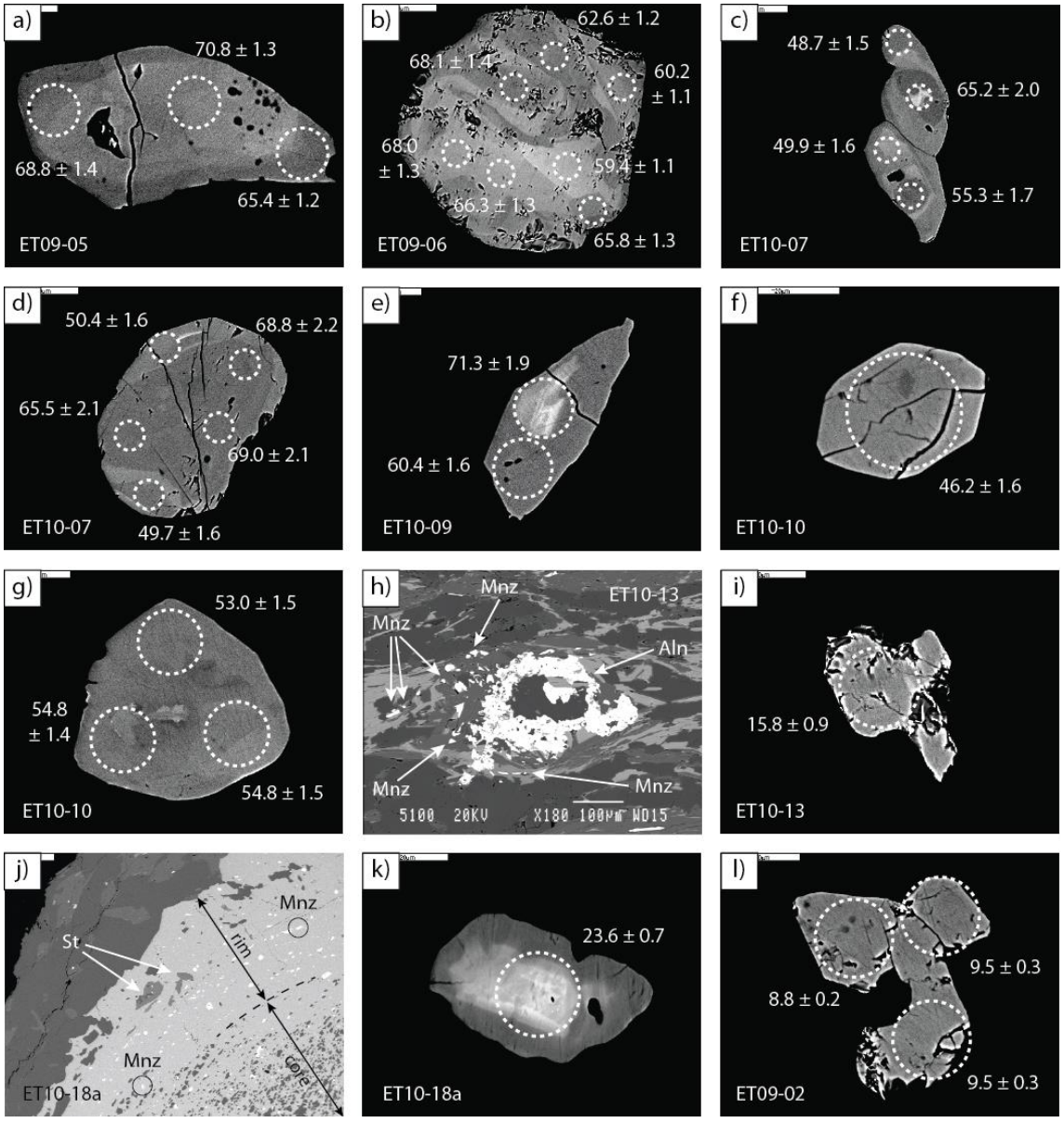


Fig. 6.17 – SEM BSE images of monazite for samples from the B-L-M region. Dashed circles indicate the position of individual spot analyses and U–Pb ages given are those after correction for common lead. In all monazite images, BSE contrast levels are fixed so that greyscale intensities are equivalent. Scale is given by spot sizes (20 µm diameter). (a) ET09-05. (b) ET09-06. (c) ET10-07. (d) ET10-07. (e) ET10-09. (f) ET10-10. (g) ET10-10. (h) Allanite in sample ET10-13 wrapped by the mylonitic foliation (running left to right) and encircled by small grains of monazite. White scale bar at bottom of image equals 100 µm. (i) ET10-13. (j) Garnet in sample ET10-18a showing the petrographic relationship between analysed monazite and staurolite inclusions in rim regions. Field of view is approximately 1 mm along long axis. (k) ET10-18a. (l) ET09-02.

Analysis	Position	Calculated age (Ma)								Corrected age (Ma)			
		$^{207}Pb/^{206}Pb$	2σ (abs)	$^{206}Pb/^{238}U$	2σ (abs)	$^{207}Pb/^{235}U$	2σ (abs)	$^{208}Pb/^{232}Th$	2σ (abs)	$^{208}Pb/^{232}Th$	2σ (abs)	$^{206}Pb/^{238}U$	2σ (abs)
ET10-07 mnz 1_1	Leucosome	142	20	50.4	1.6	52.3	1.8	49.0	2.5	48.9	5.0	50.2	1.6
ET10-07 mnz 1_2	Leucosome	212	14	49.8	1.5	53.2	1.7	51.1	2.6	50.9	5.1	49.5	1.5
ET10-07 mnz 2_1	Leucosome	139	15	49.2	1.5	51.1	1.7	48.6	2.4	48.5	4.8	49.1	1.5
ET10-07 mnz 2_2	Leucosome	112	15	50.4	1.5	51.7	1.7	51.2	2.7	51.1	5.2	50.3	1.6
ET10-07 mnz 3_1	Leucosome	156	16	50.8	1.6	53.1	1.8	49.5	2.4	49.4	4.9	50.4	1.6
ET10-07 mnz 3_2	Leucosome	411	16	51.5	1.6	59.9	2.0	49.7	2.3	49.5	4.7	50.6	1.6
ET10-07 mnz 3_3	Leucosome	1030	16	52.8	1.6	81.3	2.7	49.6	2.4	49.1	4.9	50.4	1.6
ET10-07 mnz 4_1	Leucosome	1265	60	58.8	1.8	101.1	6.6	53.3	2.6	51.7	5.0	56.0	1.8
ET10-07 mnz 4_2	Leucosome	2240	28	47.5	1.5	136.4	5.9	46.6	2.3	42.8	4.3	41.7	1.4
ET10-07 mnz 4_3	Leucosome	106	16	51.1	1.6	52.3	1.7	49.4	2.5	49.4	4.9	50.8	1.6
ET10-07 mnz 4_4	Leucosome	133	18	54.6	1.7	56.4	1.9	54.1	2.6	54.1	5.3	54.4	1.7
ET10-07 mnz 5_1	Leucosome	8	15	55.2	1.7	53.8	1.7	51.5	2.7	51.6	5.2	55.3	1.7
ET10-07 mnz 5_2	Leucosome	197	18	50.3	1.6	53.5	1.8	49.8	2.4	49.7	4.8	49.9	1.6
ET10-07 mnz 6_1	Leucosome	271	14	65.8	2.0	71.7	2.3	66.1	3.2	66.0	6.3	65.2	2.0
ET10-07 mnz 6_2	Leucosome	166	15	49.0	1.5	51.5	1.7	49.7	2.4	49.6	4.7	48.7	1.5
ET10-07 mnz 7_1	Mesosome	265	16	71.5	2.1	77.4	2.5	70.4	3.5	70.0	6.8	71.0	2.2
ET10-07 mnz 7_2	Mesosome	515	17	66.0	2.1	79.8	2.7	68.0	3.2	67.4	6.5	65.0	2.0
ET10-07 mnz 7_3	Mesosome	193	15	70.4	2.2	74.0	2.4	71.3	3.7	71.0	7.2	70.1	2.2
ET10-07 mnz 8_1	Mesosome	100	18	55.5	1.7	56.5	1.9	56.3	2.9	56.2	5.7	55.4	1.7
ET10-07 mnz 9_1	Mesosome	292	16	69.4	2.2	76.1	2.5	70.1	3.5	69.8	7.0	68.8	2.2
ET10-07 mnz 9_2	Mesosome	591	15	70.2	2.1	87.5	2.8	71.7	3.7	70.4	7.1	69.0	2.1
ET10-07 mnz 9_3	Mesosome	196	18	65.8	2.1	69.5	2.4	64.1	3.2	63.8	6.3	65.5	2.1
ET10-07 mnz 9_4	Mesosome	455	15	51.0	1.6	60.6	2.0	51.1	2.7	50.6	5.3	50.4	1.6
ET10-07 mnz 9_5	Mesosome	288	20	50.1	1.5	55.3	1.9	48.1	2.5	47.8	4.8	49.7	1.6
ET10-07 mnz 10_1	Mesosome	201	15	55.2	1.7	58.6	1.9	57.9	2.9	57.7	5.7	54.9	1.7
ET10-07 mnz 10_2	Mesosome	572	13	71.7	2.2	88.6	2.8	74.0	3.5	73.5	7.0	70.3	2.2
ET10-07 mnz 11_1	Leucosome	109	17	49.9	1.5	51.2	1.7	49.5	2.5	49.4	4.9	49.8	1.5
ET10-07 mnz 11_2	Leucosome	1388	21	51.9	1.6	95.3	3.4	51.0	2.5	48.7	4.8	49.1	1.5
ET10-07 mnz 12_1	Leucosome	1130	24	26.2	0.8	43.2	1.7	22.6	1.2	22.5	2.4	24.2	0.8
ET10-07 mnz 12_2	Leucosome	969	21	50.2	1.5	75.2	2.7	50.8	2.5	49.6	4.8	48.5	1.5
ET10-07 mnz 12_3	Leucosome	166	19	50.6	1.6	53.1	1.8	49.7	2.4	49.6	4.8	50.2	1.6
ET10-07 mnz 12_4	Leucosome	705	19	47.1	1.5	62.7	2.2	44.4	2.3	43.7	4.4	46.1	1.5
ET10-07 mnz 12_5	Leucosome	152	17	49.5	1.5	51.6	1.7	48.8	2.3	48.7	4.7	49.2	1.5
ET10-07 mnz 12_6	Leucosome	1487	28	23.2	0.8	46.0	2.0	20.8	1.1	20.6	2.1	20.2	0.7
ET10-07 mnz 12_7	Leucosome	2061	15	54.2	1.7	140.4	4.6	53.5	2.7	49.7	5.0	48.6	1.5
ET10-09 mnz 1_1	Leucosome	522	19	68.5	1.8	82.9	2.5	67.8	3.6	67.2	6.6	67.4	1.7
ET10-09 mnz 1_2	Leucosome	594	16	72.6	1.8	90.6	2.5	72.8	4.0	71.7	7.2	71.4	1.8
ET10-09 mnz 2_1	Leucosome	1003	18	75.9	2.0	113.8	3.5	75.6	3.6	74.0	6.7	73.3	2.0
ET10-09 mnz 2_2	Leucosome	806	17	72.6	2.0	99.5	3.0	68.8	3.7	67.8	6.7	70.7	1.9
ET10-09 mnz 3_1	Leucosome	354	18	73.3	1.9	82.4	2.4	71.8	4.0	71.3	7.3	72.6	1.9
ET10-09 mnz 5_1	Leucosome	575	20	73.1	1.9	90.4	2.7	74.7	3.6	74.2	6.9	71.7	1.9
ET10-09 mnz 6_1	Leucosome	146	18	64.9	1.7	67.1	2.0	67.1	3.6	66.9	6.7	64.7	1.7
ET10-09 mnz 6_2	Leucosome	589	16	73.2	1.9	91.1	2.6	75.0	3.7	74.4	6.9	71.8	1.8
ET10-09 mnz 6_3	Leucosome	964	17	73.9	1.9	108.9	3.2	73.6	3.8	72.5	7.1	71.4	1.9
ET10-09 mnz 7_1	Leucosome	686	17	72.8	1.8	94.6	2.7	73.8	3.6	73.2	6.8	71.1	1.8
ET10-09 mnz 8_1	Mesosome	970	19	74.7	2.0	110.4	3.5	73.2	3.6	72.3	6.7	72.1	2.0
ET10-09 mnz 8_2	Mesosome	554	19	72.5	1.9	88.9	2.7	69.9	3.7	69.5	6.7	71.2	1.9
ET10-09 mnz 11_1	Leucosome	379	18	70.8	1.8	80.5	2.3	72.7	3.8	72.1	6.9	70.1	1.8
ET10-09 mnz 11_2	Leucosome	499	22	62.8	1.6	75.5	2.3	65.1	3.3	64.4	6.0	61.9	1.6
ET10-09 mnz 12_1	Mesosome	476	17	87.7	2.2	103.1	2.9	92.5	4.7	91.9	8.7	86.5	2.2
ET10-09 mnz 13_1	Mesosome	453	20	72.2	1.7	84.7	2.4	71.9	3.8	71.5	6.9	71.1	1.7
ET10-09 mnz 13_2	Mesosome	645	16	68.7	1.8	87.9	2.6	69.1	3.6	68.3	6.5	67.4	1.8
ET10-09 mnz 14_1	Mesosome	702	20	73.0	1.9	95.6	2.9	72.4	3.7	71.8	6.9	71.3	1.9
ET10-09 mnz 14_2	Mesosome	192	18	60.6	1.6	64.0	1.9	60.1	3.2	59.9	5.9	60.4	1.6
ET10-09 mnz 15_1	Leucosome	513	18	74.4	2.0	89.5	2.7	67.9	3.8	67.4	6.9	73.2	2.0
ET10-09 mnz 16_1	Leucosome	363	30	66.8	1.7	75.5	2.7	66.6	3.5	66.2	6.4	66.0	1.7
ET10-09 mnz 16_2	Leucosome	209	21	68.8	1.9	72.8	2.3	69.3	3.5	69.2	6.4	68.3	1.9
ET10-09 mnz 17_1	Leucosome	576	18	64.8	1.8	80.5	2.5	64.2	3.2	63.8	5.9	63.6	1.8
ET10-09 mnz 17_2	Leucosome	1099	19	70.0	1.8	110.1	3.4	68.6	3.4	67.3	6.4	67.2	1.7
ET10-09 mnz 17_3	Leucosome	184	14	63.2	1.8	66.5	2.0	57.3	3.1	57.1	5.7	63.0	1.8
ET10-10 mnz 1_1	Leucosome	537	37	47.4	1.6	58.4	2.7	44.5	2.4	44.3	4.4	46.2	1.6
ET10-10 mnz 2_1	Leucosome	568	32	36.3	1.1	45.6	1.8	42.3	2.9	41.9	5.1	35.6	1.0
ET10-10 mnz 3_1	Inc in Grt rim	515	20	51.6	1.5	62.8	2.0	49.1	2.6	48.8	4.8	50.5	1.4
ET10-10 mnz 4_1	Leucosome	190	42	32.7	1.0	34.9	1.6	34.3	2.7	34.2	4.8	32.4	1.0
ET10-10 mnz 5_1	Inc in grt rim	608	32	57.4	1.6	72.6	2.9	53.8	2.5	53.5	4.7	55.9	1.6
ET10-10 mnz 6_1	Leucosome	1990	23	62.4	1.8	154.2	5.6	58.6	3.1	55.2	5.4	56.3	1.7
ET10-10 mnz 13_1	Inc in Grt rim	1116	21	53.4	1.4	85.7	2.7	51.2	3.0	50.4	5.4	51.0	1.3
ET10-10 mnz 14_1	Inc in Grt rim	692	22	51.9	1.4	68.4	2.2	50.8	3.0	50.5	5.4	50.5	1.4
ET10-10 mnz 14_2	Inc in Grt rim	710	39	46.4	1.3	61.9	2.8	47.2	3.6	46.9	6.4	45.1	1.3
ET10-10 mnz 15_1	Inc in Grt rim	584	25	48.8	1.3	61.4	2.1	46.6	2.6	46.4	4.7	47.5	1.3
ET10-10 mnz 16_1	Inc in Grt rim	781	29	47.3	1.3	65.1	2.5	46.8	2.9	46.5	5.2	45.8	1.3
ET10-10 mnz 17_2	Inc in Grt rim	826	48	47.9	1.5	67.3	3.6	49.8	3.9	49.5	6.9	46.1	1.5
ET10-10 mnz 17_3	Inc in Grt rim	701	29	48.0	1.4	63.7	2.4	48.6	2.9	48.4	5.3	46.5	1.4
ET10-10 mnz 18_1	Inc in Grt rim	536	26	46.1	1.2	56.8	2.0	45.3	2.4	45.0	4.4	45.1	1.2
ET10-10 mnz 18_2	Inc in Grt rim	568	21	45.0	1.2	56.3	1.8	44.9	2.5	44.6	4.6	44.0	1.2
ET10-10 mnz 19_1	Inc in Grt rim	915	19	56.0	1.5	81.6	2.6	56.4	2.9	55.9	5.3	54.0	1.5
ET10-10 mnz 19_2	Inc in Grt rim	437	24	49.3	1.3	58.1	2.0	44.6	2.5	44.3	4.6	48.5	1.3
ET10-10 mnz 20_1	Inc in Grt rim	302	20	53.5	1.5	59.4	1.9	48.1	2.5	47.8	4.6	53.0	1.5
ET10-10 mnz 20_2	Inc in Grt rim	233	17	55.2	1.4	59.4	1.7	52.9	2.9	52.6	5.3	54.8	1.4
ET10-10 mnz 20_3	Inc in Grt rim	387	22	55.5	1.5	63.8	2.1	51.9	2.8	51.7	5.1	54.8	1.5
ET10-10 mnz 21_1	Leucosome	955	21	41.8	1.1	62.6	2.1	40.0	2.3	39.6	4.1	40.0	1.1
ET10-10 mnz 21_2	Leucosome	1095	28	36.1	1.0	58.1	2.3	34.1	2.3	33.9	4.1	33.9	1.0

Table 6.9 – SC–ICP–MS U–Th–Pb ages for samples ET10-07, ET10-09 and ET10-10.

A significant cluster of analyses (n = 17/35) form a co-linear array and are interpreted using a single regression producing a U–Pb lower intercept age of 50.0 ± 0.4 Ma (MSWD = 0.97; Fig. 6.16d). When including an additional data point at $^{207}Pb/^{206}Pb$ ~ 0.06 and $^{238}U/^{206}Pb$ ~ 135, the calculated MSWD increases to 2.2 (n = 18) and so is above the limiting MSWD value of ~1.7 (calculated using the above relationship). A total of 10 monazite grains from sample ET10-09 produced 25 spot analyses yielding a range of U–Pb lower intercept ages between c. 87–60 Ma (Fig. 6.16e). All analysed grains showed consistent zoning profiles with bright cores and dark rims (Fig. 6.17e). A large population of spot analyses (n = 14/25) is interpreted via a single regression that produced a U–Pb lower intercept age of 71.3 ± 1.2 Ma (MSWD = 0.96; Fig. 6.16e). In the case of including nearby data points into this regression, the calculated MSWD increases to 3.6, which is greater than the limiting value of ~1.7 (n = 17).

ET10-10 – Kyanite-bearing migmatite

Monazite in sample ET10-10 occurs as inclusions in garnet rims and also in the leucosome; none was observed in sillimanite-bearing garnet cores. Grains exhibit euhedral to subhedral crystal faces (Fig. 6.17f–g) and are rarely larger than ~50 μm in diameter. Zoning was not observed in leucosome grains; however, faint core-rim relations exist in those grains included in garnet rims. Here, the monazite rim regions show inward bulging contacts with slightly darker core regions (Fig. 6.17g). Cores of monazite included in garnet are relatively enriched in Y_2O_3 (2.40–2.68 wt%), rims are relatively depleted (0.73–0.95 wt%) whereas grains in the leucosome have intermediate Y_2O_3 content (1.03–1.38 wt%). Monazite cores are therefore likely to have formed before peritectic garnet rim growth occurred (reaction 6.4.4), owing to their significantly higher Y_2O_3 content (Table 6.11). Relatively Y_2O_3-poor monazite grains in the leucosome most likely formed after (or simultaneously with) garnet rim growth. A total of 15 monazite grains occurring in leucosome segregations and as inclusions in garnet rims produced 24 spot analyses, of which two spot analyses from the same grain were rejected due to high common lead content. Inclusions in garnet produced a U–Pb lower intercept age range between c. 57–44 Ma, whereas grains in the leucosome yield similar old ages but also some as young as c. 33 Ma (Fig. 6.16f).

ET09-02 and ET10-13 – Mylonitised metapelite

Monazite in samples ET09-02 and ET10-13 is located in the matrix, most often surrounding large (>300 μm) allanite grains that are orientated with, and wrapped by, the dominant mylonitic foliation (Fig. 6.17h). No systematic internal zoning was observed in monazite from either sample (Fig. 6.17i and Fig. 6.17l) although ThO_2 and UO_2 content varies greatly between different grains (Table 6.11). This variation is interpreted to represent growth from the localised chemical reservoirs surrounding different parent allanite grains, which show a degree of compositional heterogeneity.

A total of 10 spot analyses were obtained from 6 monazite grains in sample ET09-02 producing a spread of U–Pb lower intercept ages from c. 9.5 Ma to c. 8.0 Ma (Fig. 6.16g). The majority of monazite in sample ET10-13 was too small (<20 μm) to produce a measurable signal during ablation; however, a total of 5 spot analyses were obtained from 3 slightly larger grains (~30 μm in diameter) giving a range of U–Pb lower intercept ages between c. 16–11 Ma (Fig. 6.16h).

Analysis	Position	Calculated age (Ma)								Corrected age (Ma)			
		$^{207}Pb/^{206}Pb$	2σ (abs)	$^{206}Pb/^{238}U$	2σ (abs)	$^{207}Pb/^{235}U$	2σ (abs)	$^{208}Pb/^{232}Th$	2σ (abs)	$^{208}Pb/^{232}Th$	2σ (abs)	$^{206}Pb/^{238}U$	2σ (abs)
ET10-13 mnz 1_1	Matrix	2847	49	20.5	0.8	86.4	6.0	13.9	2.7	12.5	4.3	15.3	0.6
ET10-13 mnz 2_1	Matrix	1185	54	11.6	0.4	19.9	1.2	10.1	0.8	10.0	1.5	10.4	0.4
ET10-13 mnz 2_2	Matrix	674	32	14.5	0.4	19.3	0.8	13.1	1.7	12.4	2.8	14.2	0.4
ET10-13 mnz 3_1	Matrix	1661	45	13.1	0.5	28.7	1.7	10.7	0.9	10.5	1.6	11.0	0.4
ET10-13 mnz 3_2	Matrix	1037	44	15.3	0.5	24.3	1.3	17.0	2.1	15.8	3.4	14.8	0.4
ET10-18a mnz 1_1	Inc in Grt core	963	31	24.7	0.7	37.5	1.5	24.9	2.0	24.2	3.4	23.8	0.6
ET10-18a mnz 1_2	Inc in Grt core	1881	24	26.1	0.7	63.3	2.4	26.2	1.3	25.7	2.3	23.1	0.7
ET10-18a mnz 2_1	Inc in Grt rim	774	37	24.9	0.7	34.6	1.5	27.2	3.7	26.1	6.2	24.3	0.7
ET10-18a mnz 3_1	Inc in Grt rim	1286	19	24.3	0.6	43.3	1.4	24.1	1.4	23.7	2.5	22.8	0.6
ET10-18a mnz 3_2	Inc in Grt rim	1142	18	24.1	0.7	40.0	1.3	24.5	1.7	23.8	3.0	23.0	0.6
ET10-18a mnz 4_1	Inc in Grt rim	1544	24	25.1	0.6	51.0	1.8	21.1	1.8	19.4	2.9	23.4	0.6
ET10-18a mnz 4_2	Inc in Grt rim	1230	21	24.6	0.7	42.7	1.5	22.8	1.4	22.3	2.4	23.3	0.6
ET10-18a mnz 5_1	Inc in Grt rim	1481	20	25.6	0.7	50.3	1.7	23.6	1.2	23.1	2.2	23.6	0.7
ET10-18a mnz 6_1	Inc in Grt rim	1308	20	24.9	0.7	44.9	1.5	24.1	1.2	23.5	2.2	23.4	0.6
ET10-18a mnz 6_2	Inc in Grt rim	1080	27	24.8	0.7	39.9	1.5	24.8	1.4	24.1	2.5	23.7	0.7
ET10-18a mnz 7_1	Inc in Grt core	2324	20	27.5	0.8	85.1	2.9	27.9	1.2	27.3	2.2	23.0	0.7
ET10-18a mnz 8_1	Inc in Grt rim	807	25	23.8	0.6	33.6	1.2	24.0	1.8	23.4	3.1	23.1	0.6
ET10-18a mnz 9_1	Inc in Grt rim	891	35	24.0	0.7	35.3	1.5	25.1	2.9	24.4	4.9	23.3	0.7
ET10-18a mnz 10_1	Inc in Grt core	1623	25	25.1	0.6	53.1	1.9	22.8	1.5	22.2	2.6	23.0	0.6
ET10-18a mnz 10_2	Inc in Grt core	705	57	24.8	0.8	33.4	2.1	27.4	5.6	26.2	9.4	24.3	0.8
ET10-18a mnz 11_1	Inc in Grt core	1674	23	24.9	0.7	54.1	1.9	21.8	1.2	21.3	2.1	22.6	0.6
ET09-02 mnz 2_2	Matrix	2546	53	10.5	0.4	38.0	2.8	9.3	1.3	8.3	2.0	8.8	0.4
ET09-02 mnz 3_2	Matrix	2021	41	8.9	0.3	23.9	1.3	17.6	5.6	10.3	5.7	8.1	0.3
ET09-02 mnz 4_1	Matrix	2494	42	9.4	0.3	32.9	1.9	7.5	1.8	5.7	2.3	8.0	0.3
ET09-02 mnz 7_1	Matrix	2667	32	10.5	0.3	40.6	2.0	13.8	3.0	10.0	3.8	8.7	0.3
ET09-02 mnz 7_2	Matrix	3477	32	11.9	0.4	75.4	3.8	14.7	4.1	7.6	3.7	8.2	0.3
ET09-02 mnz 8_1	Matrix	922	51	9.2	0.3	13.9	0.8	9.0	1.0	8.9	1.7	8.6	0.3
ET09-02 mnz 8_2	Matrix	1595	43	9.5	0.3	20.1	1.1	8.3	0.8	8.0	1.4	8.6	0.2
ET09-02 mnz 10_1	Matrix	860	40	9.0	0.3	13.2	0.6	7.4	2.2	6.3	3.2	8.8	0.2
ET09-02 mnz 10_2	Matrix	2725	30	11.4	0.3	45.7	2.1	14.8	2.9	8.7	2.9	9.5	0.3
ET09-02 mnz 10_3	Matrix	2761	24	11.6	0.3	47.5	1.9	11.4	1.5	8.6	1.9	9.5	0.3

Table 6.10 – SC–ICP–MS U–Th–Pb ages for samples ET10-13, ET10-18a and ET09-02.

ET10-18a – Mylonitised staurolite-grade metapelite

Monazite in sample ET10-18a occurs mostly as inclusions in garnet porphyroblast rims and commonly exhibits bright core regions surrounded by dull rims, clearly distinguishable in SEM BSE images (Fig. 6.17k). Rare and small (~25 μm) grains exist in the matrix with no such internal zoning.

Analysis	Petrographic position	Internal domain	SiO_2	P_2O_5	CaO	FeO	Y_2O_3	La_2O_3	Ce_2O_3	Pr_2O_3	Nd_2O_3	Sm_2O_3	Eu_2O_3	Gd_2O_3	Tb_2O_3	Dy_2O_3	Ho_2O_3	Er_2O_3	Tm_2O_3	Yb_2O_3	Lu_2O_3	PbO	ThO_2	UO_2	**Total**
ET09-05 Mnz 2	Leucosome	Bright core (Fig. 6.17a)	0.00	29.25	1.54	1.17	1.26	13.29	26.75	3.30	10.00	1.64	b.d.l	1.20	0.29	1.05	0.25	0.30	0.08	0.08	b.d.l	0.21	5.92	1.53	**99.10**
ET09-05 Mnz 2	Leucosome	Dull rim (Fig. 6.17a)	0.05	29.18	1.34	0.83	1.01	12.35	25.86	3.04	10.45	2.27	0.09	1.66	0.04	0.98	0.35	0.34	0.06	0.10	0.22	0.18	7.87	0.84	**99.12**
ET09-05 Mnz 2	Leucosome	Dull rim (Fig. 6.17a)	0.19	29.33	1.62	0.14	0.85	12.65	26.91	3.47	11.30	2.27	0.04	1.83	0.15	0.77	b.d.l	0.03	0.07	0.17	0.19	0.24	6.44	1.43	**100.10**
ET09-05 Mnz 4	Inclusion in Grt rim	Bright core	0.00	30.22	1.46	0.25	1.59	13.15	26.64	2.97	10.36	2.26	0.21	1.53	b.d.l	0.86	0.18	0.23	0.00	b.d.l	0.11	0.09	5.96	1.80	**99.86**
ET09-05 Mnz 4	Inclusion in Grt rim	Dull rim	0.15	29.29	1.09	0.12	1.52	12.05	26.03	3.49	12.66	3.01	0.02	2.34	0.32	0.99	0.07	0.34	0.24	0.05	b.d.l	0.09	5.13	1.19	**100.18**
ET09-05 Mnz 4	Inclusion in Grt rim	Dull rim	0.02	29.52	1.14	0.27	1.80	10.49	24.47	3.52	12.88	4.00	0.42	3.38	0.49	1.11	0.15	0.21	0.00	0.05	0.11	0.12	6.40	1.74	**102.28**
ET09-06 Mnz 3	Leucosome	Bright region (Fig. 6.17b)	0.77	27.72	3.03	0.00	0.14	11.63	23.11	2.81	7.95	1.13	0.00	1.05	0.47	0.41	0.01	0.06	0.13	0.19	0.17	0.11	16.86	2.15	**99.89**
ET09-06 Mnz 3	Leucosome	Dull region (Fig. 6.17b)	1.29	26.65	0.59	0.08	0.84	15.56	27.96	3.30	9.30	1.84	0.32	1.61	0.33	0.26	b.d.l	0.22	0.10	0.04	0.12	0.04	9.47	0.20	**100.08**
ET09-06 Mnz 3	Leucosome	Dull region (Fig. 6.17b)	0.46	28.05	1.37	0.06	0.51	15.06	26.05	2.45	8.24	1.32	0.00	0.84	0.21	0.65	0.00	0.30	0.20	0.16	0.39	0.05	11.04	0.84	**98.24**
ET09-06 Mnz 3	Leucosome	Mid-bright region (Fig. 6.17b)	0.82	27.65	1.23	0.07	0.59	15.36	26.79	2.53	8.40	1.41	0.11	0.85	0.00	0.37	0.07	0.32	0.07	0.17	0.00	0.17	10.34	0.47	**97.78**
ET09-06 Mnz 3	Leucosome	Mid-bright region (Fig. 6.17b)	0.54	28.33	1.94	0.07	0.21	14.45	26.09	2.83	8.06	1.22	0.00	0.97	0.09	0.44	b.d.l	0.28	0.01	b.d.l	0.20	0.20	11.30	1.23	**98.46**
ET10-07 Mnz 6	Leucosome	Bright core (Fig. 6.17c)	2.74	23.59	0.74	0.11	1.91	11.31	23.07	2.94	10.44	1.74	0.39	1.75	0.34	0.49	b.d.l	b.d.l	b.d.l	0.10	b.d.l	b.d.l	17.41	0.19	**99.24**
ET10-07 Mnz 6	Leucosome	Bright core (Fig. 6.17c)	1.90	24.76	0.79	0.09	1.93	11.99	23.87	2.71	10.40	1.88	0.26	1.85	0.28	0.41	b.d.l	0.03	0.01	b.d.l	0.17	0.02	14.46	0.44	**98.28**
ET10-07 Mnz 5	Leucosome	Dark core (Fig. 6.17c)	0.03	30.23	1.21	0.01	4.08	13.53	26.88	2.80	10.68	1.83	0.17	1.48	0.21	0.94	0.20	0.49	0.19	0.16	0.27	0.08	4.51	1.24	**101.24**
ET10-07 Mnz 5	Leucosome	Dark core (Fig. 6.17c)	0.03	30.25	1.00	0.02	3.78	13.68	27.28	3.03	10.59	1.98	0.19	1.67	0.28	0.97	0.25	0.45	b.d.l	b.d.l	b.d.l	0.03	4.68	0.92	**101.08**
ET10-07 Mnz 5	Leucosome	Mid-bright rim (Fig. 6.17c)	0.13	29.37	1.36	0.09	3.41	13.22	26.38	3.22	10.71	2.43	0.36	2.12	0.49	0.79	0.15	0.36	0.00	b.d.l	b.d.l	0.04	6.07	1.22	**101.91**
ET10-07 Mnz 5	Leucosome	Mid-bright rim (Fig. 6.17c)	0.06	29.30	1.65	0.04	3.16	13.06	26.04	3.17	10.41	2.34	0.47	2.02	0.35	0.62	b.d.l	0.25	0.03	b.d.l	b.d.l	0.15	7.75	1.04	**101.93**
ET10-07 Mnz 9	Mesosome	Broad dull core (Fig. 6.17d)	0.15	29.71	1.04	0.01	3.14	13.99	27.69	3.34	11.04	1.45	0.01	1.48	0.27	0.55	b.d.l	b.d.l	b.d.l	b.d.l	b.d.l	0.12	4.80	1.28	**100.09**
ET10-07 Mnz 9	Mesosome	Broad dull core (Fig. 6.17d)	0.20	29.34	0.94	0.12	3.09	14.29	28.10	2.95	10.84	1.76	0.17	1.57	0.28	0.84	0.06	0.50	0.23	0.06	0.03	b.d.l	4.69	0.46	**100.52**
ET10-07 Mnz 9	Mesosome	Thin brighter rim (Fig. 6.17d)	0.08	29.77	1.49	0.25	3.37	12.91	26.09	2.80	10.47	2.20	0.17	1.58	0.06	0.74	b.d.l	0.31	b.d.l	b.d.l	b.d.l	0.03	6.79	1.09	**100.19**
ET10-07 Mnz 9	Mesosome	Thin brighter rim (Fig. 6.17d)	0.18	28.95	1.51	0.21	3.10	13.14	25.83	2.85	10.33	2.38	0.26	2.04	0.41	0.67	b.d.l	0.27	0.04	0.10	0.10	b.d.l	7.22	0.92	**100.51**
ET10-09 Mnz 14	Mesosome	Bright core (Fig. 6.17e)	1.35	27.94	2.15	0.11	2.94	11.37	22.48	2.57	9.10	1.49	0.27	1.45	0.27	0.62	b.d.l	0.13	0.03	b.d.l	0.17	0.06	14.82	1.29	**100.62**
ET10-09 Mnz 14	Mesosome	Bright core (Fig. 6.17e)	1.30	28.20	2.16	0.14	3.00	11.75	22.39	2.40	8.79	1.46	0.26	1.37	0.33	0.75	0.01	0.23	b.d.l	b.d.l	b.d.l	0.05	15.36	0.75	**100.68**
ET10-09 Mnz 14	Mesosome	Bright core (Fig. 6.17e)	0.80	29.36	1.75	0.07	3.01	12.06	23.40	2.31	9.32	1.06	0.08	1.17	0.15	0.62	b.d.l	0.23	b.d.l	0.09	0.11	0.17	11.78	0.73	**98.26**
ET10-09 Mnz 14	Mesosome	Dull rim (Fig. 6.17e)	0.21	29.98	0.83	0.28	2.75	14.44	28.32	3.09	11.57	1.88	0.06	1.58	b.d.l	0.52	b.d.l	0.16	b.d.l	b.d.l	b.d.l	0.07	4.05	0.64	**100.42**
ET10-09 Mnz 14	Mesosome	Dull rim (Fig. 6.17e)	0.06	29.24	1.11	0.13	3.40	14.31	27.80	2.93	10.96	1.96	0.47	1.58	0.18	0.27	b.d.l	0.15	0.31	0.18	0.25	0.16	5.82	0.25	**101.51**
ET10-09 Mnz 14	Mesosome	Dull rim (Fig. 6.17e)	0.24	29.02	1.25	0.10	2.65	14.28	27.31	2.85	10.57	1.86	0.12	1.45	0.33	0.74	b.d.l	b.d.l	b.d.l	b.d.l	b.d.l	0.03	5.33	1.29	**99.40**
ET10-10 Mnz 1	Leucosome	Body (Fig. 6.17f)	0.45	28.83	1.19	0.05	1.07	15.00	29.12	3.52	12.23	1.75	0.16	0.59	0.08	0.11	b.d.l	0.08	b.d.l	b.d.l	b.d.l	0.10	6.63	0.52	**101.48**
ET10-10 Mnz 1	Leucosome	Body (Fig. 6.17f)	0.37	29.07	1.27	0.08	1.03	14.66	28.25	3.18	11.34	1.69	0.12	0.92	0.25	b.d.l	b.d.l	0.16	b.d.l	b.d.l	b.d.l	0.19	0.06	7.08	0.07	**99.79**
ET10-10 Mnz 1	Leucosome	Body (Fig. 6.17f)	0.43	30.09	1.22	0.10	1.38	14.62	28.49	2.81	11.36	1.80	0.10	1.33	0.25	0.05	b.d.l	b.d.l	b.d.l	b.d.l	b.d.l	0.06	5.84	0.32	**100.25**
ET10-10 Mnz 1	Leucosome	Body (Fig. 6.17f)	0.85	29.63	1.09	0.08	1.32	14.69	27.97	2.86	11.29	2.01	0.30	1.30	0.29	0.28	0.05	0.09	0.05	b.d.l	0.13	b.d.l	5.74	0.26	**100.28**
ET10-10 Mnz 20	Inclusion in Grt rim	Broad dull core (Fig. 6.17g)	0.01	30.08	1.19	0.99	2.40	13.83	25.88	2.87	10.21	1.52	0.20	1.37	0.10	0.50	0.01	0.04	b.d.l	b.d.l	b.d.l	b.d.l	5.46	0.57	**97.22**
ET10-10 Mnz 20	Inclusion in Grt rim	Broad dull core (Fig. 6.17g)	0.09	30.14	1.31	0.33	2.68	14.39	26.90	3.00	10.44	2.08	0.07	1.73	0.13	0.55	b.d.l	0.29	b.d.l	b.d.l	0.03	0.04	5.84	1.16	**101.21**
ET10-10 Mnz 20	Inclusion in Grt rim	Dull rim (Fig. 6.17g)	0.12	28.73	1.29	1.13	0.90	14.97	28.08	3.21	11.17	1.88	0.17	1.28	0.27	0.17	0.13	0.11	b.d.l	b.d.l	0.10	0.01	6.46	0.13	**100.31**
ET10-10 Mnz 20	Inclusion in Grt rim	Dull rim (Fig. 6.17g)	0.08	29.42	1.30	1.16	0.73	15.43	28.63	3.03	11.18	1.77	0.05	0.97	0.06	0.25	b.d.l	0.14	0.08	0.13	b.d.l	0.04	6.12	0.22	**100.80**
ET10-10 Mnz 20	Inclusion in Grt rim	Dull rim (Fig. 6.17g)	0.16	28.08	1.09	0.77	0.95	15.09	28.86	3.25	11.74	2.03	0.25	0.93	0.06	0.04	b.d.l	b.d.l	b.d.l	b.d.l	b.d.l	0.29	b.d.l	6.12	0.39	**100.08**
ET10-10 Mnz 20	Inclusion in Grt rim	Dull rim (Fig. 6.17g)	0.20	28.34	1.23	0.68	0.80	15.09	27.86	2.85	10.80	2.17	0.30	1.58	0.30	0.06	b.d.l	0.09	0.05	b.d.l	0.00	0.04	5.81	0.27	**98.51**
ET10-13 Mnz 1	Matrix adjacent to Aln	Body (Fig. 6.17i)	0.00	29.53	0.93	0.23	0.16	13.73	28.90	3.19	11.80	1.96	0.22	1.36	0.03	0.42	0.04	0.29	0.17	0.20	0.15	0.25	4.10	0.27	**97.93**
ET10-13 Mnz 1	Matrix adjacent to Aln	Body (Fig. 6.17i)	0.02	29.11	1.31	0.28	0.40	12.97	27.83	3.54	11.45	2.31	0.38	1.90	0.55	0.91	0.01	0.28	0.00	0.22	0.38	0.02	5.20	0.35	**99.38**
ET10-13 Mnz 1	Matrix adjacent to Aln	Body (Fig. 6.17i)	0.06	29.47	0.77	0.07	0.18	13.90	30.44	3.63	12.39	1.96	0.37	1.61	0.38	0.63	0.00	0.22	0.09	b.d.l	b.d.l	0.19	1.74	0.57	**98.69**
ET10-13 Mnz 1	Matrix adjacent to Aln	Body (Fig. 6.17i)	0.00	29.24	1.20	0.45	0.36	13.98	28.28	3.21	11.26	2.16	0.00	1.61	0.36	0.72	0.14	0.13	0.03	b.d.l	b.d.l	0.27	4.76	0.36	**98.50**
ET10-13 Mnz 1	Matrix adjacent to Aln	Body (Fig. 6.17i)	0.36	29.37	0.53	0.20	0.14	14.33	31.66	3.37	12.65	1.99	0.21	1.16	0.07	0.32	0.04	0.05	b.d.l	b.d.l	b.d.l	0.20	0.42	0.55	**97.59**
ET10-18a Mnz 2	Inclusion in Grt rim	Bright core (Fig. 6.17k)	2.62	24.10	2.36	0.81	1.89	10.00	18.31	2.21	7.92	1.87	0.38	1.98	0.10	0.49	b.d.l	0.14	0.14	b.d.l	b.d.l	0.19	24.86	0.15	**100.54**
ET10-18a Mnz 2	Inclusion in Grt rim	Bright core (Fig. 6.17k)	2.75	24.15	2.31	1.30	1.65	9.94	18.61	2.00	7.95	1.70	0.41	1.62	0.11	0.59	0.05	0.37	b.d.l	b.d.l	b.d.l	0.12	22.24	0.62	**98.49**
ET10-18a Mnz 2	Inclusion in Grt rim	Bright core (Fig. 6.17k)	1.43	25.64	2.43	1.06	1.74	10.79	19.29	1.78	7.93	1.81	0.39	1.80	b.d.l	0.58	b.d.l	0.10	b.d.l	0.03	0.16	0.10	20.64	0.80	**98.50**
ET10-18a Mnz 2	Inclusion in Grt rim	Dull rim (Fig. 6.17k)	0.15	28.59	1.05	1.42	1.24	14.42	28.30	2.73	11.33	2.03	0.37	1.45	0.17	0.32	b.d.l	0.27	0.25	0.11	0.05	0.09	5.67	0.78	**100.80**
ET10-18a Mnz 2	Inclusion in Grt rim	Dull rim (Fig. 6.17k)	0.16	28.13	1.61	1.40	1.09	14.14	27.01	3.17	11.00	1.97	0.39	1.32	0.36	0.08	0.06	0.19	0.20	0.14	0.31	b.d.l	6.87	1.61	**101.21**
ET10-18a Mnz 2	Inclusion in Grt rim	Dull rim (Fig. 6.17k)	0.06	28.89	0.71	1.15	1.11	15.55	29.89	3.30	11.97	1.67	0.29	1.38	0.32	0.30	0.02	0.08	0.00	0.08	b.d.l	0.02	2.97	0.70	**100.45**
ET09-02 Mnz 10	Matrix adjacent to Aln	Body (Fig. 6.17l)	0.00	29.18	1.25	0.20	1.36	13.46	28.26	3.74	11.65	2.14	0.23	1.48	0.23	0.77	0.02	0.16	0.11	0.19	b.d.l	0.05	5.64	0.35	**100.46**
ET09-02 Mnz 10	Matrix adjacent to Aln	Body (Fig. 6.17l)	0.00	29.41	0.56	0.30	2.31	15.76	29.13	3.34	12.16	2.39	0.39	1.84	0.33	0.78	0.16	0.18	0.05	0.01	0.15	0.02	0.86	0.54	**100.69**
ET09-02 Mnz 10	Matrix adjacent to Aln	Body (Fig. 6.17l)	0.00	29.25	0.84	0.37	2.11	14.73	27.70	3.14	11.69	2.28	0.49	2.11	0.32	0.47	0.00	0.10	b.d.l	b.d.l	b.d.l	0.03	3.75	0.63	**99.99**
ET09-02 Mnz 10	Matrix adjacent to Aln	Body (Fig. 6.17l)	0.00	29.12	0.36	0.08	1.79	16.29	30.02	3.21	12.08	2.20	0.47	1.68	0.34	0.70	0.32	0.36	0.00	b.d.l	0.13	b.d.l	1.22	0.32	**100.70**
ET09-02 Mnz 10	Matrix adjacent to Aln	Body (Fig. 6.17l)	0.00	30.61	1.03	0.18	2.12	15.31	27.62	2.93	11.20	1.95	0.00	1.42	0.14	0.47	0.00	0.13	0.26	0.03	0.16	0.02	5.12	0.27	**100.98**

Table 6.11 – Monazite compositions for all analysed migmatite and mylonite samples ET09-05, ET09-06, ET10-07, ET10-09, ET10-10, ET10-13, ET10-18a and ET09-02 shown in weight % oxide.

Grains in garnet are occasionally located in the outermost inclusion-rich core regions, but the majority exists in rims that contain staurolite inclusions (Fig. 6.17j). Compositional analysis of monazite in garnet reveals that bright cores are extremely enriched in ThO2 (20.64–24.86 wt%; Table 6.11) and have relatively higher Y2O3 content than duller rim regions (1.65–1.89 wt% compared to 1.09–1.24 wt% respectively; Table 6.11). A total of 19 spot analyses from 12 monazites were obtained, of which three spot analyses on two grains from the matrix were rejected due to large amounts of common lead. The remaining 16 analyses from both garnet outermost cores and rims exhibit a co-linear relationship and were interpreted with a single regression to a lower intercept U–Pb age of 23.6 ± 0.3 Ma (Fig. 6.16i) with an MSWD = 1.6.

6.5.2. Interpretation of monazite geochronology

A common feature of samples in this study, especially those that have undergone anatexis, is a spread of common lead corrected U–Pb ages, even in the same monazite grain (e.g. Fig. 6.17b). This is also seen in analyses that have low common lead and lie close to concordia (e.g. Fig. 6.16a), therefore are affected by the correction procedure to a lesser extent. An independent check on ^{238}U–^{206}Pb ages is provided by ^{232}Th–^{208}Pb age data (chapter 3.5.2), which provide a very high correlation factor between all analyses ($R^2 = 0.962$; Fig. 6.16j), suggesting that this spread of ages between (and within) each sample dataset is real. Foster *et al*. (2002) investigated similar dispersals in upper amphibolite-facies metapelites and concluded that they could occur through one of four mechanisms: the continuous growth/recrystallisation of monazite during a single metamorphic event, discontinuous growth during several events, mixing of different age domains during the ablation process or diffusive lead loss at peak temperatures. Parrish (1990) has suggested that the latter effect, diffusive lead loss, is extremely uncommon in monazite so is excluded as a possibility in this case. The utmost care was taken to avoid simultaneously analysing multiple domains during ablation, although mixing of domains in the third dimension (with an ablation pit depth of between c. 12–15 μm) is an uncontrollable factor; however, it is thought unlikely that mixing could account for the total dispersion in every sample. Therefore, the age ranges observed are considered to reflect protracted growth during either prograde to peak metamorphism and/or during partial melting. The identification of chemical zonation (especially in Y_2O_3 content) in the majority of monazite in

anatectic samples supports this conclusion. Distinct boundaries between domains in some samples (e.g. ET10-07; Fig. 6.17d) indicates punctuated events, whereas others are more chaotic and gradational (e.g. ET09-06; Fig. 6.17b) suggesting continual growth/recrystallisation (ibid).

Sillimanite-grade partial melting

The onset of sillimanite-grade partial melting is best constrained by monazite in leucosome domains, which in sample ET10-09 partly lie on a common lead trajectory with a U–Pb lower intercept age of 71.3 ± 1.2 Ma (Fig. 6.16e). Similar ages are obtained from samples ET09-05 (c. 72 Ma; Fig. 6.16a), ET09-06 (c. 73 Ma; Fig. 6.16b) and ET10-07 (c. 71 Ma; Fig. 6.16d), suggesting that sillimanite-grade crustal anatexis initiated at similar times in all samples. As a result of its petrographic location (enclosed in biotite in the mesosome) the older analysis (c. 87 Ma) in sample ET10-09 (Fig. 6.16e) is interpreted to represent prograde metamorphic growth in unknown subsolidus *P–T* conditions. Younger ages suggest that partial melting continued for an extended period of time, an interpretation that can again be made for all four sillimanite-grade migmatite samples (Fig. 6.16a–e). For example, in sample ET10-07 monazite rims provide a significant cluster of spot analyses at 50.0 ± 0.4 Ma (Fig. 6.16d, Fig. 6.17c–d) suggesting that high-grade conditions were sustained for *at least* 20 Myr and that melting may have occurred throughout this period in several 'pulses'.

Kyanite-grade partial melting

Monazite in sample ET10-10 occurs as inclusions in garnet rims that surround sillimanite-bearing cores. Sillimanite-grade metamorphism in this sample is therefore interpreted to have occurred prior to c. 57 Ma, the oldest monazite inclusion age obtained (Fig. 6.16f). Kyanite-grade metamorphism and melting is thus constrained between the upper and lower limits of c. 57 Ma and c. 33 Ma. Dispersion along concordia by a relatively small number of results (n = 22) does not allow elucidation of whether monazite crystallisation occurred in a single event or over an extended period of time. Y_2O_3-rich cores in monazite inclusions in garnet rims appear to have formed during prograde metamorphism, when garnet was present (i.e. sillimanite-grade cores), but not abundant (i.e. before kyanite-grade rim growth). Old ages of c. 57 Ma, providing a minimum age for sillimanite-grade conditions in sample ET10-10, are consistent with the ages of anatexis obtained in sillimanite migmatite samples ET09-05, ET09-06, ET10-07 and ET10-09 (above). Alternatively,

they may be interpreted as representing prograde growth during burial to kyanite-grade conditions of partial melting. As a result of the interpreted peritectic nature of the garnet rims in this sample, the youngest monazite inclusion in garnet is taken to represent a minimum age (c. 44 Ma) for the initiation of partial melting. The youngest age of c. 33 Ma obtained from monazites in the leucosome are interpreted to provide a maximum age on the cessation of melting, suggesting that kyanite-grade anatectic conditions were sustained for 11 Myr.

Mylonitisation along the MYLP fault

A U–Pb age of 23.6 ± 0.3 Ma was obtained from monazite grains located in garnet outer core and rim regions of sample ET10-18a, the latter domain also hosting staurolite inclusions (Fig. 6.17j). The age is interpreted as dating the peak staurolite-garnet assemblage based on the petrographic association of both minerals, or at least providing a maximum age for this event. Further support for this interpretation comes from the systematic decrease in Y_2O_3 content from monazite cores to rims, indicating simultaneous crystallisation with garnet outer core and rim regions, with both minerals drawing Y_2O_3 from the same matrix reservoir.

U–Pb age ranges of c. 9.5–8.0 Ma (ET09-02) and c. 16–11 Ma (ET10-13) are interpreted to date the breakdown of allanite to monazite during bulk shearing. As discussed in chapter 3.4.1, allanite is commonly observed to first form at the expense of low-grade monazite during prograde metamorphism of a metapelite at the biotite isograd, at temperatures of approximately 450 ± 25 °C (Smith & Barreiro, 1990; Wing *et al*., 2003). The presence of monazite mantling allanite in mylonite samples ET10-13 and ET09-02 (e.g. Fig. 6.17h) suggests that the reverse of this reaction, the breakdown of allanite, has occurred. Chlorite in microfold hinges (Fig. 6.12a) and garnet strain shadows (Fig. 6.12b) confirm that shearing continued into the chlorite-zone during exhumation out of the biotite isograd/allanite stability field.

6.6. Thermobarometry of metamorphic units

Monazite-bearing samples underwent thermobarometric investigation in order to constrain *P–T* conditions of peak metamorphism and, where relevant, subsequent deformation. THERMOCALC in AvePT mode was used to calculate peak *P–T* conditions for garnet-bearing samples. The input activities of all end-members are presented in Appendix 11.5. No result was obtained for garnet-free

samples ET09-02 or ET10-09, as the algorithm failed to find enough independent reactions for a result fitting 95% confidence. Garnet outer rim compositions were used for calculations, except when diffusional cation exchange or resorption had occurred between garnet and adjacent ferromagnesian matrix phases, when inner-rim garnet compositions were used instead (cf. Kohn & Spear, 2000). A fluid composition of pure H_2O was assumed for all samples except for ET10-10 due to the presence of graphite (below). All calculated uncertainty is subsequently quoted at 1 S.D.

6.6.1. Sillimanite-grade migmatisation

In order to calculate peak *P–T* conditions of sillimanite-grade metamorphism, fluid-independent equilibria are preferred due to the uncertain activity of H_2O in equilibrium with partial melt and remaining solid phases. However, as dehydration reactions are the most effective geothermometers, peak temperatures obtained using such equilibria for samples ET09-05 and ET10-07 carry extremely large uncertainties of ± 197 °C and ± 267 °C respectively (Table 6.12). Furthermore, AvePT failed to calculate a result for sample ET09-06 in these conditions.

Instead, given that muscovite compositions indicate high-temperatures of crystallisation, *P–T* conditions considering both muscovite and H_2O were calculated in order to provide minimum temperatures for this event. Considering these additional phases produced results of 6.3 ± 1.2 kbar and 751 ± 32 °C (ET09-05), 5.2 ± 1.5 kbar and 735 ± 42 °C (ET09-06) and 5.8 ± 1.1 kbar and 729 ± 29 °C (ET10-07), which are taken to represent conditions of muscovite crystallisation on cooling from peak conditions. These data agree with experimental results for the minimum conditions required to form granitic partial melts via muscovite-dehydration (Pëto, 1976).

This period of high-temperature metamorphism, sustained for ~21 Myr, would result in significant intracrystalline cation diffusion in garnet, leading to compositional homogenisation by means of the relaxation of any prograde growth zoning profiles, as currently observed in both samples (Fig. 6.8a–b). Caddick *et al.* (2010) show that the preservation of fully unmodified compositional zoning in garnet porphyroblasts up to 3 mm in diameter in pelitic lithologies requires the complete burial and exhumation cycle to have a duration of <10 Myr, with a peak temperature of 600 °C. By contrast, a garnet grain 3 mm in diameter that is heated up to 750 °C over 20 Myr at a rate typical of regional metamorphism would show significant modification of core compositions at

peak in all cations Fe, Mg, Ca and Mn (Caddick *et al*., 2010). Inflections in spessartine content at the rims of each analysed garnet are therefore interpreted to be the result of cooling during post-peak exhumation allowing for cation exchange with matrix phases. At a certain point on the retrograde path, cation exchange became inefficient and the final compositional profiles were locked in.

Sample	Calculation assemblage	XH_2O	T (°C)	1 S.D.	P (kbar)	1 S.D.	Cor	Sig Fit	N	End-members excluded
ET09-05	Grt, Kfs, Pl, Bt, Sil, Ilm, Qz	N/A	818	197	6.4	2.6	0.81	0.83	5	none
ET09-06	Grt, Kfs, Pl, Bt, Sil, Qz	NO RESULT								
ET10-07	Grt, Kfs, Pl, Bt, Sil, Ilm, Qz	N/A	730	267	5.1	3.5	0.80	1.57	5	none
ET09-05	Grt, Kfs, Ms, Pl, Bt, Sil, Ilm, Qz, H_2O	1.0	751	32	6.3	1.2	0.92	0.71	10	cel
ET09-06	Grt, Kfs, Ms, Pl, Bt, Sil, Qz, H_2O	1.0	735	42	5.2	1.5	0.92	1.36	8	spss, cel
ET10-07	Grt, Kfs, Ms, Pl, Bt, Sil, Ilm, Qz, H_2O	1.0	729	29	5.8	1.1	0.91	0.90	9	spss
ET10-10	Grt, Bt, Ky, Qz, Pl, Ms, Rt, H_2O	1.0	712	21	10.6	1.0	0.78	0.29	5	ru, cel, fcel
ET10-10	Grt, Bt, Ky, Qz, Pl, Ms, Rt, H_2O	0.9	698	20	10.4	1.0	0.78	0.23	5	ru, cel, fcel
ET10-10	Grt, Bt, Ky, Qz, Pl, Ms, Rt	N/A	683	76	10.2	1.4	0.86	0.24	4	ru, cel, fcel
ET10-13	Grt, Ms, Pl, Bt, Chl, Qz, H_2O	1.0	577	13	6.9	0.8	0.32	0.42	7	clin, pa
ET10-18a	Grt, Ms, Pl, Bt, Chl, Qz, H_2O	1.0	538	13	7.0	0.7	0.19	0.85	6	ames, clin, pa

Table 6.12 – THERMOCALC AvePT results for samples from the B-L-M region. Cor = correlation, Sig Fit = significant fit, N = number of independent reactions used in calculation (after Powell & Holland, 1994).

6.6.2. Kyanite-grade migmatisation

Sample ET10-10 documents two separate metamorphic stages at sillimanite- and kyanite-grade respectively. The *P–T* conditions of early sillimanite-grade metamorphism could not be determined directly, since the inclusion population in host garnet cores was unsuitable for thermobarometry, although AvePT allowed investigation into peak conditions for kyanite-grade metamorphism and partial melting. Fluid-absent equilibria produced results of 10.2 ± 1.4 kbar and 683 ± 76 °C (Table 6.12), again with a large uncertainty. However, the tonalitic nature of leucosomes implies a high water activity during partial melting (Conrad *et al.*, 1988) and so tighter constraints can be obtained by including a metamorphic fluid in AvePT calculations.

The presence of graphite in the mesosome foliation indicates its presence during peak metamorphism, thus the coexisting metamorphic fluid must have been diluted with a proportion of CO_2. Fluid composition was constrained to $XH_2O = 0.9$ in accordance with the maximum predicted carbon content of a metamorphic fluid coexisting with graphite at the *P–T* conditions previously estimated by fluid-independent equilibria (Ohmoto & Kerrick, 1977). Calculation with this fluid composition produced AvePT results of 10.4 ± 1.0 kbar and 698 ± 20 °C (Table 6.12). For comparison, these conditions are slightly lower than, but within uncertainty of, those assuming a

fluid composition of $XH_2O = 1.0$, which produced results of 10.6 ± 1.0 kbar and 712 ± 21 °C (Table 6.12). Thus, the former results using a fluid composition $XH_2O = 0.9$ are taken as a reliable estimate of conditions of peak kyanite-grade anatexis.

As opposed to garnet observed in sillimanite-grade units, substantial compositional zoning is preserved in sample ET10-10. This is interpreted to be a combined result of three factors: the generally larger porphyroblast size (up to 8 mm in diameter), the lower temperature of peak metamorphism (cf. ~750 °C; chapter 6.6.1) and the shorter duration at peak metamorphism. Although some intracrystalline cation diffusion is interpreted to have occurred at core-rim interfaces (chapter 6.4.1), the shorter duration at a relatively lower peak temperature means that significant relaxation of compositional gradients in sample ET10-10 garnet did not occur. Caddick *et al*. (2010) suggests that a grain 3 mm in diameter held at temperature of 700 °C would first experience significant modification of its core composition in the cations Fe, Mg and Mn after ~10 Myr. As the intracrystalline diffusion of Ca is markedly slower than Fe, Mg and/or Mn, there would be minor change to grossular profiles under these conditions (ibid). Hence, the analysed grain in sample ET10-10 should be able to retain substantial compositional gradients between core and rim regions for the duration of peak metamorphism, with only minor diffusional relaxation occurring where compositional gradients exist close to the rim, as observed.

6.6.3. Mylonitisation of metapelites and prior prograde metamorphism

The garnet-ilmenite thermometer calibration of Pownceby *et al.* (1987) was used to calculate the temperature range over which initial prograde garnet growth occurred in samples ET10-13 and ET10-18a, prior to mylonitisation. This was possible as a result of abundant ilmenite inclusions throughout garnet cores and inner rims and an associated strong correlation with spessartine content in both samples (Fig. 6.15). All SEM-microprobe compositional analyses used in calculations are given in Table 6.13. Calculated temperatures range between 555–597 °C (± 30 °C) for sample ET10-13 (five data pairs) and 549–611 °C (± 30 °C) for sample ET10-18a (ten data pairs).

Ilmenite inclusions in the outermost rims of garnet in both samples contains a negligible Mn content, therefore no result was obtained from this thermometer in this instance. Despite this, staurolite inclusions in sample ET10-18a garnet rim regions allow an estimation of peak *P–T*

conditions. The stability field of staurolite has been calculated by Wei *et al.* (2004) in the model system $MnO–K_2O–FeO–MgO–Al_2O_3–SiO_2–H_2O$ (MnKFMASH) for an average pelite composition (taken from Mahar *et al.*, 1997). Here, staurolite is stable between ~560–650 °C at mid-crustal pressures (~5–9 kbar), in agreement with the above estimates of prograde temperatures. As a result, the stability field of staurolite is taken as a reliable estimate of peak conditions for these samples.

Sample	Pair	Mineral	SiO_2	TiO_2	Al_2O_3	FeO	MnO	MgO	CaO	Na_2O	K_2O	**Total**	Si	Ti	Al	Fe^{2+}	Mn	Mg	Ca	Na	K	**Total**	Ox	XFe	XMn	T (°C)
ET10-13	1	Grt	35.84	0.11	20.99	33.57	0.75	1.42	6.78	0.00	0.00	**99.47**	2.95	0.01	1.97	2.26	0.05	0.17	0.59	0.00	0.00	**8.00**	12	0.98	0.02	597
		Ilm	0.25	51.97	0.20	46.36	0.16	0.41	0.09	0.00	0.03	**99.47**	0.01	0.99	0.01	0.97	0.00	0.02	0.00	0.00	0.00	**2.00**	3	1.00	0.00	
	2	Grt	36.04	0.22	20.38	33.45	1.85	1.27	6.61	0.00	0.00	**99.82**	2.94	0.01	1.96	2.24	0.13	0.16	0.57	0.00	0.00	**8.00**	12	0.95	0.05	590
		Ilm	0.09	51.83	0.09	45.56	0.33	0.39	0.11	0.07	0.01	**98.47**	0.00	1.00	0.00	0.97	0.01	0.01	0.00	0.00	0.00	**2.00**	3	0.99	0.01	
	3	Grt	36.37	0.26	20.50	31.81	2.98	1.13	7.18	0.00	0.00	**100.22**	2.94	0.01	1.97	2.12	0.20	0.13	0.61	0.00	0.00	**7.99**	12	0.91	0.09	574
		Ilm	0.10	51.57	0.22	44.95	0.58	0.45	0.07	0.05	0.02	**98.02**	0.00	0.99	0.01	0.96	0.01	0.02	0.00	0.00	0.00	**2.00**	3	0.99	0.01	
	4	Grt	36.51	0.20	20.64	29.67	4.58	0.98	7.25	0.00	0.04	**99.86**	2.95	0.01	1.96	2.00	0.32	0.12	0.63	0.00	0.00	**8.00**	12	0.86	0.14	565
		Ilm	0.17	52.33	0.24	45.66	1.07	0.37	0.06	0.00	0.03	**99.92**	0.00	1.00	0.01	0.95	0.02	0.01	0.00	0.00	0.00	**2.00**	3	0.98	0.02	
	5	Grt	35.65	0.12	20.48	28.88	4.91	1.03	7.21	0.00	0.02	**98.29**	2.94	0.01	1.97	1.99	0.34	0.12	0.64	0.00	0.00	**8.00**	12	0.85	0.15	555
		Ilm	0.39	52.00	0.25	45.33	1.08	0.38	0.02	0.01	0.01	**99.48**	0.01	0.99	0.01	0.95	0.02	0.01	0.00	0.00	0.00	**2.00**	3	0.98	0.02	
ET10-18a	1	Grt	35.46	0.07	20.22	38.13	0.76	2.79	0.61	0.03	0.00	**98.07**	2.94	0.00	1.98	2.64	0.05	0.34	0.05	0.00	0.00	**8.01**	12	0.98	0.02	611
		Ilm	0.16	54.43	0.18	44.83	0.19	0.19	0.01	0.00	0.00	**100.00**	0.00	1.03	0.01	0.95	0.00	0.01	0.00	0.00	0.00	**2.00**	3	1.00	0.00	
	2	Grt	36.35	0.07	20.02	38.88	1.48	1.32	1.81	0.00	0.00	**99.93**	2.94	0.00	1.97	2.66	0.10	0.16	0.16	0.00	0.00	**8.00**	12	0.96	0.04	604
		Ilm	0.15	51.72	0.14	46.56	0.29	0.09	0.04	0.00	0.01	**99.00**	0.00	0.99	0.00	0.99	0.01	0.00	0.00	0.00	0.00	**2.00**	3	0.99	0.01	
	3	Grt	36.41	0.07	20.52	35.56	3.49	0.94	3.00	0.00	0.00	**99.98**	2.95	0.00	1.98	2.46	0.24	0.11	0.27	0.00	0.00	**8.01**	12	0.91	0.09	599
		Ilm	0.12	53.10	0.18	46.08	0.66	0.23	0.02	0.02	0.03	**100.44**	0.00	1.00	0.01	0.96	0.01	0.01	0.00	0.00	0.00	**1.99**	3	0.99	0.01	
	4	Grt	36.18	0.09	20.67	31.64	5.68	0.90	4.33	0.00	0.00	**99.51**	2.95	0.01	1.97	2.20	0.39	0.11	0.38	0.00	0.00	**8.01**	12	0.85	0.15	595
		Ilm	1.52	51.96	1.04	43.47	0.97	0.24	0.47	0.28	0.12	**100.06**	0.04	0.96	0.03	0.91	0.02	0.01	0.01	0.01	0.00	**2.00**	3	0.98	0.02	
	5	Grt	36.28	0.10	19.98	33.96	6.58	0.94	2.36	0.00	0.00	**100.19**	2.94	0.01	1.97	2.30	0.46	0.12	0.21	0.00	0.00	**8.01**	12	0.83	0.17	594
		Ilm	0.18	54.40	0.20	44.63	1.16	0.32	0.06	0.03	0.00	**100.98**	0.00	1.01	0.01	0.92	0.02	0.01	0.00	0.00	0.00	**1.98**	3	0.97	0.03	
	6	Grt	35.70	0.10	20.69	30.82	7.33	0.79	4.44	0.00	0.01	**99.87**	2.94	0.01	1.97	2.10	0.50	0.10	0.39	0.00	0.00	**8.01**	12	0.81	0.19	592
		Ilm	0.25	52.71	0.20	43.95	1.55	0.33	0.10	0.00	0.01	**99.10**	0.01	0.99	0.01	0.94	0.03	0.01	0.00	0.01	0.00	**2.00**	3	0.97	0.03	
	7	Grt	35.77	0.05	20.00	28.63	8.82	0.61	4.95	0.00	0.02	**98.85**	2.94	0.00	1.96	1.97	0.61	0.07	0.43	0.00	0.00	**8.00**	12	0.76	0.24	576
		Ilm	0.05	52.74	0.12	42.81	1.92	0.27	0.06	0.09	0.00	**98.06**	0.00	1.01	0.00	0.91	0.04	0.01	0.00	0.00	0.00	**1.99**	3	0.96	0.04	
	8	Grt	35.57	0.02	20.41	27.22	9.60	0.64	5.51	0.00	0.00	**98.98**	2.92	0.00	1.98	1.89	0.65	0.08	0.48	0.00	0.00	**8.00**	12	0.74	0.26	559
		Ilm	0.09	53.85	0.20	43.21	2.22	0.22	0.08	0.00	0.00	**99.88**	0.00	1.03	0.01	0.90	0.05	0.01	0.00	0.00	0.00	**2.00**	3	0.95	0.05	
	9	Grt	35.79	0.15	20.30	26.80	9.56	0.69	5.66	0.00	0.00	**98.96**	2.94	0.01	1.97	1.84	0.67	0.08	0.49	0.00	0.00	**8.01**	12	0.73	0.27	550
		Ilm	0.29	54.23	0.15	43.49	2.33	0.25	0.12	0.09	0.00	**100.94**	0.01	1.02	0.00	0.91	0.05	0.01	0.00	0.00	0.00	**2.00**	3	0.95	0.05	
	10	Grt	35.76	0.14	20.58	26.98	10.01	0.64	5.90	0.00	0.01	**100.01**	2.93	0.01	1.97	1.81	0.68	0.08	0.51	0.00	0.00	**8.00**	12	0.73	0.27	549
		Ilm	1.10	53.53	0.12	42.16	2.38	0.11	0.06	0.02	0.05	**99.53**	0.03	1.01	0.00	0.90	0.05	0.00	0.00	0.00	0.00	**2.00**	3	0.95	0.05	

Table 6.13 – Mineral compositions used for garnet-ilmenite thermometry and associated calculated temperatures for samples ET10-13 and ET10-18a. Data represent SEM-microprobe analyses and so do not consider Fe^{3+} content.

The *P–T* conditions of later mylonitisation can be calculated from mineral assemblages in garnet rim strain shadows. AvePT calculations produced conditions of 6.9 ± 0.8 kbar and 577 ± 13 °C (sample ET10-13) and 7.0 ± 0.7 kbar and 538 ± 13 °C (sample ET10-18) when considering garnet outer rims and adjacent populations of neocrystallised biotite, muscovite, chlorite and plagioclase (Table 6.12). End-member activities used for AvePT calculations are given in Appendix 11.5. These temperatures are lower than those suggested for peak metamorphism and lie in the range of 350–650 °C presented by Xu *et al*. (2012) for similar mylonite from the region.

6.7. Summary and discussion

These geochronological and thermobarometric data provide tight *P–T–t* constraints on metamorphic and deformational episodes that affected units in the B-L-M region. These data are summarised below within the framework of its currently documented *P–T–t* history, and the tectonic implications for the larger-scale evolution of the southern Asian margin are discussed in chapter 8.1.2.

6.7.1. Partial melting in the B-L-M gneisses

Two types of partial melt have been identified in samples from the B-L-M region; medium-pressure sillimanite-grade K-feldspar-bearing granitic leucosomes (ET09-05, ET09-06, ET10-07, ET10-09), and higher pressure kyanite-grade K-feldspar-poor tonalitic leucosomes (ET10-10, ET10-12).

Medium-pressure granitic partial melts (ET09-05, ET09-06, ET10-07 and ET10-09)

Calculated minimum *P–T* conditions of peak metamorphism and partial melting in samples ET09-05, ET09-06 and ET10-07 are all equivalent within uncertainty, with pressures ranging between 5.2–6.3 kbar and temperatures ranging between 729–751 °C. U–Pb monazite ages obtained for the onset of partial melting in each sample (including ET10-09) are also similar (c. 71 Ma); hence it is interpreted that all sillimanite-grade migmatites in the study area share a common *P–T–t* history. Given observations of variable retrogression between samples, the highest calculated *P–T* conditions of 6.3 ± 1.2 kbar and ~750 ± 30 °C are taken to represent minimum *P–T* conditions for sillimanite-grade anatexis. This retrograde evolution is shown in Fig. 6.18a by a solid arrow – although it should be noted that absolute peak *P–T* conditions are unknown. The prograde evolution of these samples is also uncertain, except that they must have undergone muscovite-dehydration at some earlier time. As

a result, a clockwise *P–T* evolution is assumed following initial partial melting, although no evidence exists relating to the early prograde history through the subsolidus domain.

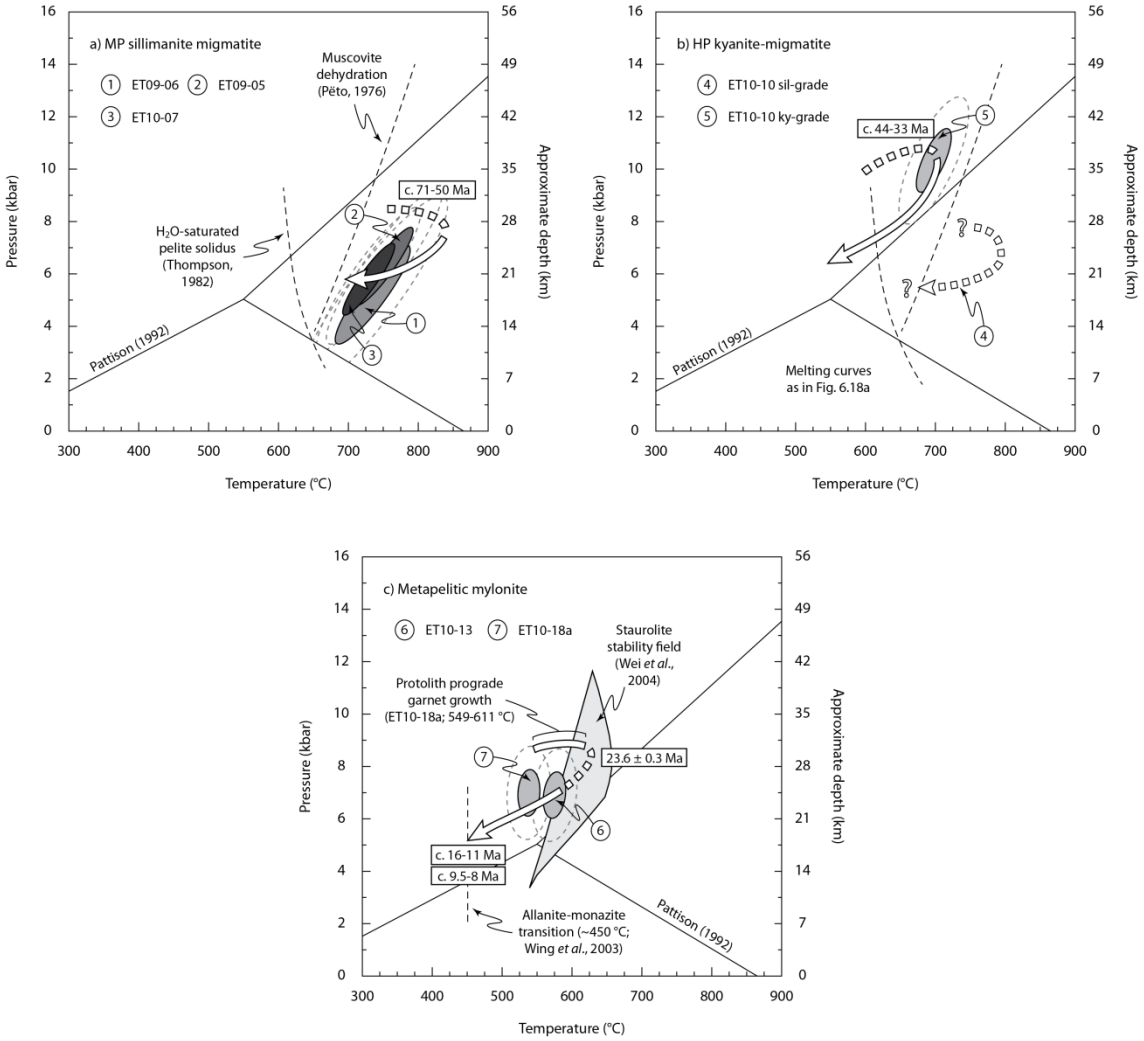


Fig. 6.18 – Interpreted *P–T–t* syntheses for samples from the B-L-M region. Solid arrows represent *P–T–t* evolution paths using calculated constraints; dashed arrows are inferred as discussed in the text. Aluminosilicate phase relations and triple point are after Pattison (1992). AvePT results, where present, are plotted as ellipses with solid and dashed lines at 1 S.D. and 2 S.D uncertainties respectively. (a) Medium-pressure sillimanite-grade migmatites ET09-05, ET09-06, ET10-07, ET10-09. (b) High-pressure kyanite-grade migmatites ET10-10, ET10-12. (c) Mylonite samples ET09-02, ET10-13, ET10-18. Staurolite stability field is taken from Wei *et al.* (2004) & Mahar *et al.* (1997).

Other sillimanite-grade migmatites and granitic melt compositions are documented in the B-L-M region, with ages constrained solely by U–Pb zircon geochronology. Zhang *et al.* (2010) report granulite-facies garnet-sillimanite-K-feldspar migmatites that formed at c. 90 Ma and which were subsequently overprinted at amphibolite-facies kyanite-grade conditions (see later). Zhang *et al.* (2010) report that these samples were collected from highway S306, north of Milin (Fig. 6.1). In addition, Guo *et al.* (2012) report granite and quartz-diorite sills intrusions into B-L-M units exposed

just east of Linzhi. According to their geological map, these samples were collected at an outcrop locality close to samples ET09-05 and ET09-06 from this study (Fig. 6.1). U–Pb zircon ages for both sills were calculated to be 64.4 ± 0.7 Ma and 63.1 ± 0.6 Ma, and analysis of Hf isotopes was interpreted to show that both were sourced from partial melting of Asian plate crustal materials. An orthogneiss from a nearby outcrop, also documented by Guo *et al.* (2012), was reported to have been metamorphosed between c. 65–46 Ma – overlapping with the c. 71–50 Ma ages described above. It is significant that the U–Pb monazite ages reported in this study largely overlap with the U–Pb zircon age data presented in previous work, given that zircon has a higher potential for inheritance in these lithologies and so zircon and monazite may not always provide evidence of the same metamorphic or anatectic event (Rubatto *et al*., 2006; Crowley *et al*., 2008). Hence, common age ranges for sillimanite-grade partial melting across the B-L-M region of the EHS shows that this event was widespread and of great importance to the tectonic evolution of the south Asian margin.

The mechanism behind such an extensive episode of crustal melting was interpreted by Guo *et al*. (2012) to be aesthenospheric upwelling, resulting in a high heat flow to the lower crust, caused by rollback of the northward subducted Neo-Tethyan oceanic slab. However, this interpretation seems to be slightly conjectural, as insufficient evidence currently exists (or was offered) to track the southward progression of crustal melting; an effect that would be expected with a diachronous event such as slab rollback. Instead, an alternative source of heat is presented by the observation that the southern Lhasa block (including a large proportion of the B-L-M region; Fig. 6.1) contains abundant calc-alkaline volcanic rocks and subduction-related granites of the Gangdese batholith (see chapter 1.5.2). Ages for these units span the Jurassic to Early Eocene, with a major episode of pluton emplacement documented at c. 66–57 Ma (Wen *et al*., 2008; Chiu *et al*., 2009; Lee *et al*., 2009). Such a large volume of magma could provide a regional-scale source of heat for initiating melting of the adjacent crust. A similar mechanism has been proposed for the formation of mid-crustal kyanite- and sillimanite-bearing metapelites that are now exposed as the exhumed roots of the Idaho–Bitterroot (Cordilleran) continental-margin batholith in north America (Foster *et al.*, 2001) and the Coast Mountains magmatic arc in British Columbia (Rusmore *et al.*, 2005). Although kyanite- and sillimanite-bearing metamorphic rocks are rare outside of the B-L-M region elsewhere along the >2000 km long southern margin of the Asian plate, this is interpreted to be a result of the generally

shallow depths of batholith exposure in these regions. Potentially similar exhumed migmatitic units described in the Nyainqentanglha Shan in central Tibet are inferred to be of Cretaceous-Tertiary age (Kidd *et al.,* 1988; Kapp *et al.,* 2005), although no age data are provided to support this claim. Further discussion of the regional-scale magmatism in the B-L-M region is given in chapter 8.1.2.

High-pressure kyanite-grade tonalitic partial melts (ET10-10)

Sample ET10-10 records high-pressure metamorphism and anatexis at peak *P–T* conditions of 10.4 ± 1.0 kbar and 698 ± 20 °C (Fig. 6.18b) with a vapour phase composition of XH_2O ~0.9, consistent with the presence of graphite in the mesosome foliation. At that pressure, the calculated temperature is insufficient for dehydration melting reactions to occur, but is more-than-sufficient for fluid-saturated melting of a metasediment (Patiño Douce & Harris, 1998; García-Casco *et al.*, 2003). Monazite inclusions in garnet rims suggest that partial melting commenced no later than c. 44 Ma, continuing for *at least* 11 Myr as shown by younger euhedral monazite (c. 33 Ma) in leucosomes. Exhumation from peak conditions until melt crystallisation cannot have been isothermal, as kyanite shows no evidence of retrograde transition to sillimanite. Such changes are thought to occur with minimal overstepping in suprasolidus assemblage fields (e.g. Pattison & Begin, 1994). Hence, the partial retrograde path in Fig. 6.18b is described with a solid line, although as with the sillimanite-grade migmatites described above, the early prograde history is uncertain.

Two separate occurrences of high-pressure kyanite-bearing migmatite have been documented recently from the core of the EHS (Namche Barwa Group) by Guilmette *et al.* (2011) and Zeng *et al.* (2012). The former study reported anatexis as the result of biotite-dehydration at high-pressure granulite-facies conditions of 15–16 kbar and ~850 °C (with no age constraints), producing a granitic partial melt, whereas the latter study documents Ca-rich/K-poor trondhjemitic leucosomes that formed at ~24–25 Ma (U–Pb zircon) via water-fluxed melting reactions (with no *P–T* constraints). Age data from the latter study suggests that some units of the Namche Barwa Group (Indian plate) experienced high-pressure melting ~5–9 Myr later than the event recorded in sample ET10-10. However, leucosomes of granitic composition documented in the former study indicates that these two occurrences of high-pressure melting within the syntaxis are not directly related.

Kyanite-bearing migmatitic paragneiss from the Asian plate B-L-M region is documented by Zhang *et al.* (2010) and was reportedly collected from an outcrop close to that of sample ET10-10 in this study (Fig. 6.1). Calculated peak *P–T* conditions reported by Zhang *et al.* (2010) of 8–11 kbar and 590–660 °C are also similar to those of 10.4 ± 1.0 kbar and 698 ± 20 °C calculated for sample ET10-10. Furthermore, akin to the evolution described by Zhang *et al.* (2010), sillimanite inclusions in garnet cores in sample ET10-10 indicate early garnet growth at lower pressure (possibly higher temperature?) conditions compared to the kyanite-grade anatectic matrix assemblage (Fig. 6.18b). The *P–T* conditions of this early event could not be calculated, therefore it is unclear whether sample ET10-10 records a poly-metamorphic history or whether sillimanite was included in garnet during a lower pressure stage of a single prograde *P–T* evolution. The latter case, a continuous evolution from sillimanite- to kyanite-grade seems unlikely as such an evolution would require a very steep positive slope (in *P–T* space) in order to remain below the wet solidus at mid-crustal pressures, thus avoiding melting to form a granitic leucosome, but whilst evolving from within the stability field of sillimanite (a minimum temperature of ~550 °C at ~4.25 kbar; Pattison, 1992).

The former scenario of two separate and distinct metamorphic events is thus preferred (dashed line on Fig. 6.18b), especially given the occurrence of older sillimanite-grade migmatites to the north (ET09-05, ET09-06, ET10-07 and ET10-09). The c. 36–33 Ma U–Pb zircon ages reported by Zhang *et al.* (2010) for kyanite-grade metamorphism are interpreted to date the same event as the c. 44–33 Ma U–Pb monazite data from sample ET10-10. Whether the prior sillimanite-grade metamorphism documented at c. 90 Ma by Zhang *et al.* (2010) and at c. 71–50 Ma (this study) represents two distinct thermal pulses, or reflects a protracted c. 40 Myr regional metamorphic event is unknown at this point and will require further investigation of suitable samples from the region. This kyanite-grade melting event is interpreted to be the result of crustal thickening associated with the India-Asia collision, and is distinctly different in character from the prior sillimanite-grade melting that was interpreted to require a pre-collisional heat source (see chapter 8.1.2 for further discussion).

6.7.2. Mylonite formation along the MYLP fault

The present day north-western margin of the EHS is expressed as a major ductile shear zone with a prominent band of mylonite that cuts across kyanite- and sillimanite-grade rocks in the B-L-M

region (Fig. 6.1). Mylonite from the southern section of the shear zone, situated very close to the outcrop locality for sample ET10-18a (Fig. 6.1), was dated by Xu *et al.* (2012). Their study reports U–Pb ages of 31.3 ± 0.3 Ma and 25.5 ± 0.6 Ma from metamorphic overgrowths on zircon rims in a mylonitised garnet-bearing paragneiss and amphibole-bearing felsic orthogneiss respectively (ibid). These ages slightly predate a U–Pb monazite age of 23.6 ± 0.3 Ma obtained for pre-mylonitisation staurolite-grade metamorphism in sample ET10-18a, although it should be emphasised again that the provenance of these mylonites is debated. Given that the shear zone truncates high-grade metamorphic units on both the Indian and Asian plates, it is possible that some mylonitised metasediments within the zone represent deformed units of either continental margin, rather than necessarily representing sheared packets of marine sediments and oceanic crust that once formed part of the Neo-Tethyan Ocean prior to the India-Asia collision (as concluded by Zhang *et al*., 2010).

Samples ET10-13 and ET09-02, collected from a separate locality along strike of sample ET10-18a (Fig. 6.1), produced U–Pb monazite data suggesting that both were undergoing ductile shear and exhuming through the ~450 °C isotherm between c. 16–11 Ma and c. 9.5–8.0 Ma respectively (Fig. 6.18c). Xu *et al.* (2012) provide data that corroborate this interpretation with an Ar–Ar biotite age of 9.6 ± 0.2 Ma obtained from a sheared amphibolite that was collected from the same locality, which was interpreted by their study as representing cooling through the closure temperature of ~300 °C. From analysis of numerous mylonites along the shear zone, they concluded that two major shearing events in the region occurred at c. 22–18 Ma and c. 6–2 Ma.

7. Red River shear zone

Part of the work presented here forms the basis of the paper Palin et al. (2013) published in the Journal of Metamorphic Geology (cf. chapter 10.2.2).

7.1. Chapter introduction

The tectonic configuration and evolution of south-east Asia is a topic of ardent study by the geological community, with particular interest in the relationship between the India-Asia collision and four high-grade metamorphic massifs that exist along the RRSZ (chapter 1.4.4). Lithologies in these massifs provide geochronological evidence for an extended metamorphic history, with major events documented by numerous workers to have occurred during both the Triassic and Eocene-Oligocene reportedly associated with the Indosinian and Himalayan orogenies respectively. However, extensive strike-slip shear deformation and transpressive exhumation of these units since the Oligocene-Miocene has hindered the interpretation of these events as pre-mylonitisation petrographic features are poorly preserved. In addition, all previous studies of these units have relied upon conventional thermobarometry to investigate changing *P–T* conditions in the massif, which carry relatively large associated uncertainties when compared to the potential accuracy that can be attained through thermodynamic phase equilibria modelling. The reported *P–T* data by these works also show a wide spread in calculated conditions. In response to this problem, samples of relatively undeformed anatectic paragneiss and associated granite dykes were collected from the DNCV region of the RRSZ by M.P. Searle, S.-L. Chung, M.-W. Yeh and T.T. Anh. These units have been used in a study that integrates pseudosection construction with *in-situ* monazite geochronology to better constrain the *P–T–t* history of the DNCV massif and have provided new insight into the link between the timing of high-grade metamorphism in Vietnam and the India-Asia collision.

7.2. Geological setting

The RRSZ is a major geological discontinuity that stretches for >1000 km across south-east Asia (Fig. 1.6) and separates the South China and Indochina crustal blocks. The DNCV in North Vietnam is the southernmost metamorphic core complex exposed along this shear zone and occurs as a ~250 km long NW–SE trending antiform that is bound by the Red River fault to the south-west and the Song Chay fault to the north-east (Fig. 7.1). Both faults are associated with steeply dipping mylonitic

fabrics (Nam *et al.*, 1998; Leloup *et al.*, 2001) that truncate gently dipping metamorphic fabrics in the massif core (Searle 2006; Anczkiewicz *et al.*, 2007; Yeh *et al.*, 2008). As the degree of strike-slip related deformation varies strongly across the antiform, previous workers have suggested that the relatively undeformed high-grade metamorphic and magmatic rocks in the massif core have been vertically (passively) exhumed with little deformation (e.g. Anczkiewicz *et al.*, 2007).

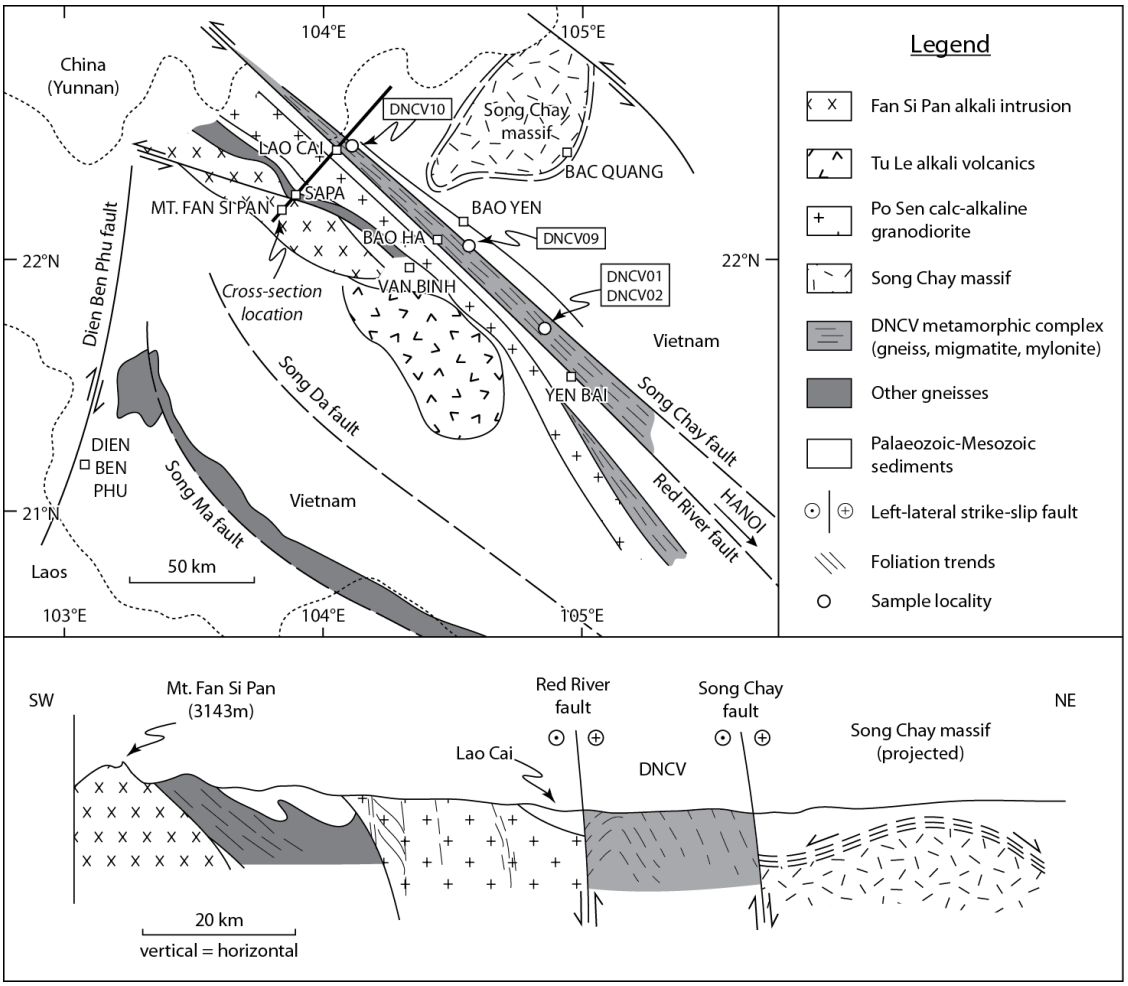


Fig. 7.1 – Geological map of the DNCV and environs (after Lacassin *et al.*, 1998; Jolivet *et al.*, 2001; Searle, 2006).

A variety of lithologies exist in and around the DNCV. High-grade metamorphic units in the antiform itself comprise abundant pelitic gneisses and migmatites, alongside discrete layers of amphibolite and lenses of marble (Leloup *et al.*, 2001). The Song Chay massif lies outside of the DNCV to the north-east (Fig. 7.1) and is an exhumed metamorphic core complex primarily composed of orthogneiss, schist and amphibolite (Yan *et al.*, 2006) that is thought to have an equivalent pre-shearing tectonothermal history to the deep-crustal units in the DNCV (Jolivet *et al.*, 1999, 2001; Searle, 2006). Numerous potassic alkaline igneous rocks occur in the region, as well as

being present elsewhere along the RRSZ (Chung *et al*., 2008). Prominent examples associated with the DNCV include the Fan Si Pan alkaline granite-syenite intrusion, Tu Le alkali volcanics and calc-alkaline hornblende-bearing granodiorites of the Po Sen batholith (Fig. 7.1). These units are located outside of the shear zone and are largely undeformed (Searle, 2006).

7.2.1. Geochronology

Numerous previous studies have investigated the tectonothermal evolution of North Vietnam through multi-system geochronology performed on a range of lithologies from in and around the DNCV massif. Carter *et al.* (2001) report a U–Pb zircon age of 245 ± 5 Ma from orthogneiss located in the core of the antiform, which was interpreted to represent an episode of high-temperature ductile deformation of the metamorphic basement of North Vietnam associated with the Indosinian orogeny (between c. 250–190 Ma; Metcalfe, 2000). Ruby-bearing marble from the north-eastern flank of the antiform was studied by Garnier *et al.* (2005) and produced similar U–Pb ages from zircon included in spinel, which was interpreted to have formed during the Late Permian (256.6 ± 9.4 Ma) with a *'possible re-opening of the U–Pb system'* during the Triassic (231.7 ± 5.6 Ma). Further evidence for Triassic metamorphism is documented by Yan *et al.* (2006) from orthogneiss from the Song Chay massif that contains zircon with magmatic cores and metamorphic rim overgrowths with U–Pb ages of 799 ± 10 Ma and 237 ± 15 Ma respectively. Gilley *et al.* (2003) document *in-situ* Th–Pb monazite ages from samples of metapelitic schist from the Song Chay massif between c. 255–203 Ma, whereas monazite from anatectic paragneiss in the DNCV was reported to contain several domains with different Th–Pb ages, indicative of multiple metamorphic episodes (Kohn *et al.*, 2005). Monazite included in garnet produced ages ranging between c. 220–44 Ma, whereas matrix grains produced similar old ages, but also some as young as c. 21 Ma (Gilley *et al*., 2003). Older ages were interpreted to be relics of Indosinian metamorphism whereas grains that had not been shielded in garnet were suggested to have been variably reset during high-temperature Tertiary metamorphism.

Nam *et al.* (1998) report K–Ar ages from hornblende-bearing amphibolite (~28 Ma) and biotite-bearing gneiss (~24 Ma) that were interpreted to represent the timing of exhumation of the massif through the 500 °C and 300 °C isotherms respectively. Similar K-feldspar, muscovite and biotite Ar–Ar data presented by Leloup *et al.* (2001) suggest that cooling of the massif below ~250

°C had occurred by ~23 Ma. This is corroborated by Maluski *et al.* (2001) who report muscovite fish in sheared gneiss from the northern flank of the antiform with an Ar–Ar plateau age of 24 ± 2 Ma alongside apatite fission-track ages of 18 ± 1 Ma and 22 ± 2 Ma. These data suggest that the exhumation of the massif from mid to shallow crustal levels occurred quickly during the Miocene.

7.2.2. Thermobarometry

Despite extensive study, disagreement exists concerning the absolute *P–T* conditions for various tectonic stages of evolution of the DNCV. Early investigation by Nam *et al.* (1998) suggested peak metamorphic conditions of 6–7 kbar and 630–720 °C, sufficient only for muscovite-dehydration melting to occur. However, subsequent work has proposed higher-grade *P–T* conditions with a wide range between 4.7–8.8 kbar and 735–830 °C (Gilley *et al.*, 2003; Anczkiewicz *et al.*, 2007; Leloup *et al.*, 2001), sufficient for the onset of biotite-dehydration melting. Through a combination of microstructural criteria and conventional thermobarometry performed on a suite of metapelitic units across the DNCV, Leloup *et al.* (2001) suggested that this metamorphic evolution is characterised by a single clockwise *P–T* path. Documented *P–T* conditions of strike-slip shearing and retrograde equilibration range between 3.5 ± 1 kbar and 655 ± 75 °C (Leloup *et al.*, 2001), 2.9–3.3 kbar and 630–670 °C (Pham Van *et al.*, 2004) and 400–560 °C at a pressure less than ~3.8 kbar (Nam *et al.*, 1998). This latter study constrained pressures of deformation by retrograde andalusite crystals rimming K-feldspar porphyroclasts in a sample of mylonite. These data are summarised in Table 7.1.

Stage	Lithology	Location	*P–T* conditions (with error)	Method	Study
Peak	Amphibolite	Core of antiform	690 ± 30 °C, 7.3 ± 0.9 kbar	Grt-Hbl[1], Grt-Hbl-Pl[2]	Nam *et al.* (1998)
Peak	Metapelite	Core of antiform	690 + 30/-60 °C, 6.2 +1.4/-1.7 kbar	Grt-Bt[1], GASP[2]	Nam *et al.* (1998)
Peak	Metapelite	Core of antiform	735 ± 65 °C, 4.7 ± 1.7 kbar	Grt-Bt[1], GASP[2]	Leloup *et al.* (2001)
Peak	Metapelite	Core of antiform	780–830 °C, 7.5–8.8 kbar	Grt-Bt[1], GRAIL[2]	Gilley *et al.* (2003)
Peak	Metapelite	Core of antiform	810 ± 60 °C, 5.6 ± 1.5 kbar	THERMOCALC AvePT	Anczkiewicz *et al.* (2007)
Peak	Metapelite	SW limb of antiform	820 ± 60 °C, 7 ± 1.6 kbar	THERMOCALC AvePT	Anczkiewicz *et al.* (2007)
Peak	Metaperidotite	Core of antiform	700–800 °C, 8 kbar	Phase relations in $MgO–Al_2O_3–SiO_2–H_2O$	Anczkiewicz *et al.* (2007)
Retrograde	Metapelite	Core of antiform	680–840 °C between 2–8 kbar	Grt-Bt[1]	Gilley *et al.* (2003)
Retrograde	Marble	Luc Yen	<3.8 kbar	Andalusite inclusion in ruby	Pham Van *et al.* (2004)
Retrograde	Marble	Luc Yen	630–670 °C, 2.9–3.3 kbar	Not stated	Garnier *et al.* (2005)
Retrograde-shearing	Metapelite	Core of antiform	655 ± 75 °C, 3.5 ± 1 kbar	Grt-Bt[1], GASP[2], THERMOCALC AvePT	Leloup *et al.* (2001)
Shearing	Mylonite	Core of antiform	480 ± 80 °C, <4 kbar	Grt-Bt[1], andalusite on K-feldspar rim	Nam *et al.* (1998)
Shearing	Metapelite	Core of antiform	500–700 °C	Qz-Fsp microfabric analysis	Anczkiewicz *et al.* (2007)

Table 7.1 – *P–T* estimates for various stages in the evolution of the DNCV massif. Conventional methods of thermobarometry are marked as follows: [1] = thermometer [2] = barometer.

7.3. Petrography and mineral chemistry

Samples used in this study were collected from several outcrops within the DNCV antiform by M.P. Searle, S.-L. Chung, M.-W. Yeh and T.T. Anh (Fig. 7.1). Samples of paragneiss (DNCV01) and

leucosome (DNCV10) were collected in order to investigate the timing and *P–T* conditions of peak metamorphism and migmatisation, whereas cross-cutting (DNCV02) and sheared (DNCV09) granitic dykes were collected in order to place constraints on the timing of deformation. Samples DNCV01 and DNCV02 were collected ~19 km north-west of Yen Bai town at GPS co-ordinates 21° 48’ 00” N and 104° 54’ 32” E. Sample DNCV09 was collected from ~8 km south-east of Bao Yen at GPS co-ordinates 22° 02’ 11” N and 104° 31’ 57” E and sample DNCV10 was collected outside of Lao Cai at GPS co-ordinates 22° 28’ 57” N and 104° 02’ 23” E. As only DNCV01 underwent SEM-microprobe analysis, mineral compositional data are restricted to this sample.

7.3.1. DNCV01

As sample DNCV01 was collected from the transpressively-uplifted core of the antiform, it lacks the strike-slip shear fabrics that are prominent in mylonitic units located at both flanks (Searle, 2006; Anczkiewicz *et al.,* 2007; Yeh *et al.,* 2008). At outcrop scale, DNCV01 resembles a stromatic migmatite with pale bands of leucosome between darker mesosome regions of variable thickness (Fig. 7.2a). At thin section scale, however, the boundary between leucosome and mesosome regions is less distinct. Microstructural analysis reveals a peak metamorphic assemblage of garnet, sillimanite, biotite, plagioclase, K-feldspar and quartz, with minor amounts of apatite, monazite, zircon and pyrite. Within the studied thin sections, subhedral-to-anhedral porphyroblasts of garnet were observed to range between 1–5 mm in diameter (Fig. 7.2b–c) and some display partial rim replacement by biotite, plagioclase and sillimanite, with or without chlorite (e.g. Fig. 7.2b). Core regions of the largest porphyroblasts contain numerous inclusions of quartz, biotite, K-feldspar, plagioclase, sillimanite and rutile, and are surrounded by broader inclusion-poor regions (Fig. 7.2c).

All examined garnet grains exhibit systematic compositional zoning, a representative profile of which is presented in Fig. 7.3. Very little compositional variation occurs in core regions, which contain 25–27% pyrope, 7–8% grossular, 61–63% almandine and 3–4% spessartine. However, significant deviation occurs in thin outer rim regions where compositions are approximately 20–21% pyrope, 5% grossular, 70–71% almandine and 5% spessartine (Table 7.2 & Fig. 7.3). Plagioclase occurs as inclusions in garnet cores and as large porphyroblasts in the leucosome, the latter being up to 8 mm in diameter and containing occasional inclusions of quartz, biotite and K-feldspar.

Sample	Mineral	Location	SiO_2	TiO_2	Al_2O_3	Fe_2O_3	FeO	MnO	MgO	CaO	Na_2O	K_2O	**Total**	Si	Ti	Al	Fe^{3+}	Fe^{2+}	Mn	Mg	Ca	Na	K	**Sum**	Ox	XMg	XCa	Al(iv)	Al(vi)	Alm	Prp	Grs	Sps
DNCV01	Bt	Matrix adjacent to Grt rim	35.45	2.78	18.88	0.00	17.49	0.06	12.09	0.10	0.25	10.28	**97.40**	2.63	0.16	1.65	0.00	1.09	0.00	1.34	0.01	0.04	0.97	**7.89**	11	0.55	-	1.37	0.28	-	-	-	-
	Bt	Inclusion in Grt core	35.71	5.04	17.81	0.00	13.64	0.04	13.65	0.10	0.30	9.89	**96.18**	2.64	0.28	1.55	0.00	0.84	0.00	1.50	0.01	0.05	0.93	**7.80**	11	0.64	-	1.37	0.18	-	-	-	-
	Bt	Mesosome foliation	34.95	4.14	17.98	0.00	17.03	0.01	11.16	0.00	0.14	10.24	**95.65**	2.64	0.24	1.60	0.00	1.08	0.00	1.26	0.00	0.03	0.99	**7.83**	11	0.54	-	1.36	0.24	-	-	-	-
	Chl	Infill within Grt fracture	25.64	0.01	21.68	0.00	33.81	0.15	6.21	0.02	0.00	0.03	**87.55**	2.82	0.00	2.81	0.00	3.11	0.02	1.02	0.00	0.00	0.00	**9.78**	14	0.25	-	-	-	-	-	-	-
	Grt	Outer rim	37.13	0.06	21.12	1.51	29.41	1.99	5.67	2.03	0.02	0.01	**98.95**	2.94	0.00	2.00	0.07	2.07	0.14	0.64	0.14	0.00	0.00	**8.00**	12	0.24	-	-	-	0.69	0.21	0.05	0.05
	Grt	Core	36.71	0.00	21.63	1.64	28.07	1.34	7.02	2.54	0.07	0.01	**99.03**	2.91	0.00	2.01	0.08	1.85	0.09	0.82	0.22	0.01	0.00	**8.00**	12	0.31	-	-	-	0.62	0.27	0.08	0.03
	Kfs	Leucosome	63.20	0.52	19.38	0.04	0.00	0.00	0.35	0.10	0.91	16.17	**100.67**	2.95	0.00	1.05	0.00	0.00	0.00	0.00	0.01	0.06	0.93	**5.00**	8	-	0.01	-	-	-	-	-	-
	Kfs	Inclusion in Grt core	62.28	0.21	18.86	0.37	0.00	0.04	0.26	0.12	1.21	15.65	**99.00**	2.94	0.00	1.04	0.01	0.00	0.00	0.00	0.01	0.09	0.90	**5.00**	8	-	0.01	-	-	-	-	-	-
	Ms	Infill within Sil boudinage	48.54	0.00	36.27	0.00	0.82	0.00	0.40	0.61	0.28	10.22	**97.14**	3.14	0.00	2.77	0.00	0.05	0.00	0.04	0.04	0.04	0.84	**6.92**	11	0.46	-	0.86	1.91	-	-	-	-
	Pl	Leucosome	56.92	0.03	26.87	0.00	0.05	0.00	0.31	8.13	6.24	0.46	**98.99**	2.57	0.00	1.43	0.00	0.00	0.00	0.02	0.39	0.55	0.03	**5.00**	8	-	0.41	-	-	-	-	-	-
	Pl	Leucosome away from Grt	58.23	0.02	26.11	0.00	0.00	0.02	0.29	7.33	6.81	0.23	**99.04**	2.62	0.00	1.39	0.00	0.00	0.00	0.02	0.35	0.60	0.02	**5.00**	8	-	0.36	-	-	-	-	-	-
	Pl	Inclusion in Grt core	53.83	0.00	29.19	0.24	0.00	0.00	0.33	10.96	4.76	0.43	**99.74**	2.44	0.00	1.56	0.01	0.00	0.00	0.02	0.53	0.42	0.03	**5.00**	8	-	0.55	-	-	-	-	-	-
	Pl	Matrix adjacent to Grt rim	57.00	0.00	27.08	0.59	0.00	0.06	0.38	8.21	6.46	0.18	**99.96**	2.56	0.00	1.43	0.02	0.00	0.00	0.03	0.39	0.56	0.01	**5.00**	8	-	0.41	-	-	-	-	-	-

Table 7.2 – Mineral compositions for sample DNCV01

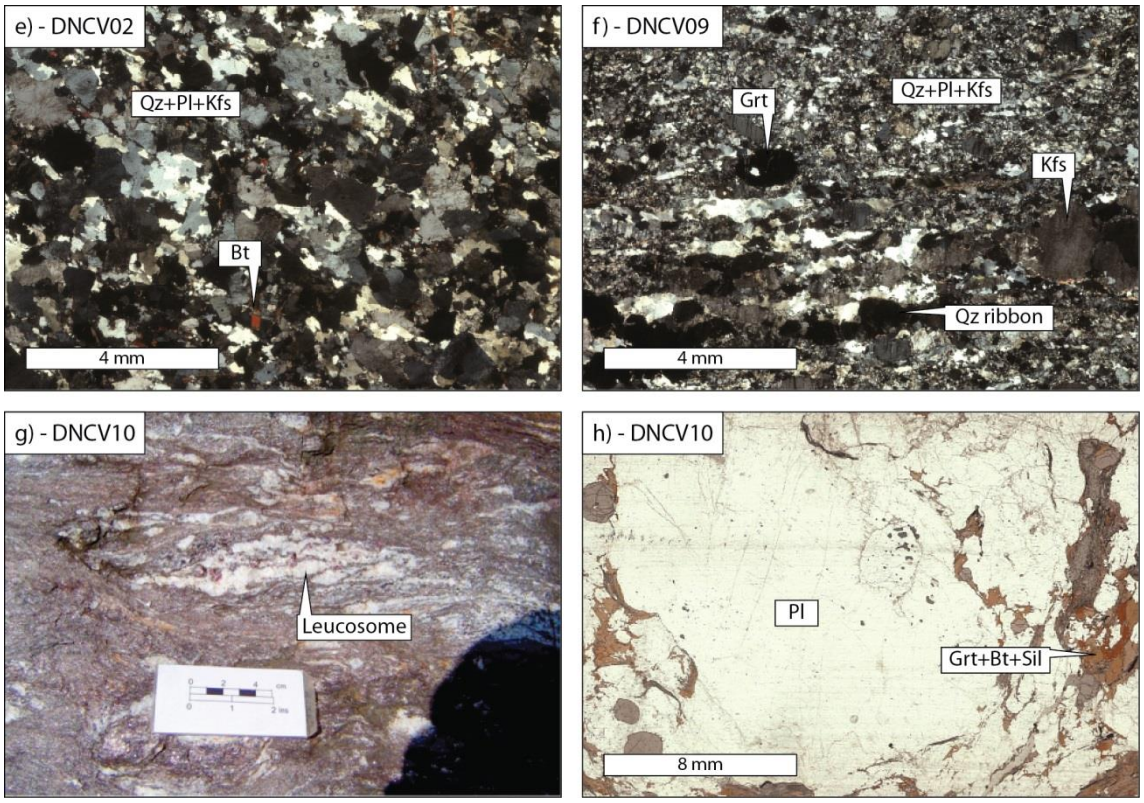
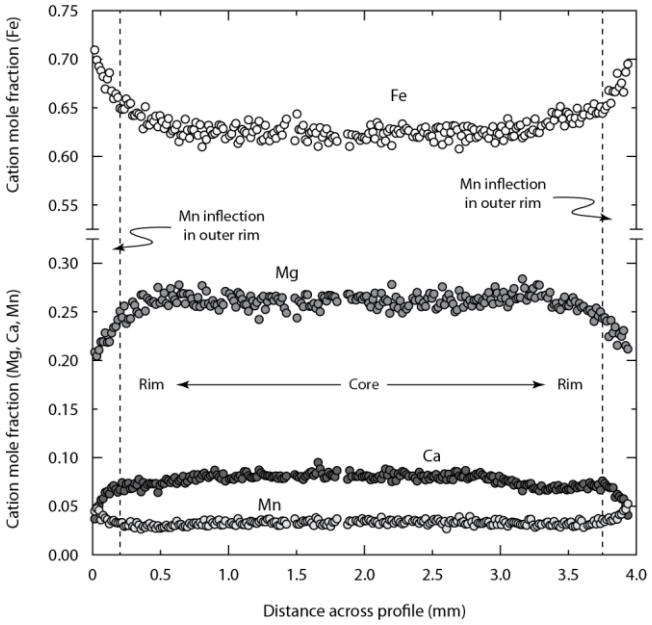


Fig. 7.2 – Field photographs and thin section images of samples from the DNCV (overleaf). (a) Outcrop photograph of sample DNCV01 with cm-scale stromatic differentiation of leucosome and mesosome (b) Sample DNCV01 showing partial replacement of garnet by biotite, sillimanite and occasional chlorite (plane polarised light). (c) Detail of inclusion-rich garnet cores in sample DNCV01, which commonly contain quartz and plagioclase with minor biotite (plane polarised light). (d) Outcrop photograph of undeformed granite dyke sample DNCV02, which cross-cuts migmatitic folia in host gneiss. (e) Sample DNCV02 showing a typical igneous assemblage of quartz, plagioclase, K-feldspar and minor biotite (viewed under crossed polars). (f) Sheared granite dyke sample DNCV09 showing ribbons of quartz that contain a medium-strong crystallographic preferred orientation and wrap larger clasts of K-feldspar and garnet (viewed under crossed polars). (g) Outcrop photograph of migmatite leucosome segregation DNCV10. (h) Sample DNCV10 showing a typical leucosome domain containing plagioclase megacrysts (plane polarised light).

K-feldspar occurs as inclusions in garnet cores and as porphyroblasts up to 5 mm in diameter in the leucosome. Sillimanite occurs as prismatic laths that occur up to 10 mm in length. Biotite exists primarily as sub-millimetre-sized grains in the mesosome foliation (Fig. 7.2a), but also occurs as inclusions in garnet cores, partially replacing garnet rims and as finely recrystallised grains in strain shadows that are aligned with the foliation (Fig. 7.2b). Rare chlorite occurs along fractures in garnet. Compositions of minerals in each textural position are given in Table 7.2.

Fig. 7.3 – Garnet compositional profile for sample DNCV01 (overleaf). Line profile is non-continuous due to traverse crossing inclusions and fractures.



7.3.2. DNCV02

Undeformed granite dyke sample DNCV02 cross-cuts sample DNCV01 (Fig. 7.2d) and is largely isotropic, exhibiting an undeformed igneous microstructure dominated by coarse crystalline aggregates of K-feldspar, plagioclase and quartz alongside minor biotite and accessory zircon, monazite and apatite (Fig. 7.2e). Rare chlorite and muscovite are present, associated with biotite and feldspar respectively, and are therefore likely to be post-crystallisation low-temperature alteration products. Representative grain sizes are shown in Fig. 7.2e.

7.3.3. DNCV09

Sample DNCV09 is a well-foliated granitic dyke that is aligned parallel to mylonitic fabrics in host gneisses located at the north-eastern flank of the antiform and has a 140° NW–SE aligned stretching lineation (M.P. Searle *pers comms*, 2012). This relationship implies emplacement prior to strike-slip deformation and that the intrusion has undergone shearing along with host gneiss units (e.g. Searle, 2006). Sample DNCV09 exhibits a similar mineralogy to sample DNCV02, with the addition of minor garnet (Fig. 7.2f). Garnet, K-feldspar and plagioclase clasts are wrapped by ribbons of quartz (Fig. 7.2f) and biotite flakes are commonly aligned alongside these ribbons. Thin regions of recrystallised muscovite partially surround K-feldspar rims and accessory zircon, monazite and apatite are also present. Representative grain sizes are shown in Fig. 7.2f.

7.3.4. DNCV10

DNCV10 was sampled as a bulbous leucosome segregation in paragneiss, which can occur up to ~5 cm in thickness (M.P. Searle *pers comms*, 2012; Fig. 7.2g) and are characterised by megacrysts of K-feldspar and plagioclase in excess of 20 mm in diameter alongside smaller quartz, garnet, biotite, sillimanite, apatite, monazite and zircon (Fig. 7.2h). Petrographically, these segregations are thicker domains of the leucocratic material described for sample DNCV01.

7.4. Thermobarometry and pseudosection modelling

Due to the large variation in peak metamorphic conditions reported for units of the DNCV (Table 7.1), pseudosections were constructed to provide tighter constraints on the *P–T* evolution. *P–T* pseudosection construction and interpretation has been shown to be the most effective method of investigation for the metamorphic evolution of high-temperature and partially melted rocks, in place of conventional thermobarometry (e.g. Halpin *et al.,* 2007; Indares *et al.,* 2008). This is following advances in thermodynamic modelling of the effects of melt loss in metapelites (White & Powell, 2002) and updated activity-composition relationships for ferro-magnesian minerals coexisting with silicate melt (White *et al.,* 2007), which allow more realistic reproduction of natural assemblages and compositions. *P–T* pseudosections are also extremely useful for estimating peak metamorphic conditions in these situations by identifying the stability fields of particular mineral assemblages in *P–T* space, which eliminates problems associated with conventional thermobarometry whereby the resetting of mineral compositions during cooling may produce invalid results (e.g. Pattison & Begin, 1994; Kelsey *et al.,* 2003).

7.4.1. Bulk composition calculation and pseudosection construction

Multiple *P–T* pseudosections were constructed for sample DNCV01 following the general methods and parameters outlined in chapter 2.4. An initial EBC was calculated from observed mineral proportions and compositions (cf. chapter 2.4.2); however, this was later modified to account for the previous loss of melt (see chapter 7.4.3). H_2O content of the initial EBC was calculated from the proportion of biotite after adjusting stoichiometric compositions to account for the incorporation of Ti by a deprotonation substitution (Waters & Charnley, 2002; White *et al*., 2007). In this situation, instead of biotite having an ideal 2.00 atoms of H (per 11-oxygens), this is reduced by 0.24 (the Ti content for 11-oxygens) to produce a total of 1.76 H atoms (Appendix 11.6). The resulting calculated

H_2O content in the EBC is low, consistent with the preservation of a high-grade assemblage (White & Powell, 2002). The initial modelled EBC for sample DNCV01 is H_2O – 2.43; SiO_2 – 68.73; Al_2O_3 – 11.67; FeO – 5.50; MgO – 4.13; CaO – 2.17; K_2O – 2.82; Na_2O – 1.65; TiO_2 – 0.75; MnO – 0.14; O – 0.16 (mole %).

7.4.2. Pseudosections for measured bulk composition (suprasolidus *P–T* evolution)

Initial *P–T* pseudosection construction was performed using an EBC calculated from the observed mineralogy in sample DNCV01. However, leucosome networks in the DNCV gneisses combined with the partial preservation of garnet implies that a portion of melt has been lost from the rock system during its *P–T* evolution (White & Powell, 2002). Hence, such a bulk composition is appropriate to model *P–T* conditions after the loss of that melt fraction (i.e. it is valid for assessment of peak/near-peak and suprasolidus retrograde *P–T* conditions of metamorphism, but not the prograde evolution). The resulting *P–T* pseudosection for sample DNCV01, between the limits of 2–10 kbar and 700–900 °C, is presented in Fig. 7.4a. This range encompasses the majority of peak *P–T* conditions reported by previous studies and also clearly shows the relationship between subsolidus and suprasolidus assemblages. The general topology is dominated by 5- and 6-variance fields, with muscovite absent and plagioclase, ilmenite, K-feldspar and quartz present over the entire *P–T* range.

An apparent problem exists as ilmenite is calculated to be stable in every assemblage with a modal proportion ranging between 1–2%, although it was not observed in sample DNCV01. This may be explained through the inspection of calculated biotite compositions over the region of interest, which shows that THERMOCALC assigns less Ti to the biotite structure than is observed in matrix grains. At peak conditions (see below) biotite is calculated to have ~0.15 Ti cpfu, a difference of ~0.09 cations from observed values. Also, the melt model (in NCKFMASH) of White *et al.* (2007) used for modelling does not include TiO_2 as a component, although it has been demonstrated through experimental study that Ti will begin to enter silicate melt under high-*T* conditions (Gaetani *et al.,* 2008). Thus it is likely that the incongruent breakdown of biotite with increasing temperature should result in less Ti being available for the production of ilmenite than is calculated by THERMOCALC, hence the difference between observations and calculations. Alternatively, the formation of retrograde biotite (as observed; Fig. 7.2b) would require consumption of a Ti-bearing

phase and could account for the present absence of ilmenite. For these reasons, coupled with the very low calculated modal proportion, ilmenite is not discussed further for sample DNCV01.

Peak metamorphism

The peak metamorphic assemblage of grt–bt–kfs–pl–sil–qz(–melt) observed in sample DNCV01 is represented by a 6-variant field which exists between ~5.5–9.5 kbar and ~780–860 °C (Fig. 7.4a). The low-temperature limit of this field is marked by the solidus and a low-pressure limit is provided by the closely spaced 'sillimanite-out' and 'cordierite-in' field boundaries, with this exchange occurring over an interval of <0.1 kbar. Refinement of peak *P–T* conditions in this field is achieved from examination of the garnet composition just inside of the outer-rim inflections in XFe and Mn content (Fig. 7.3 & Table 7.2), both of which are characteristic features of retrograde replacement by biotite (Spear, 1993; Kohn & Spear, 2000). Isopleths of 7% grossular and 25% pyrope intersect at *P–T* conditions of ~8.5 kbar and ~805 °C, in the peak assemblage field (Fig. 7.4b), with associated uncertainties on the location of these isopleths of ± 0.1 kbar and ± 5 °C (1 S.D.) These conditions are taken to satisfactorily represent the best estimate of peak *P–T* conditions.

Post-peak suprasolidus evolution

White & Powell (2002) and Indares *et al.* (2008) suggest that the post-peak textural evolution of an anatectic rock will end on crossing the solidus when the final melt fraction crystallises, assuming that no further deformation takes place. The lack of free fluid along the grain boundary network after this point restricts further reaction, although cation diffusion may continue to alter mineral compositions if the rock remains at high-temperature. This latter effect is seen in garnet outer rims that are in contact with biotite that record grossular and pyrope contents of ~5% and 21% respectively (Fig. 7.4b). This decrease in Ca and Mg content is also consistent with equilibration down temperature and pressure (Spear, 1993).

Previous estimates of peak metamorphic conditions have suggested a range of pressures whilst still at high-temperature (Table 7.1), indicative of a steep retrograde *P–T* path from peak conditions. However, the extent of exhumation at high-grade is limited by the 5-variant field grt–bt–kfs–pl–crd–sil–qz–liq, which bounds the peak assemblage field between 5.5–7 kbar and 790–860 °C (Fig. 7.4a). The generation of further melt and the appearance of cordierite would occur with

minimal overstepping in suprasolidus assemblage fields (Pattison & Begin, 1994). Therefore, given the absence of cordierite in sample DNCV01, this boundary is treated as providing a reliable minimum pressure for post-peak exhumation.

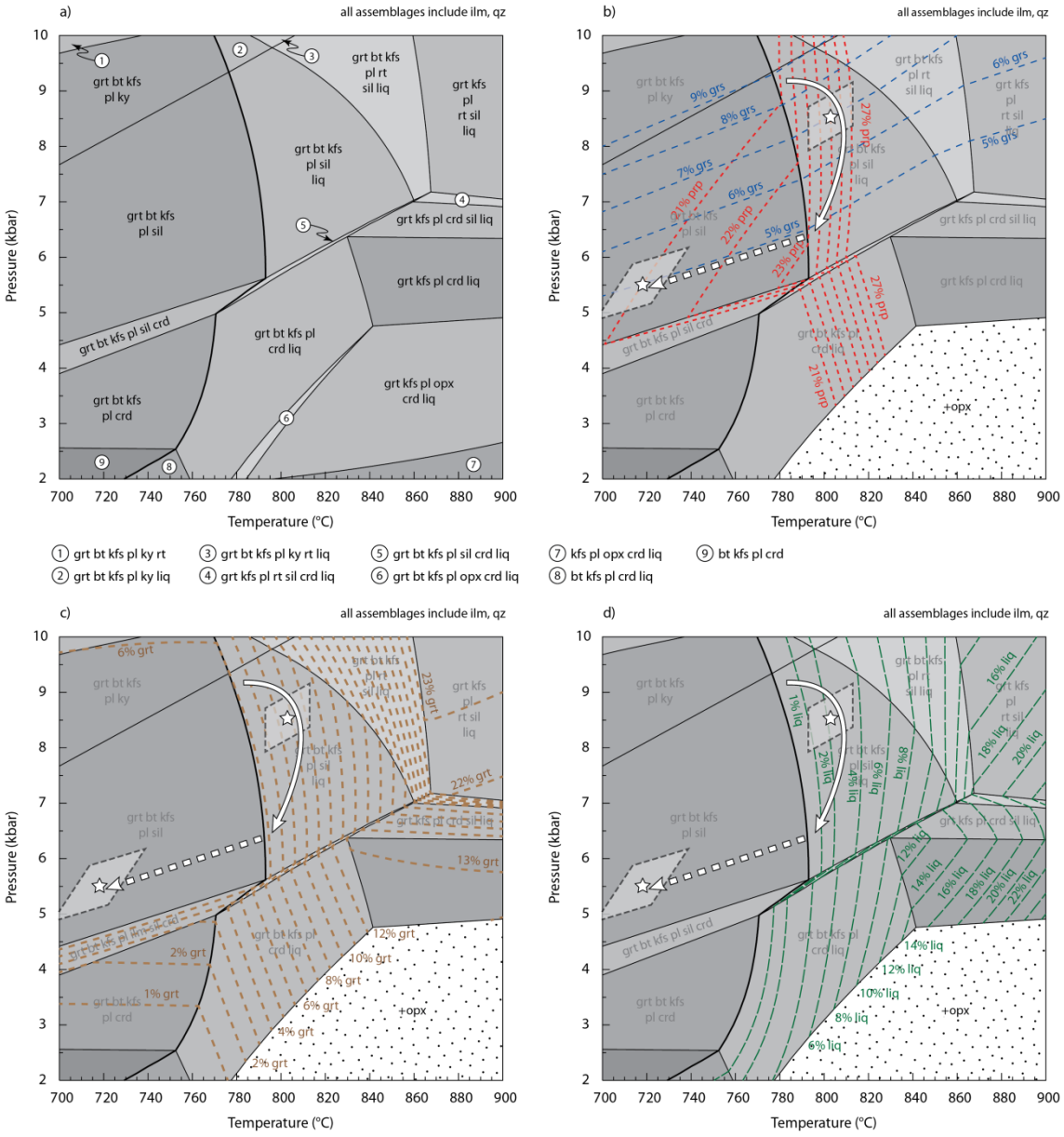


Fig. 7.4 – *P–T* pseudosection for sample DNCV01 using the observed bulk composition. White arrows and dashed boxes represent suggested *P–T* paths and conditions as discussed in the text. Some minor assemblage fields are not labelled for clarity. (a) Complete pseudosection showing calculated assemblages. (b) Isopleths of garnet grossular (grs) and pyrope (prp) content relevant to those measured in the analysed garnet. (d) Modal proportion contours for garnet (grt). (d) Modal proportion contours for silicate melt (liq).

Final melt crystallisation at the solidus is thus thought to have occurred at *P–T* conditions no lower than 5.5 kbar (at 790 °C), equivalent to a depth of ~20 km in the crust. Modal proportion contours for garnet and melt (Fig. 7.4c–d) show that both phases are produced with increasing

temperature as biotite is consumed during incongruent melting through the following reaction, in agreement with the experimental results of LeBreton & Thompson (1988):

biotite + plagioclase + aluminosilicate + quartz → K-feldspar + garnet + melt (7.4.1)

Furthermore, decompression from peak conditions to the solidus predicts a slight decrease in the modal proportion of garnet and an increase in the modal proportion of biotite (± sillimanite), consistent with observed textures (e.g. Fig. 7.2b).

7.4.3. Melt-reintegration (inferred prograde *P–T* evolution)

The *P–T* pseudosection constructed previously sufficiently explains the textural and compositional evolution of sample DNCV01 in melt-bearing assemblage fields; however, certain observed features cannot be accounted for. A large discrepancy arises in that the proportion of melt calculated to have been produced at peak *P–T* conditions is ~2% (Fig. 7.4d), far too little to account for the pervasive leucosome networks that have been reported in the region (Nam *et al*., 1998; Leloup *et al*., 2001). Subsolidus topologies also fail to account for the occurrence of biotite-plagioclase-quartz composite inclusions in garnet cores, which exhibit lobate shapes against host porphyroblasts (e.g. Fig. 7.2c). Similar features have previously been described as evidence for garnet growth in a suprasolidus environment (Waters, 2001; Indares *et al*., 2008; Guilmette *et al*., 2011). Given that the modal proportion of garnet present along the previously calculated solidus is ~6% (Fig. 7.4c), garnet-forming reactions would require an unreasonably large overstep in order to delay initial growth until it coexisted with melt. Both inconsistencies however can be resolved by accounting for the previous loss of melt from the current bulk composition.

Once melt accumulation in an anatectic rock reaches a critical threshold, a portion of that melt may be lost, creating an open-system environment (Vanderhaege, 2001). The composition of such a melt is dependent on *P–T* conditions of formation (White & Powell, 2002), and melt extraction may occur continuously or in several discrete episodes (Sawyer, 1994). This open system behaviour, coupled with inherent uncertainty regarding the proportion and composition of melt lost, suggests that recovering a bulk composition representative of the *exact protolith* is very unlikely. Despite this, previous investigation has shown that various melt loss scenarios do not change the subsolidus and suprasolidus topologies or the compositions of peritectic phases in a significant manner (White &

Powell, 2002). Therefore, with certain assumptions, it is possible to calculate an approximate bulk composition suitable for prograde modelling. In the interest of minimising uncertainty, the melt-loss scenario chosen is that of a single extraction event. In the event that this is unrealistic for the DNCV as a whole, the results at least represent a defensible end-member case.

Calculation of a melt-reintegrated bulk composition

The calculation of a melt-reintegrated bulk composition (MRBC) was performed by the addition of a proportion of melt to the actual bulk composition in order to displace the solidus down-temperature to H_2O-saturated conditions, following the method of White *et al*. (2004). Given the previously stated point by White & Powell (2002), a nominal pressure of 9 kbar was chosen for obtaining the composition of reintegrated melt. This is higher than conditions inferred for melt crystallisation and so allows for a clockwise *P–T* evolution for the DNCV gneisses, as previously detailed by Leloup *et al.* (2001). The composition of reintegrated melt (calculated at 779 °C and 9 kbar on Fig. 7.4) for DNCV01 is H_2O – 7.93; SiO_2 – 67.88; Al_2O_3 – 14.12; FeO – 0.31; MgO – 0.06; CaO – 0.71; K_2O – 5.83; Na_2O – 3.17 (oxide weight %). This is equivalent to Si – 1.65; Al – 0.40; Fe^{2+} – 0.01; Mg – 0.00; Ca – 0.01; Na – 0.13; K – 0.18; H – 0.98 cpfu (on an 8-oxygen basis; White *et al.*, 2007).

In order to obtain the correct proportion of this melt that would 'just saturate' the solidus, 'gmin' calculations were performed at a fixed pressure of 7 kbar over a temperature range of 620–700 °C (with an interval of 5 °C). The gmin function of THERMOCALC (using the *dogmin yes* script) allows Gibbs energy minimisation calculations to be performed on all possible assemblages within a user-defined set of phases at any *P–T* conditions. Hence, the stable assemblage (with the lowest G) can be calculated for a specified pressure and temperature. If this function is performed over a range of *P–T* conditions, it is possible to delimit the change in stable assemblage – in this case to examine when the H_2O-out and liq-in field boundaries meet. Different bulk compositions were calculated using incremental additions of melt (in 5 volume % intervals) to the previously calculated total bulk composition. It can be seen from Fig. 7.5 that the solidus becomes water saturated between the additions of 45% (bulk composition on left hand side of figure) and 50% melt (bulk composition on right hand side of figure). Thus, the volume of melt added to sample DNCV01 to produce the MRBC was 50% and the total volume proportion present before loss was ~33% (i.e. (50/150)*100).

The MRBC for sample DNCV01 is H_2O – 6.09; SiO_2 – 68.03; Al_2O_3 – 10.85; FeO – 4.39; MgO – 3.26; CaO – 1.83; K_2O – 2.97; Na_2O – 1.87; TiO_2 – 0.59; MnO – 0.11; O – 0.13 (mole %).

```
THERMOCALC 3.33
the main output is in the file, "tc-DNCV01-ptpseudo-o.txt"
other (eg drawpd) output is in the file, "tc-DNCV01-ptpseudo-dr.txt"

calcs use:

reading a-x datafile, "tc-DNCV01-MnNCKFMASHTO.txt"...
hb liq cd st g opx ctd chl bi mu pa ksp pl ilm sp mt
hem and sill ru ky zo q H2O

phases ignored this run: hb hem zo (from script)
choose from: liq cd st g opx ctd chl bi mu pa ksp pl ilm
sp mt and sill ru ky q H2O
q - automatically included (from script)
(last time was: liq g bi mu pl ilm q H2O)
which phases : (nothing input)
(last time was: liq g bi mu pl ilm q H2O)
max variance of equilibria to be looked at : 8

specification of PT window:
P range over which equilibria to be calculated
P window: P low,high : 7
T range over which equilibria to be calculated
T window: T low,high : 640 660
use the T interval in the datafile script ? no
T window : 640 <-> 660°C :T interval : 1
use the P interval in the datafile script ? yes
composition (from script)
   H2O  SiO2 Al2O3  CaO   MgO   FeO   K2O  Na2O  TiO2   MnO    O
 5.784 68.005 10.898  1.848  3.326  4.475  2.957  1.858  0.599  0.120  0.130
<================================================>
phases : liq, g, bi, mu, pl, ilm, H2O, (q)

...
...
(calculations deleted for space)
...
...

Gibbs energy minimisation info

 P(kbar)  T(°C) liq   g  bi  mu  pl ilm   q H2O   n        G      del
   7.00   620.0  -   ¥  ¥  ¥  ¥  ¥  ¥  -   6  -962.08496   0.06435
   7.00   630.0  -   ¥  ¥  ¥  ¥  ¥  ¥  -   6  -963.26428   0.06280
   7.00   640.0  -   ¥  ¥  ¥  ¥  ¥  ¥  -   6  -964.45209   0.06099
   7.00   650.0  -   ¥  ¥  ¥  ¥  ¥  ¥  -   5  -965.64832   0.05892
   7.00   660.0  -   ¥  ¥  ¥  ¥  ¥  ¥  -   5  -966.85284   0.05661
   7.00   670.0  -   ¥  ¥  ¥  ¥  ¥  ¥  -   6  -968.06573   0.05392
   7.00   680.0  ¥   ¥  ¥  ¥  ¥  ¥  ¥  -   9  -969.28705   0.00013
   7.00   690.0  ¥   ¥  ¥  ¥  ¥  ¥  ¥  -  11  -970.51715   0.00057
   7.00   700.0  ¥   ¥  ¥  ¥  ¥  ¥  ¥  -  11  -971.75623   0.00137

(Use these results at your own risk!)

more phase diagram calculations ? yes
calcs use:

reading a-x datafile, "tc-DNCV01-MnNCKFMASHTO.txt"...
hb liq cd st g opx ctd chl bi mu pa ksp pl ilm sp mt
hem and sill ru ky zo q H2O

phases ignored this run: hb hem zo (from script)
choose from: liq cd st g opx ctd chl bi mu pa ksp pl ilm
sp mt and sill ru ky q H2O
q - automatically included (from script)
(last time was: liq g bi mu pl ilm q H2O)
which phases : (nothing input)
(last time was: liq g bi mu pl ilm q H2O)
max variance of equilibria to be looked at : 7

specification of PT window:
P range over which equilibria to be calculated
P window: P low,high : 7
T range over which equilibria to be calculated
T window: T low,high : 600 700
use the T interval in the datafile script ? no
T window : 600 <-> 700°C :T interval : 10
use the P interval in the datafile script ? yes
composition (from script)
   H2O  SiO2 Al2O3  CaO   MgO   FeO   K2O  Na2O  TiO2   MnO    O
 6.083 67.948 10.837  1.828  3.256  4.385  2.966  1.868  0.589  0.110  0.130
<================================================>

...
...
(calculations deleted for space)
...
...

Gibbs energy minimisation info

 P(kbar)  T(°C) liq   g  bi  mu  pl ilm   q H2O   n        G      del
   7.00   620.0  -   ¥  ¥  ¥  ¥  ¥  ¥  ¥  10  -960.62781   0.00052
   7.00   630.0  -   ¥  ¥  ¥  ¥  ¥  ¥  ¥  10  -961.80615   0.00064
   7.00   640.0  -   ¥  ¥  ¥  ¥  ¥  ¥  ¥   9  -962.99335   0.00074
   7.00   650.0  -   ¥  ¥  ¥  ¥  ¥  ¥  ¥   9  -964.18933   0.00056
   7.00   660.0  -   ¥  ¥  ¥  ¥  ¥  ¥  ¥   9  -965.39404   0.00014
   7.00   670.0  ¥   ¥  ¥  ¥  ¥  ¥  ¥  -  10  -966.60797   0.00055
   7.00   680.0  ¥   ¥  ¥  ¥  ¥  ¥  ¥  -   9  -967.83099   0.00112
   7.00   690.0  ¥   ¥  ¥  ¥  ¥  ¥  ¥  -  10  -969.06299   0.00137
   7.00   700.0  ¥   ¥  ¥  ¥  ¥  ¥  ¥  -  10  -970.30396   0.00171

(Use these results at your own risk!)

more phase diagram calculations ? no
================================================
all done - hit return to exit ? yes
```

Fig. 7.5 – Gmin output for DNCV01 used to find proportion of melt required for reintegration.

Results

A *P–T* pseudosection has been calculated for the MRBC between the *P–T* limits of 2–10 kbar and 600–800 °C (Fig. 7.6a). This allows interpretation of phase relations above and below the H_2O-saturated solidus, which has a steep positive *P–T* slope in garnet-bearing assemblages, and a negative *P–T* slope in garnet-absent (K-feldspar-present) assemblages. This topology and position in *P–T* space is consistent with the calculations of White *et al.* (2007) for a similar bulk composition and suggests that the MRBC appears to be a plausible representation of the initial protolith.

Contours for modal proportion of silicate melt in Fig. 7.6b show that melt production across the wet solidus in garnet-bearing assemblages is negligible (~1%). It is not until fluid-absent

muscovite-dehydration occurs across the quadrivariant field grt–bt–kfs–pl–sil–qz–liq that melt generation reaches significant volumes, increasing from 4% to 12% over a very small temperature interval. Contours for calculated modal proportion of garnet (Fig. 7.6b) allow interpretation of possible conditions of garnet core growth in terms of the melting history. Although garnet cores lack prograde compositional zoning and the early stages of the *P–T* evolution are therefore poorly constrained, rough interpretations can be made. The absence of muscovite inclusions in garnet cores could be taken to suggest that garnet grew over a steep *P–T* gradient, initially nucleating in muscovite-absent fields (e.g. path A on Fig. 7.6b). Indeed, growth here leading up to previously established peak *P–T* conditions would mimic the inclusion suites observed and fit the interpreted criterion of core growth in the suprasolidus field. However, this scenario would require the protolith to have sat along an initial geothermal gradient of at least 50 °C/km (assuming a crustal density of 2800 kg/m^3) before initial garnet nucleated (e.g. at ~670 °C, 3.5 kbar on Fig. 7.6b). The subsequent approach to peak metamorphic conditions would then require a pressure increase of ~5 kbar, equivalent to burial from 12 km to 30 km, over a relatively small increase in temperature of just ~120 °C, suggesting evolution along an effective geotherm of ~7 °C/km.

An alternative interpretation along a more reasonable initial geotherm of 25–30 °C/km (path B on Fig. 7.6b) allows initial garnet growth to occur at ~600 °C and 6 kbar in an assemblage containing biotite, muscovite, plagioclase, ilmenite and H_2O. Contours for garnet modal proportion (Fig. 7.6c) show that growth in muscovite-bearing assemblages is minor mostly pressure-dependent. It is not until K-feldspar is produced as a result of muscovite-dehydration along the *effective solidus* that the proportion of garnet increases significantly with increasing temperature. Therefore evolution along such a gradient would not be expected to trap many subsolidus minerals in garnet core regions as a result of extremely slow growth rates (if any) in these assemblages.

Although both *P–T* paths satisfy the microstructural observation that garnet core growth occurred in the presence of melt, an evolution similar to path B is preferred as it seems unlikely that garnet first grew at low-pressure high-temperature conditions (path A; Fig. 7.6d). Although possible, such a high geothermal gradient would require a significant source of heat and would disagree with the data provided by Leloup *et al*. (2001) who suggested that metamorphic units of the DNCV have followed a clockwise *P–T* path with no evidence of initial thermal anomalies.

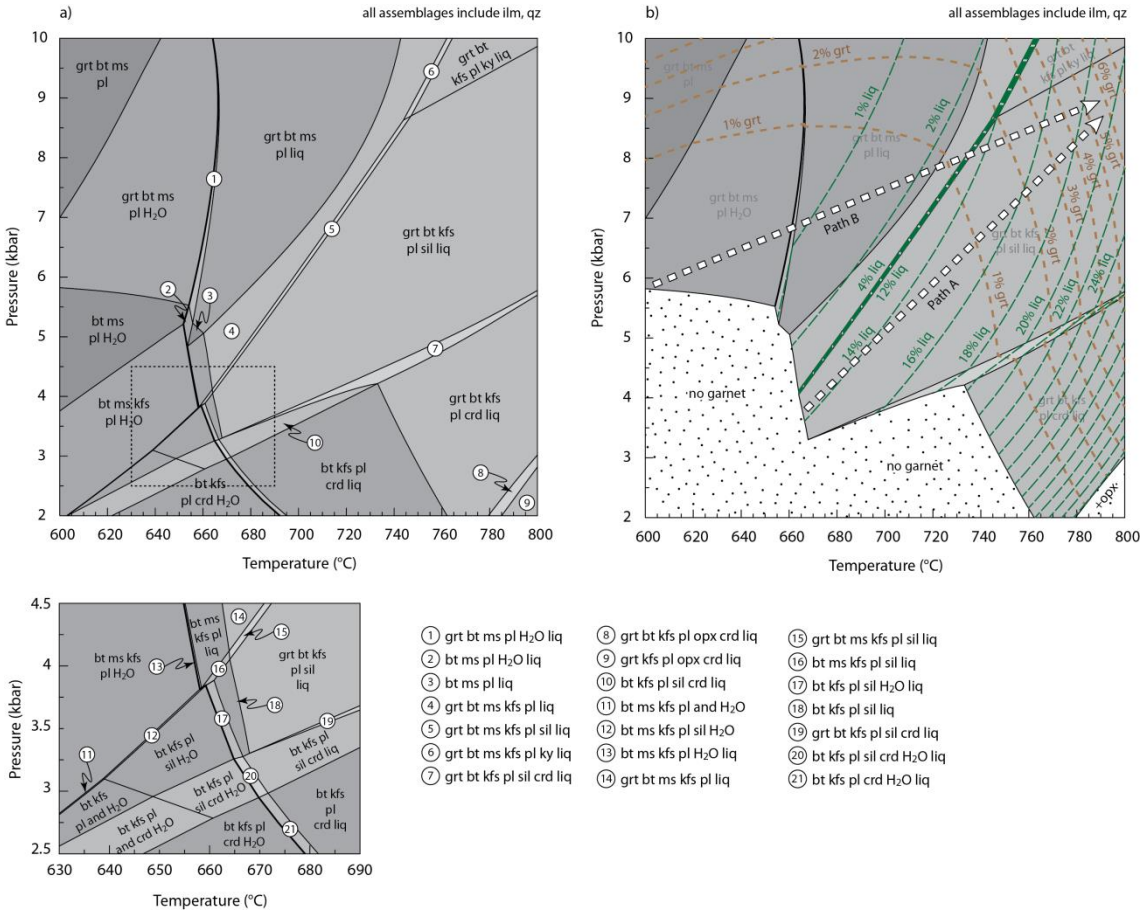


Fig. 7.6 – *P–T* pseudosection for sample DNCV01 using the MRBC. White dashed arrows represent *P–T* paths discussed in the text. Some minor assemblage fields are not labelled for clarity. (a) Sample DNCV01. Dashed box represents location of inset. (b) DNCV01 isomode contours for garnet (grt) and silicate melt (liq).

7.4.4. *P–T* conditions of retrograde metamorphism

Although *P–T* pseudosections constructed using observed bulk compositions should theoretically be able to examine retrograde processes, the sluggishness of retrograde reactions in the absence of melt or fluid has been noted in numerous previous studies of high-grade rocks (e.g. Pattison & Begin, 1994; Guiraud *et al.*, 2001; White & Powell, 2002). Localised retrograde alterations in garnet strain shadows demonstrate that the total bulk rock composition is not a good proxy for the volume of reacting matrix during the subsolidus evolution of the sample. This interpretation is supported by the observation that not all garnet grains suffer retrogression to the same degree or are replaced by exactly the same products. As a result, the investigation of *P–T* conditions that sample DNCV01 experienced during exhumation through the subsolidus domain was performed with conventional thermobarometry under the assumption that local equilibrium was achieved where recrystallisation occurred, but not over the whole rock volume.

Assemblage	Mineral	SiO_2	TiO_2	Al_2O_3	FeO	MnO	MgO	CaO	Na_2O	K_2O	**Total**
1	Bt	33.43	2.13	18.58	18.79	0.01	12.37	0.17	0.24	8.22	**93.94**
	Grt	36.57	0.09	21.36	32.16	2.00	5.52	1.68	0.14	0.00	**99.51**
	Pl	56.72	0.01	26.55	0.38	0.00	0.29	7.97	6.52	0.19	**98.63**
2	Bt	34.41	2.70	18.33	16.98	0.06	11.74	0.10	0.34	9.99	**94.64**
	Grt	36.41	0.03	21.37	32.42	2.34	5.29	1.58	0.16	0.03	**99.64**
	Pl	56.56	0.08	26.50	0.47	0.02	0.29	7.98	6.51	0.16	**98.55**
3	Bt	35.89	3.07	18.77	17.13	0.04	12.29	0.07	0.41	9.98	**97.65**
	Grt	36.49	0.02	21.24	32.55	2.43	4.93	1.43	0.05	0.01	**99.14**
	Pl	57.00	0.00	27.08	0.53	0.06	0.38	8.21	6.46	0.18	**99.89**

Table 7.3 – Mineral compositions for strain shadow assemblages in DNCV01 used to calculate *P–T* conditions of retrograde metamorphism. Garnet compositions represent extreme outer rim analyses in direct contact with neocrystallised grains of biotite, plagioclase, sillimanite and quartz in strain shadows.

P–T conditions of garnet breakdown were calculated using TWQ version 2.3 (Berman, 1991, 2007) using the thermodynamic dataset of Berman (1988) with solution models for plagioclase (Furhman & Lindsley, 1988), garnet and biotite (Berman & Aranovich, 1996). This method was used after THERMOCALC AvePT was unable to find results fitting 95% confidence using its own algorithm. Garnet outer rim compositions were used in conjunction with recrystallised biotite, plagioclase, sillimanite and quartz located in strain shadows (Table 7.3). These allowed two independent reactions to be found:

$$\text{grossular} + \text{quartz} + 2\ \text{sillimanite} = 3\ \text{anorthite} \qquad (7.4.2)$$

$$\text{phlogopite} + \text{almandine} = \text{annite} + \text{pyrope} \qquad (7.4.3)$$

Three strain shadow assemblages produced intersecting equilibria at *P–T* conditions of ~4.5 kbar and ~700 °C (assemblage 1), ~4.9 kbar and ~675 °C (assemblage 2) and ~4.0 kbar and ~640 °C (assemblage 3). An uncertainty of ± 1 kbar and ± 50 °C is assumed for each of these results. As a result, the approximate *P–T* conditions for garnet strain shadow recrystallisation can be delimited roughly between ~4–5 kbar and ~640–700 °C, indicating that exhumation to crustal depths of ~15 km occurred whilst still at amphibolite-facies temperatures.

7.5. U–Th–Pb monazite geochronology

Accessory monazite is present in all studied samples and was analysed using two different methods. Geochronological analysis of grains from sample DNCV01 was performed using *in-situ* laser ablation ICP-MS from thin section in order to provide textural relationships for the ages obtained, as described in chapter 3.4. Analysed grains existed both in the rock matrix and as inclusions in garnet

porphyroblasts, the latter being targeted due to the potential for preserving evidence of early metamorphic events, or at least to provide a maximum age constraint on the timing of garnet growth. Geochronological analysis of monazite from samples DNCV02, DNCV09 and DNCV10, where textural relations were not required, was performed using laser ablation ICP-MS of separated crystals from grain mounts by R.R. Parrish in June 2010 (Appendix 11.1). Subsequent analysis and interpretation of this data was performed by the author (R.M. Palin) for this thesis case study.

7.5.1. Analytical techniques

All geochronological analysis was performed at the Natural Environment Research Council (NERC) Isotope Geosciences Laboratory, UK, on two separate occasions following the methods outlined in chapter 3.5.1. As samples DNCV02, DNCV09 & DNCV10 were analysed on a Nu Plasma MC–ICP–MS by R.R. Parrish, only data in the U–Pb isotope system were obtained. Sample DNCV01 was analysed on a Nu Attom SC–ICP–MS; therefore, both U–Pb and Th–Pb isotopic data are documented. Interpretations of both datasets follow the methodologies outlined in chapter 3.5.2. SEM-microprobe compositional analyses of various monazite domains in samples DNCV02, DNCV09 & DNCV10 are presented in Table 7.4. The compositions shown are taken from the relevant grains shown in Fig. 7.7. SEM-microprobe comositional analyses of monazite domains in DNCV01 are presented in Table 7.6 and represent those taken from grains in Fig. 7.9.

7.5.2. Monazite chemistry and U–Th–Pb ages

As described in chapter 3.4.2, particular compositional characteristics of monazite can be used to investigate possible coexisting mineral assemblages with which a particular grain (or internal domain) grew. In particular, the combined Y+HREE concentration may be linked to episodes of formation (or breakdown) of garnet. If monazite growth occurs during prograde metamorphism *before* garnet nucleation then it will typically have a significantly higher Y+HREE content than a similar grain that formed *during* or *after* garnet growth had occurred (e.g. Yang & Pattison, 2006). Additionally, although monazite is commonly present in migmatitic rocks, it is reported by some studies to have a relatively low solubility in peraluminous melts (Montel, 1993; Wolf & London, 1995). Therefore, pre-anatectic (prograde) monazite may be preserved alongside younger grains that are directly associated with partial melting processes, the latter being likely to have a lower Y_2O_3

content than the former where garnet has crystallised during the interim period. However, retrograde processes that result in the replacement of garnet by biotite, for example during melt crystallisation, would release Y_2O_3 back into the reacting matrix and allow for the growth of young Y(+HREE)-rich monazite (Pyle & Spear, 2003; Kohn *et al*., 2005). These compositional characteristics are combined with grain morphology and internal zoning patterns in order to discriminate between multiple generations of monazite growth, so providing a robust petrographic interpretation of ages obtained.

7.5.3. LA–MC–ICP–MS separated grain U–Pb ages

SEM compositional analysis and image acquisition for these samples was performed by D.J. Waters and U–Pb geochronological analysis was performed by R.R. Parrish (Appendix 11.1). Subsequent interpretation of these data has been performed as part of this thesis work.

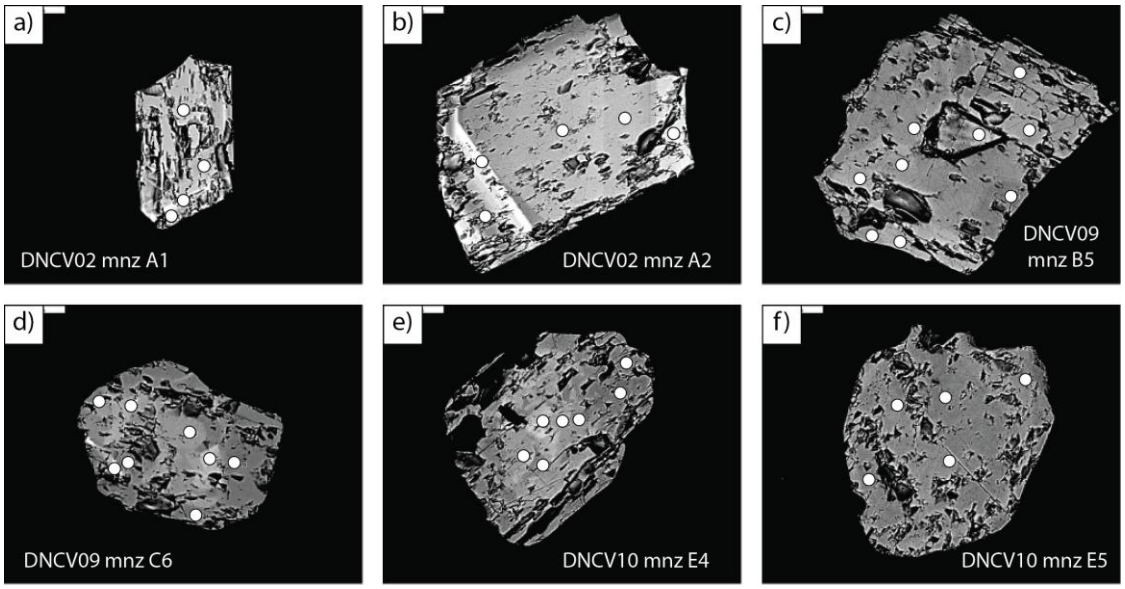


Fig. 7.7 – SEM BSE images of monazite in samples DNCV02, DNCV09 and DNCV10. Labels stating sample and grain number are equivalent to compositional spot analyses in Table 7.4, the locations of which are marked by small filled circles. These spots do not demarcate the location of LA–MC–ICP–MS spot localities. Field of view for all images is ~300 µm in width. Compositional analysis and image acquisition for these samples was performed by D.J. Waters.

DNCV02 – Undeformed granite dyke

Monazite separated from sample DNCV02 exhibits distinct euhedral and prismatic outlines (Fig. 7.7a; grain A1), indicative of a magmatic origin (Ayers *et al*., 1999). Internal zoning profiles highlighted in SEM BSE contrast images vary from being homogenous to having concentric or oscillatory zoning, with alternating bright and dark bands (Fig. 7.7b; grain A2). Such zoning is largely a function of ThO_2 content, with bright bands containing up to 18.98 wt% and duller regions

containing as little as 9.36 wt% (Table 7.4). UO_2 content ranges between 0.29–1.37 wt% in the analysed grains. A total of 20 spot analyses obtained from 7 grains (A1, A2, A6, A7, B4, B5 and B6) were initially interpreted using a single regression on a Tera-Wasserburg plot resulting in a U–Pb lower intercept age of 25.2 ± 0.3 Ma (MSWD = 3.1; Fig. 7.8a). As a result of the undeformed nature of the granite dyke, this age would normally be interpreted as the timing of dyke intrusion; however, the associated MSWD is too large to comfortably represent a single statistical population. In lieu of this, a mean age with a 2 S.D. uncertainty, 25.2 ± 1.4 Ma, is reported instead as representing the timing of emplacement of sample DNCV02. The cause of an apparent drift towards younger ages in some analyses is uncertain, but does not significantly change the main result or age interpretation.

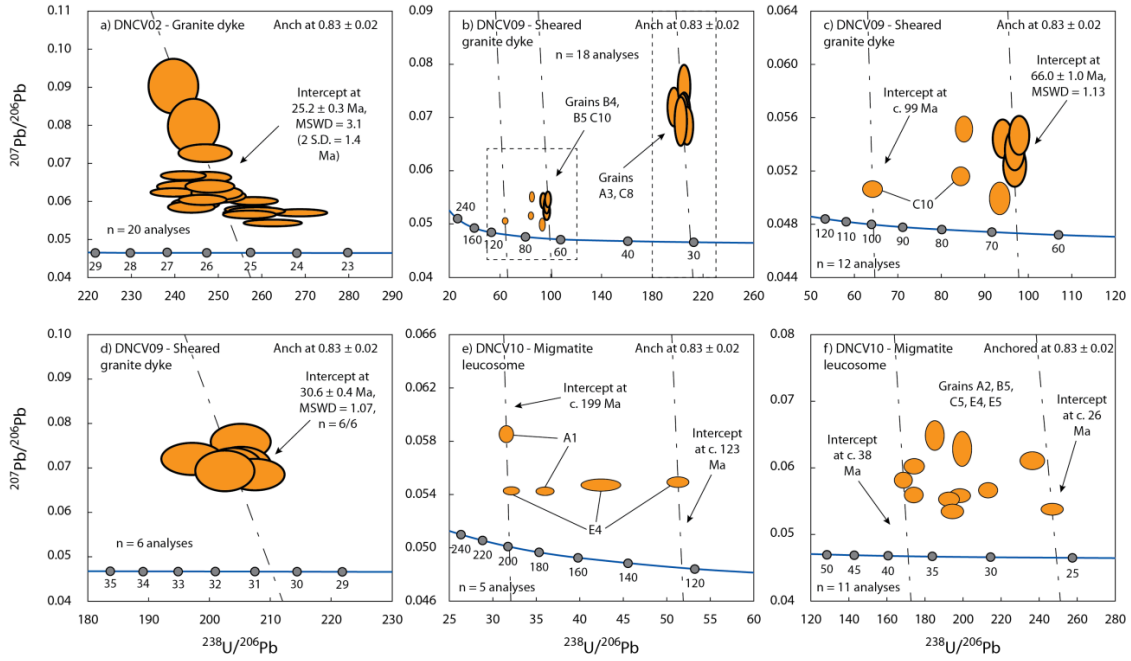


Fig. 7.8 – Tera-Wasserburg plots for samples DNCV02, DNCV09 and DNCV10. Dashed lines indicate regressions from a common lead ratio of 0.83 ± 0.02 and all ages denote intersections with concordia. Bold ellipses represent analyses included in regressions. (a) DNCV02. (b) DNCV09 all analyses. (c) DNCV09 selected analyses. (d) DNCV09 selected analyses. (e) DNCV10 selected analyses. (f) DNCV10 selected analyses.

DNCV09 – Sheared granite dyke

Monazite from sample DNCV09 shows a variety of internal compositional zoning patterns and morphologies. Rare grains exhibit euhedral and prismatic outlines (e.g. Fig. 7.7c) resembling those observed in sample DNCV02 with internal compositional zoning weakly identifiable in SEM BSE contrast images. The majority of grains are subhedral and contain irregular and patchy internal zoning (e.g. Fig. 7.7d), which suggests that they have a metamorphic origin (Ayers *et al.*, 1999).

Analysis	Petrographic position	Internal domain	SiO_2	P_2O_5	CaO	FeO	Y_2O_3	La_2O_3	Ce_2O_3	Pr_2O_3	Nd_2O_3	Sm_2O_3	Eu_2O_3	Gd_2O_3	Tb_2O_3	Dy_2O_3	Ho_2O_3	Er_2O_3	Tm_2O_3	Yb_2O_3	Lu_2O_3	PbO	ThO_2	UO_2	**Total**
DNCV02 Mnz A1	Groundmass	Body (Fig. 7.7a)	0.41	28.80	1.80	0.04	2.50	12.50	24.97	2.91	8.38	1.75	b.d.l	1.68	0.15	0.83	b.d.l	0.29	b.d.l	b.d.l	b.d.l	b.d.l	13.17	1.37	**101.56**
DNCV02 Mnz A1	Groundmass	Body (Fig. 7.7a)	0.06	29.26	1.60	0.08	1.32	13.88	26.04	2.49	8.67	1.22	b.d.l	0.85	0.03	0.69	b.d.l	b.d.l	0.18	0.20	b.d.l	0.01	11.18	1.14	**98.89**
DNCV02 Mnz A1	Groundmass	Rim (Fig. 7.7b)	0.02	29.71	1.28	0.01	0.97	14.39	27.12	2.59	9.02	1.91	b.d.l	1.42	0.32	1.13	0.13	0.17	0.08	0.16	0.18	0.18	9.36	1.06	**101.23**
DNCV02 Mnz A2	Groundmass	Bright band (Fig. 7.7b)	1.49	26.23	1.49	0.00	0.42	12.06	23.64	2.98	8.55	1.17	b.d.l	1.08	b.d.l	0.70	b.d.l	0.38	b.d.l	b.d.l	b.d.l	b.d.l	18.98	0.40	**99.58**
DNCV02 Mnz A2	Groundmass	Body (Fig. 7.7b)	0.15	28.75	1.75	0.00	1.05	12.89	24.69	2.41	8.46	1.83	0.04	1.71	0.31	0.89	b.d.l	0.31	b.d.l	b.d.l	b.d.l	0.04	13.74	1.25	**100.27**
DNCV02 Mnz A6	Groundmass	Rim	0.82	26.73	1.67	0.02	0.42	12.88	23.45	2.34	7.90	1.95	0.33	1.63	0.59	0.58	b.d.l	b.d.l	b.d.l	b.d.l	b.d.l	0.00	15.09	0.29	**96.70**
DNCV02 Mnz A6	Groundmass	Body	0.49	28.67	1.31	0.09	0.88	13.37	25.53	2.97	9.19	1.42	b.d.l	1.17	0.01	0.33	b.d.l	0.16	b.d.l	b.d.l	b.d.l	0.11	13.10	0.82	**99.62**
DNCV02 Mnz A6	Groundmass	Body	0.99	28.33	1.61	0.00	0.88	13.00	25.03	2.31	8.13	1.53	0.02	1.30	b.d.l	0.56	b.d.l	0.28	0.02	b.d.l	0.01	0.07	15.25	0.86	**100.17**
DNCV02 Mnz A7	Groundmass	Body	0.92	27.64	1.51	0.00	0.68	12.95	24.31	2.69	8.39	1.81	0.08	1.25	b.d.l	0.41	b.d.l	0.27	0.13	0.35	0.39	0.20	15.78	1.03	**100.79**
DNCV02 Mnz B5	Groundmass	Rim	0.94	27.17	1.51	0.00	0.94	13.54	25.57	2.59	8.49	1.79	0.20	1.33	b.d.l	0.26	b.d.l	b.d.l	b.d.l	b.d.l	0.05	b.d.l	14.34	0.64	**99.35**
DNCV02 Mnz B5	Groundmass	Body	1.14	27.38	1.53	0.00	0.84	13.40	25.45	2.92	8.56	1.58	b.d.l	0.97	b.d.l	0.28	b.d.l	0.15	b.d.l	b.d.l	b.d.l	0.27	15.79	0.53	**100.79**
DNCV02 Mnz B5	Groundmass	Rim	0.94	27.94	1.40	0.00	0.83	13.50	25.56	2.43	8.26	1.67	0.29	1.76	0.43	0.60	b.d.l	b.d.l	b.d.l	b.d.l	0.01	0.01	14.47	0.87	**100.97**
DNCV02 Mnz B6	Groundmass	Body	0.00	28.83	1.38	0.11	0.92	14.66	27.13	2.66	8.93	1.59	b.d.l	1.38	0.22	0.47	b.d.l	0.01	b.d.l	b.d.l	b.d.l	0.07	10.03	0.85	**99.22**
DNCV09 Mnz A3	Groundmass	Body	0.00	31.05	1.51	0.01	0.00	14.30	29.56	3.50	12.09	2.01	b.d.l	1.05	b.d.l	0.27	b.d.l	0.07	b.d.l	0.28	b.d.l	b.d.l	7.85	0.18	**103.76**
DNCV09 Mnz A3	Groundmass	Rim	0.00	30.39	1.08	0.00	0.00	14.49	30.80	3.18	11.87	1.81	b.d.l	0.26	b.d.l	0.02	b.d.l	b.d.l	0.03	0.10	b.d.l	b.d.l	6.07	0.69	**100.79**
DNCV09 Mnz C8	Groundmass	Body	0.00	30.67	1.14	0.00	0.00	15.29	31.69	3.48	12.22	1.82	0.17	0.88	0.13	b.d.l	b.d.l	b.d.l	b.d.l	b.d.l	b.d.l	0.01	5.81	0.31	**103.63**
DNCV09 Mnz C8	Groundmass	Body	0.00	30.34	1.59	0.08	0.00	14.08	29.24	3.37	11.84	2.09	b.d.l	1.44	0.11	0.03	b.d.l	0.32	b.d.l	b.d.l	0.07	b.d.l	8.88	0.72	**104.21**
DNCV09 Mnz C6	Groundmass	Medium-bright core (Fig. 7.7d)	0.94	27.37	0.32	0.04	0.00	14.91	30.98	3.76	11.99	1.30	b.d.l	1.26	0.43	0.55	0.29	0.18	0.20	0.07	b.d.l	0.22	8.70	0.08	**103.60**
DNCV09 Mnz C6	Groundmass	Dull body (Fig. 7.7d)	0.00	29.89	1.13	0.02	0.00	15.82	31.95	3.61	12.37	1.53	b.d.l	0.20	b.d.l	0.20	0.17	b.d.l	b.d.l	b.d.l	b.d.l	0.05	5.50	0.21	**102.65**
DNCV09 Mnz B4	Groundmass	Body	0.00	29.94	1.26	0.03	0.00	14.30	30.40	3.31	11.85	1.90	b.d.l	1.40	0.62	0.28	b.d.l	b.d.l	0.01	0.11	0.27	0.14	6.36	0.31	**102.48**
DNCV09 Mnz B4	Groundmass	Body	0.00	30.89	1.42	0.06	0.73	13.25	28.47	3.78	11.35	1.91	b.d.l	1.69	0.31	1.21	0.59	0.29	b.d.l	0.28	0.03	0.01	7.03	0.35	**103.66**
DNCV09 Mnz B4	Groundmass	Body	0.00	30.08	1.31	0.03	0.00	14.73	30.96	3.21	12.28	1.93	0.39	1.28	0.25	0.25	0.16	0.10	b.d.l	b.d.l	b.d.l	0.16	6.54	0.21	**103.86**
DNCV09 Mnz B5	Groundmass	Dull body (Fig. 7.7c)	0.00	30.01	1.30	0.03	0.00	13.91	29.91	3.37	11.75	1.83	b.d.l	1.37	b.d.l	0.23	b.d.l	0.01	0.01	0.07	0.04	0.20	7.29	0.45	**101.77**
DNCV09 Mnz B5	Groundmass	Bright mantle (Fig. 7.7c)	0.00	30.37	1.32	0.04	0.00	14.16	29.33	2.87	11.26	2.03	0.27	1.53	0.56	0.36	b.d.l	b.d.l	0.22	0.15	b.d.l	0.24	8.54	0.49	**103.76**
DNCV09 Mnz B5	Groundmass	Bright rim (Fig. 7.7c)	0.00	30.09	1.41	0.00	0.00	14.15	29.27	3.06	11.33	1.58	0.03	0.98	0.27	0.48	0.05	0.17	0.26	0.31	0.13	b.d.l	9.18	0.49	**103.24**
DNCV09 Mnz B5	Groundmass	Dull rim (Fig. 7.7c)	0.00	30.33	1.20	0.06	0.00	15.02	31.48	3.85	11.86	1.68	b.d.l	0.61	b.d.l	0.03	0.10	b.d.l	b.d.l	0.33	b.d.l	0.08	6.35	0.34	**103.32**
DNCV10 Mnz A2	Leucosome	Dull body	0.00	30.88	1.07	0.00	1.26	13.39	28.85	2.88	11.25	2.17	0.45	1.80	0.44	0.90	b.d.l	0.02	b.d.l	b.d.l	b.d.l	0.01	4.89	0.83	**101.10**
DNCV10 Mnz A2	Leucosome	Bright mottled patch	0.00	29.73	1.51	0.08	0.00	13.99	28.96	3.40	11.20	2.38	b.d.l	0.99	b.d.l	0.42	0.21	0.22	b.d.l	0.22	0.12	0.04	6.93	0.76	**101.18**
DNCV10 Mnz B5	Leucosome	Body	0.00	30.28	1.17	0.07	0.00	14.42	29.12	2.74	11.18	2.33	0.16	1.77	0.14	0.47	b.d.l	0.15	b.d.l	b.d.l	b.d.l	b.d.l	5.49	0.71	**100.21**
DNCV10 Mnz E4	Leucosome	Bright mottled patch (Fig. 7.7e)	0.00	30.00	1.55	0.00	0.00	13.45	28.19	2.88	11.49	1.80	0.03	1.28	0.09	0.25	b.d.l	0.10	0.41	b.d.l	b.d.l	0.13	8.98	0.23	**100.87**
DNCV10 Mnz E4	Leucosome	Duller mottled patch (Fig. 7.7e)	0.00	30.27	1.27	0.00	0.00	13.97	29.48	3.42	11.53	1.61	b.d.l	1.57	0.54	0.46	b.d.l	b.d.l	0.55	0.31	b.d.l	0.06	5.56	0.71	**101.31**
DNCV10 Mnz E4	Leucosome	Duller mottled patch (Fig. 7.7e)	0.00	30.82	1.27	0.09	0.70	13.19	27.87	2.97	11.07	2.24	0.14	1.61	0.26	0.81	0.25	0.65	0.44	0.29	b.d.l	0.07	5.60	1.14	**101.48**
DNCV10 Mnz E5	Leucosome	Body (Fig. 7.7f)	0.00	30.76	1.19	0.07	1.18	13.18	27.93	3.00	11.14	1.54	b.d.l	1.21	b.d.l	0.79	b.d.l	0.35	0.11	0.12	0.21	0.04	5.03	0.98	**98.84**
DNCV10 Mnz E5	Leucosome	Body (Fig. 7.7f)	0.00	30.18	1.23	0.02	0.00	14.02	29.24	2.70	10.89	1.88	b.d.l	1.65	0.23	0.68	b.d.l	0.22	0.17	0.01	0.04	0.18	5.69	0.91	**99.95**
DNCV10 Mnz E5	Leucosome	Body (Fig. 7.7f)	0.00	29.90	1.18	0.14	0.00	14.65	30.33	3.35	11.67	1.82	b.d.l	1.00	b.d.l	b.d.l	b.d.l	b.d.l	b.d.l	b.d.l	0.16	0.08	6.03	0.49	**100.78**
DNCV10 Mnz E5	Leucosome	Body (Fig. 7.7f)	0.00	29.92	1.12	0.07	0.00	14.64	30.27	3.03	11.58	1.91	b.d.l	1.14	0.21	0.59	0.11	b.d.l	b.d.l	b.d.l	b.d.l	0.13	5.68	0.65	**101.04**
DNCV10 Mnz E5	Leucosome	Body (Fig. 7.7f)	0.00	30.67	1.01	0.07	0.07	14.96	30.56	3.51	11.37	1.70	b.d.l	1.39	b.d.l	0.66	b.d.l	b.d.l	b.d.l	0.25	b.d.l	0.14	4.43	0.42	**101.20**

Table 7.4 – Monazite compositions from samples DNCV02, DNCV09 and DNCV10 shown in weight % oxide (overleaf). Individual domains in selected monazites are equivalent to domains highlighted in images in Fig. 7.7. Compositional analysis and image acquisition was performed by D.J. Waters.

Analysis	Position	Calculated age (Ma)						Corrected age (Ma)	
		$^{207}Pb/^{206}Pb$	2σ (abs)	$^{206}Pb/^{238}U$	2σ (abs)	$^{207}Pb/^{235}U$	2σ (abs)	$^{206}Pb/^{238}U$	2σ (abs)
DNCV02 mnz A1_1	Groundmass	662	39	26.0	0.7	36.8	1.5	25.3	0.7
DNCV02 mnz A1_2	Groundmass	597	35	25.1	0.7	30.6	1.1	24.7	0.7
DNCV02 mnz A2_1	Groundmass	559	37	25.0	0.7	31.0	1.2	24.7	0.7
DNCV02 mnz A2_2	Groundmass	527	38	23.9	0.7	29.3	1.1	23.6	0.7
DNCV02 mnz A2_3	Groundmass	534	35	24.9	0.7	32.1	1.2	24.5	0.7
DNCV02 mnz A6_1	Groundmass	890	63	26.5	0.9	36.3	1.7	26.0	0.9
DNCV02 mnz A6_2	Groundmass	608	51	26.3	0.8	33.4	1.6	25.9	0.8
DNCV02 mnz A7_1	Groundmass	948	47	26.6	0.7	37.9	1.4	25.9	0.7
DNCV02 mnz A7_2	Groundmass	551	47	26.4	0.8	33.1	1.5	26.0	0.7
DNCV02 mnz A7_3	Groundmass	630	44	26.8	0.8	35.8	1.4	26.3	0.8
DNCV02 mnz B4_1	Groundmass	580	43	24.8	0.8	30.6	1.3	24.5	0.8
DNCV02 mnz B4_2	Groundmass	441	37	25.0	0.8	30.3	1.2	24.7	0.8
DNCV02 mnz B4_3	Groundmass	505	40	24.5	0.8	28.6	1.2	24.3	0.8
DNCV02 mnz B5_1	Groundmass	659	50	25.7	0.8	33.8	1.7	25.2	0.8
DNCV02 mnz B5_2	Groundmass	772	55	25.8	0.8	34.3	1.7	25.3	0.8
DNCV02 mnz B5_3	Groundmass	677	48	26.1	0.8	33.8	1.4	25.6	0.8
DNCV02 mnz B6_1A	Groundmass	1084	68	26.3	0.8	44.7	5.6	25.2	0.9
DNCV02 mnz B6_1B	Groundmass	874	51	25.9	0.8	35.5	1.6	25.4	0.8
DNCV02 mnz B6_2A	Groundmass	955	82	26.8	0.8	51.4	5.8	25.3	0.9
DNCV02 mnz B6_2B	Groundmass	692	53	26.0	0.9	40.4	2.2	25.2	0.8
DNCV09 mnz A3_1	Groundmass	906	82	31.4	1.0	50.5	4.0	30.2	1.0
DNCV09 mnz A3_2	Groundmass	835	82	31.3	1.0	47.1	3.9	30.4	1.0
DNCV09 mnz A3_3	Groundmass	820	73	32.6	1.1	49.9	3.8	31.6	1.1
DNCV09 mnz B4_1	Groundmass	269	43	68.1	2.2	77.9	3.8	67.5	2.1
DNCV09 mnz B4_2	Groundmass	238	43	68.6	2.3	72.2	3.5	68.4	2.2
DNCV09 mnz B4_3	Groundmass	204	45	66.2	2.4	73.1	4.0	65.8	2.3
DNCV09 mnz B5_1	Groundmass	529	34	75.2	2.3	86.8	3.5	74.5	2.2
DNCV09 mnz B5_2	Groundmass	330	48	66.2	2.0	74.6	3.8	65.7	2.0
DNCV09 mnz B5_3	Groundmass	342	47	65.5	2.1	75.3	3.7	64.9	2.0
DNCV09 mnz C10_1	Groundmass	228	30	75.9	2.5	82.2	3.2	75.5	2.4
DNCV09 mnz C10_2	Groundmass	180	24	99.7	4.7	104.9	5.5	99.4	4.5
DNCV09 mnz C8_1	Groundmass	849	85	31.5	1.0	47.1	4.2	30.6	1.0
DNCV09 mnz C8_2	Groundmass	794	78	31.0	1.0	45.2	3.5	30.1	0.9
DNCV09 mnz C8_3	Groundmass	710	93	31.8	1.0	46.8	4.4	30.8	1.0
DNCV10 mnz A1_1	Leucosome	354	16	176.6	6.9	191.6	8.2	175.5	6.5
DNCV10 mnz A1_2	Leucosome	409	14	201.1	7.1	231.3	9.7	199.0	6.7
DNCV10 mnz A2_1	Leucosome	308	34	26.1	0.8	30.1	1.2	25.8	0.8
DNCV10 mnz A2_2	Leucosome	327	33	30.2	0.9	36.5	1.5	29.8	0.9
DNCV10 mnz B5_1	Leucosome	322	36	32.4	1.2	38.7	1.8	32.0	1.2
DNCV10 mnz B5_2	Leucosome	331	37	33.4	1.3	39.4	1.8	33.0	1.2
DNCV10 mnz B5_3	Leucosome	346	38	34.7	1.2	47.9	2.8	33.9	1.2
DNCV10 mnz C5_1	Leucosome	476	37	38.1	1.4	47.2	2.2	37.6	1.4
DNCV10 mnz C5_2	Leucosome	431	38	36.9	1.5	47.3	2.3	36.2	1.4
DNCV10 mnz E4_1A	Leucosome	388	18	150.2	10.8	166.2	12.9	149.0	10.0
DNCV10 mnz E4_1B	Leucosome	389	15	197.6	7.7	212.6	9.2	196.5	7.3
DNCV10 mnz E4_2	Leucosome	393	19	124.5	4.1	139.8	5.1	123.4	3.9
DNCV10 mnz E4_3	Leucosome	351	33	27.2	1.0	35.5	1.7	26.7	1.0
DNCV10 mnz E5_1	Leucosome	324	37	32.2	1.1	43.2	2.8	31.6	1.0
DNCV10 mnz E5_2	Leucosome	362	39	33.1	1.3	37.8	1.9	32.8	1.3
DNCV10 mnz E5_3	Leucosome	388	41	36.9	1.4	44.0	2.1	36.5	1.3

Table 7.5 – MC–ICP–MS U–Pb ages for samples DNCV02, DNCV09 and DNCV10. Data were obtained by R.R. Parrish.

A total of 22 spot analyses were obtained from 7 grains, of which 4 analyses on 2 grains were rejected due to an anomalously low Th signal. The remaining 18 spot analyses, from 5 grains (A3, B4, B5, C10 and C8), cluster into two separate populations (Fig. 7.8b). Old grains B4, B5 and C10 produced 12 spot analyses yielding U–Pb ages as old as c. 99 Ma (Fig. 7.8c). A single regression, interpreted to pass through four spots on grains B4 and B5, resulted in a U–Pb lower intercept age of 66.0 ± 1.0 Ma (MSWD = 1.13; Fig. 7.8c). Six spot analyses from younger grains A3 and C8 are interpreted as a single population, producing a regression with a U–Pb lower intercept age of 30.6 ± 0.4 Ma (MSWD = 1.07; Fig. 7.8d). Grains in the older cluster commonly contain higher ThO_2 (6.35–

9.18 wt%) and lower UO_2 (0.21–0.49 wt%) than younger grains, which have 5.81–8.88 wt% ThO_2 and 0.18–0.72 wt% UO_2 (Table 7.4). The U–Pb lower intercept age of 66.0 ± 1.0 Ma obtained from older grains with euhedral morphologies (e.g. grain B5; Fig. 7.7c) is interpreted as the timing of dyke intrusion. The younger U–Pb lower intercept age of 30.6 ± 0.4 Ma obtained from grains with metamorphic characteristics (e.g. grain C6; Fig. 7.7d) is taken to represent the timing of recrystallisation of pre-existing monazite. Grain C10, which is older, is interpreted to be a xenocryst from the host DNCV gneiss.

DNCV10 – Leucosome segregation

Monazite in sample DNCV10 ranges from being sub-rounded to sub-idioblastic and has varied internal zoning patterns. Some grains contain mottled patches in core regions (Fig. 7.7e) whereas others appear to fully lack zoning (Fig. 7.7f). These textures and morphologies suggest a metamorphic origin (Ayers *et al*., 1999) and grains have a typically low ThO_2 content (4.43–8.98 wt%). A total of 16 spot analyses from 6 grains (A1, A2, B5, C5, E4 and E5) formed two distinct populations. Five spot analyses on grains A1 and E4 produced U–Pb ages between c. 199–123 Ma (Fig. 7.8e) whereas the remaining 11 analyses produced younger ages of c. 38–26 Ma (Fig. 7.8f). One grain (E4) produced three spot ages between c. 198–123 Ma and a fourth of c. 26 Ma. This spread likely represents partial recrystallisation of old (Triassic?) metamorphic monazite during deformation. The cluster of young ages in the majority of grains is interpreted to represent monazite formation during crystallisation of partial melt that was produced during Tertiary metamorphism.

7.5.4. LA–SC–ICP–MS *in-situ* U–Th–Pb ages

DNCV01 – Stromatic migmatite

Sample DNCV01 contains monazite in the leucosome and as inclusions in garnet rims; none were found in inclusion-rich garnet cores. Grains are subhedral and either have numerous compositional domains visible in SEM BSE contrast imagery (e.g. Fig. 7.9b) or lack clear zonation (e.g. Fig. 7.9d). A total of 66 spot analyses were obtained from 20 grains, with no strong correlation between U–Th–Pb ages obtained and textural position. A single monazite located in the matrix (grain 1; Fig. 7.9a) produced 4 spot analyses that allowed a regression on a Tera-Wasserburg plot to a lower intercept U–Pb age of 150.4 ± 1.8 Ma (MSWD = 0.90, Fig. 7.10b). This grain contains a bright interior with

relatively high Y_2O_3 (0.61–1.26 wt%) and UO_2 (0.87–1.31 wt%), surrounded by a duller mantle/rim with lower Y_2O_3 and UO_2 of 0.56–0.96 wt% and 0.05–0.38 wt% respectively. Th–Pb analysis of this grain produced a weighted average common lead corrected age of 149.7 ± 5.9 Ma (MSWD = 0.13).

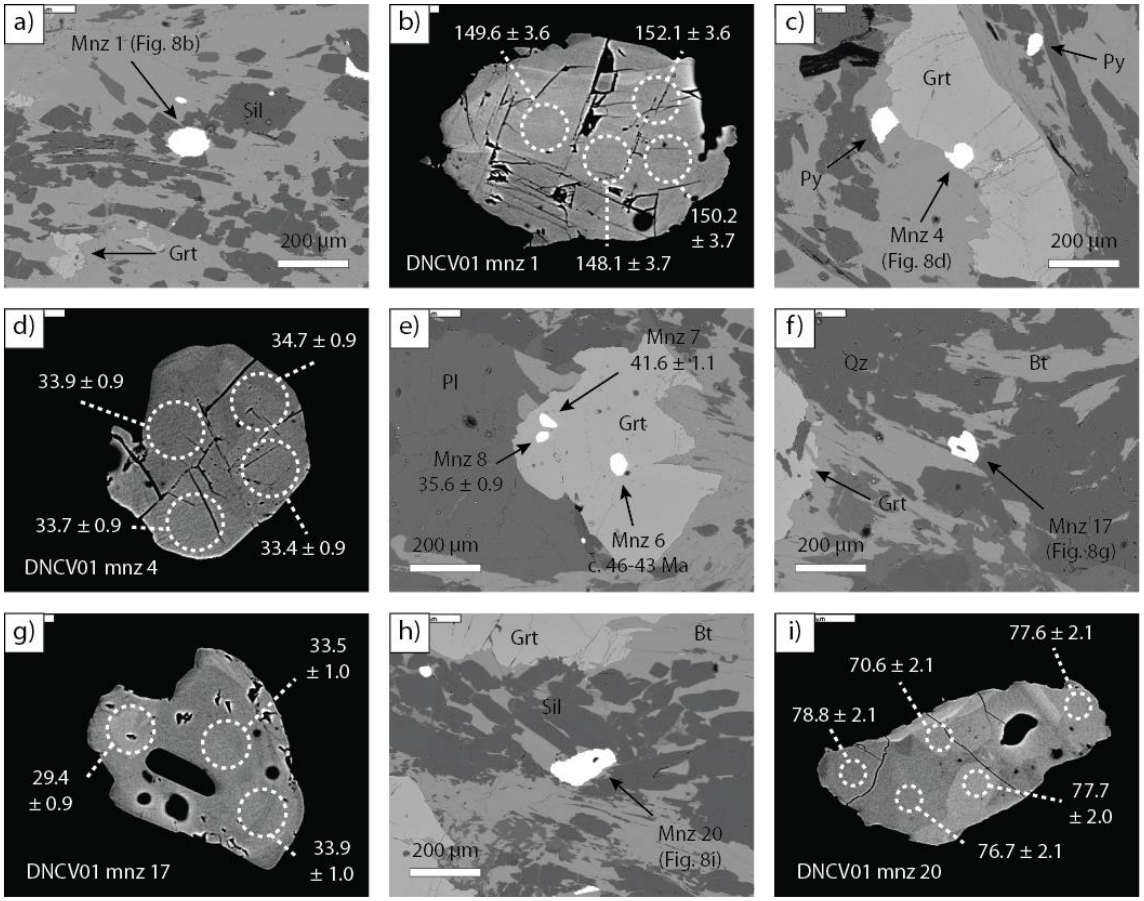


Fig. 7.9 – SEM BSE images and petrographic positions of monazite in sample DNCV01. Labels with sample and grain number are equivalent to analyses in Table 7.6. In monazite images scale is given by spot size (20 µm in diameter).

Inclusions in garnet show a spread of lower intercept U–Pb ages between c. 83–35 Ma (Fig. 7.10a & Table 7.7) and other grains located in the matrix (excluding grain 1) show a range between c. 83–29 Ma (Fig. 7.10c & Table 7.7). These data points (excluding grain 1) show a positive correlation between $^{207}Pb/^{206}Pb$ and $^{238}U/^{206}Pb$ ratios that trends towards the origin, which is interpreted to be the result of variable amounts of excess ^{206}Pb that was incorporated into different grains/domains during the crystallisation process (cf. Fig. 3.2b). As discussed in chapter 3.3, the incorporation of excess ^{206}Pb results in calculated $^{238}U–^{206}Pb$ ages appearing older than the true crystallisation ages (Parrish, 1990) and so these data are interpreted in relation to both the U–Pb and Th–Pb isotopic systems, the latter being unaffected by this process. Where a good correlation exists between U–Pb and Th–Pb ages, one can interpret that the age reliably represents the crystallisation age.

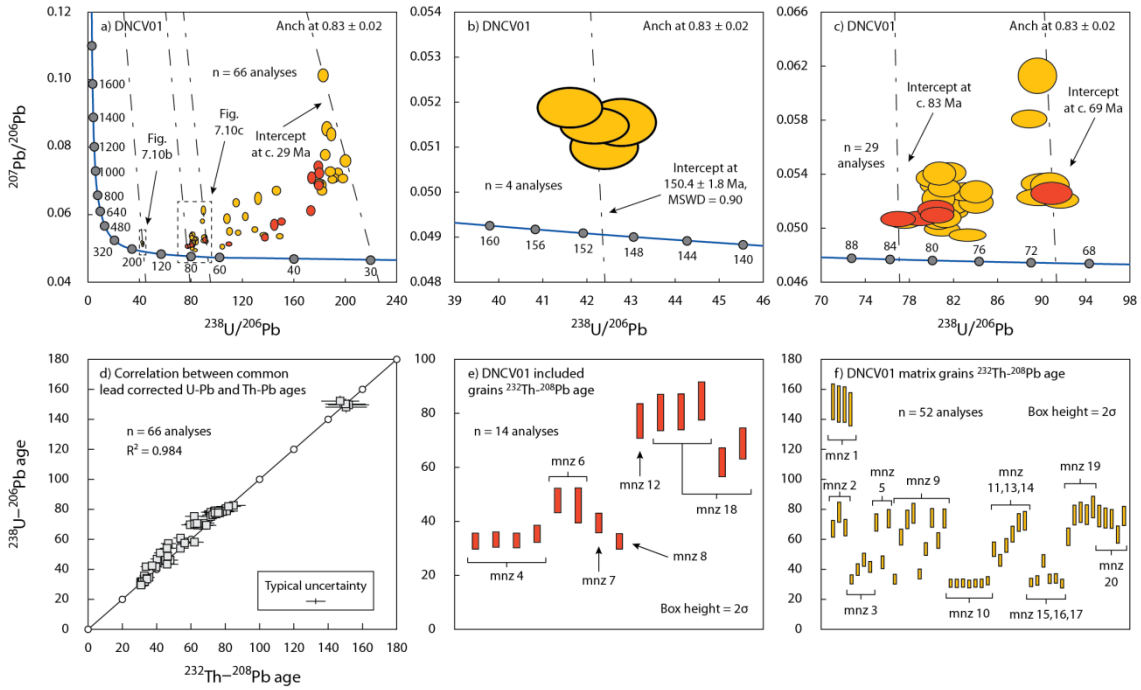


Fig. 7.10 – Tera-Wasserburg and Th–Pb box plots for sample DNCV01. Dashed lines on Tera-Wasserburg plots indicate regressions from a common lead ratio of 0.83 ± 0.02. All ages denote intersections with concordia. Bold ellipses represent analyses used in regressions. Red represents analyses from monazite included in garnet and yellow represents matrix grains. (a) DNCV01 all analyses. (b) DNCV01 selected analyses. (c) DNCV01 selected analyses. (d) Correlation between common lead corrected U–Pb and Th–Pb ages. A 1:1 line is shown for reference with circles at 20 Myr intervals. (e) Weighted average Th–Pb age plot for monazite grains included in garnet. (f) Weighted average Th–Pb age plot for monazite grains in the matrix.

The youngest grain partially included in garnet (grain 4; Fig. 7.9c–d) produced 4 spots with a lower intercept U–Pb age of 35.0 ± 0.4 Ma (MSWD = 1.8) and a weighted average common lead corrected Th–Pb age of 33.7 ± 1.4 Ma (MSWD = 0.64). These data provide a maximum age constraint for the timing of garnet rim growth in sample DNCV01. Other grains included in garnet produced similar young ages from c. 46–36 Ma (Fig. 7.9e). A single grain in the matrix (grain 17; Fig. 7.9f) produced 3 spots with U–Pb ages ranging between c. 34–29 Ma (Fig. 7.9g). This grain contains a thin Y_2O_3-rich rim region (1.07–1.24 wt%) surrounding a Y_2O_3-poor core region (0.56–0.84 wt%), the youngest spot located in this high-Y_2O_3 rim. An increase in Y_2O_3 content likely indicates monazite growth as a result of the breakdown of garnet; thus, this age represents either the timing of melt crystallisation or subsolidus retrograde breakdown.

Table 7.6 – Monazite compositions from sample DNCV01 shown in weight % oxide (overleaf). Individual domains in selected monazites are equivalent to domains highlighted in images in Fig. 7.9.

Analysis	Petrographic position	Internal domain	SiO_2	P_2O_5	CaO	FeO	Y_2O_3	La_2O_3	Ce_2O_3	Pr_2O_3	Nd_2O_3	Sm_2O_3	Eu_2O_3	Gd_2O_3	Tb_2O_3	Dy_2O_3	Ho_2O_3	Er_2O_3	Tm_2O_3	Yb_2O_3	Lu_2O_3	PbO	ThO_2	UO_2	**Total**
DNCV01 Mnz 1	Matrix	Bright interior (Fig. 7.9b)	0.22	27.41	1.15	0.14	0.86	14.38	27.30	2.67	11.09	2.18	0.28	1.47	0.22	0.01	b.d.l	0.15	0.00	b.d.l	0.03	0.06	6.35	1.31	**97.29**
DNCV01 Mnz 1	Matrix	Bright interior (Fig. 7.9b)	0.06	26.76	0.97	0.03	0.86	14.29	28.34	3.18	10.86	1.77	0.11	1.30	b.d.l	0.13	b.d.l	0.12	0.06	b.d.l	b.d.l	0.07	5.38	0.87	**95.17**
DNCV01 Mnz 1	Matrix	Bright interior (Fig. 7.9b)	0.10	27.13	1.13	0.09	0.87	14.36	27.88	3.17	10.92	1.69	0.03	1.39	0.08	0.22	b.d.l	0.02	b.d.l	b.d.l	b.d.l	0.06	6.52	1.10	**96.75**
DNCV01 Mnz 1	Matrix	Bright interior (Fig. 7.9b)	0.04	27.65	0.98	0.12	0.61	14.99	28.72	2.83	10.99	1.64	0.10	0.96	0.05	0.14	0.14	0.25	0.29	0.10	b.d.l	0.04	5.52	1.07	**97.23**
DNCV01 Mnz 1	Matrix	Bright interior (Fig. 7.9b)	0.35	26.72	1.04	0.12	1.26	14.02	27.98	3.10	11.01	1.65	0.11	1.07	0.04	0.05	b.d.l	0.01	0.02	b.d.l	0.10	0.14	5.39	0.96	**95.14**
DNCV01 Mnz 1	Matrix	Dull mantle/rim (Fig. 7.9b)	0.11	26.96	1.12	0.10	0.96	13.99	28.06	2.98	11.24	1.91	0.28	1.08	0.13	b.d.l	b.d.l	0.12	b.d.l	b.d.l	0.05	b.d.l	6.35	0.05	**95.51**
DNCV01 Mnz 1	Matrix	Dull mantle/rim (Fig. 7.9b)	0.01	28.24	1.09	0.12	0.61	14.75	29.24	2.99	11.72	1.61	0.11	1.35	0.43	0.13	b.d.l	b.d.l	b.d.l	b.d.l	b.d.l	0.03	5.99	0.07	**98.49**
DNCV01 Mnz 1	Matrix	Dull mantle/rim (Fig. 7.9b)	0.07	28.23	1.19	0.12	0.82	14.76	29.23	2.99	11.19	1.65	0.06	0.81	b.d.l	0.05	0.03	0.08	b.d.l	b.d.l	0.08	0.02	6.52	0.38	**98.27**
DNCV01 Mnz 1	Matrix	Dull mantle/rim (Fig. 7.9b)	0.11	27.59	1.10	0.16	0.56	14.46	28.60	3.09	11.04	1.67	0.23	1.09	0.06	b.d.l	b.d.l	b.d.l	0.16	0.29	0.18	0.09	5.87	0.10	**96.46**
DNCV01 Mnz 4	Inclusion in Grt rim	Body (Fig. 7.9d)	0.12	27.52	0.90	0.55	1.04	15.24	29.01	2.90	10.79	1.79	0.12	0.89	0.20	0.09	b.d.l	0.10	0.18	0.01	0.18	b.d.l	5.34	0.09	**97.06**
DNCV01 Mnz 4	Inclusion in Grt rim	Body (Fig. 7.9d)	0.17	30.52	1.42	0.27	0.95	14.93	28.94	3.14	10.83	1.65	0.08	0.68	b.d.l	0.07	b.d.l	b.d.l	b.d.l	b.d.l	b.d.l	0.07	5.80	0.38	**99.90**
DNCV01 Mnz 4	Inclusion in Grt rim	Body (Fig. 7.9d)	0.16	29.55	1.29	0.43	0.96	14.80	28.38	2.72	10.87	1.87	0.27	1.14	0.23	0.01	b.d.l	b.d.l	b.d.l	b.d.l	b.d.l	0.02	5.91	0.45	**99.05**
DNCV01 Mnz 4	Inclusion in Grt rim	Body (Fig. 7.9d)	0.23	29.03	1.31	0.24	1.05	14.87	28.05	2.73	10.32	1.74	0.09	0.90	0.25	0.22	0.10	0.08	b.d.l	0.01	b.d.l	0.03	4.92	0.04	**96.21**
DNCV01 Mnz 4	Inclusion in Grt rim	Body (Fig. 7.9d)	0.16	27.70	1.04	0.27	0.61	15.29	29.36	2.78	10.97	1.50	0.23	0.45	b.d.l	0.02	0.08	0.22	b.d.l	b.d.l	b.d.l	b.d.l	5.51	0.06	**96.25**
DNCV01 Mnz 6	Inclusion in Grt rim	Body	0.16	27.70	0.89	0.31	0.95	14.62	29.07	3.22	10.83	1.76	0.00	1.12	0.07	0.18	b.d.l	b.d.l	b.d.l	b.d.l	0.10	0.16	5.36	0.31	**96.80**
DNCV01 Mnz 6	Inclusion in Grt rim	Body	0.04	27.10	1.04	0.27	0.75	14.41	27.90	2.89	10.96	1.78	0.28	1.43	0.35	0.12	b.d.l	0.02	b.d.l	b.d.l	b.d.l	0.05	5.62	0.48	**95.51**
DNCV01 Mnz 6	Inclusion in Grt rim	Body	0.05	27.16	1.04	0.35	0.66	14.40	28.50	2.98	10.88	1.79	0.18	1.01	0.20	0.00	0.02	0.02	0.23	b.d.l	0.08	0.03	6.05	0.59	**96.22**
DNCV01 Mnz 6	Inclusion in Grt rim	Body	0.03	28.48	1.13	0.37	0.69	14.88	29.06	2.98	11.40	1.83	0.21	1.43	0.12	b.d.l	b.d.l	0.06	b.d.l	b.d.l	b.d.l	0.03	6.57	0.54	**99.80**
DNCV01 Mnz 6	Inclusion in Grt rim	Body	0.05	28.37	0.91	0.40	1.07	15.02	29.74	3.25	11.22	1.76	b.d.l	1.28	0.18	0.30	b.d.l	0.18	0.18	b.d.l	b.d.l	b.d.l	5.14	0.36	**99.41**
DNCV01 Mnz 7	Inclusion in Grt rim	Body	0.05	27.31	1.23	0.48	0.70	14.57	27.59	2.53	10.30	1.74	0.17	1.29	0.53	0.38	0.01	0.01	0.02	b.d.l	b.d.l	b.d.l	7.05	0.64	**96.60**
DNCV01 Mnz 7	Inclusion in Grt rim	Body	0.12	27.16	0.99	0.41	1.03	14.38	28.60	3.29	11.24	1.85	0.25	1.18	0.29	0.23	b.d.l	0.05	0.12	b.d.l	b.d.l	0.02	5.46	0.48	**97.16**
DNCV01 Mnz 7	Inclusion in Grt rim	Body	0.08	27.17	1.08	0.74	0.80	14.06	27.85	3.29	10.86	1.87	0.14	1.24	0.22	0.25	0.02	0.06	0.08	0.03	0.10	0.07	5.85	0.15	**96.00**
DNCV01 Mnz 7	Inclusion in Grt rim	Body	0.16	27.38	1.30	0.60	0.84	14.07	27.47	3.05	10.78	1.64	0.02	1.10	0.04	0.05	b.d.l	0.18	b.d.l	b.d.l	0.04	0.08	6.99	0.42	**96.21**
DNCV01 Mnz 7	Inclusion in Grt rim	Body	0.09	27.73	1.09	1.03	1.02	14.20	28.30	2.96	10.97	1.79	0.11	1.19	0.28	0.19	b.d.l	b.d.l	b.d.l	0.08	0.14	0.05	5.69	0.67	**97.59**
DNCV01 Mnz 8	Inclusion in Grt rim	Body	0.02	28.74	1.06	0.71	0.93	15.23	30.18	3.32	11.46	1.41	0.28	0.79	b.d.l	b.d.l	b.d.l	b.d.l	0.02	0.12	b.d.l	b.d.l	6.30	0.32	**100.89**
DNCV01 Mnz 8	Inclusion in Grt rim	Body	0.12	27.95	1.09	0.70	0.60	14.87	29.25	3.09	11.17	1.81	0.14	0.86	0.17	0.18	b.d.l	b.d.l	0.14	b.d.l	b.d.l	0.10	6.23	0.35	**98.81**
DNCV01 Mnz 8	Inclusion in Grt rim	Body	0.10	29.06	1.07	0.83	0.74	15.54	29.94	3.03	11.00	1.58	0.08	0.95	0.15	b.d.l	b.d.l	b.d.l	b.d.l	b.d.l	b.d.l	0.07	5.51	0.25	**99.88**
DNCV01 Mnz 8	Inclusion in Grt rim	Body	0.08	28.30	1.05	1.11	0.62	15.20	29.91	3.19	11.21	1.65	0.03	0.53	b.d.l	0.01	0.04	b.d.l	0.00	b.d.l	0.12	0.03	5.77	0.35	**99.20**
DNCV01 Mnz 17	Matrix	Thin bright rim (Fig. 7.9g)	0.08	28.99	1.33	0.27	1.07	14.05	28.02	3.37	11.80	1.82	0.12	1.25	b.d.l	0.06	b.d.l	0.25	b.d.l	b.d.l	0.08	b.d.l	6.93	0.22	**99.68**
DNCV01 Mnz 17	Matrix	Thin bright rim (Fig. 7.9g)	0.00	28.63	1.25	0.19	1.24	13.40	26.88	3.05	11.42	1.88	0.27	1.47	0.38	0.65	0.21	0.10	b.d.l	0.02	0.09	0.12	7.03	0.32	**98.59**
DNCV01 Mnz 17	Matrix	Thin bright rim (Fig. 7.9g)	0.01	27.67	1.23	0.24	1.12	13.85	27.14	3.05	11.41	1.90	0.16	1.26	0.17	0.26	b.d.l	0.07	b.d.l	b.d.l	0.08	b.d.l	6.77	0.27	**96.67**
DNCV01 Mnz 17	Matrix	Dull body/core (Fig. 7.9g)	0.03	27.53	0.94	0.08	0.56	15.13	28.99	3.04	10.79	1.64	0.04	0.74	0.06	b.d.l	b.d.l	0.05	b.d.l	b.d.l	b.d.l	0.14	5.51	0.40	**95.68**
DNCV01 Mnz 17	Matrix	Dull body/core (Fig. 7.9g)	0.22	28.46	1.12	0.09	0.84	15.43	29.55	3.22	11.11	1.75	0.12	0.88	0.10	0.03	0.03	b.d.l	b.d.l	b.d.l	b.d.l	b.d.l	6.12	0.30	**99.39**
DNCV01 Mnz 17	Matrix	Dull body/core (Fig. 7.9g)	0.04	27.80	1.00	0.10	0.64	14.75	29.04	3.64	11.39	1.65	0.09	0.87	0.15	0.09	b.d.l	b.d.l	b.d.l	b.d.l	b.d.l	0.04	5.74	0.27	**97.33**
DNCV01 Mnz 17	Matrix	Dull body/core (Fig. 7.9g)	0.08	27.38	1.28	0.18	0.81	13.43	26.73	3.10	11.10	1.88	0.26	1.74	0.50	0.49	b.d.l	b.d.l	b.d.l	b.d.l	b.d.l	0.07	7.16	0.48	**96.67**
DNCV01 Mnz 18	Inclusion in Grt rim	Bright spot	1.05	25.30	1.78	0.16	1.00	12.69	22.60	2.53	9.66	1.75	0.01	1.30	0.25	0.27	0.15	0.03	b.d.l	b.d.l	b.d.l	0.09	14.13	0.55	**95.29**
DNCV01 Mnz 18	Inclusion in Grt rim	Bright spot	0.85	26.44	1.69	0.17	1.32	13.30	23.83	2.47	9.82	1.74	0.04	1.53	0.33	0.47	0.00	b.d.l	0.02	b.d.l	b.d.l	0.00	12.63	0.78	**97.43**
DNCV01 Mnz 18	Inclusion in Grt rim	Bright spot	1.04	25.57	1.85	0.13	1.24	12.70	22.69	2.34	9.63	1.89	0.20	1.56	0.23	0.22	b.d.l	0.36	b.d.l	b.d.l	0.17	b.d.l	13.93	0.64	**96.39**
DNCV01 Mnz 18	Inclusion in Grt rim	Dull body	0.02	28.50	0.93	0.11	0.74	15.08	29.44	2.72	11.25	2.02	0.28	1.21	b.d.l	b.d.l	b.d.l	0.14	0.10	0.02	0.15	0.13	5.39	0.52	**98.74**
DNCV01 Mnz 18	Inclusion in Grt rim	Dull body	0.03	27.99	1.09	0.24	0.85	14.79	29.18	3.46	11.59	1.76	0.16	0.68	b.d.l	0.11	b.d.l	0.06	0.11	0.03	0.04	0.16	5.92	0.19	**98.43**
DNCV01 Mnz 18	Inclusion in Grt rim	Dull body	0.07	28.15	1.13	0.25	1.07	15.13	29.52	3.23	11.33	1.91	0.06	1.08	0.00	0.00	b.d.l	b.d.l	b.d.l	0.06	0.14	0.06	5.84	0.45	**99.50**

Analysis	Position	Calculated age (Ma)								Corrected age (Ma)			
		$^{207}Pb/^{206}Pb$	2σ (abs)	$^{206}Pb/^{238}U$	2σ (abs)	$^{207}Pb/^{235}U$	2σ (abs)	$^{208}Pb/^{232}Th$	2σ (abs)	$^{208}Pb/^{232}Th$	2σ (abs)	$^{206}Pb/^{238}U$	2σ (abs)
DNCV01 mnz 1_1	Matrix	241	15	150.3	3.5	155.8	3.9	152.7	5.8	151.9	11.9	149.6	3.6
DNCV01 mnz 1_2	Matrix	266	15	149.0	3.6	156.1	4.0	151.1	5.9	150.4	12.1	148.1	3.7
DNCV01 mnz 1_3	Matrix	263	12	151.1	3.6	157.9	3.8	150.8	5.8	150.1	11.8	150.2	3.7
DNCV01 mnz 1_4	Matrix	280	13	153.1	3.5	161.1	3.8	147.7	5.4	147.0	11.1	152.1	3.6
DNCV01 mnz 2_1	Matrix	290	18	69.9	1.7	76.6	2.1	67.5	2.9	67.4	5.6	69.2	1.7
DNCV01 mnz 2_2	Matrix	374	23	79.4	1.9	89.7	2.8	78.7	3.5	78.4	6.7	78.4	1.9
DNCV01 mnz 2_3	Matrix	534	16	72.1	1.7	87.6	2.4	68.4	2.8	68.1	5.5	70.7	1.7
DNCV01 mnz 3_1	Matrix	893	32	35.4	0.9	51.8	2.0	33.9	1.6	33.7	3.0	33.7	0.9
DNCV01 mnz 3_2	Matrix	770	39	48.6	1.3	66.5	2.9	40.5	2.1	40.2	3.9	46.8	1.3
DNCV01 mnz 3_3	Matrix	415	30	58.4	1.6	67.8	2.6	46.9	2.4	46.8	4.4	57.2	1.6
DNCV01 mnz 3_4	Matrix	585	29	52.5	1.3	65.9	2.3	42.1	1.9	42.0	3.6	50.9	1.3
DNCV01 mnz 4_1	Inc in Grt rim	1051	29	35.9	0.9	56.6	2.1	33.1	1.6	32.9	3.0	33.7	0.9
DNCV01 mnz 4_2	Inc in Grt rim	995	30	35.8	0.9	54.8	2.1	33.6	1.5	33.4	2.8	33.4	0.9
DNCV01 mnz 4_3	Inc in Grt rim	891	28	35.8	0.9	52.3	1.9	33.3	1.4	33.1	2.7	33.9	0.9
DNCV01 mnz 4_4	Inc in Grt rim	957	33	37.0	0.9	55.6	2.2	35.7	1.7	35.6	3.1	34.7	0.9
DNCV01 mnz 5_1	Matrix	231	22	78.9	1.8	83.9	2.4	71.7	2.9	71.6	5.7	78.1	1.9
DNCV01 mnz 5_2	Matrix	374	19	47.0	1.4	53.9	1.8	45.2	2.3	45.1	4.2	46.2	1.4
DNCV01 mnz 5_3	Matrix	329	19	78.9	1.9	87.6	2.4	74.3	3.1	74.2	6.1	77.9	1.9
DNCV01 mnz 6_1	Inc in Grt rim	341	30	46.7	1.2	52.9	1.9	48.0	2.5	47.9	4.5	46.1	1.2
DNCV01 mnz 6_2	Inc in Grt rim	493	43	44.4	1.2	53.7	2.5	46.3	3.7	46.1	6.5	43.4	1.2
DNCV01 mnz 7_1	Inc in Grt rim	529	27	42.8	1.1	52.6	1.9	39.7	2.0	39.6	3.6	41.6	1.1
DNCV01 mnz 8_1	Inc in Grt rim	647	34	37.1	0.9	48.3	1.9	32.9	1.5	32.8	2.9	35.6	0.9
DNCV01 mnz 9_1	Matrix	842	27	43.9	1.3	62.3	2.4	34.0	1.8	33.8	3.3	41.8	1.3
DNCV01 mnz 9_2	Matrix	316	23	76.2	1.8	84.2	2.5	62.1	2.8	61.9	5.3	75.3	1.8
DNCV01 mnz 9_3	Matrix	224	21	79.5	1.8	84.3	2.4	73.7	3.2	73.6	6.2	78.8	1.9
DNCV01 mnz 9_4	Matrix	294	27	79.5	1.9	86.8	2.8	77.9	3.5	77.7	6.6	78.7	1.9
DNCV01 mnz 9_5	Matrix	356	22	43.1	1.0	49.2	1.5	37.4	1.8	37.3	3.3	42.4	1.0
DNCV01 mnz 9_6	Matrix	221	22	61.5	1.5	65.7	1.9	53.9	2.2	53.9	4.3	60.8	1.5
DNCV01 mnz 9_7	Matrix	377	20	78.5	1.8	88.8	2.5	74.8	3.3	74.7	6.2	77.3	1.9
DNCV01 mnz 9_8	Matrix	650	30	71.5	1.8	91.5	3.3	59.8	2.8	59.5	5.2	69.7	1.8
DNCV01 mnz 9_9	Matrix	360	19	80.0	2.0	89.8	2.6	74.5	3.3	74.2	6.3	79.0	2.0
DNCV01 mnz 10_1	Matrix	1327	32	34.6	1.0	62.5	2.6	31.2	1.4	31.1	2.7	30.9	0.9
DNCV01 mnz 10_2	Matrix	1289	30	34.0	0.8	60.3	2.3	31.2	1.5	31.0	2.7	30.6	0.8
DNCV01 mnz 10_3	Matrix	997	27	33.1	0.8	50.9	1.8	31.4	1.5	31.2	2.8	31.0	0.8
DNCV01 mnz 10_4	Matrix	954	25	33.6	0.8	50.6	1.7	30.8	1.4	30.6	2.6	31.6	0.8
DNCV01 mnz 10_5	Matrix	941	21	33.9	0.8	50.6	1.6	31.3	1.4	31.1	2.6	31.9	0.8
DNCV01 mnz 10_6	Matrix	951	25	32.5	0.8	48.8	1.7	31.2	1.5	31.1	2.8	30.5	0.8
DNCV01 mnz 10_7	Matrix	1141	27	34.9	0.9	57.4	2.1	32.9	1.4	32.8	2.7	31.5	0.9
DNCV01 mnz 11_1	Matrix	400	21	55.0	1.3	63.6	1.9	53.9	2.6	53.8	4.8	54.0	1.3
DNCV01 mnz 11_2	Matrix	437	22	49.6	1.2	58.4	1.8	46.6	2.1	46.4	3.9	48.7	1.2
DNCV01 mnz 12_1	Inc in Grt rim	240	17	79.6	2.0	85.0	2.4	77.5	3.3	77.3	6.4	78.9	2.0
DNCV01 mnz 13_1	Matrix	562	35	59.5	1.9	73.6	3.2	56.4	2.4	56.3	4.6	57.5	1.9
DNCV01 mnz 13_2	Matrix	337	26	70.6	1.8	78.9	2.6	63.9	2.8	63.8	5.3	69.4	1.8
DNCV01 mnz 14_1	Matrix	282	23	76.2	1.8	83.0	2.5	71.7	3.1	71.6	5.9	75.2	1.9
DNCV01 mnz 14_2	Matrix	316	19	77.3	1.8	85.3	2.4	72.9	3.3	72.7	6.2	76.2	1.9
DNCV01 mnz 15_1	Matrix	1648	23	35.2	1.0	74.8	2.7	32.0	1.5	31.7	2.8	31.7	0.9
DNCV01 mnz 15_2	Matrix	1009	26	34.1	1.0	52.7	2.0	33.1	1.7	33.0	3.2	31.9	0.9
DNCV01 mnz 16_1	Matrix	727	27	55.8	1.6	74.5	2.8	46.3	2.2	46.0	4.2	54.0	1.6
DNCV01 mnz 17_1	Matrix	905	28	35.8	1.0	52.6	2.0	34.3	1.7	34.1	3.1	33.9	1.0
DNCV01 mnz 17_2	Matrix	841	26	35.4	1.0	50.4	1.8	34.5	1.7	34.3	3.2	33.5	1.0
DNCV01 mnz 17_3	Matrix	1095	31	32.1	0.9	51.8	2.1	31.0	1.6	30.9	2.9	29.4	0.9
DNCV01 mnz 18_1	Inc in Grt rim	229	16	81.1	2.2	86.2	2.5	80.6	3.5	80.4	6.7	80.5	2.2
DNCV01 mnz 18_2	Inc in Grt rim	258	21	79.7	2.1	85.7	2.7	80.8	3.4	80.7	6.6	78.9	2.2
DNCV01 mnz 18_3	Inc in Grt rim	227	17	83.2	2.2	88.3	2.6	84.9	3.6	84.7	7.0	82.6	2.3
DNCV01 mnz 18_4	Inc in Grt rim	256	19	58.6	1.6	63.7	2.0	62.2	2.8	62.0	5.3	58.1	1.7
DNCV01 mnz 18_5	Inc in Grt rim	311	23	70.5	1.9	77.9	2.6	69.1	3.0	69.0	5.7	69.4	1.9
DNCV01 mnz 19_1	Matrix	343	21	71.2	2.0	79.7	2.6	62.2	3.1	62.1	5.8	70.2	2.0
DNCV01 mnz 19_2	Matrix	284	18	78.6	2.1	85.6	2.5	76.7	3.4	76.5	6.6	77.8	2.1
DNCV01 mnz 19_3	Matrix	337	19	79.5	2.0	88.5	2.6	78.6	3.5	78.3	6.8	78.6	2.1
DNCV01 mnz 19_4	Matrix	286	22	78.2	2.3	85.2	2.9	76.9	3.4	76.7	6.6	77.5	2.3
DNCV01 mnz 19_5	Matrix	222	18	82.6	2.2	87.5	2.6	82.0	3.7	81.9	7.1	81.9	2.3
DNCV01 mnz 20_1	Matrix	193	16	79.1	2.1	82.9	2.4	76.2	3.9	75.9	7.2	78.8	2.1
DNCV01 mnz 20_2	Matrix	172	14	76.9	2.0	80.0	2.2	74.8	3.6	74.6	6.7	76.7	2.1
DNCV01 mnz 20_3	Matrix	250	16	78.4	2.0	84.1	2.3	74.1	3.2	73.9	6.3	77.7	2.0
DNCV01 mnz 20_4	Matrix	299	18	71.4	2.1	78.5	2.5	63.7	3.1	63.5	5.8	70.6	2.1
DNCV01 mnz 20_5	Matrix	272	20	78.4	2.1	84.9	2.6	76.1	3.3	75.9	6.4	77.6	2.1

Table 7.7 – SC–ICP–MS U–Th–Pb ages for sample DNCV01

A curious and unexpected result of geochronological analysis of monazite from sample DNCV01 is that many matrix grains produced U–Pb and Th–Pb ages between c. 83–69 Ma (Fig. 7.10c). Such results are not randomly distributed throughout grains; instead multiple spot analyses on individual grains indicate that they are not outliers (e.g. grain 20; Fig. 7.9h–i). Similar Cretaceous ages in previous studies have been interpreted (and subsequently discarded) as a result of mixing of age domains on ablation, although the locations of spot analyses on grain 20 (Fig. 7.9i), for example,

show that they are demonstrably analysing individual domains. Coupled with the strong correlation between U–Pb and Th–Pb ages (R^2 = 0.984; Fig. 7.10d) for all analyses obtained for sample DNCV01, this suggests that a significant monazite-forming event occurred at this time. Box plots for Th–Pb ages (Fig. 7.10e–f) demonstrate spot analysis age variation between (and in) each analysed grain, and it can be seen that a number of analysed grains contain such ages.

7.5.5. Interpretation of monazite geochronology

Dyke emplacement, peak metamorphism and the timing of exhumation

Deformed (DNCV09) and undeformed (DNCV02) granitic dykes cross-cutting host gneisses in the DNCV massif tightly constrain the timing of regional metamorphism and ductile shear fabric formation. A U–Pb lower intercept age of 25.2 ± 1.4 Ma (DNCV02) gives a minimum age on the termination of migmatitic fabric development in the core of the antiform. Towards both massif flanks, these high-grade metamorphic fabrics are truncated by mylonites associated with both steeply dipping bounding faults. Monazite grains with igneous features in deformed dyke DNCV09 suggest that emplacement in the north-eastern flank of the antiform occurred at 66.0 ± 1.0 Ma and younger grains with metamorphic features suggest that shearing had initiated by 30.6 ± 0.4 Ma. This latter result is supported by rare high-Y_2O_3 rims on matrix grains in sample DNCV01 (grain 17; Table 7.6) with a Th–Pb age of 30.9 ± 2.9 Ma, indicating that an episode of monazite growth occurred as a result of the breakdown of garnet during exhumation. This age is similar to K–Ar cooling ages for hornblende of c. 28 Ma and biotite of c. 24 Ma reported by Nam *et al*. (1998), which they interpreted as representing the timing of exhumation of the DNCV massif through the 500 °C and 300 °C isotherms respectively. The oldest Tertiary monazite age (c. 38 Ma) obtained from leucosome segregation DNCV10 provides an upper bound on the timing of partial melting in the massif core. The youngest monazite inclusion in garnet rim regions in sample DNCV01, which produced a Th–Pb age of 33.7 ± 1.4 Ma (grain 4; Table 7.7), shows that partial melting must have continued at least up to this point (as garnet is produced from the prograde breakdown of biotite). Younger grains in both samples (DNCV10 and DNCV01) may also have formed as a result of anatexis, but were not later included into garnet.

Prograde metamorphism

Unlike the Tertiary tectonothermal events, the timing of earlier metamorphism in the DNCV massif is harder to quantify from this dataset. A previous *in-situ* study of monazite in similar DNCV paragneiss by Gilley *et al*. (2003) produced a wide range of Th–Pb ages between c. 220–21 Ma, with some of the oldest ages obtained from inclusions in garnet (cf. sample V-220 in that study). These old ages were interpreted by the authors to document pre-existing (Indosinian) monazite, whereas younger ages were attributed to resetting and recrystallisation during Tertiary deformation. Similar Triassic U–Pb ages (c. 199 Ma) were obtained from grains A1 and E4 from leucosome sample DNCV10, fitting with the interpretation that the DNCV gneisses initially underwent metamorphism during the Indosinian orogeny, although whether or not these samples also experienced partial melting during this event is undeterminable from the available petrographic and age data.

Evidence for both metamorphic events has been found by almost all previous studies with the recognition of two main clusters of age data. However, in this work, a significant number of Late Cretaceous U–Pb lower intercept age ages (n = 29/66) have been calculated to lie between c. 83–69 Ma (Fig. 7.10c) and multiple spot analyses on the same grains (e.g. grain 20; Fig. 7.9i) show that this result is not merely a result of mixing of age domains. Given that no tectonic or metamorphic events of this age have been proposed by past studies of the DNCV (or other RRSZ core complexes) the possible causes of this result are discussed below.

7.6. Summary and discussion

7.6.1. Timing and *P–T* conditions of metamorphism and partial melting

Previous studies of metamorphic lithologies from the DNCV have relied solely on conventional thermobarometry for the examination of changing *P–T* conditions. In particular, the garnet-biotite thermometer has been frequently used to calculate temperatures of peak metamorphism, often using biotite inclusions in garnet cores and inner rims (Nam *et al.,* 1998; Leloup *et al.,* 2001; Gilley *et al.,* 2003). However, the nature of these inclusions means that they cannot document true peak *P–T* conditions, having been incorporated during prograde metamorphism. Other studies (Anczkiewicz *et al.,* 2007) have used matrix biotite in contact with garnet rims to calculate peak conditions using the same methodology, although it is a well-known issue for high-grade rocks that modification of phase compositions will occur as a result of diffusional equilibration during cooling (e.g. Kohn & Spear,

2000). Aside from this problem, Indares *et al.* (2008) showed that large proportions of matrix biotite in migmatites may be formed retrogressively during crystallisation of a melt; hence the analysed grain may never have been present at peak conditions. *P–T* data obtained through both methods thus document minimum conditions of metamorphism. As a result, it is unsurprising that many of the calculated *P–T* conditions (within uncertainty) fall along the calculated post-peak *P–T* path obtained through the above pseudosection modelling (Fig. 7.11a–b).

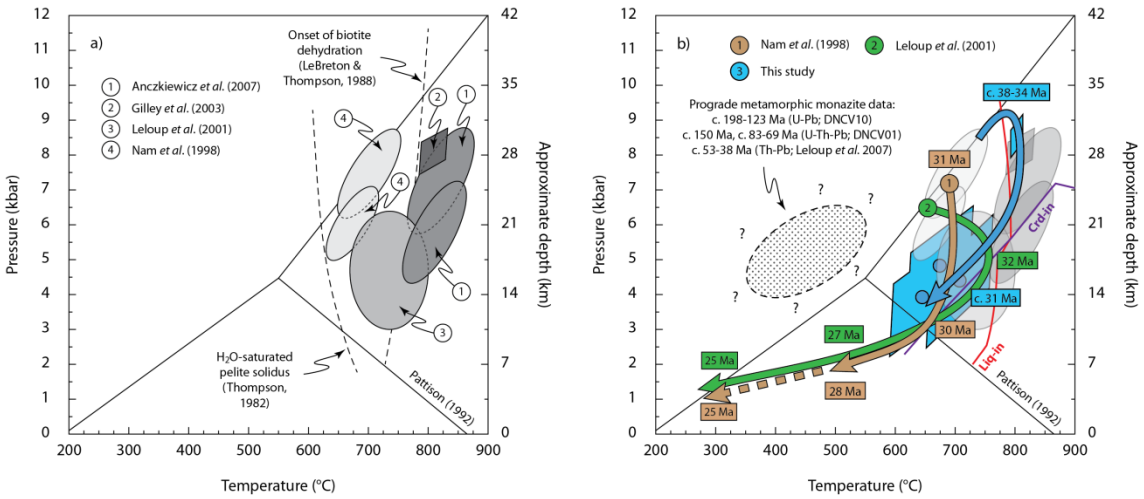


Fig. 7.11 – *P–T* synthesis for the DNCV massif. (a) Previous peak *P–T* estimates for metamorphosed units of the DNCV. Approximate depth scale is calculated assuming 3.5 km per 1 kbar. (b) Regional *P–T–t* evolution. TWQ results for *P–T* conditions of strain shadow assemblage formation in sample DNCV01 are marked by bold circles with uncertainty parallelograms of ± 1 kbar and ± 50°C. Crd-in and Liq-in boundaries are taken from Fig. 7.6a. The ellipse representing prograde metamorphic conditions is schematic and for illustration purposes only. Aluminosilicate phase relations and triple point are after Pattison (1992).

P–T pseudosection modelling suggests that conditions of 8.5 kbar and 805 °C were reached for peak metamorphism and partial melting, equivalent to a depth of 30 km depth in the crust. U–Th–Pb analysis of monazite suggests that this event occurred between c. 38 Ma, the oldest leucosome monazite (DNCV10) and c. 34 Ma, the youngest inclusion in garnet rims (DNCV01). Following a period of melt loss, crystallisation of the remaining melt fraction occurred during exhumation of sample DNCV01 at c. 31 Ma (Fig. 7.11b), indicated by the growth of high-Y_2O_3 monazite during garnet breakdown. This is corroborated by the coeval shearing of dyke DNCV09 at 30.6 ± 0.4 Ma, located on the flank of the DNCV, which is also coincident with the initiation of shearing (c. 31 Ma) proposed by Cao *et al.* (2011) in the Diancang Shan in Yunnan. Cross-cutting dyke sample DNCV02, which lacks evidence of shear deformation, was intruded at 25.2 ± 1.4 Ma,

thus providing constraining the cessation of regional metamorphic fabric development in the core of the antiform. These new data suggest that partial melting in the DNCV likely initiated earlier than has been previously thought and that exhumation occurred almost immediately after peak metamorphic conditions were reached. The range of monazite ages between 32.5–21.5 Ma that are reported by Leloup *et al*. (2007) are interpreted to represent the timing of high-temperature metamorphism caused by shear heating along the RRSZ (Fig. 7.12). By contrast, this study's data suggest that the duration of peak metamorphism and anatexis only spans 4 Myr (c. 38–34 Ma), and that the younger monazite ages in the range proposed by Leloup *et al.* (2007) resulted from retrograde exhumation and garnet breakdown as documented above (cf. grain 17; Fig. 7.9f).

7.6.2. Late Cretaceous monazite ages

In addition to the geochronological data showing that gneisses of the DNCV massif experienced initial metamorphism during the Triassic and subsequently during the Tertiary, evidence of a significant episode of monazite crystallisation during the Late Cretaceous (c. 83–69 Ma; Fig. 7.11) is reported. If these data are representative of the evolution of the entire DNCV massif, the cause of such an event is not apparent when considering the traditional palaeogeographic reconstructions of south-east Asia during this period, which mostly show that North Vietnam had experienced a period of tectonic quiescence following termination of the Indosinian orogeny (e.g. Metcalfe, 2002 and references therein). However, recent palaeomagnetic studies of terrestrial sediments by Takemoto *et al*. (2005) and Charusiri *et al*. (2006) suggest that a significant rotation of the Indochina and South China blocks may have occurred prior to and during the Jurassic-Cretaceous, reportedly facilitated by motion along the Red River and Song Ma faults. This result is contrary to the continental extrusion model, where total displacement along these faults is a result of the India-Asia collision, and these data suggest that these fault zones may have an extensive history prior to 50 Ma.

Alternatively, if these data are not representative of the DNCV as a whole, and are a special case, a different explanation must be made. Patchy internal zoning characterised by *'irregularly shaped subequant zones with distinct backscattered intensity associated with embayments, fractures and inclusions'* has been described by Ayers *et al*. (1999) as a texture associated with recrystallisation during *in-situ* hydrothermal alteration of pre-existing monazite. This mechanism,

allowing for a suitable source of fluid input, would permit recrystallisation of matrix monazite in the absence of a metamorphic or deformational episode. Evidence of magmatism in North Vietnam during the Late Cretaceous has recently been given by Roger *et al*. (2012), who report a U–Pb zircon emplacement age of 87.3 ± 1.2 Ma for a granite intrusion that is situated ~150 km north-west of the DNCV. Furthermore, sample DNCV09 in this study represents a granite intrusion into the DNCV gneisses, albeit volumetrically small, that was emplaced at 66.0 ± 1.0 Ma. These examples evidently show that magmatic activity has been occurring in and around North Vietnam prior to any deformation associated with the India-Asia collision. On solidification of these igneous bodies, substantial amounts of water may have been liberated into the neighbouring rocks and thus provide a plausible mechanism for fluid-assisted recrystallisation of monazite.

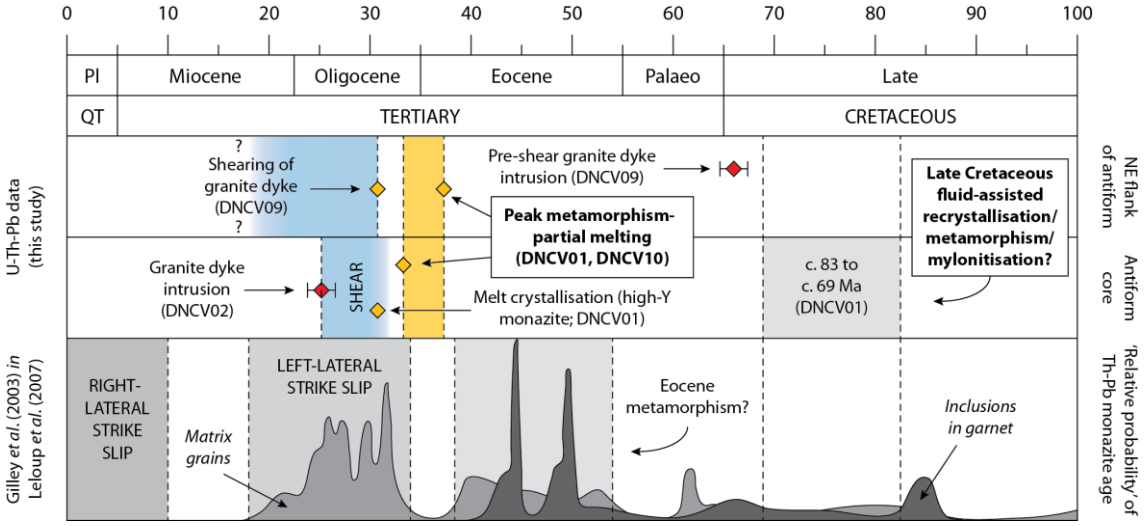


Fig. 7.12 – Summary timechart for geochronological data obtained in this study compared against Th–Pb monazite data presented in Leloup *et al.* (2007). Blue gradient boxes denote shearing at each locality.

Although hydrothermal alteration appears to be a likely explanation for the age data described above in this study, further possibilities exist. Geochronological data obtained by Gilley *et al*. (2003) and discussed in Leloup *et al*. (2007) show two significant crystallisation events during the Eocene, the latter study suggesting that they provide possible evidence for additional metamorphism at this time (Fig. 7.12). The complexity of geochronological datasets typically produced by DNCV paragneiss samples (e.g. Gilley *et al*., 2003; this study) shows that unravelling the thermal history of these units is extremely difficult, although of great importance for the understanding of the tectonic evolution of the RRSZ and south-east Asia. With studies suggesting an extended tectonic history for the RRSZ (Charusiri *et al*., 2006), it is possible that rocks now exposed along the RRSZ (or RRF)

have experienced multiple discrete deformational episodes, with more recent Late Eocene-Oligocene high-grade metamorphism having eliminated the majority of evidence by recrystallising older grains. The interpretation that monazite crystallisation was induced by hydrothermal fluid infiltration is the preferred explanation for the data described above, although further investigation is required in order to corroborate or refute these possible scenarios.

8. Conclusions and discussion

8.1. Regional studies

The four case studies presented in this thesis describe new tectonic and metamorphic episodes in each region. Important interpretations can be made when these data are considered within the framework of the HKTO as a whole, and in addition some remarkable similarities are revealed.

8.1.1. Deep subduction of the leading edge of the Indian plate

Analysis of mafic eclogite sample L08-03A has provided new *P–T* data that describe parts of the prograde, peak and retrograde evolution of the TMM, thus elucidating the conditions of subduction and transient exhumation of the Indian plate margin during the Eocene. Geochronological analysis of constituent minerals was not achieved in this study but, by integrating the above *P–T* data with published age constraints, a direct comparison can be made with the Kaghan massif in northern Pakistan, which hosts the only other UHP eclogites of Tertiary age within the Himalayan Range and is located ~450 km from Tso Morari along strike to the north-west (Fig. 1.2). *P–T* pseudosection modelling of compositional zoning recorded in a garnet porphyroblast, in addition to conventional thermobarometry and AvePT calculations, suggest metamorphism from prograde *P–T* conditions of ~22.5 kbar and ~525 °C to peak conditions of 25.5–27.5 kbar and 630–645 °C (Fig. 8.1). Prograde, peak and retrograde *P–T* data for eclogites from Kaghan have been presented by Kaneko *et al.* (2003), Gough (2002) *in* Parrish *et al.* (2006), and Wilke *et al.* (2010). Calculated *P–T* paths from these studies are shown in Fig. 8.1 and it can be seen that peak UHP conditions are higher than those calculated from sample L08-03A, ranging between c. 28–32 kbar and c. 650–750 °C.

It is notable, however, that these data have all been obtained using various calibrations of the garnet-clinopyroxene thermometer and garnet-clinopyroxene-phengite barometer. Štípská & Powell (2005) showed via a Monte Carlo error propagation method that a 1% relative error on the weight % compositional analysis of omphacite (thus propagating through to the calculation of XFe^{3+} content) results in a minimum uncertainty of ± 70 °C (1 S.D.) that applies to temperatures obtained from the garnet-clinopyroxene thermometer. By calculating a higher Fe^{2+} content, the result is biased up-temperature (ibid), hence, data obtained via this method may represent over-estimates of peak temperature. By contrast, Krogh Ravna & Terry (2004) report an error of just ± 0.32 kbar (1 S.D)

that is applicable to the garnet-clinopyroxene-phengite barometer, therefore maximum pressure can usually be better constrained. A discussion of the possible reasons behind the lack of UHP indicators in sample L08-03A is given in chapter 5.6.1, although by considering the above uncertainties, the differences in peak eclogite-facies *P–T* conditions between Tso Morari sample L08-03A (25.5–27.5 kbar and 630–645 °C) and those from Kaghan (c. 28–32 kbar and c. 650–750 °C) become minor. Thus, both Himalayan eclogites are interpreted to record similar peak conditions and were similarly subducted to maximum ~100 km depth, given that the reported existence of microdiamond in Tso Morari by Mukherjee *et al*. (2005) is unconfirmed by the peer-review process.

A notable feature of the *P–T* paths for the Kaghan eclogite (shown in Fig. 8.1) is a region of common *P–T* conditions at c. 10–12 kbar and c. 650–700 °C that was calculated in all studies by conventional thermobarometry performed on symplectite colonies and other matrix constituents (data from Kaneko *et al*., 2003; Gough, 2002 *in* Parrish *et al*., 2006; Wilke *et al*., 2010). The retrograde evolution of sample L08-03A to a similar pressure was investigated via *P*–M(H_2O) pseudosections constructed at a fixed temperature of 640 °C (chapter 5.5.4.1). This showed that it is possible to replicate the compositional zoning present within retrograde matrix amphibole as well as calculating a very similar volume proportion to that observed, with growth initiating at 23–25 kbar and continuing to ~12 kbar during the addition of H_2O. Although other minor differences between observed and calculated petrographic features exist (chapter 5.5.4.1), this result gives additional weight to the idea that the *P–T* histories of Kaghan and the TMM are, in part, quite similar.

Despite this, one feature of the calculated *P–T* history for sample L08-03A is fully discrepant with the calculated paths for Kaghan shown in Fig. 8.1. Thermobarometry performed on symplectite colonies in sample L08-03A has indicated growth at *P–T* conditions of 10.3–13.9 kbar and 461–554 °C, with an apparent evolution from low-pressure eclogite-facies, through epidote-amphibolite-facies into blueschist-facies (chapter 5.5.4.2). Given that the thermobarometers chosen for this work accounted for the symplectite assemblage as well as for the unknown activity of SiO_2 and H_2O, there is no good explanation for the calculated data. It has been shown by many studies (chapter 5.2) that the TMM experienced a Barrovian-type prograde metamorphic overprint following the exhumation of eclogitic units to the lower-middle crust. The path calculated via symplectite thermobarometry, however, is orientated to suggest exhumation back to the surface with no further metamorphism. If

this trajectory is real, it must therefore be a part of the M2-to-M3 evolution and marks the final stage of initial exhumation, before the units were caught up in the early stages of the subsequent prograde overprint. In this case, the lack of M4 assemblages/microstructures within mafic eclogite could then be explained by the total removal of fluid from the grain boundary network during retrograde mineral growth, restricting further reaction. Otherwise, this result is best explained as an artefact of the thermobarometric methods used and its cause is unknown.

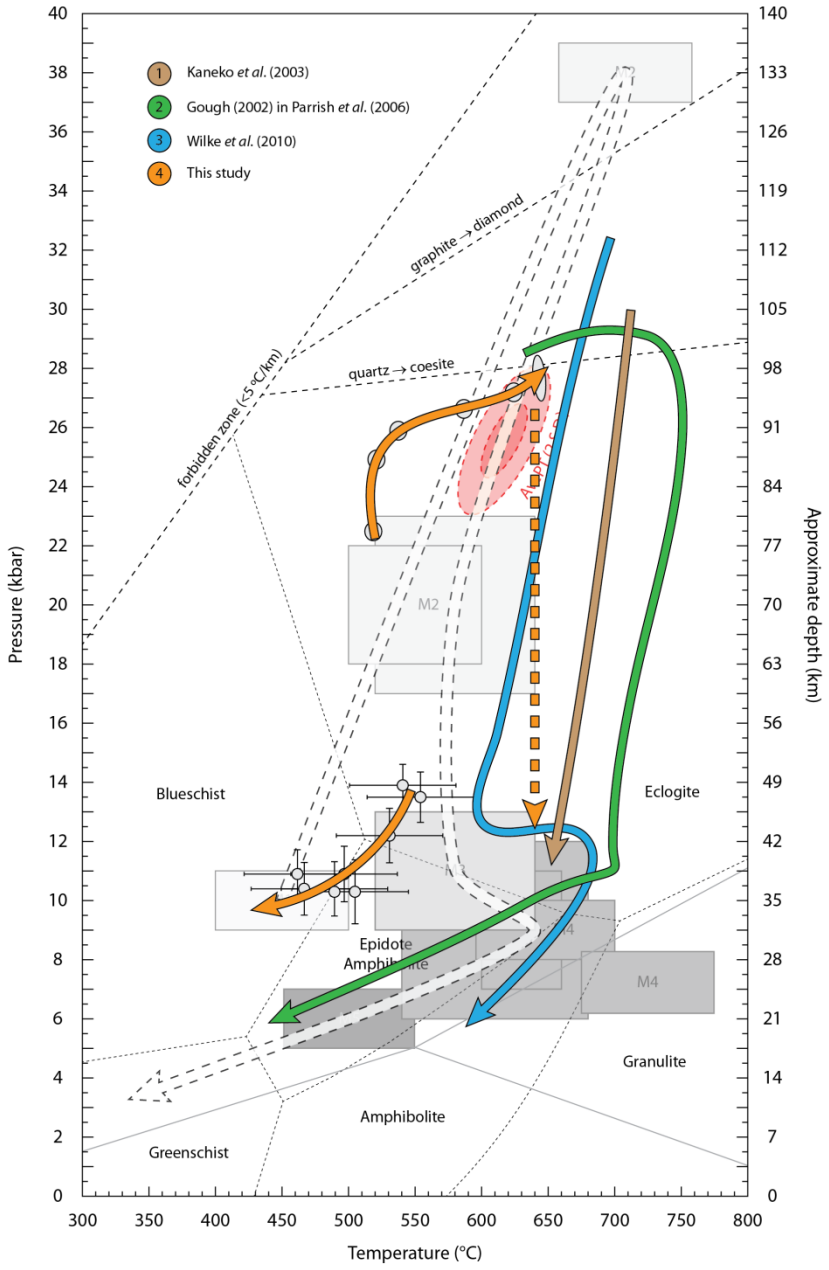


Fig. 8.1 – Comparison of *P–T* data between sample L08-03A and the Kaghan eclogitic massif. *P–T* estimates for different metamorphic episodes (M1–M5) and generalised *P–T* path for the TMM are the same as those shown in Fig. 5.2. *P–T* paths for the reported evolution of eclogite from Kaghan are shown by various studies alongside *P–T* data obtained in this study from sample L08-03A relating to the TMM. See text for discussion.

Although the above data from sample L08-03A demonstrate a remarkable similarity to the evolution of the Kaghan eclogitic massif, suggesting a laterally similar subduction event along the leading edge of the Indian plate during the Eocene, there is a significant difference in the calculated rates of exhumation. St-Onge *et al.* (2013) report a minimum exhumation rate of 12 mm/yr for units of the TMM based on a U–Pb zircon age of 50.8 ± 1.4 Ma for peak M2 conditions (c. 27–28 kbar) from mafic eclogite and a Th–Pb monazite age of 45.3 ± 1.1 Ma for the timing of the peak M4 overprint in host orthogneiss (c. 7 kbar). This rate is marginally faster than that of 7 mm/yr reported by de Sigoyer *et al.* (2004), who used similar data from de Sigoyer *et al.* (2000) and Sachan *et al.* (2001). These estimates are both significantly slower than rates of ~30–80 mm/yr and 86–143 mm/yr that have been proposed for Kaghan by Parrish *et al.* (2006) and Wilke *et al.* (2010) respectively. Despite this large difference the exhumation rates reported by St-Onge *et al.* (2013) and de Sigoyer *et al.* (2004) represent minima, as they are constrained by ages obtained on peak eclogite-facies (M2) conditions and peak amphibolite-facies Barrovian overprinting (M4). The exhumation of eclogites based upon a two-stage model (Duchene *et al.*, 1997; Walsh & Hacker, 2004; Beaumont *et al.*, 2009 and others) shows that the first stages of exhumation to the lower levels of the continental crust are extremely fast, whereas the final stages of exhumation, which in the case of units of the TMM involves a prograde metamorphic episode up to amphibolite-facies, takes a longer time. Thus, as the exact time interval between M2 and M3 metamorphism is unconstrained there is scope for increasing the interpreted minimum rate during initial exhumation, although it is doubtful that it could increase by approximately one order of magnitude to match the rates reported for Kaghan.

8.1.2. Metamorphism and magmatism along the southern Asian margin

Two regional case studies in this thesis document metamorphism, magmatism and deformation that affected the southern Asian margin prior to, during, and after initial collision with India. These two regions, the Karakoram metamorphic complex, north of the western Himalayan syntaxis in Pakistan, and the eastern Himalayan syntaxis, south-east Tibet, are >2000 km apart along strike (Fig. 1.1) and yet numerous similarities in their tectonothermal evolution are recorded. The following discussion summarises and compares the data that have been produced for both areas, but ultimately focuses on

interpretations that can be made for the south Lhasa block, due to the potential to directly compare these data with the nearby Indian plate units of the eastern Himalayan syntaxis.

In a study of peraluminous metapelites from the Karakoram metamorphic complex, two kyanite-grade metapelites from the Baltoro region show evidence of having reached similar peak *P–T* conditions of ~7.4–8.0 kbar and ~640–660 °C. Sample T17 indicates that garnet growth occurred over a pressure increase of ~2.6 kbar and a temperature increase of ~100 °C sometime after c. 22 Ma from an initial geothermal gradient of ~30 °C/km. The timing of kyanite-grade metamorphism coincides with emplacement ages for components of the BPU (c. 25–13 Ma; Table 4.1), suggesting that granite intrusions may have provided the heat source required to create this elevated initial geotherm and magmatic over-accretion could be responsible for the increase in pressure. This mechanism is particularly favoured here as similar kyanite-grade metapelites situated away from early deformed components of the BPU record open clockwise *P–T* loops during metamorphism (Rolland *et al*., 2001) that are characteristic of rocks undergoing crustal thickening in a continent-continent collisional setting (Thompson & England, 1984). A kyanite-grade overprint (~7.8 kbar, 645 °C) of sillimanite-grade rocks in the Hunza Valley occurred at 28.2 ± 0.8 Ma, leading to the replacement of sillimanite by kyanite and the formation of garnet-rim overgrowths in sample 20-199. This particular overprint is only partially exposed in the lower sillimanite-zone, possibly due to varying degrees of exhumation and erosion, and its structural and temporal relationship to units of the 'kyanite-zone' further south is unknown. Finally, a U–Pb monazite age of 105.5 ± 0.8 Ma also obtained from sample 20-199 reveals evidence of andalusite-grade contact metamorphism associated with subduction-related magmatism that formed the HPU of the Karakoram batholith.

An investigation into rocks of the south Asian margin on the north-western flank of the EHS has produced petrographic and geochronological constraints on metamorphic and deformational events that affected south-east Tibet. Migmatites located in the B-L-M region contain sillimanite-grade leucosomes that formed between c. 71–50 Ma at *P–T* conditions above 6.3 ± 1.2 kbar and 750 ± 30 °C. These are interpreted to represent a muscovite-dehydration sillimanite-grade melting event in the south Lhasa block that likely resulted from conductive heat transfer to the middle crust via the proximity of emplacement of the Gangdese batholith (chapter 6.7.1). Subsequent higher pressure and lower temperature kyanite-grade metamorphism and fluid-saturated K-feldspar-absent partial

melting occurred between c. 44–33 Ma at *P–T* conditions of 10.4 ± 1.0 kbar and 698 ± 25 °C, interpreted to be associated with crustal thickening and burial during the India-Asia collision. Evidence for a later staurolite-grade prograde metamorphic episode that reached a maximum temperature of 650 °C at 23.6 ± 0.3 Ma is given by monazite inclusions in garnet porphyroblast rims that exist as porphyroclasts in a now-mylonitised metapelite. However, as the provenance of the mylonite protolith is uncertain, this event cannot be unequivocally assigned to the B-L-M region. The timing of mylonitisation and exhumation of similar metapelites along the MYLP fault has been constrained with U–Pb dating of syn-shearing monazite growth between c. 16–11 and c. 9.5–8.0 Ma.

A comparison between these two regions is easily drawn. Although the KMC is laterally equivalent to the Qiangtang block of central Tibet (chapter 1.4.3), it is situated north of the western Himalayan syntaxis and contains rocks that document the tectonothermal evolution of the southern Asian margin during closure of the Neo-Tethys Ocean and collision of the Indian plate (e.g. Searle, 1991). Fig. 8.2 summarises major magmatic and metamorphic events in the KMC, the B-L-M region and the EHS according to the currently available geochronological data (including this study).

It can be seen that the extended period of pre-collision sillimanite-grade metamorphism and partial melting documented in the B-L-M region is quite similar in duration to that observed in the Hunza Valley region of the KMC, although the interpreted causes differ. Whereas sillimanite-grade partial melting in the B-L-M region between c. 71–50 Ma is interpreted to have been caused by coeval emplacement of the Gangdese batholith throughout the Late Cretaceous, with a major intrusion event in the Palaeocene between c. 66–57 Ma, equivalent calc-alkaline subduction-related plutons in the Hunza Valley (the HPU) have intrusion ages of c. 95–105 Ma (Table 4.1), much older than high-grade metamorphism between c. 63–44 Ma (chapter 1.5.3). Instead, this latter sillimanite-grade metamorphism and crustal melting was interpreted by Searle *et al*. (2010a) to be the result of prolonged crustal thickening. Although the HPU is a composite batholith with many components still to be studied (Debon *et al.*, 1987; M.P. Searle *pers comms*, 2010), thus providing the possibility that younger intrusions could have resulted from continued subduction of the Neo-Tethys Ocean prior to the India-Asia collision, these data are currently unavailable. As a result, it is concluded that both pre-collisional sillimanite-grade partial melting events, although superficially similar in their ~20 Myr duration and Late Cretaceous-Palaeocene timing, are simply coincidental.

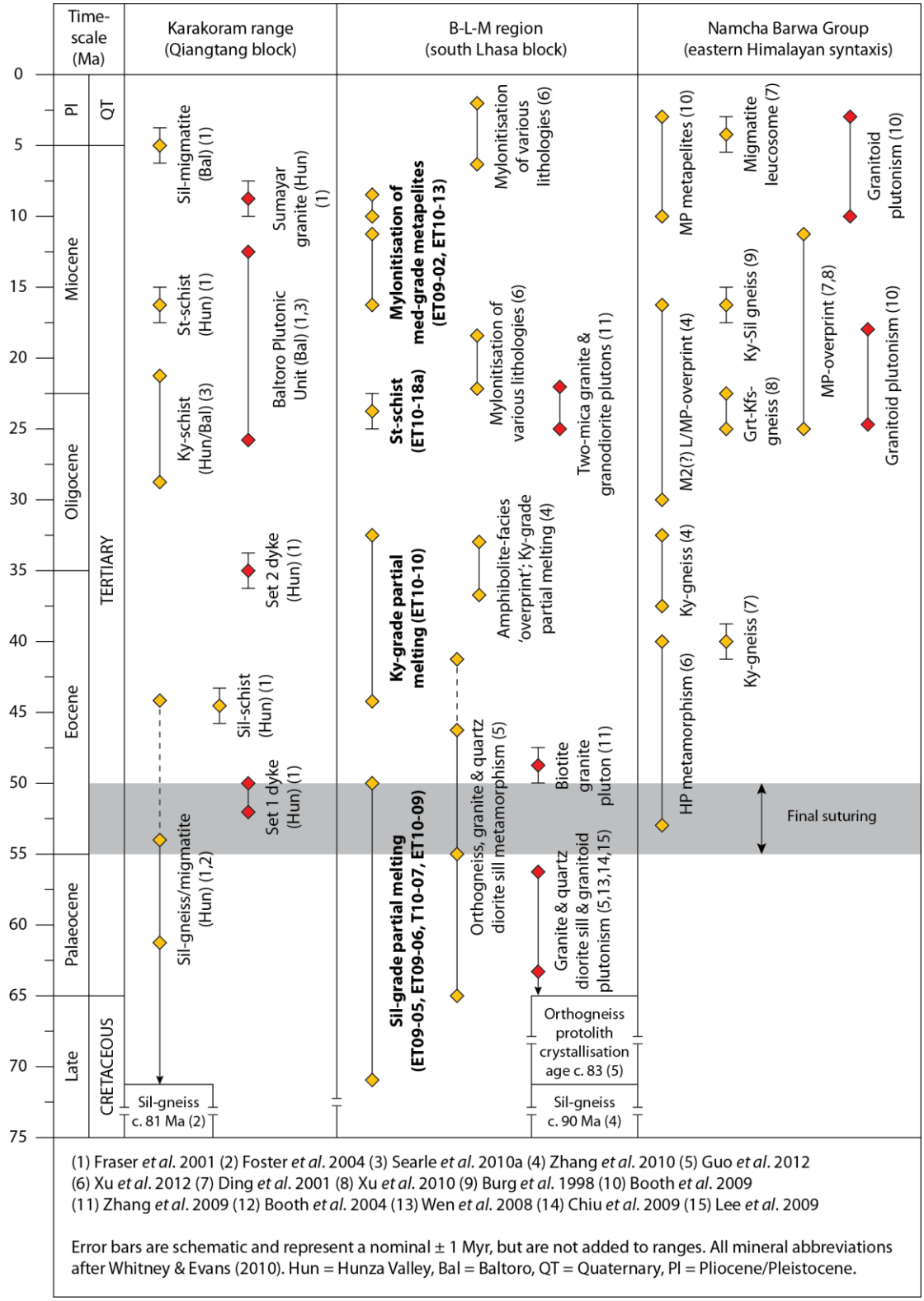


Fig. 8.2 – Comparative magmatic-metamorphic evolution timechart for selected regions. Shaded bar represents the timing of final suturing during the India-Asia collision (after Searle *et al.*, 1987; Green *et al.*, 2008). Bold data relating to the B-L-M region of the south Lhasa block are those from this study.

Post-collisional magmatism in the KMC is prevalent in the Baltoro region, with monzogranite and two-mica leucogranite components of the BPU emplaced between c. 25–13 Ma (Table 4.1).

Searle *et al*. (2010a) interpreted the BPU to have resulted from widespread crustal melting of the middle-lower Karakoram crust associated with deformation caused by the India-Asia collision, as it intrudes into and across these older metamorphic units. In the B-L-M region, Zhang *et al.* (2009) document very similar large granite plutons that intrude across older metamorphic units and adjacent components of the Gangdese batholith (Fig. 6.1), with U–Pb zircon emplacement ages of 25.4 ± 0.3 Ma and 22 ± 1 Ma. The same study also showed via isotope geochemistry that these bodies were sourced from a combination of garnet-bearing crustal rocks and Gangdese batholith. Kyanite-bearing migmatite sample ET10-10 documented in this study shows that post-collisional crustal melting was occurring in the B-L-M region between c. 44–33 Ma and could be theorised as a potential source rock for such intrusions. Although the minimum time gap between these events is large (at least ~8 Myr), and does not fully support this particular case, these data serve to highlight some fundamental tectonic, petrographic and geochronological similarities in the evolution of the Asian margin in the vicinity of both Himalayan syntaxes prior to, during and following the India-Asia collision.

Implications for the evolution of the EHS region; evidence for a paired metamorphic belt?

Before assessing the implications of the new data given in this study for the evolution of the EHS as a whole, it is useful to revise the current understanding of the tectonothermal history of the B-L-M region. The relevant data are summarised below and orientated on a map of the region in Fig. 8.3:

- c. 90 Ma – Granulite-facies metamorphism at 9–13 kbar and 830–900 °C, recorded in sillimanite-bearing paragneiss that outcrops north of Milin (Zhang *et al*., 2010).
- 83.4 ± 1.2 Ma – Orthogneiss magmatic protolith emplacement, east of Linzhi, interpreted by Guo *et al*. (2012) from Hf isotopes to represent a depleted mantle or juvenile crust source.
- c. 71–50 Ma – Sillimanite-grade metamorphism and muscovite-dehydration melting above 6.3 ± 1.2 kbar and 750 ± 30 °C, data from four outcrops near Bayi and Linzhi (this study).
- c. 66–57 Ma – A major emplacement episode of units of the Gangdese batholith along the length of the south Lhasa block (Wen *et al*., 2008; Chiu *et al*., 2009; Lee *et al*., 2009).
- c. 65–46 Ma – Metamorphism of orthogneiss magmatic protolith (above) to unknown *P–T* conditions (Guo *et al*., 2012).

- 64.4 ± 0.7 Ma and 63.1 ± 0.6 Ma – Granite and quartz-diorite sills intruded into B-L-M orthogneiss and paragneiss, east of Linzhi, interpreted by Guo *et al*. (2012) from Hf isotopes to be sourced from partial melting of crustal materials.
- 55.1 ± 1.3 Ma and 41.4 ± 2.3 Ma – Metamorphism of granite sill (above) to unknown *P–T* conditions (Guo *et al*., 2012).
- 49.1 ± 0.4 Ma – Biotite granite sheet (~6m wide) intruded into B-L-M gneiss, south-west of Linzhi, interpreted by Zhang *et al*. (2009) from isotope geochemistry to be sourced from a combination of garnet-bearing crustal material and Gangdese batholith.
- c. 44–33 Ma – Kyanite-grade metamorphism and fluid-saturated melting at 10.4 ± 1.0 kbar and 698 ± 20 °C, recorded in sample ET10-10 collected south-west of Linzhi (this study).
- c. 36–33 Ma – Amphibolite-facies metamorphism at 8–11 kbar and 590–660 °C recorded in kyanite-bearing paragneiss outcropping south-west of Linzhi (Zhang *et al*., 2010).
- 25.4 ± 0.3 Ma and 22 ± 1 Ma – Lunan and Bayi two-mica granite and granodiorite plutons, >1000 km^2 and ~250 km^2 in areal extent respectively, east of Bayi and Linzhi, intruding across metamorphic units, interpreted by Zhang *et al*. (2009) from isotope geochemistry to be sourced from a combination of garnet-bearing crustal material and Gangdese batholith.
- 23.6 ± 0.3 Ma – Staurolite-grade metamorphism to a maximum temperature of 650 °C in a metapelite that has since been exhumed and mylonitised along the MYLP fault (this study).
- c. 22–18, c. 16–11, c. 9.5–8.0 Ma and c. 6–2 Ma – Exhumation and mylonitisation of units (of uncertain provenance) exposed along the MYLP fault from just south of Milin to north of Linzhi (Xu *et al*., 2012; this study)

Several previous studies have used subsets of the above data to interpret the post-collisional evolution of the southern Asian margin in and around the EHS. The following section discusses one specific tectonic scenario that has been presented by Zhang *et al*. (2010), which suggests that the Indian and Asian margins acted as *paired metamorphic belts* during the Oligocene. This scenario is favoured by this study as it manages to account for many of the features described above and provides a good fit with the known *P–T–t* constraints for both the Namche Barwa Group and rocks within the B-L-M region.

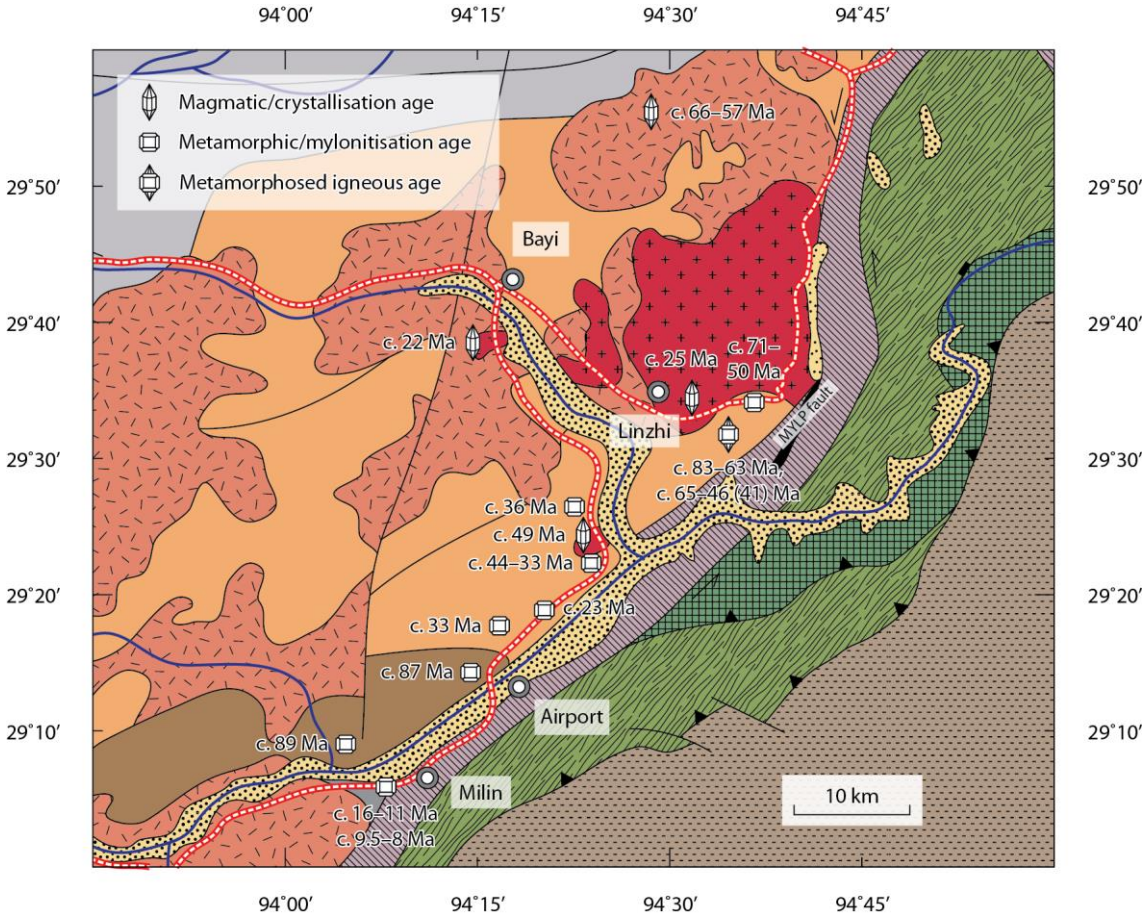


Fig. 8.3 – Map summary of geochronological data currently available for the B-L-M region. All patterns, fills and other markings relevant to geological units are equivalent to those in Fig. 6.1. See text for discussion of data.

The concept of 'paired metamorphic belts' was first proposed by Miyashiro (1961) to describe the spatial and temporal relationship between two adjacent suites of rocks, one characterised by a low geothermal gradient (low d*T*/d*P*) and the other characterised by a high geothermal gradient (high d*T*/d*P*). This original definition applied to an oceanic island arc subduction setting where the low geotherm applied to subduction zone metamorphism and the high geotherm to metamorphism taking place in a backarc environment (ibid). Subsequent studies have extended this definition to include suites of rocks occurring in continent-continent collisional systems (Brown, 2009), in particular within the north-west and east Himalaya (Kumar, 1978 and Goscombe & Hand, 2000 respectively). In a recent review of the topic, Brown (2010) states that the paired metamorphic belt concept is '*particularly useful in subduction-to-collision orogenic systems [for example the HKTO], where the suture and lower plate materials will register the imprint of low-to-intermediate dT/dP and the upper plate will register penecontemporaneous high dT/dP metamorphism commonly manifested at*

shallow crustal levels by the occurrence of granites in the rock record'. In order to verify this, one should therefore look for blueschist, eclogite or high-pressure granulite assemblages in lower plate rocks and medium-to-low pressure amphibolite- or granulite-facies assemblages in the upper plate.

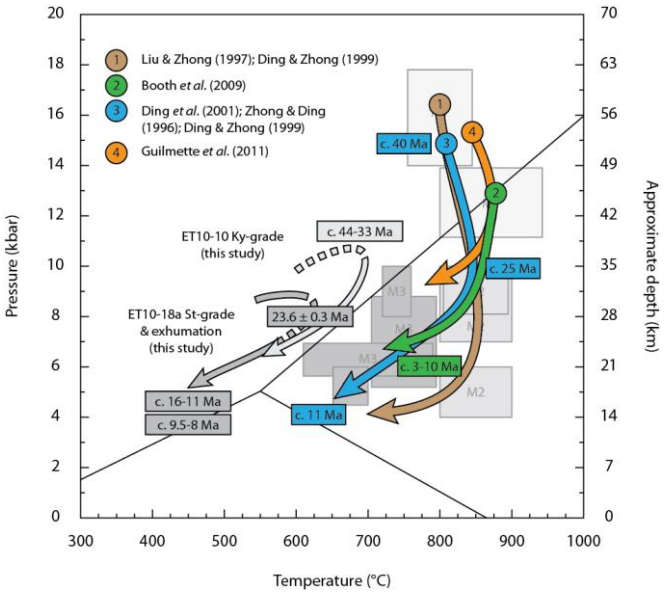


Fig. 8.4 – Paired metamorphic belts within the EHS? A comparison of post-collisional *P–T–t* paths for units of the south Lhasa block (B-L-M region; this study) with those of the Namche Barwa Group (other studies as numbered).

P–T–t data relevant to the hypothesis that metamorphic units of the B-L-M region (Asian/upper plate) and the Namche Barwa Group (Indian/lower plate) may represent a paired metamorphic belt are shown in Fig. 8.4. In addition, cartoon cross-sections showing the evolving India-Asis collision at relevant time periods since c. 70 Ma are shown in Fig. 8.5. High-grade units from the core of the syntaxis (the Namche Barwa Group) experienced high-pressure granulite-facies metamorphism at peak pressures up to 18 kbar (Liu & Zhong, 1997; Ding & Zhong, 1999) and peak temperatures up to 950 °C (Booth *et al.*, 2009) between c. 40–24 Ma (U–Pb zircon; Ding *et al.*, 2001; Zhang *et al.*, 2010; Xu *et al.*, 2010). These units show apparent peak thermal gradients of less than 15 °C/km. Furthermore, a sample of garnet-pyroxenite examined by Zhang *et al.* (2007) suggests that eclogite-facies peak conditions of 26–28 kbar at 800–900 °C were reached by some rocks of the Namche Barwa Group during subduction. Xu *et al.* (2012) reportedly dated this eclogite-facies event at 53.9 ± 1.1 Ma by U–Pb analysis of zircon from a sample of mylonitised felsic gneiss; however, as noted previously, given the uncertain provenance of units within the shear zone, this age does not necessarily apply to the Namche Barwa Group. In contrast to these high-pressure granulite-facies units of the Namche Barwa Group, post-collisional kyanite-grade

metamorphism and partial melting on the Asian plate (sample ET10-10) occurred at significantly lower *P–T* conditions of 10.4 ± 1.0 kbar and 698 ± 20 °C, which is equivalent to a higher geothermal gradient for peak metamorphism of ~20 °C/km. This latter event is dated at c. 44–33 Ma, initiating slightly earlier than the Indian-plate 'equivalent'.

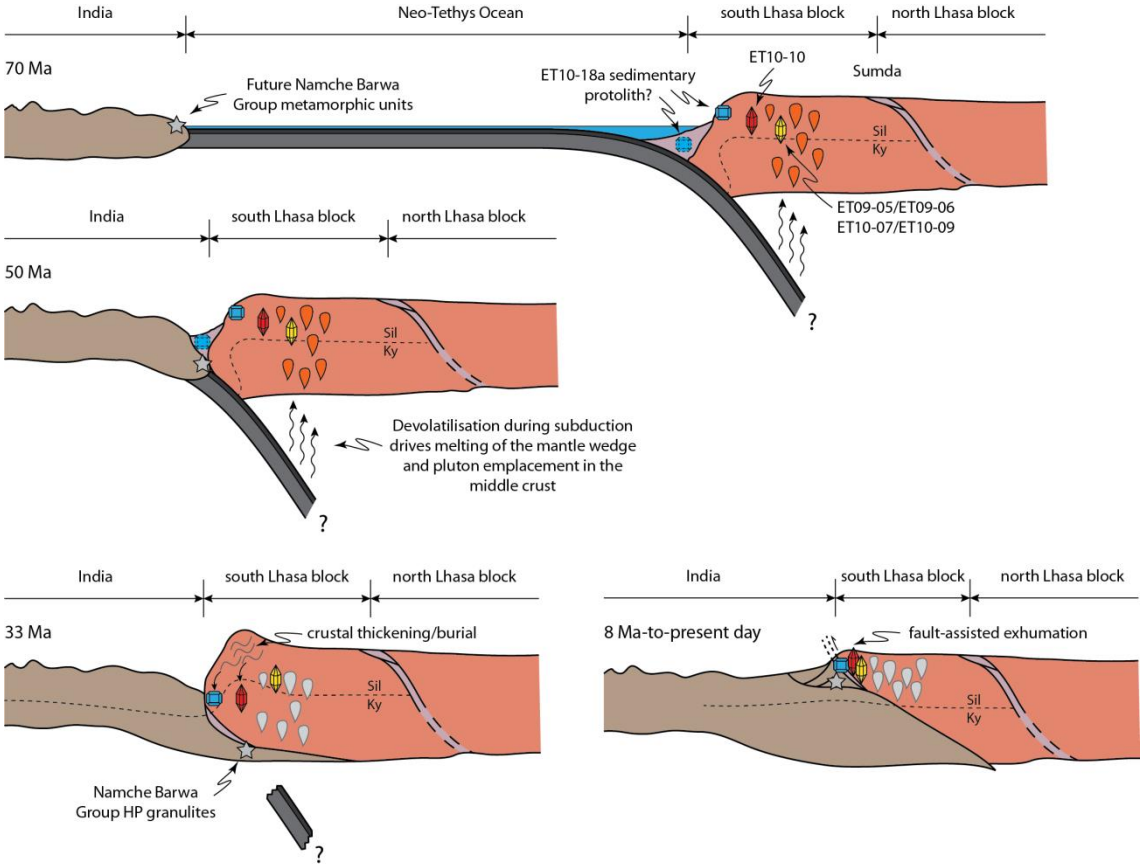


Fig. 8.5 – Cartoon cross-sections of the India-Asia collision over since 70 Ma. Drawings are not to scale and are used solely to illustrate the interpreted evolution of dated samples in this study.

Following this high-pressure event, units of the Namche Barwa Group underwent almost-isothermal decompression to the mid-crust, reaching pressures of 4–10 kbar by c. 25 Ma whilst still at granulite-facies temperatures (Fig. 8.4; Zhong & Ding, 1996; Liu & Zhong, 1997; Ding & Zhong, 1999; Ding *et al.*, 2001). This event occurred concurrently with a prograde staurolite-grade metamorphic event, thought to have affected the B-L-M region (sample ET10-18), that peaked at 23.6 ± 0.3 Ma. Exhumation of Namche Barwa Group units during the Oligocene-Miocene is marked by a medium-pressure, medium-temperature amphibolite-facies overprint with *P–T* conditions between 4.5–10 kbar and 600–800 °C (Zhong & Ding, 1996; Ding & Zhong, 1999; Booth *et al.*, 2009; Burg *et al.*, 1998). The timing of this overprint is poorly constrained, with a total range

between c. 30–8 Ma having been proposed (Ding *et al.*, 2001; Xu *et al.*, 2010; Burg *et al.*, 1998; Zhang *et al.*, 2010; Zhang *et al.*, 2012) although Booth *et al*. (2009) suggests that this could have occurred as late as c. 10–3 Ma.

Thermal modelling has shown that for a sequence of rocks undergoing the same burial and exhumation cycle, an initially deeper rock will experience peak metamorphic conditions at a later time than a shallower rock (e.g. England & Thompson, 1984; Thompson & England, 1984). The absolute difference in peak *P–T* conditions and the time that they are reached is a function of the difference in initial depth in the pile (ibid). Using these relationships with the above *P–T–t* data, it can be interpreted that rocks of the south Lhasa block/B-L-M region and Indian plate Namche Barwa Group may have formed a paired metamorphic belt during the Eocene based upon metamorphism documented in sample ET10-10 whereby the slight offset in peak metamorphic ages lends further support to the paired metamorphic belt hypothesis in addition to the difference in peak thermal gradients. The exact provenance of mylonitised staurolite-grade sample ET10-18a is uncertain, as it was collected from within the shear zone that divides the B-L-M lithologies from the Namche Barwa Group. However, if it does represent a prograde event that affected the B-L-M region, given that the prograde metamorphism is distinctly different in character from the Namche Barwa Group units that were undergoing exhumation from high-pressure granulite-facies conditions at the time, then this new data would provide further support for coupling during the Oligocene. Even if sample ET10-18a represents a sheared packet of marine sediment from the Neo-Tethyan Ocean, as suggested by Zhang *et al*. (2010), it still provides valuable *P–T* and age constraints on prograde metamorphism that was occurring at the Indian and Asian plate interface following initial collision. Finally, ages obtained from sample ET09-02, collected from along strike of the same band of mylonitised units, shows that these lithologies were exhumed through the ~450 °C isotherm as recently as c. 8 Ma.

In final support of this hypothesis, Brown (2010) suggested that a common result of paired metamorphism in a continent-continent collision setting should be the late emplacement of crustally-derived granites in the upper plate. Fieldwork performed in this study recognised numerous ‘S-type’ granitic bodies in the B-L-M region just east of Bayi (chapter 6.3.1), although restrictions did not allow an estimation of size for these bodies. In addition, Zhang *et al*. (2009) report large post-collisional granite plutons that represent a significant addition of magma to the B-L-M region (Fig.

8.3) and which intrude across older and/or pre-collisional metamorphic and magmatic units. These bodies, and smaller sills reported by Guo *et al.* (2012), have geochemical signatures indicating that they have a mixed source of Asian garnet-bearing crustal material and Gangdese batholith. Although the pre-collisional sillimanite-grade partial melting described in this study cannot be a source, the younger kyanite-grade partial melts (sample ET10-10) that formed between c. 44–33 Ma represent a potential candidate; although anatexis in this unit still predates granite emplacement by at least ~8 Myr. Despite this, these crustal melt bodies in the B-L-M region have no equivalent (in terms of volume) in the Namche Barwa Group and therefore provide additional support to the paired metamorphic belt hypothesis.

8.1.3. Lithospheric-scale strike-slip faults and the continental extrusion hypothesis

The continental extrusion hypothesis, first proposed by Tapponnier *et al.* (1982), suggests that c. 40–60% of the northward convergence of India with Asia has been accommodated by the lateral displacement of rigid continental blocks away from the indenter (India), assisted by motion along lithospheric-scale strike-slip faults (Tapponnier *et al.*, 1986; Peltzer & Tapponnier, 1988). In this model, the south-eastward extrusion of Indochina during the Tertiary has been accommodated by movement along along the RRSZ, the Sagaing fault and the Wang Chao fault (Fig. 1.6) in south-east Asia (Leloup *et al.*, 1993, 1995, 2001; Tapponnier *et al.*, 1986, 1990, 2001). However, numerous multidisciplinary studies have subsequently discredited this hypothesis as a viable mechanism for accommodating a *large* proportion of the total shortening across the HKTO (a full description of the data and arguments are reviewed in Searle *et al.*, 2011), Tertiary metamorphism and magmatism is nonetheless documented in rocks exposed along the RRSZ – the cause of which remains debated.

Numerous studies that support the continental extrusion hypothesis have suggested that the high-temperatures recorded within the Xuelong Shan, Diancang Shan, Ailao Shan and DNCV are a direct result of Tertiary shear heating along the RRSZ (Tapponnier *et al.*, 1990; Leloup *et al.*, 1993, 1995, 2001, 2007). A steady-state 1-dimensional conductive model constructed by Leloup *et al.* (1999) showed that shear heating of the middle-lower crust at a slip rate of 4 cm/yr could cause an increase in ambient crustal temperature of ~150 °C, that may then result in metamorphism and partial melting. However, later modelling reported by Gilley *et al.* (2003) considered time-dependent

conduction in 2-dimensions and showed that up to 20 Myr of continual shearing (at the same slip rate) would only raise temperatures by 60–80 °C. Although this result showed that a degree of heating would occur as a result of fault motion, it is does not constitute a suitable cause for the entireity of prograde metamorphism (documented to have occurred over a temperature range of at least 150 °C; chapter 7.6.1).

A tenet of the continental extrusion hypothesis is that the lithospheric-scale strike-slip faults cut through the entire crust and thus terminate at the Moho (e.g. Leloup *et al.*, 1995). Using this condition, an alternative heat source for high-temperature metamorphism in the Ailao Shan metamorphic core complex was proposed by Leloup & Kienast (1993), whereby advection of heat up through the shear zone by ascending magmas induced crustal anatexis. This theory was largely based on the existence of numerous alkali syenite-monzonite intrusions, in all metamorphic complexes of the RRSZ, with U–Pb zircon ages of c. 35–32 Ma (Schärer *et al*., 1994; Zhang & Schärer, 1999; Liang *et al.,* 2007). Although these ages are roughly coincident with U–Pb and Th–Pb monazite ages for peak metamorphism (and crustal melting) within DNCV paragneiss (Gilley *et al*., 2003; this work), other alkali intrusions also occur over a wide region of Yunnan and Vietnam outside of the shear zone and are hence unlikely to be directly associated with strike-slip shearing (Chung *et al*., 1997, 2008; Searle 2006; Yeh *et al.,* 2008). Furthermore, Searle (2006) and Chung *et al*. (2008) argue that the bodies within the RRSZ are volumetrically insignificant and cannot have provided sufficient heat to produce the total volume of high-grade paragneiss that is exposed today.

Work performed in this study has shown that a sample of weakly deformed anatectic paragneiss from the core of the DNCV antiform reached peak metamorphic conditions of ~8.5 kbar and ~805 °C between c. 38–34 Ma, these ages being constrained by monazite located in leucosome segregations and as inclusions in garnet rim regions. Exhumation initially followed a steep retrograde *P–T* path with final melt crystallisation at the solidus occurring at pressures no less than 5.5 kbar at 790 °C, equivalent to ~20 km depth in the crust. Further exhumation in the subsolidus domain led to the breakdown of garnet at conditions between ~4–5 kbar and ~640–700 °C, an event that instigated the formation of high-Y_2O_3 rims on matrix monazite at c. 31 Ma. Hence, the main high-grade metamorphism and melting event occurred in less than 7 Myr. Although these data provide a precise and detailed description of the *P–T–t* evolution of DNCV paragneiss, they do not

provide any insight into the tectonic or thermal mechanisms responsible. Neither the short duration documented for peak metamorphism and partial melting, nor the large temperature range of >150 °C inferred for prograde metamorphism and garnet growth support the hypothesis of continental extrusion and shear heating inducing metamorphism. In addition, a quite unexpected result of the geochronological work in this study is the production of a significant cluster of U–Th–Pb monazite ages between c. 83–69 Ma recording an episode of monazite crystallisation during the Late Cretaceous. This event is interpreted to be (most likely) related to fluid liberation into host paragneiss following the emplacement of magmatic units, especially given recent age data describing the occurrence of such bodies with a Cretaceous age elsewhere in North Vietnam (e.g. Roger *et al*., 2012). However, regardless of its cause, the event predates the India-Asia collision by nearly 20 Myr and is likely to be wholly unrelated.

8.2. Implications for pseudosection modelling

The effect that the continual fractionation of cations into garnet during porphyroblast growth has on calculated prograde and peak *P–T* conditions has been investigated with similar pseudosection modelling case studies of a metapelitic schist from the KMC and a mafic eclogite from the TMM. Remarkably, the conclusions that are drawn from either sample differ significantly, such that understanding why this discrepancy occurs has important implications for the modelling process.

Pseudosection modelling of sample T17, a peraluminous kyanite-grade metapelite from the Baltoro region of the KMC, suggests that a calculated prograde *P–T* path is petrographically more reliable when fractionation of cations into garnet can be implemented. This is a fully expected result that has also been demonstrated by numerous other workers that have investigated the problem (e.g. Marmo *et al*., 2002; Evans, 2004; Konrad-Schmolke *et al*., 2008 and others). Garnet porphyroblasts that grow in a metapelitic bulk composition as a result of prograde metamorphism through the amphibolite-facies should show strong compositional zoning profiles from core to rim (Woodsworth, 1977; Pattison & Tinkham, 2009). Consequently, it is clear that a rock's EBC must also evolve throughout the growth history of garnet – the extent to which this occurs depending on the volume of garnet created. As such, when considering fractionation in sample T17, the modal proportions and compositions of the calculated peak metamorphic assemblage matched observed parameters to a

higher degree of accuracy than without accounting for this effect (chapter 4.6.2). Indeed, the calculated 'total volume discrepancy' between observed and calculated phase proportions was only 7.9% for the fractionated case, nearly half of the total for an unfractionated system (15.2%). A total discrepancy as small as this may even simply represent natural variation in calculated volume proportions throughout the sample. Even though garnet in sample T17 constitutes only 4.25% of the total rock volume (Appendix 11.6), grains are almandine-rich (Fig. 4.6) and hence the major compositional effect of cation fractionation is the influence on the Fe–Mg distribution in coexisting ferro-magnesian matrix phases such as biotite (Table 4.8).

Following this reasoning, a rock that contains a larger volume proportion of garnet should give a more pronounced result. An opportunity to test this theory was provided by mafic eclogite sample L08-03A from the TMM, in which garnet comprises ~30% of the total rock volume; a proportion that was consistent throughout multiple thin sections. As the process of cation sequestration also becomes increasingly important towards the latter stages of garnet growth, assuming a spherical geometry, it is unsurprising that the prograde *P–T* paths calculated with and without fractionation exhibited diversion towards their latter stages. However, this diversion for a fractionated EBC occurred towards lower peak pressure (25.5 kbar; Fig. 5.12e), a result that is known to be erroneous given the documented occurrence of coesite in the massif that indicates peak pressures of >28 kbar at a temperature of ~650 °C. Additionally, an attempt to use the maximum measured Si content of phengite to constrain peak pressure showed a poorer correlation on the calculated pseusdosections when fractionation was applied (Fig. 5.13). Possible causes of this result that are specific to sample L08-03A are discussed in chapter 5.6.1; however, the technique that was used (outlined in chapter 4.6.2) suffers from certain limitations that are common to the theoretical process in general, regardless of whatever method of fractionation is actually employed.

Firstly, in order to successfully initiate a fractionation procedure one must examine the most primitive composition of a garnet, that is to say the *actual* core, which requires a thin section to achieve a crystallographically-central cut on the porphyroblast of interest. Actual core compositions are required so that calculated isopleths will intersect within error of the garnet-in field boundary on a total bulk rock pseudosection (Evans, 2004). Compositional isopleths representing a 'non-central cut' should intersect at higher *P–T* conditions in garnet-bearing assemblage fields, giving the

appearance of delayed nucleation owing to an apparent temperature overstep before 'core' growth. As a result, if garnet modal proportion for assumed core growth is non-zero, the calculated volume of garnet produced for each subsequent fractionation step will be underestimated.

This problem was encountered in sample L08-03A where it was petrographically interpreted that garnet cores grew at some earlier time before the inner, middle and outer rims (which all grew during one prograde episode). An attempt to circumvent this problem was made by manually removing the garnet cores from the total bulk rock composition used for the starting point for fractionation. Here, core regions comprised ~20% of the garnet grain and therefore ~6% of the total rock volume (Fig. 5.4). However, the location of the first isopleth intersection point for both fractionated and unfractionated paths 'overstepped' this proportion greatly, by producing a garnet modal proportion (of the rock) of ~19–20%. Although the calculated peak modal proportion of ~32% matches the observed value extremely well (30% volume proportion), an excess of ~14% garnet was 'missing' from the EBC prior to the start of fractionation.

It is notable when considering the above situation that even if a truly central cut is obtained, the measured core composition may still have been modified to some degree from its original composition at first nucleation, even if nucleation occurs at low-temperature conditions of the upper greenschist or lower amphibolite-facies (Caddick *et al.*, 2010). Although intracrystalline cation diffusion is extremely slow at these *P–T* conditions, the small radii of just-nucleated and newly forming grains may still permit the relaxation of concentration gradients (ibid). This compositional modification will again result in calculated isopleths intersecting at higher-grade conditions than they should do and cause a problem for the initiation of the fractionation process.

An additional assumption that applies to all methodologies is that of 100% efficient fractionation, whereby once cations have entered a garnet they cannot leave and are permanently eliminated from the EBC. Thus, in situations where garnet is partly consumed during prograde metamorphism, for example in the formation of staurolite as documented by Florence & Spear (1993), it is computationally difficult to replicate this effect. In this case, the user would need to determine the exact modal proportion and composition of the garnet that was consumed in order for the exact amount of cations to be added back into the EBC. This effect would not simply be replicated on a calculated pseudosection with a fractionated bulk composition, as it is impossible for

a phase to be calculated with a negative mass. A final and significant consideration is that the fractionation process assumes that all grains throughout the sample formed simultaneously with a similar growth rate; a process that may not be true if growth kinetics are dominantly diffusion-controlled (Carlson, 2011). In this latter case of diffusion control, the calculated modal proportion of garnet at peak metamorphism may be correct if the rock achieved full chemical and textural equilibrium, although compositions and proportions of phases calculated during prograde metamorphism would likely be spurious given that modelling programs cannot account for variations in mineral growth rate at different points throughout a system.

It is therefore readily acknowledged following the above concerns that one must be extremely careful in identifying the 'perfect' garnet to model in this way. A more indirect method of manipulating an EBC has been shown in chapter 7.4 with the reintegration of lost melt and appeared to be very successful. In both situations, the petrologist is trying to replicate the conditions present during prograde metamorphism as accurately as possible in order to maximise the reliability of the calculated data. Consideration of the theoretical basis for cation fractionation and melt reintegration dictates that accounting for changes in an EBC during metamorphism must replicate the evolution of natural system more accurately than with a fixed EBC. Even though it is impractical to suggest minimum conditions for when these methods should be applied (e.g. a minimum garnet volume in a rock, or a minimum amount of melt generated during anatexis), it is clear that employing these techniques wherever possible should be encouraged.

8.3. On the application of different thermobarometric techniques to different lithologies

Various techniques have been applied different lithologies in this thesis with the aim of extracting as precise *P–T(–t)* information as possible in order to interpret the tectonic evolution of each case study region. This has involved both conventional thermobarometry (chapter 2.3.1) and phase equilibria modelling (chapter 2.3.2). Although a discussion of the relative magnitude of average uncertainty that is associated with each technique (chapter 2.3.3) would imply that phase equilibria modelling should be the favoured method for such investigations, it cannot be applied uncritically.

In the first case, a suite of pelitic mylonites from the EHS was examined (chapter 6.6.3) with the aim of constraining the *P–T* conditions of prograde and peak metamorphism, prior to shearing

during exhumation. Samples ET10-13 and ET10-18a both contain garnet porphyroblasts that preserve prograde compositional growth zoning (chapter 6.4.2) and so, prior to mylonitisation, these units would likely have been petrographically similar to the Barrovian-type metapelitic schist sample T17 documented in the KMC case study that was successfully analysed using the pseudosection approach to produce a well-constrained prograde *P–T* path. However, it was shown that only a rough estimate of the prograde temperature range could be calculated for these mylonites using garnet-ilmenite cation exchange thermometry, and peak metamorphism was delimited on the basis of petrographic arguments given the inclusion of staurolite in the outermost garnet rim portions. No explicit pressure constraints were obtained. The significant difference between EHS samples ET10-13 and ET10-18a and KMC sample T17 is the degree of post-peak deformation that has occurred.

As a good estimate of the effective bulk composition is required for pseudosection analysis, one must account for any mass transport outside of the interpreted system boundaries that may have occurred in a rock during its history. Field evidence exists in outcrop for samples ET10-13 and ET10-18a to show intense folding and telescoping of the various protoliths (Fig. 6.10) during mylonitisation, which indicates that material that was at one time localised has likely since been distributed over a wider area (at least larger than the scale of a single thin section or hand sample). Thus, the bulk composition that is *currently* represented by the mineralogy observed in a thin section of sample ET10-18a is unlikely to be the same as it was for peak metamorphism. Microstructural evidence for the fragmentation of peak metamorphic (?) staurolite porphyroblasts (Fig. 6.12e) supports this, and highlights an additional problem with applying the pseudosection approach to strongly sheared lithologies – the deformation process eliminates prograde and peak microfabrics and textural relationships. These features can be used to verify features that may occur along the calculated *P–T* paths in the pseudosection approach (cf. sample T17) and so confidence is also lost in the petrographic interpretation where these are absent. In addition, mass transport may be extended to consider the effects of fluid migration and possible metasomatism through the addition or removal of key components in solution. A petrographic study of mafic eclogite sample L08-03A from the TMM has shown that the addition of a H_2O-bearing metamorphic fluid is necessary to reproduce the post-peak hydrated mineral assemblage (chapter 5.6). Although there is limited scope to replicate the petrographic effects of variable-composition fluids on different metamorphic mineral

assemblages using THERMOCALC at this time, future improvements in the program's capability may allow detailed investigation into this problem.

A second case to consider is the occurrence of mosaic equilibrium (chapter 2.3), which was encountered in examination of the subsolidus retrograde evolution of sample DNCV01, where localised breakdown of garnet formed a lower-temperature assemblage in strain shadows (chapter 7.4.4). In the investigation of the earlier history of sample DNCV01, the loss of melt was accounted for by adjustment of the effective bulk composition, which produced geologically sensible information regarding the prograde and peak metamorphic conditions. However, it is non-trivial to assess the degree of rock-wide 'communication' that exists during subsolidus metamorphism in a fluid-poor environment. One might then consider restricting the extent of the system boundaries to explicitly assess the mineralogical changes that occurred in the vicinity of the garnet porphyroblast rims, although it is simpler to revert to methods that are unconstrained by mass-balance criteria; namely conventional thermobarometry, as was shown.

The future of pseudosection construction and analysis for THERMOCALC users looks very bright as a result of the imminent public release of an updated internally consistent dataset (ds-6; Holland & Powell, 2011) and the continual efforts by numerous research groups to improve and extend activity-composition models to better fit natural and experimental data. Dataset ds-6 will provide thermodynamic data for new end-members containing elements such as sulphur and zirconium, which have previously been unavailable for consideration in modelling work and will allow petrographic investigation of new rock types and mineralisation processes. However, no amount of expansion of the available thermodynamic data can circumvent the problems associated with effective bulk composition calculations (and also those limitations outlined in chapter 8.2), so the petrologist will always be required to consider employing a range of thermobarometric methods to solve tectonic problems, as the work in this thesis has attempted to show.

8.4. Future work

The results of this work have highlighted several future research directions. From a regional perspective, the continued investigation of the response of the southern Asian plate margin to the India-Asia collision is extremely important in order to complete our understanding of the along-

strike evolution of the HKTO. Given that very little opportunity for this exists in central Tibet, this would preferentially be achieved by further field and laboratory investigation of units of the KMC and EHS. By exposing deep crustal metamorphic rocks of Tertiary age that belong to the Asian plate these regions hold the key this problem. Tectonothermal data collected from the EHS has been interpreted to suggest that the Indian and Asian plates may have acted as a paired metamorphic belt since ~44 Ma; therefore, it is questionable as to whether this can be seen elsewhere along the Himalayan Range. In a review of the evolution of the Paleoproterozoic Trans-Hudson orogen, north America and Canada, St-Onge *et al*. (2006) reports similarities in the evolution of both syntaxis regions. Additional comparison is made between the Trans-Hudson orogen and the HKTO, with the suggestion of similar evolutionary traits having occurred over a broadly similar timescale (ibid). A preliminary comparison of the tectonic and metamorphic evolution of both Himalayan syntaxes is given in chapter 6.2.2, although more high resolution *P*–*T*–*t* data will allow the best chance of investigating this idea.

The modelling work performed in this study has also instigated an important idea for future research. Although fervent study has been dedicated to the issue, directly relating the timing of REE-bearing accessory mineral growth to major events in the evolution of a metamorphic rock remains problematic (chapter 3.4.1). Correctly linking the timing of monazite crystallisation to calculated *P*–*T* conditions is of prime importance for accurately determining the rates of tectonic processes and breakthroughs in this field have far-reaching implications for petrochronologists worldwide. Given that compositional characteristics of monazite can be linked to the formation or breakdown of minerals such as garnet (chapter 3.4.2), REEs could even be incorporated into the cation fractionation process. Preliminary investigations (e.g. Spear, 2010) have had success in integrating REE-bearing accessory minerals into pseudosection modelling; however, none have considered the critical effect of evolving bulk compositions during major mineral growth.

9. Reference list

Allen, C.R., Gillespie, A.R., Han, Y., Sieh, K.E., Zhang, B., Zhu, C., 1984. Red River and associated faults, Yunnan province, China: Quaternary geology, slip rates and seismic hazard. *Geol Soc Am Bull*, **95**, 686–700.

Allen, T., Chamberlain, P.C., 1991. Metamorphic evidence for an inverted crustal section, with constraints on the Main Karakoram thrust, Baltistan, northern Pakistan. *J Metamorph Geol*, **9**, 403–418.

Anczkiewicz, R., Viola, G., Müntener, O., Thirlwall, M.F., Villa, I.M., Quong, N.Q., 2007. Structure and shearing conditions in the Day Nui Con Voi massif: Implications for the evolution of the Red River shear zone in northern Vietnam. *Tectonics*, **26**, TC2002.

Angiboust, S., Langdon, R., Agard, P., Waters, D.J., Chopin, C., 2011. Eclogitization of the Monviso eclogite (W. Alps) and implications on subduction dynamics. *J Metamorph Geol*, **30**, 37–61.

Ashworth, J.R., 1975. The sillimanite zone of the Huntly-Portsoy area in the north-east Dalradian, Scotland. *Geol Mag*, **112**, 113–136.

Ashworth, J.R., 1979. Textural and mineralogical evolution of migmatites. *Geol Soc Lond Spec Pub*, **8**, 357–361.

Atkins, P.W., Overton, T., Rourke, J.P., Weller, M., Armstrong, F.A., 2010. Shriver & Atkins' inorganic chemistry. Oxford University Press, Oxford.

Auzanneau, E., Schmidt, M.W., Vielzeuf, D., Connolly, J.A., 2010. Titanium in phengite: a geobarometer for high-temperature eclogites. *Contrib Mineral Petr*, **159**, 1–24.

Ayers, J.C., Miller, C., Gorisch, B., Milleman, J., 1999. Textural development of monazite during high-grade metamorphism: Hydrothermal growth kinetics, with implications for U–Th–Pb geochronology. *Am Mineral*, **84**, 1766–1780.

Barrow, G., 1893. On an intrusion of muscovite-biotite gneiss in the southeast Highlands of Scotland, and its accompanying metamorphism. *Quart Jour Geol Soc Lond*, **49**, 330–358.

Barrow, G., 1912. On the geology of the Lower Dee-side and the southern Highland Border. *Geol Assoc Lond Proc*, **23**, 274–290.

Beaumont, C., Jamieson, R.A., Butler, J.P., Warren, C.J., 2009. Crustal structure: A key constraint on the mechanism of ultra-high-pressure rock exhumation. *Earth Planet Sc Lett*, **287**, 116–129.

Becquerel, H., 1896. Sur les radiations émises par phosphorescence. *Comptes Rendus*, **122**, 420–421.

Berman, R.G., 1988. Internally-consistent thermodynamic data for stoichiometric minerals in the system Na_2O–K_2O–CaO–MgO–FeO–Fe_2O_3–Al_2O_3–SiO_2–TiO_2–H_2O–CO_2. *J Petrol*, **29**, 445–522.

Berman, R.G., 1991. Thermobarometry using multi-equilibrium calculations: a new technique, with petrological applications. *The Canadian Mineralogist*, **29**, 833–855.

Berman, R.G., 2007. WinTWQ (version 2.3): A software package for performing internally-consistent thermobarometric calculations. Geological Survey of Canada, Open File 5462 (revised).

Berman, R.G., Aranovich, L.Y., 1996. Optimized standard state and mixing properties of minerals 1. Model calibration for olivine, orthopyroxene, cordierite, garnet, and ilmenite in the system FeO–MgO–CaO–Al_2O_3–SiO_2–TiO_2. *Contrib Mineral Petr*, **126**, 1–24.

Bertrand, J.M., Kienast, J.R., Pinardon, J.L., 1988. Structure and metamorphism of the Karakoram gneisses in the Braldu-Baltoro Valley (north Pakistan). *Geodynamica Acta*, **2**, 135–150.

Bilham, R., Larson, K., Freymueller, J., 1997. GPS measurements of present-day convergence across the Nepal Himalaya. *Nature*, **386**, 61–64.

Booth, A.L., Zeitler, P.K., Kidd, W.S.F, Wooden, J., Liu, Y., Idleman, B., Hren, M., Page Chamberlain, C., 2004. U–Pb zircon constraints on the tectonic evolution of southeastern Tibet, Namche Barwa area. *Am J Sci*, **304**, 889–929.

Booth, A.L., Page Chamberlain, C., Kidd, W.S.F., Zeitler, P.K., 2009. Constraints on the metamorphic evolution of the eastern Himalayan syntaxis from geochronologic and petrologic studies of Namche Barwa. *Geol Soc Am Bull*, **121**, 385–407.

Bowen, N.L., 1940. Progressive metamorphism of siliceous limestone and dolomites. *J Geol*, **48**, 225–274.

Brandon, C., Romanowicz, B., 1986. A ‘no-lid’ zone in the central Qiangtang platform of Tibet: Evidence from pure path phase velocity measurements of long period Rayleigh waves. *J Geophys Res*, **91**, 6547–6564.

Brown, L.D., Zhao, W., Nelson, K.D., Hauck, M., Alsdorf, D., Ross, A., Cogan, M., Liu, X., Che, J., 1996. Bright spots, structure and magmatism in southern Tibet from INDEPTH seismic reflection profiling. *Science*, **274**, 1688–1690.

Brown, M., 2002. Retrograde processes in migmatites and granulites revisited. *J Metamorph Geol*, **20**, 25–40.

Brown, M., 2007. Metamorphic conditions in orogenic belts: a record of secular change. *Int Geol Rev*, **49**, 193–234.

Brown, M., 2009. Metamorphic patterns in orogenic systems and the geological record. In: Cawood, P.A., Kroner, A. (Eds.), Accretionary Orogens in Space and Time. *Geol Soc Lond Spec Pub*, **318**, 37–74.

Brown, M., 2010. Paired metamorphic belts revisited. *Gondwana Res*, **18**, 46–59.

Burg, J.P., Davy, P., Nievergelt, P., Oberli, F., Seward, D., Diao, Z., Meier, M., 1997. Exhumation during crustal folding in the Namche Barwa syntaxis. *Terra Nova*, **9**, 117–123.

Burg, J.P., Nievergelt, P., Oberli, F., Seward, D., Davy, P., Maurin, J.-C., Diao, Z., Meier, M., 1998. The Namche Barwa syntaxis: evidence for exhumation related to compressional crustal folding. *J Asian Earth Sci*, **16**, 239–252.

Caddick, M.J., Konopásek, J., Thompson, A.B., 2010. Preservation of garnet growth zoning and the duration of prograde metamorphism. *J Petrol*, **51**, 2327–2347.

Cao, S., Liu, J., Leiss, B., Neubauer, F., Genser, J., Zhao, C., 2011. Oligo-Miocene shearing along the Ailao Shan–Red River shear zone: Constraints from structural analysis and zircon U/Pb geochronology of magmatic rocks in the Diancang Shan massif, SE Tibet, China. *Gondwana Res*, **19**, 975‑993.

Caporali, A., 2000. The gravity field of the Karakoram Mountain Range and surrounding areas. *Geol Soc Lond Spec Pub*, **170**, 7–23.

Carlson, W.D., 2006. Rates of Fe, Mg, Mn, and Ca diffusion in garnet. *Am Mineral*, **91**, 1–11.

Carlson, W.D., 2011. Porphyroblast crystallization: linking processes, kinetics, and microstructures. *Int Geol Rev*, **53**, 406–445.

Carson, C.J., Powell, R., Clarke, G.L., 1999. Calculated mineral equilibria for eclogites in CaO–Na_2O–FeO–MgO–Al_2O_3–SiO_2–H_2O: application to the Pouébo Terrane, Pam Peninsula, New Caledonia. *J Metamorph Geol*, **17**, 9–24.

Carson, C.J., Clarke, G.L., Powell, R., 2000. Hydration of eclogite, Pam Peninsula, New Caledonia. *J Metamorph Geol*, **18**, 79–90.

Carson, C.J., Berman, R.G., Stern, R.A., Sanborn-Barrie, M., Skulski, T., Sandeman, H.A.I., 2004. Age constraints on the Paleoproterozoic tectonometamorphic history of the Committee Bay region, western Churchill Province, Canada: evidence from zircon and in situ monazite SHRIMP geochronology. *Can J Earth Sci*, **41**, 1049–1076.

Carswell, D.A., O'Brien, P.J., Wilson, R.N., Zhai, M., 1997. Thermobarometry of phengite-bearing eclogites in the Dabie Mountains of central China. *J Metamorph Geol*, **15**, 239–252.

Carter, A., Roques, D., Bristow, C., Kinny, P., 2001. Understanding Mesozoic accretion in Southeast Asia: Significance of Triassic thermotectonism (Indosinian orogeny) in Vietnam. *Geology*, **29**, 211–214.

Charusiri, P., Imsamut, S., Zhuang, Z., Ampaiwan, T., Xu, X., 2006. Paleomagnetism of the earliest Cretaceous to early late Cretaceous sandstones, Khorat Group, north-east Thailand: Implications for tectonic plate movement of the Indochina block. *Gondwana Res*, **9**, 310–325.

Chen, W.P., Molnar, P., 1983. Focal depths of intracontinental and intraplate earthquakes and their implications for the thermal and mechanical properties of the lithosphere. *J Geophys Res*, **88**, 4183–4214.

Cherniak, D.J., Watson, E.B., Grove, M., 2004. Pb diffusion in monazite: A combined RBS/SIMS study. *Geochim Cosmochim Ac*, **68**, 829–840.

Chinner, G.A., 1962. Almandine in thermal aureoles. *J Petrol*, **3**, 316–340.

Chiu, H.Y., Chung, S.L., Wu, F.Y., Liu, D.Y., Liang, Y.H., Lin, I.J., Iizuka, Y., Xie, L.W., Wang, Y.B., Chu, M.F., 2009. Zircon U–Pb and Hf isotopic constraints from eastern Trans-Himalayan batholiths on the pre-collisional magmatic and tectonic evolution in southern Tibet. *Tectonophysics*, **477**, 3–19.

Chung, S.-L., Lee, T.-Y., Lo, C.-H., Wang, P., Chen, C.-Y., Yem, N.T., Hoa, T.T., Genyao, W., 1997. Intraplate extension prior to continental extrusion along the Ailao Shan–Red River shear zone. *Geology*, **25**, 311–314.

Chung, S.-L., Liu, D.Y., Ji, J.Q., Chu, M.F., Lee, H.Y., Wen, D.J., Lo, C.H., Lee, T.-Y., Qian, Q., Zhang, Q., 2003. Adakites from continental collision zones: melting of thickened lower crust beneath southern Tibet. *Geology*, **31**, 1021–1024.

Chung, S.-L., Chu, M.F., Zhang, Y., Xie, Y., Lo, C.H., Lee, T.-Y., Lan, C.Y., Li, X., Zhang, Q., Wang, Y., 2005. Tibetan tectonic evolution inferred from spatial and temporal variations in post-collisional magmatism. *Earth Sci Rev*, **68**, 173–196.

Chung, S.-L., Searle, M.P., Yeh, M.-W., 2008. The age of the potassic alkaline igneous rocks along the Ailao Shan–Red River shear zone: Implications for the onset age of left-lateral shearing: A discussion. *J Geol*, **116**, 201–204.

Coggon, R., Holland, T.J.B., 2002. Mixing properties of phengitic micas and revised garnet-phengite thermobarometers. *J Metamorph Geol*, **20**, 683–696.

Conrad, W.K., Nicholls, I.A., Wall, V.J., 1988. Water saturated and undersaturated melting at 10 kbar: evidence for the origin of silicic magmas in the Taupo volcanic zone, New Zealand, and other occurrences. *J Petrol*, **29**, 765–803.

Copley, A., Avouac, J.-P., Royer, J.-Y., 2010. India-Asia collision and the Cenozoic slowdown of the Indian plate: Implications for the forces driving plate motions. *J Geophys Res*, **115**, B03410.

Cottle, J.M., Searle, M.P., Horstwood, M.S.A., Waters, D.J., 2009a. Timing of midcrustal metamorphism, melting and deformation in the Mount Everest Region of Southern Tibet revealed by U–(Th)–Pb geochronology. *J Geol*, **117**, 643–664.

Cottle, J.M., Jessup, M.J., Newell, D.L., Horstwood, M.S.A., Noble, S.R., Parrish, R.R., Waters, D.J., Searle, M.P., 2009b. Geochronology of granulitized eclogite from the Ama Drime Massif: implications for the tectonic evolution of the South Tibetan Himalaya. *Tectonics*, **28**, TC1002.

Craw, D., Koons, P.O., Zeitler, P.K., Kidd, W.S.F., 2005. Fluid evolution and thermal structure in the rapidly exhuming gneiss complex of Namche Barwa-Gyala Peri, eastern Himalayan syntaxis. *J Metamorph Geol*, **23**, 829–845.

Crawford, M.B., Searle, M.P., 1992. Field relationships and geochemistry of pre-collisional (India-Asia) granitoid magmatism in the central Karakoram, northern Pakistan. *Tectonophysics*, **206**, 171–192.

Crawford, M.B., Searle, M.P., 1993. Collision-related granitoid magmatism and crustal structure of the Hunza Karakoram, north Pakistan. *Geol Soc Lond Spec Pub*, **74**, 53–68.

Crowley, J.L., Schoene, B., Boring, S.A., 2007. U–Pb dating of zircon in the Bishop Tuff at the millennial scale. *Geology*, **35**, 1123–1126.

Crowley, J.L., Brown, R.L., Gervais, F., Gibson, H.D., 2008. Assessing inheritance of zircon and monazite in granitic rocks from the Monashee Complex, Canadian Cordillera. *J Petrol*, **49**, 1915–1929.

Crowley, J.L., Waters, D.J., Searle, M.P., Bowring, S.A., 2009. Pleistocene melting and rapid exhumation of the Nanga Parbat massif, Pakistan: age and *P–T* conditions of accessory mineral growth in migmatite and leucogranite. *Earth Planet Sc Lett*, **288**, 408–420.

Cruciani, G., Franceschelli, M., Marco Elter, F., Puxeddu, M., Utzeri, D., 2008. Petrogenesis of Al-silicate-bearing trondhjemitic migmatites from NE Sardinia, Italy. *Lithos*, **102**, 554–574.

De Sigoyer, J., Guillot, S., Lardeaux, J.-M., Mascle, G., 1997. Glaucophane-bearing eclogites in the Tso Morari dome (eastern Ladakh, NW Himalaya). *Eur J Mineral*, **9**, 1073–1083.

De Sigoyer, J., Chavagnac, V., Blichert-Toft, J., Villa, I.M., Luais, B., Guillot, S., Cosca, M., Mascle, G., 2000. Dating the Indian continental subduction and collisional thickening in the northwest Himalaya: Multichronology of the Tso Morari eclogites. *Geology*, **28** 487–490.

De Sigoyer, J., Guillot, S., Dick, P., 2004. Exhumation of the ultrahigh-pressure Tso Morari unit in eastern Ladakh (NW Himalaya): a case study. *Tectonics*, **23**, TC3003

Debon, F., Le Fort, P., Dautel, D., Sonet, J., Zimmermann, J.L., 1987. Granites of western Karakoram and northern Kohistan (Pakistan): A composite mid-Cretaceous to upper Cenozoic magmatism. *Lithos*, **20**, 19–40.

Deer, W.A., Howie, R.A., Zussman, J., 1992. An Introduction to the Rock Forming Minerals, 2nd edition, Longman Scientific & Technical, Harlow, Essex, England.

Desio, A., 1964. Geological tentative map of the Western Karakorum, scale 1/500000. Institute of Geology, Milano University, Milano.

Dewey, J.F., Shackleton, R.M., Chengfa, C., Yiyin, S., 1988. The tectonic evolution of the Tibetan plateau. *Phil Trans Roy Soc Lond. Ser A*, **327**, 379–413.

Diener, J.F.A., Powell, R., White, R.W., Holland, T.J.B., 2007. A new thermodynamic model for clino- and orthoamphiboles in the system Na_2O–CaO–FeO–MgO–Al_2O_3–SiO_2–H_2O–O. *J Metamorph Geol*, **25**, 631–656.

Ding, L., Zhong, D.L., 1999. Metamorphic characteristics and geotectonic implications of the high-pressure granulites from Namjagbarwa, eastern Tibet. *Sci China Ser D,* **42**, 491–505.

Ding, L., Zhong, D.L., Yin, A., Kapp, P., Harrison, T.M., 2001. Cenozoic structural and metamorphic evolution of the eastern Himalayan syntaxis (Namche Barwa). *Earth Planet Sc Lett*, **192**, 423–438.

DiPietro, J.A., Pogue, K.R., 2004. Tectonostratigraphic subdivisions of the Himalaya: A view from the west. *Tectonics*, **23**, TC5001.

Dong, X., Zhang, Z., Liu, F., Wang, W., Yu, F., Shen, K., 2011. Zircon U–Pb geochronology of the Nyainqentanglha Group from the Lhasa terrane: New constraints on the Triassic orogeny of the south Tibet. *J Asian Earth Sci*, **42**, 732–739.

Droop, G.T.R., Lombardo, B., Pognante, U., 1990. Formation and distribution of eclogite facies rocks in the Alps. In: Carswell, D.A., (Eds.), Eclogite facies rocks. Glasgow, Blackie, 225–259.

Duchene, S., Lardeaux, J.M., Albarede, F., 1997. Exhumation of eclogites: Insights from depth-time path analysis. *Tectonophysics*, **280**, 125–140.

England, P.C., Richardson, S.W., 1977. The influence of erosion upon the mineral facies of rocks from different metamorphic environments. *J Geol Soc Lond*, **134**, 201–213.

England, P.C., Thompson, A.B., 1984. Pressure-temperature-time paths of regional metamorphism I. Heat transfer during the evolution of regions of thickened continental crust. *J Petrol*, **25**, 894–928.

Engvik, A.K., Austrheim, H., Erambert, M., 2001. Interaction between fluid flow, fracturing and mineral growth during eclogitization, an example from the Sunnfjord area, Western Gneiss Region, Norway. *Lithos*, **57**, 111–141.

Epard, J.-L., Steck, A., 2008. Structural development of the Tso Morari ultra-high-pressure nappe of the Ladakh Himalaya. *Tectonophysics*, **451**, 242–264.

Erambert, M., Austrheim, H., 1993. The effect of fluid and deformation on zoning and inclusion patterns in polymetamorphic garnets. *Contrib Mineral Petr*, **115**, 204–214.

Eskola, P., 1915. On the relations between the chemical and mineralogical composition in the metamorphic rocks of the Orijarvi region. *Bull Comm Geol Fin*, **44**.

Eskola, P., 1920. The mineral facies of rocks. *Norsk Geol Tidsskrift,* **6**, 143–194.

Eskola, P., 1921. On the eclogites of Norway. *Vide Skrifter, I Mat Nat Klasse*, **8**, 1–118.

Evans, B.W., 2007. Landmark papers: Metamorphic petrology. Mineralogical Society of America, Washington D.C.

Evans, B.W., Guidotti, C.V., 1966. The sillimanite-potash feldspar isograd in Western Maine, U.S.A. *Contrib Mineral Petr,* **12**, 25–62.

Evans, T.P., 2004. A method for calculating effective bulk composition modification due to crystal fractionation in garnet-bearing schist: implications for isopleth thermobarometry. *J Metamorph Geol,* **22**, 547–557.

Faure, G., 1986. Principles of Isotope Geology, 2nd edition. John Wiley & Sons, New York.

Ferry, J.M., Spear, F.S., 1978. Experimental calibration of the partitioning of Fe and Mg between biotite and garnet. *Contrib Mineral Petr*, **66**, 113–117.

Fielding, E., Isacks, B., Barazangi, M., Duncan, C., 1994. How flat is Tibet? *Geology*, **22**, 163–167.

Finger, F., Broska, I., Roberts, M.P., Schermaier, A., 1998. Replacement of primary monazite by apatite-allanite-epidote coronas in amphibolite-facies granite gneiss from the eastern Alps. *Am Mineral*, **83**, 248–258.

Finnegan, N.J., Hallet, B., Montgomery, D.R., Zeitler, P.K., Stone, J.O., Anders, A.M., Yuping, L., 2008. Coupling of rock uplift and river incision in the Namche Barwa-Gyala Peri massif, Tibet. *Geol Soc Am Bull*, **120**, 142–155.

Florence, F.P., Spear, F.S., 1991. Effects of diffusional modification of garnet growth zoning on *P–T* path calculations. *Contrib Mineral Petr*, **107**, 487–500.

Florence, F.P., Spear, F.S., 1993. Influences of reaction history and chemical diffusion on *P–T* calculations for staurolite schists from the Littleton Formation, northwestern New Hampshire. *Am Mineral*, **78**, 345–359.

Foster, D.A., Schafer, C., Fanning, C.M., Hyndman, D.W., 2001. Relationships between crustal partial melting, plutonism, orogeny, and exhumation: Idaho–Bitterroot batholith. *Tectonophysics*, **342**, 313–350.

Foster, G.L., Parrish, R.R., 2003. Metamorphic monazite and the generation of *P–T–t* paths. In: Vance, D., *et al*., (Eds.), Geochronology: Linking the isotopic record with petrology and textures. *Geol Soc Lond Spec Pub*, **220**, 25–47.

Foster, G.L., Kinny, P., Vance, D., Prince, C., Harris, N., 2000. The significance of monazite U–Th–Pb age data in metamorphic assemblages; a combined study of monazite and garnet chronometry. *Earth Planet Sc Lett*, **181**, 327–340.

Foster, G.L., Gibson, H.D., Parrish, R.R., Horstwood, M.S.A., Fraser, J.E., Tindle, A., 2002. Textural, chemical and isotopic insights into the nature and behavior of metamorphic monazite. *Chem Geol*, **191**, 183–207.

Foster, G.L., Parrish, R.R., Horstwood, M.S.A., Chenery, S., Pyle, J., Gibson, H.D., 2004. The generation of prograde *P–T–t* points and paths; a textural, compositional and chronological study of metamorphic monazite. *Earth Planet Sc Lett*, **228**, 125–142.

Fraser, J.E., 2000. The structural and metamorphic evolution of the deep crust in the Hunza Karakoram, Pakistan. D.Phil thesis, University of Oxford.

Fraser, J.E., Searle, M.P., Parrish, R.R., Noble, S.R., 2001. Chronology of deformation, metamorphism, and magmatism in the southern Karakoram Mountains. *Geol Soc Am Bull*, **113**, 1443–1455.

Frost, B.R., Chacko, T., 1989. The granulite uncertainty principle: limitations on thermobarometry in granulites. *J Geol*, **97**, 435–450.

Furhman, M.L., Lindsley, D.H., 1988. Ternary-feldspar modelling and thermometry. *Am Mineral*, **73**, 201–215.

Gaetani, G.A., Asimow, P.D., Stolper, E.M., 2008. A model for rutile saturation in silicate melts with applications to eclogite partial melting in subduction zones and mantle plumes. *Earth Planet Sc Lett*, **272**, 720–729.

Gaetani, M., Garzanti, E., 1991. Multicyclic history of the northern India continental margin (northwestern Himalaya). *Am Assoc Petrol Geol Bull*, **75**, 1427–1446.

Ganguly, J., Cheng, W., Tirone, M., 1996. Thermodynamics of aluminosilicate garnet solid solution: new experimental data, an optimized model, and thermometry applications. *Contrib Mineral Petr*, **126**, 137–151.

García-Casco, A., Torres-Roldán, R.L., Millán, G., Monie, P., Haissen, F., 2001. High-grade metamorphism and hydrous melting of metapelites in the Pinos terrane (W. Cuba): Evidence for crustal thickening and extension in the northern Caribbean collisional belt. *J Metamorph Geol*, **19**, 699–715.

García-Casco, A., Haissen, F., Castro, A., El-Hmidi, H., Torres-Roldán, R.L., Millán, G., 2003. Synthesis of staurolite in melting experiments of a natural metapelite: Consequences for the phase relations in low-temperature pelitic migmatites. *J Petrol*, **44**, 1727–1757.

Garnier, V., Ohnenstetter, D., Giuliani, G., Maluski, H., Deloule, E., Phan Trong, T., Pham Van, L., Hoàng Quang, V., 2005. Age and significance of ruby-bearing marble from the Red River shear zone, northern Vietnam. *Can Mineral*, **43**, 1315–1329.

Geng, Q., Guitang, P., Zheng, L., Chen, Z., Fisher, R.D., Sun, Z., Ou, C., Dong, H., Wang, X., Li, S., Lou, X., Fu, H., 2006. The eastern Himalayan syntaxis: major tectonic domains, ophiolitic mélanges and geologic evolution. *J Asian Earth Sci*, **27**, 265–285.

Gerya, T.V., Maresch, W.V., 2004. Metapelites of the Kanskiy granulite complex (Eastern Siberia): Kinked *P–T* paths and a geodynamic model. *J Petrol*, **45**, 1393–1412.

Gerya, T.V., Perchuk, L.L., van Reenen, D.D., Smit, C.A., 2000. Two-dimensional numerical modelling of pressure-temperature-time paths for the exhumation of some granulite facies terrains in the Precambrian. *J Geodyn*, **30**, 17–35.

Gibson, H.D., Carr, S.D., Brown, R.L., Hamilton, M.A., 2004. Correlations between chemical and age domains in monazite, and metamorphic reactions involving major pelitic phases: an

integration of ID-TIMS and SHRIMP geochronology with Y–Th–U X-ray mapping. *Chem Geol*, **211**, 237–260.

Gilley, L.D., Harrison, T.M., Leloup, P.H., Ryerson, F.J., Lovera, O.M., Wang, J.-H., 2003. Direct dating of left-lateral deformation along the Red River shear zone, China and Vietnam. *J Geophys Res*, **108**, 2127–2148.

Girard, M., 2001. Metamorphism and tectonics of the transition between non metamorphic Tethyan Himalaya sediments and the north Himalayan Crystalline Zone (Rupshu area, Ladakh, north-west India). *Mem Géol (Lausanne)*, **35**, 1–100.

Girard, M., Bussy, F., 1999. Late Pan-African magmatism in the Himalaya: new geochronological and geochemical data from the Ordovician Tso Morari metagranites (Ladakh, NW India). *Schweiz Min Petrog Mitt*, **79**, 399–417.

Girardeau, J., Marcous, J., Allegre, C.J., Bassoullet, J.P., Tang, Y., Xuchang, X., Yougong, Z., Xibin, W., 1984. Tectonic environment and geodynamic significance of the Neo-Cimmerian Donqiao ophiolite, Bangong-Nujiang suture zone, Tibet. *Nature*, **307**, 27–31.

Godin, L., Parrish, R.R., Brown, R.L., Hodges, K.V., 2001. Crustal thickening leading to exhumation of the Himalayan metamorphic core of central Nepal: Insight from U–Pb geochronology and ^{40}Ar–^{39}Ar thermochronology. *Tectonics*, **20**, 729–747.

Godin, L., Grujic, D., Law, R.D., Searle, M.P., 2006. Channel flow, ductile extrusion and exhumation in continental collision zones: an introduction. In: Law, R.D., *et al*., (Eds.), Channel flow, ductile extrusion and exhumation in continental collision zones. *Geol Soc Lond Spec Pub*, **268**, 1–23.

Goscombe, B., Hand, M., 2000. Contrasting *P–T* paths in the Eastern Himalaya, Nepal: Inverted isograds in a paired metamorphic mountain belt. *J Petrol*, **41**, 1673–1719.

Gough, S.J., 2002, Subduction-related metamorphism, structure and tectonic evolution of the Kohistan arc and Main Mantle thrust zone, Pakistan Himalaya. DPhil thesis, University of Oxford.

Gouzu, C., Itaya, T., Hyodo, H., Ahmad, T., 2006. Cretaceous isochron ages from K–Ar and ^{40}Ar/^{39}Ar dating of eclogitic rocks in the Tso Morari Complex, western Himalaya, India. *Gondwana Res*, **9**, 426–440.

Green, E.C.R., Holland, T.J.B., Powell, R., 2007. An order-disorder model for omphacitic pyroxenes in the system jadeite–diopside–hedenbergite–acmite, with applications to eclogite rocks. *Am Mineral*, **92**, 1181–1189.

Green, N.L., Usdansky, S.I., 1986. Ternary-feldspar mixing relations and thermobarometry. *Am Mineral*, **71**, 1100–1108.

Green, O.R., Searle, M.P., Corfield, R.I., Corfield, R.M., 2008. Cretaceous-Tertiary carbonate platform evolution and the age of the India-Asia collision along the Ladakh Himalaya (north-west India). *J Geol*, **116**, 331–353.

Grujic, D., Warren, C., Wooden, J.L., 2011. Rapid synconvergent exhumation of Miocene-aged lower orogenic crust in the eastern Himalaya. *Lithosphere*, **3**, 346–366.

Guidiotti, C.V., 1984. Micas in metamorphic rocks. In: Bailey, S.W. (Eds.), Micas. *Rev Min Geochem Min Soc Am*, **13**, Washington, D.C.

Guillot, S., de Sigoyer, J., Lardeaux, J.M., Mascle, G., 1997. Eclogitic metasediments from the Tso Morari area (Ladakh, Himalaya): evidence for continental subduction during India-Asia convergence. *Contrib Mineral Petr*, **128**, 197–212.

Guillot, S., Mahéo, G., de Sigoyer, J., Hattori, K.H., Pêcher, A., 2008. Tethyan and Indian subduction viewed from the Himalayan high- to ultrahigh-pressure metamorphic rocks. *Tectonophysics*, **451**, 225–241.

Guilmette, C., Indares, A., Hébert, R., 2011. High-pressure anatectic paragneiss from the Namche Barwa, eastern Himalayan syntaxis: Textural evidence for partial melting, phase equilibria modelling and tectonic implications. *Lithos*, **124**, 66–81.

Guiraud, M., Powell, R., Rebay, G., 2001. H_2O in metamorphism and unexpected behaviour in the preservation of metamorphic mineral assemblages. *J Metamorph Geol*, **19**, 445–454.

Guo, L., Zhang, H-F., Harris, N., Parrish, R., Zu, W-C., Shi, Z-L., 2012. Paleogene crustal anatexis and metamorphism in Lhasa terrane, eastern Himalayan syntaxis: Evidence from U–Pb zircon ages and Hf isotopic compositions of the Nyingchi Complex. *Gondwana Res*, **21**, 100–111.

Halpin, J.A., Clarke, G.L., White, R.W., Kelsey, D.E., 2007. Contrasting *P–T–t* paths for Neoproterozoic metamorphism in MacRobertson and Kemp Lands, east Antarctica. *J Metamorph Geol*, **25**, 683–701.

Hammarstrom, J.M., Zen, E., 1986. Aluminium in hornblende: an empirical igneous geobarometer. *Am Mineral*, **71**, 1297–1313.

Hao, J., Chai, Y., Li, J., 1999. Original tectonic setting of the Tsangpo ophiolite and sedimentary evolution of the Xigaze forearc basin. *Chinese J Geol (Sci Geol Sinica)*, **34**, 1–9 (in Chinese with English abstract).

Harte, B., Henley, K.J., 1966. Occurrence of compositionally zoned almanditic garnets in regionally metamorphosed rocks. *Nature*, **210**, 689–692.

Hawkins, D.P., Bowring, S.A., 1999. U–Pb monazite, xenotime and titanite geochronological constraints on the prograde to post-peak metamorphic thermal history of Palaeoproterozoic migmatites from the Grand Canyon, Arizona. *Contrib Mineral Petr*, **134**, 150–169.

Helgeson, H.C., Delaney, J.M., Nesbitt, H.W., Bird, D.K., 1978. Summary and critique of the thermodynamic properties of rock-forming minerals. *Am J Sci*, **278A**, 1–229.

Henry, D.J., Guidotti, C.V., Thompson, J.A., 2005. The Ti-saturation surface for low-to-medium-pressure metapelitic biotites: Implications for geothermometry and Ti-substitution mechanisms. *Am Mineral*, **90**, 316–328.

Hestmark, G., 2011. The meaning of 'metamorphic' – Charles & Mary Lyell in Norway, 1837. *Nor J Geol*, **91**, 247–275.

Hildebrand, P.R., Noble, S.R., Searle, M.P., Parrish, R.R., Shakirullah, S., 1998. Tectonic significance of 24 Ma crustal melting in the eastern Hindu Kush, Pakistan. *Geology*, **26**, 865–960.

Hildebrand, P.R., Noble, S.R., Searle, M.P., Waters, D.J., Parrish, R.R., 2001. An old origin for an active mountain range – the eastern Hindu Kush, north-west Pakistan. *Geol Soc Am Bull*, **113**, 625–639.

Hodges, K.V., 2000. Tectonics of the Himalaya and southern Tibet from two perspectives. *Geol Soc Am Bull*, **112**, 324–350.

Hodges, K.V., Parrish, R.R., Searle, M.P., 1996. Tectonic evolution of the central Annapurna range, Nepalese Himalayas. *Tectonics*, **15**, 1264–1291.

Holland, T.J.B., 1990. Activities in omphacitic solid solutions: an application of Landau theory to mixtures. *Contrib Mineral Petr*, **105**, 446–453.

Holland, T.J.B., 2009. AX: A program to calculate activities of mineral end-members from chemical analyses. http://www.esc.cam.ac.uk/research/research-groups/holland/ax, last updated 5th February 2009.

Holland, T.J.B., Blundy, J.D., 1994. Non-ideal interactions in calcic amphiboles and their bearing on amphibole-plagioclase thermometry. *Contrib Mineral Petr*, **116**, 433–447.

Holland, T.J.B., Powell, R., 1990. An internally-consistent thermodynamic dataset with uncertainties and correlations: the system Na_2O–K_2O–CaO–MgO–FeO–Fe_2O_3–Al_2O_3–SiO_2–TiO_2–C–H_2–O_2. *J Metamorph Geol*, **8**, 89–124.

Holland, T.J.B., Powell, R., 1998. An internally-consistent thermodynamic dataset for phases of petrological interest. *J Metamorph Geol*, **16**, 309–344.

Holland, T.J.B., Powell, R., 2003. Activity-composition relations for phases in petrological calculations: an asymmetric multicomponent formulation. *Contrib Mineral Petr*, **145**, 492–501.

Holland, T.J.B., Powell, R., 2011. An improved and extended internally consistent thermodynamic dataset for phases of petrological interest, involving a new equation of state for solids. *J Metamorph Geol*, **29**, 333–383.

Holland, T.J.B., Baker, J.M., Powell, R., 1998. Mixing properties and activity-composition relationships of chlorites in the system MgO–FeO–Al_2O_3–SiO_2–H_2O. *Eur J Mineral*, **10**, 395–406.

Hollister, L.S., 1966. Garnet zoning: An interpretation based on the Rayleigh fractionation model. *Science*, **154**, 1647–1651.

Horstwood, M.S.A., 2008. Data reduction strategies, uncertainty assessment and interpretation of LA-(MC-)ICP-MS isotope data. In: Sylvester, P., (Eds.), Laser ablation ICP-MS in the earth sciences: Current practices and outstanding issues. *Min Assoc Can Short Course Ser*, **40**, 283–303.

Hoschek, G., 2001. Thermobarometry of metasediments and metabasites from the eclogite zone of the Hohe Tauern, Eastern Alps, Austria. *Lithos*, **59**, 127–150.

Hsü, K., Guitang, P., Sengör, A.M.C., 1995. Tectonic evolution of the Tibetan Plateau: A working hypothesis based on the archipelago model of orogenesis. *Int Geol Rev*, **37**, 473–508.

Indares, A., White, R.W., Powell, R., 2008. Phase equilibria modelling of kyanite-bearing anatectic paragneiss from the central Grenville Province. *J Metamorph Geol*, **26**, 815–836.

Jaffey, A.H., Flynn, K.F., Glendenin, L.E., Bentley, W.C., Essling, A.M., 1971. Precision measurement of half-lives and specific activities of ^{235}U and ^{238}U. *Phys Rev*, **4**, 1889–1906.

Janots, E., Brunet, F., Goffé, B., Poinssot, C., Burchard, M., Cemič, L., 2007. Thermochemistry of monazite-(La) and dissakisite-(La): implications for monazite and allanite stability in metapelites. *Contrib Mineral Petr*, **154**, 1–14.

Janots, E., Engi, M., Berger, A., Allaz, J., Schwarz, J.-O., Spandler, C., 2008. Prograde metamorphic sequence of REE minerals in pelitic rocks of the Central Alps: implications for allanite-monazite-xenotime phase relations from 250 to 610 °C. *J Metamorph Geol*, **26**, 509–526.

Johnson, M.R.W., 2002. Shortening budgets and the role of continental subduction during the India-Asia collision. *Earth-Sci Rev*, **59**, 101–123.

Jolivet, L., Maluski, H., Beyssac, O., Goffé, B., Lepvrier, C., Thi, P.T., Van Vuong, N., 1999. Oligocene-Miocene Bu Khang extensional gneiss dome in Vietnam: Geodynamic implications. *Geology*, **27**, 67–70.

Jolivet, L., Beyssac, O., Goffé, B., Avigad, D., Lepvrier, C., Maluski, H., Thang, T.T., 2001. Oligo-Miocene midcrustal subhorizontal shear zone in Indochina. *Tectonics*, **20**, 46–57.

Kaneko, Y., Katayama, I., Yamamoto, H., Misawa, K., Ishikawa, M., Rehman, H.U., Kausar, A.B., Shiraishi, K., 2003. Timing of Himalayan ultrahigh-pressure metamorphism: Sinking rate and subduction angle of the Indian continental crust beneath Asia. *J Metamorph Geol*, **21**, 589–599.

Kapp, P., Yin, A., Manning, C.E., Harrison, T.M., Taylor, M.H., Ding, L., 2003. Tectonic evolution of the early Mesozoic blueschist-bearing Qiangtang metamorphic belt, central Tibet. *Tectonics*, **22**, 1043–1070.

Kapp, J.L.D., Harrison, T.M., Kapp, P., Grove, M., Lovera, O., Lin, D., 2005. Nyainqentanglha Shan: A window into the tectonic, thermal, and geochemical evolution of the Lhasa block, southern Tibet. *J Geophys Res*, **110**, B08413.

Kellett, D.A., Grujic, D., Erdmann, S., 2009. Miocene structural reorganization of the South Tibetan detachment, eastern Himalaya: Implications for continental collision. *Lithosphere*, **1**, 259–281.

Kellett, D.A., Grujic, D., Warren, C., Cottle, J., Jamieson, R., Tenzin, T., 2010. Metamorphic history of a syn-convergent orogen-parallel detachment: the South Tibetan detachment system, Bhutan Himalaya. *J Metamorph Geol*, **28**, 785–808.

Kelsey, D.E., White, R.W., Powell, R., 2003. Orthopyroxene-sillimanite-quartz assemblages: distribution, petrology, quantitative *P–T–X* constraints and *P–T* paths. *J Metamorph Geol*, **21**, 439–453.

Kelsey, D.E., Powell, R., 2011. Progress in linking accessory mineral growth and breakdown to major mineral evolution in metamorphic rocks: a thermodynamic approach in the Na_2O–CaO–K_2O–FeO–MgO–Al_2O_3–SiO_2–H_2O–TiO_2–ZrO_2 system. *J Metamorph Geol*, **29**, 151–166.

Kelvin, W.T., 1863. On the secular cooling of the earth. *Trans Royal Soc Edinburgh*, **23**, 157–170.

Kidd, W.S.F., Pan, Y., Chang, C., Coward, M.P., Dewey, J.F., Gansser, A., Molnar, P., Shackleton, R.M., Sun, Y., 1988. Geological mapping of the 1985 Chinese-British Tibetan (Xizang-Qinghai) Plateau Geotraverse route. *Phil Trans Roy Soc Lond. Ser A.*, **327**, 287–305.

King, J., Harris, N., Argles, T., Parrish, R.R., Zhang, H., 2011. Contribution of crustal anatexis to the tectonic evolution of Indian crust beneath southern Tibet. *Geol Soc Am Bull*, **123**, 218–239.

Kohn, M.J., Malloy, M.A., 2004. Formation of monazite via prograde metamorphic reactions among common silicates: implications for age determinations. *Geochim Cosmochim Ac*, **68**, 101–113.

Kohn, M.J., Spear, F.S., 2000. Retrograde net transfer reaction insurance for pressure-temperature estimates. *Geology*, **28**, 1127–1130.

Kohn, M.J., Wieland, M.S., Parkinson, C.D., Upreti, B.N., 2005. Five generations of monazite in Langtang gneisses: implications for chronology of the Himalayan metamorphic core. *J Metamorph Geol*, **23**, 399–406.

Konrad-Schmolke, M., O'Brien, P.J., de Capitani, C., Carswell, D.A., 2008. Garnet growth at high- and ultra-high-pressure conditions and the effect of element fractionation on mineral modes and composition. *Lithos*, **103**, 309–332.

Kosarev, G., Kind, R., Sobolev, S.V., Yuan, X., Hanka, W., Oreshin, S., 1999. Seismic evidence for a detached Indian lithospheric mantle beneath Tibet. *Science*, **283**, 1306–1309.

Koziol, A.M., Newton, R.C., 1988. Redetermination of the anorthite breakdown reaction and improvement of the plagioclase-garnet-Al_2SiO_5-quartz barometer. *Am Mineral*, **73**, 216–223.

Krenn, E., Ustaszewski, K., Finger, F., 2008. Detrital and newly formed metamorphic monazite in amphibolite-facies metapelites from the Motajica Massif, Bosnia. *Chem Geol*, **254**, 164–174.

Krogh Ravna, E.J., 2000. The garnet–clinopyroxene Fe^{2+}–Mg geothermometer: an updated calibration. *J Metamorph Geol*, **18**, 211–219.

Krogh Ravna, E.J., Terry, M.P., 2004. Geothermobarometry of UHP and HP eclogites and schists – an evaluation of equilibria among garnet–clinopyroxene–kyanite–phengite–coesite/quartz. *J Metamorph Geol*, **22**, 579–592.

Kumar, S., 1978. Presence of paired metamorphic belts in the northwest Himalaya. *Tectonophysics*, **46**, 117–133.

Lacassin, R., Leloup, P.H., Trinh, P.T., Tapponnier, P., 1998. Unconformity of red sandstones in North Vietnam: field evidence for Indosinian orogeny in northern Indochina? *Terra Nova*, **10**, 106–111.

Le Fort, P., 1975. Himalayas: The collided range. Present knowledge of the continental arc. *Am J Sci*, **275A**, 1–44.

Le Fort, P., Michard, A., Sonet, J., Zimmermann, J.L., 1983. Petrography, geochemistry and geochronology of some samples from the Karakoram Axial Batholith, Pakistan. In: Shams, F.A. (Eds.), Granites of the Himalayas, Karakoram and Hindu Kush. University of Lahore, Lahore, 277–387.

Leake, B.E., Woolley, A.R., Arps, C.E.S., Birch, W.D., Gilbert, M.C., Grice, J.D., Hawthorne, F.C., Kato, A., Kisch, H.J., Krivovichev, V.G., Linthout, K., Laird, J., Mandarino, J.A., Maresch, W.V., Nickel, E.H., Rock, N.M., Schumacher, J.C., Smith, D.C., Stephenson, N.C.N., Ungaretti, L., Whittaker, E.J.W., Youzhi, G., 1997. Nomenclature of amphiboles: Report of

the subcommittee on amphiboles of the International Mineralogical Association commission on new minerals and mineral names. *Can Mineral*, **35**, 219–246.

Leake, B.E., Woolley, A.R., Birch, W.D., Burke, E.A.J., Ferraris, G., Grice, J.D., Hawthorne, F.C., Kisch, H.J., Krivovichev, V.G., Schumacher, J.C., Stephenson, N.C.N., Whittaker, E.J.W., 2004. Nomenclature of amphiboles: Additions and revisions to the International Mineralogical Association's amphibole nomenclature. *Am Mineral*, **89**, 883–887.

LeBreton, N., Thompson, A.B., 1988. Fluid-absent (dehydration) melting of biotite in metapelites in the early stages of crustal anatexis. *Contrib Mineral Petr*, **99**, 226–237.

Lee, H.Y., Chung, S.L., Lo, C.H., Ji, J.Q., Lee, T.-Y., Qian, Q., Zhang, Q., 2009. Eocene Neotethyan slab breakoff in southern Tibet inferred from the Linzizong volcanic record. *Tectonophysics*, **477**, 20–35.

Leech, M.L., Singh, S., Jain, A.K., 2007. Continuous metamorphic zircon growth and interpretation of U–Pb SHRIMP dating: An example from the western Himalaya. *Int Geol Rev*, **49**, 313–328.

Leloup, P.H., Kienast, J.-R., 1993. High-temperature metamorphism in a major strike-slip shear zone: the Ailao Shan-Red River, People's Republic of China. *Earth Planet Sc Lett*, **118**, 213–234.

Leloup, P.H., Harrison, T.M., Ryerson, F.J., Wenji, C., Qi, L., Tapponnier, P., Lacassin, R., 1993. Structural, petrological and thermal evolution of a Tertiary ductile strike-slip shear zone, Diancang Shan, Yunnan. *J Geophys Res*, **98**, 6715–6743.

Leloup, P.H., Lacassin, R., Tapponnier, P., Schärer, U., Dalai, Z., Xiaohan, L., Liangshang, Z., Shaocheng, J., Phan Trong, T.T., 1995. The Ailao Shan-Red River shear zone (Yunnan, China), Tertiary transform boundary of Indochina. *Tectonophysics*, **251**, 3–84.

Leloup, P.H., Ricard, Y., Battaglia, J., Lacassin, R., 1999. Shear heating in continental strike-slip shear zones: Model and field examples. *Geophys J Int*, **136**, 19–40.

Leloup, P.H., Arnaud, N., Lacassin, R., Kienast, J.-R., Harrison, T.M., Phan Trong, T.T., Replumaz, A., Tapponnier, P., 2001. New constraints on the structure, thermochronology, and timing of the Ailao Shan-Red River shear zone, SE Asia. *J Geophys Res*, **106**, 6683–6732.

Leloup, P.H., Tapponnier, P., Lacassin, R., 2007. Discussion on the role of the Red River shear zone, Yunnan and Vietnam, in the continental extrusion of south-east Asia. *J Geol Soc Lond*, **164**, 1253–1260.

Lemennicier, Y., Le Fort, P., Lombardo, B., Pêcher, A., Rolfo, F, 1996. Tectonometamorphic evolution of the central Karakorum (Baltistan – northern Pakistan). *Tectonophysics*, **260**, 119–143.

Liang, H.-Y., Campbell, I.H., Allen, C.M., Sun, W.-D., Yu, H.-X., Xie, Y.-W., Zhang, Y.-Q., 2007. The age of the potassic alkaline igneous rocks along the Ailao Shan-Red River shear zone: implications for the onset age of left-lateral shearing. *J Geol*, **115**, 231–242.

Lin, T.-H., Chung, S.-L., Chiu, H.-Y., Wu, F.-Y., Yeh, M.-W., Searle, M.P., Iizuka, Y., 2012. Zircon U–Pb and Hf isotope constraints from the Ailao Shan–Red River shear zone on the tectonic and crustal evolution of southwestern China. *Chem Geol*, **291**, 23–37.

Liu, Y., Zhong, D., 1997. Petrology of high-pressure granulites from the eastern Himalayan syntaxis. *J Metamorph Geol*, **15**, 451–466.

Liu, Y., Berner, Z., Massonne, H.-J., Zhong, D., 2006. Carbonatite-like dykes from the eastern Himalayan syntaxis: geochemical, isotopic, and petrogenetic evidence for melting of metasedimentary carbonate rocks within the orogenic crust. *J Asian Earth Sci*, **26**, 105–120.

Liu, Z.Q., 1988. Geologic Map of the Qinghai-Xizang Plateau and its neighbouring regions (scale at 1:1,500,000). Chengdu Institute of Geology and Mineral Resources. Beijing: Geologic Publishing House

Ludwig, K.R., 2003. User's Manual for Isoplot 3.00: A Geochronological Toolkit for Microsoft Excel; *Berkeley Geochronology Center Spec Pub*; no. 4, Berkeley, California.

Lyell, C., 1833. Principles of Geology, being an attempt to explain the former changes of the Earth's surface, by reference to causes now in operation (Vol. 3). London, John Murray.

Lyell, C., 1838. Elements of Geology. London, John Murray.

Mahar, E.M., Baker, J.M., Powell, R., Holland, T.J.B., Howell, N., 1997. The effect of Mn on mineral stability in metapelites. *J Metamorph Geol*, **15**, 223–238.

Mahéo, G., Bertrand, H., Guillot, S., Villa, I.M., Keller, F., Capiez, P., 2004. The south Ladakh ophiolites (north-west Himalaya, India): an intra-oceanic tholeiitic arc origin with implication for the closure of the Neo-Tethys. *Chem Geol*, **203**, 273–303.

Maluski, H., Lepvrier, C., Jolivet, L., Carter, A., Roques, D., Beyssac, O., Trong Tang, T., Duc Thang, N., Avigad, D., 2001. Ar–Ar and fission-track ages in the Song Chay Massif: Early Triassic and Cenozoic tectonics in northern Vietnam. *J Asian Earth Sci*, **19**, 233–248.

Marmo, B.A., Clarke, G.L., Powell, R., 2002. Fractionation of bulk rock composition due to porphyroblast growth: effects on eclogite facies mineral equilibria, Pam Peninsula, New Caledonia. *J Metamorph Geol*, **20**, 151–165.

Massonne, H.-J., 2012. Formation of amphibole and clinozoisite-epidote in eclogite owing to fluid infiltration during exhumation in a subduction channel. *J Petrol*, **53**, 1969–1998.

Matthews, M., Harte, B., Prior, D., 1992. Mantle garnets: A cracking yarn. *Geochim Cosmochim Ac*, **56**, 2633–2642.

McKenzie, D., Bickle, M.J., 1988. The volume and composition of melt generated by extension of the lithosphere. *J Petrol*, **29**, 625–679.

Medaris, G., Jelinek, E., Misar, Z., 1995. Czech eclogites; terrane settings and implications for Variscan tectonic evolution of the Bohemian Massif. *Eur J Mineral*, **7**, 7–28.

Messiga, B., Bettini, E., 1990. Reactions behaviour during kelyphite and symplectite formation – a case-study of mafic granulites and eclogites from the Bohemian Massif. *Eur J Mineral*, **2**, 125–144.

Metcalfe, I., 2000. The Bentong-Raub suture zone. *J Asian Earth Sci*, **18**, 691–712.

Metcalfe, I., 2002. Palaeozoic and Mesozoic geological evolution of the SE Asian region: multidisciplinary constraints and implications for biogeography. In: Hall, R., Holloway, J.D. (Eds.), Biogeography and geological evolution of SE Asia, 25–42, Backhuys Publishers, Holland.

Meyre, C., de Capitani, C., Partzsch, J.H., 1997. A ternary solid solution model for omphacite and its application to geothermobarometry of eclogites from the Middle Adula nappe (Central Alps, Switzerland). *J Metamorph Geol*, **15**, 687–700.

Miller, C.F., Stoddard, E.F., Bradfish, L.J., Dollase, W.A., 1981. Composition of plutonic muscovite: genetic implications. *Can Mineral*, **19**, 25–34.

Miyashiro, A., 1961. Evolution of metamorphic belts. *J Petrol*, **2**, 277–311.

Molnar, P., Stock, J.M., 2009. Slowing of India's convergence with Eurasia since 20 Ma and its implications for Tibetan mantle dynamics. *Tectonics*, **28**, TC3001.

Montel, J.-M., 1993. A model for monazite/melt equilibrium and application to the generation of granitic magmas. *Chem Geol*, **110**, 127–146.

Montel, J.-M., Kornprobst, J., Vielzeuf, D., 2000. Preservation of old U–Th–Pb ages in shielded monazite: Example from the Beni Bousera Hercynian kinzigites (Morocco). *J Metamorph Geol*, **18**, 335–342.

Morton, A.C., Hallsworth, C.R., 1999. Processes controlling the composition of heavy mineral assemblages in sandstones. *Sediment Geol*, **124**, 3–29.

Mukherjee, B., Sachan, H.K., Ogasawaray, Y., Muko, A., Yoshioka, N., 2003. Carbonate-bearing UHPM rocks from the Tso-Morari region, Ladakh, India: petrological implications. *Int Geol Rev*, **45**, 49–69.

Mukherjee, B., Sachan, H.K., Ahmad, T., 2005. A new occurrence of microdiamond from Indus Suture Zone, Himalaya: possible origin. In: Mascle, G., Lavé, J., (Eds.), 20th Himalaya-Karakoram-Tibet Workshop, Special Extended Abstracts Volume. *Géologie Alpine, Mémoir Hors Série*, **44**, 136.

Murphy, M.A., Harrison, T.M., 1999. Relationship between leucogranites and the Qomolangma detachment in the Rongbuk Valley, south Tibet. *Geology*, **27**, 831–834.

Nam, T.N., Toriumi, M., Itaya, T., 1998. *P–T–t* paths and post-metamorphic exhumation of the Day Nui Con Voi shear zone in Vietnam. *Tectonophysics*, **290**, 299–318.

Nelson, K.D., Zhao, W., Brown, L.D., Kuo, J., Che, J., Liu, X., Klemperer, S.L., Makovsky, Y., Meissner, R., Mechie, J., Kind, R., Wenzel, F., Ni, J., Nabelek, J., Leshou, C., Tan, H., Wei, W., Jones, A.G., Booker, J., Unsworth, M., Kidd, W.S.F., Hauck, M., Alsdorf, D., Ross, A., Cogan, M., Wu, C., Sandvol, E., Edwards, M., 1996. Partially molten middle crust beneath southern Tibet: Synthesis of project INDEPTH results. *Science*, **274**, 1684–1688.

Noble, S.R., Searle, M.P., 1995. Age of crustal melting and leucogranite formation from U–Pb zircon and monazite dating in the Western Himalaya, Zanskar, India. *Geology,* **23**, 1135–1138.

O'Brien, P.J., 1997a. Garnet zoning and reaction textures in overprinted eclogites, Bohemian Massif, European Variscides: a record of their thermal history during exhumation. *Lithos*, **41**, 119–133.

O'Brien, P.J., 1997b. Granulite facies overprints of eclogites: short-lived events deduced from diffusion modelling. In: Qian, X *et al.,* (Eds.), Precambrian geology and metamorphic petrology. *Proc 30th Int Geol Con*, **17**, 157–171.

O'Brien, P.J., 2006. The age of deep, steep continental subduction in the north-west Himalaya: Relating zircon growth to metamoprhic history. Comment on: 'The onset of India-Asia continental collision: Early, steep subduction required by the timing of UHP metamorphism in the western Himalaya' by Mary L. Leech, S. Singh, A.K. Jain, Simon L. Klemperer and R.M. Manickavasagam, Earth and Planetary Science Letters 234 (2005) 83–97. *Earth Planet Sc Lett*, **245**, 814–816.

O'Brien, P.J., Vrána, S., 1995. Eclogites with a short–lived granulite facies overprint in the Moldanubian Zone, Czech Republic: petrology, geochemistry and diffusion modelling of garnet zoning. *Geol Rund*, **84**, 473–488.

O'Brien, P.J., Zotov, N., Law, R., Khan, M.A., Jan, M.Q., 2001. Coesite in Himalayan eclogite and implications for models of India-Asia collision. *Geology*, **29**, 435–438.

Ohmoto, H., Kerrick, D.M., 1977. Devolatilization equilibria in graphitic systems. *Am J Sci*, **277**, 1013–1044.

Orville, P.M., 1972. Plagioclase cation exchange equilibria with aqueous chloride solution: results at 700 °C and 200 bars in the presence of quartz. *Am J Sci*, **272**, 234–272.

Olimpio, J.C., Anderson, D.E., 1978. The relationship between chemical and textural (optical) zoning in metamorphic garnets, South Morar, Scotland. *Am Mineral,* **63**, 677–689.

Palin, R.M., Searle, M.P., Waters, D.J., Horstwood, M.S.A., Parrish, R.R., 2012. Combined thermobarometry and geochronology of peraluminous metapelites from the Karakoram

metamorphic complex, North Pakistan; New insight into the tectonothermal evolution of the Baltoro and Hunza regions. *J Metamorph Geol*, **30**, 793–820.

Palin, R.M., Searle, M.P., Waters, D.J., Horstwood, M.S.A., Parrish, R.R., Roberts, N.M.W., Horstwood, M.S.A., Yeh, M.-W., Chung, S.-L., Anh, T.T., 2013 A geochronological and petrological study of anatectic paragneiss and associated granite dykes from the Day Nui Con Voi metamorphic core complex, North Vietnam; constraints upon the timing of metamorphism within the Red River shear zone. *J Metamorph Geol*, **31**, 359–387.

Pandey, A., Leech, M., Milton, A., Singh, P., Verma, P.K., 2010. Evidence of former majoritic garnet in Himalayan eclogite points to 200-km-deep subduction of Indian continental crust. *Geology,* **38**, 399–402.

Parrish, R.R., 1990. U–Pb dating of monazite and its application to geological problems. *Can J Earth Sci*, **27**, 1431–1450.

Parrish, R.R., Tirrul, R., 1989. U–Pb age of the Baltoro granite, northwest Himalaya, and implications for zircon inheritance and monazite U–Pb systematics. *Geology*, **17**, 1076–1079.

Parrish, R.R., Gough, S.J., Searle, M.P., Waters, D.J., 2006. Plate velocity exhumation of ultrahigh-pressure eclogites in the Pakistan Himalaya. *Geology*, **34**, 989–992.

Passchier, C.W., Trouw, R.A.J., 2005. Microtectonics, 2nd edition. Springer, Berlin.

Patiño Douce, A.E., Harris, N., 1998. Experimental constraints on Himalayan anatexis. *J Petrol*, **39**, 689–710.

Pattison, D.R.M., 1992. Stability of andalusite, sillimanite and the Al_2SiO_5 triple point: constraints from the Ballachulish Aureole, Scotland. *J Geol*, **100**, 423–446.

Pattison, D.R.M., 2003. Petrogenetic significance of orthopyroxene-free garnet plus clinopyroxene plus plagioclase ± quartz-bearing metabasites with respect to the amphibolite and granulite facies. *J Metamorph Geol,* **21**, 21–34.

Pattison, D.R.M., Begin, N.J., 1994. Hierarchy of closure temperatures in granulites and the importance of an intergranular exchange medium (melt?) in controlling maximum Fe-Mg exchange temperatures. *Mineral Mag*, **58A**, 694–695.

Pattison, D.R.M., Tinkham, D.K., 2009. Interplay between equilibrium and kinetics in prograde metamorphism of pelites: an example from the Nelson aureole, British Columbia. *J Metamorph Geol*, **27**, 249–279.

Pattison, D.R.M., Tracy, R.J., 1991. Phase equilibria and thermobarometry of metapelites. *Rev Mineral*, **26**, 105–206.

Peltzer, G., Tapponnier, P., 1988. Formation and evolution of strike-slip faults, rifts and basins during the India–Asia collision: an experimental approach. *J Geophys Res*, **93**, 15085–15117.

Peterson, E.M., Grove, M., 2010. Growth conditions of symplectic muscovite + quartz: Implications for quantifying retrograde metamorphism in exhumed magmatic arcs. *Geology*, **38**, 1071–1074.

Pëto, P., 1976. An experimental investigation of melting relations involving muscovite and paragonite in the silica-saturated portion of the system K_2O–Na_2O–Al_2O_3–SiO_2–H_2O to 15 kbar total pressure. *Prog Exp Petrol, NERC London, 3rd Report*, 41–45.

Petterson, M.G., Windley, B.F., 1985. Rb–Sr dating of the Kohistan arc batholith in the Himalaya of north Pakistan and tectonic implications. *Earth Planet Sc Lett*, **74**, 54–75.

Pham Van, L., Hoàng Quang, V., Garnier, V., Giuliani, G., Ohnenstetter, D., 2004. Marble-hosted ruby from Vietnam. *Can Gemm*, **25**, 83–95.

Philpotts, A.R., Ague, J.J., 2009. Principles of igneous and metamorphic petrology, 2nd edition. Cambridge publishing.

Powell, R., 1978. Equilibrium thermodynamics in petrology: an introduction. London, Harper and Row.

Powell, R., Holland, T.J.B., 1988. An internally consistent thermodynamic dataset with uncertainties and correlations: 3. Application to geobarometry, worked examples and a computer program. *J Metamorph Geol*, **6**, 173–204.

Powell, R., Holland, T.J.B., 1994. Optimal geothermometry and geobarometry. *Am Mineral*, **79**, 120–133.

Powell, R., Holland, T.J.B., 2008. On thermobarometry. *J Metamorph Geol*, **26**, 155–179.

Powell, R., Holland, T.J.B., Worley, B., 1998. Calculating phase diagrams involving solid solutions via non-linear equations, with examples using THERMOCALC. *J Metamorph Geol*, **16**, 577–588.

Pownceby, M.I., Wall, V.J., O'Neill, H.St.C., 1987. Fe–Mn partitioning between garnet and ilmenite: experimental calibration and applications. *Contrib Mineral Petr*, **97**, 116–126.

Pullen, A., Kapp, P., Gehrels, G.E., Ding, L., Zhang, Q., 2011. Metamorphic rocks in central Tibet: Lateral variations and implications for crustal structure. *Geol Soc Am Bull*, **123**, 585–600.

Pyle, J.M., Spear, F.S., 1999. Yttrium zoning in garnet: coupling of major and accessory phases during metamorphic reactions. *Geol Mat Res*, **1**, 1–49.

Pyle, J.M., Spear, F.S., 2003. Four generations of accessory-phase growth in low-pressure migmatites from SW New Hampshire. *Am Mineral*, **88**, 338–351.

Råheim, A., Green, D.H., 1975. *P–T* paths of natural eclogites during metamorphism – a record of subduction. *Lithos*, **8**, 317–328.

Rai, S.S., Priestley, K., Gaur, V.K., Mitra, S., Singh, M.P., Searle, M.P., 2006. Configuration of the Indian Moho beneath the north-west Himalaya and Ladakh. *Geophys Res Lett*, **33**, L15308.

Rasmussen, B., Muhling, J.R., 2009. Reactions destroying detrital monazite in greenschist-facies sandstones from the Witwatersrand basin, South Africa. *Chem Geol*, **264**, 311–327.

Robinson, A.C., 2009. Geologic offsets across the northern Karakorum fault: Implications for its role and terrane correlations in the western Himalayan-Tibetan orogen. *Earth Planet Sc Lett*, **273**, 123–130.

Roger, F., Maluski, H., Lepvrier, C., Van, T.V., Paquette, J.-L., 2012. LA–ICP–MS zircons U–Pb dating of Permo-Triassic and Cretaceous magmatism in Northern Vietnam – Geodynamical implications. *J Asian Earth Sci*, **48**, 72–82.

Rolland, Y., Mahéo, G., Guillot, S., Pêcher, A., 2001. Tectono-metamorphic evolution of the Karakorum Metamorphic complex (Dassu-Askole area, north-east Pakistan): exhumation of mid-crustal H*T*-M*P* gneisses in a convergent context. *J Metamorph Geol*, **19**, 717–737.

Rolland, Y., Carrio-Schaffhauser, E., Sheppard, S.M.F., Pêcher, A., Esclauze, L., 2006. Metamorphic zoning and geodynamic evolution of an inverted crustal section (Karakorum margin, north Pakistan), evidence for two metamorphic events. *Int J Earth Sci*, **95**, 288–305.

Rubatto, D., Williams, I.S., Buick, I.S., 2001. Zircon and monazite response to prograde metamorphism in the Reynolds Range, central Australia. *Contrib Mineral Petr*, **140**, 458–468.

Rubatto, D., Hermann, J., Buick, I.S., 2006. Temperature and bulk composition control on the growth of monazite and zircon during low-pressure anatexis (Mount Stafford, Central Australia). *J Petrol*, **47**, 1973–1996.

Rusmore, M.E., Woodsworth, G.J., Gehrels, G.E., 2005. Two-stage exhumation of midcrustal arc rocks, Coast Mountains, British Columbia. *Tectonics*, **24**, TC5013.

Rutherford, E., Soddy, F., 1902. The cause and nature of radioactivity. Part 1. *Phil Mag*, **4**, 370–396.

Sachan, H.K., Mukherjee, N.K., Ogasawara, Y., Mayurama, S., Pandey, A.A.K.M., Yoshioka, N., Ishida, H., 2001. Discovery of coesite from Indian Himalaya: Consequences on Himalayan tectonics. Abstract presented at Ultrahigh-Pressure Minerals Workshop, Waseda University, Tokyo, Japan.

Sachan, H.K., Mukherjee, B.K., Ogasawara, Y., Maruyama, S., Ishida, H., Muko, A., Yoshioka, N., 2004. Discovery of coesite from Indus Suture Zone (ISZ), Ladakh, India: Evidence for deep subduction. *Eur J Mineral*, **16**, 235–240.

Sawyer, E.W., 1994. Melt segregation in the continental crust. *Geology*, **22**, 1019–1022.

Schärer, U., 1984. The effect of initial Th-230 disequilibrium on young U–Pb ages – The Makalu Case, Himalaya. *Earth Planet Sc Lett*, **67**, 191–204.

Schärer, U., Copeland, P., Harrison, T.M., Searle, M.P., 1990. Age, cooling history and origin of post-collisional leucogranites in the Karakoram batholith, a multisystem isotope study. *J Geol*, **98**, 233–251.

Schärer, U., Tapponnier, P., Lacassin, R., Leloup, P.H., Zhong, D., Ji, S., 1994. Duration of the strike-slip movements in large shear zones: The Red River belt, China. *Earth Planet Sc Lett*, **97**, 379–397.

Schmitz M.D., Schoene B., 2007. Derivation of isotope ratios, errors and error correlations for U-Pb geochronology using ^{205}Pb–^{235}U–(^{233}U)-spike isotope dilution thermal ionization mass spectrometric data. *Geochem Geophy Geosyst*, **8**, Q08006.

Searle, M.P., 1991. Geology and Tectonics of the Karakoram Mountains. John Wiley & Sons, New York.

Searle, M.P., 1996. Geological evidence against large-scale pre-Holocene offsets along the Karakoram fault: implications for the limited extrusion of the Tibetan Plateau. *Tectonics*, **15**, 171–186.

Searle, M.P., 2006. Role of the Red River shear zone, Yunnan and Vietnam, in the continental extrusion of south-east Asia. *J Geol Soc Lond*, **163**, 1025–1036.

Searle, M.P., Tirrul, R., 1991. Structural and thermal evolution of the Karakoram crust. *J Geol Soc Lond*, **148**, 65–82.

Searle, M.P., Rex, A.J., Tirrul, R., Windley, B.F., St-Onge, M., Hoffman, P., 1986. A geological profile across the Baltoro Karakoram Range. *Geol Bull Univ Peshawar,* **19**, 1–12.

Searle, M.P., Windley, B.F., Coward, M.P., Cooper, D.J.W., Rex, A.J., Rex, D., Tingdong, L., Xuchang, X., Jan, M.Q., Thakur, V.C., Kumar, S., 1987. The closing of the Tethys and the tectonics of the Himalayas. *Geol Soc Am Bull*, **98**, 678–701.

Searle, M.P., Rex, A.J., Tirrul, R., Rex, D.C., Barnicoat, A., Windley, B.F., 1989. Metamorphic, magmatic and tectonic evolution of the Central Karakoram in the Biafo-Baltoro-Hushe regions of northern Pakistan. *Geol Soc Am Spec Paper,* **232**, 47–74.

Searle, M.P., Crawford, M.B., Rex, A.J., 1992. Field relations, geochemistry and emplacement of the Baltoro granite, Central Karakoram. *Trans Royal Soc Edinburgh: Earth Sci*, **83**, 519–538.

Searle, M.P., Parrish, R.R., Hodges, K.V., Hurford, A., Ayres, M.W., Whitehouse, M.J., 1997. Shisha Pangma leucogranite, South Tibetan Himalaya: Field relations, geochemistry, age, origin and emplacement. *J Geol*, **105**, 295–317.

Searle, M.P., Waters, D.J., Dransfield, M.W., Stephenson, B.J., Walker, C.B., Walker, J.D., Rex, D.C., 1999. Thermal and mechanical models for the structural and metamorphic evolution of the Zanskar High Himalaya. In: MacNiocaill, C., Ryan, P., (Eds.), Continental tectonics. *Geol Soc Lond Spec Pub*, **164**, 139–156.

Searle, M.P., Simpson, R.L., Law, R.D., Parrish, R.R., Waters, D.J., 2003. The structural geometry, metamorphic and magmatic evolution of the Everest massif, High Himalaya of Nepal – south Tibet. *J Geol Soc Lond*, **160**, 345–366.

Searle, M.P., Law, R.D., Jessup, M., 2006. Crustal structure, restoration and evolution of the Greater Himalaya in Nepal–South Tibet: implications for channel flow and ductile extrusion of the

middle crust. In: Law, R.D., *et al*., (Eds.), Channel flow, ductile extrusion and exhumation in continental collision zones. *Geol Soc Lond Spec Pub*, **268**, 355–378.

Searle, M.P., Cottle, J.M., Streule, M.J., Waters, D.J., 2009. Crustal melt granites and migmatites along the Himalaya: melt source, segregation, transport and granite emplacement mechanisms. *Earth Environ Sci Trans Royal Soc Edinburgh*, **100**, 1–15.

Searle, M.P., Parrish, R.R., Thow, A.V., Noble, S., Phillips, R.J., Waters, D.J., 2010a. Anatomy, age and evolution of a collisional mountain belt: the Baltoro granite batholith and Karakoram metamorphic complex, Pakistani Karakoram. *J Geol Soc Lond*, **167**, 183–202.

Searle, M.P., Yeh, M.-W., Lin, T.-H, Chung, S.-L., 2010b. Structural constraints on the timing of left-lateral shear along the Red River shear zone in the Ailao Shan and Diancang Shan Ranges, Yunnan, south-west China. *Geosphere*, **6**, 1–23.

Searle, M.P., Elliott, J.R., Phillips, R.J., Chung, S.-L., 2011. Crustal-lithospheric structure and extrusion of Tibet. *J Geol Soc Lond*, **168**, 633–672.

Seward, D., Burg, J.-P., 2008. Growth of the Namche Barwa Syntaxis and associated evolution of the Tsangpo Gorge: Constraints from structural and thermochronological data. *Tectonophysics*, **451**, 282–289.

Shaw, D.M., 1956. Geochemistry of pelitic rocks. Part III: Major elements and general geochemistry. *Geol Soc Am Bull*, **87**, 919–934.

Shen, K., Wang, J., Dong, X., 2010. Fluid inclusions of the high-pressure granulites from the Namche Barwa complex of the eastern Himalayan syntaxis, Tibet: Fluid composition and evolution in the continental subduction-zone. *J Asian Earth Sci*, **38**, 44–56.

Sibson, R.H., 1986. Earthquakes and rock deformation in crustal fault zones. *Ann Rev Earth Planet Sci*, **14**, 149–175.

Simpson, R.L., Parrish, R.R., Searle, M.P., Waters, D.J., 2000. Two episodes of monazite crystallization during metamorphism and crustal melting in the Everest region of the Nepalese Himalaya. *Geology*, **28**, 403–406.

Smith, H.A., 1993, Characterisation and timing of metamorphism within the Indo-Asian suture zone, Himalayas, northern Pakistan. PhD thesis, Hanover, New Hampshire, Dartmouth College.

Smith, H.A., Barreiro, B., 1990. Monazite U–Pb dating of staurolite-grade metamorphism in pelitic schists. *Contrib Mineral Petr*, **105**, 602–615.

Song, S.G., Zhang, L.F., Niu, Y., Wei, C.J., Liou, J.G., Shu, G.M., 2007. Eclogite- and carpholite-bearing metasedimentary rocks in the North Qilian suture zone, north-west China: implications for Early Palaeozoic cold oceanic subduction and water transport into mantle. *J Metamorph Geol*, **25**, 547–563.

Spear, F.S., 1993. Metamorphic phase equilibria and pressure-temperature-time paths. Mineralogical Society of America, Monograph Series, Washington, D.C.

Spear, F.S., 2010. Monazite-allanite phase relations in metapelites. *Chem Geol*, **279**, 55–62.

Spear, F.S., Florence, F.P., 1992. Thermobarometry in granulites: pitfalls and new approaches. *Precambrian Res*, **55**, 209–241.

Spear, F.S., Pyle, J.M., 2002. Apatite, monazite, and xenotime in metamorphic rocks. In: Kohn, M.J., *et al*., (Eds.), Metamorphic phosphates: geochemical, geobiological and material importance. *Rev Min Geochem Min Soc Am*, **48**, 293–335, Washington, D.C.

Spear, F.S., Pyle, J.M., 2010. Theoretical modelling of monazite growth in a low-Ca metapelite. *Chem Geol*, **273**, 111–119.

Spear, F.S., Selverstone, J., 1983. Quantitative *P–T* paths from zoned minerals: theory and tectonic applications. *Contrib Mineral Petr*, **83**, 348–357.

Spear, F.S., Kohn, M.J., Florence, F.P., Menard, T., 1990. A model for garnet and plagioclase growth in pelitic schists: implications for thermobarometry and *P–T* path determinations. *J Metamorph Geol*, **8**, 683–696.

Spear, F.S., Kohn, M.J., Cheney, J.T., 1999. *P–T* paths from anatectic pelites. *Contrib Mineral Petr*, **134**, 17–32.

Stacey, J.S., Kramers, J.D., 1975. Approximation of terrestrial lead isotope evolution by a 2-stage model. *Earth Planet Sc Lett*, **26**, 207–221.

Steck, A., Spring, L., Vannay, J.-C., Masson, H., Bucher, H., Stutz, E., Marchant, R., Tièche, J.-C., 1993. The tectonic evolution of the northwestern Himalaya in eastern Ladakh and Lahul, India. *Geol Soc Lond Spec Pub*, **74**, 265–276.

Steiger, R., Jäger, E., 1977. Subcommission on geochronology: convention on the use of decay constants in geo-and cosmochronology. *Earth Planet Sc Lett*, **36**, 359–362.

Štípská, P., Powell, R., 2005. Constraining the *P–T* path of a MORB-type eclogite using pseudosections, garnet zoning and garnet-clinopyroxene thermometry: an example from the Bohemian Massif. *J Metamorph Geol*, **23**, 725–743

St-Onge, M.R., Rayner, N., Palin, R.M., Searle, M.P., Waters, D.J., 2013. Integrated pressure-temperature-time constraints for the Tso Morari dome (Northwest India): Implications for the burial and exhumation path of UHP units in the western Himalaya. *J Metamorph Geol,* **31**, 469–504.

St-Onge, M.R., Searle, M.P., Wodicka, N., 2006. Trans-Hudson Orogen of North America and Himalaya-Karakoram-Tibetan Orogen of Asia: Structural and thermal characteristics of the lower and upper plates. *Tectonics,* **25**, TC4006.

Streule, M.J., Strachan, R.A., Searle, M.P., Law, R.D., 2010. Comparing Tibet-Himalayan and Caledonian crustal architecture, evolution and mountain building processes. *Geol Soc Lond Spec Pub*, **335**, 207–232.

Stüwe, K., 1997. Effective bulk composition changes due to cooling: a model predicting complexities in retrograde reaction textures. *Contrib Mineral Petr*, **129**, 43–52.

Stüwe, K., Powell, R., 1995. *P–T* paths from modal proportions: application to the Koralm Complex, Eastern Alps. *Contrib Mineral Petr*, **119**, 83–93.

Takasu, A., 1989. *P–T* histories of peridotite and amphibolite tectonic blocks in the Sambagawa metamorphic belt, Japan. In: Daly, J.S., *et al*. (Eds.), The evolution of metamorphic belts. *Geol Soc Lond Spec Pub*, **43**, 533–538.

Takemoto, K., Halim, N., Otofuji, Y-I., Tri, T.V., De, L.V., Hada, S., 2005. New paleomagnetic constraints on the extrusion of Indochina: Late Cretaceous results from the Song Da terrane, northern Vietnam. *Earth Planet Sc Lett*, **229**, 273–285.

Tapponnier, P., Molnar, P., 1977. Active faulting and tectonics in China. *J Geophys Res*, **82**, 2905–2930.

Tapponnier, P., Mattauer, M., Proust, F., Cassaigneau, C., 1981. Mesozoic ophiolites, sutures, and large-scale tectonic movements in Afghanistan. *Earth Planet Sc Lett,* **52**, 355–371.

Tapponnier, P., Peltzer, G., Ledain, A.Y., Armijo, R., Cobbold, P.R., 1982. Propagating extrusion tectonics in Asia: New insights from simple experiments with plasticine. *Geology*, **10**, 611–616.

Tapponnier, P., Peltzer, G., Armijo, R., 1986. On the mechanics of the collision between India and Asia. In: Coward, M.P., Ries, A.C. (Eds.), Collision tectonics. *Geol Soc Lond Spec Pub*, **19**, 115–157.

Tapponnier, P., Lacassin, R., Leloup, P.H., Schärer, U., Dalai, Z., Haiwei, W., Xiaohan, L., Shaocheng, J., Lianshang, Z., Jiayou, Z., 1990. The Ailao Shan-Red River metamorphic belt: Tertiary left-lateral shear between Indochina and South China. *Nature*, **343**, 431–437.

Tapponnier, P., Zhiqin, X., Roger, F., Meyer, B., Arnaud, N., Wittlinger, G., Yang, J., 2001. Oblique stepwise rise and growth of the Tibet Plateau. *Science*, **294**, 1671–1677.

Thompson, A.B., 1982. Dehydration melting of pelitic rocks and the generation of H_2O-undersaturated granitic liquids. *Am J Sci*, **282**, 1567–1595.

Thompson, A.B., England. P.C., 1984. Pressure-temperature-time paths of regional metamorphism II. Their inference and interpretation using mineral assemblages in metamorphic rocks. *J Petrol*, **25**, 929–955.

Thow, A.V., 2004. Tectonic, metamorphic and magmatic evolution of the Central Karakoram crust, Northern Pakistan. DPhil thesis, University of Oxford.

Tilley, C.E., 1924. The facies classification of metamorphic rocks. *Geol Mag*, **61**, 167–171.

Tracy, R.J., 1982. Compositional zoning and inclusions in metamorphic minerals. In: Ferry, J.M., (Eds.), Characterization of metamorphism through mineral equilibria. *Rev Min Geochem Min Soc Am*, **10**, Washington, D.C.

Treloar, P.J., Rex, D.C., Guise, P.G., Coward, M.P., Searle, M.P., Windley, B.F., Petterson, M.G., Jan, M.Q., Luff, I.W., 1989. K–Ar and Ar–Ar geochronology of the Himalayan collision in NW Pakistan: Constraints on the timing of suturing, deformation, metamorphism and uplift. *Tectonics*, **8**, 881–909.

Tsujimori, T., Sisson, V.B., Liou, J.G., Harlow, G.E., Sorensen, S.S., 2006. Very-low-temperature record of the subduction process: A review of worldwide lawsonite eclogites. *Lithos*, **92**, 609–624.

Turner, F.J., 1981. Metamorphic petrology: Mineralogical, field and tectonic aspects (2nd edition). New York, McGraw-Hill.

Tyler, I.M., Ashworth, J.R., 1982. Sillimanite-potash feldspar assemblages in graphitic pelites, Strontian area, Scotland. *Contrib Mineral Petr*, **81**, 18–29.

Van Hinsbergen, D.J.J., Kapp, P., Dupont-Nivet, G., Lippert, P.C., DeCelles, P.G., Torsvik, T.H., 2011. Restoration of Cenozoic deformation in Asia and the size of Greater India. *Tectonics*, **30**, TC5003.

Vance, D., Harris, N., 1999. Timing of prograde metamorphism in the Zanskar Himalaya. *Geology*, **27**, 395–398.

Vance, D., Mahar, E., 1998. Pressure-temperature paths from *P–T* pseudosections and zoned garnets: potential, limitations and examples from the Zanskar Himalaya, NW India. *Contrib Mineral Petr*, **132**, 225–245.

Vanderhaege, O., 2001. Melt segregation, pervasive melt migration and magma mobility in the continental crust: the structural record from pores to orogens. *Phy Chem Earth; Part A – Solid Earth Geodesy*, **26**, 213–223.

Vannay, J.-C., Hodges, K.V., 1996. Tectonometamorphic evolution of the Himalayan metamorphic core between the Annapurna and Dhaulagiri, central Nepal. *J Metamorph Geol*, **14**, 635–656.

Villa, I.M., Lemennicier, Y., Le Fort, P., 1996. Late Miocene to Early Pliocene tectonometamorphism and cooling in south-central Karakorum and Indus-Tsangpo suture, Chogo Lungma area (NE Pakistan). *Tectonophysics*, **260**, 201–214.

Vine, F.J., Matthews, D.H., 1963. Magnetic anomalies over oceanic ridges. *Nature*, **199**, 947–949.

Viskupic, K., Hodges, K.V., 2001. Monazite–xenotime thermochronometry: methodology and an example from the Nepalese Himalaya. *Contrib Mineral Petr*, **141**, 233–247.

Waage, P., Guldberg, C.M., 1864. Studies concerning affinity. *Norw Ac Sci Lett*, translated by H.I. Abrash (1986) and re-published in the *Jour Chem Ed*, **63**, 1044–1047.

Walker, C.B., Searle, M.P., Waters, D.J., 2001. An integrated tectonothermal model for the evolution of the High Himalaya in western Zanskar with constraints from thermobarometry and metamorphic modelling. *Tectonics*, **20**, 810–833.

Walsh, E.O., Hacker, B.R., 2004. The fate of subducted continental margins: Two-stage exhumation of the high-pressure to ultrahigh-pressure Western Gneiss complex, Norway. *J Metamorph Geol*, **22**, 671–689.

Wark, D.A., Watson, E.B., 2006. TitaniQ: a titanium-in-quartz geothermometer. *Contrib Mineral Petr*, **152**, 743–754.

Waters, D.J., 2001. The significance of prograde and retrograde quartz-bearing intergrowth microstructures in partially melted granulite-facies rocks. *Lithos*, **56**, 97–110.

Waters, D.J., 2002. Clinopyroxene-amphibole-plagioclase symplectites in Norwegian eclogites: microstructures, chemistry and the exhumation *P–T* path. Mineralogical Society, Winter Conference, Derby.

Waters, D.J., Charnley, N.R., 2002. Local equilibrium in polymetamorphic gneiss and the titanium substitution in biotite. *Am Mineral*, **87**, 383–396.

Waters, D.J., Martin, H.N., 1993. Geobarometry in phengite–bearing eclogites (abstract). *Terra Nova*, **5**, 410–411.

Wei, C.J., Song, S.G., 2008. Chloritoid-glaucophane schist in the north Qilian orogen, NW China: phase equilibria and *P–T* path from garnet zonation. *J Metamorph Geol*, **26**, 301–316.

Wei, C.J., Powell, R., Clarke, G., 2004. Calculated phase equilibria for low- and medium-pressure metapelites in the KFMASH and KMnFMASH systems. *J Metamorph Geol*, **22**, 495–508.

Wells, P.R.A., 1980. Thermal models for the magmatic accretion and subsequent metamorphism of continental crust. *Earth Planet Sc Lett*, **46**, 253–265.

Wen, D.R., Liu, D.Y., Chung, S.L., Chu, M.F., Ji, J.Q., Zhang, Q., Song, B., Lee, T.Y., Yeh, M.-W., Lo, C.H., 2008. Zircon SHRIMP U–Pb ages of the Gangdese batholith and implications for Neotethyan subduction in south Tibet. *Chem Geol*, **252**, 191–201.

Wendt, I., Carl, C., 1991. The statistical distribution of the mean squared weighted deviation. *Chem Geol*, **86**, 275–285.

Wetherill, G.W., 1956a. An interpretation of the Rhodesia and Witwatersrand age patterns. *Geochim Cosmochim Ac*, **9**, 290–292.

Wetherill, G.W., 1956b. Discordant uranium-lead ages, I. *Trans, Am Geophys Union*, **37**, 320–327.

Wetherill, G.W., 1966. Radioactive decay constants and energies. Handbook of Physical Constants. *Geol Soc Am Mem*, **97**, 513–519.

White, R.W., 2010. Tutorial for using the readbulkinfo (rbi) script. THERMOCALC website, http://www.metamorph.geo.uni-mainz.de/thermocalc/tutorials/index.html

White, R.W., Powell, R., 2002. Melt loss and the preservation of granulite facies mineral assemblages. *J Metamorph Geol*, **20**, 621–632.

White, R.W., Powell, R., Holland, T.J.B., Worley, B.A., 2000. The effect of TiO_2 and Fe_2O_3 on metapelitic assemblages at greenschist and amphibolite facies conditions: mineral equilibria calculations in the system K_2O–FeO–MgO–Al_2O_3–SiO_2–H_2O–TiO_2–Fe_2O_3. *J Metamorph Geol*, **18**, 497–511.

White, R.W., Powell, R., Holland, T.J.B., 2001. Calculation of partial melting in the system Na_2O–CaO–K_2O–FeO–MgO–Al_2O_3–SiO_2–H_2O (NCKFMASH). *J Metamorph Geol*, **19**, 139–153.

White, R.W., Powell, R., Clarke, G.L., 2002. The interpretation of reaction textures in Fe-rich metapelitic granulites of the Musgrave Block, central Australia: constraints from mineral equilibria calculations in the system K_2O–FeO–MgO–Al_2O_3–SiO_2–H_2O–TiO_2–Fe_2O_3. *J Metamorph Geol*, **20**, 41–55.

White, R.W., Powell, R., Halpin, J.A., 2004. Spatially-focussed melt formation in aluminous metapelites from Broken Hill, Australia. *J Metamorph Geol*, **22**, 825–845.

White, R.W., Pomroy, N.E., Powell, R., 2005. An *in-situ* metatexite-diatexite transition in upper amphibolite-facies rocks from Broken Hill, Australia. *J Metamorph Geol*, **23**, 579–602.

White, R.W., Powell, R., Holland, T.J.B., 2007. Progress relating to calculation of partial melting equilibria for metapelites. *J Metamorph Geol*, **25**, 511–527.

Whitney, D.L., Evans, B.W., 2010. Abbreviations for names of rock-forming minerals. *Am Mineral*, **95**, 185–187.

Whitney, D.L., Irving, A.J., 1994. Origin of K-poor leucosomes in a metasedimentary migmatite complex by ultrametamorphism, syn-metamorphic magmatism and subsolidus processes. *Lithos*, **32**, 173–192.

Wilke, F.D.H., O'Brien, P.J., Altenberger, U., 2010. Multi-stage reaction history in different eclogite types from the Pakistan Himalaya and implications for exhumation processes. *Lithos*, **114**, 70–85.

Williams, I.S., 2001. Response of detrital zircon and monazite, and their U–Pb isotopic systems, to regional metamorphism and host-rock partial melting, Cooma Complex, southeastern Australia. *Aust Jour Earth Sci*, **48**, 557–580.

Winchester, J.A., 1974. The control of whole-rock content of CaO and Al_2O_3 on the occurrence of the aluminium silicate polymorphs in amphibolite-facies pelites. *Geol Mag*, **111**, 205–211.

Wing, B.A., Ferry, J.M., Harrison, T.M., 2003. Prograde destruction and formation of monazite and allanite during contact and regional metamorphism of pelites: petrology and geochronology. *Contrib Mineral Petr*, **145**, 228–250.

Wintsch, R.P., 1975. Solid-fluid equilibria in the system $KAlSi_3O_8$–$NaAlSi_3O_8$–Al_2SiO_5-SiO_2–H_2O–HCl. *J Petrol*, **16**, 57–79.

Wittlinger, G., Farra, V., Vergne, J., 2004. Lithospheric and upper mantle stratifications beneath Tibet: New insights from Sp conversions. *Geophys Res Lett*, **31**, L19615.

Wolf, M.B., London, D., 1995. Incongruent dissolution of REE- and Sr-rich apatite in peraluminous granitic liquids; differential apatite, monazite, and xenotime solubilities during anatexis. *Am Mineral*, **80**, 765–775.

Wolf, M.B., Wyllie, P.J., 1994. Dehydration-melting of amphibolite at 10kbar: the effects of temperature and time. *Contrib Mineral Petr*, **115**, 369–383.

Woodhead, J.D., Hergt, J.M., 2001. Strontium, neodymium and lead isotope analyses of NIST glass certified reference materials: SRM 610, 612, 614. *Geostand News*, **25**, 261–266.

Woodsworth, G.J., 1977. Homogenisation of zoned garnets from pelitic schists. *Can Mineral*, **15**, 230–242.

Xu, W.-C., Zhang, H.-F., Parrish, R.R., Harris, N., Guo, L., Yuan, H.-L., 2010. Timing of granulite facies metamorphism in the eastern Himalayan syntaxis and its tectonic implications. *Tectonophysics*, **485**, 231–244.

Xu, Z., Ji, S., Cai, Z., Zeng, L., Geng, Q., Cao, H., 2012. Kinematics and dynamics of the Namche Barwa Syntaxis, eastern Himalaya: Constraints from deformation, fabrics and geochronology. *Gondwana Res*, **21**, 19–36.

Yan, D.P., Zhou, M.-F., Wang, C.Y., Xia, B., 2006. Structural and geochronological constraints on the tectonic evolution of the Dulong-Song Chay tectonic dome in Yunnan province, south-west China. *J Asian Earth Sci*, **28**, 332–353.

Yang, J., Xu, Z., Li, Z., Xu, X., Li, T., Ren, Y., Li, H., Chen, S., Robinson, P.T., 2009. Discovery of an eclogite belt in the Lhasa block, Tiet: A new border for Paleo-Tethys? *J Asian Earth Sci*, **34**, 76–89.

Yang, P.S., Pattison, D., 2006. Genesis of monazite and Y zoning in garnet from the Black Hills, South Dakota. *Lithos*, **88**, 233–253.

Yeh, M.-W., Lee, T.-Y., Lo, C-H., Chung, S.-L., Lan, C.-Y., Anh, T.T., 2008. Structural evolution of the Day Nui Con Voi metamorphic complex: Implications on the development of the Red River shear zone, North Vietnam. *J Struct Geol*, **30**, 1540–1553.

Yin, A., Harrison, T.M., 2000. Geologic evolution of the Himalayan-Tibetan orogen. *Ann Rev Earth Planet Sci*, **28**, 211–280.

Yin, A., Nie, S., 1996. A Phanerozoic palinspastic reconstruction of China and its neighbouring regions. In: Yin, A., Harrison, T.M., (Eds.), The tectonics of Asia. Cambridge University Press, Cambridge.

Yu, Z., Zheng, A.Z., 1979. Unpublished geologic map of the Lhasa region at a scale of 1:1,000,000 and geologic report, Xizang Bureau of Geology and Mineral Resources.

Zack, T., Moraes, R., Kronz, A., 2004. Temperature dependence of Zr in rutile: empirical calibration of a rutile thermometer. *Contrib Mineral Petr*, **148**, 471–488.

Zeitler, P.K., 1985. Cooling history of the NW Himalaya, Pakistan. *Tectonics*, **4**, 127–151.

Zeitler, P.K., Meltzer, A.S., Koons, P.O., Craw, D., Hallet, B., Page Chamberlain, C., Kidd, W.S.F., Park, S.K., Seeber, L., Bishop, M., Shroder, J., 2001. Erosion, Himalayan geodynamics, and the geomorphology of metamorphism. *Geol Soc Am Today*, **11**, 4–9.

Zeng, L., Gao, L.E., Dong, C., Tang, S., 2012. High-pressure melting of metapelite and the formation of Ca-rich granitic melts in the Namche Barwa Massif, southern Tibet. *Gondwana Res*, **21**, 138–151.

Zhang, H., Harris, N., Guo, L., Xu, W., 2009. The significance of Cenozoic magmatism from the western margin of the eastern syntaxis, southeast Tibet. *Contrib Mineral Petr*, **160**, 83–98.

Zhang, K.J., Cai, J.X., Zhang, Y.X., Zhao, T.P., 2006. Eclogites from central Qiangtang, northern Tibet (China) and tectonic implications. *Earth Planet Sc Lett*, **245**, 722–729.

Zhang, L.S., Schärer, U., 1999. Age and origin of magmatism along the Cenozoic Red River shear belt, China. *Contrib Mineral Petr*, **134**, 67–85.

Zhang, R.Y., Liou, J.G., Zheng, Y.F., Fu, B., 2003. Transition of UHP eclogites to gneissic rocks of low-amphibolite facies during exhumation: evidence from the Dabie terrane, central China. *Lithos*, **70**, 269–291.

Zhang, Z.M., Zheng, L.L., Wang, J.L., Zhao, X.D., Shi, C., 2007. Garnet pyroxenite in the Namjagbarwa Group-complex in the eastern Himalayan tectonic syntaxis, Tibet, China: evidence for subduction of the Indian continent beneath the Eurasian plate at 80–100 km depth. *Geol Bull China*, **26**, 1–12 (in Chinese with English abstract).

Zhang, Z.M., Zhao, G.C., Santosh, M., Wang, J.L., Dong, X., Liou, J.G., 2010. Two stages of granulite facies metamorphism in the eastern Himalayan syntaxis, south Tibet: petrology, zircon geochronology and implications for the subduction of Neo-Tethys and the Indian continent beneath Asia. *J Metamorph Geol*, **28**, 719–733.

Zhang, Z.M., Dong, X., Santosh, M., Liu, F., Wang, W., Yiu, F., Hu, Z., Shen, K., 2012. Petrology and geochronology of the Namche Barwa Complex in the eastern Himalayan syntaxis, Tibet: Constraints on the origin and evolution of the north-eastern margin of the Indian Craton. *Gondwana Res*, **21**, 123–137.

Zhao, G.C., Cawood, P.A., Wilde, S.A., Lu, L., 2001. High–pressure granulites (retrograded eclogites) from the Hengshan Complex, North China craton: petrology and tectonic implications. *J Petrol*, **42**, 1141–1170.

Zhong, D.L., Ding, L., 1996. Discovery of high-pressure basic granulite in Namjagbarwa area, Tibet, China. *Chinese Sci Bull*, **41**, 87–88 (in Chinese with English abstract).

10. Additional information

10.1. Conference proceedings

Data and results from case studies in this thesis have been presented by myself and colleagues at the following conferences:

St-Onge, M.R., Rayner, N., **Palin, R.M.,** Searle, M.P., Waters, D.J. *Integrated pressure-temperature-time constraints for the Tso Morari dome (NW India) Part II: Implications for the burial and exhumation path of UHP units in the western Himalaya.* Himalaya-Karakoram-Tibet (HKT) conference, Kathmandu, Nepal. November 2012. Link

Rayner, N., **Palin, R.M.,** St-Onge, M.R., Searle, M.P., Waters, D.J. *Integrated pressure-temperature-time constraints for the Tso Morari dome (NW India) Part I: In situ U–Pb geochronology of monazite and zircon.* Himalaya-Karakoram-Tibet (HKT) conference, Kathmandu, Nepal. November 2012. Link

Palin, R.M., St-Onge, M.R., Rayner, N., Searle, M.P., Waters, D.J. *The tectonothermal evolution of the Tso Morari massif; petrology and geochronology of a mafic eclogite.* Oral presentation, European Mineralogical Conference (EMC), Frankfurt, Germany. September 2012. Link

Palin, R.M., Searle, M.P., St-Onge, M.R., Waters, D.J., Roberts, N.M.W., Horstwood, M.S.A., Parrish, R.R., Weller, O., Chen, S., Yang, J. *High-grade metamorphism and crustal anatexis on the northwestern flank of the eastern Himalayan syntaxis.* Oral presentation, Metamorphic Studies Group (Geol. Soc. London) meeting, Cambridge, UK. March 2012.

Palin, R.M., Searle, M.P., Waters, D.J., Horstwood, M.S.A. Parrish, R.R. *Duration of metamorphism in the Karakoram metamorphic complex.* Oral presentation, Himalaya-Karakoram-Tibet (HKT) conference, Canmore, Canada. July 2011. Link

Palin, R.M., Searle, M.P., Waters, D.J. *Insights into the effect of garnet fractionation on resultant P–T paths.* Oral presentation, Metamorphic Studies Group (Geol. Soc. London) meeting, Cambridge, UK. March 2010.

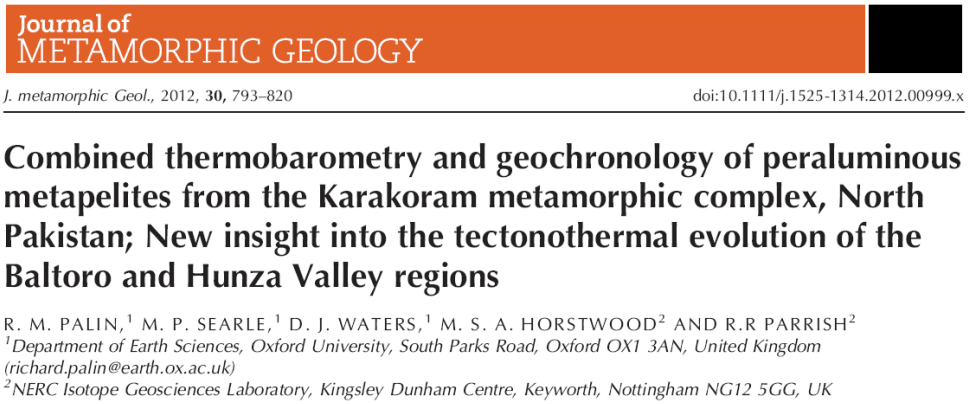
Palin, R.M., Searle, M.P., Waters, D.J. *P–T–t paths and tectonic correlation in the Karakoram metamorphic complex.* Oral presentation, Metamorphic Studies Group (Geol. Soc. London) meeting, Cambridge, UK. March 2008.

10.2. Peer-reviewed work

The following research papers have been published during the course of my postgraduate research:

10.2.1. Palin *et al*. (2012) – The Karakoram metamorphic complex

Work presented in chapter 4 has been published in the Journal of Metamorphic Geology (doi: 10.1111/j.1525-1314.2012.00999.x) as:



Journal of METAMORPHIC GEOLOGY

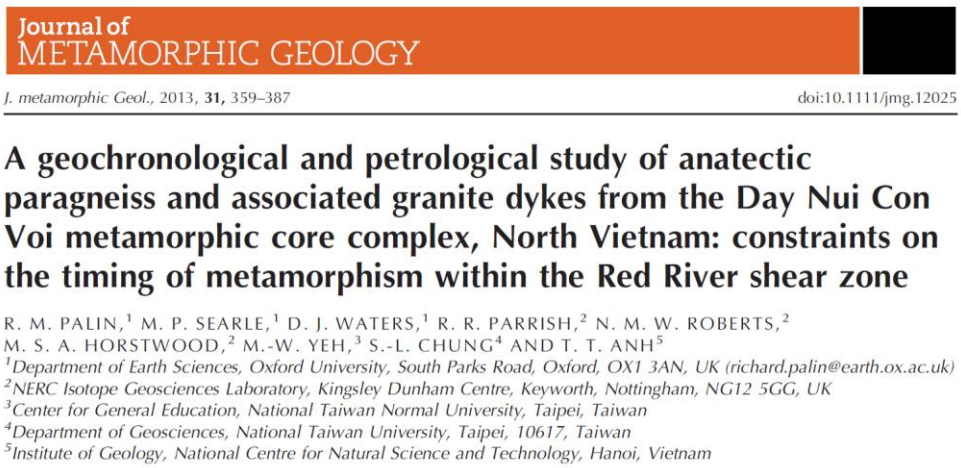
J. metamorphic Geol., 2012, **30**, 793–820 doi:10.1111/j.1525-1314.2012.00999.x

Combined thermobarometry and geochronology of peraluminous metapelites from the Karakoram metamorphic complex, North Pakistan; New insight into the tectonothermal evolution of the Baltoro and Hunza Valley regions

R. M. PALIN,[1] M. P. SEARLE,[1] D. J. WATERS,[1] M. S. A. HORSTWOOD[2] AND R.R PARRISH[2]
[1]*Department of Earth Sciences, Oxford University, South Parks Road, Oxford OX1 3AN, United Kingdom (richard.palin@earth.ox.ac.uk)*
[2]*NERC Isotope Geosciences Laboratory, Kingsley Dunham Centre, Keyworth, Nottingham NG12 5GG, UK*

10.2.2. Palin *et al*. (2013) – The Day Nui Con Voi metamorphic massif

Work presented in chapter 7 has been published in the Journal of Metamorphic Geology (doi: 10.1111/jmg.12025) as:



Journal of METAMORPHIC GEOLOGY

J. metamorphic Geol., 2013, **31**, 359–387 doi:10.1111/jmg.12025

A geochronological and petrological study of anatectic paragneiss and associated granite dykes from the Day Nui Con Voi metamorphic core complex, North Vietnam: constraints on the timing of metamorphism within the Red River shear zone

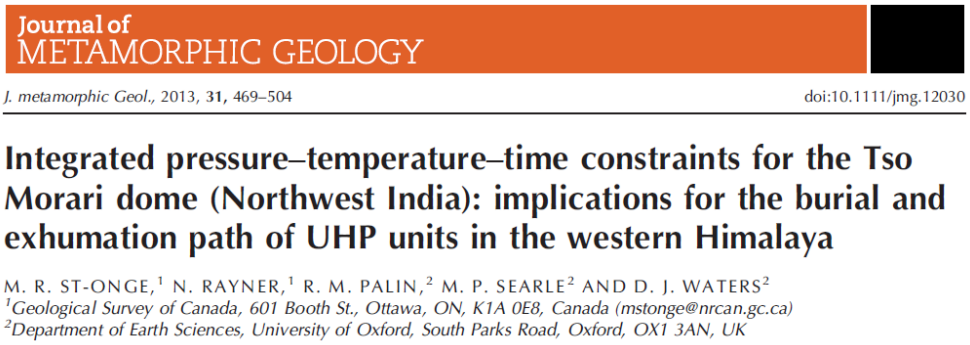
R. M. PALIN,[1] M. P. SEARLE,[1] D. J. WATERS,[1] R. R. PARRISH,[2] N. M. W. ROBERTS,[2] M. S. A. HORSTWOOD,[2] M.-W. YEH,[3] S.-L. CHUNG[4] AND T. T. ANH[5]
[1]*Department of Earth Sciences, Oxford University, South Parks Road, Oxford, OX1 3AN, UK (richard.palin@earth.ox.ac.uk)*
[2]*NERC Isotope Geosciences Laboratory, Kingsley Dunham Centre, Keyworth, Nottingham, NG12 5GG, UK*
[3]*Center for General Education, National Taiwan Normal University, Taipei, Taiwan*
[4]*Department of Geosciences, National Taiwan University, Taipei, 10617, Taiwan*
[5]*Institute of Geology, National Centre for Natural Science and Technology, Hanoi, Vietnam*

10.2.3. Palin *et al*. (in press) – The eastern Himalayan syntaxis

Work presented in chapter 6 is in press in the journal Gondwana Research as: Palin, R.M., Searle, M.P., St-Onge, M.R., Waters, D.J., Roberts, N.M.W., Horstwood, M.S.A., Parrish, R.R., Weller, O., Chen, S., Yang, J. Monazite geochronology and petrology of kyanite- and sillimanite-grade migmatites from the northwestern flank of the eastern Himalayan syntaxis.

10.2.4. St-Onge *et al*. (2013) – The Tso Morari massif

Work presented in chapter 5 has been published in the Journal of Metamorphic Geology (doi: 10.1111/jmg.12030) as:



Journal of
METAMORPHIC GEOLOGY

J. metamorphic Geol., 2013, **31**, 469–504 doi:10.1111/jmg.12030

Integrated pressure–temperature–time constraints for the Tso Morari dome (Northwest India): implications for the burial and exhumation path of UHP units in the western Himalaya

M. R. ST-ONGE,[1] N. RAYNER,[1] R. M. PALIN,[2] M. P. SEARLE[2] AND D. J. WATERS[2]
[1]*Geological Survey of Canada, 601 Booth St., Ottawa, ON, K1A 0E8, Canada (mstonge@nrcan.gc.ca)*
[2]*Department of Earth Sciences, University of Oxford, South Parks Road, Oxford, OX1 3AN, UK*

10.3. A historical account of the methods used for metamorphic petrology

This thesis focuses on the most 'up-to-date' methodologies for the investigation and quantification of metamorphic *P–T(–t)* conditions, although this approach is the result of an extended series of innovations and discoveries that span nearly two centuries. Following the pioneering efforts of Charles Lyell in 1833, who devised the word 'metamorphic' to describe rocks that had been '*changed by heat*' (chapter 2), the first significant attempt to assess metamorphic 'intensity' on a regional scale was only achieved 60 years later, in 1893, by George Barrow. Barrow documented progressive changes in metamorphic mineral assemblages across the south-east Highlands of Scotland and concluded that the appearance of each particular (index) mineral was the result of reaching progressively-higher *P–T* conditions of peak metamorphism (Barrow, 1893, 1912). A continuation of this work by Tilley (1924) formulated the concept of *metamorphic grade* and introduced the field-term *isograd* for the boundary between two index mineral zones, based on the notion that the mineral-forming reaction in question took place over a narrow range of pressure and temperature conditions. However, divisions in metamorphic grade such as 'low', 'medium' or 'high' were only of use in the same metamorphic area and offered a poor comparison between different regions worldwide, with no standardisation. Furthermore, it was known at the time that two rocks of different bulk compositions would develop different mineral assemblages at the same *P–T* conditions; therefore they were difficult to directly compare with one another.

A preliminary solution to this problem was formulated by Eskola (1915, 1920), who performed a qualitative subdivision of *P*–*T* conditions relevant to crustal lithologies into groups called *metamorphic facies*. This classification, later to be extended by Turner (1981), grouped or separated a wide variety of metamorphic rocks according to two simple tenets: those that had formed under broadly equivalent *P*–*T* conditions, but contained different mineral assemblages, represented different bulk compositions (protoliths). By contrast, for a sequence of protoliths of broadly similar bulk compositions, different mineral assemblages indicated metamorphism under different *P*–*T* conditions. The metamorphic facies concept has proven to be extremely useful in regional-scale studies, although it does not allow quantitative analysis of peak *P*–*T* conditions that a rock reached. Most reactions that bound each facies are dehydration reactions, so their position in *P*–*T* space depends on other factors (e.g. fluid composition or activity), meaning that new methods that could produce quantitative *P*–*T* data (with associated uncertainties) were clearly needed.

Bowen (1940) made the first in-depth attempt to quantify changing metamorphic phase equilibria by considering sequential devolatilisation reactions in a limestone, graphically representing them in *P*–*T* space and producing the first petrogenetic grid. This was possible owing to rocks such as limestones containing minerals that had relatively pure compositions (e.g. calcite, tremolite, forsterite, and diopside), with thermodynamic data being readily available for such end-member materials. However, the subsequent application of this technique to other lithologies stalled due to an abundance of minerals that exhibit solid solution between end-member compositions, alongside the belief held by many geologists that metamorphism could not be described by equilibrium processes alone (N.B. this belief is reported in Evans, 2007).

During the latter half of the 20th century two major achievements instigated a change in this inertia. Firstly, the advent of the electron microprobe allowed rapid and easy acquisition of mineral compositional data, which was complemented by technological advances in experimental petrology that vastly enhanced the quantity and quality of thermodynamic data for a range of materials. This led to the compilation of broad thermodynamic databases specifically relevant to the metamorphic petrology community (e.g. Helgeson *et al.*, 1978; Berman, 1988; Holland & Powell, 1990). Secondly, the formulation of literature describing the application of thermodynamic methods and

principles to metamorphic petrology (Wood & Fraser, 1977; Powell, 1978) provided the required theoretical background and tools.

The ability to acquire absolute *P–T* conditions of interest allowed detailed investigation into the tectonothermal evolution of metamorphic rocks through conventional thermobarometry and petrogenetic grid construction. When coupled with geochronological data, this provided insight into the rates of tectonic processes. Early *P–T(–t)* paths produced through a combination of field study, petrography, thermobarometry and geochronology considered mafic eclogite formation during subduction (Råheim & Green, 1975), medium- to high-grade amphibolite-facies rocks in continent-continent collisional orogenies (Spear & Selverstone, 1983; Spear *et al*., 1990) and anatectic pelites in high-grade metamorphic terranes (Spear *et al*., 1999). However, persistent problems affect such methods, such as the diffusional alteration of mineral compositions at high-temperature (Florence & Spear, 1991), so that debates on the accuracy and validity of such data continues today (e.g. Frost & Chacko, 1989; Spear & Florence, 1992, Powell & Holland, 2008)

A new milestone in the field of thermobarometry occurred with the production of internally-consistent thermodynamic databases and associated computer software capable of manipulating this information to the user's requirements (e.g. THERMOCALC; Powell & Holland, 1988; Holland & Powell, 1998). In particular, using a specific rock bulk composition to construct a phase equilibria diagram (pseudosection) that is uniquely relevant to a sample is an invaluable interpretive tool (see chapter 2.4). As the quality of thermodynamic data and activity-composition models for phases of interest improve, this method will provide greater and greater confidence in calculated results. The ability to fully describe the equilibrium state of a system under analysis allows calculated *P–T* trajectories to be supported through comparisons of calculated proportions and compositions of minerals with those observed in the sample (e.g. Stüwe & Powell, 1995). Such *P–T* paths can also be tested against numerical geodynamic simulations (e.g. Gerya *et al*. 2000, Gerya & Maresch, 2004) or conversely can be compared to predicted *P–T* paths for different tectonic scenarios such as thermal models for collisional orogenesis (e.g. England & Thompson, 1984; Thompson & England, 1984). Although pseudosection construction and analysis is not applicable to all rock types, it is a powerful tool that currently offers the best potential for accurate and reliable acquisition of *P–T* data in most rock types (discussed in Powell & Holland, 2008) and hence is the preferred method in this study.

11. Appendices

11.1. Description of external contributions

Chapter 4 (KMC) – This chapter was written by R.M. Palin. Fieldwork and sample collection was conducted by M.P. Searle, J. Fraser and A. Thow. Co-author manuscript reviews were given by M.P. Searle, D.J. Waters, M.S.A. Horstwood and R.R. Parrish. Journal and editorial reviews were given by C. Clark, two anonymous reviewers and R. White. U–Pb geochronology was performed in July 2010 by R.M. Palin at NIGL with assistance from M.S.A. Horstwood and V. Pashley.

Chapter 5 (TMM) – This chapter was written by R.M. Palin. Fieldwork and sample collection was conducted by M.P. Searle and M.R. St-Onge. Co-author manuscript reviews of the petrographic analysis and phase equilibria modelling of sample L08-03A were given by M.R. St-Onge, D.J. Waters, and M.P. Searle. Journal and editorial reviews were given by M. Kohn, C. Groppo, D. Kellett, two anonymous reviewers and M. Brown.

Chapter 6 (EHS) – This chapter was written by R.M. Palin. Fieldwork and sample collection for ET09- samples was performed by M.P. Searle and M.R. St-Onge, whereas fieldwork and sample collection for ET10- samples was conducted by R.M. Palin. Co-author manuscript reviews were given by M.P. Searle, D.J. Waters, M.R. St-Onge, R.R. Parrish, M.S.A. Horstwood, N.M.W. Roberts and O. Weller. Journal and editorial reviews were given by A. Indares, A. Zagorevski and two anonymous reviewers. U–Th–Pb geochronology was performed in February 2012 by R.M. Palin at NIGL with assistance from M.S.A. Horstwood and N.M.W. Roberts. Mass spectrometer technical specifications and working conditions given in Appendix 11.3 were provided by N.M.W. Roberts.

Chapter 7 (DNCV) – This chapter was written by R.M. Palin. Fieldwork and sample collection was conducted by M.P. Searle, M.-W. Yeh, S.-L. Chung and T.T. Anh. Co-author manuscript reviews were given by M.P. Searle, D.J. Waters, M.S.A. Horstwood, N.M.W. Roberts and R.R. Parrish. Journal and editorial reviews were given by A. Robinson, J. Halpin and R. White. Compositional analysis and SEM image acquisition for monazite in samples DNCV02, DNCV09 and DNCV10 were performed by D.J. Waters. U–Pb monazite analyses were conducted by in June 2010 by R.R. Parrish at NIGL. U–Th–Pb monazite analyses were performed in February 2012 by R.M. Palin at NIGL with assistance from M.S.A. Horstwood and N.M.W. Roberts.

11.2. U–(Th–)Pb isotopic data for MC–ICP–MS and SC–ICP–MS analyses

The following data obtained during geochronological analysis supplement the relevant tables presented in chapters 6.5 and 7.5. These isotopic data were used to construct Tera-Wasserburg plots in order to interpret U–Pb ages. As described in chapter 3.5, Th–Pb isotopic ratios were only obtained during work performed on the Nu Attom SC–ICP–MS.

								Ratios										
Analysis	Position	^{204}Pb cps	^{206}Pb (mV)	Pb (ppm)	Th (ppm)	U (ppm)	Th/U ratio	$\frac{^{206}Pb}{^{204}Pb}$	1σ (%)	$\frac{^{238}U}{^{206}Pb}$	1σ (%)	$\frac{^{207}Pb}{^{206}Pb}$	1σ (%)	$\frac{^{207}Pb}{^{235}U}$	1σ (%)	$\frac{^{206}Pb}{^{238}U}$	1σ (%)	Rho
K146 Mnz 1-1	Matrix	464	0.3	18	3245	177	18	35	28	241.1	0.6	0.18089	2.2	0.1034	2.3	0.00415	0.6	0.26
K146 Mnz 1-3	Matrix	202	0.2	15	2660	153	17	66	99	247.0	0.7	0.13566	3.3	0.0757	3.3	0.00405	0.7	0.20
K146 Mnz 3-1	Inc in grt rim	191	0.3	17	1715	156	11	80	79	227.3	1.6	0.22614	4.7	0.1372	5.0	0.00440	1.6	0.33
K146 Mnz 3-2	Inc in grt rim	60	0.2	15	2577	139	19	218	319	232.0	1.4	0.21253	4.2	0.1263	4.4	0.00431	1.4	0.31
K146 Mnz 3-3	Inc in grt rim	68	0.2	13	2895	135	21	176	127	247.0	0.4	0.14194	3.3	0.0792	3.4	0.00405	0.4	0.12
K146 Mnz 4-1	Inc in grt rim	263	0.2	14	3720	146	25	48	36	253.9	1.1	0.16629	2.9	0.0903	3.1	0.00394	1.1	0.35
K146 Mnz 4-2	Inc in grt rim	349	0.2	13	3620	141	26	34	40	257.5	1.3	0.16929	3.5	0.0907	3.7	0.00388	1.3	0.36
K146 Mnz 6-1	Inc in kyanite	269	0.2	16	4285	179	24	54	52	268.3	0.5	0.13945	2.9	0.0717	2.9	0.00373	0.5	0.17
K146 Mnz 6-2	Inc in kyanite	380	0.2	17	3561	179	20	40	26	255.7	0.4	0.14901	2.6	0.0804	2.7	0.00391	0.4	0.14
K146 Mnz 6-3	Inc in kyanite	153	0.3	19	3557	197	18	112	85	250.7	0.4	0.14101	2.5	0.0775	2.5	0.00399	0.4	0.17
K146 Mnz 6-4	Inc in kyanite	35	0.2	13	2664	138	19	325	165	262.6	0.5	0.13548	3.6	0.0711	3.7	0.00381	0.5	0.13
K146 Mnz 7-1	Matrix	71	0.2	15	2945	162	18	189	212	265.6	0.5	0.14000	3.1	0.0727	3.1	0.00376	0.5	0.15
K146 Mnz 7-2	Matrix	116	0.3	19	3790	191	20	143	146	251.3	0.6	0.16067	2.7	0.0882	2.8	0.00398	0.6	0.21
K146 Mnz 7-3	Matrix	115	0.3	20	4263	206	21	152	104	257.2	0.6	0.14864	2.3	0.0797	2.4	0.00389	0.6	0.25
K146 Mnz 7-4	Matrix	5	0.2	14	3085	156	20	2636	2681	260.6	0.5	0.13998	3.2	0.0741	3.3	0.00384	0.5	0.17
K146 Mnz 8-1	Matrix	150	0.2	14	3177	145	22	82	107	257.8	0.5	0.13913	3.3	0.0744	3.4	0.00388	0.5	0.15
K146 Mnz 8-2	Matrix	38	0.2	12	2944	131	23	286	599	259.9	0.4	0.14293	3.6	0.0758	3.6	0.00385	0.4	0.10
K146 Mnz 8-3	Matrix	139	0.2	14	2407	149	16	87	151	268.3	0.4	0.13166	3.6	0.0677	3.6	0.00373	0.4	0.12
K146 Mnz 9-1	Matrix	268	0.2	14	2104	150	14	47	45	256.1	0.5	0.15554	3.3	0.0837	3.3	0.00391	0.5	0.14
20-199 Mnz 1-1	Inc in grt core	155	0.3	24	1891	58	33	137	103	59.0	0.5	0.07217	5.7	0.1688	5.7	0.01696	0.5	0.08
20-199 Mnz 1-2	Inc in grt core	237	0.4	26	b.d.l	62	-	98	68	59.6	0.5	0.06366	3.9	0.1474	4.0	0.01679	0.5	0.13
20-199 Mnz 1-3	Inc in grt core	184	0.3	23	b.d.l	56	-	113	82	59.0	0.5	0.07387	6.0	0.1727	6.0	0.01695	0.5	0.08
20-199 Mnz 2-1	Inc in grt rim	318	0.2	17	385	117	3	47	30	171.2	1.4	0.19000	6.7	0.1530	6.8	0.00584	1.4	0.21
20-199 Mnz 2-2	Inc in grt rim	251	0.2	16	b.d.l	114	-	57	48	171.8	1.3	0.19396	6.6	0.1556	6.7	0.00582	1.3	0.19
20-199 Mnz 2-3	Inc in grt rim	318	0.3	18	b.d.l	124	-	51	38	167.6	1.6	0.19848	5.9	0.1633	6.1	0.00597	1.6	0.26
20-199 Mnz 3-1	Inc in grt rim	213	0.2	9	270	83	3	52	61	216.7	1.4	0.08696	5.5	0.0553	5.7	0.00461	1.4	0.25
20-199 Mnz 3-2	Inc in grt rim	53	0.1	8	214	62	3	168	304	200.4	1.4	0.10274	5.8	0.0707	6.0	0.00499	1.4	0.23
20-199 Mnz 3-3	Inc in grt rim	51	0.2	11	584	94	6	245	394	215.1	1.4	0.08046	5.3	0.0516	5.5	0.00465	1.4	0.26
20-199 Mnz 3-4	Inc in grt rim	249	0.1	5	691	37	19	22	57	195.8	1.5	0.13119	7.6	0.0924	7.7	0.00511	1.5	0.19
20-199 Mnz 4-1	Inc in grt rim	40	0.1	5	1751	25	70	146	554	122.9	1.5	0.25469	4.0	0.2856	4.3	0.00813	1.5	0.34
20-199 Mnz 4-2	Inc in grt rim	225	0.1	7	1556	28	55	36	54	103.9	3.7	0.25126	3.6	0.3333	5.1	0.00962	3.7	0.72
20-199 Mnz 4-3	Inc in grt rim	99	0.0	2	875	8	111	23	101	97.0	1.4	0.47534	6.7	0.6759	6.8	0.01031	1.4	0.21
ET09-05 mnz 2_1	Leucosome	96	6.6	103	2200	379	6	50	797	92.8	1.0	0.05040	0.4	0.0749	1.1	0.01077	1.0	0.92
ET09-05 mnz 2_2	Leucosome	17	8.3	129	2161	519	4	927	53	97.6	0.9	0.05091	0.4	0.0719	1.0	0.01025	0.9	0.94
ET09-05 mnz 2_3	Leucosome	71	7.7	119	2061	443	5	1230	35	90.1	0.9	0.05108	0.4	0.0781	1.0	0.01109	0.9	0.91
ET09-05 mnz 4_1	Inc in grt rim	260	8.1	126	1858	484	4	900	61	93.3	0.9	0.04805	0.4	0.0710	1.0	0.01072	0.9	0.92
ET09-05 mnz 4_2	Inc in grt rim	155	4.3	66	1957	248	8	366	68	90.3	0.9	0.05088	0.6	0.0777	1.1	0.01107	0.9	0.82
ET09-05 mnz 4_3	Inc in grt rim	305	7.5	118	1714	499	3	201	274	102.0	0.9	0.04816	0.4	0.0651	1.0	0.00980	0.9	0.92
ET09-05 mnz 4_4	Inc in grt rim	297	6.5	102	2500	382	7	1043	31	89.0	0.8	0.05810	0.7	0.0900	1.1	0.01124	0.8	0.76
ET09-05 mnz 4_5	Inc in grt rim	269	5.2	81	2505	300	8	795	63	88.3	0.9	0.05120	0.5	0.0799	1.0	0.01132	0.9	0.89
ET09-05 mnz 4_6	Inc in grt rim	210	7.6	119	1744	500	3	313	121	99.8	0.9	0.04821	0.5	0.0666	1.0	0.01002	0.9	0.89
ET09-05 mnz 4_7	Inc in grt rim	308	6.5	101	1790	435	4	431	98	103.7	1.0	0.05801	4.5	0.0771	4.6	0.00964	1.0	0.23
ET09-05 mnz 4_8	Inc in grt rim	10	6.0	94	1868	365	5	45	3526	92.8	0.9	0.05023	0.5	0.0746	1.0	0.01078	0.9	0.88
ET09-05 mnz 5_1	Leucosome	156	7.5	118	2150	455	5	619	141	94.1	0.9	0.04891	0.4	0.0717	1.0	0.01063	0.9	0.90
ET09-05 mnz 5_2	Leucosome	338	5.5	86	2275	329	7	1333	31	91.1	0.8	0.05038	0.5	0.0763	1.0	0.01098	0.8	0.85
ET09-06 mnz 1_1	Leucosome	106	3.0	39	4627	148	31	358	56	91.8	1.0	0.05297	1.1	0.0795	1.5	0.01089	1.0	0.68
ET09-06 mnz 1_2	Leucosome	44	3.9	51	4858	182	27	231	246	88.3	1.0	0.04887	0.7	0.0763	1.2	0.01132	1.0	0.84
ET09-06 mnz 1_3	Leucosome	120	6.3	81	5057	318	16	1083	51	94.8	1.0	0.04989	0.7	0.0726	1.2	0.01055	1.0	0.81
ET09-06 mnz 1_4	Leucosome	28	6.5	84	2225	336	7	35	1075	97.3	1.0	0.05016	0.8	0.0711	1.3	0.01028	1.0	0.76
ET09-06 mnz 1_5	Leucosome	16	7.4	95	4660	396	12	1200	48	100.7	1.2	0.04846	0.4	0.0663	1.3	0.00993	1.2	0.94
ET09-06 mnz 1_6	Leucosome	305	5.8	74	5043	404	12	423	283	132.6	1.1	0.04738	0.5	0.0493	1.2	0.00754	1.1	0.91
ET09-06 mnz 1_7	Leucosome	364	6.5	84	5539	397	14	244	139	113.3	1.0	0.04837	0.5	0.0589	1.2	0.00883	1.0	0.89
ET09-06 mnz 3_1	Leucosome	106	6.1	79	4115	332	12	48	706	102.3	1.0	0.04795	0.4	0.0646	1.1	0.00977	1.0	0.92
ET09-06 mnz 3_2	Leucosome	219	10.3	133	4470	582	8	1029	89	106.5	1.0	0.04773	0.4	0.0618	1.0	0.00939	1.0	0.94
ET09-06 mnz 3_3	Leucosome	112	5.1	66	5194	252	21	430	126	93.6	1.0	0.05183	0.5	0.0763	1.1	0.01068	1.0	0.90
ET09-06 mnz 3_4	Leucosome	23	6.3	82	5342	317	17	1106	60	94.1	1.0	0.04979	0.4	0.0730	1.1	0.01063	1.0	0.92
ET09-06 mnz 3_5	Leucosome	217	5.7	74	4488	294	15	255	204	96.5	1.0	0.04944	0.5	0.0706	1.1	0.01036	1.0	0.90
ET09-06 mnz 3_6	Leucosome	262	6.7	87	4214	383	11	1038	49	108.0	1.0	0.04737	0.4	0.0605	1.1	0.00926	1.0	0.92
ET09-06 mnz 3_7	Leucosome	687	8.9	115	6003	449	13	879	13	95.2	1.0	0.06487	1.9	0.0939	2.1	0.01050	1.0	0.48

Table 11.1 – MC–ICP–MS isotopic data for samples K146, 20-199, ET09-05 and ET09-06

Analysis	Position	^{204}Pb cps	^{206}Pb (mV)	Pb (ppm)	Th (ppm)	U (ppm)	Th/U ratio	Ratios															
								$^{206}Pb/^{204}Pb$	1σ (%)	$^{238}U/^{206}Pb$	1σ (%)	$^{207}Pb/^{206}Pb$	1σ (%)	$^{208}Pb/^{206}Pb$	1σ (%)	$^{207}Pb/^{235}U$	1σ (%)	$^{206}Pb/^{238}U$	1σ (%)	Rho	$^{208}Pb/^{232}Th$	1σ (%)
ET10-07 mnz 1_1	Leucosome	147	4.2	19	3442	430	8	20	78	127.5	1.6	0.04888	0.8	2.52	1.70	0.0529	1.8	0.00784	1.6	0.88	0.0024	2.6
ET10-07 mnz 1_2	Leucosome	35	5.7	27	3212	602	5	122	172	129.0	1.5	0.05036	0.6	1.78	1.66	0.0538	1.7	0.00775	1.5	0.93	0.0025	2.5
ET10-07 mnz 2_1	Leucosome	95	5.1	24	3334	532	6	13	113	130.4	1.5	0.04882	0.6	1.97	1.72	0.0516	1.7	0.00767	1.5	0.92	0.0024	2.5
ET10-07 mnz 2_2	Leucosome	19	5.6	26	3297	584	6	100	86	127.4	1.5	0.04826	0.6	1.84	1.63	0.0522	1.7	0.00785	1.5	0.92	0.0025	2.6
ET10-07 mnz 3_1	Leucosome	107	4.5	21	6312	451	14	229	100	126.4	1.6	0.04918	0.7	4.32	1.88	0.0536	1.7	0.00791	1.6	0.91	0.0024	2.4
ET10-07 mnz 3_2	Leucosome	108	3.6	17	7220	366	20	66	72	124.7	1.5	0.05498	0.7	6.06	1.78	0.0608	1.7	0.00802	1.5	0.91	0.0025	2.3
ET10-07 mnz 3_3	Leucosome	721	4.1	19	10365	401	26	157	46	121.7	1.6	0.07357	0.8	7.68	1.82	0.0834	1.7	0.00822	1.6	0.90	0.0025	2.4
ET10-07 mnz 4_1	Leucosome	797	6.4	30	5830	549	11	359	64	109.1	1.6	0.08282	3.1	3.05	1.69	0.1047	3.5	0.00917	1.6	0.46	0.0026	2.4
ET10-07 mnz 4_2	Leucosome	1756	4.0	18	4275	429	10	143	6	135.3	1.6	0.14105	1.6	3.09	1.71	0.1437	2.3	0.00739	1.6	0.70	0.0023	2.5
ET10-07 mnz 4_3	Leucosome	47	3.8	17	6001	381	16	57	87	125.6	1.5	0.04813	0.7	4.88	1.69	0.0528	1.7	0.00796	1.5	0.91	0.0024	2.5
ET10-07 mnz 4_4	Leucosome	110	5.5	26	4515	516	9	112	113	117.6	1.5	0.04869	0.8	2.81	1.72	0.0571	1.7	0.00850	1.5	0.89	0.0027	2.4
ET10-07 mnz 5_1	Leucosome	140	8.2	38	3146	771	4	135	134	116.4	1.5	0.04590	0.6	1.24	1.62	0.0544	1.7	0.00859	1.5	0.93	0.0026	2.6
ET10-07 mnz 5_2	Leucosome	349	4.2	19	6953	430	16	13	133	127.5	1.6	0.05005	0.8	5.05	1.80	0.0541	1.8	0.00784	1.6	0.89	0.0025	2.4
ET10-07 mnz 6_1	Leucosome	203	4.8	22	5158	373	14	96	115	97.4	1.6	0.05168	0.6	4.40	1.72	0.0732	1.7	0.01027	1.6	0.93	0.0033	2.4
ET10-07 mnz 6_2	Leucosome	188	5.1	24	6250	538	12	178	106	131.0	1.6	0.04938	0.7	3.82	1.65	0.0520	1.7	0.00764	1.6	0.92	0.0025	2.4
ET10-07 mnz 7_1	Mesosome	317	4.7	22	2405	338	7	108	123	89.7	1.5	0.05153	0.7	2.28	1.61	0.0792	1.7	0.01115	1.5	0.91	0.0035	2.5
ET10-07 mnz 7_2	Mesosome	237	4.2	20	3251	329	10	167	123	97.1	1.6	0.05762	0.8	3.20	1.73	0.0818	1.7	0.01030	1.6	0.90	0.0034	2.4
ET10-07 mnz 7_3	Mesosome	192	5.7	26	2152	420	5	134	110	91.1	1.5	0.04995	0.6	1.68	1.64	0.0756	1.7	0.01098	1.5	0.92	0.0035	2.6
ET10-07 mnz 8_1	Mesosome	2	6.1	28	3211	559	6	92	100	115.7	1.6	0.04802	0.8	1.86	1.65	0.0572	1.7	0.00864	1.6	0.90	0.0028	2.6
ET10-07 mnz 9_1	Mesosome	90	4.1	19	2418	303	8	126	75	92.4	1.6	0.05214	0.7	2.55	1.68	0.0778	1.7	0.01082	1.6	0.91	0.0035	2.5
ET10-07 mnz 9_2	Mesosome	305	4.9	23	2161	359	6	78	91	91.4	1.5	0.05964	0.7	1.97	1.66	0.0900	1.7	0.01095	1.5	0.91	0.0036	2.6
ET10-07 mnz 9_3	Mesosome	163	4.7	22	2704	369	7	10	85	97.4	1.6	0.05002	0.8	2.29	1.69	0.0708	1.8	0.01027	1.6	0.90	0.0032	2.5
ET10-07 mnz 9_4	Mesosome	179	4.3	20	3584	428	8	2	81	125.8	1.6	0.05606	0.7	2.60	1.64	0.0615	1.7	0.00795	1.6	0.92	0.0025	2.7
ET10-07 mnz 9_5	Mesosome	235	4.1	19	3359	424	8	103	96	128.3	1.6	0.05206	0.9	2.39	1.62	0.0560	1.8	0.00780	1.6	0.87	0.0024	2.6
ET10-07 mnz 10_1	Mesosome	238	5.3	24	2985	492	6	240	186	116.3	1.5	0.05014	0.7	2.03	1.72	0.0594	1.7	0.00860	1.5	0.92	0.0029	2.5
ET10-07 mnz 10_2	Mesosome	275	3.9	18	4509	284	16	206	112	89.4	1.5	0.05914	0.6	5.27	1.74	0.0912	1.6	0.01118	1.5	0.93	0.0037	2.4
ET10-07 mnz 11_1	Leucosome	121	4.7	22	3738	487	8	92	88	128.6	1.5	0.04821	0.7	2.46	1.64	0.0517	1.7	0.00778	1.5	0.91	0.0025	2.6
ET10-07 mnz 11_2	Leucosome	957	4.8	22	3699	485	8	310	34	123.6	1.5	0.08823	1.1	2.40	1.70	0.0984	1.9	0.00809	1.5	0.82	0.0025	2.5
ET10-07 mnz 12_1	Leucosome	87	0.7	3	6274	134	47	35	12	245.2	1.6	0.07735	1.2	13.02	1.66	0.0435	2.0	0.00408	1.6	0.80	0.0011	2.7
ET10-07 mnz 12_2	Leucosome	319	4.3	20	3766	444	8	389	76	128.0	1.5	0.07139	1.0	2.75	1.74	0.0769	1.8	0.00781	1.5	0.83	0.0025	2.4
ET10-07 mnz 12_3	Leucosome	256	3.6	17	5445	364	15	185	78	126.9	1.6	0.04939	0.8	4.70	1.68	0.0536	1.8	0.00788	1.6	0.89	0.0025	2.4
ET10-07 mnz 12_4	Leucosome	367	4.1	19	4002	449	9	116	66	136.2	1.6	0.06291	0.9	2.70	1.65	0.0637	1.8	0.00734	1.6	0.87	0.0022	2.6
ET10-07 mnz 12_5	Leucosome	414	4.2	19	4692	437	11	188	46	129.8	1.5	0.04910	0.7	3.33	1.74	0.0521	1.7	0.00770	1.5	0.90	0.0024	2.4
ET10-07 mnz 12_6	Leucosome	173	0.4	2	6502	92	71	16	7	276.8	1.6	0.09296	1.5	20.88	1.62	0.0463	2.2	0.00361	1.6	0.74	0.0010	2.6
ET10-07 mnz 12_7	Leucosome	1885	4.9	23	4378	463	9	196	12	118.4	1.5	0.12731	0.8	2.98	1.74	0.1483	1.7	0.00845	1.5	0.88	0.0027	2.5
ET10-09 mnz 1_1	Leucosome	295	2.6	19	3392	363	9	97	56	93.7	1.3	0.05779	0.9	3.00	1.18	0.0851	1.5	0.01068	1.3	0.83	0.0034	2.6
ET10-09 mnz 1_2	Leucosome	99	3.2	23	2673	407	7	12	48	88.3	1.2	0.05973	0.7	2.14	1.16	0.0933	1.5	0.01133	1.2	0.86	0.0036	2.7
ET10-09 mnz 2_1	Leucosome	435	3.2	23	3934	397	10	224	82	84.4	1.3	0.07260	0.9	3.24	1.29	0.1186	1.6	0.01185	1.3	0.83	0.0037	2.4
ET10-09 mnz 2_2	Leucosome	249	2.3	17	3381	302	11	141	51	88.3	1.4	0.06599	0.8	3.51	1.19	0.1030	1.6	0.01132	1.4	0.85	0.0034	2.7
ET10-09 mnz 3_1	Leucosome	156	2.7	19	2657	345	8	61	94	87.4	1.3	0.05359	0.8	2.50	1.09	0.0845	1.5	0.01144	1.3	0.85	0.0036	2.8
ET10-09 mnz 5_1	Leucosome	115	2.9	21	5334	372	14	82	80	87.7	1.3	0.05923	0.9	4.71	1.33	0.0931	1.6	0.01140	1.3	0.82	0.0037	2.4
ET10-09 mnz 6_1	Leucosome	200	4.1	29	3354	589	6	242	90	98.8	1.3	0.04896	0.8	1.89	1.18	0.0683	1.5	0.01012	1.3	0.86	0.0033	2.7
ET10-09 mnz 6_2	Leucosome	301	3.1	22	5167	396	13	188	88	87.6	1.3	0.05960	0.7	4.42	1.24	0.0939	1.5	0.01142	1.3	0.86	0.0037	2.5
ET10-09 mnz 6_3	Leucosome	365	3.3	24	5615	418	13	221	52	86.8	1.3	0.07123	0.8	4.42	1.35	0.1132	1.5	0.01152	1.3	0.84	0.0036	2.6
ET10-09 mnz 7_1	Leucosome	295	3.2	23	6329	414	15	226	74	88.0	1.3	0.06234	0.8	4.98	1.30	0.0976	1.5	0.01136	1.3	0.85	0.0037	2.5
ET10-09 mnz 8_1	Mesosome	437	2.8	20	5945	339	18	130	52	85.7	1.4	0.07143	0.9	5.54	1.31	0.1149	1.7	0.01166	1.4	0.82	0.0036	2.4
ET10-09 mnz 8_2	Mesosome	137	1.6	12	3090	207	15	13	45	88.4	1.3	0.05864	0.9	4.62	1.18	0.0915	1.6	0.01132	1.3	0.83	0.0035	2.6

Table 11.2 – SC–ICP–MS isotopic data for samples ET10-07, ET10-09,ET10-10, ET10-13, ET10-18a and ET09-02

Analysis	Position	^{204}Pb cps	^{206}Pb (mV)	Pb (ppm)	Th (ppm)	U (ppm)	Th/U ratio	^{206}Pb/^{204}Pb	1σ (%)	^{238}U/^{206}Pb	1σ (%)	^{207}Pb/^{206}Pb	1σ (%)	^{208}Pb/^{206}Pb	1σ (%)	^{207}Pb/^{235}U	1σ (%)	^{206}Pb/^{238}U	1σ (%)	Rho	^{208}Pb/^{232}Th	1σ (%)
ET10-09 mnz 11_1	Leucosome	53	2.9	21	2482	393	6	39	137	90.6	1.3	0.05418	0.8	2.09	1.13	0.0825	1.5	0.01104	1.3	0.85	0.0036	2.6
ET10-09 mnz 11_2	Leucosome	114	3.3	24	3662	498	7	64	118	102.2	1.3	0.05719	1.0	2.52	1.09	0.0772	1.6	0.00979	1.3	0.79	0.0032	2.5
ET10-09 mnz 12_1	Mesosome	174	3.5	26	4063	378	11	145	106	73.0	1.3	0.05659	0.8	3.67	1.27	0.1069	1.5	0.01370	1.3	0.86	0.0046	2.5
ET10-09 mnz 13_1	Mesosome	86	2.5	18	3783	322	12	29	58	88.8	1.2	0.05602	0.9	3.83	1.19	0.0869	1.5	0.01126	1.2	0.80	0.0036	2.6
ET10-09 mnz 13_2	Mesosome	312	2.6	19	3554	351	10	65	64	93.3	1.3	0.06118	0.7	3.29	1.19	0.0904	1.5	0.01072	1.3	0.87	0.0034	2.6
ET10-09 mnz 14_1	Mesosome	284	2.7	19	5210	344	15	45	48	87.8	1.3	0.06280	0.9	4.80	1.24	0.0987	1.6	0.01140	1.3	0.82	0.0036	2.6
ET10-09 mnz 14_2	Mesosome	53	3.6	26	3222	550	6	46	107	105.8	1.3	0.04994	0.8	1.91	1.14	0.0651	1.5	0.00945	1.3	0.87	0.0030	2.7
ET10-09 mnz 15_1	Leucosome	178	2.2	16	3212	283	11	49	92	86.2	1.4	0.05756	0.8	3.32	1.15	0.0921	1.6	0.01161	1.4	0.86	0.0034	2.8
ET10-09 mnz 16_1	Leucosome	210	2.3	16	3481	316	11	50	46	96.1	1.3	0.05381	1.3	3.51	1.09	0.0772	1.9	0.01041	1.3	0.71	0.0033	2.6
ET10-09 mnz 16_2	Leucosome	49	2.3	17	3461	319	11	157	115	93.3	1.4	0.05031	0.9	3.64	1.16	0.0744	1.6	0.01072	1.4	0.84	0.0034	2.5
ET10-09 mnz 17_1	Leucosome	168	2.2	16	4214	321	13	46	53	98.9	1.4	0.05923	0.8	4.22	1.24	0.0826	1.6	0.01011	1.4	0.85	0.0032	2.5
ET10-09 mnz 17_2	Leucosome	439	2.8	21	5087	382	13	137	47	91.6	1.3	0.07615	1.0	4.22	1.29	0.1146	1.6	0.01091	1.3	0.80	0.0034	2.5
ET10-09 mnz 17_3	Leucosome	135	4.6	34	3130	707	4	220	152	101.4	1.4	0.04976	0.6	1.33	1.12	0.0676	1.6	0.00986	1.4	0.93	0.0028	2.7
ET10-10 mnz 1_1	Leucosome	104	0.4	3	1567	63	25	17	9	135.5	1.7	0.05818	1.7	7.50	1.09	0.0592	2.4	0.00738	1.7	0.71	0.0022	2.7
ET10-10 mnz 2_1	Leucosome	102	0.7	5	1586	162	10	23	21	177.2	1.5	0.05904	1.5	3.65	1.05	0.0459	2.1	0.00564	1.5	0.70	0.0021	3.4
ET10-10 mnz 3_1	Inc in grt rim	86	1.0	7	2732	154	18	22	29	124.4	1.4	0.05762	0.9	5.44	1.10	0.0638	1.7	0.00804	1.4	0.84	0.0024	2.7
ET10-10 mnz 4_1	Leucosome	100	0.3	2	941	83	11	28	11	196.7	1.5	0.04988	1.8	3.85	1.03	0.0350	2.3	0.00508	1.5	0.64	0.0017	3.9
ET10-10 mnz 5_1	Inc in grt rim	46	0.8	6	2558	121	21	56	21	111.9	1.4	0.06011	1.5	6.24	1.13	0.0741	2.0	0.00894	1.4	0.70	0.0027	2.4
ET10-10 mnz 6_1	Leucosome	262	0.8	6	1267	113	11	35	31	102.8	1.5	0.12230	1.3	3.34	1.09	0.1640	2.0	0.00973	1.5	0.75	0.0029	2.7
ET10-10 mnz 13_1	Inc in grt rim	281	1.0	7	3081	173	18	61	41	120.3	1.3	0.07680	1.0	5.49	1.14	0.0880	1.6	0.00831	1.3	0.78	0.0025	2.9
ET10-10 mnz 14_1	Inc in grt rim	207	1.1	8	3786	192	20	134	35	123.7	1.3	0.06251	1.0	6.29	1.14	0.0697	1.7	0.00808	1.3	0.79	0.0025	2.9
ET10-10 mnz 14_2	Inc in grt rim	55	0.3	2	1393	68	20	5	9	138.3	1.4	0.06304	1.8	6.72	1.06	0.0628	2.3	0.00723	1.4	0.62	0.0023	3.8
ET10-10 mnz 15_1	Inc in grt rim	21	0.8	6	3282	146	22	6	31	131.6	1.3	0.05947	1.1	6.99	1.15	0.0623	1.8	0.00760	1.3	0.76	0.0023	2.8
ET10-10 mnz 16_1	Inc in grt rim	1	0.6	4	2240	112	20	9	14	135.8	1.4	0.06519	1.4	6.50	1.08	0.0662	2.0	0.00736	1.4	0.70	0.0023	3.1
ET10-10 mnz 17_2	Inc in grt rim	89	0.2	2	1097	44	25	14	7	134.1	1.6	0.06664	2.3	8.48	1.05	0.0685	2.8	0.00746	1.6	0.56	0.0025	3.9
ET10-10 mnz 17_3	Inc in grt rim	189	0.5	4	2389	96	25	68	23	133.7	1.4	0.06279	1.3	8.36	1.08	0.0647	2.0	0.00748	1.4	0.73	0.0024	3.0
ET10-10 mnz 18_1	Inc in grt rim	101	0.9	7	3477	194	18	16	20	139.3	1.3	0.05816	1.2	5.82	1.18	0.0575	1.8	0.00718	1.3	0.74	0.0022	2.7
ET10-10 mnz 18_2	Inc in grt rim	140	1.1	8	3431	231	15	109	32	142.8	1.3	0.05902	1.0	4.73	1.17	0.0570	1.6	0.00700	1.3	0.81	0.0022	2.8
ET10-10 mnz 19_1	Inc in grt rim	96	1.3	10	4409	216	20	61	44	114.6	1.4	0.06955	0.9	6.67	1.17	0.0837	1.6	0.00873	1.4	0.83	0.0028	2.5
ET10-10 mnz 19_2	Inc in grt rim	154	1.5	11	3862	286	13	28	57	130.2	1.4	0.05560	1.1	3.98	1.14	0.0589	1.7	0.00768	1.4	0.79	0.0022	2.8
ET10-10 mnz 20_1	Inc in grt rim	138	2.1	15	3649	374	10	92	49	119.9	1.4	0.05239	0.9	2.88	1.18	0.0602	1.6	0.00834	1.4	0.84	0.0024	2.6
ET10-10 mnz 20_2	Inc in grt rim	198	3.4	25	3751	578	6	264	71	116.4	1.3	0.05083	0.7	2.03	1.16	0.0602	1.5	0.00859	1.3	0.86	0.0026	2.7
ET10-10 mnz 20_3	Inc in grt rim	125	1.6	12	3562	280	13	91	52	115.6	1.3	0.05438	1.0	3.87	1.15	0.0649	1.7	0.00865	1.3	0.81	0.0026	2.7
ET10-10 mnz 21_1	Leucosome	123	0.6	5	3117	143	22	24	26	153.9	1.3	0.07093	1.0	6.94	1.11	0.0636	1.7	0.00650	1.3	0.79	0.0020	2.8
ET10-10 mnz 21_2	Leucosome	56	0.3	2	2956	79	37	1	11	178.1	1.5	0.07601	1.4	11.64	1.07	0.0588	2.0	0.00562	1.5	0.72	0.0017	3.3

Table 11.2 (continued) – SC–ICP–MS isotopic data for samples ET10-07, ET10-09,ET10-10, ET10-13, ET10-18a and ET09-02

Analysis	Position	^{204}Pb cps	^{206}Pb (mV)	Pb (ppm)	Th (ppm)	U (ppm)	Th/U ratio	^{206}Pb/^{204}Pb	1σ (%)	^{238}U/^{206}Pb	1σ (%)	^{207}Pb/^{206}Pb	1σ (%)	^{208}Pb/^{206}Pb	1σ (%)	^{207}Pb/^{235}U	1σ (%)	^{206}Pb/^{238}U	1σ (%)	Rho	^{208}Pb/^{232}Th	1σ (%)
ET10-13 mnz 1_1	Matrix	46	0.0	0.2	281	13	21	0	2	314.4	2.0	0.20251	3.0	4.75	1.01	0.0888	3.6	0.00318	2.0	0.55	0.0007	9.9
ET10-13 mnz 2_1	Matrix	50	0.1	1	2562	69	37	7	3	554.4	1.6	0.07953	2.7	10.54	1.03	0.0198	3.2	0.00180	1.6	0.52	0.0005	4.1
ET10-13 mnz 2_2	Matrix	121	0.5	3	803	241	3	29	11	444.5	1.5	0.06199	1.5	0.94	1.01	0.0192	2.1	0.00225	1.5	0.70	0.0006	6.3
ET10-13 mnz 3_1	Matrix	135	0.1	1	2114	54	39	1	2	491.1	1.8	0.10200	2.4	9.62	1.02	0.0286	3.0	0.00204	1.8	0.58	0.0005	4.4
ET10-13 mnz 3_2	Matrix	64	0.4	3	659	199	3	35	13	419.5	1.5	0.07384	2.2	1.17	1.01	0.0243	2.6	0.00238	1.5	0.57	0.0008	6.1
ET10-18a mnz 1_1	Inc in grt core	53	0.5	4	1276	175	7	23	15	260.7	1.3	0.07119	1.5	2.33	1.03	0.0376	2.0	0.00384	1.3	0.66	0.0012	4.0
ET10-18a mnz 1_2	Inc in grt core	181	0.4	3	3862	137	28	21	12	246.8	1.4	0.11509	1.3	9.07	1.10	0.0643	1.9	0.00405	1.4	0.73	0.0013	2.4
ET10-18a mnz 2_1	Inc in grt rim	112	0.3	2	423	122	3	13	13	258.8	1.4	0.06498	1.8	1.24	1.01	0.0346	2.3	0.00386	1.4	0.63	0.0013	6.8
ET10-18a mnz 3_1	Inc in grt rim	198	0.7	5	4286	274	16	18	17	264.9	1.3	0.08371	1.0	5.02	1.08	0.0436	1.7	0.00377	1.3	0.80	0.0012	3.0
ET10-18a mnz 3_2	Inc in grt rim	132	1.0	7	3016	379	8	36	27	267.1	1.4	0.07780	0.9	2.62	1.06	0.0402	1.6	0.00374	1.4	0.84	0.0012	3.6
ET10-18a mnz 4_1	Inc in grt rim	248	0.8	6	1749	308	6	45	16	256.7	1.3	0.09581	1.3	1.55	1.04	0.0515	1.8	0.00390	1.3	0.71	0.0010	4.2
ET10-18a mnz 4_2	Inc in grt rim	162	0.8	6	4225	309	14	49	20	261.5	1.4	0.08135	1.1	4.16	1.09	0.0429	1.8	0.00382	1.4	0.78	0.0011	3.0
ET10-18a mnz 5_1	Inc in grt rim	142	0.7	5	4823	228	21	3	31	251.5	1.4	0.09266	1.1	6.38	1.07	0.0508	1.8	0.00398	1.4	0.79	0.0012	2.6
ET10-18a mnz 6_1	Inc in grt rim	165	0.8	6	4022	268	15	13	28	258.1	1.4	0.08468	1.0	4.53	1.07	0.0452	1.7	0.00387	1.4	0.79	0.0012	2.5
ET10-18a mnz 6_2	Inc in grt rim	76	0.9	7	2774	313	9	53	18	259.9	1.4	0.07544	1.3	2.76	1.04	0.0400	1.9	0.00385	1.4	0.72	0.0012	2.8
ET10-18a mnz 7_1	Inc in grt rim	292	0.5	3	5339	138	39	11	10	233.6	1.4	0.14807	1.2	12.66	1.19	0.0874	1.8	0.00428	1.4	0.76	0.0014	2.1
ET10-18a mnz 8_1	Inc in grt rim	95	0.7	5	1744	283	6	83	36	270.6	1.4	0.06603	1.2	2.08	1.06	0.0336	1.8	0.00370	1.4	0.75	0.0012	3.7
ET10-18a mnz 9_1	Inc in grt rim	75	0.4	3	845	142	6	6	12	267.6	1.4	0.06875	1.7	2.01	1.02	0.0354	2.2	0.00374	1.4	0.64	0.0012	5.7
ET10-18a mnz 10_1	Inc in grt core	217	0.6	4	3906	220	18	50	26	256.6	1.3	0.09995	1.4	5.19	1.07	0.0537	1.9	0.00390	1.3	0.68	0.0011	3.3
ET10-18a mnz 10_2	Inc in grt core	130	0.1	1	160	57	3	5	4	259.2	1.6	0.06290	2.7	1.01	1.00	0.0335	3.1	0.00386	1.6	0.52	0.0014	10.3
ET10-18a mnz 11_1	Inc in grt core	97	0.6	5	5664	246	23	66	23	258.6	1.3	0.10272	1.2	6.53	1.10	0.0548	1.8	0.00387	1.3	0.74	0.0011	2.7
ET09-02 mnz 2_2	Matrix	152	0.1	1	1172	117	10	7	3	610.7	2.0	0.16887	3.2	2.76	1.01	0.0381	3.8	0.00164	2.0	0.53	0.0005	6.8
ET09-02 mnz 3_2	Matrix	12	0.1	1	99	114	1	0	2	721.6	1.6	0.12442	2.3	0.49	1.00	0.0238	2.8	0.00139	1.6	0.57	0.0009	16.0
ET09-02 mnz 4_1	Matrix	17	0.1	1	380	77	5	5	4	684.4	1.7	0.16370	2.5	1.23	1.00	0.0330	3.0	0.00146	1.7	0.56	0.0004	11.8
ET09-02 mnz 7_1	Matrix	169	0.1	1	339	109	3	4	2	614.0	1.6	0.18155	1.9	1.28	1.00	0.0408	2.5	0.00163	1.6	0.65	0.0007	11.1
ET09-02 mnz 7_2	Matrix	13	0.1	0.4	149	48	3	0	1	539.0	1.6	0.30132	2.1	1.36	1.00	0.0771	2.6	0.00186	1.6	0.60	0.0007	13.9
ET09-02 mnz 8_1	Matrix	227	0.2	1	2821	175	16	8	3	698.3	1.5	0.06979	2.5	5.00	1.02	0.0138	2.9	0.00143	1.5	0.51	0.0004	5.5
ET09-02 mnz 8_2	Matrix	48	0.2	1	2383	172	14	5	6	678.7	1.4	0.09848	2.3	3.86	1.02	0.0200	2.7	0.00147	1.4	0.51	0.0004	5.1
ET09-02 mnz 10_1	Matrix	56	0.2	1	277	185	1	8	6	714.0	1.4	0.06773	1.9	0.40	1.00	0.0131	2.4	0.00140	1.4	0.59	0.0004	14.7
ET09-02 mnz 10_2	Matrix	180	0.2	1	351	162	2	6	5	562.9	1.5	0.18797	1.8	0.88	1.01	0.0460	2.4	0.00178	1.5	0.63	0.0007	9.7
ET09-02 mnz 10_3	Matrix	265	0.2	2	863	180	5	14	7	553.5	1.4	0.19224	1.5	1.53	1.01	0.0479	2.0	0.00181	1.4	0.69	0.0006	6.4

Table 11.2 (continued) – SC–ICP–MS isotopic data for samples ET10-07, ET10-09,ET10-10, ET10-13, ET10-18a and ET09-02

Analysis	Position	^{204}Pb cps	^{206}Pb (mV)	Pb (ppm)	Th (ppm)	U (ppm)	Th/U ratio	Ratios										
								$\frac{^{206}Pb}{^{204}Pb}$	1σ (%)	$\frac{^{238}U}{^{206}Pb}$	1σ (%)	$\frac{^{207}Pb}{^{206}Pb}$	1σ (%)	$\frac{^{207}Pb}{^{235}U}$	1σ (%)	$\frac{^{206}Pb}{^{238}U}$	1σ (%)	Rho
DNCV02 mnz A1_1	Groundmass	160	1.7	97	6099	333	18	25	435	247.7	1.4	0.06635	1.5	0.0369	2.0	0.00404	1.4	0.70
DNCV02 mnz A1_2	Groundmass	115	1.9	101	6542	382	17	59	562	256.7	1.4	0.05696	1.1	0.0306	1.8	0.00390	1.4	0.78
DNCV02 mnz A2_1	Groundmass	158	1.7	95	6070	347	17	119	127	257.2	1.5	0.05790	1.2	0.0310	1.9	0.00389	1.5	0.77
DNCV02 mnz A2_2	Groundmass	84	1.7	96	6088	349	17	138	275	268.8	1.5	0.05707	1.1	0.0293	1.9	0.00372	1.5	0.81
DNCV02 mnz A2_3	Groundmass	114	1.8	105	6695	367	18	240	92	258.1	1.4	0.06015	1.1	0.0321	1.8	0.00387	1.4	0.78
DNCV02 mnz A6_1	Groundmass	132	1.2	106	6633	230	29	137	47	242.4	1.7	0.06395	1.6	0.0364	2.3	0.00413	1.7	0.75
DNCV02 mnz A6_2	Groundmass	222	1.0	82	5063	194	26	48	134	244.8	1.5	0.05938	1.8	0.0335	2.3	0.00409	1.5	0.64
DNCV02 mnz A7_1	Groundmass	130	1.6	84	4857	304	16	46	190	242.0	1.4	0.06683	1.1	0.0381	1.8	0.00413	1.4	0.78
DNCV02 mnz A7_2	Groundmass	59	1.8	91	5433	338	16	77	170	243.8	1.5	0.05856	1.7	0.0331	2.2	0.00410	1.5	0.66
DNCV02 mnz A7_3	Groundmass	2	1.6	121	7232	288	25	74	87	239.7	1.4	0.06241	1.2	0.0359	1.9	0.00417	1.4	0.78
DNCV02 mnz B4_1	Groundmass	134	1.9	73	4268	373	11	262	53	258.9	1.6	0.05749	1.2	0.0306	2.0	0.00386	1.6	0.81
DNCV02 mnz B4_2	Groundmass	15	1.9	90	5398	386	14	61	195	257.2	1.6	0.05659	1.2	0.0303	2.0	0.00389	1.6	0.79
DNCV02 mnz B4_3	Groundmass	81	2.0	85	5067	390	13	162	105	262.5	1.7	0.05437	1.1	0.0286	2.0	0.00381	1.7	0.84
DNCV02 mnz B5_1	Groundmass	10	1.1	84	5048	223	23	6	1079	250.3	1.6	0.06146	1.9	0.0339	2.4	0.00400	1.6	0.65
DNCV02 mnz B5_2	Groundmass	66	1.3	104	6316	261	24	35	207	249.7	1.6	0.06223	1.9	0.0344	2.5	0.00400	1.6	0.63
DNCV02 mnz B5_3	Groundmass	131	1.4	156	9254	266	35	14	554	246.4	1.5	0.06046	1.4	0.0338	2.1	0.00406	1.5	0.71
DNCV02 mnz B6_1A	Groundmass	269	1.5	79	4762	292	16	161	81	244.3	1.6	0.07983	5.9	0.0451	6.2	0.00409	1.6	0.26
DNCV02 mnz B6_1B	Groundmass	314	1.5	76	4666	288	16	73	303	248.1	1.5	0.06401	1.7	0.0356	2.3	0.00403	1.5	0.66
DNCV02 mnz B6_2A	Groundmass	261	1.7	86	5337	322	17	102	85	239.7	1.6	0.09035	5.2	0.0520	5.5	0.00417	1.6	0.29
DNCV02 mnz B6_2B	Groundmass	341	1.7	85	5452	329	17	232	108	247.0	1.6	0.07274	2.1	0.0406	2.7	0.00405	1.6	0.61
DNCV09 mnz A3_1	Groundmass	64	0.4	80	3814	72	53	10	275	205.1	1.6	0.07588	3.5	0.0510	3.9	0.00488	1.6	0.41
DNCV09 mnz A3_2	Groundmass	92	0.4	80	3871	73	53	3	558	205.2	1.6	0.07071	3.8	0.0475	4.1	0.00487	1.6	0.38
DNCV09 mnz A3_3	Groundmass	153	0.5	77	3665	84	44	25	99	197.2	1.7	0.07204	3.3	0.0504	3.7	0.00507	1.7	0.46
DNCV09 mnz B4_1	Groundmass	199	1.3	150	3251	119	27	94	128	94.1	1.6	0.05444	1.7	0.0798	2.4	0.01063	1.6	0.68
DNCV09 mnz B4_2	Groundmass	135	1.3	151	3271	121	27	196	77	93.4	1.7	0.04995	1.6	0.0737	2.3	0.01070	1.7	0.72
DNCV09 mnz B4_3	Groundmass	89	1.2	139	3100	117	27	87	103	96.9	1.8	0.05242	2.0	0.0746	2.7	0.01032	1.8	0.67
DNCV09 mnz B5_1	Groundmass	54	1.8	162	3065	149	21	58	172	85.2	1.5	0.05516	1.2	0.0893	1.9	0.01174	1.5	0.80
DNCV09 mnz B5_2	Groundmass	389	1.1	149	3209	100	32	52	65	96.9	1.5	0.05360	1.9	0.0763	2.4	0.01032	1.5	0.63
DNCV09 mnz B5_3	Groundmass	424	1.1	150	3141	103	30	138	33	97.9	1.6	0.05469	1.8	0.0770	2.4	0.01021	1.6	0.66
DNCV09 mnz C10_1	Groundmass	206	2.5	147	2805	204	14	15	1001	84.5	1.6	0.05162	0.9	0.0843	1.8	0.01184	1.6	0.87
DNCV09 mnz C10_2	Groundmass	233	3.8	233	3024	234	13	620	50	64.2	2.3	0.05065	0.8	0.1089	2.5	0.01559	2.3	0.95
DNCV09 mnz C8_1	Groundmass	263	0.3	80	3976	69	57	26	55	203.9	1.5	0.07020	4.0	0.0475	4.3	0.00490	1.5	0.36
DNCV09 mnz C8_2	Groundmass	4	0.4	87	4422	81	54	17	177	207.5	1.5	0.06851	3.4	0.0455	3.7	0.00482	1.5	0.41
DNCV09 mnz C8_3	Groundmass	276	0.3	79	4010	61	66	36	30	202.5	1.6	0.06935	4.4	0.0472	4.6	0.00494	1.6	0.34
DNCV10 mnz A1_1	Leucosome	392	7.2	318	2547	261	10	118	516	36.0	1.9	0.05426	0.4	0.2077	2.0	0.02777	1.9	0.98
DNCV10 mnz A1_2	Leucosome	722	8.2	377	2338	265	9	869	18	31.6	1.7	0.05854	0.7	0.2558	1.9	0.03169	1.7	0.92
DNCV10 mnz A2_1	Leucosome	408	2.0	50	2636	484	5	281	33	246.9	1.6	0.05380	1.1	0.0300	1.9	0.00405	1.6	0.82
DNCV10 mnz A2_2	Leucosome	576	2.1	60	3033	448	7	98	42	213.2	1.5	0.05665	1.3	0.0366	2.0	0.00469	1.5	0.76
DNCV10 mnz B5_1	Leucosome	240	1.8	54	2797	349	8	69	124	198.3	1.9	0.05584	1.2	0.0388	2.2	0.00504	1.9	0.83
DNCV10 mnz B5_2	Leucosome	454	1.7	54	2872	329	9	284	85	192.6	1.9	0.05531	1.3	0.0396	2.3	0.00519	1.9	0.82
DNCV10 mnz B5_3	Leucosome	470	1.6	58	3122	303	10	231	86	185.2	1.8	0.06488	2.3	0.0483	2.9	0.00540	1.8	0.62
DNCV10 mnz C5_1	Leucosome	469	1.6	79	3503	268	13	43	392	168.7	1.9	0.05817	1.4	0.0476	2.3	0.00593	1.9	0.81
DNCV10 mnz C5_2	Leucosome	153	1.6	67	3017	274	11	169	54	174.4	2.0	0.06026	1.3	0.0476	2.4	0.00573	2.0	0.85
DNCV10 mnz E4_1A	Leucosome	371	5.7	447	3079	246	13	491	47	42.4	3.6	0.05472	0.6	0.1778	3.6	0.02357	3.6	0.99
DNCV10 mnz E4_1B	Leucosome	683	7.5	447	3079	244	13	1171	145	32.1	1.9	0.05429	0.4	0.2330	2.0	0.03112	1.9	0.98
DNCV10 mnz E4_2	Leucosome	241	5.2	298	2797	271	10	617	115	51.3	1.6	0.05494	0.5	0.1477	1.7	0.01949	1.6	0.96
DNCV10 mnz E4_3	Leucosome	490	2.0	47	2822	480	6	106	160	236.4	1.8	0.06109	1.4	0.0356	2.3	0.00423	1.8	0.78
DNCV10 mnz E5_1	Leucosome	399	1.7	58	2954	328	9	60	91	199.5	1.7	0.06287	2.7	0.0434	3.2	0.00501	1.7	0.51
DNCV10 mnz E5_2	Leucosome	426	1.5	62	2934	303	10	291	34	194.4	2.0	0.05348	1.3	0.0379	2.4	0.00514	2.0	0.83
DNCV10 mnz E5_3	Leucosome	460	1.4	72	2933	246	12	83	48	174.1	1.9	0.05595	1.4	0.0443	2.3	0.00574	1.9	0.80

Table 11.3 – MC–ICP–MS isotopic data for samples DNCV02, DNCV09 and DNCV10

Analysis	Position	^{204}Pb cps	^{206}Pb (mV)	Pb (ppm)	Th (ppm)	U (ppm)	Th/U ratio	Ratios													
								^{206}Pb/^{204}Pb	1σ (%)	^{238}U/^{206}Pb	1σ (%)	^{207}Pb/^{206}Pb	1σ (%)	^{208}Pb/^{206}Pb	1σ (%)	^{207}Pb/^{235}U	1σ (%)	^{206}Pb/^{238}U	1σ (%)	Rho	^{208}Pb/^{232}Th	1σ (%)
DNCV01 mnz 1_1	Matrix	160	12.9	97	4244	718	6	114	434	42.4	1.2	0.05101	0.6	1.90	1.49	0.1659	1.4	0.02359	1.2	0.88	0.0076	1.9
DNCV01 mnz 1_2	Matrix	231	10.4	79	4312	576	7	99	269	42.8	1.2	0.05156	0.7	2.35	1.49	0.1662	1.4	0.02338	1.2	0.88	0.0075	2.0
DNCV01 mnz 1_3	Matrix	107	9.5	72	4011	526	8	226	243	42.2	1.2	0.05148	0.5	2.44	1.46	0.1683	1.3	0.02371	1.2	0.92	0.0075	1.9
DNCV01 mnz 1_4	Matrix	61	10.6	80	4505	579	8	143	246	41.6	1.2	0.05188	0.6	2.40	1.38	0.1719	1.3	0.02403	1.2	0.90	0.0073	1.9
DNCV01 mnz 2_1	Matrix	50	2.0	15	3955	243	16	92	52	91.7	1.2	0.05210	0.8	4.89	1.20	0.0783	1.4	0.01091	1.2	0.84	0.0033	2.2
DNCV01 mnz 2_2	Matrix	123	2.3	17	3789	241	16	43	49	80.7	1.2	0.05406	1.0	4.94	1.21	0.0923	1.6	0.01239	1.2	0.76	0.0039	2.3
DNCV01 mnz 2_3	Matrix	14	1.8	14	4338	211	21	31	63	88.9	1.2	0.05811	0.8	6.13	1.31	0.0902	1.4	0.01125	1.2	0.85	0.0034	2.1
DNCV01 mnz 3_1	Matrix	15	0.5	4	3750	120	31	23	19	181.4	1.3	0.06882	1.6	9.53	1.15	0.0523	2.0	0.00551	1.3	0.64	0.0017	2.4
DNCV01 mnz 3_2	Matrix	94	0.7	5	3542	118	30	3	21	132.1	1.3	0.06486	1.9	7.89	1.12	0.0677	2.3	0.00757	1.3	0.58	0.0020	2.6
DNCV01 mnz 3_3	Matrix	158	0.9	7	3543	128	28	23	16	109.9	1.4	0.05508	1.4	6.97	1.15	0.0691	2.0	0.00910	1.4	0.72	0.0023	2.5
DNCV01 mnz 3_4	Matrix	72	0.7	5	3795	112	34	38	19	122.2	1.2	0.05947	1.3	8.68	1.15	0.0671	1.8	0.00818	1.2	0.67	0.0021	2.3
DNCV01 mnz 4_1	Inc in grt rim	75	0.5	3	4413	107	41	20	16	179.0	1.3	0.07435	1.4	12.31	1.15	0.0573	1.9	0.00559	1.3	0.67	0.0016	2.4
DNCV01 mnz 4_2	Inc in grt rim	74	0.4	3	4621	95	49	0	11	179.7	1.3	0.07233	1.5	15.07	1.16	0.0555	1.9	0.00556	1.3	0.66	0.0017	2.2
DNCV01 mnz 4_3	Inc in grt rim	101	0.4	3	3851	99	39	49	14	179.4	1.3	0.06873	1.3	11.58	1.21	0.0528	1.8	0.00558	1.3	0.69	0.0016	2.2
DNCV01 mnz 4_4	Inc in grt rim	41	0.4	3	4372	91	48	8	14	173.8	1.2	0.07098	1.6	14.81	1.13	0.0563	2.0	0.00575	1.2	0.60	0.0018	2.4
DNCV01 mnz 5_1	Matrix	57	1.8	14	4108	193	21	71	43	81.2	1.2	0.05078	0.9	6.14	1.29	0.0862	1.5	0.01231	1.2	0.78	0.0036	2.1
DNCV01 mnz 5_2	Matrix	0	1.2	9	4294	212	20	9	22	136.6	1.5	0.05406	0.8	6.18	1.19	0.0546	1.7	0.00732	1.5	0.87	0.0022	2.5
DNCV01 mnz 5_3	Matrix	62	1.6	12	4001	170	24	80	68	81.2	1.2	0.05301	0.8	7.03	1.26	0.0901	1.5	0.01232	1.2	0.82	0.0037	2.1
DNCV01 mnz 6_1	Inc in grt rim	50	0.6	5	1780	117	15	44	19	137.4	1.3	0.05328	1.3	5.03	1.12	0.0535	1.9	0.00728	1.3	0.70	0.0024	2.6
DNCV01 mnz 6_2	Inc in grt rim	18	0.2	2	912	45	20	6	10	144.8	1.4	0.05703	1.9	6.79	1.03	0.0543	2.4	0.00691	1.4	0.58	0.0023	4.0
DNCV01 mnz 7_1	Inc in grt rim	19	0.7	6	3654	145	25	17	16	150.3	1.3	0.05798	1.2	7.38	1.13	0.0532	1.8	0.00665	1.3	0.74	0.0020	2.5
DNCV01 mnz 8_1	Inc in grt rim	3	0.5	4	3702	106	35	15	11	173.1	1.2	0.06122	1.6	9.99	1.13	0.0488	2.0	0.00578	1.2	0.62	0.0016	2.3
DNCV01 mnz 9_1	Matrix	26	0.5	4	3981	94	42	16	17	146.4	1.5	0.06715	1.3	10.47	1.11	0.0633	2.0	0.00683	1.5	0.76	0.0017	2.6
DNCV01 mnz 9_2	Matrix	150	1.4	11	3080	160	19	53	46	84.1	1.2	0.05271	1.0	5.03	1.18	0.0865	1.6	0.01190	1.2	0.75	0.0031	2.3
DNCV01 mnz 9_3	Matrix	172	1.8	14	3537	195	18	121	56	80.6	1.2	0.05062	0.9	5.39	1.22	0.0866	1.5	0.01240	1.2	0.79	0.0037	2.2
DNCV01 mnz 9_4	Matrix	94	1.9	14	3195	197	16	144	55	80.6	1.2	0.05219	1.2	5.05	1.29	0.0892	1.7	0.01240	1.2	0.72	0.0039	2.2
DNCV01 mnz 9_5	Matrix	33	1.0	8	3744	202	18	45	25	149.0	1.2	0.05363	1.0	5.21	1.14	0.0496	1.5	0.00671	1.2	0.77	0.0019	2.4
DNCV01 mnz 9_6	Matrix	40	1.2	9	3688	170	22	37	35	104.3	1.2	0.05056	1.0	6.07	1.19	0.0668	1.5	0.00959	1.2	0.77	0.0027	2.1
DNCV01 mnz 9_7	Matrix	120	1.8	13	4471	191	23	30	50	81.7	1.2	0.05413	0.9	7.04	1.22	0.0914	1.5	0.01224	1.2	0.80	0.0037	2.2
DNCV01 mnz 9_8	Matrix	95	1.0	8	3379	123	27	52	31	89.6	1.3	0.06131	1.4	7.16	1.19	0.0943	1.9	0.01116	1.3	0.67	0.0030	2.3
DNCV01 mnz 9_9	Matrix	28	1.5	11	2572	157	16	121	44	80.1	1.2	0.05374	0.9	4.81	1.22	0.0925	1.5	0.01248	1.2	0.82	0.0037	2.2

Table 11.4 – SC–ICP–MS isotopic data for sample DNCV01

Analysis	Position	^{204}Pb cps	^{206}Pb (mV)	Pb (ppm)	Th (ppm)	U (ppm)	Th/U ratio	Ratios														^{208}Pb/^{232}Th	1σ (%)
								^{206}Pb/^{204}Pb	1σ (%)	^{238}U/^{206}Pb	1σ (%)	^{207}Pb/^{206}Pb	1σ (%)	^{208}Pb/^{206}Pb	1σ (%)	^{207}Pb/^{235}U	1σ (%)	^{206}Pb/^{238}U	1σ (%)	Rho			
DNCV01 mnz 10_1	Matrix	158	0.3	2	5670	71	80	4	7	185.6	1.4	0.08549	1.7	22.39	1.18	0.0635	2.2	0.00539	1.4	0.64	0.0015	2.3
DNCV01 mnz 10_2	Matrix	75	0.3	3	5908	85	70	13	15	189.1	1.2	0.08384	1.5	20.38	1.16	0.0611	2.0	0.00529	1.2	0.63	0.0015	2.4
DNCV01 mnz 10_3	Matrix	129	0.5	4	5128	122	42	19	13	194.2	1.2	0.07238	1.3	12.38	1.17	0.0514	1.8	0.00515	1.2	0.67	0.0016	2.4
DNCV01 mnz 10_4	Matrix	82	0.5	4	5455	130	42	15	18	191.4	1.2	0.07089	1.2	12.20	1.24	0.0511	1.7	0.00523	1.2	0.71	0.0015	2.2
DNCV01 mnz 10_5	Matrix	41	0.6	4	6119	149	41	32	17	189.9	1.2	0.07044	1.0	12.16	1.17	0.0511	1.6	0.00527	1.2	0.75	0.0015	2.2
DNCV01 mnz 10_6	Matrix	113	0.5	4	5654	146	39	32	14	198.1	1.3	0.07077	1.2	11.92	1.14	0.0493	1.8	0.00505	1.3	0.72	0.0015	2.4
DNCV01 mnz 10_7	Matrix	142	0.3	2	5949	75	79	7	9	184.3	1.3	0.07776	1.4	23.50	1.26	0.0582	1.9	0.00542	1.3	0.70	0.0016	2.2
DNCV01 mnz 11_1	Matrix	49	1.1	9	3951	178	22	42	43	116.6	1.2	0.05469	1.0	6.91	1.10	0.0647	1.6	0.00858	1.2	0.79	0.0027	2.4
DNCV01 mnz 11_2	Matrix	151	1.4	11	4154	246	17	80	31	129.6	1.2	0.05562	1.0	5.04	1.21	0.0592	1.6	0.00772	1.2	0.77	0.0023	2.2
DNCV01 mnz 12_1	Inc in grt rim	110	2.1	16	3263	224	15	53	43	80.5	1.2	0.05098	0.7	4.59	1.29	0.0873	1.5	0.01242	1.2	0.86	0.0038	2.1
DNCV01 mnz 13_1	Matrix	128	0.6	5	3694	84	44	31	19	107.9	1.6	0.05885	1.6	13.13	1.20	0.0752	2.3	0.00927	1.6	0.70	0.0028	2.1
DNCV01 mnz 13_2	Matrix	9	1.1	8	3987	133	30	17	28	90.8	1.3	0.05319	1.2	8.56	1.09	0.0808	1.7	0.01102	1.3	0.74	0.0032	2.2
DNCV01 mnz 14_1	Matrix	102	1.2	9	3776	138	27	17	34	84.0	1.2	0.05192	1.0	8.16	1.21	0.0852	1.6	0.01190	1.2	0.77	0.0036	2.2
DNCV01 mnz 14_2	Matrix	52	1.5	11	3759	160	23	63	69	82.9	1.2	0.05271	0.8	6.97	1.23	0.0876	1.5	0.01206	1.2	0.82	0.0036	2.2
DNCV01 mnz 15_1	Matrix	171	0.5	4	4669	113	41	14	11	182.7	1.4	0.10132	1.3	11.97	1.16	0.0765	1.9	0.00547	1.4	0.75	0.0016	2.3
DNCV01 mnz 15_2	Matrix	128	0.6	4	5631	127	44	12	8	188.3	1.4	0.07281	1.3	13.90	1.14	0.0533	1.9	0.00531	1.4	0.74	0.0016	2.6
DNCV01 mnz 16_1	Matrix	209	1.3	8	4393	166	26	39	34	115.1	1.5	0.06357	1.3	6.90	1.23	0.0762	1.9	0.00869	1.5	0.76	0.0023	2.4
DNCV01 mnz 17_1	Matrix	114	0.5	4	4201	110	38	15	10	179.4	1.4	0.06920	1.3	11.70	1.18	0.0532	1.9	0.00558	1.4	0.72	0.0017	2.4
DNCV01 mnz 17_2	Matrix	77	0.5	4	4243	114	37	16	11	181.8	1.4	0.06710	1.3	11.53	1.19	0.0509	1.9	0.00550	1.4	0.74	0.0017	2.5
DNCV01 mnz 17_3	Matrix	40	0.4	3	5360	95	57	8	14	200.1	1.4	0.07599	1.6	17.52	1.17	0.0524	2.1	0.00500	1.4	0.66	0.0015	2.6
DNCV01 mnz 18_1	Inc in grt rim	110	3.0	20	4140	273	15	43	92	79.0	1.4	0.05074	0.7	4.74	1.32	0.0886	1.5	0.01266	1.4	0.89	0.0040	2.2
DNCV01 mnz 18_2	Inc in grt rim	108	2.0	13	3258	185	18	13	53	80.4	1.4	0.05138	0.9	5.81	1.28	0.0881	1.6	0.01244	1.4	0.83	0.0040	2.1
DNCV01 mnz 18_3	Inc in grt rim	104	3.7	24	4758	326	15	36	66	77.0	1.3	0.05069	0.7	4.83	1.38	0.0908	1.5	0.01299	1.3	0.88	0.0042	2.1
DNCV01 mnz 18_4	Inc in grt rim	31	2.7	17	4439	335	13	51	46	109.4	1.4	0.05134	0.8	4.54	1.22	0.0647	1.6	0.00914	1.4	0.87	0.0031	2.3
DNCV01 mnz 18_5	Inc in grt rim	113	1.4	9	4173	145	29	15	37	90.9	1.4	0.05259	1.0	8.92	1.24	0.0798	1.7	0.01100	1.4	0.80	0.0034	2.2
DNCV01 mnz 19_1	Matrix	32	1.8	12	3734	191	20	50	49	90.1	1.4	0.05333	0.9	5.51	1.20	0.0816	1.7	0.01110	1.4	0.84	0.0031	2.5
DNCV01 mnz 19_2	Matrix	71	2.4	16	3994	223	18	13	45	81.5	1.3	0.05197	0.8	5.55	1.33	0.0879	1.5	0.01227	1.3	0.86	0.0038	2.2
DNCV01 mnz 19_3	Matrix	110	2.6	17	3430	239	14	7	56	80.6	1.3	0.05320	0.8	4.59	1.38	0.0911	1.5	0.01241	1.3	0.84	0.0039	2.2
DNCV01 mnz 19_4	Matrix	153	2.7	17	3516	250	14	157	67	81.9	1.5	0.05200	1.0	4.34	1.35	0.0876	1.8	0.01221	1.5	0.83	0.0038	2.2
DNCV01 mnz 19_5	Matrix	117	3.2	21	4453	285	16	138	106	77.5	1.4	0.05059	0.8	5.01	1.27	0.0900	1.6	0.01290	1.4	0.87	0.0041	2.3
DNCV01 mnz 20_1	Matrix	81	3.6	24	1814	335	5	25	58	81.0	1.3	0.04996	0.7	1.67	1.15	0.0851	1.5	0.01235	1.3	0.88	0.0038	2.6
DNCV01 mnz 20_2	Matrix	162	5.2	34	2343	491	5	123	159	83.3	1.3	0.04950	0.6	1.48	1.19	0.0820	1.5	0.01201	1.3	0.91	0.0037	2.4
DNCV01 mnz 20_3	Matrix	1	2.6	17	3839	246	16	84	84	81.7	1.3	0.05120	0.7	4.74	1.36	0.0864	1.4	0.01224	1.3	0.88	0.0037	2.2
DNCV01 mnz 20_4	Matrix	136	1.8	12	3556	184	19	112	39	89.7	1.5	0.05230	0.8	5.55	1.15	0.0804	1.7	0.01114	1.5	0.88	0.0032	2.4
DNCV01 mnz 20_5	Matrix	68	2.2	14	3908	203	19	93	38	81.7	1.3	0.05169	0.9	5.83	1.31	0.0872	1.6	0.01224	1.3	0.84	0.0038	2.2

Table 11.4 (continued) – SC–ICP–MS isotopic data for sample DNCV01

11.3. Mass spectrometer technical specifications and operating conditions

The following specifications were written and provided on request to R.M. Palin by N.M.W. Roberts as a requirement for inclusion in the research papers Palin *et al*. (2012, 2013). As such, they are presented in this thesis for reference only.

Geochronological analyses of monazite performed in July 2010 were undertaken on a Nu Instruments Nu-Plasma MC–ICP–MS, whereas those acquired in February 2012 used a Nu Attom SC–ICP–MS. In all cases laser ablation was performed using the following parameters: 5 Hz, 1.9–2.2 j/cm^2, 10 second washout and a 30 second ablation time. Data processing for all analyses used the time-resolved function on the Nu Instruments' software, an in-house Excel spreadsheet for data reduction and error propagation and the add-in Isoplot for data presentation (Ludwig, 2003). The Nu Attom SC–ICP–MS was used in peak-jumping mode with measurement on a MasCom secondary electron multiplier. Measurement strategy and data reduction are the same as for U–Pb analyses on the Nu Plasma, except that on the Attom the following masses are measured in each sweep: ^{202}Hg, ^{204}Pb+Hg, ^{206}Pb, ^{207}Pb, ^{208}Pb, ^{232}Th, and ^{235}U. One hundred sweeps of the measured masses are integrated in each run, roughly taking 0.22 seconds. Dwell times on each mass are 400 μs on ^{207}Pb and ^{235}U, and 200 μs on all other masses; the switching between masses takes 40 μs. Since ^{208}Pb and ^{232}Th are large signals relative to other masses in monazites, these masses use the attenuation mechanism on the Nu Attom, which reduces the signal by ~350 times. Since ^{235}U is measured, ^{238}U is calculated from ^{235}U*137.88. Uncertainty propagation followed the method of Horstwood (2008), which includes a contribution from the external reproducibility of a reference material for the ratios ^{206}Pb/^{238}U and ^{208}Pb/^{232}Th, which is ~3% (2σ) and ~4% (2σ) respectively. ^{204}Pb intensity was below the detection limit in all analyses and the accuracy of ^{238}U–^{206}Pb ages are within 3% according to measurement of secondary reference materials. For analyses obtained on the Nu Plasma MC–ICP–MS, a secondary reference material weighted mean ^{238}U–^{206}Pb age was calculated to be 566 ± 5 Ma for 'Manangotry' (559 ± 1 Ma (2 S.D.), ID-TIMS ^{238}U–^{206}Pb age based on two concordant points; Appendix 11.4). For analyses obtained on the Nu Attom SC–ICP–MS, secondary reference material weighted mean ^{238}U–^{206}Pb ages were calculated to be 524 ± 15 Ma for 'Moacyr' (515.6 ± 1.4 Ma (2 S.D.), ID-TIMS ^{238}U–^{206}Pb average age; Appendix 11.4) and 566 ± 16 for 'Manangotry'(559 ± 1 Ma (2 S.D.), ID-TIMS ^{238}U–^{206}Pb age based on two concordant points; Appendix 11.4).

11.4. ID-TIMS data for Stern, Moacyr and Manangotry monazite materials

The following data were obtained at the NERC Isotope Geosciences Laboratory, UK by other workers and were compiled by M.S.A. Horstwood for inclusion in the research paper Palin *et al.* (2013). As such, they are presented in this thesis for reference only.

(a)	(b)	(c)	(b)	(d)	(d)	(e)	(h)	(g)	(h)	(g)
Reference material	U-Th-Pb isotopic data and compositional parameters						Ratios before common-Pb correction			
	U (ppm)	Th/U ratio	Pb (ppm)	Pb*/Pb^c	Pb^c (pg)	$^{206}Pb/^{204}Pb$	$^{238}U/^{206}Pb$	err	$^{207}Pb/^{206}Pb$	err
Stern										
m1	132	17.97	62.7	1669	3.76	18383	12.12	0.097	0.057047	0.570
m2	177	17.91	83.8	1283	6.53	14115	12.10	0.090	0.057427	0.422
m3	40	18.14	19.0	1281	1.48	14052	12.11	0.115	0.056861	0.927
m7	217	18.02	103.5	1564	6.61	17126	12.07	0.244	0.057294	0.270
m8	81	18.25	39.1	974	4.02	10590	12.10	0.122	0.057240	0.908
m2 2nd lot	801	18.06	382.4	2105	18.16	22881	12.07	0.149	0.057434	0.203
Moacyr										
m1	66	54.24	85.3	663	12.84	2633	12.00	0.093	0.061932	0.348
m2	47	52.64	58.4	809	7.21	3308	12.02	0.100	0.060637	0.501
Manangotry										
m1	43	86.00	91.7	1882	4.87	4771	11.24	0.116	0.061199	0.506
m3	54	86.73	119.8	4323	2.77	10956	11.04	0.098	0.059678	0.403
m6	70	86.10	152.4	3710	4.11	9430	11.04	0.094	0.059924	0.317
m1 2nd lot	562	87.69	1244.1	6038	20.61	14914	11.15	0.114	0.059714	0.092

	(f)	(f)	(g)	(f)	(g)	(f)	(g)		(f)	(g)	(f)	(g)	(f)	(g)
Reference material	Ratios after common-Pb correction								Isotopic age (Ma)					
	$^{208}Pb/^{206}Pb$	$^{207}Pb/^{206}Pb$	err	$^{207}Pb/^{235}U$	err	$^{206}Pb/^{238}U$	err	Cor	$^{207}Pb/^{206}Pb$	2σ	$^{207}Pb/^{235}U$	2σ	$^{206}Pb/^{238}U$	2σ
Stern														
m1	5.571	0.056885	0.084	0.646750	0.168	0.082459	0.089	0.976	487.1	1.9	506.5	0.7	510.8	0.4
m2	5.549	0.056865	0.085	0.647618	0.167	0.082599	0.085	0.985	486.3	1.9	507.0	0.7	511.6	0.4
m3	5.619	0.056861	0.088	0.647280	0.174	0.082561	0.095	0.959	486.2	1.9	506.8	0.7	511.4	0.5
m7	5.576	0.056825	0.102	0.648966	0.287	0.082828	0.243	0.940	484.8	2.2	507.8	1.1	513.0	1.2
m8	5.654	0.056887	0.105	0.648176	0.188	0.082637	0.104	0.898	487.2	2.3	507.4	0.8	511.8	0.5
m2 2nd lot	5.593	0.056901	0.095	0.649712	0.210	0.082813	0.149	0.916	487.7	2.1	508.3	0.8	512.9	0.7
Moacyr														
m1	16.781	0.056821	0.108	0.649121	0.191	0.082854	0.090	0.958	484.6	2.4	507.9	0.8	513.1	0.4
m2	16.289	0.056826	0.100	0.648858	0.187	0.082813	0.094	0.962	484.8	2.2	507.8	0.7	512.9	0.5
Manangotry														
m1	26.933	0.058761	0.116	0.718548	0.201	0.088689	0.111	0.879	558.2	2.5	549.8	0.9	547.78	0.6
m3	27.063	0.058819	0.088	0.733974	0.174	0.090502	0.093	0.959	560.4	1.9	558.9	0.7	558.51	0.5
m6	26.847	0.058748	0.091	0.732403	0.175	0.090418	0.092	0.955	557.8	2.0	558.0	0.7	558.01	0.5
m1 2nd lot	27.410	0.058787	0.087	0.726301	0.185	0.089606	0.114	0.936	559.2	1.9	554.4	0.8	553.21	0.6

N.B. errors (err) on isotopic ratios before and after correction for common-Pb are percentage (%) errors whereas 2σ errors on ages are absolute

(a) m1, m2 etc. are labels for fractions composed of single monazite grains or fragments

(b) Nominal U and total Pb concentrations subject to uncertainty in photomicrographic estimation of weight

(c) Model Th/U ratio calculated from radiogenic $^{208}Pb/^{206}Pb$ ratio and $^{207}Pb/^{235}U$ age.

(d) Pb* and Pb^c represent radiogenic and common-Pb, respectively; mol % ^{206}Pb* with respect to radiogenic, blank and initial common Pb.

(e) Measured ratio corrected for spike and fractionation only. Daly analyses, based on analysis of NBS-981 and NBS-982.

(f) Corrected for fractionation, spike, and common-Pb; up to 1 pg of common-Pb was assumed to be procedural blank: $^{206}Pb/^{204}Pb = 18.60 \pm 0.80\%$; $^{207}Pb/^{204}Pb = 15.69 \pm 0.32\%$; $^{208}Pb/^{204}Pb = 38.51 \pm 0.74\%$ (all uncertainties 1-sigma). Excess over blank was assigned to initial common-Pb. Calculations are based on the decay constants of Jaffey *et al*. (1971).

(g) 2-sigma errors are propagated using the algorithms of Schmitz & Schoene (2007) and Crowley *et al*. (2007).

(h) Corrected for fractionation, spike, and blank Pb only.

Table 11.5 – ID-TIMS data for Stern, Moacyr and Manangotry monazite reference materials

11.5. THERMOCALC AvePT calculation end-member activities

The following activities were used in AvePT calculations and were calculated from SEM-microprobe compositional analyses by the program AX (Holland, 2009). Data are given as pairs of calculated activity and associated error e.g. activity of pyrope in garnet (K146) = 0.0044 ± 0.00277.

		Sample																					
		K146		T17		20-199		L08-03A		ET09-05		ET09-06		ET10-07		ET10-10		ET10-13		ET10-18a	
Garnet																							
	py	0.0044	0.00277	0.0087	0.0049	0.0068	0.00402	0.0810	0.0235	0.0031	0.00204	0.003	0.00198	0.00138	0.000981	0.0193	0.0093	0.0036	0.00232	0.003	0.00198
	gr	0.00085	0.00063	0.0030	0.0020	0.00133	9.48E-04	0.0245	0.0111	6.10E-05	5.07E-05	1.17E-04	9.53E-05	7.50E-05	6.19E-05	0.0071	0.00417	0.00106	7.69E-04	0.0035	0.00227
	alm	0.41	0.0615	0.3100	0.0465	0.31	0.0465	0.0720	0.0221	0.30	0.045	0.29	0.0435	0.35	0.0525	0.20	0.031	0.43	0.0645	0.37	0.0555
	sps	-	-	-	-	-	-	-	-	0.002	0.00138	-	-	0.0025	0.00168	-	-	-	-	-	-
Biotite																					
	phl	0.0340	0.0136	0.047	0.0173	0.057	0.0198	-	-	0.0173	0.00783	0.0151	0.0077	0.0145	6.73E-03	0.111	0.0296	0.058	0.0201	0.045	0.0168
	ann	0.0620	0.0204	0.039	0.0153	0.042	0.0161	-	-	0.064	0.0207	0.13	0.0319	0.10	2.58E-02	0.015	0.00766	0.048	0.0175	0.068	0.0214
	east	0.0380	0.0148	0.052	0.0186	0.058	0.0201	-	-	0.025	0.0106	0.017	0.01	0.019	0.00847	0.072	0.0231	0.052	0.0186	0.045	0.0168
Chlorite																					
	clin	-	-	-	-	-	-	-	-	-	-	-	-	-	-	-	-	0.024	0.0103	0.0049	0.00254
	daph	-	-	-	-	-	-	-	-	-	-	-	-	-	-	-	-	0.027	0.0119	0.078	0.023
	ames	-	-	-	-	-	-	-	-	-	-	-	-	-	-	-	-	0.0292	0.012	0.01	0.00486
Staurolite																					
	mst	0.00063	5.35E-04	0.0066	0.00405	-	-	-	-	-	-	-	-	-	-	-	-	-	-	-	-
	fst	0.50	0.10	0.26	0.052	-	-	-	-	-	-	-	-	-	-	-	-	-	-	-	-
Plagioclase																					
	an	0.52	0.0359	0.70	0.035	0.51	0.0367	-	-	0.42	0.0424	0.39	0.0435	0.70	0.0174	0.57	0.0316	0.45	0.0408	0.50	0.0375
	ab	0.68	0.034	0.57	0.0316	0.69	0.0345	-	-	0.73	0.0365	0.75	0.075	0.49	0.0191	0.62	0.031	0.73	0.0365	0.70	0.035
K-feldspar																					
	san	-	-	-	-	-	-	-	-	0.90	0.045	0.88	0.044	0.93	0.0465	-	-	-	-	-	-
	ab	-	-	-	-	-	-	-	-	0.68	0.034	0.76	0.038	0.486	0.0193	-	-	-	-	-	-
White mica																					
	mu	0.71	0.071	0.71	0.071	0.69	0.034	0.36	0.036	0.72	0.072	0.66	0.066	0.79	0.079	0.65	0.065	0.72	0.072	0.72	0.072
	cel	0.0138	0.01	0.0127	0.01	0.027	0.0056	0.21	0.0393	0.022	0.01	0.024	0.01	0.016	0.01	0.04	0.0111	0.0056	0.01	0.0114	0.01
	fcel	0.0148	0.01	0.0106	0.01	0.0152	0.0035	0.035	0.00978	0.017	0.01	0.018	0.01	0.023	0.01	0.019	0.01	0.006	0.01	0.019	0.01
	pa	0.341	0.0444	0.129	0.0294	0.432	0.0216	0.449	0.0409	0.243	0.0418	0.184	0.0368	0.249	0.0421	0.479	0.039	0.281	0.0436	0.335	0.0444
Ilmenite																					
	ilm	-	-	-	-	0.94	0.047	0.94	0.047	0.92	0.046	-	-	0.84	0.042	-	-	-	-	-	-
	pnt	-	-	-	-	0.0034	0.0011	0.0013	0.0011	0.044	0.0121	-	-	0.099	0.0241	-	-	-	-	-	-
	geik	-	-	-	-	0.011	0.0027	0.022	0.0049	0.0068	0.01	-	-	0.0079	0.01	-	-	-	-	-	-
Pyroxene																					
	di	-	-	-	-	-	-	0.42	0.0424	-	-	-	-	-	-	-	-	-	-	-	-
	hed	-	-	-	-	-	-	0.14	0.041	-	-	-	-	-	-	-	-	-	-	-	-
	jd	-	-	-	-	-	-	0.44	0.0414	-	-	-	-	-	-	-	-	-	-	-	-
Talc																					
	ta	-	-	-	-	-	-	0.76	0.076	-	-	-	-	-	-	-	-	-	-	-	-
	fta	-	-	-	-	-	-	0.0002	2.83E-04	-	-	-	-	-	-	-	-	-	-	-	-

Table 11.6 – Activities for all end-members used for THERMOCALC AvePT calculations.

11.6. Phase compositions and proportions used in bulk composition calculations

The following phase compositions and volume proportions were used in the calculation of EBCs for pseudosection modelling. Each phase composition was 'optimised' for use in THERMOCALC by eliminating cations that are not considered within their model system. For example, the activity-composition coding for plagioclase only considers the phase components Na_2O–CaO–K_2O–Al_2O_3–SiO_2. If a natural analysis records trace FeO, for example, and this is kept in the bulk composition calculation, THERMOCALC will assign this FeO to an Fe-bearing phase (i.e. not plagioclase) in order to comply with mass balance constraints – thus overestimation of the molar proportions of other phases will result. All input compositions were optimised for this reason; although, in reality, phase components that are not considered within activity composition relationship codings for major phases generally exist in minor proportions, so there is a negligible effect on calculated assemblages.

	T17								
	Bt	Grt	Ilm	Ky	Ms	Pl	Qtz	Ru	St
Si	2.70	2.98		1	3.05	2.55	1		7.55
Ti	0.17		1.01					1	
Al	1.69	2.01		2	2.76	1.46			17.95
Fe^{3+}	0.00	0.05	0.00						
Fe^{2+}	1.11	2.02	0.92		0.08				2.60
Mn	0.00	0.19	0.07						0.01
Mg	1.14	0.37			0.09				1.02
Ca		0.37				0.45			
Na					0.04	0.53			
K	0.97				0.87	0.01			
H	2.00				2.00				4.00
O	11	12	3	5	11	8	2	2	46
Vol%	18	4.25	0.1	10	22	12	32.75	0.8	0.1

	DNCV01								
	Grt	Ksp	Chl	Bt	Pl	Rt	Sil	Qtz	Liq
Si	3.00	2.95	2.69	2.63	2.64		1	1	1.65
Ti				0.24		1			
Al	1.87	1.05	2.63	1.58	1.37		2		0.40
Fe^{3+}	0.13			0.06					
Fe^{2+}	1.84		2.23	1.06					0.01
Mn	0.10		0.01	0.00					
Mg	0.76		2.44	1.26					0.00
Ca	0.21				0.37				0.01
Na		0.05			0.62				0.13
K		0.95		1.00	0.02				0.18
H			8.00	1.76					0.98
O	12	8	14	11	8	2	5	2	8
Vol%	7.2	15.75	0.05	15.85	22.5	0.15	7	31.5	50

Table 11.7 – Phase compositions and proportions used for EBC calculation

	L08-03A													
	Act[1]	Brs[2]	Czo	Di[1]	Grt core	Grt rim	Mhb[3]	Mhb[1]	Omp	Pa	Ph	Pl[1]	Qz	Rt
Si	7.63	7.41	3	1.99	2.96	2.96	7.13	7.43	2.01	3.00	3.45	3.00	1	
Ti														1
Al	0.64	1.56	3	0.14	1.94	2.00	1.58	0.98	0.43	2.98	2.05	1.04		
Fe^{3+}	0.02	0.00		0.00	0.08	0.06	0.34	0.02	0.01					
Fe^{2+}	0.95	0.70		0.16	1.91	1.85	1.05	1.05	0.14	0.02	0.07			
Mn														
Mg	3.74	3.33		0.72	0.31	0.52	3.20	3.51	0.42	0.02	0.43			
Ca	1.88	1.37	2	0.86	0.80	0.61	1.35	1.86	0.51			0.02		
Na	0.22	0.85		0.13			0.44	0.34	0.47	0.84	0.04	0.94		
K										0.09	0.93			
H	2.00	2.00	1.00				2.00	2.00		2.00	2.00			
O	23	23	12.5	6	12	12	23	23	6	11	11	8	2	2
Vol%	0.75	31	3	0.75	6	24	7	0.75	12	6	5	0.75	2.5	0.5

1 = symplectite constituent 2 = matrix lath core 3 = matrix lath rim

Table 11.7 (continued) – Phase compositions and proportions used for EBC calculation